Ollscoil na hÉireann, Corcaigh

National University of Ireland, Cork



Sediment transport modelling and geomorphological assessments related to offshore renewable energy developments in the Irish Sea

Thesis presented by

Shauna Creane, BSc (Hons)

[ORCID ID: https://orcid.org/0000-0002-9637-1636]

for the degree of

Doctor of Philosophy in Engineering

Department of Civil and Environmental Engineering

School of Engineering and Architecture

University College Cork

Head of School: Prof Jorge Oliveira

Academic Supervisors: Dr Jimmy Murphy & Dr Michael O'Shea

External Advisor: Dr Mark Coughlan

2022

Table of Contents

List of figures vi
List of tables xix
Declaration xxii
Acknowledgement xxiii
Abstract xxv
Thesis output xxviii
Chapter 3 xxviii
Chapter 4 xxviii
Chapter 5 xxix
Chapter 6 xxix
Chapter 7 xxix
Appendix A xxix
Appendix B xxix
General Nomenclature xxxi
1 Introduction 1
1.1 Background to the thesis 2
1.1.1 Contribution to science 2
1.1.2 Climate targets, action plans, sustainable development goals 3
1.1.3 Impact of seabed mobility and morphodynamics on ORE developments 5
1.1.4 Impact of ORE and other anthropogenic activities on environmental stability 6
1.2 Rationale behind the thesis 6
1.3 Thesis objectives and scope 7
1.4 Thesis outline and the link between chapters 10
1.4.1 Chapter 3: The Irish Sea bed load parting zone: Is it a mid-sea hydrodynamic phenomenon or a geological theoretical concept? (Review and Original Research) 10
1.4.2 Chapter 4: Development and dynamic of sediment waves in a complex morphological and tidal dominant system: southern Irish Sea (Original Research) 11
1.4.3 Chapter 5: Estimation of suspended solids concentration from Acoustic Doppler Current Profiler in a tidally-dominated continental shelf sea setting and its use as a numerical modelling validation technique (Original Research) 11
1.4.4 Chapter 6: Hydrodynamic processes controlling sand bank mobility and long-term base stability: A case study of Arklow Bank (Original Research) 12
1.4.5 Chapter 7: Morphological modelling to investigate the role of external sediment sources, and wind and waves-induced flow on sand bank sustainability: An Arklow Bank case study (Original Research) 13
1.5 References 13

2 Literature Review 24
3 The Irish Sea Bed Load Parting Zone: Is it a mid-sea hydrodynamic phenomenon or a geological theoretical concept? 33
3.1 Introduction 36
3.2 Study Area 38
3.2.1 Geological History 40
3.2.2 Present day sediment distribution 41
3.2.3 Present day seabed morphology 42
3.2.4 Hydrodynamic Regime 50
3.2.5 Influence of wind-generated waves on seabed mobility in the Irish Sea 54
3.3 Regional net sand transport pathways 55
3.3.1 Bed load transport pathways – current knowledge 55
3.4 Hydrodynamic Modelling 58
3.5 Correlation of bed load parting zone with present day hydrodynamic regime 61
3.5.1 Transport pathways and tidal asymmetry: 62
3.5.2 BLP Zone: Origin 69
3.5.3 BLP Zone: Minor Factors influencing shape and location 72
3.5.4 BLP: Nature of opposing flows 80
3.6 Wider Implications 89
3.7 Conclusions 89
3.8 Future Work 91
3.9 Acknowledgments 92
3.10 Author statement 93
3.11 References 93
4 Development and dynamic of sediment waves in a complex morphological and tidal dominant system: southern Irish Sea 116
4.1 Introduction 119
4.1.1 Seabed morphodynamics 119
4.1.2 Study aims 128
4.2 Regional setting 128
4.3 Materials and methods 131
4.3.1 Multibeam echo sounder data acquisition and processing 131
4.3.2 Sediment wave analysis 135
4.3.3 Sediment samples 139
4.3.4 Hydrodynamic modelling 140
4.3.5 Theoretical parameters 141

4.4 Results 143
4.4.1 Sand wave characteristics 143
4.4.2 Spatial and temporal evolution of sediment waves 151
4.4.3 Comparison between sand wave characteristics, environmental parameters and theory-based indicators 170
4.5 Discussion 173
4.5.1 Connection between average net sediment wave migration directions and the wider sediment transport regime in the Irish Sea 173
4.5.2 Local variations in sand wave morphology 188
4.6 Conclusions 194
4.7 Data Availability 197
4.8 Acknowledgments 197
4.9 Author statement 198
4.10 Supplementary Material A: Methodology – sediment wave crest delineation and migration direction and rates 199
4.10.1 Crest Delineation 199
4.10.2 Sand wave migration calculation 199
4.11 Supplementary Material B: Results - statistical correlation between sediment wave dimensions and individual environmental parameters 201
4.12 References 212
5 Estimation of suspended solids concentration from Acoustic Doppler Current Profiler in a tidally-dominated continental shelf sea setting and its use as a numerical modelling validation technique 228
5.1 Introduction 230
5.2 Methods 236
5.2.1 ADCP Deployment and water sample collection 236
5.2.2 ADCP derived SSC 240
5.2.3 Numerical modelling 244
5.2.4 Generation of seabed substrate map representing the ADCP deployment time frame 256
5.3 Results 259
5.3.1 Water sample based $SSCsolids$ 259
5.3.2 ADCP based $SSCsolids$ 261
5.3.3 Comparison between ADCP-based $SSCsolids$ and Water sample based $SSCsolids$ 266
5.3.4 Suspended sediment model validation 267
5.4 Discussion 279
5.4.1 Evaluation of the ability to estimate $SSCsolids$ from ADCP relative acoustic backscatter in a shallow shelf sea environment 279

5.4.2 Evaluation of model validation techniques 281
5.4.3 Potential improvements/future work 284
5.5 Conclusions 286
5.6 Acknowledgments 287
5.7 Author Statement 288
5.8 References 288
6 Hydrodynamic processes controlling sand bank mobility and long-term base stability: A case study of Arklow Bank 302
6.1 Introduction 305
6.2 Methodology 310
6.3 Results and Discussion 314
6.3.1 General bank morphodynamics from a flood-neap tidal cycle to full lunar cycle 314
6.3.2 Detailed analysis of hydrodynamic-morphodynamic feedback loop 319
6.3.3 Summary discussion of hydrodynamic controls on Arklow Bank high mobility and bank base stability 337
6.4 Conclusions 339
6.5 Acknowledgments 342
6.6 Author Contributions 343
6.7 Supplementary Material: Numerical Modelling 343
6.7.1 Hydrodynamic Model 343
6.7.2 ST modelling set-up 346
6.8 References 352
7 Morphological modelling to investigate the role of external sediment sources, and wind and waves-induced flow on sand bank sustainability: An Arklow Bank case study 359
7.1 Introduction 362
7.2 Methods 368
7.2.1 Numerical model set-up and validation 368
7.2.2 Scenario modelling 374
7.3 Results and discussion 376
7.3.1 Mesh sensitivity analysis 376
7.3.2 Sediment budget 384
7.3.3 Influence of external sediment sources on Arklow Bank's local sediment transport regime 392
7.3.4 Impact of wind on Arklow Bank morphodynamics 400
7.3.5 Impact of wave-induced flow on Arklow Bank morphodynamics 404
7.4 Conclusion 408
7.5 Acknowledgments 411

7.6 Author statement 412
7.7 References 412
8 Conclusions and Recommendations 421
8.1 Chapter Overview 422
8.2 Conclusions to the thesis objectives 422
8.2.1 Objective 1: Improve the understanding of hydrodynamics and morphodynamics in the Irish Sea 423
8.2.2 Objective 2: Develop new methods and approaches to investigate hydrodynamics and seabed morphodynamics in an offshore setting 432
8.2.3 Objective 3: Collect and produce novel datasets that will contribute to the understanding of hydro- and morpho-dynamics in the Irish Sea 436
8.2.4 Objective 4: Facilitate the sustainable growth of anthropogenic activities in the Irish Sea 438
8.3 Impact on policy, industry and society 440
8.3.1 Policy implications 440
8.3.2 Industry implications 442
8.3.3 Society implications 443
8.4 Recommendations and future research 444
8.5 Final Remarks 447
8.6 References 447
Appendix A: Conference deliverables and co-authored peer-reviewed publications 452
Appendix B: Offshore research surveys 456

List of figures

Figure 3-1 Graphical Abstract for the peer-reviewed paper 'The Irish Sea Bed Load Parting Zone: Is it a mid-sea hydrodynamic phenomenon or a geological theoretical concept?' [1] 36

Figure 3-2 Irish Sea bathymetry with water depth referenced to mean sea level (MSL) within the study area. Main bathymetric highs and lows are indicated. Geographic locations and oceanographic features mentioned in the text are also shown. The location of the bedform derived bed load parting zone, defined by Van Landeghem et al [27], characterised by one main sediment transport convergence zone and two divergent zones, is indicated. Bathymetric metadata and Digital Terrain Model (DTM) data products have been derived from the EMODnet Bathymetry portal - http://www.emodnet-bathymetry.eu. 39

Figure 3-3 Sediment distribution across the Irish Sea and the location of the Western Irish Sea Mud Belt (WISMB). Information contained here has been derived from data that is made available under the European Marine Observation Data Network (EMODnet) Seabed Habitats initiative (http://www.emodnet-seabedhabitats.eu/), financed by the European Union under Regulation (EU) No 508/2014 of the European Parliament and of the Council of 15 May 2014 on the European Maritime and Fisheries Fund. 42

Figure 3-4 Distribution of bedforms across the southern Irish Sea. The dataset presented was developed by the HABMAP project (Habitat Mapping for Conservation and Management of the Southern Irish Sea) [11]. 44

Figure 3-5 Sediment transport pathways in the Irish Sea defined by bedform studies. Bathymetric metadata and Digital Terrain Model (DTM) data products have been derived from the EMODnet Bathymetry portal - http://www.emodnet-bathymetry.eu. 56

Figure 3-6 (A) Linear relationships between relative sea-surface phase and tidal distortion for $(AM4AM2) > 0$, adapted from Friedrichs and Aubrey [105]; (B) and (C) displays associated tidal residual bed shear stress and associated bed level change adapted from Neill and Couch [107]

calculations; Descriptions for each regime in (A) are a combined interpretation from both Friedrichs and Aubrey [105] and Neill and Couch [107]..... 66

Figure 3-7 A. Overview of interaction between M_2 tidal wave propagation through the Irish Sea with the bed form derived bed load parting zone [27] *and the approximate locations of the symmetrical tidal zones modelled by Horrillo-Caraballo et al* [31]*, B. Newly modelled residual tidal currents at the Codling Platform and Arklow Bank, C. Newly modelled residual tidal currents over the Welsh Platform, St Georges Channel (Deep 1 and 2) and Anglesey, D. Newly modelled residual tidal currents at Arklow Bank. Bathymetric metadata and Digital Terrain Model (DTM) data products have been derived from the EMODnet Bathymetry portal - http://www.emodnet-bathymetry.eu.*..... 68

Figure 3-8 The interaction of two tidal fronts in the Irish Sea, and their relationship between the tidal symmetrical zone defined by Horrillo-Caraballo et al [31], the bed load parting zone defined by Van Landeghem et al [27], and the seasonal Western Irish Sea Gyre observed by Olbert and Dabrowski [25]. Bathymetric metadata and Digital Terrain Model (DTM) data products have been derived from the EMODnet Bathymetry portal - http://www.emodnet-bathymetry.eu. 71

Figure 3-9 Irish Sea bathymetry with water depths referenced to mean sea level (MSL). The impact of large bathymetric and coastline constrictions on tidal propagation through the central Irish Sea is portrayed through two cross-sections and modelled co-tidal phase lines. Bathymetric cross-section A displays channel characteristics south of submarine constriction; bathymetric cross-section B displays channel topography over submarine constriction. Bathymetric metadata and Digital Terrain Model (DTM) data products have been derived from the EMODnet Bathymetry portal - http://www.emodnet-bathymetry.eu. 79

Figure 3-10 A. Numerically modelled mean tidal current directions across the Irish Sea, displaying a distinct panel of circulatory flow in the proximity of the bed load parting zone [27], and symmetrical tidal zone [31]; B. Numerically modelled tidal induced bed shear stress directions across the Irish Sea; C. Inset of A, mean tidal current directions overlain by numerically modelled residual (mean) tidal current vectors..... 82

Figure 3-11 A and B display the tidal oscillation zone on the east coast of Ireland; Two graphs (C and D) display time-series of water level (m) and bottom-current speed (m/s) from ADCP locations 1 and 2, revealing the change in tidal character over a spring-neap cycle in this region 86
Figure 4-1 Graphical Abstract for peer-reviewed paper 'Development and dynamics of sediment waves in a complex morphological and tidal dominant system: southern Irish Sea'..... 119
Figure 4-2 Maps showing pre-existing knowledge of Irish Sea sediment transport. (**A**) Location of the Irish Sea on the north-western European continental shelf. (**B**) Irish Sea hydrodynamic and sediment transport characteristics. The location of the bedform derived bed load parting zone, defined by Van Landeghem et al [39], characterised by one main sediment transport convergence zone and two divergent zones, is indicated. Bathymetry source: EMODnet Bathymetry Consortium [40]. (**C**) Study area displaying sediment distribution and main offshore sediment banks. Seabed substrate source: European Marine Observation Data Network (EMODnet) Seabed Habitats initiative (http://www.emodnet-seabedhabitats.eu/ [Accessed: 25 June 2021]) [41]. 123
Figure 4-3 Location of multi-beam echo sounder (MBES) bathymetry datasets analysed in this study. Available datasets at each site are presented in Table 4-2. Sites are grouped into three environments for sediment wave analysis: Independent Assemblages, Northern Banks and Southern Banks, which are indicated by blue, pink, and green polygons respectively. Bathymetry source: composite map produced from INFOMAR datasets (https://www.infomar.ie/data [Accessed: 10 June 2021]) (see section 4.3.1)..... 132
Figure 4-4 Illustration representing sediment wave (SW) characteristics used in this study. For SW "a", the figure denotes cr = SW crest, $d(cr)$ = water depth of SW crest; H = SW height; L = SW wavelength (and length components $L1$ and $L2$); $t(i)$ = time of first bathymetric survey over SW field; $c(x)$ = displacement of SW crest over time interval x; cr' = position of displaced SW crest over time interval x..... 137
Figure 4-5 Interpreted average sediment wave shape across the south-western Irish Sea. The location of (**B**) and (**C**) are provided in (**A**). Black boxes and labels indicate the location of figures in

Figure 4-6. Bathymetry source: composite map produced from INFOMAR datasets https://www.infomar.ie/data [Accessed: 10 June 2021]) (see section 4.3.1).....145
Figure 4-6 Selection of sediment wave types observed in the south-western Irish Sea; a. progressive, asymmetric, round-crested, 3-dimensional sediment waves, b. progressive, asymmetric, sharp-crested, simple, 2-dimensional sediment waves, c. progressive, asymmetric, sharp-crested, superimposed sediment waves, and d. trochoidal, sharp-crested sediment waves. A representative cross-section is given for each type. Locations are given in Figure 4-5. Bathymetry source: MOVE 2020 survey (see site 1A, 6 and 3A in Table 4-2). 146
Figure 4-7 Relationship between sediment wave heights and wavelengths in the south-western Irish Sea: (**a**) displays the results for the full dataset and for three compiled environments i.e., Southern Banks, Northern Banks and Independent Assemblages, and (**b**) displays the results for each individual study site. 151
Figure 4-8 Average annual sediment wave migration rates updated with new time-lapse multi-beam echo sounder bathymetry datasets: (**A**) an overview of south-western Irish Sea, whereby the locations of (**B**) to (**D**) are indicated; (**B**) inset of study sites 1, 6 and 7; (**C**) inset of study sites 2 and 3; (**D**) inset of study site 5. See Figure 4-3 for study site boundaries. Figure bathymetry data source: composite map produced from INFOMAR datasets (referenced to Lowest Astronomical Tide (LAT)) https://www.infomar.ie/data [Accessed: 10 June 2021]) (see section 4.3.1).....152
Figure 4-9 Sediment wave translation rates and shapes at the southern extent of Arklow Bank in the Irish Sea: (**A**) location of Arklow Bank; (**B**) sediment wave shape with locations of cross-sections a and b; (**C**) and (**D**) sediment wave translation rates.(**B**) and (**C**) bathymetry source: composite map produced from INFOMAR datasets (https://www.infomar.ie/data [Accessed: 10 June 2021]) (see section 4.3.1). (**D**) bathymetry source: 2016: INFOMAR survey; 2020: MOVE survey (see site 1B in Table 4-2) 154
Figure 4-10 Sediment wave dynamics at southern extent of Lucifer–Blackwater Bank and Holden's Bed–Long Bank complexes. (**A**) Location of analysed site. (**B**) Distribution of sediment wave migration

direction and rates. (**C**) Distribution of sediment wave shape. B and C bathymetry source: composite map produced from INFOMAR datasets (https://www.infomar.ie/data [Accessed: 10 June 2021]) (see section 4.3.1). (**D**) Cross-section 'a' location. (**E**) Cross-section 'b' location. D and E bathymetry source: site 2E in Table 4-2. 158

Figure 4-11 Sediment wave dynamics at offshore independent sediment wave assemblage at site 8 in the Irish Sea. Location of cross-sections a to e are provided in (**B**). Location of (**B**) is given in (**A**). Bathymetry source: composite map produced from INFOMAR datasets (https://www.infomar.ie/data [Accessed: 10 June 2021]) (see section 4.3.1). 168

Figure 4-12 Spatial distribution of (**A**) dimensionless Rouse number, (**B**) residual bed shear stress (N/m²) and (**C**) median grain size ($D50$) overlain by residual current velocity with location of newly analysed sediment wave assemblages. Transition zones (labelled in white as T1 to T5) refer to areas of relatively higher Rouse number, higher residual current velocity and coarse grain sizes along a residual transport pathway between offshore sand banks and independent sediment wave assemblages. 172

Figure 4-13 Newly derived sediment wave migration rates and bedload transport divergence and convergence zones overlain by modelled residual tidal current vectors at (**A**) the southern extent of Lucifer–Blackwater and Holden's Bed–Long Bank complexes, and (**B**) the southern half of Arklow Bank in the Irish Sea. Bathymetry source: composite map produced from INFOMAR datasets (https://www.infomar.ie/data [Accessed: 10 June 2021]). 174

Figure 4-14 Overview of three residual circulatory transport systems in the south-western Irish Sea connecting offshore sediment banks with independent offshore sediment wave assemblages: (**a**) Location of three circulatory systems, main offshore sediment banks mentioned in the text and areas of analysed sediment waves by this study, (**b**) circulatory system (i) outlined in the text (4.5.1.2), connecting assemblages at site 6 and site 7 with Lucifer–Blackwater Bank complex and Arklow Bank, (**c**) circulatory system (ii) outlined in the text connecting sediment wave assemblage at site 8 and the further offshore assemblage at Point 2 with Arklow Bank, and (**d**) circulatory system

(iii) outlined in the text, connecting the sediment wave assemblage at site 5 with the Lucifer–Blackwater Bank complex. Transects in A, B, and C are presented in Figure 4-15. Bathymetry source: composite map produced from INFOMAR datasets (https://www.infomar.ie/data [Accessed: 10 June 2021]) (see section 4.3.1). Seabed substrate source: EMODnet Seabed Habitats initiative (http://www.emodnet-seabedhabitats.eu/ [Accessed: 25 June 2021]) [41]. 179
Figure 4-15 Transects along residual transport pathways in each circulatory system connecting offshore sediment banks with independent offshore sediment wave assemblages. Location of transects are presented in Figure 4-14. Data used in this figure is described in section 4.3.3 to 4.3.5. Mobilisation Frequency Index (MFI) data source: Coughlan et al [64]. Seabed substrate source: EMODnet Seabed Habitats initiative (http://www.emodnet-seabedhabitats.eu/ [Accessed: 25 June 2021]) [41]..... 181
Figure 4-16 (**A**) The location of (**C**–**E**) in the south-western Irish Sea. (**Bi**,**Bii**): The Shields curve [87] overlain with values of $Re*$ and Fs derived from the sediment surface samples calculated under mean and maximum current velocities, respectively. Sampling locations are displayed in C to E, which form a 500 × 500 m grid that transects along residual circulatory cell systems 1, 2, and 3 outlined in Figure 4-14. From (**Bi**,**Bii**), each point is designated as (a) No motion or (b) Motion: Ripples, Sediment waves or Transition, the location of which are displayed in (**C**–**E**). Bathymetry source: INFOMAR (https://www.infomar.ie/data [Accessed: 10 June 2021]). 187
Figure 4-17 Schematic of sediment wave (SW) migration rate calculation, using plan-view delineation of sediment wave crests from bathymetry datasets. For SW "a", the figure denotes cr = SW crest at time of first bathymetric survey; cx = displacement of SW crest over time interval x, cr'= position of displaced SW crest over time interval x; θ = bearing perpendicular to the crest at point n. 202
Figure 5-1 A. Site map displaying the area of interest (C), numerical model mesh boundary levels and numerical model validation and calibration points; B. Three sediment sample datasets used in the sediment transport model: i) manually added artificial samples, ii) synthetic samples from Wilson et

al [66], and iii) in situ surficial sediment samples; C. Study site displaying water sampling and ADCP stations. (Bathymetry source: A: [67] C: [68]) 240
Figure 5-2 Schematic diagram of set-up of the upward-looking Teledyne RDI Workhorse Sentinel 300kHz Acoustic Doppler Current Profiler (ADCP) at the study site..... 242
Figure 5-3 Comparison between measured and simulated water levels. See Table 5-1 for location. 253
Figure 5-4 Calibration profiles of current speed and direction at each of the four ADCP locations (Table 5-2) 253
Figure 5-5 Workflow diagram of multi-beam echo sounder (MBES) processing and derivation of seabed substrate map over ADCP deployment time period 260
Figure 5-6 Scatter plot of all water sample-based $SSCsolids$ samples at stations 1 to 8..... 263
Figure 5-7 Calibration of ADCP relative acoustic backscatter data (Beam 4) using the laboratory-analysed $SSCsolids$. 266
Figure 5-8 a) Beam 4 ADCP-derived $SSCsolids$ spatial time series, b) bottom current speed and direction recorded by the ADCP, c) rose diagram of bottom current speed and direction recorded by the ADCP 266
Figure 5-9 Linear regression between water sample-based $SSCsolids$ samples and ADCP-derived $SSCsolids$ 269
Figure 5-10 Comparison of 2D modelled peak $SSCsediment$ against measured $SSCsolids$ samples at four sampling stations non-associated with ADCP deployments. Sampling station locations are presented in Figure 5-1. 272
Figure 5-11 A. Modelled residual currents, B. Modelled residual suspended sediment transport ... 274
Figure 5-12 Roses of bottom-water, mid-water, surface-water and depth-averaged ADCP-based suspended solids concentration with measured current directions from 27/09/2020 15:00 to 14/10/2020 09:00. Modelled depth-averaged suspended sediment concentration with modelled current directions over the same time period..... 276

Figure 5-13 a) Comparative time series plot of 2D modelled suspended sediment concentration against ADCP-derived suspended solids concentration, b) water level and bottom current speed recorded by the ADCP 278
Figure 5-14 Correlation between a) 2D modelled peak $SSCsediment$ and ADCP-based depth-averaged $SSCsolids$, b) 2D modelled peak $SSCsediment$ and ADCP-based minimum $SSCsolids$ and c) 2D modelled peak $SSCsediment$ and ADCP-based mid-water $SSCsolids$ 280
Figure 6-1 Graphical Abstract for peer-reviewed paper 'Hydrodynamic processes controlling sand bank mobility and long-term base stability: A case study of Arklow Bank' [1] 307
Figure 6-2 (a) Overview of Irish Sea oceanographic phenomena impacting the study site [8], [14], [24], [29]; (b) the area of interest, Arklow Bank. Panel (a) bathymetry source: EMODnet [30] where MSL is mean sea level; Panel (b) bathymetry source: INFOMAR (https://www.infomar.ie/ (accessed on 20 March 2020)) where LAT is lowest astronomical tide. 312
Figure 6-3 (a,b) Numerical model boundaries, mesh resolution levels and validation points [8], [33]. Panel (a) bathymetry source: EMODnet [30] where MSL is mean sea level; Panel (b) bathymetry source: INFOMAR (https://www.infomar.ie/ (accessed on 20 March 2020)), where LAT is lowest astronomical tide. 314
Figure 6-4 Bed level changes over various time periods calculated from extracted simulated bed levels; (a) after one ebb tidal phase, (b) after one flood tidal phase, (c) after two ebb and two flood tides, (d) after one spring-neap cycle, (e–g) after one, six and 12 lunar month simulations, (h–i) after one spring-neap cycle between simulation months five and six and 11 and 12 respectively. A −25 m water depth contour is provided based on INFOMAR bathymetry data referenced to Lowest Astronomical Tide (LAT). INFOMAR data available at: https://www.infomar.ie/, (accessed on 20 March 2020). 317
Figure 6-5 (a,b) Simulated peak ebb and flood depth-averaged currents, respectively. Bathymetry source: INFOMAR (https://www.infomar.ie/ (accessed on 20 March 2020)). 318

Figure 6-6 Simulated residual currents for the (a) first (t1mo), (b) sixth (t6mo) and (c) twelfth (t12mo) month of a one-year simulation period. Simulated bed levels at the end of each simulated month are also presented; t1mo is the simulated bed level at the end of the first month. 321
Figure 6-7 Morphodynamics and hydrodynamics at Sub-cell 1 of Arklow Bank (a) Simulated bed level change after one lunar month and associated residual current vectors, overlain by the location of the centre point of residual eddies from residual currents during each subsequent lunar month simulation whereby 't6mo' is the sixth lunar simulation month; (b) to (e) Simulated bed level over a one year simulation at cross-sections 4, 14, 10 and 17 whereby 't0' is the starting bed level and 'h', 'wk' and 'mo' is subsequent months. 323
Figure 6-8 Morphodynamics and hydrodynamics at Sub-cell 2 of Arklow Bank. (a) Simulated bed level change after one lunar month and associated residual current vectors, overlain by the location of the centre point of residual eddies from residual currents during each subsequent lunar month simulation; 't6mo' is the sixth lunar simulation month. (b,c) Simulated bed level over a one year simulation at cross-sections 23 and 27; 't0' is the starting bed level, and 'mo' is subsequent months. 327
Figure 6-9 Morphodynamics and hydrodynamics at Sub-cell 3 of Arklow Bank. (a) Simulated bed level change after one lunar month and associated residual current vectors, overlain by the location of the centre point of residual eddies from residual currents during each subsequent lunar month simulation; 't6mo' is the sixth lunar simulation month. (b) Slope derived from the resulting bed level after 10 lunar month simulation, overlain by cross-section L30. (c–f) Simulated bed level over a one year simulation at cross-sections 30, 33, 36, and 40; 't0' is the starting bed level, and 'mo' is subsequent months. 330
Figure 6-10 Morphodynamics and hydrodynamics at Sub-cell 4 of Arklow Bank. (a) Simulated bed level change after one lunar month and associated residual current vectors, overlain by the location of the centre point of residual eddies from residual currents during each subsequent lunar month simulation; 't6mo' is the sixth lunar simulation month. (b–e) Simulated bed level over a one year

simulation at cross-sections 51, 58, 65 and 71, representing 'stable' areas; 't0' is the starting bed level and 'mo' is subsequent months; (f–i) cross-sections 52, 54, 61 and 62 representing 'mobile' areas. 333

Figure 6-11 Morphodynamics and hydrodynamics at Sub-cells 5 and 6 of Arklow Bank. (**a**) Simulated bed level change after one lunar month and associated residual current vectors, overlain by the location of the centre point of residual eddies from residual currents during each subsequent lunar month simulation; 't6mo' is the sixth lunar simulation month. (**b**,**c**) Simulated bed level over a one year simulation at cross-sections 82 and 92; 't0' is the starting bed level, and 'mo' is subsequent months. 336

Figure 6-12 Morphodynamics and hydrodynamics at Sub-cells 7 and 8 of Arklow Bank. (a,b) Simulated bed level change after one lunar month and associated residual current vectors, overlain by the location of the centre point of residual eddies from residual currents during each subsequent lunar month simulation; 't6mo' is the sixth lunar simulation month. (c–e) Simulated bed level over a one year simulation at cross-sections 96, 120 and 125; 't0' is the starting bed level, and 'mo' is subsequent months. 338

Figure 6-13 A schematic diagram summarising the hydrodynamic processes driving Arklow Bank's upper slope mobility and bank base stability. 341

Figure 6-14 Comparison between measured and simulated (a) water levels from Wicklow Trough ADCP (52.95601°, −5.90135°) and Rosslare tide gauge (52.254600°, −6.334861°), and (b) current speed and directions from Arklow ADCP (52.72153°, -6.0278°). Data source: Creane et al [33]. 347

Figure 6-15 Comparison of 2D modelled peak $SSCsediment$ against measured $SSCsolids$ samples at sampling station 6 (-5.953°, 52.551°). Data source: Creane et al [33]. 353

Figure 6-16 Correlation between 2D modelled peak $SSCsediment$ and ADCP-based depth-averaged $SSCsolids$. Data source: Creane et al [33]. 354

Figure 7-1 (a) Overview of Irish Sea oceanographic phenomena impacting the study site (b), (b) the area of interest, Arklow Bank. Panel (a) bathymetry source: EMODnet [19] where MSL is mean sea

level; Panel (b) bathymetry source: INFOMAR (https://www.infomar.ie/ [Accessed on 20 March 2020]) where LAT is lowest astronomical tide.....366
Figure 7-2 (a)-(c) shows numerical model boundaries, mesh resolution levels and validation points whereby (b) specifically displays the four mesh levels used in model runs 2 to 5 and (c) displays the five mesh levels used in model run 1. Panel (a) bathymetry source: EMODnet [19] where MSL is mean sea level; Panel (b) bathymetry source: INFOMAR (https://www.infomar.ie/ [Accessed on 20 March 2020]) where LAT is lowest astronomical tide. 371
Figure 7-3 Wave model validation plots: (a) to (c) time-series plots of significant wave height (Hs), spectral zero-crossing wave period ($T02$) and mean wave direction (MWD) at M2 data point; (d) to (e) time-series plots of Hs, $T02$ and MWD at M5 data point; (g) to (j) scatter plots of Hs at M2, M5, ERA5 1 and ERA5 2 data point locations. Coordinates of each data point is provided in Table 7-1. .376
Figure 7-4 Diagram displaying Arklow Bank hydro- and morpho-dynamics under pure current conditions produced by Creane et al [17].....380
Figure 7-5 (a) and (b) displays residual currents calculated after the first lunar month simulation from Run 1 and Run 2 respectively (Table 7-2). The approximate location of the centre point of each off-bank anticlockwise residual eddy and two on-bank clockwise residual eddies, originally identified in Creane et al [17], are provided in each figure. Bathymetry source: INFOMAR (https://www.infomar.ie/ [Accessed on 20 March 2020]).....382
Figure 7-6 (a) Location of Arklow Bank in the south-western Irish Sea, (b) difference in simulated bed levels between Run 1 and Run 2 at the starting model timestep (t0), (c) difference in simulated bed levels between Run 1 and Run 2 after a 12 lunar month simulation period (t12mo). Bathymetry source: INFOMAR (https://www.infomar.ie/ [Accessed on 20 March 2020]) 383
Figure 7-7 Cross-sectional analysis of simulated bed levels of Run 2 against Run 1 in identified 'stable' zones: (b) – (i) display simulated bed level over a one year simulation at cross-sections 23, 63, 67 and 92 whereby 't0' is the starting bed level and 'h', 'wk' and 'mo' is subsequent months; (a) provides

the location of these cross-sections. Bathymetry source: INFOMAR (https://www.infomar.ie/ [Accessed on 20 March 2020]).....384
Figure 7-8 Cross-section L65 (b) displays a comparison of bed levels between interpolated INFOMAR bathymetry using the higher and lower resolution unstructured triangular meshes used in Run 1 and Run 2 respectively, against baseline INFOMAR survey data. (a) Displays the location of this cross-section. Bathymetry source: INFOMAR (https://www.infomar.ie/ [Accessed on 20 March 2020]). .385
Figure 7-9 Cross-sectional analysis of simulated bed levels of Run 2 against Run 1 in identified 'mobile' zones. (b) – (k) display simulated bed level over a one year simulation at multiple cross-sections whereby 't0' is the starting bed level and 'h', 'wk' and 'mo' is subsequent months; (a) provides the location of these cross-sections. Bathymetry source: INFOMAR (https://www.infomar.ie/ [Accessed on 20 March 2020]). 386
Figure 7-10 (a) Bathymetry map overlain by simulated accumulative total sediment load transport vectors after 12 lunar month simulation period. The identified source and sink pathways are identified along the circumference of the sediment budget cell in red and blue respectively. (b) The percentage of the total sediment entering the sediment budget cell through each source pathway over this 12 month period are presented in red. The percentage of the total sediment exiting the sediment budget cell at each sink pathway over this 12 month period is identified in blue. Bathymetry source: INFOMAR (https://www.infomar.ie/ [Accessed on 20 March 2020]).....388
Figure 7-11 (a) Bathymetry (mLAT) overlain by modelled residual currents (m/s), (b) Mean simulated SSC (g/m³) over one-year period under pure current conditions overlain by modelled residual currents (m/s), (c) Bed load versus suspended load dominance calculated from one lunar month simulation under pure current conditions overlain by modelled residual currents (m/s). Bathymetry source: INFOMAR (https://www.infomar.ie/ [Accessed on 20 March 2020]). 391
Figure 7-12 (a) Identified sink and source pathways around Arklow Bank's sediment budget cell in relation to the Wicklow Trough and Wicklow Head, (b) Simulated residual currents, after first simulation month (t1mo), over Wicklow Trough and Northern Arklow Bank, (c) Modelled

accumulative total sediment load over, after a 12 lunar month simulation, over Wicklow Trough and Northern Arklow Bank, (d) Simulated residual currents t1mo over Glassgorman Banks and Arklow Bank. Bathymetry source: INFOMAR (https://www.infomar.ie/ [Accessed on 20 March 2020])..... 393
Figure 7-13 (a) Identified sediment sink and source pathways on the circumference of Arklow Bank's sediment budget cell. Location of simulated bed level cross-sections are given. Areas designated as 'immobile zones' in Run 3 are also denoted. (b) to (d) Difference in simulated bed levels after one (t1mo), six (t6mo) and 12 (t12mo) lunar month simulations between Run 2 and Run 3 respectively (Table 7-5). (d) also displays the % total sediment load volume change between Run 3 and Run 2 at each source and sink transport pathway (see Table 7-4). (e) to (g) Cross-sections of simulated bed levels after one (t1mo), six (t6mo) and 12 (t12mo) lunar month simulations between Run 2 and Run 3 respectively). Panel (a) bathymetry source: INFOMAR (https://www.infomar.ie/ [Accessed on 20 March 2020])..... 396
Figure 7-14 (a) Identified sediment sink and source pathways on the circumference of Arklow Bank's sediment budget cell. Location of simulated bed level cross-sections are given. (b) to (d) Difference in simulated bed levels after one (t1mo), six (t6mo) and 12 (t12mo) lunar month simulations between Run 2 and Run 4 respectively (Table 7-5). (e) to (i) Cross-sections of simulated bed levels after one (t1mo), six (t6mo) and 12 (t12mo) lunar month simulations between Run 2 and Run 3 respectively. Panel (a) bathymetry source: INFOMAR (https://www.infomar.ie/ [Accessed on 20 March 2020])..... 405
Figure 7-15 (a), (c), (e) Difference in simulated bed levels after one (t1mo), six (t6mo) and 12 (t12mo) month simulation periods respectively between Run 2 and Run 5; (b), (d), (f) Difference in simulated bed levels after one, six and 12 month simulation periods respectively between Run 4 and Run 5 (see Table 7-5); (g) to (j) Cross-sections of simulated bed levels from Run 2 ('base'), Run 4 ('wind') and Run 5 ('wind and wave'). 409

List of tables

Table 2-1 Summary of the main topics discussed in this thesis alongside representative papers for that topic. 25

Table 3-2 Tidal character definition based on the phase difference between high tide and the closest preceding or succeeding peak current flow (m/s), and the areal extent of each regime according to the Irish Sea model presented by Ward et al [30] 53

Table 3-3 Comparison between modelled and measured tidal amplitudes and currents from tide gauge and ADCP locations respectively. The indices shown are bias, the root-mean-square error (RMSE), the correlation coefficient (R) and the scatter index (SI). Data source: Coughlan et al [132] 60

Table 4-1 Geometrical relationships of sediment waves from previous studies 127

Table 4-2 Details of MBES bathymetry datasets used in this study. Location of each site is presented in Figure 4-3. 134

Table 4-3 Sediment wave size classification scheme used in this study. Source: Van Landeghem et al [56] and Evans et al [79], originally adapted from Ashley [46] and Berne et al [80] 137

Table 4-4 Sediment wave characteristics for each individual study site based on first time-lapse bathymetric dataset 147

Table 4-5 Relationship between bedform heights and wavelengths in the south-western Irish Sea. The Full dataset has been broken into three environments i.e. Southern Banks, Northern Banks and Independent Assemblages, and each individual study site. 150

Table 4-6 Interpretation of Pearson correlation coefficient (r) 203

Table 4-7 Relationship between sediment wave heights (H) and wavelengths (L) in the south-western Irish Sea. The Full dataset has been broken into three environments i.e. Southern Banks, Northern Banks and Independent Assemblages, and each individual study site. 204

Table 4-8 Relationship between sediment wave heights (H), wavelengths (L), and Sand Wave Index (SWI) with Rouse Number (P) in the south-western Irish Sea. 205

Table 4-9 Relationship between sediment wave heights (H), wavelengths (L), and Sand Wave Index (SWI) with Water depth (D) in the south-western Irish Sea. 206
Table 4-10 Relationship between sediment wave heights (H), wavelengths (L), and Sand Wave Index (SWI) with median grain size ($D50$) in the south-western Irish Sea. 208
Table 4-11 Relationship between sediment wave heights (H), wavelengths (L), and Sand Wave Index (SWI) with maximum current speed ($Ucmax$) in the south-western Irish Sea. 209
Table 4-12 Relationship between sediment wave heights (H), wavelengths (L), and Sand Wave Index (SWI) with residual current speed ($Ucres$) in the south-western Irish Sea. 211
Table 4-13 Relationship between sediment wave heights (H), wavelengths (L), and Sand Wave Index (SWI) with mean current speed ($Ucmean$) in the south-western Irish Sea. 212
Table 5-1 Comparison between the simulated and observed water level data from tide gauge and ADCP locations 251
Table 5-2 Comparison between the simulated and observed current data from ADCP locations 253
Table 5-3 Details of water sampling stations including water depth of samples and resulting $SSCsolids$ 262
Table 5-4 Directly measured samples used in linear regression analysis to estimate $SSCsolids$ from ADCP relative acoustic backscatter 264
Table 5-5 Minimum, maximum and mean ADCP-based $SSCsolids$ at bottom-water, mid-water, surface water and depth-averaged, and statistics from full dataset of modelled $SSCsediment$ 276
Table 6-1 Comparison of simulated bed level changes against measured repeat bathymetry datasets at different sites in the model domain 315
Table 7-1 Comparison between the model and measured M2 and M5 datasets and model and output from the ERA5-ECMWF dataset at locations shown in Figure 7-2. The indices shown are bias, the root-mean-square error (RMSE), the correlation coefficient (R) and the scatter index (SI) 374
Table 7-2 Overview of scenario modelling 378

Table 7-3 Resolution details of the unstructured flexible triangular mesh used in scenario modelling 379

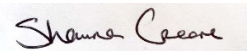
Table 7-4 Change in volume of sediment passing through each pathway in Run 3 compared to baseline model Run 2..... 397

Table 7-5 Difference in bed levels between each scenario run, along targeted cross-sections over the identified HVZs, after a simulation period of 1 month (t1mo), 6 months (t6mo) and 12 months (t12mo). For cross-section locations see Figure 7-13(a)..... 400

Table A-1 Conference deliverables during this PhD programme 456

Declaration

This is to certify that the work I am submitting is my own and has not been submitted for another degree, either at University College Cork or elsewhere. All external references and sources are clearly acknowledged and identified within the contents. I have read and understood the regulations of University College Cork concerning plagiarism and intellectual property.

Signed: 

Shauna Creane

Date: 07/10/2022

Acknowledgement

I would like to gratefully acknowledge the help from the following people throughout these years of knowledge, experiences and learning.

This research would not have been possible without the support and guidance of my supervisor Dr Jimmy Murphy, co-supervisor Dr Michael O'Shea and external advisor/employment mentor Dr Mark Coughlan. A sincere thank you to all three, for the discussions and constructive feedback that undoubtedly has improved the quality of work in my dissertation. Special thanks to Dr Mark Coughlan for his continuous support and mentorship throughout each offshore field work campaign.

Sincerest appreciation to my colleagues and friends at Gavin and Doherty Geosolutions, who provided me with continuous support through this employment-based PhD programme. A special mention to Dr Julie Clarke, Dr Cian Desmond, Dr Soroosh Jalilvand and Dr Jimmy Murphy who supported and inspired me throughout my research and industry-based endeavours.

Thank you to my family, especially my mother, Caroline Creane, for providing me with unfailing support and continuous encouragement throughout my years of study and through the process of researching and writing this thesis.

I must express my profound gratitude to my partner, Darragh O'Connor, for his constant encouragement, understanding and support throughout this academic adventure. It goes without saying that this PhD would have been much harder without him by my side.

A special thank you to my friends in the Belpark Triathlon Club for giving me the space to enjoy life beyond this work.

Lastly, I would like to thank the Irish Research Council and Gavin and Doherty Geosolutions who funded this employment-based postgraduate programme (grant no. EBPPG/2019/158).

Abstract

A combination of in-situ geophysical, geological and oceanographic datasets, and advanced numerical modelling tools are used to: improve the understanding of hydrodynamics and morphodynamics in the Irish Sea, develop new methods and approaches to investigate hydrodynamics and seabed morphodynamics in an offshore setting, collect and produce novel datasets that will contribute to this scientific field, and facilitate the sustainable growth of anthropogenic activities in the Irish Sea. These new methods and approaches include, using process-based indicators to understand sediment wave development and distribution, utilising ADCP-based SSC_{solids} as a numerical model calibration tool, and the application of a 'sediment budget' to an offshore sand bank to understand external influences on the stability of its morphodynamic system.

Results provide hydrodynamic proof underpinning the presence of the bed load parting (BLP) in central Irish Sea and associated divergent sediment transport pathways driving sediment dispersal across this tidally-dominated continental shelf sea. Analysis of tidal propagation through the Irish Sea Basin concludes that the origin of the BLP is mainly attributed to the intersection of the north and south tidal fronts at an inclined angle due to Coriolis Forcing and coastline interactions. Minor factors impacting the shape and location of the BLP are the change in tidal character at (a) abrupt bathymetry changes, (b) headlands and intricate coastline topography, and (c) large-scale constrictions. These outcomes set the basis of understanding for the thesis.

Building upon this knowledge, analysis of targeted, high resolution, time-lapse bathymetry datasets in the south-western Irish Sea reveals sediment waves in a range of sizes (height = 0.1 to 25.7 m, and wavelength = 17 to 983 m), occurring in water depths of 8.2 to 83 mLAT,

and migrating at a rate of 1.1 to 79 m/yr. Combined with numerical modelling outputs, a strong divergence of sediment transport pathways from the previously understood predominantly southward flow in the south Irish Sea is revealed. Furthermore, a new source and sink mechanism are defined for offshore independent sediment wave assemblages, whereby each sediment wave field is supported by circulatory residual current cells originating from offshore sand banks. Reliable sediment transport modelling is required to investigate these physical processes further, therefore, the need for cost-effective sediment validation datasets for 2D sediment transport models is addressed, utilising ADCP-based datasets.

A robust spatial timeseries of ADCP-based SSC_{solids} was successfully calculated in an offshore, tidally-dominated setting. Three new validation techniques are deemed advantageous in developing an accurate 2D suspended sediment transport, including i) validation of 2D modelled suspended sediment concentration ($SSC_{sediment}$) using water sample-based SSC_{solids}, ii) validation of the flood-ebb characteristics of 2D modelled suspended load transport and $SSC_{sediment}$ using ADCP-based datasets and iii) validation of the 2D modelled peak $SSC_{sediment}$ over a spring-neap cycle using the ADCP-based SSC_{solids}. The robust coupled hydrodynamic and sediment transport model produced from this research is used as a tool of investigation in subsequent chapters.

The complex hydrodynamic processes controlling upper slope mobility and long-term base stability of Arklow Bank are determined. Results reveal a flood and ebb tidal current dominance on the west and east side of the bank respectively, ultimately generating a large anticlockwise residual current eddy encompassing the entire bank. The positioning of multiple off-bank anticlockwise residual current eddies on the edge of this cell is shown to both

facilitate and inhibit east-west fluctuations of the upper slopes of the bank and control long-term bank base stability. Within Arklow Bank's morphological cell, eight morphodynamically and hydrodynamically unique bank sections or 'sub-cells' are identified, whereby a complex morphodynamic-hydrodynamic feedback loop is present. The local east-west fluctuation of the upper slopes of the bank is driven by migratory on-bank stationary and transient clockwise residual eddies and the development of 'narrow' residual current cross-flow zones. Together these processes drive upper slope mobility but maintain long term bank base stability.

A sediment budget was successfully estimated for an offshore linear sand bank, Arklow Bank, whereby seven source and nine sink pathways are identified. The restriction of sediment sources off the southern extent of Arklow Bank impact erosion and accretion patterns in the mid and northern sections of the bank after just one lunar month simulation. Where tidal current is the primary driver of sand bank morphodynamics, wind- and wave-induced flow is shown to alter sediment distribution patterns.

This advanced body of work forms a robust scientific evidence-base to facilitate the sustainable growth of offshore renewable developments.

Thesis output

The following chapters are either published peer-reviewed journal papers or are currently under review in an international journal. For each paper, I was the first author, where I was both responsible for the decision making in the approach to the study and for writing the original draft. I was also responsible for the construction of the methodology, formal analysis, visualisation and conceptualisation for each body of work. I was the lead in the investigation process which included undertaking the role as co-chief scientist for two offshore research surveys in 2020, and the role of chief scientist for two later offshore research surveys in 2021 (Appendix B). This field work allowed the collection of critical geophysical, geological and oceanographic datasets all of which fed directly into these papers. The supervisors were responsible for reviewing and editing the original draft of each paper and greatly helped improve the quality of work by providing mentorship, feedback and criticism during the conceptualisation phase, numerical model design and development, and during analysis of results. Additionally, the supervisors provided continuous support and guidance in the planning and execution of offshore field work, especially during the two earliest surveys.

Chapter 3

S. Creane, M. O'Shea, M. Coughlan, and J. Murphy, "The Irish Sea bed load parting zone: Is it a mid-sea hydrodynamic phenomenon or a geological theoretical concept?," *Estuarine, Coastal and Shelf Science*, vol. 263, p. 107651, 2021, doi: 10.1016/j.ecss.2021.107651.

Chapter 4

S. Creane, M. Coughlan, M. O'Shea, and J. Murphy, "Development and dynamics of sediment waves in a complex morphological and tidal dominant system: southern Irish Sea," *Geosciences*, vol. 12, no. 12, p. 46, 2022, doi: 10.3390/geosciences12120431.

Chapter 5

S. Creane, M. O'Shea, M. Coughlan, and J. Murphy, "Estimation of suspended solids concentration from Acoustic Doppler Current Profiler in a tidally-dominated continental shelf sea setting and its use as a numerical modelling validation technique," *Coastal Engineering*, under review.

Chapter 6

S. Creane, M. O'Shea, M. Coughlan, and J. Murphy, "Hydrodynamic processes controlling sand bank mobility and long-term base stability: A case study of Arklow Bank," *Geosciences*, vol. 13, no. 2, p. 60, 2023, doi: 10.3390/geosciences13020060.

Chapter 7

S. Creane, M. O'Shea, M. Coughlan, and J. Murphy, "Morphological modelling to investigate the role of external sediment sources, and wind and wave-induced flow on sand bank sustainability: A case study of Arklow Bank," *Continental Shelf Research*, under review.

Appendix A

Multiple conference poster and oral presentations; one co-authored conference paper; one co-authored peer-reviewed journal paper.

Appendix B

Two offshore research survey campaigns split into four survey legs:

M. Coughlan and S. Creane, "Mobility of Sediment Waves and Sand Banks in the Irish Sea (MOVE 1), Leg 1 and 2," 2020. Cruise report: CV20010 and CV20036.

S. Creane and M. Coughlan, "Mobility of Sediment Waves and Sand Banks in the Irish Sea Phase 2 (MOVE 2), Leg 1," 2021. Cruise report: CV21035.

S. Creane, R. Strachan, and F. Butchek, “Mobility of Sediment Waves and Sand Banks in the Irish Sea Phase 2 (MOVE 2) Leg 2,” 2021. Cruise report: CV21034.

General Nomenclature

A list of nomenclature used in this thesis is outlined below.

ADCP	Acoustic Doppler Current Profiler
BGS	British Geological Survey
BLP	Bed Load Parting
GSI	Geological Survey Ireland
HVZs	High Vulnerability Zones
LAT	Lowest Astronomical Tide
LCOE	Levelized Cost of Energy
MBES	Multibeam echo sounder
MFI	Mobilisation Frequency Index
MSL	Mean Sea Level
OWF	Offshore Wind Farm
RSSI	Returned Signal Strength Indicator
RMSE	Root Mean Square Error
SWI	Sand Wave Index
M_2	Principle lunar semi-diurnal constituent
M_4	Quarter-diurnal non-linear harmonic overtide of M_2
S_2	Principle solar semi-diurnal constituent
GW	Gigawatt
m	Metre
°	Degrees
km	Kilometres
m/s	Metres per second
ka BP	Thousand years before present
%	Percent
SI	Scatter Index
τ_b	Bottom shear stress
C_d	Drag coefficient
M	Manning number
g	Acceleration due to gravity
$\overline{\mathrm{U}}$	Depth-averaged velocity
A_{M_4}	Amplitude of M_4
A_{M_2}	Amplitude of M_2
ϕ_{M_4}	Phase of M_4
ϕ_{M_2}	Phase of M_2
mm/yr	Millimetre per year
kHz	kiloHertz
cm	Centimetre
D_{50}	Median grain size
P	Rouse number

w_s	Particle settling velocity
ρ_s	Density of particle
ρ	Density of a fluid
μ	Dynamic viscosity
u_*	Shear velocity
k	von Karman constant
z_0	hydraulic roughness
F_s	Entrainment function
Re_*	Shear Reynolds number
τ_{cr}	Critical shear stress
τ_c	Current-induced bed shear stress
τ_{cw}	Wave-induced bed shear stress
$U_{c_{max}}$	Maximum current speed
$U_{c_{res}}$	Residual current speed
$U_{c_{mean}}$	Mean current speed
SSC_{solids}	Suspended solids concentration
$SSC_{sediment}$	Suspended sediment concentration
RL	Reverberation level
$2TL$	Two-way travel transmission losses
SL	Source level
TS	Target strength of suspended sediment
E	Measured Returned Signal Strength Indicator (RSSI) amplitude recorded by the ADCP for each bin along each beam, in counts
E_r	Amplitude seen by the ADCP in the absence of any signal or the baseline amplitude
α_s	absorption coefficient for sediments
α_w	Absorption coefficient due to water
c_1	Speed of sound in the water used by the ADCP
c'	Average sound speed from the transducer to the range cell
T	Temperature
S	Salinity
R_0	Rayleigh Distance
ψ	Near field correction for spreading loss
f_1	Boric acid
f_2	Magnesium sulphate
f	Frequency of the ADCP
dB	Decibel
°C	Degrees Celsius
ppm	Parts per million
SSC_v	Dimensionless volumetric sediment concentration
θ	Shields parameter

C	Chezy number
τ''	Form drag
τ'	Skin friction
c_e	Equilibrium mass concentration
mg/L	Milligram per liter
2D	Two-dimensional
3D	Three-dimensional
2DV	Two-dimensional vertical
H_s	Significant wave height
T_p	Peak wave period
T_{02}	Mean spectral wave zero-upcrossing period
T_s	Significant wave period
MWD	Mean wave direction
S_{xx}, S_{yy}, S_{xy}	Three components of wave radiation stresses

1 Introduction

1.1 Background to the thesis

1.1.1 Contribution to science

Tidal wave propagation into a channel or sea, that is constricted by landmasses with convoluted coastlines and underlain by intricate bathymetries, give rise to highly complex oceanographic phenomena [1]–[3]. Many variables controlling and influencing these phenomena are generally well understood such as tidal wave propagation [4], tidal harmonic variations including the generation of shallow water tidal constituents [1], density-driven circulation [5], wave-current interaction [6], and storm surge [7], [8]. The resulting hydrodynamic forces exert shear stress on the seabed, whereby if the threshold of motion of sediments is exceeded, grains will be mobilised [9], giving rise to a range of erosional and depositional bedforms [10]. In the Irish Sea, located on the north-western European continental shelf, this complex interaction between the hydrodynamic and sediment transport regimes is highly under-studied and their inter-related relationship is yet to be fully understood. This is a major gap in scientific knowledge to date.

The Irish Sea is bound to the west and east by two landmasses, the Island of Ireland and Great Britain respectively. This tidally-dominated continental shelf sea opens to the Celtic Sea to the south via the St Georges Channel, and to the Atlantic Ocean via the North Channel. Within this region, a number of studies have compiled regional sediment classification maps [11]–[15], identified a mosaic of bedforms that are erosional, depositional, mobile and moribund in nature [16]–[20], with less studies investigating bedform migration dynamics [21], [22]. Broad net bed load sediment transport pathways have been defined [21], [23], [24] yet the hydrodynamic regime underpinning these physical movements is not fully supported. Additionally, only a limited amount of studies have investigated seabed mobility on a regional

scale through numerical modelling [25]. Investigation into how local and regional scale sediment transport systems are defined, how they interact with one another, and defining hydrodynamic support for these processes is imperative. To date, this knowledge is poorly understood in the Irish Sea and in many other tidally-dominated shelf seas around the globe.

This thesis sets out to understand the complex hydrodynamic regime driving seabed mobility and morphodynamics in the Irish Sea and elucidate these phenomena as an entire system in terms of sediment source, sediment sink, the mechanism of movement and the drivers of this movement. Subsequently, the wealth of knowledge, the abundance of newly obtained datasets, the development of novel methods and techniques, and other state-of-the-art outputs produced from this body of work will form a substantial contribution to the scientific community. This work will not only advance the scientific knowledge of the Irish Sea but will also inform processes, techniques and methods that can be applied to tidally-dominated shelf seas on a global level.

1.1.2 Climate targets, action plans, sustainable development goals

Applications of this scientific contribution is at the forefront of policy, industry and society due to the ongoing global climate crisis. Both the Paris Agreement 2015 [26] and Glasgow Climate Pact 2021 [27] set a target to limit global temperature rise to 1.5 °C above pre-industrial levels [28]. Consequently, international groups and national governments have set stringent climate action targets in order to accelerate the decarbonisation of industry and society [29].

The 2020 European Commission's Green Deal [30] originally set a target of a 40 % share of renewable energy by 2030. Due to recent energy resource issues stemming from the war in Ukraine with Russia, REPowerEU [31], [32] has recently increased this goal from 40 % to 45 %

with the intension of reducing Europe's reliance on external energy resources. As a result, a large-scale offshore wind deployment is expected around Europe. In particular, the United Kingdom has set a commitment of up to 50 GW of offshore wind by 2030 [33], some of which is earmarked for the eastern Irish Sea. In Ireland, the first and only existing offshore wind farm (OWF) is the Arklow Wind Park Phase 1, a seven-turbine 25 MW offshore wind farm (OWF), located in the western Irish Sea, co-developed between SSE and GE Energy in 2004. However, the offshore wind sector in Ireland has picked up momentum with the Maritime Area Planning Bill (MAP) [34] signed into law on the 23 December 2021 and the Department of Environment, Climate and Communications (DECC) publishing the timeline for the first Offshore RESS (O-RESS) auction with a revised date of April 2023 [35]. Ireland's Climate Action Plan (CAP) originally set a target of 5 GW of offshore wind generation by 2030. This was revised in July 2022, increasing the target to 7 GW [36]. The updated Climate Action Plan should reflect this change in late 2022. Ireland's early phase projects will be fixed-bottom offshore wind farms (OWFs) located in the western Irish Sea. More ambitious targets are set to 30 GW of offshore wind by 2050 upon realising the opportunities of combined fixed and floating OWFs across the Irish and Celtic Seas and the Atlantic Ocean [37]. The overarching goal of both the CAP [37] and the Ireland's Programme for Government [38] is to reach net zero carbon emissions by 2050.

In addition to climate actions, in 2015, governments of all United Nations Member States adopted the United Nations 17 sustainable development goals (SDGs) [39]. These SDGs acknowledge that ending human deprivation must be addressed closely alongside tackling climate change and preserving our oceans and forests [40].

Furthermore, with the increase in demand on marine resources, the European Union set out an obligation for all 22 coastal Member States to develop a maritime spatial plan (MSP) by 31 March 2021 [41], with a minimum review period of 10 years. This EU MSP Directive was adopted in 2014 and establishes a framework for an MSP, 'aimed at promoting the sustainable growth of maritime economies, the sustainable development of marine areas and the sustainable use of marine resources' [41]. Key benefits of the MSP are the reduction of conflicts between sectors, the creation of synergies between different activities, and the protection and preservation of the environment through early identification of impact and opportunities for multiple use of the marine space.

1.1.3 Impact of seabed mobility and morphodynamics on ORE developments

The accurate characterisation of potential offshore site locations, in terms of seabed morphodynamics, sediment transport and baseline hydrodynamics, is of critical importance to understanding the engineering challenges and the environmental implication associated with offshore renewable energy developments. With the installation of offshore infrastructure on the seabed, flow is accelerated leading to locally enhanced erosion of sediment. This causes the development of local and global scour [42]–[47], and free-spanning or burial of cables and pipelines [48]. Additionally, interaction of this infrastructure with seabed morphology such as sand wave migration, and natural vertical and horizontal bed level changes on mobile sand banks, have shown to result in similar issues [49]–[51]. These bed level changes can lead to infrastructural instability and economic losses. Optimised design of offshore infrastructure [52] and associated protection structures [53], [54], as well as optimised installation methods is put in place to reduce the risk of infrastructural instability to the highest respect. To facilitate this critical decision-making process, a comprehensive understanding of baseline hydrodynamics, seabed mobility and morphodynamics is key to

implement accurate measures [44], [55], [56]. This body of work addresses these issues in the Irish Sea, outputs from which can be applied to other environments.

1.1.4 Impact of ORE and other anthropogenic activities on environmental stability

With the increase of offshore anthropogenic activities, the preservation of environmental stability is of key concern. For example, marine aggregate extraction [57], [58] has the potential to adversely affect the marine ecosystem and leave long lasting changes to the seabed and bathymetry [59], sediment composition [60] and benthic community composition [61], [62]. Furthermore, offshore renewable energy (ORE) developments have shown to alter wave propagation, tidal flow and sediment dynamics [42], [63]–[66] which can potentially adversely affect the natural environment in the near and far field [67], but also provide advantageous effects such as coastal protection [68], [69]. In order to successfully facilitate a sustainable growth in anthropogenic activities in the marine environment, a baseline understanding of the complex interconnected hydrodynamic and sediment transport regime is vital. This crucial information will support continuous long-term monitoring before, during and after installation of ORE developments and/or offshore activities. Ultimately, this will help facilitate the maintenance of environmental stability.

1.2 Rationale behind the thesis

The definition of and the inter-connected relationships between hydrodynamic and sediment transport regimes in tidally-dominated shelf seas is highly under-studied thus there is a strong need to elucidate these processes. The principle motive behind this thesis is to fill this gap in scientific knowledge and to provide high quality state-of-the-art outputs that will make a major contribution to this interconnected engineering and geoscience field of research. Secondly, this body of work will facilitate the progression of sustainable energy generation in

an offshore environment. Advanced knowledge, new methods and investigation techniques, and other state-of-the-art outputs produced from this thesis will directly support the growth of this industry and aid the transition towards a climate-resilient economy. Thirdly, this thesis aims to facilitate the growth of offshore anthropogenic activities in a sustainable manner by informing robust environmental risk assessments aimed at protecting and preserving environmental stability. A combination of geoscience and engineering approaches are used to address these issues.

1.3 Thesis objectives and scope

In order to qualify and quantify seabed change in the Irish Sea, this thesis will address the following central research question:

- What are the morphodynamic characteristics and drivers in the Irish Sea?

The narrative of this thesis aims to provide a large contribution to science with respect to this central research question, taking into consideration the application of this knowledge to the sustainable growth of offshore anthropogenic activities. This includes facilitating the synergy between offshore engineering projects and other offshore anthropogenic activities in order to tackle climate change. To address this aim, four high-level objectives and corresponding sub-objectives are as follows:

1. Improve the understanding of hydrodynamics and morphodynamics in the Irish Sea
    a. Review how the bed load parting zone (BLP) is characterised and defined in the central Irish Sea.
    b. Discuss whether the present-day hydrodynamic regime supports this BLP and the resulting divergent net sand transport pathways.
    c. If so, elucidate why the BLP develops at this location.

d. Describe the morphological characteristics of sediment waves and their spatio-temporal evolution in a tidally dominated, shallow shelf setting in NW Europe.
e. Estimate sediment wave migration rate and infer sediment transport flux, relating the data to the wider sediment transport and hydrodynamic regime of the region.
f. Investigate whether there is a relationship between sand banks and independent sediment wave assemblages.
g. Determine how the hydrodynamics and bank mobility varies along the length of Arklow Bank, what are the underlying hydrodynamic processes driving this variation and what hydrodynamic phenomena control the bank's long-term stable positioning.
h. Examine the influence of external sediment sources on Arklow Banks local sediment transport regime and bank morphodynamics and how it interacts with the wider sediment transport regime.
i. Identify the most vulnerable areas of the Arklow Bank due to wind and wave-induced flow and the nature of this impact.

2. Develop new methods and approaches to investigate hydrodynamics and seabed morpho-dynamics in an offshore setting;
    a. Using equations developed by previous authors, estimate SSC_{solids} from the acoustic amplitudes recorded by a 300kHz ADCP deployed in a tidally-dominated shallow shelf setting characterised by complex hydrodynamics and non-cohesive seabed substrate.

b. Explore different model validation techniques to validate the suspended load transport and SSC aspect using a combination of direct sampling and ADCP-estimated SSC_{solids}.

c. Evaluate the applicability and advantages of the new validation techniques presented and provide best practice recommendations for future studies.

d. Conduct a numerical model mesh sensitivity analysis to define the most efficient spatial resolution that facilitates the investigation of various processes controlling Arklow Bank morphodynamics;

e. Examine the applicability of the coastal engineering concept, 'sediment budget' to offshore linear sand bank to investigate the role of external sediment sources on the local sediment transport regime and bank morphodynamics.

3. Collect and produce novel datasets that will contribute to the understanding of hydro- and morpho-dynamics in the Irish Sea;

    a. The technical challenge of gathering data in an offshore environment is a trying one. Using multi-disciplinary offshore surveying techniques, collect geological, geophysical, metocean and oceanographic datasets that can either (i) be integrated into the development of a robust hydrodynamic, spectral wave and sediment transport model, and/or (ii) act as standalone datasets that can be analysed independently of model development. These datasets aid the success of Objectives 1, 2 and 4 and can be used in future research and commercial investigations beyond this thesis.

4. Facilitate the sustainable growth of anthropogenic activities in the Irish Sea.

a. Link knowledge obtained from Objective, 1, 2 and 3 to understand their application to the sustainable growth of anthropogenic activities in the Irish Sea

1.4 Thesis outline and the link between chapters

This nine-chapter thesis, presented as a thesis by publication, investigates the characteristics and drivers of seabed morphodynamics in the Irish Sea. Chapter 1 and 2 are the Introduction and Literature Review chapters, Chapter 8 provides the thesis Conclusions, whereas Chapter 3 to 7 corresponds to an individual paper and can be read independently with corresponding supplementary material and references.

At the time of production of the final version of this thesis (July 2023), chapters 3, 4 and 6 are published in international journals following peer-review, while chapters 5 and 7 are currently under review. Accordingly, each chapter in this thesis closely resembles the published or submitted manuscripts. The link between each chapter and a summary of chapters 3 to 7 are given as follows:

1.4.1 Chapter 3: The Irish Sea bed load parting zone: Is it a mid-sea hydrodynamic phenomenon or a geological theoretical concept? (Review and Original Research)

Chapter 3 is published as an 'Invited Article' in a peer-reviewed international journal. This chapter investigates the highly complex morpho- and hydro-dynamic regimes in the central Irish Sea through a comprehensive review of existing literature, and analysis of new MIKE 21 numerical modelling outputs and observational data. The study aims to determine whether the bed load parting zone in this region is fully supported by underlying hydrodynamics, and if proven, elucidate its origin. Furthermore, the high complexity of hydro- and morpho-dynamic processes around sand banks and the degenerate amphidromic point in the south-

western Irish Sea is explored and discussed. Findings from this study ultimately facilitates efficient marine spatial planning, underpinning a movement towards a climate resilient economy. The integrated approach used in this body of work can be applied to tidally-dominated continental shelves beyond the Irish Sea. This chapter provides the reader with a suitable background to the thesis.

1.4.2 Chapter 4: Development and dynamic of sediment waves in a complex morphological and tidal dominant system: southern Irish Sea (Original Research)

In Chapter 4, high-resolution time-lapse bathymetry datasets (Appendix B), hydrodynamic numerical modelling outputs and various theoretical parameters are used to describe the morphological characteristics of sediment waves and their spatio-temporal evolution in a hydrodynamic and morphodynamic complex region of the Irish Sea. This chapter builds upon the knowledge produced from Chapter 3 to ultimately investigate the environmental parameters underpinning seabed morphodynamics in tidally-dominated shelf seas, using the south-western Irish Sea as a case study. Furthermore, a complex sediment exchange relationship between offshore sand banks and offshore independent sediment wave fields are revealed for the first time. This forms the basis of investigation for Chapters 5, 6 and 7. The methods, datasets and concepts produced from this body of work can be applied to tidally-dominated continental shelves beyond the Irish Sea.

1.4.3 Chapter 5: Estimation of suspended solids concentration from Acoustic Doppler Current Profiler in a tidally-dominated continental shelf sea setting and its use as a numerical modelling validation technique (Original Research)

Chapter 5 addresses the need for cost-effective sediment validation datasets for two-dimensional (2D) sediment transport models by investigating the applicability of four new

suspended load validation techniques in an offshore, tidally-dominated setting (the south-western Irish Sea). This involves integrating an estimated spatial time series of suspended solids concentration (SSC_{solids}) derived from acoustic doppler current profiler (ADCP) acoustic backscatter with several in situ water sample-based SSC_{solids} datasets. Results from this body of work shows that the multi-disciplinary method of collecting in situ metocean and sediment dynamic data via acoustic instruments could be a cost-efficient data collection method for future offshore renewable energy developments and other engineering and scientific projects. This chapter builds upon the gaps identified in Chapter 3. Furthermore, it uses a combination of acoustic, oceanographic, geophysical and geological datasets collected during field work, outlined in Appendix B, to develop a robust sediment transport model which will be used as a tool of investigation in Chapter 6 and 7.

1.4.4 Chapter 6: Hydrodynamic processes controlling sand bank mobility and long-term base stability: A case study of Arklow Bank (Original Research)

The validated, dynamically coupled, 2D hydrodynamic and sediment transport model developed in Chapter 5 is used as a base in Chapter 6 to investigate the hydrodynamic processes controlling the highly upper mobile layer of Arklow Bank while maintaining overall long-term bank base stability. Further validation details of this model in terms of bed load transport is provided. Arklow Bank is an offshore linear sand bank in the south-western Irish Sea that is positioned at the centre of two out of three circulatory residual transport pathways identified in Chapter 4, whereby sediment is exchanged between offshore sand banks and offshore independent sediment wave fields. This bedform also hosts Ireland's only offshore wind farm, Arklow Wind Park Phase 1 which is earmarked for further expansion. Results from this study elucidates the hydrodynamic processes controlling both bedform mobility and bedform stability, which directly improves the ability to assess the risk of environmental

instability due to increased offshore anthropogenic activities. The advanced knowledge revealed from this study provides the basis of understanding for Chapter 7.

1.4.5 Chapter 7: Morphological modelling to investigate the role of external sediment sources, and wind and waves-induced flow on sand bank sustainability: An Arklow Bank case study (Original Research)

Chapter 7 builds upon both the knowledge of hydrodynamic processes driving Arklow Bank morphodynamics revealed in Chapter 6 and the complex inter-connected sediment transport pathways identified in Chapter 4 to assess the dependency of Arklow Bank's local sediment transport regime on external sediment sources. Additionally, scenario modelling is used to identify vulnerable areas of this offshore linear sand bank to wind and wave-forcing, and to examine the nature of this impact. A new spectral wave model is developed and validated for the Irish Sea, outputs from which aid this investigation. Given the particular complexity of the interconnected sediment transport pathways in the south-western Irish Sea revealed from this chapter, combined with knowledge from Chapter 3, 4 and 6, the risk of seabed instability arising from increased anthropogenic seabed disturbances is high. Robust environmental risk assessments that considers identified processes from this thesis are key to reducing the risk of environmental instability.

1.5 References

[1] E. P. Kvale, "The origin of neap-spring tidal cycles," *Marine Geology*, vol. 235, no. 1–4, pp. 5–18, 2006, doi: 10.1016/j.margeo.2006.10.001.

[2] A. I. Olbert, M. Hartnett, and T. Dabrowski, "Long-term inter-annual variability of a cyclonic gyre in the western Irish Sea," *Continental Shelf Research*, vol. 31, no. 13, pp. 1343–1356, 2011, doi: http://dx.doi.org/10.1016/j.csr.2011.05.010.

[3] A. E. Hill, J. Brown, and L. Fernand, “The summer gyre in the western Irish Sea: Shelf sea paradigms and management implications,” *Estuarine, Coastal and Shelf Science*, vol. 44, pp. 83–95, 1997, doi: 10.1016/S0272-7714(97)80010-8.

[4] J. M. Horrillo-Caraballo, Y. Yin, I. Fairley, H. Karunarathna, I. Masters, and D. E. Reeve, “A comprehensive study of the tides around the Welsh coastal waters,” *Estuarine, Coastal and Shelf Science*, vol. 254, p. 107326, 2021, doi: 10.1016/j.ecss.2021.107326.

[5] K. J. Horsburgh and A. E. Hill, “A three-dimensional model of density-driven circulation in the Irish Sea,” *Journal of Physical Oceanography*, vol. 33, no. 2, pp. 343–365, 2003, doi: 10.1175/1520-0485(2003)033<0343:ATDMOD>2.0.CO;2.

[6] X. Zhang, R. Simons, J. Zheng, and C. Zhang, “A review of the state of research on wave-current interaction in nearshore areas,” *Ocean Engineering*, vol. 243, p. 110202, 2022, doi: 10.1016/j.oceaneng.2021.110202.

[7] A. I. Olbert and M. Hartnett, “Storms and surges in Irish coastal waters,” *Ocean Modelling*, vol. 34, no. 1–2, pp. 50–62, 2010, doi: 10.1016/j.ocemod.2010.04.004.

[8] J. Poulose, A. D. Rao, and P. K. Bhaskaran, “Role of continental shelf on non-linear interaction of storm surges, tides and wind waves: An idealized study representing the west coast of India,” *Estuarine, Coastal and Shelf Science*, vol. 207, pp. 457–470, 2018, doi: 10.1016/j.ecss.2017.06.007.

[9] R. Soulsby, “Dynamics of Marine Sands,” *Thomas Telford Publications*, vol. 249.

[10] D. A. V. Stow, F. J. Hernández-Molina, E. Llave, M. Sayago-Gil, V. Díaz-del Río, and A. Branson, “Bedform-velocity matrix: The estimation of bottom current velocity from bedform observations,” *Geology*, vol. 37, no. 4, pp. 327–330, 2009, doi:

10.1130/G25259A.1.

[11] D. R. Tappin, R. A. Chadwick, A. A. Jackson, R. T. R. Wingfield, and N. J. P. Smith, *United Kingdom offshore regional report: The geology of Cardigan Bay and the Bristol Channel*. London: HMSO for the British Geological Survey, 1994.

[12] D. I. Jackson, A. A. Jackson, D. J. A. Evans, R. T. R. Wingfield, R. P. Barnes, and M. J. Arthur, *United Kingdom offshore regional report: the geology of the Irish Sea*. London: HMSO for the British Geological Survey, 1995.

[13] M. Kozachenko, R. Fletcher, G. Sutton, X. Monteys, K. Van Landeghem, A. Wheeler, Y. Lassoued, A. Cooper, and C. Nicoll, *A geological appraisal of marine aggregate resources in the southern Irish Sea. Technical report produced for the Irish Sea Marine Aggregates Initiative (IMAGIN) project funded under the INTERREG IIIA Community Initiative Programme 2000-2006*. University College Cork, Ireland, 2008.

[14] British Geological Survey, "BGS Datasets: Seabed sediments 250K," 2020. https://www.bgs.ac.uk/datasets/marine-sediments-250k/

[15] S. L. Ward, S. P. Neill, K. J. J. Van Landeghem, and J. D. Scourse, "Classifying seabed sediment type using simulated tidal-induced bed shear stress," *Marine Geology*, vol. 367, pp. 94–104, 2015, doi: 10.1016/j.margeo.2015.05.010.

[16] K. A. Robinson, K. Ramsay, C. Lindenbaum, N. Frost, J. Moore, D. Petrey, and T. Darbyshire, *Habitat Mapping for Conservation and Management of the Southern Irish Sea (HABMAP). II: Modelling & Mapping*, vol. 5, no. 2. 2009.

[17] K. J. J. Van Landeghem, A. J. Wheeler, N. C. Mitchell, and G. Sutton, "Variations in sediment wave dimensions across the tidally dominated Irish Sea, NW Europe,"

Marine Geology, vol. 263, no. 1–4, pp. 108–119, 2009, doi: 10.1016/j.margeo.2009.04.003.

[18] C. L. Mellet, D. Long, G. Carter, R. C. Chiverrell, and K. J. J. Van Landeghem, "Geology of the seabed and shallow subsurface: The Irish Sea. British Geological Survey Commissioned Report, CR/15/057," 2015.

[19] J. E. Hanna and J. A. G. Cooper, "Mesoscale Morphological Changes on Linear, Nearshore Sandbanks, Co.Wexford, SE Ireland.," *Journal of Coastal Research*, vol. 36, pp. 356–364, 2002, doi: 10.2112/1551-5036-36.sp1.356.

[20] A. J. Wheeler, J. Walshe, and G. D. Sutton, "Geological appraisal of the Kish, Burford, Bray and Fraser Banks, Outer Dublin Bay Area," in *Marine Resources Series*, Dublin: Marine Institute, 2000.

[21] K. J. J. Van Landeghem, K. Uehara, A. J. Wheeler, N. C. Mitchell, and J. D. Scourse, "Post-glacial sediment dynamics in the Irish Sea and sediment wave morphology: Data-model comparisons," *Continental Shelf Research*, vol. 29, no. 14, pp. 1723–1736, 2009, doi: 10.1016/j.csr.2009.05.014.

[22] K. J. J. Van Landeghem, J. H. Baas, N. C. Mitchell, D. Wilcockson, and A. J. Wheeler, "Reversed sediment wave migration in the Irish Sea, NW Europe: A reappraisal of the validity of geometry-based predictive modelling and assumptions," *Marine Geology*, vol. 295–298, pp. 95–112, 2012, doi: 10.1016/j.margeo.2011.12.004.

[23] P. T. Harris, C. B. Pattiaratchi, M. B. Collins, and R. W. Dalrymple, "What is a bedload parting?," in *Tidal signatures in modern and ancient sediments*, B. W. Flemming and A. Bartholoma, Eds. 1995. doi: 10.1002/9781444304138.ch1.

[24] R. D. Pingree and D. K. Griffiths, “Sand transport paths around the British Isles resulting from M2 and M4 tidal interactions,” *Journal of the Marine Biological Association of the United Kingdom*, vol. 59, no. 2, pp. 497–513, 1979, doi: https://doi.org/10.1017/S0025315400042806.

[25] M. Coughlan, M. Guerrini, S. Creane, M. O’Shea, S. L. Ward, K. J. J. Van Landeghem, J. Murphy, and P. Doherty, “A new seabed mobility index for the Irish Sea: modelling seabed shear stress and classifying sediment mobilisation to help predict erosion, deposition, and sediment distribution,” *Continental Shelf Research*, vol. 229, p. 104574, 2021, doi: https://doi.org/10.1016/j.csr.2021.104574.

[26] UNFCCC, “The Paris Agreement,” in *Paris Climate Change Conference*, 2015.

[27] UNFCCC, “Glasgow Climate Pact,” in *Conference of the Parties serving as the meeting of the Parties to the Paris Agreement*, 2021.

[28] IPCC, “Global Warming of 1.5°C. An IPCC Special Report on the impacts of global warming of 1.5°C above pre-industrial levels and related global greenhouse gas emission pathways, in the context of strengthening the global response to the threat of climate change,” V. Masson-Delmotte, P. Zhai, H.-O. Pörtner, D. Roberts, J. Skea, P. R. Shukla, A. Pirani, W. Moufouma-Okia, C. Péan, R. Pidcock, S. Connors, J. B. R. Matthews, Y. Chen, X. Zhou, M. I. Gomis, E. Lonnoy, T. Maycock, M. Tignor, and T. Waterfield, Eds. 2018.

[29] European Commission, “The 2030 Climate target plan,” Brussels, 2020.

[30] European Commission, “Fit for 55: Delivering the EU’s 2030 Climate Target on the way to climate neutrality,” Brussels, 2021.

[31] European Commission, “REPowerEU: A plan to rapidly reduce dependence on Russian fossil fuels and fast forward the green transition,” *Press Release*, 2022. https://ec.europa.eu/commission/presscorner/detail/en/IP_22_3131 (accessed Sep. 27, 2022).

[32] European Aluminium and Solar Power Europe, “Europe’s Renewables & Raw Materials Associations Unite with Cities & Academics Behind a 45 % European Renewables Target for 2030,” *Press Release*, 2022.

[33] National Grid ESO, “Pathway to 2030: A holistic network design to support offshore wind deployment for net zero,” 2022.

[34] Government of Ireland, *An Bille um Pleanáil Limistéir Mhuirí, Maritime Area Planning Bill*, no. 104. 2021.

[35] Government of Ireland and EIRGRID, “Renewable Electricity Support Scheme: ORESS 1 Auction Timetable,” 2022. [Online]. Available: https://www.eirgridgroup.com/site-files/library/EirGrid/ORESS-1-Auction-Timetable-(OR1AT).pdf

[36] Department of the Taoiseach, “Government announces sectoral emissions ceilings, settling Ireland on a pathway to turn the tide on climate change,” *Press Release*, 2022. https://www.gov.ie/en/press-release/dab6d-government-announces-sectoral-emissions-ceilings-setting-ireland-on-a-pathway-to-turn-the-tide-on-climate-change/ (accessed Sep. 27, 2022).

[37] Department of the Environment Climate and Communications, “Climate Action Plan 2021,” 2021.

[38] Department of the Taoiseach, “Programme for Government,” 2020. [Online].

Available: https://www.gov.ie/en/publication/7e05d-programme-for-government-our-shared-future/

[39] United Nations, “Transforming our world: the 2030 Agenda for Sustainable Development,” in *UN General Assembly*, 2015. doi: 10.1163/15718093-12341375.

[40] F. Fuso Nerini, B. Sovacool, N. Hughes, L. Cozzi, E. Cosgrave, M. Howells, M. Tavoni, J. Tomei, H. Zerriffi, and B. Milligan, “Connecting climate action with other Sustainable Development Goals,” *Nature Sustainability*, vol. 2, no. 8, pp. 674–680, 2019, doi: 10.1038/s41893-019-0334-y.

[41] European Union, “Directive 2014/89/EU of the European Parliment and of the Council of 23 July 2014 establishing a framework for maritime spatial planning,” *Offical Journal of the European Union*, pp. 135–145, 2014.

[42] R. A. Lind and R. J. S. Whitehouse, “Understanding and Assessing Scour Development at Offshore Structures,” *Journal of Oilfield Technology*, vol. 5, no. 6, pp. 63–67, 2012.

[43] R. J. S. Whitehouse, J. Harris, J. Sutherland, and J. Rees, “An assessment of field data for scour at offshore wind turbine foundations,” in *4th International Conference on Scour and Erosion Tokyo*, 2008, pp. 329–335.

[44] R. J. S. Whitehouse and J. M. Harris, “Scour prediction offshore and soil erosion testing,” in *Proceedings of the International Conference on Offshore Mechanics and Arctic Engineering - OMAE*, 2014. doi: 10.1115/OMAE2014-24271.

[45] J. M. Harris, R. J. S. Whitehouse, and J. Sutherland, “Marine scour and offshore wind - Lessons learnt and future challenges,” in *Proceedings of the International Conference on Offshore Mechanics and Arctic Engineering - OMAE*, 2011, vol. 5, pp. 849–858. doi:

10.1115/OMAE2011-50117.

[46] B. M. Sumer, R. J. S. Whitehouse, and A. Tørum, “Scour around coastal structures: A summary of recent research,” *Coastal Engineering*, vol. 44, no. 2, pp. 153–190, 2001, doi: 10.1016/S0378-3839(01)00024-2.

[47] T. U. Peterson, B. M. Sumer, J. Fredsøe, D. R. Fuhrman, and E. D. Christensen, “Scour around Offshore Wind Turbine Foundations,” Technical University of Denmark. Department of Mechanical Engineering., 2014.

[48] M. Yaghoobi, S. Mazaheri, and E. Jabbari, “Determining Natural Frequency of Free Spanning Offshore Pipelines by Considering the Seabed Soil Characteristics,” *Journal of the Persian Gulf*, vol. 3, no. 8, pp. 25–34, 2012.

[49] R. Morelissen, S. J. M. H. Hulscher, M. A. F. Knaapen, A. A. Németh, and R. Bijker, “Mathematical modelling of sand wave migration and the interaction with pipelines,” *Coastal Engineering*, vol. 48, no. 3, pp. 197–209, 2003, doi: 10.1016/S0378-3839(03)00028-0.

[50] A. J. Couldrey, T. Benson, M. A. F. Knaapen, K. V Marten, and R. J. S. Whitehouse, “Morphological evolution of a barchan dune migrating past an offshore wind farm foundation,” *Earth Surface Processes and Landforms*, vol. 45, no. 12, pp. 2884–2896, 2020, doi: https://doi.org/10.1002/esp.4937.

[51] R. J. S. Whitehouse, J. M. Harris, J. Sutherland, and J. Rees, “The nature of scour development and scour protection at offshore windfarm foundations,” *Marine Pollution Bulletin*, vol. 62, no. 1, pp. 73–88, 2011, doi: 10.1016/j.marpolbul.2010.09.007.

[52] J. van der Tempel, M. B. Zaaijer, and H. Subroto, “The effects of Scour on the design of offshore wind turbines,” in *Proceedings of the 3rd International Conference on Marine Renewable Energy*, 2004, pp. 27–35.

[53] H. H. Chen, R. Y. Yang, and H. H. Hwung, “Study of hard and soft countermeasures for scour protection of the jacket-type offshore wind turbine foundation,” *Journal of Marine Science and Engineering*, vol. 2, no. 3, pp. 551–567, 2014, doi: 10.3390/jmse2030551.

[54] W. Lengkeek, K. Didderen, M. Teunis, F. Driessen, J. W. P. Coolen, O. G. Bos, S. A. Vergouwen, T. C. Raaijmakers, M. B. de Vries, and M. van Koningsveld, “Eco-friendly design of scour protection: potential enhancement of ecological functioning in offshore wind farms: Towards an implementation guide and experimental set-up,” Bureau Waardenburg. Wageningen Marine Research. Deltares. TU Delft. Commissioned by Ministry of Economic Affairs, The Netherlands, 2017.

[55] L. Chen and W. H. Lam, “Methods for predicting seabed scour around marine current turbine,” *Renewable and Sustainable Energy Reviews*, vol. 29, pp. 683–692, 2014, doi: 10.1016/j.rser.2013.08.105.

[56] J. M. Harris and R. J. S. Whitehouse, “Scour management – a risk based approach,” in *Proceedings of the 6th International Conference of Scour and Erosion (ICSE-6)*, 2012.

[57] G. Sutton, *Irish Sea Marine Aggregate Initiative (IMAGIN) Project Synthesis Report Including: Geological Assessment, Environmental Assessment, Morphodynamic Modelling Web-based GIS System, Cost Benefit Analysis, Aggregate Resources and Markets-Wales.*, Marine Env., no. 36. 2008.

[58] A. F. Velegrakis, A. Ballay, S. Poulos, R. Radzevičius, V. Bellec, and F. Manso, "European marine aggregates resources: Origins, usage, prospecting and dredging techniques," *Journal of Coastal Research*, no. 51, pp. 1–14, 2010, doi: 10.2112/SI51-002.1.

[59] F. Mielck, H. C. Hass, R. Michaelis, L. Sander, S. Papenmeier, and K. H. Wiltshire, "Morphological changes due to marine aggregate extraction for beach nourishment in the German Bight (SE North Sea)," *Geo-Marine Letters*, vol. 39, no. 1, pp. 47–58, 2019, doi: 10.1007/s00367-018-0556-4.

[60] S. E. Crowe, D. C. Bergquist, D. M. Sanger, and R. F. Van Dolah, "Physical and Biological Alterations Following Dredging in Two Beach Nourishment Borrow Areas in South Carolina's Coastal Zone," *Journal of Coastal Research*, vol. 32, no. 4, pp. 875–889, 2016, doi: 10.2112/JCOASTRES-D-15-00075.1.

[61] L. Wyns, M. Roche, F. Barette, V. Van Lancker, K. Degrendele, K. Hostens, and A. De Backer, "Near-field changes in the seabed and associated macrobenthic communities due to marine aggregate extraction on tidal sandbanks: A spatially explicit bio-physical approach considering geological context and extraction regimes," *Continental Shelf Research*, vol. 229, p. 104546, 2021, doi: 10.1016/j.csr.2021.104546.

[62] A. De Backer, N. Breine, H. Hans, E. Pecceu, J. Ranson, G. Van Hoey, J. Wittoeck, K. Hostens, and H. Kris, "Ecological assessment of intense aggregate dredging activity on the Belgian part of the North Sea," in *Belgian marine sand: a scarce resource?: Study Day, 9 June 2017, Hotel Andromeda - Ostend*, 2017.

[63] I. Fairley, I. Masters, and H. Karunarathna, "The cumulative impact of tidal stream

turbine arrays on sediment transport in the Pentland Firth," *Renewable Energy*, vol. 80, pp. 755–769, 2015, doi: 10.1016/j.renene.2015.03.004.

[64] M. Baeye and M. Fettweis, "In situ observations of suspended particulate matter plumes at an offshore wind farm, southern North Sea," *Geo-Marine Letters*, vol. 35, no. 4, pp. 247–255, 2015, doi: 10.1007/s00367-015-0404-8.

[65] C. Auguste, J. R. Nader, P. Marsh, I. Penesis, and R. Cossu, "Modelling the influence of Tidal Energy Converters on sediment dynamics in Banks Strait, Tasmania," *Renewable Energy*, vol. 188, pp. 1105–1119, 2022, doi: 10.1016/j.renene.2022.02.077.

[66] A. Rivier, A.-C. Bennis, G. Pinon, V. Magar, and M. Gross, "Parameterization of wind turbine impacts on hydrodynamics and sediment transport," *Ocean Dynamics*, vol. 66, no. 10, pp. 1285–1299, 2016, doi: 10.1007/s10236-016-0983-6.

[67] L. Bat, M. Sezgin, and F. Sahin, "Impacts of OWF installations on fisheries: A Literature Review," *Journal of Coastal Life Medicine*, vol. 1, no. 3, pp. 241–252, 2013, doi: 10.12980/jclm.1.2013j17.

[68] F. Onea, L. Rusu, G. B. Carp, and E. Rusu, "Wave farms impact on the coastal processes—A case study area in the portuguese nearshore," *Journal of Marine Science and Engineering*, vol. 9, no. 3, pp. 1–20, 2021, doi: 10.3390/jmse9030262.

[69] J. Abanades, D. Greaves, and G. Iglesias, "Wave farm impact on the beach profile: A case study," *Coastal Engineering*, vol. 86, pp. 36–44, 2014, doi: 10.1016/j.coastaleng.2014.01.008.

2 Literature Review

Chapters 3 to 7 of this thesis integrate a substantial, state-of-the-art literature review supporting the scope and objectives of this thesis. The main topics discussed, and associated representative papers, are summarised in Table 2-1.

Table 2-1 Summary of the main topics discussed in this thesis alongside representative papers for that topic.

Topic	Representative papers
Interaction between sediment dynamics and offshore infrastructure	A. Rivier, A.-C. Bennis, G. Pinon, V. Magar, and M. Gross, "Parameterization of wind turbine impacts on hydrodynamics and sediment transport," *Ocean Dynamics*, vol. 66, no. 10, pp. 1285–1299, 2016, doi: 10.1007/s10236-016-0983-6. M. Baeye and M. Fettweis, "In situ observations of suspended particulate matter plumes at an offshore wind farm, southern North Sea," *Geo-Marine Letters*, vol. 35, no. 4, pp. 247–255, 2015, doi: 10.1007/s00367-015-0404-8. I. Fairley, I. Masters, and H. Karunarathna, "The cumulative impact of tidal stream turbine arrays on sediment transport in the Pentland Firth," *Renewable Energy*, vol. 80, pp. 755–769, 2015, doi: 10.1016/j.renene.2015.03.004. R. J. S. Whitehouse, J. M. Harris, J. Sutherland, and J. Rees, "The nature of scour development and scour protection at offshore windfarm foundations," *Marine Pollution Bulletin*, vol. 62, no. 1, pp. 73–88, 2011, doi: 10.1016/j.marpolbul.2010.09.007. S. P. Neill, P. E. Robins, and I. Fairley, "The Impact of Marine Renewable Energy Extraction on Sediment Dynamics," in *Marine Renewable Energy:*

	Resource Characterization and Physical Effects, Z. Yang and A. Copping, Eds. Springer International Publishing, 2017, pp. 279–304. doi: 10.1007/978-3-319-53536-4_12. M. Yaghoobi, S. Mazaheri, and E. Jabbari, "Determining Natural Frequency of Free Spanning Offshore Pipelines by Considering the Seabed Soil Characteristics," *Journal of the Persian Gulf*, vol. 3, no. 8, pp. 25–34, 2012. B. M. Sumer, J. Fredsøe, and N. Christiansen, "Scour around vertical pile in waves," *Journal of Waterway, Port, Coastal, and Ocean Engineering*, vol. 118, no. 1, pp. 15–31, 1992, doi: 10.1061/(ASCE)0733-950X(1992)118:1(15). C. Jones, J. Magalen, and J. Roberts, "Wave energy converter (WEC) array effects on wave, current, and sediment circulation: Monteray Bay, CA," Sandia National Laboratories, Santa Cruz, CA; Albuquerque, New Mexico, 2014.
Seabed morphodynamics	J. Krabbendam, A. Nnafie, H. de Swart, B. Borsje, and L. Perk, "Modelling the past and future evolution of tidal sand waves," *Journal of Marine Science and Engineering*, vol. 9, no. 10, 2021, doi: 10.3390/jmse9101071. S. Leenders, J. H. Damveld, J. Schouten, R. Hoekstra, T. J. Roetert, and B. W. Borsje, "Numerical modelling of the migration direction of tidal sand waves over sand banks," *Coastal Engineering*, vol. 163, p. 103790, 2021, doi: 10.1016/j.coastaleng.2020.103790.

J. M. Damen, T. A. G. P. van Dijk, and S. J. M. H. Hulscher, “Spatially Varying Environmental Properties Controlling Observed Sand Wave Morphology,” *Journal of Geophysical Research: Earth Surface*, vol. 123, no. 2, pp. 262–280, 2018, doi: 10.1002/2017JF004322.

S. P. Neill and S. J. Couch, “Impact of Tidal Energy Converter (TEC) Array Operation on Sediment Dynamics,” in *9th European Wave and Tidal Energy Conference (EWTEC)*, 2011.

G. H. P. Campmans, P. C. Roos, H. J. de Vriend, and S. J. M. H. Hulscher, “The Influence of Storms on Sand Wave Evolution: A Nonlinear Idealized Modeling Approach,” *Journal of Geophysical Research: Earth Surface*, vol. 123, no. 9, pp. 2070–2086, 2018, doi: 10.1029/2018JF004616.

M. Z. Li, J. Shaw, B. J. Todd, V. E. Kostylev, and Y. Wu, “Sediment transport and development of banner banks and sandwaves in an extreme tidal system: Upper Bay of Fundy, Canada,” *Continental Shelf Research*, vol. 83, pp. 86–107, 2014, doi: 10.1016/j.csr.2013.08.007.

B. W. Borsje, W. M. Kranenburg, P. C. Roos, J. Matthieu, and S. J. M. H. Hulscher, “The role of suspended load transport in the occurrence of tidal sand waves,” *Journal of Geophysical Research: Earth Surface*, vol. 119, pp. 701–716, 2014, doi: https://doi.org/10.1002/2013JF002828.

K. R. Dyer and D. A. Huntley, “The origin, classification and modelling of sand banks and ridges,” *Continental Shelf Research*, vol. 19, no. 10, pp. 1285–1330, 1999, doi: 10.1016/S0278-4343(99)00028-X.

K. J. J. Van Landeghem, J. H. Baas, N. C. Mitchell, D. Wilcockson, and A. J. Wheeler, “Reversed sediment wave migration in the Irish Sea, NW Europe: A reappraisal of the validity of geometry-based predictive modelling and assumptions,” *Marine Geology*, vol. 295–298, pp. 95–112, 2012, doi: 10.1016/j.margeo.2011.12.004.

D. A. V. Stow, F. J. Hernández-Molina, E. Llave, M. Sayago-Gil, V. Díaz-del Río, and A. Branson, “Bedform-velocity matrix: The estimation of bottom current velocity from bedform observations,” *Geology*, vol. 37, no. 4, pp. 327–330, 2009, doi: 10.1130/G25259A.1.

K. J. J. Van Landeghem, A. J. Wheeler, N. C. Mitchell, and G. Sutton, “Variations in sediment wave dimensions across the tidally dominated Irish Sea, NW Europe,” *Marine Geology*, vol. 263, no. 1–4, pp. 108–119, 2009, doi: 10.1016/j.margeo.2009.04.003.

P. Blondeaux and G. Vittori, “A model to predict the migration of sand waves in shallow tidal seas,” *Continental Shelf Research*, vol. 112, pp. 31–45, 2016, doi: 10.1016/j.csr.2015.11.011.

I. Fairley, I. Masters, and H. Karunarathna, “Numerical modelling of storm and surge events on offshore sandbanks,” *Marine Geology*, vol. 371, pp. 106–119, 2016, doi: 10.1016/j.margeo.2015.11.007.

I. Colosimo, P. L. M. de Vet, D. S. van Maren, A. J. H. M. Reniers, J. C. Winterwerp, and B. C. van Prooijen, “The impact of wind on flow and

	sediment transport over intertidal flats," *Journal of Marine Science and Engineering*, vol. 8, no. 11, pp. 1–26, 2020, doi: 10.3390/jmse8110910.
Geological history of the Irish Sea	C. D. Clark, A. L. C. Hughes, S. L. Greenwood, C. Jordan, and H. P. Sejrup, "Pattern and timing of retreat of the last British-Irish Ice Sheet," *Quaternary Science Reviews*, vol. 44, pp. 112–146, 2012, doi: 10.1016/j.quascirev.2010.07.019. D. Praeg, S. McCarron, D. Dove, C. Ó Cofaigh, G. Scott, X. Monteys, L. Facchin, R. Romeo, and P. Coxon, "Ice sheet extension to the Celtic Sea shelf edge at the Last Glacial Maximum," *Quaternary Science Reviews*, vol. 111, pp. 107–112, 2015, doi: 10.1016/j.quascirev.2014.12.010. S. L. Ward, S. P. Neill, J. D. Scourse, S. L. Bradley, and K. Uehara, "Sensitivity of palaeotidal models of the northwest European shelf seas to glacial isostatic adjustment since the Last Glacial Maximum," *Quaternary Science Reviews*, vol. 151, pp. 198–211, 2016, doi: 10.1016/j.quascirev.2016.08.034. D. Small, R. K. Smedley, R. C. Chiverrell, J. D. Scourse, C. Cofaigh, G. A. T. Duller, S. McCarron, M. J. Burke, D. J. A. Evans, D. Fabel, D. M. Gheorghiu, G. S. P. Thomas, S. Xu, and C. D. Clark, "Trough geometry was a greater influence than climate-ocean forcing in regulating retreat of the marine-based Irish-Sea Ice Stream," *Bulletin of the Geological Society of America*, vol. 130, no. 11–12, pp. 1981–1999, 2018, doi: 10.1130/B31852.1.

Sediment transport pathways	K. J. J. Van Landeghem, K. Uehara, A. J. Wheeler, N. C. Mitchell, and J. D. Scourse, “Post-glacial sediment dynamics in the Irish Sea and sediment wave morphology: Data-model comparisons,” *Continental Shelf Research*, vol. 29, no. 14, pp. 1723–1736, 2009, doi: 10.1016/j.csr.2009.05.014. R. Holmes and D. R. Tappin, “DTI Strategic Environmental Assessment Area 6, Irish Sea, seabed and surficial geology and processes.” British Geological Survey Commissioned Report, CR/05/057, p. 82, 2005. [Online]. Available: http://nora.nerc.ac.uk/11259/ M. A. Johnson, N. H. Kenyon, R. H. Belderson, and A. H. Stride, “Sand transport,” in *Offshore Tidal Sands: Processes and Deposits*, A. H. Stride, Ed. Chapman and Hall, 1982, pp. 58–94. doi: 10.1007/978-94-009-5726-8_4. M. Z. Li, C. G. Hannah, W. A. Perrie, C. C. L. Tang, R. H. Prescott, and D. A. Greenberg, “Modelling seabed shear stress, sediment mobility, and sediment transport in the bay of fundy,” *Canadian Journal of Earth Sciences*, vol. 52, no. 9, pp. 757–775, 2015, doi: 10.1139/cjes-2014-0211. M. A. F. Knaapen, “Sandwave migration predictor based on shape information,” *Journal of Geophysical Research: Earth Surface*, vol. 110, no. 4, pp. 1–9, 2005, doi: 10.1029/2004JF000195. J. J. Daniell, “Bedload parting in western Torres Strait, northern Australia,” *Continental Shelf Research*, vol. 93, pp. 58–69, 2015, doi: 10.1016/j.csr.2014.11.008.

P. E. Robins, S. P. Neill, M. J. Lewis, and S. L. Ward, “Characterising the spatial and temporal variability of the tidal-stream energy resource over the northwest European shelf seas,” *Applied Energy*, vol. 147, pp. 510–522, 2015, doi: 10.1016/j.apenergy.2015.03.045.

J. M. Horrillo-Caraballo, Y. Yin, I. Fairley, H. Karunarathna, I. Masters, and D. E. Reeve, “A comprehensive study of the tides around the Welsh coastal waters,” *Estuarine, Coastal and Shelf Science*, vol. 254, p. 107326, 2021, doi: 10.1016/j.ecss.2021.107326.

R. D. Pingree and D. K. Griffiths, “Sand transport paths around the British Isles resulting from M2 and M4 tidal interactions,” *Journal of the Marine Biological Association of the United Kingdom*, vol. 59, no. 2, pp. 497–513, 1979, doi: https://doi.org/10.1017/S0025315400042806.

P. T. Harris, C. B. Pattiaratchi, M. B. Collins, and R. W. Dalrymple, “What is a bedload parting?,” in *Tidal signatures in modern and ancient sediments*, B. W. Flemming and A. Bartholoma, Eds. 1995. doi: 10.1002/9781444304138.ch1.

R. H. Belderson, “Bed-load partings and convergences at the entrance to the White Sea, U.S.S.R., and between Cape Cod and Georges Bank, U.S.A.,” *Marine Geology*, vol. 28, no. 1–2, pp. 65–75, 1978.

J. D. Rosati, “Concepts in sediment budgets,” *Journal of Coastal Research*, vol. 21, no. 2, pp. 307–322, 2005, doi: 10.2112/02-475A.1.

Estimation of ADCP-derived suspended solids concentration in an offshore setting.	J. Mullison, "Backscatter estimation using broadband acoustic doppler current profilers - updated," in *ASCE Hydraulic Measurements & Experimental Methods Conference*, 2017. M. Guerrero, N. Rüther, S. Haun, and S. Baranya, "A combined use of acoustic and optical devices to investigate suspended sediment in rivers," *Advances in Water Resources*, vol. 102, pp. 1–12, 2017, doi: 10.1016/j.advwatres.2017.01.008. M. N. Landers, T. D. Straub, M. S. Wood, and M. M. Domanski, "Sediment acoustic index method for computing continuous suspended-sediment concentrations," in *U.S. Geological Survey Techniques and Methods: Book 3, Applications of Hydraulics*, U.S. Department of the Interior; U.S. Geological Survey, 2016, p. 63. doi: http://dx.doi.org/10.3133/tm3C5. A. Dwinovantyo, H. M. Manik, T. Prartono, and S. Susilohadi, "Quantification and Analysis of Suspended Sediments Concentration Using Mobile and Static Acoustic Doppler Current Profiler Instruments," *Advances in Acoustics and Vibration*, vol. 2017, 2017, doi: 10.1155/2017/4890421. R. J. Urick, *Principles of underwater sound*. New York: McGraw-Hill, 1975.

3 The Irish Sea Bed Load Parting Zone: Is it a mid-sea hydrodynamic phenomenon or a geological theoretical concept?

The Irish Sea Bed Load Parting Zone: Is it a mid-sea hydrodynamic phenomenon or a geological theoretical concept?

Shauna Creane[1,2,3], Michael O'Shea[1,2], Mark Coughlan[4,5,3], Jimmy Murphy[1,2]

[1]School of Civil & Environmental Engineering, University College Cork, College Road, T12 K8AF Cork, Ireland; shauna.creane@ucc.ie (S.C.); michaeloshea@ucc.ie (M.O.); jimmy.murphy@ucc.ie (J.M.)

[2]SFI Research Centre for Energy, Climate and Marine (MaREI), Beaufort Building, Environmental Research Institute, University College Cork, Ringaskiddy, P43 C573 Cork, Ireland

[3]Gavin and Doherty Geosolutions, Unit A2, Nutgrove Office Park, Rathfarnham, D14 X627 Dublin, Ireland

[4]School of Civil Engineering, University College Dublin, Belfield, D04 N2E5 Dublin, Ireland; mark.coughlan@icrag-centre.org (M.C.)

[5]SFI Research Centre for Applied Geosciences (iCRAG), O'Brien Centre for Science East, University College Dublin, D04 N2E5 Dublin, Ireland

Abstract

On tidally-dominated shelf seas, hydrodynamic flow exerts shear stress on the seabed, inducing sediment transport and seabed evolution. Net sediment transport pathways and associated bed load partings zones (the 'head' of sediment transport pathways) are important elements of this sediment dispersal process. A robust comprehension of these dynamics on a local and regional scale are crucial for a range of offshore activities, including the rapidly

growing offshore renewable energy industry. Previous studies infer a bedload parting zone (BLP) in the central Irish Sea, yet this predominantly bedform-derived BLP remains to be fully supported by underlying hydrodynamics. This study reviews how sediment transport pathways in the Irish Sea are defined to date, investigates whether a hydrodynamic regime capable of supporting this inferred BLP exists, and if proven, aims to elucidate its origin.

Tidal asymmetry indicators, derived from the phase and amplitude relationships of numerically modelled M_2 and M_4 tidal constituents, reveal the existence of a symmetrical tidal zone in the proximity of the inferred BLP. New numerically modelled residual tidal current and bed shear stress vectors reinforce the presence of this distinct tidal character change and further reveal strong opposing tidal flows extending from this region, thus supporting the presence of a tidal flow capable of producing divergent bedload patterns. Analysis of tidal propagation through the Irish Sea Basin concludes that the origin of the BLP is mainly attributed to the intersection of the north and south tidal fronts at an inclined angle due to Coriolis Forcing and coastline interactions. Minor factors impacting the shape and location of the BLP are the change in tidal character at (a) abrupt bathymetry changes, (b) headlands and intricate coastline topography, and (c) large-scale constrictions. Further investigation into localised morphodynamics is needed. These findings are highly valuable to efficient marine spatial planning, underpinning a movement towards a climate resilient economy. The integrated approach used in this body of work can be applied to tidally-dominated continental shelves beyond the Irish Sea.

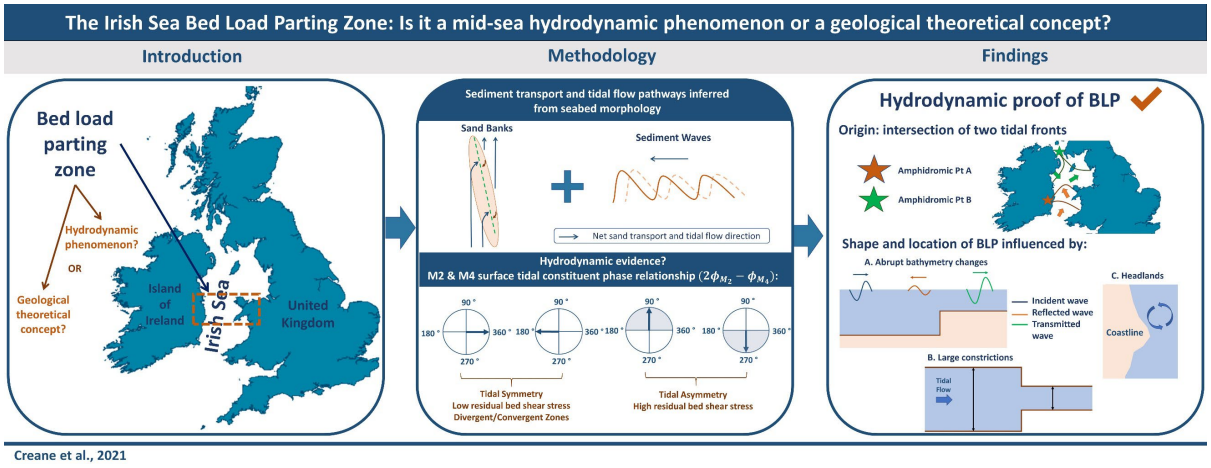


Figure 3-1 Graphical Abstract for the peer-reviewed paper 'The Irish Sea Bed Load Parting Zone: Is it a mid-sea hydrodynamic phenomenon or a geological theoretical concept?' [1]

3.1 Introduction

The recent increase in activity related to offshore infrastructure developments in the Irish Sea has led to a greater focus on seabed morphodynamics and sediment mobility. With 2030 offshore wind capacity targets at 57 GW (combined UK and Republic of Ireland) [1]–[3], shallow water depths (20 – 60 m) particularly in the western Irish Sea provide suitable conditions to optimise fixed-bottom offshore wind energy plants [4]. Potentially inhibiting these offshore infrastructure developments are the challenging ground conditions present through the existing complex hydrodynamic and morphodynamic regime. Hydrodynamic forces acting on a cohesionless seabed induces bedload sediment transport and seabed evolution. Regions of high seabed mobility and intricate seabed topography generates high potential for free-spanning and burial of cables and pipelines [5], [6], and scour formation around turbine foundations [7], [8], inherently leading to critical infrastructural instability. According to Stehly and Beiter [9], substructure and foundation attribute 10% of the Levelised Cost of Energy (LCOE) of fixed-bottom offshore wind farms, and so they present a significant engineering cost that needs to be safe-guarded. Additionally, a qualitative understanding of

seabed dynamics is paramount for key economic exploits such as a) the need to monitor volume of marine aggregates [10], b) the location and evolution of benthic habitats directly impacting fisheries [11], [12], c) the dispersal of dredged material, and d) the impact of coastal flooding and erosion protection measures [13], [14]. The heightened demand on the seafloor for offshore activities calls for efficient and progressive marine spatial planning. A firm understanding of the hydrodynamics underpinning seabed evolution is paramount to facilitate this progression.

Bed load parting zones are areas of maximum bed shear stress [15], [16] that mark the 'head' of divergent sediment transport pathways, hence are important components of the sediment dispersal regime on tidally-dominated continental shelves. The current widely accepted conceptual model, first introduced by Stride [17], [18], Belderson and Stride [19] and Kenyon and Stride [20], builds upon the concept that tidal current velocity decreases along a pathway from this region, along which sand particles are transported. An ideal sequence of bedforms associated with this reduction in current velocity is presented by Belderson and Stride [19], consisting of scour zones (winnowed lag gravel deposits and/or exposed bedrock), sand ribbons, sand waves and sand banks, and finally mud deposits. Current velocity and sediment supply conditions determine whether this full progressive bedform pattern is present. Bed load partings have been described in both semi-diurnal and mixed tidally-dominated shelf seas, including the western European shelf sea [15], Cape Cod (US), White Sea (Russia) [21], and Torres Strait (Australia) [22]. Understanding the hydrodynamics driving the origin and location of these zones is imperative to elucidating present day sediment dispersal patterns across tidally-dominated shelf seas. This knowledge will form a foundation for future predicted changes in the sediment dispersal regime under potential sea level rise due to climate change.

The general dynamics of the tidal regime in the Irish Sea is well known, for example, the seasonal formation of the Western Irish Sea Gyre [23]–[25], and the nature of tidal resonance in the Bristol Channel [26]. However, there is little understanding of the interaction between hydrodynamics and seabed morphodynamics in the central Irish Sea where a bed load parting zone is inferred [27]. The bed load parting zone and subsequent divergent net sand transport pathways in the Irish Sea have previously been defined predominately through bedform geometric parameters [27], [28]with a lesser use of modelled tidal induced bed shear stress [16]. However, significant inconsistencies exist between these theoretical pathways in relation to the current understanding of underlying hydrodynamics. Scientific validation of these pathways under present day conditions have yet to be fully supported. Without the support of physical processes capable of driving and underpinning this inferred bed load parting zone, this dynamic phenomenon is under threat of becoming a redundant concept.

This paper will address the following:

a) Review how the bed load parting zone (BLP) is characterised and defined in the central Irish Sea;
b) Discuss whether the present-day hydrodynamic regime supports this BLP and the resulting divergent net sand transport pathways;
c) If so, elucidate why the BLP develops at this location.

3.2 Study Area

Located on the north-western European Shelf, the Irish Sea is a semi-enclosed body of water connected to the Atlantic Ocean by two openings; the North Channel and St Georges Channel (Figure 3-2). The circulation pattern in the Irish Sea is driven by tidal forcing, wind shear stress and baroclinic flow, which in turn is a major driver of seabed mobility, sediment distribution

and morphodynamics [24], [29]–[31]. Due to a complex basin geometry, rapidly changing bathymetry and an intricate coastline, a complicated tidal regime exists. The area of the central and southern Irish Sea bound by the 52.2 to 53.5 latitudes is the focus area of this study which incorporates the inferred bed load parting zone and the degenerate amphidromic point located on the east coast of Ireland (Figure 3-2).

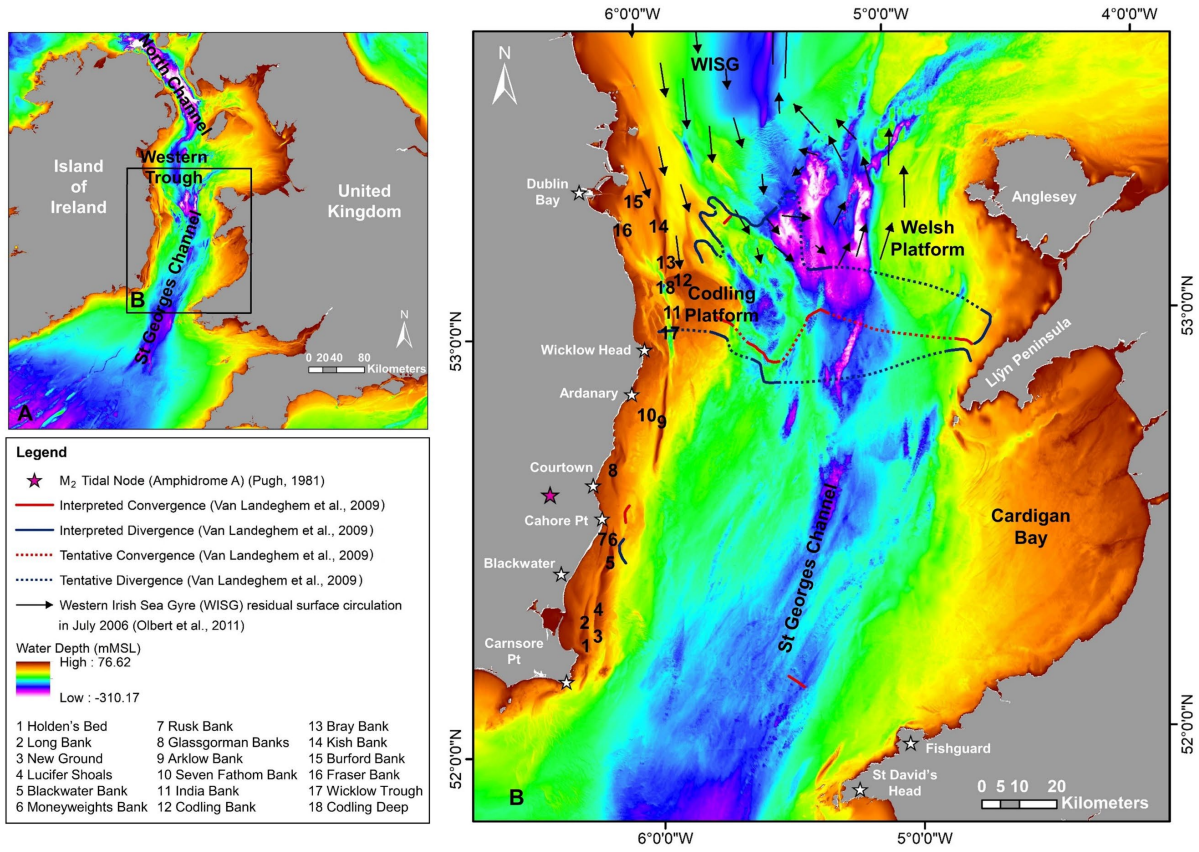


Figure 3-2 Irish Sea bathymetry with water depth referenced to mean sea level (MSL) within the study area. Main bathymetric highs and lows are indicated. Geographic locations and oceanographic features mentioned in the text are also shown. The location of the bedform derived bed load parting zone, defined by Van Landeghem et al [27]*, characterised by one main*

sediment transport convergence zone and two divergent zones, is indicated. Bathymetric metadata and Digital Terrain Model (DTM) data products have been derived from the EMODnet Bathymetry portal - http://www.emodnet-bathymetry.eu.

3.2.1 Geological History

The present-day seabed morphology of the Irish Sea has been largely sculpted by ice stream advance and retreat during the last glaciation, followed by marine transgression establishing present-day hydrodynamics which reworked much of the glacial and post-glacial sediments. Changes in tidal current velocities and relative sea level (RSL) during this post-glacial marine transgression are two fundamental environmental factors to understanding present-day seabed morphology in the Irish Sea. The Last Glacial Termination is the period of onset of Irish Sea Ice Sheet (ISIS) deglaciation off the north-western European continental shelf through to onset of the Holocene [32]. This period is associated with ice-marginal episodic re-advance during overall deglaciation (Clogher Head Stadial and Killard Stadial), streamlining, and drumlin formation [33]–[35]. Oscillations in ice sheet dynamics analysed by numerous studies [35]–[38] highlight the complexity of ice margin retreat through Irish Sea Basin. This time period in the Irish Sea Basin is associated with unique erosional and depositional processes [39], [40], and an abundance of sediment supply. In order to produce a local accumulation of sediment during this period, a hydrodynamic and sediment regime must exist so that there is a higher sediment input over sediment output into the local system. According to Dyer and Huntley [41], the most common situations for regional sand accumulation are; a reversal in sand transport direction involving bed-load convergence, or a reduction in bed shear stress along a transport path until threshold motion is reached. Evidence of a complex, highly variable post glacial hydrodynamic regime, and reversals in peak bed shear stress directions over time, especially in the south and central Irish Sea, is highlighted by numerous paleo-tidal modelling studies [42]–[45]. This combined with an abundant sediment supply support the

presence of an adequate hydrodynamic and sediment regime for submarine bedform (e.g. sediment bank) formation during this time period.

3.2.2 Present day sediment distribution

Seabed sediment distribution of the Irish Sea has been characterised by multiple studies [27], [46]–[51]. The southern part of the Irish Sea is dominated by coarse, non-cohesive sands and gravels (Figure 3-3). In regions where sediment supply is limited, the upper mobile layer of Holocene sediments may be limited or absent resulting in the exposure of the Pleistocene glacial till, or rarely exposed bedrock. In areas of high sediment supply, a transition from coarse-lag gravels and gravelly sands into thick mobile sand sheets (up to 40 m thick) are evident. The transition into cohesive muds is evident in parts, especially around the Western Irish Sea Mud Belt, reflecting changes in current flow dynamics and settling velocities to a low energetic environment [52]–[55].

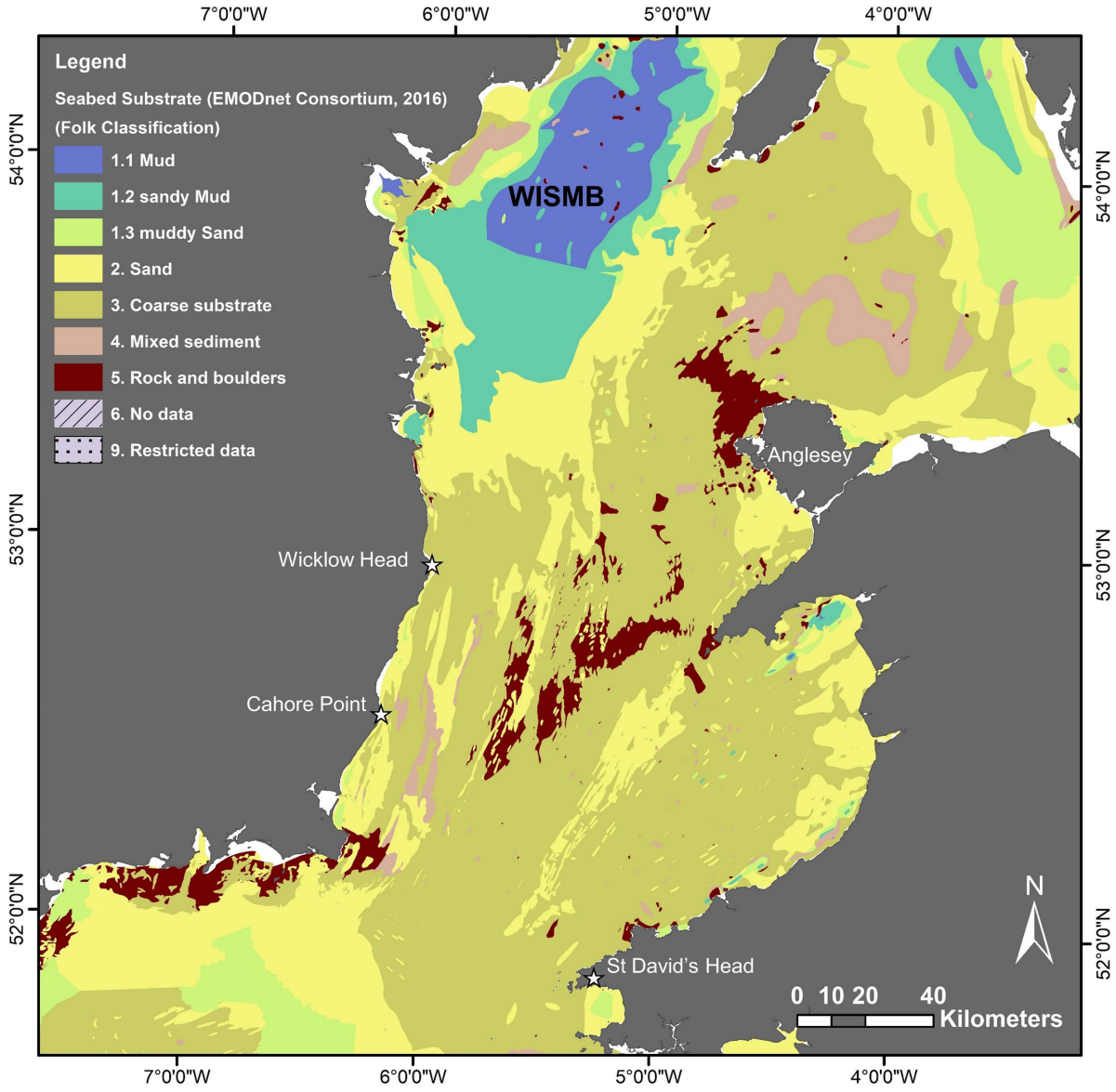


Figure 3-3 Sediment distribution across the Irish Sea and the location of the Western Irish Sea Mud Belt (WISMB). Information contained here has been derived from data that is made available under the European Marine Observation Data Network (EMODnet) Seabed Habitats initiative (http://www.emodnet-seabedhabitats.eu/), financed by the European Union under Regulation (EU) No 508/2014 of the European Parliament and of the Council of 15 May 2014 on the European Maritime and Fisheries Fund.

3.2.3 Present day seabed morphology

Due to the highly dynamic, complex nature of hydrodynamics across the Irish Sea, a huge variety of bedforms develop (Figure 3-4) [11], [34], [48], [51], [53], [56]–[58]. Two main

categories of submarine geological features have been described by Stow et al [59]; (1) Linear bedforms that develop elongated and parallel to flow direction, and (2) transverse bedforms which are regular undulating features occurring perpendicular to flow. To date, the plan- and cross-sectional analysis of sediment banks (linear bedforms) and sediment waves (transverse bedforms) are used to define bed load transport pathways in the Irish Sea and are so paramount to understanding seabed evolution over time.

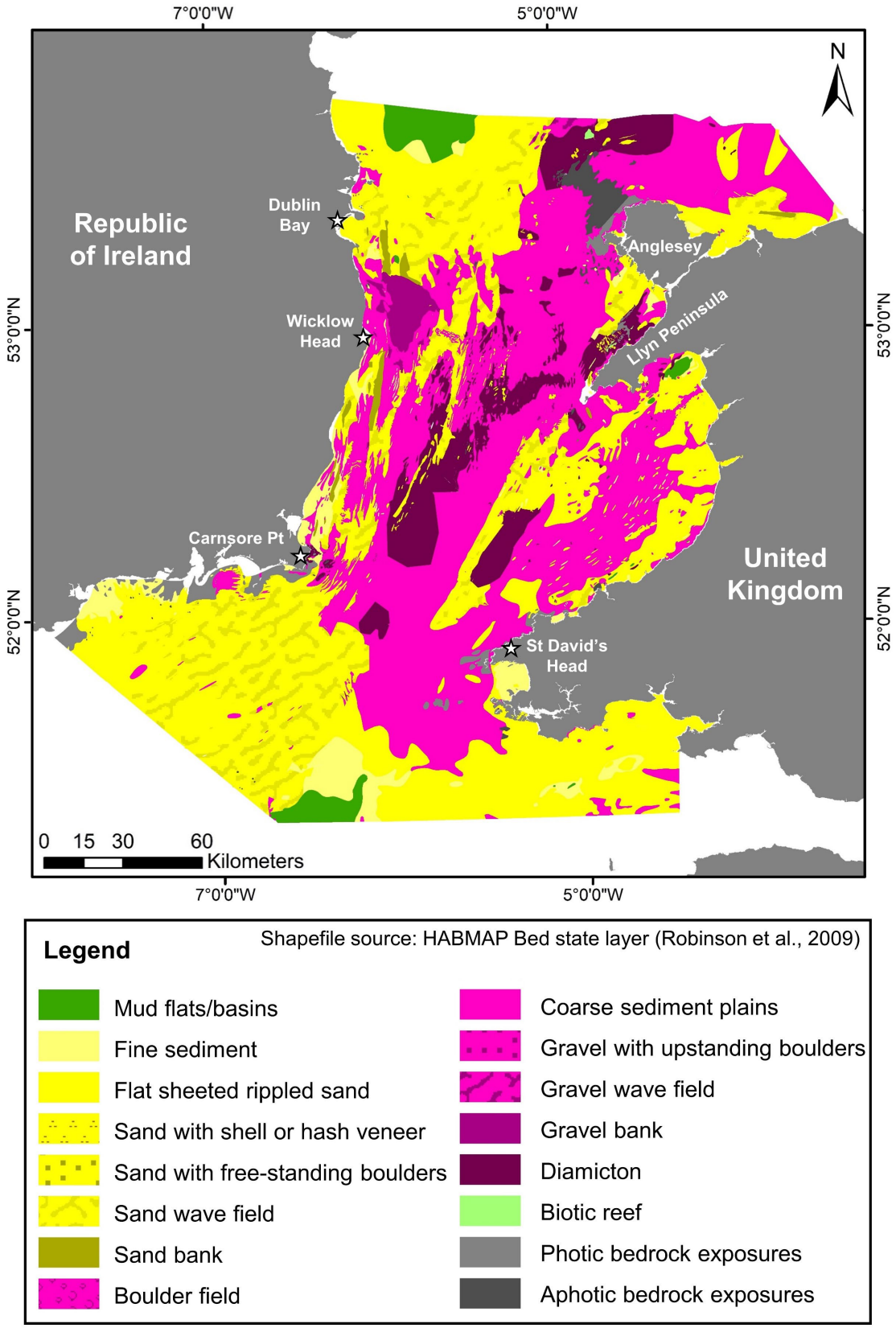


Figure 3-4 Distribution of bedforms across the southern Irish Sea. The dataset presented was developed by the HABMAP project (Habitat Mapping for Conservation and Management of the Southern Irish Sea) [11].

3.2.3.1 Sediment waves

Sediment waves are prominent transverse bedforms in the south-western Irish Sea (Figure 3-4). An extensive study has been undertaken by Van Landeghem et al [57], using a classification scheme modified from Ashley [60] and Berne et al [61], to characterise the variations of sediment wave geometries across the Irish Sea shelf. These flow-transverse bedforms were found at a wide range of shapes and sizes and are exposed to a multitude of environmental factors such as highly variable sediment composition and varying water depths (some up to 179 m deep). Transverse progressive sediment waves were found in single or compound form, occurring isolated or in sediment wave assemblages. These were in either two-dimensional or three-dimensional patterns. Large (0.44 – 2.8 m high; 10 – 100 m spacing), trochoidal (nearly symmetrical to symmetrical: see Van Landeghem et al [57]) waves were identified either isolated or in a regularly spaced sediment wave assemblage. Barchan dunes (crescent-shaped: see Couldrey et al [62]) were the last type identified, located in the St Georges channel. Analysis of statistics derived from their two-dimensional profiles supports the concept that sediment waves are hydrodynamically analogue features however site-specific predictability of their geometric characteristics remains poor [57].

Mathematical modelling studies [63] supports the idea that transverse bedforms in tide-dominated areas arise from a fundamental instability of the flat seabed subject to tidal currents, where as a result, sediment transport converge towards the crest of seafloor irregularities [64]–[66]. The growth mechanism of these bedforms remains to be fully understood, however, under uni-directional flow conditions, sediment transport is found to be dominantly in the direction of asymmetry [67]. Johnson et al [28] supports this statement to be mostly true under bi-directional flow. Numerous studies have used this concept to

derive net sand transport pathways [27], [28], [68], [69]. Most recently, Van Landeghem et al [27] uses sediment wave derived statistics to inform residual bed stress directions and bed load transport pathways in the central Irish Sea. This will be discussed further in section 3.3.1.

These bedforms have also been studied to estimate migration rates through geometric predictions [58], [69]–[71] and through mathematical modelling using eddy viscosity and bed shear stress parameters [66], [72]. A study [58] that uses time-lapse bathymetry data to analyse sediment wave migration challenges the previous assumption that bedform migration is dominantly in the direction of asymmetry. A sand wave is symmetrical when the difference between the length of the gentle slope and the length of the steep slope, divided by the total length of the given sand wave is equal to zero. It is fully asymmetrical when equal to 1 [73]. Observations include; a) reversals in sediment wave asymmetry over time, and b) counter-current bedform migration. These controversial findings induce high caution on the use of sediment wave geometric parameters from a single snapshot in time to predict sediment wave mobility, thus bedload transport pathways.

As noted in section 3.2.1, in natural environments, asymmetry of modern sediment waves may not always be the result of present-day hydrodynamics but originate from periods of lower sea levels and higher current velocities [27], [74], [75]. For very large (> 2.8 m high; > 100 m spacing) [57], [60], [61] moribund sediment waves in the Irish Sea (some reaching 36 m high), present-day energy conditions have been considered inadequate to produce such significant growth [27]. It is suggested that these morphological features are remnants of stronger tidal flows [42]–[45], or glaciomarine deposits related to marine transgression post Last Glacial Maximum (LGM) [27], [47], [48], [76], [77].

3.2.3.2 Sediment Banks

Sediment banks are widespread across the European continental shelf, having formed under a variety of conditions [41], [78], [79]. In the western Irish Sea, a series of coast-parallel bedforms are located in approximately 20 – 40 m water depth, rising to only a couple of metres below sea level (Figure 3-2; Figure 3-4). These elongated ridges have been used to inform regional sediment transport pathways and to indicate and/or confirm BLP zones (e.g. Southern Bight of the North Sea [80] mainly through analysis of admiralty charts and early echo sounding technologies [28], [68], [81]. A variety of studies characterise these sandbanks as being 'active', displaying a highly mobile top layer of surficial sediments [48], [56], [82], however, there is a significant paucity of high spatial and temporal resolution sand bank morphodynamic and seabed stability studies under present day hydrodynamics. These complex bathymetries create divergence from the net northward flow and increase the complexity of sediment transport pathways in this region, yet the extent of this divergence and driving factors is poorly understood.

It has been previously understood that open linear ridges are aligned parallel to the residual tidal current [83], however subsequent studies involving numerical modelling and geophysical data interpretation reveal an oblique orientation to peak tidal flow [84]–[86]. This orientation was found to be generally from 7 ° to 15 ° and can either be an anticlockwise or clockwise deflection. In the northern hemisphere, Coriolis Force is thought to be a controlling factor where sand banks orientate anticlockwise [28], [41], however this has yet to be found true in the Southern Hemisphere. Exceptions to this concept has been found through field and numerical modelling studies [28], [87]. The principle of sand transport rate lagging behind a change of current speed during a tidal cycle, described in Johnson et al [28], has been

described as a factor influencing this oblique alignment of the bedform axis to the peak tidal current.

This oblique alignment exposes one side of the bank to the flood tidal phase and leaves the other side exposed to the ebb phase. This generates a flood and ebb dominance in terms of sediment transport on either flank of the ridge [88]. On active sand banks, this is generally reflected in the sand wave asymmetry where sand wave asymmetry faces opposite directions on either side of the bank [41], [89]. Furthermore, from the bank base to the bank crest, sand wave crest alignment changes orientation towards the crest. An implication of convergence at the crest has been recognised by Caston [90] where sand crest angles were found to be 40 ° on the gentle slope but 30 ° on the steeper slope. Identification and analysis of symmetrical sand waves at the ends of the bank have led to the conclusion of sediment circulation around and over the ridges is what maintains them [90], [91]. Huthnance [92] supports the observations by Caston [90] by providing an explanation for the development and maintenance of sandbanks through fluid-dynamics. On the other hand, Johnson et al [28] suggests that circulation of water around the bank does not imply a closed sand circulation pattern. Most recently, modelled residual currents and their vorticity reveals potential circulatory flow patterns around sand banks in the Irish Sea [31]. Residual gyre patterns around headlands and sandbanks result from the transfer of vorticity from the tide to residual flow [31], [93], [94]. Evidence of strong positive vorticity over sandbanks and negative vorticity over associated channels off the east coast of Ireland (e.g. Arklow Bank) indicate relatively strong residual gyre patterns in this region [31]. This can be used as a diagnostic tool to infer sediment transport trends [31].

Where sand waves on sand banks express local sand transport dynamics, the regional scale net transport directions can be inferred by the interpreting the plan view outline of the sand bank where the end pointing in the direction of the net sand transport direction is generally long and pointed but the opposite end can be wider and more rounded [28]. Zimmerman [94] cautions this technique by arguing that the feedback mechanism within the current flow-bedform interaction should be considered, whereby current flow properties directly influence the growth and development of seabed morphological features and resulting bedforms simultaneously alter and constrain flow dynamics above. This is particularly important in the Irish Sea where active morphological features such as sandbanks and sand waves are composed of mobile sediments. The importance of this feedback mechanism within this hydrodynamic-morphodynamic coupled system is confirmed by sandbank evolution studies [95], [96]. Consequently, attentiveness has been recommended surrounding the use of single snapshot bathymetric surveys to predict tidal residuals. This technique is best used as an indicative tool [31].

3.2.3.3 Sedimentary plateaus and deeps

A series of troughs and channels add to the intricate morphology of the Irish Sea Basin [47]. The St Georges Channel is the main offshore bathymetric deep in the south and central Irish Sea, extending approximately 160 km long and 170 m deep, connecting with the North Channel via the Western Trough [34], [47] (Figure 3-2). In the central Irish Sea, the narrowing and notable deepening of the St. Georges Channel is bordered by abrupt changes in water depth in the form of protruding sedimentary plateaus. On the western edge of this trough, a plateau of relatively shallow bathymetry (< -20 mMSL) extends eastwards from the Codling Bank, henceforth will be referred to as the Codling Platform. Similarly, the Welsh Platform

protrudes south-westwards from Anglesey at a similar latitude. Along the eastern boundary of the Codling Platform and isolated from the main St Georges Channel are a suggested 'linked-valley' system [40] comprising Codling Deep and Wicklow Trough (Figure 3-2). These features are understood to constrain tidal flow and so have been assessed previously for tidal energy potential [54]. The seafloor of these deeps comprise a complex morphology of coarse lag deposits (sand to boulder), sediment wave fields, and irregular transverse and sub parallel ridges [40], [97].

3.2.4 Hydrodynamic Regime

Tidal flow is the main physical driver of seabed mobility in the Irish Sea. The propagation of tidal waves from the deep ocean into shallow shelf seas is well documented [29], [31], [98], [99]. The flood tidal flow enters the Irish Sea from the Atlantic Ocean through the St Georges Channel and the North Channel moving northwards and southwards respectively. They intersect on the east and west side of the Isle of Man, resulting in tidal mixing and complex circulation patterns i.e. the Western Irish Sea Gyre (Figure 3-2) [25], [100]. The ebb tidal phase occurs in the reverse direction. Residual flow in the Irish Sea is northward [31], [101]. Tidal current vectors in the Irish Sea are dominated by the M_2 and S_2 constituents, whereby M_2 displays a greater dominance. These are predominately quasi-symmetrical and rectilinear in shape, indicating a rapid change between flood and ebb current flows [31], [102]. However, circular ellipses are present in fewer localities, signalling an almost constant tidal current speed as the current direction changes, for example, east and south of Isle of Man, the entrance to the Bristol Channel and areas of Cardigan Bay [31], [102]. This basic semi-diurnal tide period is 12 hours 25 minutes underlain by fortnightly (springs/neaps), monthly, six monthly (equinoctial springtides) and yearly time scale tidal cycles [103].

In addition to this complex tidal regime, a degenerate amphidromic point has been pinpointed on the east coast of Ireland, geographically located between Cahore Point and Courtown (Figure 3-2). Paleo tidal modelling by Ward et al [45] details the change in tidal amplitudes through the north-western European shelf seas from 21 ka BP (ka BP = thousand years before present) to present, from which the dynamic nature of this degenerate amphidrome is evident. During deglaciation, the degenerate amphidrome is simulated to move progressively northwards, as the Irish Sea is flooded, until 12 ka BP. Beyond 12 ka BP, it moved progressively eastwards until reaching its current position on the south-east coast of Ireland. Pugh [29] also proves the location of the amphidromic point to be highly variable over a spring-neap cycle, displaying a daily movement of 70 km in a direction perpendicular to NNE-SSW trending St. Georges channel axis. The amphidromic point tends to be degenerate up to 40 km inland during spring tides but migrates into the Irish Sea during neap tides. Tidal ranges increase from this degenerate amphidromic point in the Irish Sea [30], [31]. Mean spring peak tidal flow is approximately 1 m/s in the southwestern Irish Sea with regions offshore Wicklow Head and Carnsore Point displaying relatively higher velocities (exceeding 2 m/s) [30], [54]. On a local scale, complex flow patterns occur commonly as a result of complex local bathymetric changes, resulting in flow separation, which create transient eddies and vortices liable to trap sediments and form seabed sedimentary structures [104]. This tidal distortion is mainly due to propagation of tidal currents into shoaling water [31], [105]–[107].

The Western Irish Sea Gyre (WISG) (Figure 3-2) is a dominant oceanographic feature creating a density-driven component to Irish Sea circulation. Numerous studies have detailed various aspects of the WISG including mechanism of formation [108], [109], 3-D modelling of flow

circulation [110]–[112], impact of seasonal circulation on transport [23], long term analysis of the flows in relation to climate change [113], and impact of seasonal gyre changes on scour processes [114]. In this region, weak tides and relatively deep waters, up to 100 m, lead to weaker vertical mixing in the water column [109]. As a result, solar heating causes rapid thermal stratification during spring of each year and continually grows in strength into a well-formed two-layer structure until a rapid linear decline at the beginning of August [25]. Due to persistent weak tidal velocities and solar heating, a dome of cold water is trapped beneath a warm top layer in the water column. On the flanks of this dome, the change between tidally mixed waters and stratified water column occurs rapidly with sharp horizontal density gradients extending over 10 km. The sharpest tidal mixing fronts are found to be located at the southern and eastern flanks. Sharp sloping density gradients causes baroclinicity which provides geostrophic cyclonic surface flow. It has been found that this causes a reversal to the net northward flow to southwards [25]. In addition, seasonal changes effect retention time of materials immensely in this region whereby more material is removed from the Western Irish Sea when stratification is at its strongest [25]. This may have important impact of sediment transport in this local area and the wider Irish Sea.

3.2.4.1 Hydrodynamic influence on seabed mobility in the Irish Sea

A ‘standing wave’ or a ‘symmetrical tide’ system consists of an ebb and flood phase of equal duration and relatively equal velocity strength. In a standing wave system, slack tide coincides with high and low water, and flood and ebb peak current flows occur at mid water. As peak ebb and flood current speeds occur at similar water depths, bed frictional forces of similar strength are exerted over both tidal phases, resulting in no overall sediment transport. In contrast, a progressive wave system or tidal asymmetry is when the ebb and flood tidal phases are of unequal duration [30], [105]. This is the result of wave propagation into shallow water

i.e. along a coastal shelf, approaching sediment banks or shoaling waters [106], [115], [116]. Tidal propagation as a shallow water wave in this instance is a non-linear propagation process whereby the main principles include quadratic bottom friction, convergence and continuity [106], [115], [117], [118]. In progressive wave systems, peak flood and ebb current flows occur at high and low water. Varying water depth between peak flood and peak ebb current flow cause an exertion of enhanced frictional forces on the seabed at low water, resulting in higher flood current velocities in comparison to ebb currents [30]. This results in a higher net sediment transportation in the dominant tidal phase. Many oceanic and shallow shelf environments display a combination of these two classifications i.e. are 'partially-progressive' [30], [31]. Table 3-2 defines the characteristics of each of these classifications according to Ward et al [30].

Table 3-2 Tidal character definition based on the phase difference between high tide and the closest preceding or succeeding peak current flow (m/s), and the areal extent of each regime according to the Irish Sea model presented by Ward et al [30]

Regime	Phase difference (Δ T, hours)	Areal extent of Irish Sea (%) according to Ward et al [30]
Progressive	≤ 1	16
Partially-progressive	1 < Δ T ≤ 2	32
Standing	> 2	52

Tidal distortion is represented in the form of harmonics of single astronomical constituent, for example, M_4 is a quarter-diurnal non-linear harmonic overtide of M_2 [105], [107], [119]. The generation mechanisms of these harmonics have been studied using shallow-water equations [118], and the effect of tidal asymmetry on seabed morphology has been studied on various levels of detail [106], [107], [120]. Previous studies have shown that shallow

systems tend to be flood dominant and deeper systems tend to be ebb dominant [105], [116], [120], [121]. This has a major impact on sediment transport. For example, in a flood dominated tidal asymmetric system where the ebb phase duration is relatively longer, there is an implication of a higher velocity, higher intensity current occurrence during the shorter flood phase [119], [122]. This increased flow velocity in turn exerts higher shear stress forces on the seabed sediment. If this shear stress increases further and incipient motion threshold is exceeded, enhanced bedload sediment transport will follow. Continued increased shear stress will result in resuspension and entrainment of sediment into the water column and transported as suspended load. This leads to a net sediment transport in the flood direction. In ebb dominant conditions, the opposite is found to be true [123]. Alternatively, the longer duration of the ebb or flood phase could cause net sand transport in that direction [28]. However, the latter situation is more common. Clearly, the magnitude of shear stress exerted on the seabed at any point in time, and the duration over which critical shear stress is exceeded are dependent variables of sediment transport [106]. Studies have found that sediment transport is predominately in the direction of the tidal current ellipse [28], [52]. Concurrently, the magnitude of sediment transport depends on the magnitude of current velocity to the third power [124].

3.2.5 Influence of wind-generated waves on seabed mobility in the Irish Sea

Wind-generated waves have a profound influence on coastal flooding, coastal erosion, nearshore sediment transport dynamics and offshore sand bank morphodynamics [125]–[128]. In shallow water, where oscillatory wave motion reaches the seafloor, critical shear stress and the mode of sediment transport is affected. The complex interaction between tidal currents and wind driven flows can specifically have a large impact on residual sediment

transport pathways [129], whereby in regions of low tidal amplitude, even moderate wind speeds can reverse residual tidal flows [22], [130]. Similarly, numerical modelling works reveal that the interaction between storm waves and tidal currents not only increase bed shear stresses on sand banks, resulting in net erosion and sediment transport, but further influence the direction of net sediment transport associated with these bedforms [131]. Nevertheless, tidally-driven flows are revealed to be the dominant physical process driving sediment mobilisation in the Irish Sea, where wave-induced bed shear stress dominance is mainly restricted to < 10 km and < 20 km from the western and eastern coastlines respectively [132]. Consequently, this study does not consider wind-generated waves as a critical factor influencing the development and modification of the bed load parting zone in the Irish Sea.

3.3 Regional net sand transport pathways

The direction of asymmetrical sediment waves and the alignment of sand banks derived from geophysical data interpretation, in combination with tidal current analysis and sediment distribution patterns, has been used to infer residual bed stress directions and broad scale net sand transport pathways in the Irish Sea [27], [28], [47], [68], [81]. This section looks at how these sediment transport pathways in the Irish Sea have been quantified to date.

3.3.1 Bed load transport pathways – current knowledge

Dobson et al [68] illustrates the distribution and orientation of sand waves, sand ribbons and tidal current ridges in the south Irish Sea derived from geological and geophysical data collected in the Irish Sea between 1962 – 1969. The produced map shows clear north-south trending bedforms reflecting tidal current trends in the region (Figure 3-5).

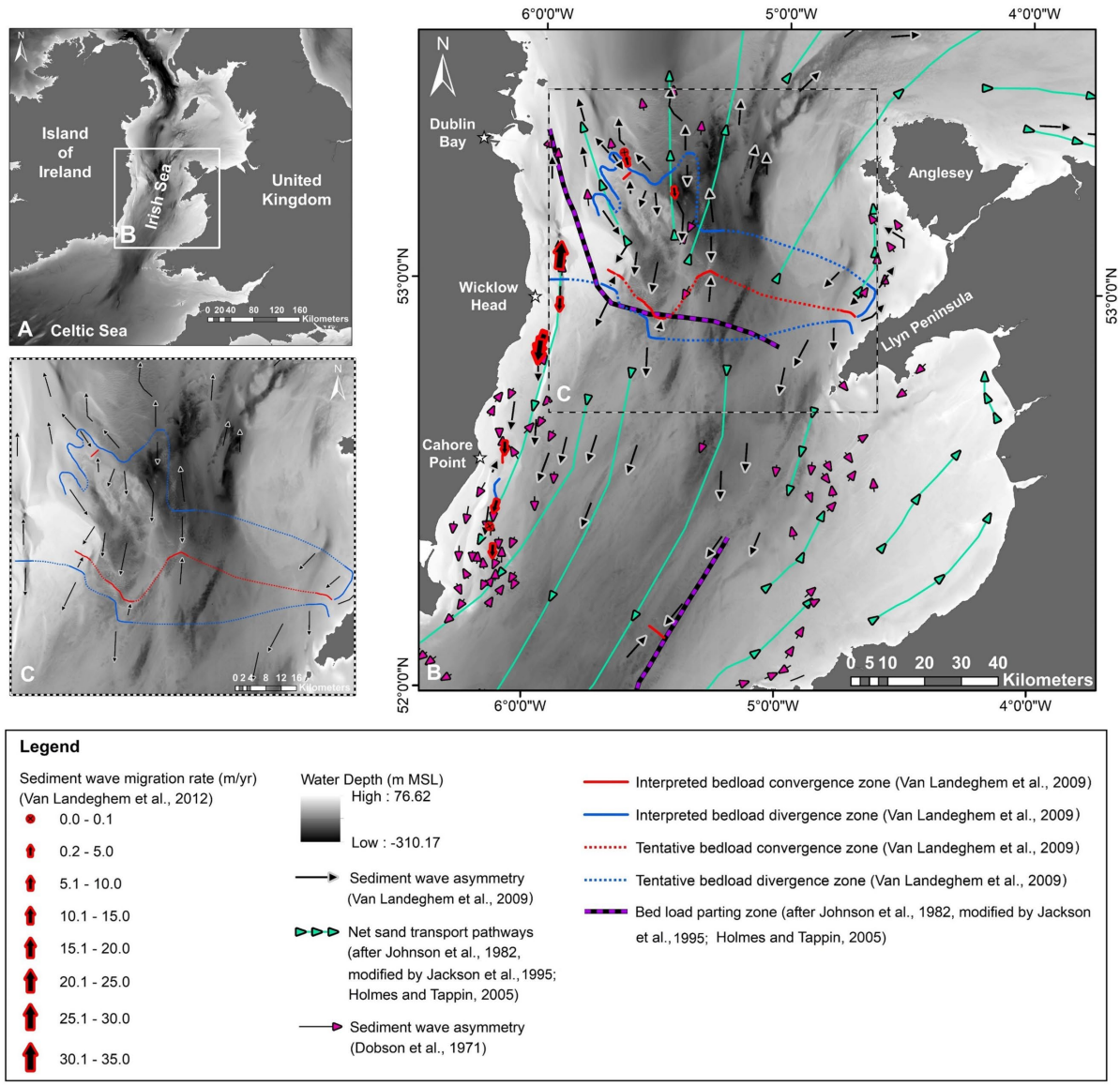


Figure 3-5 Sediment transport pathways in the Irish Sea defined by bedform studies. Bathymetric metadata and Digital Terrain Model (DTM) data products have been derived from the EMODnet Bathymetry portal - http://www.emodnet-bathymetry.eu.

Johnson et al [28] further provides a composite map of all previously published available data to infer regional scale net sand transport directions. The composite map was produced due to the good agreement of seabed evidence with the direction of the stronger tidal flow illustrated on tidal atlases and charts. The location of the bed load parting zone in the western Irish Sea stretches eastwards from the Irish coastline just above Wicklow Head across into the Irish Sea. From this zone, regional scale net sand transport extends southwards out into the

Celtic Sea, and northwards towards Dublin Bay. A strong correlation exists between these net sand transport directions and the numerically modelled maximum bottom shear stress by Pingree and Griffiths [16] however, the exact location of the bed load parting zone (BLP) is not highlighted in the model. Johnson et al [28] provides strong evidence that suggests these net sand transport pathways in offshore locations are mainly due to tidal distortion giving rise to transport in the direction of the stronger of the ebb or flood peak tidal current.

Holmes and Tappin [81] modified these pathways based on data from Pantin [133], Jackson et al [47], Kenyon and Cooper [91] and interpretations from DTI [134] SEA6 survey datasets (Figure 3-5). The principle bed load parting and convergence zones correlate well with early iterations. However, adjustments have been made to the nearshore sand parting zone in the western Irish Sea following interpretations from locations and geometries of banner banks on admiralty charts. This presents an extension of the nearshore southward trending sand transport pathway from Wicklow Head to Dublin Bay, thus shifting the nearshore section of the bed load parting zone northwards.

Van Landeghem et al [27] re-examines this work in more detail using the direction of asymmetry derived from two-dimensional cross-sectional profiles over large (0.44 – 2.8 m high; 10 – 100 m spacing) to very large (> 2.8 m high; > 100 m spacing) sediment waves in the Irish Sea. Results show that derived trends in the central Irish Sea broadly agree with previous studies (Figure 3-5). The bed load parting zone in the western Irish Sea proposed by Van Landeghem et al [27] conflicts with suggested by Holmes and Tappin [81], but correlates more closely with earlier studies [28], [68]. Van Landeghem et al [27] also provides a greater detailed description of convergence/divergence zone locations in the western Irish Sea in comparison to previous iterations [28], [81]. For example, a bedload separation is interpreted

on the western side of and parallel to Blackwater Bank. These northward trending asymmetric sand waves are limited by the appearance of a convergence zone immediately north of the bank. In deeper parts of the Irish Sea and Celtic Sea, bedform asymmetry is predominately to the south. The western Irish Sea divergence/convergence patterns around Codling Bank are also described using the variations of asymmetrical sand wave directions, but sometimes variations along the same crest line persist.

Van Landeghem et al [27] also describes temporal variability of bedload transport in the Irish Sea through a combination of geological and geophysical data interpretation and paleo-tidal modelling outputs [44], [74]. It is noted that the three zones of divergence, convergence and divergence respectively identified in the central Irish Sea do not extend to the land-ward side of the coast-parallel sand banks. Large to very large sediment waves in this region are associated with higher sediment wave migration rates and are so observed to be active under the present-day hydrodynamic regime. Large to very large sediment waves located further offshore exhibit very little to no migration and are so considered to be moribund or adapting very slowly to hydrodynamic changes. In the case of smaller sediment waves travelling on and over large to very large sediment waves, Van Landeghem et al [27] proposes to revise the assumption that this is indicative of active migration [28] and suggests retaining the interpretation of these larger, coarse-grained sediment waves as slow-moving or moribund. Van Landeghem et al [58] adds to these defined net sand transport directions by including sand wave migration rates in areas where repeat bathymetry data was available (Figure 3-5).

3.4 Hydrodynamic Modelling

A fully validated, two-dimensional, hydrodynamic model covering the entire Irish Sea, developed using the Danish Hydraulics Institute's MIKE 21 suite of tools [135], [136], was used

to simulate bed shear stress and tidal current u and v magnitude components for a one-month period. The hydrodynamic model was validated using in situ water elevation data from thirteen tide gauges along the Irish and UK coastlines, and in situ current magnitude and direction measurements from four Acoustic Doppler Current Profilers (ADCP) [132]. The location of these validation points and resulting comparisons between modelled and observed values are presented in Table 3-3. The correlation coefficient (R) is a measure of the linear correlation between the measured and modelled data. The scatter index (SI) takes the root mean square error (RMSE) of the difference between the measured and modelled values and normalises the RMSE using the mean of the measured data. Bias is expressed as the mean difference between modelled and measured data. In general, a good agreement is shown between simulated and measured values. Full model extent and validation details are outlined in Coughlan et al [132].

Table 3-3 Comparison between modelled and measured tidal amplitudes and currents from tide gauge and ADCP locations respectively. The indices shown are bias, the root-mean-square error (RMSE), the correlation coefficient (R) and the scatter index (SI). Data source: Coughlan et al [132]

Comparison between:	Location	Bias (m for tidal amplitudes; m/s for currents)	RMSE (m for tidal amplitudes; m/s for currents)	*R*	SI (%)
Modelled and measured tidal elevation amplitudes from tide gauge locations	Ballycotton (51.8278°, -8.0007°)	-0.06	0.17	0.99	17.76
	Bangor (54.665°, -5.669167°)	-0.28	0.16	0.99	21.13
	Dunmore (52.1477°, -6.9919°)	-0.23	0.14	0.99	15.22
	Fishguard (52.01272°, -4.982778°)	-0.02	0.15	0.99	17.33
	Ilfracombe (51.211139°, -4.112389°)	0.01	0.25	0.99	12.06
	Milford Haven (51.70686°, -5.050639°)	-0.02	0.17	1.00	11.40
	Millport (55.74969°, -4.904667°)	-0.06	0.21	0.97	28.25
	Portpatrick (54.84242°, -5.118889°)	-0.04	0.15	0.99	16.72
	Portrush (55.2°, -6.666667°)	-0.03	0.13	0.97	35.60
	Rosslare (52.254600°, -6.334861°)	-0.01	0.13	0.97	31.71
	Wexford (52.3385°, -6.4589°)	-0.09	0.18	0.94	49.30
	Heysham (54.03369°, -2.912361°)	-0.07	0.59	0.97	27.68
	Holyhead (53.30889°, -4.630556°)	0.02	0.12	1.00	9.73
Modelled and measured current data from ADCP locations	Kish Bank 1 (53.28422°, -5.9361°)	-0.03	0.08	0.89	26.28
	Kish Bank 2 (53.16978°, -5.912767°)	-0.07	0.13	0.88	32.96
	Wicklow Trough (52.95601°, -5.90135°)	-0.08	0.21	0.83	32.14
	Lucifer Bank (52.3867°, -6.2183°)	-0.04	0.11	0.85	29.61

The MIKE 21 hydrodynamic model [136] determines bottom shear stress, τ_b, by quadratic friction law:

$$\tau_b = C_d \rho \overline{U}^2 \quad (1)$$

Where C_d is a drag coefficient, ρ is the density of the fluid medium in seawater and $\overline{U}$ is the depth averaged velocity. The drag coefficient is determined as;

$$C_d = \frac{g}{(Mh^{1/6})^2} \quad (2)$$

Where h is the total water depth and g is the acceleration due to gravity and M is the Manning number. A constant Manning number of 32 $m^{(1/3)}s^{-1}$ was applied in this case. Model outputs were interpolated on to a 1 km² grid where the residual bed shear stress and residual tidal currents were calculated.

3.5 Correlation of bed load parting zone with present day hydrodynamic regime

The highly complex nature of bedform evolution, highlighted in section 3.2.1 and 3.2.3, arises many uncertainties surrounding the robustness of the predominately bedform-derived net sediment transport pathways in the Irish Sea. To challenge the existence and the accuracy of these pathways, this section poses two research questions;

a. Does the present-day hydrodynamic regime support the bed load parting zone (BLP) and the resulting divergent sediment transport pathways in the central Irish Sea?
b. If so, why does the BLP develop at this location?

Many studies provide numerous theoretical suggestions for the general formation of BLPs across the European continental shelf [28]. Similar indistinct concepts have been used to specifically explain the central Irish Sea BLP. For example, its existence is said to be due to the

change in tidal parameters across the basin as tidal ranges increase from the degenerate amphidromic point located near Cahore Point [27], or that this BLP aligns with the precise location of a tidal node that intersects the coastline where tidal ranges are zero, and tidal current velocities and bed shear stress local maxima are high [15]. While Harris et al [15] defines this BLP zone as Type A, those associated with flow accelerations at a tidal node, instead of Type B, those formed under flow accelerations generated by local restrictions, this study proposes a more complex understanding of the generation of a BLP at this location using tidal constituent analysis, numerically modelled residual tidal currents and numerically modelled residual tidal-induced bed shear stress.

3.5.1 Transport pathways and tidal asymmetry:

Evidence from numerically modelled bed shear stress [16], [50] concludes that net sand transport pathways result from the distortion of the M_2 tidal constituent by its first harmonic. In a progressive wave system, the phase relationship between M_2 and M_4 constituents is such that a flood or ebb dominance exists (section 3.2.4.1). This in turn corresponds to no reversals of peak current direction and associated lack of bed load convergence/divergence zones. The lack of regional scale bed load partings and convergence zones offshore in the Celtic and North Seas [16], [28] confirm these findings.

Pingree and Griffiths [16] also note that bed load partings (BLP) coincide with regions exhibiting a local maximum in peak bed shear stress. Numerically modelled maximum bed shear stress vectors by Ward et al [50] supports this finding whereby divergence patterns correlate well with the general location of regional scale bed-load parting zone in the central Irish Sea defined by bedform studies [27], [81]. In this way, recent hydrodynamic modelling studies that generate tidal asymmetry indicators can be used to infer bed shear stress

patterns, which in turn directly influence net sand transport pathways. For example, Horrillo-Caraballo et al [31] uses two methods to measure tidal asymmetry in the Irish Sea;

(a) the total tidal distortion factor, that calculates the ratio of the M_4 amplitude to the M_2 amplitude (A_{M_4}/A_{M_2}), and

(b) the tidal dominance factor that uses harmonic analysis to derive the phase relationship between M_2 and M_4 tidal constituents, $(2\phi_{M_2} - \phi_{M_4})$.

Although the superposition of M_2 and M_4 tidal constituents results in a distorted tide, when flood and ebb tidal currents are equal, the magnitude of bed shear stress is also equal (based on the assumption of quadratic friction law), resulting in an absent sediment transport residual. This occurs when

$$2\phi_{M_2} = \phi_{M_4} + 90° \quad (3)$$

where ϕ is the phase of the tidal constituent noted in its subscript. Furthermore, maximum tidal asymmetry and maximum residual bed shear stress occur when

$$2\phi_{M_2} = \phi_{M_4} \quad (4)$$

thus a plot of $2\phi_{M_2} - \phi_{M_4}$ ultimately quantifies asymmetry [107]. These parameters have been used to indicate tidal asymmetry by many studies [16], [105], [107], [137].

The total tidal distortion factor [31] reveals the highest distortion at the M_2 degenerate amphidromic point on the east coast of Ireland (section 3.2.4) (Figure 3-2), with a relatively high distortion factor stretching northeast of Wicklow Head in the vicinity of the suggested bed load parting zone. However, tidal distortion within the vicinity of the amphidromic point should be interpreted with caution. Distortion in estuaries for example is attributed to the dissipation of frictional energy in shallow waters and energy transfer from the M_2 and M_4 tidal

constituents through nonlinear processes. In tidal shallow continental shelf sea locations such as this, the large distortion factor can be attributed to the higher dominance of the M_4 constituent in the total tide. This is attributed to the diminishing M_2 amplitudes at the M_2 degenerate amphidrome [31]. Additionally, the increasing amplitudes of the M_4 constituent away from its nodal point, off Carnsore Point, may be a contributing factor [31], [138]. Further complexity of tidal propagation in this region is driven by the cyclic movement of the semi-diurnal tidal node over a spring-neap cycle [29]. Using tidal distortion alone to infer sediment dynamics and bed level changes may also be subject to misinterpretation in standing wave zones. The sum of the M_2 and M_4 constituents in a standing wave circumstance (high distortion factor), as pointed out by Neill and Couch [107], represents enhanced bed shear stress in both the flood and ebb tidal flow directions yet does not represent tidal dominance. Subsequently, a net residual sediment transport direction is absent. In this way tidal distortion must be accompanied with tidal dominance factor in order to fully understand net sand transport pathways.

The tidal dominance factor is used to determine whether a tidal system is symmetric or asymmetric, thus indicating whether a flood or ebb dominance exists [105]. As outlined in section 3.2.4.1, tidal current asymmetry (velocity constituents) [139], [140], hence net sand transport pathways, can be inferred from tidal duration asymmetry (sea surface constituents). In particular, the methodology presented by Neill and Couch [107] relates the resulting tidal current dominance factor to tidal residual bed shear stress and bed level change. By adapting this method to sea surface constituents [105], data presented by Horrillo-Caraballo et al [31] and similar sea surface modelling studies can be utilised efficiently to understand sediment dynamics.

When employing the tidal dominance factor $(2\phi_{M_2} - \phi_{M_4})$ to sea surface derived M_2 and M_4 constituents, a symmetrical tide theoretically occurs at 360 ° and 180 ° phase differences [105]. This is associated with;

a) equal flood and ebb tidal duration phases,

b) long period of nearly stationary sea surface height at low and high water respectively,

c) inferred equal ebb and flood current velocities,

d) high bed level changes due to the presence of convergence or divergent zones, and

e) relatively low residual bed shear stress in comparison to tidal asymmetric zones [107].

Where 0 ° to 180 ° and 180 ° to 360 ° indicates a flood dominant and ebb dominant tide respectively, and maximum sediment accumulation and maximum sediment erosion is expected to occur at 0° and 180°. In contrast, maximum tidal asymmetry theoretically occurs at 90° and 270° [105], [107], [137], [140]. This is associated with the highest residual bed shear stresses and low bed level changes [107]. This is summarised in Figure 3-6.

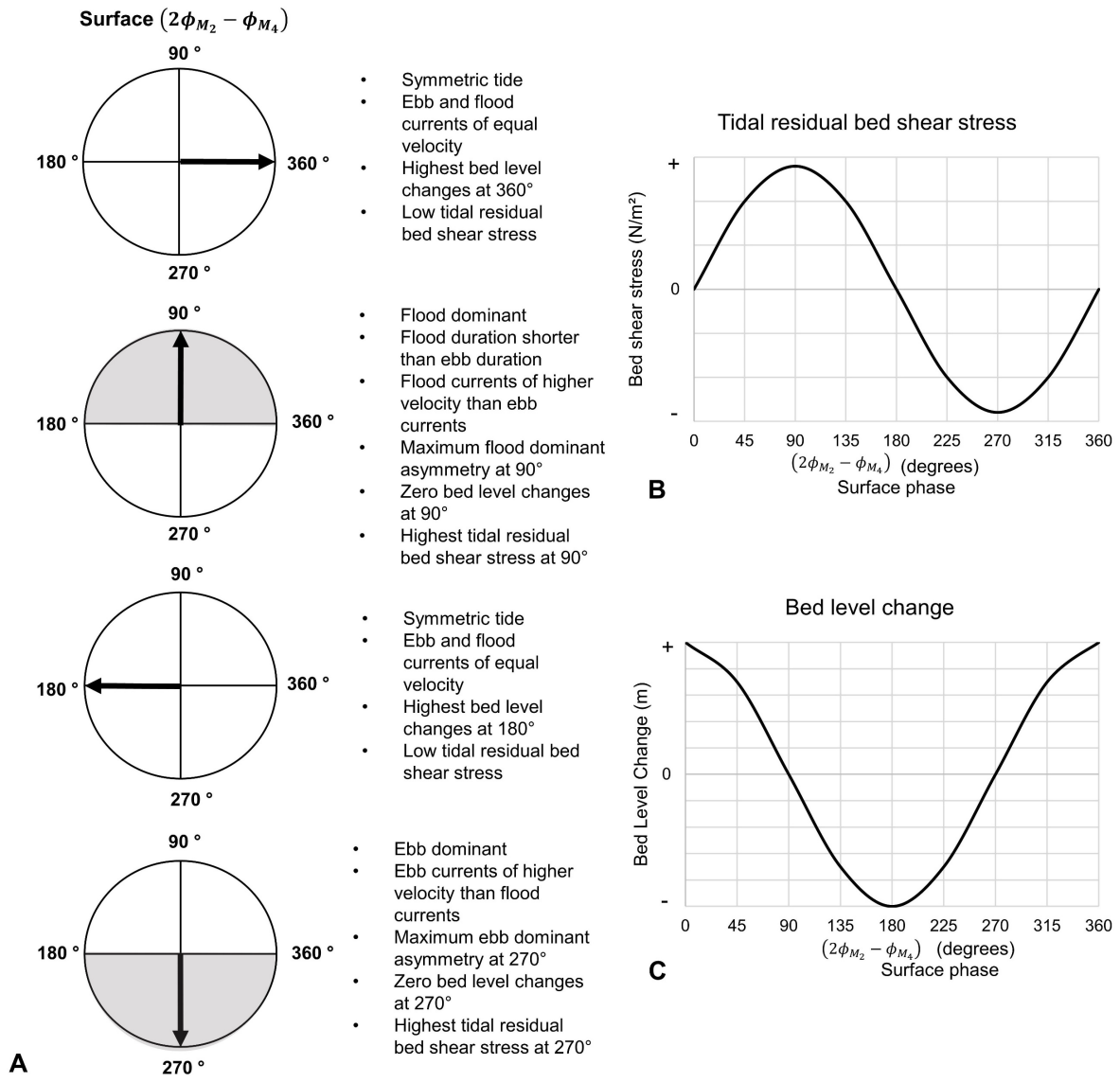


Figure 3-6 (A) Linear relationships between relative sea-surface phase and tidal distortion for $(A_{M_4}/A_{M_2}) > 0$*, adapted from Friedrichs and Aubrey* [105]*; (B) and (C) displays associated tidal residual bed shear stress and associated bed level change adapted from Neill and Couch* [107] *calculations; Descriptions for each regime in (A) are a combined interpretation from both Friedrichs and Aubrey* [105] *and Neill and Couch* [107]

Using this adaptation, two significant maximum symmetrical tidal zones are evident in the southern Irish Sea from Horrillo-Caraballo et al [31] (Figure 3-7);

(i) A 180 ° phase relationship geographically beginning at Ardanary on the east coast of Ireland (approximately 5.5 km wide), extending eastwards to north-eastwards

following the edge contour of Codling Platform. A distinct northward movement and threefold spatial increase of this zone is evident from the Codling Platform into relatively deeper waters of the St Georges Channel. An exception to this is the southward extension of ebb-dominated partially asymmetric zone that coincides with a relatively shallow topography (~ -65 mMSL), between Deep 2 (~ -120 mMSL) directly east of Codling Platform and the Main St Georges Channel (referred to as Deep 1) (~ -170 mMSL). From Deep 1, this zone continues to extend eastwards across the Irish Sea narrowing once again when reaching the Welsh Platform, connecting with the UK coastline at Anglesey.

(ii) Extending eastwards from Blackwater, County Wexford across to Fishguard/St David's Head on the west coast of Wales (~ 0 ° or 360 ° phase difference) (Location 2 in Figure 3-7).

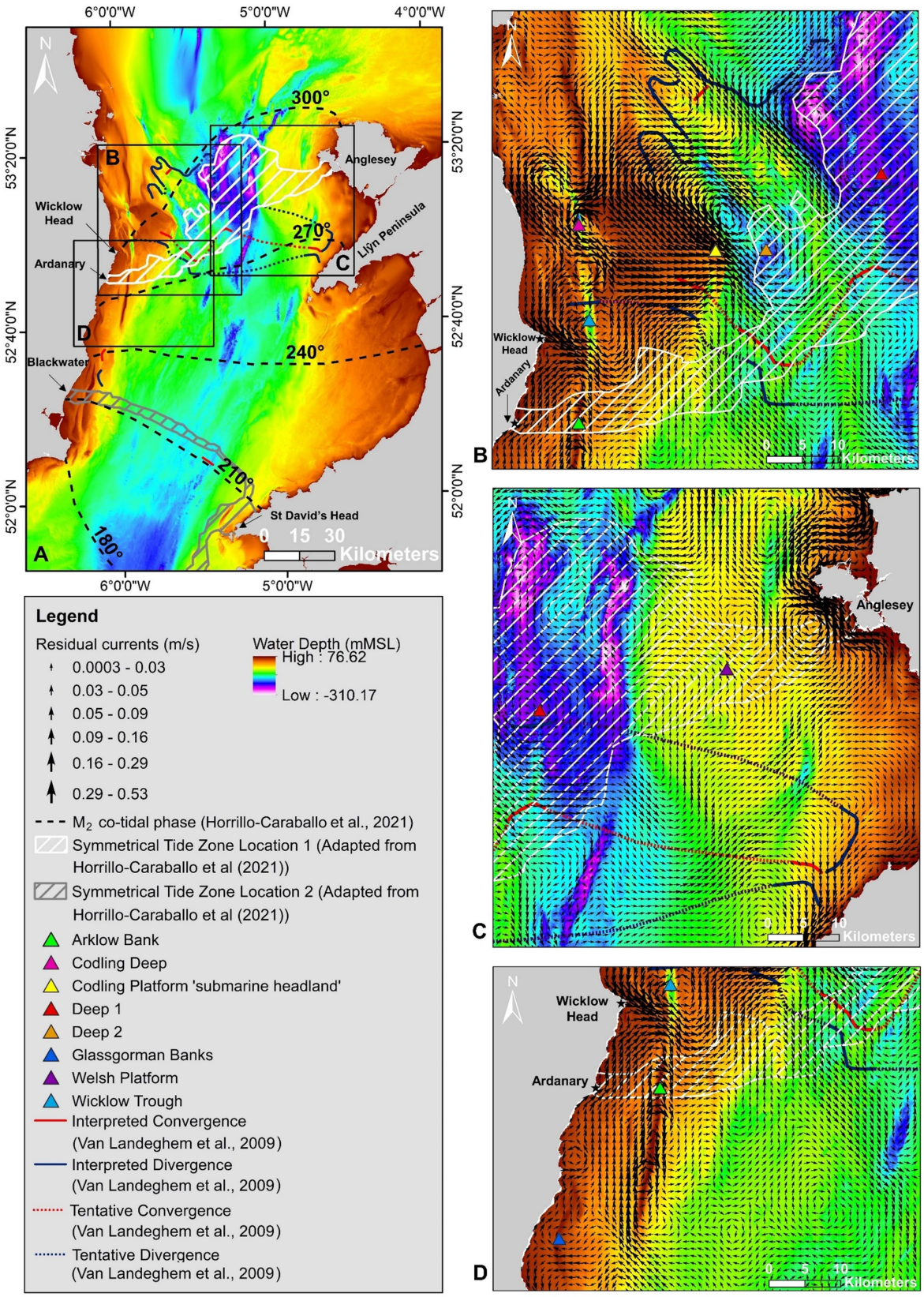


Figure 3-7 A. Overview of interaction between M_2 tidal wave propagation through the Irish Sea with the bed form derived bed load parting zone [27] *and the approximate locations of the symmetrical tidal zones modelled by Horrillo-Caraballo et al*

[31]*, B. Newly modelled residual tidal currents at the Codling Platform and Arklow Bank, C. Newly modelled residual tidal currents over the Welsh Platform, St Georges Channel (Deep 1 and 2) and Anglesey, D. Newly modelled residual tidal currents at Arklow Bank. Bathymetric metadata and Digital Terrain Model (DTM) data products have been derived from the EMODnet Bathymetry portal - http://www.emodnet-bathymetry.eu.*

These divergent and convergent standing wave zones correlate quantitatively with similar calculations for tidal asymmetry carried out by Robins et al [137], and with Ward et al [30] whereby the tidal system is characterised into progressive and standing wave systems based on the time difference between high water and the closest preceding or succeeding peak current flow.

3.5.2 BLP Zone: Origin

The complex BLP in the western Irish Sea, as indicated by Van Landeghem et al [27] correlates well with the divergent nature of the hydrodynamic system indicated by the tidal dominance factor at Symmetrical Tidal Zone Location 1 (Figure 3-7). Newly modelled residual currents and residual tidal induced bed shear stress supports the change from a progressive to standing wave system across the central Irish Sea at this location. The nature of this symmetrical zone is indicative of relatively low bed shear stress and high bed level change. Residual currents and bed shear stress vectors support this by highlighting a distinct panel of relatively low magnitude circulatory vectors stretching from south the Codling Platform across the central Irish Sea to Anglesey on the UK coastline, aligning precisely with the 180 ° tidal dominance zone (Figure 3-7; Figure 3-10). Similarly, these circulatory residual vectors correlate well with high positive and negative residual vorticity values [31] associated with complex seabed and coastline topography in this region and along the east coast of Ireland. A high bed level change resulting in an overall BLP is further supported by sediment distribution patterns (section 3.2.2) whereby winnowing of sandy sediments reveal gravel-

dominated lag deposits and exposed bedrock. This correlates with 'scour zones' indicated by Harris et al [15] and earlier sand transport conceptual models whereby an erosive basal layer is said to occur at the head of a sand transport path [17]–[20].

Analysis of numerically modelled M_2 tidal wave propagation in the Irish Sea reveals that tidal mixing between northward and southward propagating tidal waves may be the main factor influencing the presence of this symmetrical zone. The propagation of the M_2 tidal wave from the Atlantic Ocean, into the St Georges Channel, and through the Irish Sea Basin, is highly complex. When considering the Irish Sea as a rectangular entity, the continental shelf sea's dimensions are one quarter of the M_2 wavelength wide and is considered ideal for the generation of tidal resonance [28], [29], [31]. Tidal resonance is noted as a contributing factor to large tidal ranges in areas such as the Bristol Channel [26]. In reality, the Irish Sea basin comprises an intricate coastline and highly variable water depths (Figure 3-8) which interferes with tidal wave propagation. As the dominant M_2 tidal wave propagates into the Irish Sea through the St Georges Channel, Coriolis accelerations force the tidal flow to the right, resulting in high tidal ranges on the eastern edge of the basin and tidal dampening on the western edge. The tidal flow is unable to continue flowing to the right due to the interference with the coastline, therefore the crest moves northward, maintaining high tidal ranges on the Welsh coast [30], [31]. The tidal wave is continuously deflected in this way by Coriolis Force, and reflected by intricate topographies, to form an anticlockwise rotary wave around this M_2 nodal point on the east coast of Ireland (Amphidrome A) (Figure 3-8). Another anticlockwise rotating amphidrome is located in the North Channel whereby the tidal node (Amphidrome B), and thus point of zero tidal ranges, is located offshore rather than degenerate. Using co-tidal lines as indicators (Figure 3-8), the interaction between these two tidal fronts is

appointed as both the main cause of the standing wave zone in this region and the dominant physical process driving the intricate bed load divergence zone defined by bedform studies.

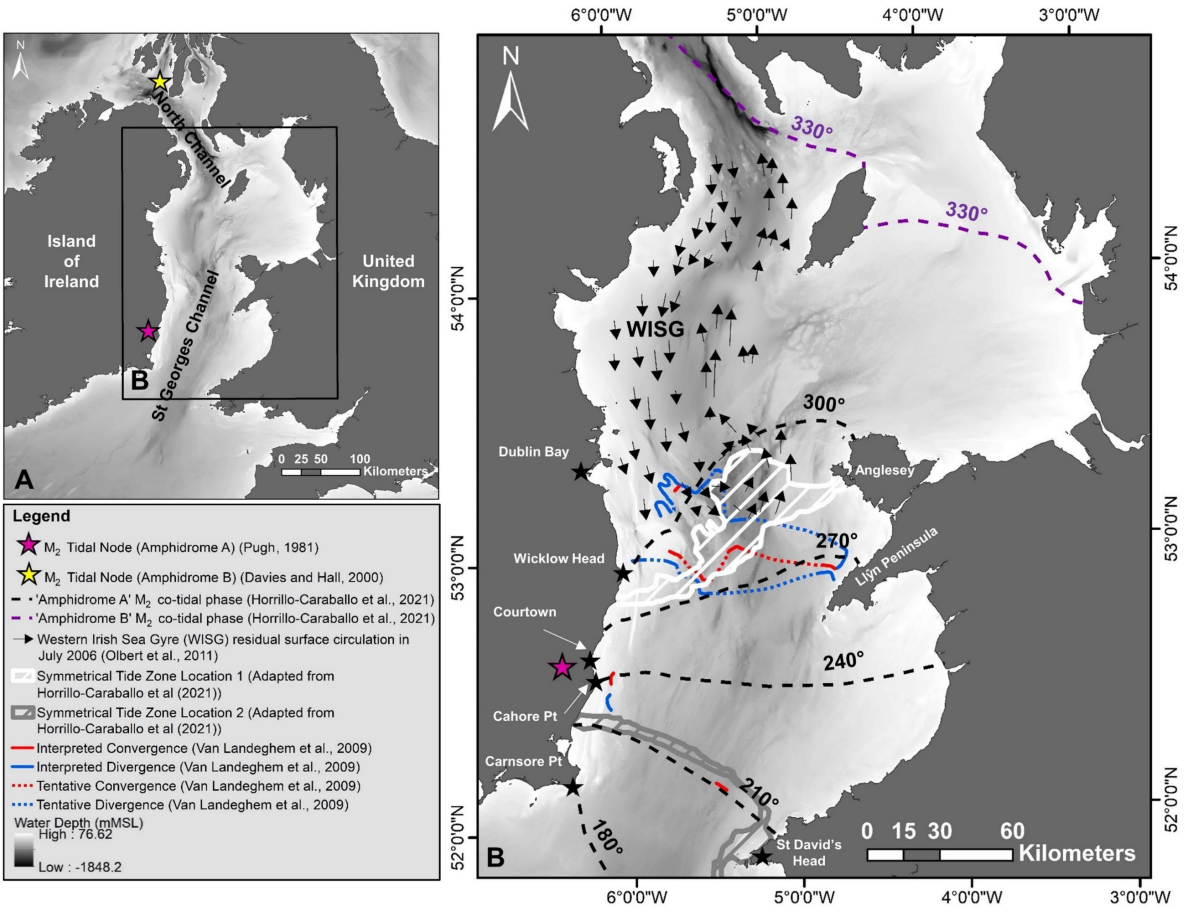


Figure 3-8 The interaction of two tidal fronts in the Irish Sea, and their relationship between the tidal symmetrical zone defined by Horrillo-Caraballo et al [31]*, the bed load parting zone defined by Van Landeghem et al* [27]*, and the seasonal Western Irish Sea Gyre observed by Olbert and Dabrowski* [25]*. Bathymetric metadata and Digital Terrain Model (DTM) data products have been derived from the EMODnet Bathymetry portal - http://www.emodnet-bathymetry.eu.*

Due to the angular nature of the tidal wave crests as they propagate through the North and South Irish Sea around each nodal point, Figure 3-8 indicates that their intersection on the east coast of Ireland theoretically should occur along the inclined northwards moving tidal crest at approximately Wicklow Head, extending north-eastwards towards North Anglesey. For example, both the anticlockwise rotational nature of Amphidrome B, and the position of

its 330 ° tidal phase which extends from the southern extent of the Isle of Man, implies that the southward flooding tide propagates into the western Irish Sea and along the eastern coast before the northward tidal wave crest propagates past Anglesey. This implies an intersection along the inclined crest of the northward flowing tidal wave. Similar cotidal line characteristics are evident for the S_2 and N_2 tidal waves [31].

3.5.3 BLP Zone: Minor Factors influencing shape and location

Local divergence and convergence zones within the overall bed load parting zone [27] cause alterations from the typical 'S' or bow-shaped BLP [15], [28]. This is analogous to other BLPs on the European continental shelf i.e. in the North Channel of the Irish Sea, in the entrance to the White Sea, and in the Southern Bight of the North Sea [28]. This alteration could be attributed to the complex local scale hydrodynamic system both modifying and being modified by the intricate seabed morphology (section 3.2.3) and the convoluted coastline topography of the Irish Sea. In this way, suggested contributing factors to the location and shape of this tidal symmetric zone, and thus bed load parting zone, are the change in tidal character at (a) abrupt changes in bathymetry, (b) headlands and intricate coastline topography, and (c) large-scale constrictions.

The constraining nature of the symmetrical zone along contour limit of the Codling Platform (Figure 3-7; Figure 3-8) indicates a strong influence of the large sedimentary platform on the BLP southern limit. Estuarine and limited coastal studies [141], [142] show that cross-sectional changes (reduction or expansion), such as a distinct step in bathymetry, can alter the tidal wave character by generating a partial standing wave system and amplification of the tidal wave due to shoaling. As a result, shallow water constituents generated from the M_2 constituent are significantly amplified [141], thus impacting tidal induced bed shear stress

and sediment transport dynamics. Where a wave encounters a sudden change in water depth, its propagation speed slows more readily over shallower water in comparison to the adjacent deeper water. The propagation speed on either side of the depth change becomes unaligned so that the wave characteristics cannot continue propagating unchanged across changing bathymetry. Consequently, as the propagating wave continues into shoaling water, part of the wave continues forward, yet part of the wave is reflected back into the deeper water. This partially reflected wave converges with the incoming wave, generating a partial standing wave system. Although a real estuary and a shallow continental shelf system is much more complex than a single channel model, this underlying concept could be applied to the south-western Irish Sea and be a contributing factor to the complex BLP presented by Van Landeghem et al [27].

At certain locations along the eastern boundary of the Codling Platform, water depth changes by 50 m and 84 m over < 1 km and 3 km respectively. This abrupt change in bathymetry constrains and alters the nature of tidal propagation in this region, thus enhancing the complexity of sediment dynamics in the BLP. Residual current and residual bed shear stress patterns confirm this concept. A northward residual current pathway is evident between the Wicklow coastline and the eastern side of the Arklow-Seven Fathom Bank complex (Figure 3-7). At Wicklow Head, this residual flow intersects with a residual southward flow resulting in refraction of the pathways eastwards, circulating around the northern extent of Arklow Bank and southern extent of the Wicklow Trough respectively. The area at which the residual currents splits into two parts i.e. (i) a southward flow along the eastern side of Arklow Bank and (ii) a north-eastward to eastward flow towards and across Codling Platform, aligns with the location of the symmetrical tide zone defined by the M_2 and M_4 phase relationship $(2\phi_{M_2} - \phi_{M_4})$ [31]. Residual bed shear stresses follow a similar pattern.

Moreover, numerous low-magnitude, rotational, residual flow patterns characterise the immediate deep-water zone of the tidal wave–Codling Platform interaction, aligning directly with the southern and eastern edge contour of the Codling Platform (Figure 3-7). This standing wave zone contrasts to the progressive nature of the enhanced residual current and bed shear stress magnitudes flowing across the relatively shallow (~ -20 mMSL) sedimentary platform. These high magnitude currents are also supported by many numerical modelling studies and in situ measurements [30], [50], [54] whereby tidal amplification due to increased frictional forces in shoaling water provides an explanation for its occurrence. The intersection of these enhanced residual flows with the submarine 'headland' of the Codling Platform (Figure 3-7), marks the separation of residual flows into clockwise and anticlockwise rotational movement north and south of this point respectively. At the centre and/or at the turning points of these residual eddies, a significant reduction in bed shear stress and current magnitudes arise. This reinforces the high impact of an abrupt bathymetric change at altering the nature of a propagating tidal wave. These residual gyres off the north and south extent of the submarine headland also coincide with the distinct divergent and convergent zones defined by Van Landeghem et al [27] presenting a potential cause for its location. Residual bed shear stresses follow a similar pattern to residual currents and thus sediment transport pathways may be inferred.

The extension of the 20 m contour from the Welsh coastline between Llŷn Peninsula and Anglesey is limited in comparison to the Irish coastline (Figure 3-9). A relative reduction in seabed morphological features is also evident. This reduces the amount and magnitude of abrupt bathymetry changes on the east coast of the Irish Sea, thus reducing the potential for alteration of the tidal character by abrupt steps in bathymetry. This provides a potential contributing factor to the evidently larger buffer zone of partially-progressive tidal wave on

the east coast of the Irish Sea between Llŷn Peninsula and Anglesey, in comparison to the west coast. This zone is supported by the extension of relatively low magnitude, rotary residual currents in this region. This helps to explain the notable impact of the Welsh Platform (~ -50 mMSL) on constraining the symmetrical zone on the eastern side of the Irish Sea, yet to a lesser degree than the Codling Platform.

In other areas of this inferred BLP zone, the narrow symmetrical tidal zone is broken by the southward extension of numerous patches of asymmetry causing the intermixing of symmetrical zones with areas of maximum tidal asymmetry. These areas are associated with high magnitude residual current and bed shear stress patterns, high peak current velocities (> 2 m/s) [30], and high magnitude divergent peak bed shear stress patterns [16], [50]. Approximately 15 km north-east of the Codling Platform is an example of this phenomenon whereby an elongated asymmetric zone protrudes southwards into the previously outlined pure symmetrical tidal zone (Figure 3-7). This area of high bed shear stress, low bed level changes and enhanced southward residual flow overlies the border of an abrupt bathymetric change between the continental shelf (~ -66 mMSL) and the relatively deep St Georges Channel (Deep 1 in Figure 3-7 and Figure 3-9) (~ -160 mMSL). Subsequently, interference of the propagating tidal wave with the shallowing continental shelf presents a credible contributory factor to shape alteration of the BLP in this region.

Headland associated eddies has also been suggested as a contributor to this complex nature of sediment dynamics within relatively large BLPs [28]. Generated headland eddies will be different for both ebb and flood tides. The direction of sediment dispersal from the BLP largely depends on the point's relative position to the nearest flood- or ebb-current eddy [28]. This will contribute to the curvature of the BLP. Flow dynamics around headlands also have

significant impact on sand bank development and maintenance [143], [144]. The residual gyres generated at headlands [31] and submerged headland-like bathymetries, including (i) Llŷn Peninsula, (ii) Anglesey, and (iii) Codling Platform, align well with the shape of the bed load parting zone indicated by Van Landeghem et al [27]. Maximum tidal asymmetry along the coastlines of Anglesey and Llŷn Peninsula [31] correlate well with enhanced residual currents and bed shear stresses and reinforce the idea that the tidal mixing is altered both by coastline topography and intricate bathymetry.

Concurrently, deep channels are suggested to enhance sediment transport in the opposite direction to the dominant tidal phase [27]. The presence of the linked-valley system (section 3.2.3.3) west of the Codling Platform presents a potential mechanism for the constriction of localised flow and alteration of sand transport from the main BLP. Due to the north-south trending orientation of this linked valley system, there is a question on whether these enhanced flows impact the stability and/or sediment supply to sand banks directly south of this location i.e. Arklow Bank and Seven Fathom Bank (Figure 3-7). Further investigation is needed into (a) whether this is a contributing factor to their dynamic morphology and to what magnitude they may be impacted, or (b) whether sand bank sediment circulation is a closed system as proposed by Huthnance [92] and suggested by Horrillo-Caraballo et al [31] (section 3.2.3.2). Numerical modelling works to date [30], [31], [50] fail to resolve both the intricate local convergent and divergent zones indicated by Van Landeghem et al [27], and localised sediment transport pathways over this highly morphodynamic region. Nevertheless, newly simulated residual bed shear stress patterns reveal a circulatory flow pattern around Arklow Bank, displaying a flood- and ebb- dominance on the west and east sides of the bank respectively. However, this does not necessarily indicate a closed circulatory sediment transport system around the bank. Sediment transport pathways inferred both from residual

currents and residual bed shear stress patterns show the potential pathways for additional sediment to be transferred in and out the dynamic circulatory cell. These two avenues include;

a) the southward residual flow located north of Wicklow Head, that refracts south-eastward at this headland to continue along the northern tip of Arklow Bank and southern tip of Wicklow Trough, finally connecting with the southward ebb-dominant flow along the eastern side of the bank;
b) the north-western residual flow cutting across the southern tip of Arklow Bank, originating from the bed load parting zone in the central Irish Sea yet reflected at the second symmetrical zone delineated by the tidal dominance factor located along the Blackwater-Fishguard transect.

Clearly, although a circulatory flow around Arklow Bank is apparent, a closed sediment dynamic system is not evident. However, no evidence supports the constraint residual tidal flow by Codling Deep or Wicklow Trough either. Instead residual pathways refract towards the shallower edges of these bathymetric deeps. In any case, this diversion of tidal wave crests away from bathymetric channels will also create local scale divergent and convergent patterns within the overall BLP, altering its shape. A combination of in situ measurements and local scale model development is necessary to elucidate this complex morphodynamic system at a higher resolution.

Additionally, this BLP is in the proximity of a large constriction. This large constriction is constrained by a) coastline topography, i.e. headlands at Wicklow Head (Figure 3-10), Llŷn Peninsula, and Anglesey (Figure 3-9), and b) rapidly changing bathymetry, i.e. Codling and Welsh Platforms causing a submarine constriction of the relatively deep St Georges Channel

(Figure 3-9). From cross-section A to cross-section B (Figure 3-9) an extension of an averaged 20 m and 50 m water depth is evident from the west and east coasts of the Irish Sea basin respectively. Flow accelerations due to local constrictions have been determined the cause of bed load parting zones elsewhere on the European Continental Shelf such as Dover Strait and Chenal du Four [15], [28]. However, the constriction in this case is suggested as a contribution to the accelerated tidal propagation over the St Georges Channel, thus pushing the interaction between two tidal waves northwards in this region and altering the shape of the bed load parting zone. Enhanced northward propagation of the tidal wave in the central Irish Sea over the constrained St Georges Channel is evident in the 180 ° phase relationship between M_2 and M_4 constituents [31]. Similarly, M_2 constituent co-tidal phase lines (300 °) of the tidal wave, associated with Amphidrome A, clearly show a bulge-like acceleration of the tidal wave over this constricted zone in comparison to other areas of the Irish Sea, such as the 240 ° co-phase line. Flow accelerations due to constrictions are combined with the concept that waves travel faster in deeper water than in shallow water. Therefore, tidal wave propagation is evidently faster over the St Georges Channel in comparison to the much shallower Codling Platform and Welsh Platform.

Evidence presented above clearly show that the modification of the tidal character at abrupt bathymetric changes, and along intricate seabed and coastline topographies, has a profound influence on the shape and location of the tidal symmetrical zone, hence bed load parting zone, in the central Irish Sea.

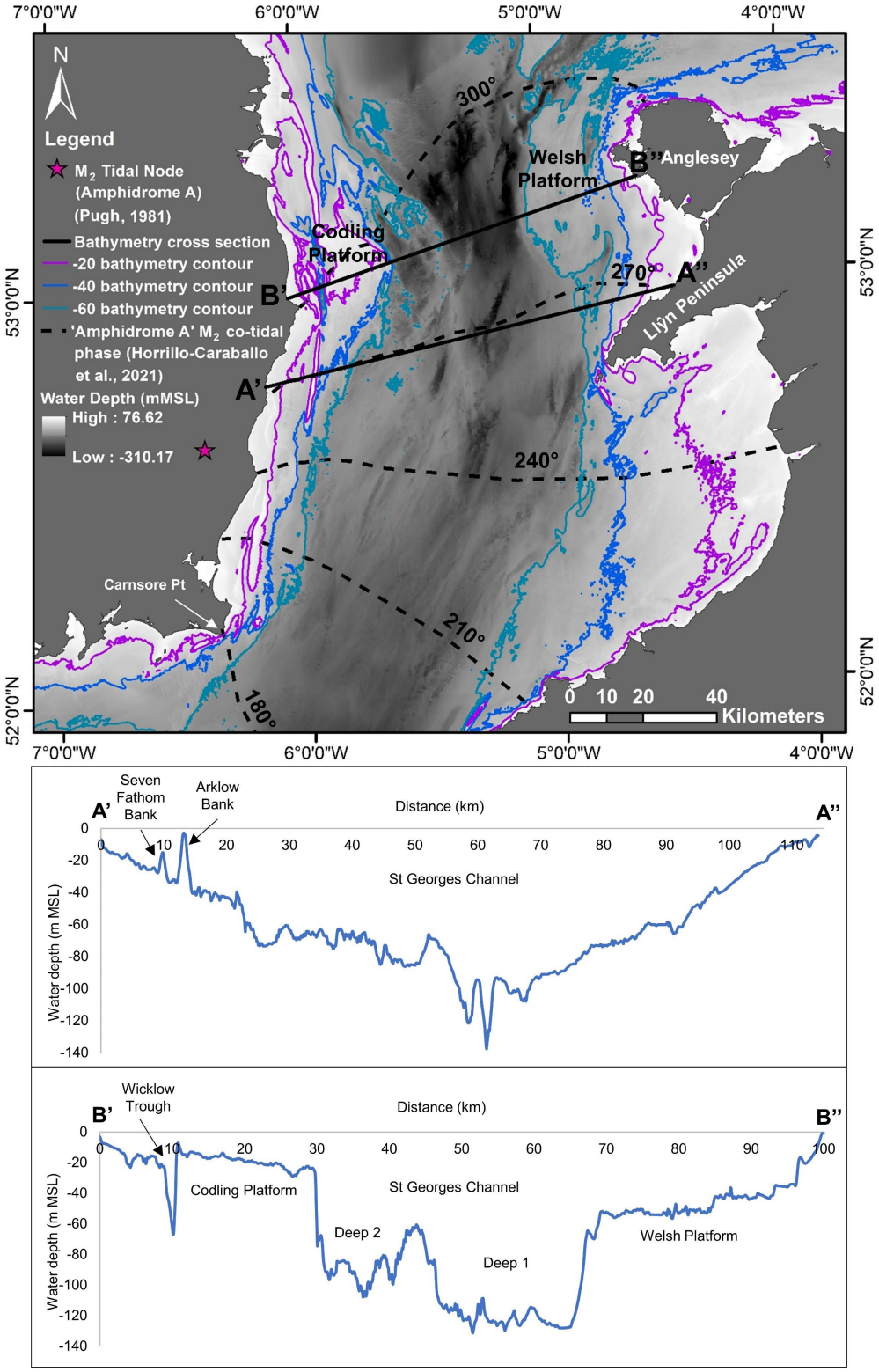


Figure 3-9 Irish Sea bathymetry with water depths referenced to mean sea level (MSL). The impact of large bathymetric and coastline constrictions on tidal propagation through the central Irish Sea is portrayed through two cross-sections and modelled co-tidal phase lines. Bathymetric cross-section A displays channel characteristics south of submarine constriction; bathymetric cross-section B displays channel topography over submarine constriction. Bathymetric metadata and Digital

Terrain Model (DTM) data products have been derived from the EMODnet Bathymetry portal - http://www.emodnet-bathymetry.eu.

3.5.4 BLP: Nature of opposing flows

Confirmation of opposing flows extending north and south from this symmetrical zone is necessary to quantify the central Irish Sea as a bed load parting zone. A progressive wave system, and strong rectilinear, elongated current ellipses dominates the south Irish Sea. Cardigan Bay is an exception of this where broad, circular ellipses are evident [31]. This correlates well with the classification presented by Ward et al [30].

Southward net sand transport directions derived from bedform studies (Figure 3-5) do not agree with the flood dominant tidal system in the southern half of the Irish Sea, as indicated by the tidal dominance factor [31], whereby flood and ebb dominance is characterised as phase differences between 0 ° to 180 °, and 180 ° to 360 ° respectively [31], [140]. As outlined in section 3.2.4.1, the most common direction of sand transport is in the direction of the shorter tidal phase (in this case flood tidal flow) due to higher bed shear stress exerted on the seabed inflicted by increased tidal current velocities during the shorter phase [122]. However, southward net sand transport pathways in this region indicate that the net sand transport is in the direction of the longer duration tidal phase (ebb flow). Residual currents and residual bed shear stress patterns clearly support this finding. This is further supported by modelled peak bed shear stresses [50].

The residual currents flow southward from the bedload parting zone along the axis of the St Georges Channel (Figure 3-10). As this flow interacts with the second tidal symmetric zone along the Blackwater-Fishguard transect, partial flow continues southward exiting the Irish Sea Basin. Furthermore, partial flow gradually undergoes a clockwise rotation in this region

and pushes north-westward across the southern tip of Arklow Bank and along the east coast of Ireland. Residual bed shear stresses rotate to a lesser degree at the second symmetrical zone along the Blackwater-Fishguard transect, yet a dominant nearshore northward flow, similar to residual currents, is evident (Figure 3-10). This northward residual sediment transport pathway is supported by the flood-dominated tidal flow characterised by the tidal dominance factor by [31]. Early bedform interpretation studies [68] and more recently numerically modelled peak bed shear stresses [50] further reinforces these dynamics. This reiterates the point outlined in section 3.2.4.1 whereby the consideration of both the duration over which sediment is mobilised, and peak current velocity is necessary to understand sediment dynamics on a shallow continental shelf.

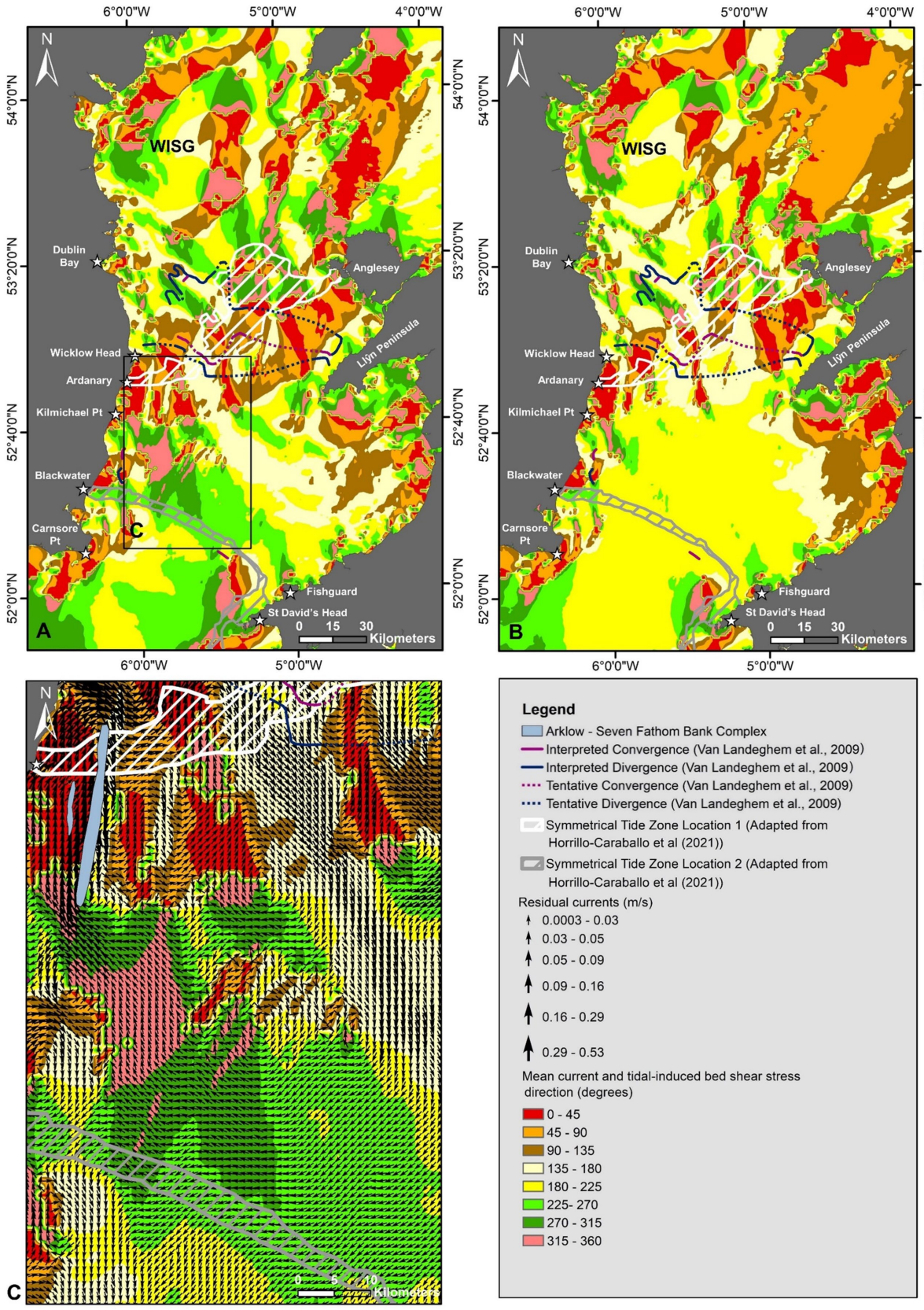


Figure 3-10 A. Numerically modelled mean tidal current directions across the Irish Sea, displaying a distinct panel of circulatory flow in the proximity of the bed load parting zone [27]*, and symmetrical tidal zone* [31]*; B. Numerically modelled tidal induced*

bed shear stress directions across the Irish Sea; C. Inset of A, mean tidal current directions overlain by numerically modelled residual (mean) tidal current vectors

In this region, a combined strong tidal distortion factor and an approximate 90 ° tidal dominance factor suggests the absence of convergence and divergence zones resulting in low bed level changes. However, this does not fully reflect the nature of sediment transport pathways in this region of the Irish Sea. Residual currents and bed shear stresses indicate convergent and divergent flow patterns in isolated areas of this indicated tidal asymmetric zone. The presence of both progressive and trochoidal sediment waves, and sediment banks, also indicate the potential for complex localised sediment transport trends, including accumulation zones. The question on whether some of these bedforms are active in the present-day hydrodynamic regime or attributed to periods of higher current velocities during post-glacial sea level rise (section 3.2.1) needs to be investigated further. Furthermore, section 3.2.3 highlight a) the impact of regional hydrodynamic patterns on morphological development, and b) the ability of sand bank complexes at controlling and altering regional flow patterns which in turn impacts morphological growth and seabed stability. Net sand transport pathways derived from bedforms and numerical modelling efforts to date fail to fully resolve the complexity of the physical interactions associated with sand banks and associated features. Previous studies [31], [56], [68], [82] indicate intricate hydrodynamic flow and sediment transport patterns surrounding the Arklow-Seven Fathom Bank, Glassgorman Bank, and the Lucifer-Blackwater Bank complexes. This intricate seabed evolution reflects complex localised transport pathways driven by tidal distortion and increased wave action in shoaling waters, the full interaction of these physical phenomena is yet to be understood.

One hydrodynamic characteristic of the western Irish Sea region that is not fully resolved by many numerical modelling studies [30], [31], [50] is the daily fluctuation of the semi diurnal tidal amphidrome. As outlined in section 3.2.4, the complexity of the physical interactions between Coriolis Force, pressure gradients, and coastal and submarine topography results in a dynamic tidal system in this region of the Irish Sea. The semi-diurnal amphidrome fluctuates in an east-west direction by 70 km over a spring-neap tidal cycle with the tidal node located in the Irish Sea during neaps, and located 40 km inland, creating a degenerate amphidromic point, during springs [29]. This zone of oscillation is outlined in Figure 3-11. The highly dynamic nature of the amphidromic point suggests that at multiple points along this zone, the tidal signal should experience a highly distorted both standing wave and progressive wave characteristics over a spring-neap cycle, moreover, a standing wave system during neap tides but a progressive wave system. This in turn has significant impact on the sediment transport. Relatively lower current velocities during neap tides, exert lower bed shear stresses on the seabed in comparison to spring currents. This phenomenon, mixed with little to no tidal asymmetry, resulting from the pure nature of the amphidromic point at this time, results in high bed level changes due to the potential presence of convergence/divergence zones. Tidal symmetry is supported on a course scale by the bed load divergence zone indicated by modelled peak bed shear stresses [50], by bed form convergent zones outlined by Van Landeghem et al [27], and from tidal dominance factor presented by Robins et al [137] and Horrillo-Caraballo et al [31].

In contrast, as the semi-diurnal amphidrome migrates inland during spring tides, the zone of oscillation in the Irish Sea theoretically is associated with a) higher M_2 constituent amplitudes, b) high distortion due to shallow water nature of the seabed, c) high spring current velocities, and c) higher bed shear stresses. All of which lead to higher net sediment mobility rates. This

higher seabed mobility rate in combination with a potential shift towards tidal asymmetry, that results from a degenerate tidal node, gives rise to net sand transport in the dominant tidal phase.

To examine the tidal node oscillation zone defined by Pugh [29], two Acoustic Doppler Current Profiler (ADCP) datasets, located within approximately 11 km of the zone (Figure 3-11), were analysed using the method defined by Ward et al [30] (Table 3-2). Observed changes in the tidal character over a spring-neap cycle correlates well with the suggested east-west fluctuation of the tidal node. ADCP 2 records a partially progressive wave during neaps and a progressive wave during springs. This coincides with the position of the tidal node onshore during springs, causing a progressive wave character, however progression of the tidal node (standing wave nodal point) eastwards during springs, influences a slightly more partially-progressive nature of the tidal wave. Contrastingly, a progressive and standing wave is observed during neap and spring tides respectively at ADCP1. This more northern, nearshore ADCP exhibits a standing wave when the tidal node is degenerate and a progressive wave system when located further away offshore. A paucity of numerical models or other study methods that resolve this phenomenon is evident. Further study into the bi-characterisation of the tidal signal into both progressive and standing wave systems over a spring-neap tidal cycle is needed to fully understand sediment transport trends in this region.

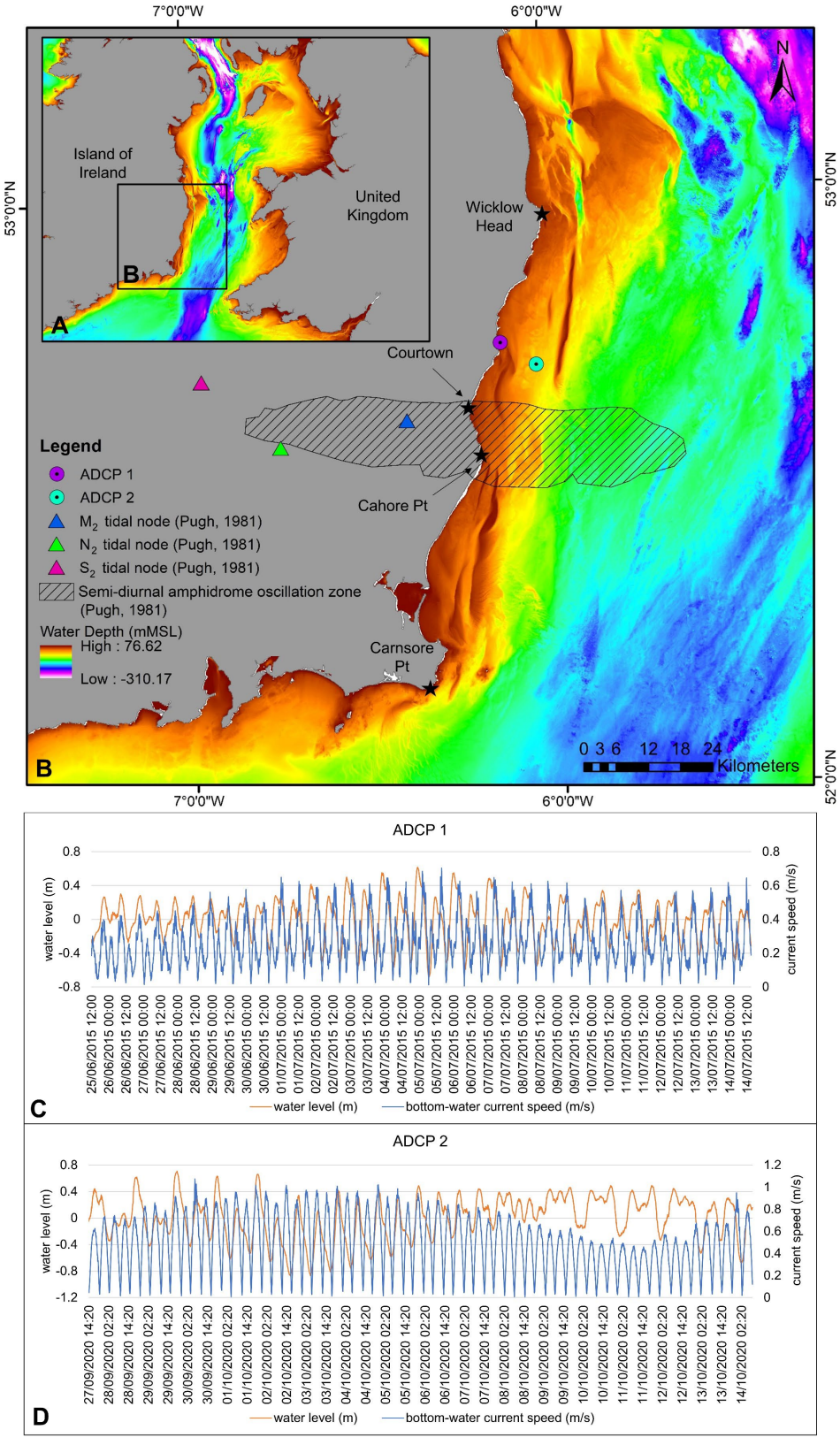


Figure 3-11 A and B display the tidal oscillation zone on the east coast of Ireland; Two graphs (C and D) display time-series of water level (m) and bottom-current speed (m/s) from ADCP locations 1 and 2, revealing the change in tidal character over a spring-neap cycle in this region

As the north-westward tidal wave continues past Anglesey, low current velocities and characteristics of a standing to partially-standing wave dominate in the western Irish Sea [30], [31]. Potential contributors to these phenomena are; a) continuous tidal mixing with the southward moving tidal wave b) tidal wave structural alteration due to eastern and northern boundary coastal reflection and interference, and c) tidal energy dissipation due to propagation into a wider shelf area after passing through large scale constrictions. This low velocity hydrodynamic system is reflected by the depositional nature of the Western Irish Sea Mud Belt (WISMB) (Figure 3-3). The development of the seasonal Western Irish Sea Gyre (WISG) (section 3.2.4) (Figure 3-8), shifts the regional northward residual flow southwards along the east coast of Ireland from April to September each year. Depth-averaged currents over June to September 1990 specifically show the extent of this reversed residual flow south of Dublin Bay [145], in the proximity of the most northern bed load divergence zone [27]. The development of the WISG may enhance southward flow in this region at a seasonal scale, impacting both bed load and suspended load transport patterns. Additional relatively strong residual northward flows are evident, from both currents and bed shear stresses, supported by the ebb-dominant tide determined by the tidal dominance factor [31].

These opposing residual current and bed shear stress patterns indicates the presence of a tidal flow capable of transporting sediment out of this region. This provides strong hydrodynamic evidence that the BLP indicated by bedform studies and early numerical modelling studies [16] exists at this location.

The nature of sediment dispersal across the Irish Sea may be subjected to change under predicted future sea level rise (SLR). The IPCC's projected SLR rate over the next century is 1.8 – 5.9 mm/yr [146], with some authors estimating an upper bound of 14 – 20 mm/yr [147],

[148]. This magnitude of SLR not only inherently increases the risk of coastal flooding and erosion [128], [149], but also has a major impact on tidal ranges both near- and offshore, at a global and European scale [150], [151]. As a tidal wave propagates as a shallow water wave, an increase in water depth due to sea level rise will increase the celerity of the wave. Similarly, as the frequency of the wave remains constant, the tidal wave wavelength will also increase with increasing water depth. This increased celerity and wavelength of the tidal wave as it propagates through a basin will ultimately alter the location of the existing amphidromes, directly impacting the spatial pattern of tidal ranges [150].

Under both 2 m and 10 m future sea level rise scenarios, Pickering et al [150] predicts a migration of the M_2 amphidromes both in the Irish Sea and in the wider European continental shelf. The position change of these amphidromes evidently cause a coherent change in the spatial distribution of tidal amplitude across these seas. In comparison to present day trends, there is a predicted increase in tidal amplitude in the western Irish Sea of 0.05 - 0.15 m and 0.2 - 0.5 m for 2 m and 10 m SLR scenarios respectively, and a decrease in the southernmost Irish Sea of 0.05 - 0.15 m and 0.2 - 0.5 m for 2 m and 10 m SLR scenarios respectively. Markedly, the M_2 tidal response to sea level rise is non-linear between the 2 m and 10 m scenarios. Moreover, changes in S_2 tidal amplitudes have an additional and important influence on spring and neap tides, with shallow water constituents further exhibiting change. Evidently, the resultant tidal constituent changes, due to predicted future sea level rise, could directly alter the location of tidal mixing zones. In the Irish Sea, this shift could directly impact the location and shape of the bed load parting zone, consequently modifying the associated sediment dispersal regime. Therefore, potential tidal constituent changes due to future SLR could impact efficient marine spatial planning.

3.6 Wider Implications

A regional and local scale understanding of sediment dynamics and hydrodynamics is imperative to a wide range of disciplines both within the Irish Sea [152] and other tidally-dominated continental shelves, e.g. the English Channel [153], Bay of Fundy [12], [98], and the Australian continental shelf [154]. Net sediment transport pathways and associated bed load parting zones are important components and resultants of these two physical phenomena. This study proves that a robust understanding of the interaction of tidal current flow with intricate coastline and seabed topography as a tidal wave propagates across a continental shelf is necessary to elucidate these trends. The combined use of;

a. numerically modelled co-tidal phases of individual tidal constituents,
b. tidal asymmetry indicators derived from individual constituent relationships, and
c. numerically modelled residual tidal currents and tidal-induced bed shear stress vectors

in this body of work has proven successful to both a) identify and investigate the existence of bed load partings and associated divergent net sediment transport pathways, and b) understand their origin. Further incorporating sediment distribution-tidal current flow correlations [15], [19], [20], and the use of repeat geophysical time-lapse data to analyse bedform migration (e.g. Van Landeghem et al [58]) allows the easier identification and confirmation of sediment dynamics. This integrated approach can easily be applied to regions outside the Irish Sea.

3.7 Conclusions

The main conclusions can be summarised as follows:

1. The nearshore northward net sand transport pathway off the east coast of Ireland indicated by early bedform interpretation studies [68] is supported by underlying hydrodynamics and peak bed shear stress patterns on a quantitative scale. This is further supported by newly modelled residual tidal currents and bed shear stresses. This is not represented in other bedform derived transport pathways studies.
2. The body of work presented by Van Landeghem et al [27], [57], [58] is similarly supported and provides an excellent base characterisation study of seabed mobility in the Irish Sea. However, in situ observations of mobile bedforms is needed to fully understand the driving factors behind net sand transport pathways in the direction of the longer tidal phase, opposite to what is most commonly expected.
3. Residual tidal currents and mean tidal bed shear stress patterns reveal an open circulatory flow around Arklow Bank which indicates a strong divergence from earlier-defined net sand transport pathways.
4. The presence of the BLP in the central Irish Sea is supported by;
    a. the reduced magnitude and circulatory nature of both mean tidal currents and mean tidal bed shear stresses,
    b. the existence of opposing residual flows from this zone,
    c. the coincident succession of symmetrical and asymmetrical tidal character (defined by tidal constituents) both within and bounding the overall divergent zone,
    d. numerically modelled peak bed shear stresses, and
    e. sediment distribution patterns.
5. This paper debunks the classification by Harris et al [15] whereby the BLP is determined as Type A: those associated with flow accelerations under tidal nodes.

6. This study proposes that the origin of the BLP is mainly attributed to the intersection of the North and South tidal fronts at an inclined angle due to Coriolis Forcing and coastline interactions.
7. Minor factors influencing the shape and location of the BLP are;
    a. the alteration of the tidal character as a result of the interaction of the propagating M_2 tidal wave with a rapid change in water depth at the Codling and Welsh Platforms,
    b. the alteration of the tidal character at intricate submarine and coastline topographies,
    c. flow acceleration due to the large constriction of the St Georges Channel caused by headlands and protruding submarine plateaus.

3.8 Future Work

A combination of engineering and geoscience methods need to be utilized in order to address these issues and aid future ORE developments in the Irish Sea. These should include;

1. The adoption of a morphological modelling approach to understand the present-day dynamic system on a fine scale and predict for future changes.
2. The acquisition of precise high-resolution time-lapse swath bathymetry data over sand banks and sediment waves will allow the analysis of both short-term and long-term bedform migration patterns and bedform stability.
3. By combining repeat geophysical data with sediment sampling and long-term hydrodynamic monitoring equipment, a better understanding of temporal changes could be garnered at a higher resolution.

4. A combination of sub-surface geophysical data and ground-truthing sediment core sampling could be used to inform long-term bedform migration, stability and geological origin.
5. Newly interpreted ADCP datasets support the presence of the semi-diurnal tidal node oscillation zone on the south-western coast of the Irish Sea. Further work is needed to understand the full extent of this phenomenon and the impact of this on sediment transport in this region.

3.9 Acknowledgments

SC is funded by the Irish Research Council (IRC) through grant EBPPG/2019/158 (Employment-Based Postgraduate Programme Scholarship). MC is funded under an Irish Research Council Enterprise Partnership Scheme Postdoctoral Fellowship (EPSPD/2020/109) and in part by a research grant from Science Foundation Ireland (SFI) under Grant Number 13/RC/2092, with support from Gavin and Doherty Geosolutions Ltd and the Geological Survey of Ireland (GSI). The authors are grateful for access to the numerical model and one ADCP dataset developed and obtained respectively through the industry-academic collaboration project involving Gavin and Doherty Geosolutions, University College Dublin (iCRAG) and University College Cork (MaREI), supported by the Marine Institute under the Marine Research Programme 2014-2020 (Grant-Aid Agreement No. IND/18/18). Ship time on the RV Celtic Voyager was funded by the Marine Institute through the 2020-2021 ship-time programme under the National Marine Research and Innovation Strategy 2017-2021. The authors would gratefully like to acknowledge the Mobility of Sediment Waves and Sand Banks in the Irish Sea (MOVE) (CV20010 and CV20036) shipboard crew and scientists, and land-based Marine Institute and INFOMAR personnel for assistance with ADCP data acquisition.

3.10 Author statement

Shauna Creane: Conceptualization, Methodology, Investigation, Formal Analysis, Writing – Original Draft, Writing - Review & Editing, Visualisation, Validation.

Michael O'Shea: Supervision, Conceptualization, Writing – Review & Editing.

Mark Coughlan: Supervision, Writing – Review & Editing.

Jimmy Murphy: Supervision, Conceptualization, Writing – Review & Editing.

3.11 References

[1] Department of the Environment Climate and Communications, "Climate Action Plan 2021," 2021.

[2] European Commission, "REPowerEU: A plan to rapidly reduce dependence on Russian fossil fuels and fast forward the green transition," *Press Release*, 2022. https://ec.europa.eu/commission/presscorner/detail/en/IP_22_3131 (accessed Sep. 27, 2022).

[3] National Grid ESO, "Pathway to 2030: A holistic network design to support offshore wind deployment for net zero," 2022.

[4] J. Guinan, C. McKeon, E. O'keeffe, X. Monteys, F. Sacchetti, M. Coughlan, and C. N. Aonghusa, "INFOMAR data supports offshore energy development and marine spatial planning in the Irish offshore via the EMODnet geology portal," *Quarterly Journal of Engineering Geology and Hydrogeology*, vol. 54, 2020, doi: 10.1144/qjegh2020-033.

[5] R. Morelissen, S. J. M. H. Hulscher, M. A. F. Knaapen, A. A. Németh, and R. Bijker, "Mathematical modelling of sand wave migration and the interaction with pipelines,"

Coastal Engineering, vol. 48, no. 3, pp. 197–209, 2003, doi: 10.1016/S0378-3839(03)00028-0.

[6] M. Yaghoobi, S. Mazaheri, and E. Jabbari, "Determining Natural Frequency of Free Spanning Offshore Pipelines by Considering the Seabed Soil Characteristics," *Journal of the Persian Gulf*, vol. 3, no. 8, pp. 25–34, 2012.

[7] B. M. Sumer, J. Fredsøe, and N. Christiansen, "Scour around vertical pile in waves," *Journal of Waterway, Port, Coastal, and Ocean Engineering*, vol. 118, no. 1, pp. 15–31, 1992, doi: 10.1061/(ASCE)0733-950X(1992)118:1(15).

[8] R. J. S. Whitehouse, J. M. Harris, J. Sutherland, and J. Rees, "The nature of scour development and scour protection at offshore windfarm foundations," *Marine Pollution Bulletin*, vol. 62, no. 1, pp. 73–88, 2011, doi: 10.1016/j.marpolbul.2010.09.007.

[9] T. J. Stehly and P. C. Beiter, "2018 Cost of Wind Energy Review. Technical Report NREL/TP-5000-74598.," National Renewable Energy Laboratory (NREL), Golden, Colorado, 2020.

[10] G. Sutton, *Irish Sea Marine Aggregate Initiative (IMAGIN) Project Synthesis Report Including: Geological Assessment, Environmental Assessment, Morphodynamic Modelling Web-based GIS System, Cost Benefit Analysis, Aggregate Resources and Markets-Wales.*, Marine Env., no. 36. 2008.

[11] K. A. Robinson, K. Ramsay, C. Lindenbaum, N. Frost, J. Moore, D. Petrey, and T. Darbyshire, *Habitat Mapping for Conservation and Management of the Southern Irish Sea (HABMAP). II: Modelling & Mapping*, vol. 5, no. 2. 2009.

[12] B. R. Wilson, C. J. Brown, J. A. Sameoto, M. Lacharité, A. M. Redden, and V. Gazzola, "Mapping seafloor habitats in the Bay of Fundy to assess megafaunal assemblages associated with Modiolus modiolus beds," *Estuarine, Coastal and Shelf Science*, vol. 252, 2021, doi: 10.1016/j.ecss.2021.107294.

[13] M. J. Lewis, S. P. Neill, and A. J. Elliott, "Interannual variability of two offshore sand banks in a region of extreme tidal range," *Journal of Coastal Research*, vol. 31, no. 2, pp. 265–275, 2015, doi: 10.2112/JCOASTRES-D-14-00010.1.

[14] M. R. Phillips and A. L. Jones, "Erosion and tourism infrastructure in the coastal zone: Problems, consequences and management," *Tourism Management*, vol. 27, no. 3, pp. 517–524, 2006, doi: 10.1016/j.tourman.2005.10.019.

[15] P. T. Harris, C. B. Pattiaratchi, M. B. Collins, and R. W. Dalrymple, "What is a bedload parting?," in *Tidal signatures in modern and ancient sediments*, B. W. Flemming and A. Bartholoma, Eds. 1995. doi: 10.1002/9781444304138.ch1.

[16] R. D. Pingree and D. K. Griffiths, "Sand transport paths around the British Isles resulting from M2 and M4 tidal interactions," *Journal of the Marine Biological Association of the United Kingdom*, vol. 59, no. 2, pp. 497–513, 1979, doi: https://doi.org/10.1017/S0025315400042806.

[17] A. H. Stride, "Current-swept sea floors near the southern half of Great Britain," *Quarterly Journal of the Geological Society*, vol. 119, no. 1–4, pp. 175–197, 1963.

[18] A. H. Stride, "Sediment transport by the North Sea," in *North Sea Science*, E. Goldberg, Ed. Cambridge, MA: MIT Press, 1973, pp. 103–130.

[19] R. H. Belderson and A. H. Stride, "Tidal current fashioning of a basal bed," *Marine*

Geology, vol. 4, no. 4, pp. 237–257, 1966.

[20] N. H. Kenyon and A. H. Stride, “The tide-swept continental shelf sediments between the Shetland Isles and France,” *Sedimentology*, vol. 14, no. 3–4, pp. 159–173, 1970.

[21] R. H. Belderson, “Bed-load partings and convergences at the entrance to the White Sea, U.S.S.R., and between Cape Cod and Georges Bank, U.S.A.,” *Marine Geology*, vol. 28, no. 1–2, pp. 65–75, 1978.

[22] J. J. Daniell, “Bedload parting in western Torres Strait, northern Australia,” *Continental Shelf Research*, vol. 93, pp. 58–69, 2015, doi: 10.1016/j.csr.2014.11.008.

[23] T. Dabrowski and M. Hartnett, “Modelling travel and residence times in the eastern Irish Sea,” *Marine Pollution Bulletin*, vol. 57, no. 1–5, pp. 41–46, 2008, doi: 10.1016/j.marpolbul.2008.03.014.

[24] T. Dabrowski, M. Hartnett, and A. I. Olbert, “Influence of seasonal circulation on flushing of the Irish Sea,” *Marine Pollution Bulletin*, vol. 60, no. 5, pp. 748–758, 2010, doi: 10.1016/j.marpolbul.2009.11.018.

[25] A. I. Olbert, M. Hartnett, and T. Dabrowski, “Long-term inter-annual variability of a cyclonic gyre in the western Irish Sea,” *Continental Shelf Research*, vol. 31, no. 13, pp. 1343–1356, 2011, doi: http://dx.doi.org/10.1016/j.csr.2011.05.010.

[26] C. Gao and T. A. A. Adcock, “On the tidal resonance of the bristol channel,” *International Journal of Offshore and Polar Engineering*, vol. 27, no. 2, pp. 177–183, 2017, doi: 10.17736/ijope.2017.as19.

[27] K. J. J. Van Landeghem, K. Uehara, A. J. Wheeler, N. C. Mitchell, and J. D. Scourse, “Post-glacial sediment dynamics in the Irish Sea and sediment wave morphology:

Data-model comparisons," *Continental Shelf Research*, vol. 29, no. 14, pp. 1723–1736, 2009, doi: 10.1016/j.csr.2009.05.014.

[28] M. A. Johnson, N. H. Kenyon, R. H. Belderson, and A. H. Stride, "Sand transport," in *Offshore Tidal Sands: Processes and Deposits*, A. H. Stride, Ed. Chapman and Hall, 1982, pp. 58–94. doi: 10.1007/978-94-009-5726-8_4.

[29] D. T. Pugh, "Tidal amphidrome movement and energy dissipation in the Irish Sea," *Geophysical Journal of the Royal Astronomical Society*, vol. 67, no. 2, pp. 515–527, 1981, doi: 10.1111/j.1365-246X.1981.tb02763.x.

[30] S. L. Ward, P. E. Robins, M. J. Lewis, G. Iglesias, M. R. Hashemi, and S. P. Neill, "Tidal stream resource characterisation in progressive versus standing wave systems," *Applied Energy*, vol. 220, pp. 274–285, 2018, doi: 10.1016/j.apenergy.2018.03.059.

[31] J. M. Horrillo-Caraballo, Y. Yin, I. Fairley, H. Karunarathna, I. Masters, and D. E. Reeve, "A comprehensive study of the tides around the Welsh coastal waters," *Estuarine, Coastal and Shelf Science*, vol. 254, p. 107326, 2021, doi: 10.1016/j.ecss.2021.107326.

[32] G. H. Denton, R. F. Anderson, J. R. Toggweiler, R. L. Edwards, J. M. Schaefer, and A. E. Putnam, "The last glacial termination," *Science*, vol. 328, no. 5986, pp. 1652–1656, 2010, doi: 10.1126/science.1184119.

[33] W. Evans, S. Benetti, F. Sacchetti, D. W. T. Jackson, P. Dunlop, and X. Monteys, "Bedforms on the northwest Irish Shelf: indication of modern active sediment transport and over printing of paleo-glacial sedimentary deposits," *Journal of Maps*, vol. 11, no. 4, pp. 561–574, 2015, doi: 10.1080/17445647.2014.956820.

[34] C. L. Mellet, D. Long, G. Carter, R. C. Chiverrell, and K. J. J. Van Landeghem, "Geology

of the seabed and shallow subsurface: The Irish Sea. British Geological Survey Commissioned Report, CR/15/057," 2015.

[35] D. Small, R. K. Smedley, R. C. Chiverrell, J. D. Scourse, C. Cofaigh, G. A. T. Duller, S. McCarron, M. J. Burke, D. J. A. Evans, D. Fabel, D. M. Gheorghiu, G. S. P. Thomas, S. Xu, and C. D. Clark, "Trough geometry was a greater influence than climate-ocean forcing in regulating retreat of the marine-based Irish-Sea Ice Stream," *Bulletin of the Geological Society of America*, vol. 130, no. 11–12, pp. 1981–1999, 2018, doi: 10.1130/B31852.1.

[36] C. D. Clark, A. L. C. Hughes, S. L. Greenwood, C. Jordan, and H. P. Sejrup, "Pattern and timing of retreat of the last British-Irish Ice Sheet," *Quaternary Science Reviews*, vol. 44, pp. 112–146, 2012, doi: 10.1016/j.quascirev.2010.07.019.

[37] R. C. Chiverrell, I. M. Thrasher, G. S. P. Thomas, A. Lang, J. D. Scourse, K. J. J. Van Landeghem, D. McCarroll, C. D. Clark, C. Ó. Cofaigh, D. J. A. Evans, and C. K. Ballantyne, "Bayesian modelling the retreat of the Irish Sea Ice Stream," *Journal of Quaternary Science*, vol. 28, no. 2, pp. 200–209, 2013, doi: 10.1002/jqs.2616.

[38] D. Praeg, S. McCarron, D. Dove, C. Ó Cofaigh, G. Scott, X. Monteys, L. Facchin, R. Romeo, and P. Coxon, "Ice sheet extension to the Celtic Sea shelf edge at the Last Glacial Maximum," *Quaternary Science Reviews*, vol. 111, pp. 107–112, 2015, doi: 10.1016/j.quascirev.2014.12.010.

[39] C. D. Clark, J. C. Ely, S. L. Greenwood, A. L. C. Hughes, R. Meehan, I. D. Barr, M. D. Bateman, T. Bradwell, J. Doole, D. J. A. Evans, C. J. Jordan, X. Monteys, X. M. Pellicer, and M. Sheehy, "BRITICE Glacial Map, version 2: a map and GIS database of glacial

landforms of the last British–Irish Ice Sheet," *Boreas*, vol. 47, pp. 11–27, 2018, doi: 10.1111/bor.12273.

[40] M. Coughlan, Z. Tóth, K. J. J. Van Landeghem, S. McCarron, and A. J. Wheeler, "Formational history of the Wicklow Trough: a marine-transgressed tunnel valley revealing ice flow velocity and retreat rates for the largest ice stream draining the late-Devensian British–Irish Ice Sheet," *Journal of Quaternary Science*, vol. 35, no. 7, pp. 907–919, 2020, doi: 10.1002/jqs.3234.

[41] K. R. Dyer and D. A. Huntley, "The origin, classification and modelling of sand banks and ridges," *Continental Shelf Research*, vol. 19, no. 10, pp. 1285–1330, 1999, doi: 10.1016/S0278-4343(99)00028-X.

[42] S. L. Bradley, G. A. Milne, I. Shennan, and R. Edwards, "An improved glacial isostatic adjustment model for the British Isles," *Journal of Quaternary Science*, vol. 26, no. 5, pp. 541–552, 2011, doi: 10.1002/jqs.1481.

[43] J. D. Scourse, S. L. Ward, A. Wainwright, S. L. Bradley, and K. Uehara, "The role of megatides and relative sea level in controlling the deglaciation of the British–Irish and Fennoscandian ice sheets," *Journal of Quaternary Science*, vol. 33, no. 2, pp. 139–149, 2018, doi: 10.1002/jqs.3011.

[44] K. Uehara, J. D. Scourse, K. J. Horsburgh, K. Lambeck, and A. P. Purcell, "Tidal evolution of the northwest European shelf seas from the Last Glacial Maximum to the present," *Journal of Geophysical Research: Oceans*, vol. 111, no. 9, pp. 1–15, 2006, doi: 10.1029/2006JC003531.

[45] S. L. Ward, S. P. Neill, J. D. Scourse, S. L. Bradley, and K. Uehara, "Sensitivity of

palaeotidal models of the northwest European shelf seas to glacial isostatic adjustment since the Last Glacial Maximum," *Quaternary Science Reviews*, vol. 151, pp. 198–211, 2016, doi: 10.1016/j.quascirev.2016.08.034.

[46] D. R. Tappin, R. A. Chadwick, A. A. Jackson, R. T. R. Wingfield, and N. J. P. Smith, *United Kingdom offshore regional report: The geology of Cardigan Bay and the Bristol Channel*. London: HMSO for the British Geological Survey, 1994.

[47] D. I. Jackson, A. A. Jackson, D. J. A. Evans, R. T. R. Wingfield, R. P. Barnes, and M. J. Arthur, *United Kingdom offshore regional report: the geology of the Irish Sea*. London: HMSO for the British Geological Survey, 1995.

[48] A. J. Wheeler, J. Walshe, and G. D. Sutton, "Geological appraisal of the Kish, Burford, Bray and Fraser Banks, Outer Dublin Bay Area," in *Marine Resources Series*, Dublin: Marine Institute, 2000.

[49] M. Kozachenko, R. Fletcher, G. Sutton, X. Monteys, K. Van Landeghem, A. Wheeler, Y. Lassoued, A. Cooper, and C. Nicoll, *A geological appraisal of marine aggregate resources in the southern Irish Sea. Technical report produced for the Irish Sea Marine Aggregates Initiative (IMAGIN) project funded under the INTERREG IIIA Community Initiative Programme 2000-2006*. University College Cork, Ireland, 2008.

[50] S. L. Ward, S. P. Neill, K. J. J. Van Landeghem, and J. D. Scourse, "Classifying seabed sediment type using simulated tidal-induced bed shear stress," *Marine Geology*, vol. 367, pp. 94–104, 2015, doi: 10.1016/j.margeo.2015.05.010.

[51] M. Coughlan, M. Long, and P. Doherty, "Geological and geotechnical constraints in the Irish Sea for offshore renewable energy," *Journal of Maps*, vol. 16, no. 2, pp. 420–

431, 2020, doi: 10.1080/17445647.2020.1758811.

[52] R. H. Belderson, “Holocene sedimentation in the western half of the Irish Sea,” *Marine Geology*, vol. 2, no. 1–2, pp. 147–163, 1964, doi: 10.1016/0025-3227(64)90032-5.

[53] A. J. Wheeler and shipboard party, “Irish Sea Marine Assessment (ISMA),” in *CV0926 Cruise Report*, University College Cork, Ireland, 2009.

[54] B. Dorschel and A. J. Wheeler, “Appraisal of the Irish Sea Seabed Imaging for Tidal Energy Generation Tidal Energy Potential Assessment. INFOMAR Report INF-11-11-WHE,” INFOMAR Programme, Geological Survey Ireland, Dublin, 2012.

[55] M. Coughlan, A. J. Wheeler, B. Dorschel, M. Long, P. Doherty, and T. Mörz, “Stratigraphic model of the Quaternary sediments of the Western Irish Sea Mud Belt from core, geotechnical and acoustic data,” *Geo-Marine Letters*, vol. 39, pp. 223–237, 2019, doi: 10.1007/s00367-019-00569-z.

[56] J. E. Hanna and J. A. G. Cooper, “Mesoscale Morphological Changes on Linear, Nearshore Sandbanks, Co.Wexford, SE Ireland.,” *Journal of Coastal Research*, vol. 36, pp. 356–364, 2002, doi: 10.2112/1551-5036-36.sp1.356.

[57] K. J. J. Van Landeghem, A. J. Wheeler, N. C. Mitchell, and G. Sutton, “Variations in sediment wave dimensions across the tidally dominated Irish Sea, NW Europe,” *Marine Geology*, vol. 263, no. 1–4, pp. 108–119, 2009, doi: 10.1016/j.margeo.2009.04.003.

[58] K. J. J. Van Landeghem, J. H. Baas, N. C. Mitchell, D. Wilcockson, and A. J. Wheeler, “Reversed sediment wave migration in the Irish Sea, NW Europe: A reappraisal of the

validity of geometry-based predictive modelling and assumptions," *Marine Geology*, vol. 295–298, pp. 95–112, 2012, doi: 10.1016/j.margeo.2011.12.004.

[59] D. A. V. Stow, F. J. Hernández-Molina, E. Llave, M. Sayago-Gil, V. Díaz-del Río, and A. Branson, "Bedform-velocity matrix: The estimation of bottom current velocity from bedform observations," *Geology*, vol. 37, no. 4, pp. 327–330, 2009, doi: 10.1130/G25259A.1.

[60] G. M. Ashley, "Classification of large-scale subaqueous bedforms: a new look at an old problem; SEPM bedforms and bedding structures," *Journal of Sedimentary Petrology*, vol. 60, no. 1, pp. 160–172, 1990, doi: 10.1306/212f9138-2b24-11d7-8648000102c1865d.

[61] S. Berne, P. Castaing, E. Le Drezen, and G. Lericolais, "Morphology, internal structure, and reversal of asymmetry of large subtidal dunes in the entrance to Gironde Estuary (France)," *Journal of Sedimentary Petrology*, vol. 63, no. 5, pp. 780–793, 1993, doi: 10.1306/d4267c03-2b26-11d7-8648000102c1865d.

[62] A. J. Couldrey, T. Benson, M. A. F. Knaapen, K. V Marten, and R. J. S. Whitehouse, "Morphological evolution of a barchan dune migrating past an offshore wind farm foundation," *Earth Surface Processes and Landforms*, vol. 45, no. 12, pp. 2884–2896, 2020, doi: https://doi.org/10.1002/esp.4937.

[63] G. Besio, P. Blondeaux, M. Brocchini, and G. Vittori, "On the modeling of sand wave migration," *Journal of Geophysical Research C: Oceans*, vol. 109, no. 4, 2004, doi: 10.1029/2002JC001622.

[64] S. J. M. H. Hulscher, "Tidal-induced large-scale regular bed form patterns in a three-

dimensional shallow water model," *Journal of Geophysical Research: Oceans*, vol. 101, no. C9, pp. 20727–20744, 1996, doi: 10.1029/96JC01662.

[65] T. Gerkema, "A linear stability analysis of tidally generated sand waves," *Journal of Fluid Mechanics*, vol. 417, pp. 303–322, 2000, doi: 10.1017/S0022112000001105.

[66] G. Besio, P. Blondeaux, M. Brocchini, and G. Vittori, "Migrating sand waves," *Ocean Dynamics*, vol. 53, no. 3, pp. 232–238, 2003, doi: 10.1007/s10236-003-0043-x.

[67] R. H. Belderson and A. H. Stride, "Tidal currents and sand wave profiles in the North-eastern Irish Sea," *Nature*, vol. 222, no. 74–75, 1969.

[68] M. R. Dobson, W. E. Evans, and K. H. James, "The sediment on the floor of the southern Irish Sea," *Marine Geology*, vol. 11, no. 1, pp. 27–69, 1971, doi: 10.1016/0025-3227(71)90083-1.

[69] M. A. F. Knaapen, "Sandwave migration predictor based on shape information," *Journal of Geophysical Research: Earth Surface*, vol. 110, no. 4, pp. 1–9, 2005, doi: 10.1029/2004JF000195.

[70] Y. A. Cataño-Lopera and M. H. García, "Geometry and migration characteristics of bedforms under waves and currents. Part 2: Ripples superimposed on sandwaves," *Coastal Engineering*, vol. 53, no. 9, pp. 781–792, 2006, doi: 10.1016/j.coastaleng.2006.03.008.

[71] J. P. Xu, F. L. Wong, R. Kvitek, D. P. Smith, and C. K. Paull, "Sandwave migration in Monterey Submarine Canyon, Central California," *Marine Geology*, vol. 248, no. 3–4, pp. 193–212, 2008, doi: 10.1016/j.margeo.2007.11.005.

[72] P. Blondeaux and G. Vittori, "A model to predict the migration of sand waves in

shallow tidal seas," *Continental Shelf Research*, vol. 112, pp. 31–45, 2016, doi: 10.1016/j.csr.2015.11.011.

[73] C. H. Cheng, K. Soetaert, and B. W. Borsje, "Sediment characteristics over asymmetrical tidal sand waves in the Dutch north sea," *Journal of Marine Science and Engineering*, vol. 8, no. 6, 2020, doi: 10.3390/JMSE8060409.

[74] S. P. Neill, J. D. Scourse, and K. Uehara, "Evolution of bed shear stress distribution over the northwest European shelf seas during the last 12,000 years," *Ocean Dynamics*, vol. 60, no. 5, pp. 1139–1156, 2010, doi: 10.1007/s10236-010-0313-3.

[75] J. H. J. Terwindt, "Sand waves in the southern bight of the North Sea," *Marine Geology*, vol. 10, no. 1, pp. 51–67, 1971, doi: 10.1016/0025-3227(71)90076-4.

[76] T. Marsset, B. Tessier, J. Y. Reynaud, M. De Batist, and C. Plagnol, "The Celtic Sea banks: An example of sand body analysis from very high-resolution seismic data," *Marine Geology*, vol. 158, no. 1–4, pp. 89–109, 1999, doi: 10.1016/S0025-3227(98)00188-1.

[77] J. Scourse, K. Uehara, and A. Wainwright, "Celtic Sea linear tidal sand ridges, the Irish Sea Ice Stream and the Fleuve Manche: Palaeotidal modelling of a transitional passive margin depositional system," *Marine Geology*, vol. 259, no. 1–4, pp. 102–111, 2009, doi: 10.1016/j.margeo.2008.12.010.

[78] R. H. Belderson, R. D. Pingree, and D. K. Griffiths, "Low sea-level tidal origin of Celtic Sea sand banks - evidence from numerical modelling of M2 tidal streams," *Marine Geology*, vol. 73, pp. 99–108, 1986.

[79] C. B. Pattiaratchi and M. B. Collins, "Mechanisms for linear sandbank formation and

maintenance in relation to dynamical oceanographic observations," *Progress in Oceanography*, vol. 19, pp. 117–176, 1987.

[80] A. H. Stride, "Offshore tidal deposits: sand sheet and sand bank facies," in *Offshore Tidal Sands: Processes and Deposits*, A. H. Stride, Ed. Dordrecht: Springer, 1982, pp. 95–125. doi: 10.1007/978-94-009-5726-8_5.

[81] R. Holmes and D. R. Tappin, "DTI Strategic Environmental Assessment Area 6, Irish Sea, seabed and surficial geology and processes." British Geological Survey Commissioned Report, CR/05/057, p. 82, 2005. [Online]. Available: http://nora.nerc.ac.uk/11259/

[82] J. K. Panigrahi, P. N. Ananth, and P. A. Umesh, "Coastal morphological modeling to assess the dynamics of Arklow Bank, Ireland," *International Journal of Sediment Research*, vol. 24, no. 3, pp. 299–314, 2009, doi: 10.1016/S1001-6279(10)60005-4.

[83] T. Off, "Rhythmic Linear Sand Bodies Caused by Tidal Currents," *AAPG Bulletin*, vol. 47, no. 2, pp. 324–341, 1963, doi: 10.1306/bc743989-16be-11d7-8645000102c1865d.

[84] J. D. Smith, "Geomorphology of a Sand Ridge," *The Journal of Geology*, vol. 77, no. 1, pp. 39–55, 1969, doi: 10.1086/627407.

[85] J. M. Huthnance, "Tidal current asymmetries over the Norfolk Sandbanks," *Estuarine and Coastal Marine Science*, vol. 1, no. 1, pp. 89–99, 1973, doi: 10.1016/0302-3524(73)90061-3.

[86] I. N. McCave, "Tidal currents at the North Hinder lightship, southern North Sea: Flow directions and turbulence in relation to maintenance of sand banks," *Marine Geology*, vol. 31, no. 1–2, pp. 101–114, 1979, doi: 10.1016/0025-3227(79)90058-6.

[87] G. Besio, P. Blondeaux, and G. Vittori, “On the formation of sand waves and sand banks Hydrodynamics of unsteady boundary layers View project Investigation of Sediment Transport in Oscillatory Flow Using Direct Numerical Simulations View project On the formation of sand waves and sand banks,” *Article in Journal of Fluid Mechanics*, vol. 557, pp. 1–27, 2006, doi: 10.1017/S0022112006009256.

[88] H. Park and C. E. Vincent, “Evolution of Scroby Sands in the East Anglian coast , UK,” *Journal of Coastal Research*, pp. 868–873, 2007.

[89] T. Schmitt, N. C. Mitchell, and T. S. Ramsay, “Use of swath bathymetry in the investigation of sand dune geometry and migration around a near shore ‘banner’ tidal sandbank,” *Geological Society Special Publication*, vol. 274, pp. 53–64, 2007, doi: 10.1144/GSL.SP.2007.274.01.07.

[90] V. N. D. Caston, “Linear sand banks in the southern North Sea,” *Sedimentology*, vol. 18, no. 1–2, pp. 63–78, 1972, doi: 10.1111/j.1365-3091.1972.tb00003.x.

[91] N. H. Kenyon and B. Cooper, “Sand banks, sand transport and offshore wind farms: DTI SEA 6 Technical Report,” ABPmer for Department of Trade and Industry, London, 2005.

[92] J. M. Huthnance, “On one mechanism forming linear sand banks,” *Estuarine, Coastal and Shelf Science*, vol. 14, no. 1, pp. 79–99, 1982, doi: 10.1016/S0302-3524(82)80068-6.

[93] I. S. Robinson, “Tidal vorticity and residual circulation,” *Deep Sea Research Part A, Oceanographic Research Papers*, vol. 28, no. 3, pp. 195–212, 1981, doi: 10.1016/0198-0149(81)90062-5.

[94] J. T. F. Zimmerman, “Dynamics, diffusion and geomorphological significance of tidal residual eddies,” *Nature*, vol. 290, no. 5807, pp. 549–555, 1981, doi: 10.1038/290549a0.

[95] J. M. Horrillo-Caraballo and D. E. Reeve, “Morphodynamic behaviour of a nearshore sandbank system: The Great Yarmouth Sandbanks, U.K.,” *Marine Geology*, vol. 254, no. 1–2, pp. 91–106, 2008, doi: 10.1016/j.margeo.2008.05.014.

[96] A. Chatzirodou, H. Karunarathna, and D. E. Reeve, “Modelling 3D hydrodynamics governing island-associated sandbanks in a proposed tidal stream energy site,” *Applied Ocean Research*, vol. 66, pp. 79–94, 2017, doi: 10.1016/j.apor.2017.04.008.

[97] A. Callaway, R. Quinn, C. J. Brown, M. Service, D. Long, and S. Benetti, “The formation and evolution of an isolated submarine valley in the North Channel, Irish Sea: An investigation of Beaufort’s Dyke,” *Journal of Quaternary Science*, vol. 26, no. 4, pp. 362–373, 2011, doi: 10.1002/jqs.1460.

[98] M. Z. Li, C. G. Hannah, W. A. Perrie, C. C. L. Tang, R. H. Prescott, and D. A. Greenberg, “Modelling seabed shear stress, sediment mobility, and sediment transport in the bay of fundy,” *Canadian Journal of Earth Sciences*, vol. 52, no. 9, pp. 757–775, 2015, doi: 10.1139/cjes-2014-0211.

[99] C. Gao, “Analysis of Storm Surge and Tidal Resonance in the Bristol Channel,” University of Oxford, 2017.

[100] W. A. McKay and N. J. Pattenden, “The behaviour of plutonium and americium in the shoreline waters of the Irish Sea: A review of Harwell studies in the 1990s,” *Journal of Environmental Radioactivity*, vol. 18, no. 2, pp. 99–132, 1993, doi: 10.1016/0265-

931X(93)90075-I.

[101] K. F. Bowden, “Physical and Dynamical Oceanography of the Irish Sea,” *Elsevier Oceanography Series*, vol. 24, no. 1907, pp. 391–413, 1980, doi: 10.1016/S0422-9894(08)71357-6.

[102] I. S. Robinson, “The tidal dynamics of the Irish and Celtic Seas,” *Geophysical Journal of the Royal Astronomical Society*, vol. 56, no. 1, pp. 159–197, 1979, doi: 10.1111/j.1365-246X.1979.tb04774.x.

[103] M. J. Howarth, “Hydrography of the Irish Sea,” in *SEA6 Technical Report*, UK Department of Trade and Industry’s offshore energy-Strategic Environmental Assessment programme, 2005.

[104] G. Ferentinos and M. Collins, “Effects of shoreline irregularities on a rectilinear tidal current (eddies) and their significance in sedimentation processes (Bristol Channel),” *Journal of Sedimentary Petrology*, vol. 50, no. 4, pp. 1081–1094, 1980, doi: 10.1306/212F7B80-2B24-11D7-8648000102C1865D.

[105] C. T. Friedrichs and D. G. Aubrey, “Non-linear tidal distortion in shallow well-mixed estuaries: a synthesis,” *Estuarine, Coastal and Shelf Science*, vol. 27, no. 5, pp. 521–545, 1988, doi: 10.1016/0272-7714(88)90082-0.

[106] R. D. Moore, J. Wolf, A. J. Souza, and S. S. Flint, “Morphological evolution of the Dee Estuary, Eastern Irish Sea, UK: A tidal asymmetry approach,” *Geomorphology*, vol. 103, no. 4, pp. 588–596, 2009, doi: 10.1016/j.geomorph.2008.08.003.

[107] S. P. Neill and S. J. Couch, “Impact of Tidal Energy Converter (TEC) Array Operation on Sediment Dynamics,” in *9th European Wave and Tidal Energy Conference (EWTEC)*,

2011.

[108] A. E. Hill, J. Brown, and L. Fernand, “The western Irish Sea gyre: a retention system for Norway lobster (Nephrops norvegicus)?,” *Oceanologica Acta*, vol. 19, no. 3–4, pp. 357–368, 1996.

[109] A. E. Hill, J. Brown, and L. Fernand, “The summer gyre in the western Irish Sea: Shelf sea paradigms and management implications,” *Estuarine, Coastal and Shelf Science*, vol. 44, pp. 83–95, 1997, doi: 10.1016/S0272-7714(97)80010-8.

[110] K. J. Horsburgh, *Observations and modelling of the Western Irish Sea Gyre (Unpublished doctoral dissertation)*. University of Wales, Bangor, United Kingdom, 1999.

[111] K. J. Horsburgh and A. E. Hill, “A three-dimensional model of density-driven circulation in the Irish Sea,” *Journal of Physical Oceanography*, vol. 33, no. 2, pp. 343–365, 2003, doi: 10.1175/1520-0485(2003)033<0343:ATDMOD>2.0.CO;2.

[112] J. Xing and A. M. Davies, “The influence of shelf edge flows and wind upon the circulation on the Malin shelf and in the Irish Sea,” *Continental Shelf Research*, vol. 21, no. 1, pp. 21–45, 2001, doi: 10.1016/S0278-4343(00)00073-X.

[113] A. I. Olbert, T. Dabrowski, S. Nash, and M. Hartnett, “Regional modelling of the 21st century climate changes in the Irish Sea,” *Continental Shelf Research*, vol. 41, pp. 48–60, 2012, doi: 10.1016/j.csr.2012.04.003.

[114] A. Callaway, J. Smyth, C. J. Brown, R. Quinn, M. Service, and D. Long, “The impact of scour processes on a smothered reef system in the Irish Sea,” *Estuarine, Coastal and Shelf Science*, vol. 84, no. 3, pp. 409–418, 2009, doi: 10.1016/j.ecss.2009.07.011.

[115] USA Corps of Engineers, *Coastal Engineering Manual Part II: Coastal Hydrodynamics (EM 1110-2-1100)*, vol. 1100. Books Express Publishing, 2002.

[116] J. Dronkers, "Tidal asymmetry and estuarine morphology," *Netherlands Journal of Sea Research*, vol. 20, no. 2–3, pp. 117–131, 1986, doi: 10.1016/0077-7579(86)90036-0.

[117] C. Friedrichs and O. S. Madsen, "Nonlinear Diffusion of the Tidal Signal in Frictionally Dominated Embayments," *Article in Journal of Geophysical Research Atmospheres*, vol. 97, no. C4, pp. 5637–5650, 1992, doi: 10.1029/92JC00354.

[118] Z. N. Zhu, X. H. Zhu, and X. Guo, "Coastal tomographic mapping of nonlinear tidal currents and residual currents," *Continental Shelf Research*, vol. 143, pp. 219–227, 2017, doi: 10.1016/j.csr.2016.06.014.

[119] P. E. Speer and D. G. Aubrey, "A study of non-linear tidal propagation in shallow inlet/estuarine systems Part II: Theory," *Estuarine, Coastal and Shelf Science*, vol. 21, no. 2, pp. 207–224, 1985, doi: 10.1016/0272-7714(85)90097-6.

[120] Z. B. Wang, M. C. J. L. Jeuken, H. Gerritsen, H. J. De Vriend, and B. A. Kornman, "Morphology and asymmetry of the vertical tide in the Westerschelde estuary," *Continental Shelf Research*, vol. 22, no. 17, pp. 2599–2609, 2002, doi: 10.1016/S0278-4343(02)00134-6.

[121] C. T. Friedrichs, D. R. Lynch, and D. G. Aubrey, *Velocity Asymmetries in Frictionally-Dominated Tidal Embayments: Longitudinal and Lateral Variability*. Washington, DC: AGU, 1992. doi: https://doi.org/10.1029/CE040p0277.

[122] G. B. Airy, "On the laws of the tides on the coasts of Ireland, as inferred from an extensive series of observations made in connection with the Ordnance Survey of

Ireland," *Philosophical Transactions, The Royal Society*, vol. 135, pp. 1–124, 1845, doi: https://doi.org/10.1098/rstl.1845.0001.

[123] S. Lanzoni, "Long-term evolution and morphodynamic equilibrium of tidal channels," *Journal of Geophysical Research*, vol. 107, no. C1, 2002, doi: 10.1029/2000jc000468.

[124] R. L. Soulsby, "Dynamics of Marine Sands. A Manual for Practical Applications," *Oceanographic Literature Review*, vol. 9, no. 44, p. 947, 1997.

[125] G. H. P. Campmans, P. C. Roos, H. J. de Vriend, and S. J. M. H. Hulscher, "The Influence of Storms on Sand Wave Evolution: A Nonlinear Idealized Modeling Approach," *Journal of Geophysical Research: Earth Surface*, vol. 123, no. 9, pp. 2070–2086, 2018, doi: 10.1029/2018JF004616.

[126] P. Chowdhury and M. R. Behera, "Nearshore Sediment Transport in a Changing Climate," in *Climate Change Signals and Response*, C. Venkataraman, T. Mishra, S. Ghosh, and S. Karmakar, Eds. Singapore: Springer, 2019. doi: https://doi.org/10.1007/978-981-13-0280-0_9.

[127] I. Fairley, I. Masters, and H. Karunarathna, "Numerical modelling of storm and surge events on offshore sandbanks," *Marine Geology*, vol. 371, pp. 106–119, 2016, doi: 10.1016/j.margeo.2015.11.007.

[128] M. J. Lewis, T. Palmer, R. Hashemi, P. Robins, A. Saulter, J. Brown, H. Lewis, and S. Neill, "Wave-tide interaction modulates nearshore wave height," *Ocean Dynamics*, vol. 69, no. 3, pp. 367–384, 2019, doi: 10.1007/s10236-018-01245-z.

[129] M. P. O'Shea, "Monitoring and modelling the morphodynamic evolution of a breached barrier beach system," University College Cork, 2015. [Online]. Available:

https://cora.ucc.ie/handle/10468/3359

[130] I. Colosimo, P. L. M. de Vet, D. S. van Maren, A. J. H. M. Reniers, J. C. Winterwerp, and B. C. van Prooijen, “The impact of wind on flow and sediment transport over intertidal flats,” *Journal of Marine Science and Engineering*, vol. 8, no. 11, pp. 1–26, 2020, doi: 10.3390/jmse8110910.

[131] A. Giardino and J. Monbaliu, “Wave effects on the morphodynamic evolution of an offshore sand bank,” *Journal of Coastal Research SI*, vol. 51, pp. 127–140, 2010, doi: 10.2112/SI51-012.1.

[132] M. Coughlan, M. Guerrini, S. Creane, M. O’Shea, S. L. Ward, K. J. J. Van Landeghem, J. Murphy, and P. Doherty, “A new seabed mobility index for the Irish Sea: modelling seabed shear stress and classifying sediment mobilisation to help predict erosion, deposition, and sediment distribution,” *Continental Shelf Research*, vol. 229, p. 104574, 2021, doi: https://doi.org/10.1016/j.csr.2021.104574.

[133] H. M. Pantin, *Seabed sediments around the United Kingdom: their bathymetric and physical environment, grain size, mineral composition and associated bedforms. British Geological Survey Marine Geology Series research report, SB/90/1*. 1991.

[134] DTI, *Petroleum Potential of the United Kingdom: Promote United Kingdom 2005*. London, UK: Department of Trade & Industry, 2004.

[135] DHI Group, “MIKE 21 Toolbox: user guide.” 2017.

[136] DHI Group, “MIKE 21 Flow Model: Hydrodynamic Module User Guide.” 2017.

[137] P. E. Robins, S. P. Neill, M. J. Lewis, and S. L. Ward, “Characterising the spatial and temporal variability of the tidal-stream energy resource over the northwest European

shelf seas," *Applied Energy*, vol. 147, pp. 510–522, 2015, doi: 10.1016/j.apenergy.2015.03.045.

[138] S. L. Ward, J. A. M. Green, and H. E. Pelling, "Tides, sea-level rise and tidal power extraction on the European shelf," *Ocean Dynamics*, vol. 62, no. 8, pp. 1153–1167, 2012, doi: 10.1007/s10236-012-0552-6.

[139] M. Piano, S. P. Neill, M. J. Lewis, P. E. Robins, M. R. Hashemi, A. G. Davies, S. L. Ward, and M. J. Roberts, "Tidal stream resource assessment uncertainty due to flow asymmetry and turbine yaw misalignment," *Renewable Energy*, vol. 114, pp. 1363–1375, 2017, doi: 10.1016/j.renene.2017.05.023.

[140] L. Guo, Z. B. Wang, I. Townend, and Q. He, "Quantification of Tidal Asymmetry and Its Nonstationary Variations," *Journal of Geophysical Research: Oceans*, vol. 124, no. 1, pp. 773–787, 2019, doi: 10.1029/2018JC014372.

[141] V. Sohrt, S. S. V. Hein, E. Nehlsen, T. Strotmann, and P. Fröhle, "Model based assessment of the reflection behavior of tidal waves at bathymetric changes in estuaries," *Water (Switzerland)*, vol. 13, no. 4, 2021, doi: 10.3390/w13040489.

[142] H. Yu, H. Yu, L. Wang, L. Kuang, H. Wang, Y. Ding, S. ichi Ito, and J. Lawen, "Tidal propagation and dissipation in the Taiwan Strait," *Continental Shelf Research*, vol. 136, pp. 57–73, 2017, doi: 10.1016/j.csr.2016.12.006.

[143] S. P. Neill, J. R. Jordan, and S. J. Couch, "Impact of tidal energy converter (TEC) arrays on the dynamics of headland sand banks," *Renewable Energy*, vol. 37, no. 1, pp. 387–397, 2012, doi: 10.1016/j.renene.2011.07.003.

[144] R. J. McCarroll, G. Masselink, N. G. Valiente, M. Wiggins, T. Scott, D. C. Conley, and E.

V. King, “Impact of a headland-associated sandbank on shoreline dynamics,” *Geomorphology*, vol. 355, p. 107065, 2020, doi: 10.1016/J.GEOMORPH.2020.107065.

[145] P. E. Robins, S. P. Neill, L. Giménez, R. Stuart, S. R. Jenkins, and S. K. Malham, “Physical and biological controls on larval dispersal and connectivity in a highly energetic shelf sea,” *Limnology and Oceanography*, vol. 58, no. 2, pp. 505–524, 2013, doi: 10.4319/lo.2013.58.2.0505.

[146] G. A. Meehl, T. F. Stocker, W. D. Collins, P. Friedlingstein, A. T. Gaye, J. M. Gregory, A. Kitoh, R. Knutti, J. M. Murphy, A. Noda, S. C. B. Raper, I. G. Watterson, A. J. Weaver, and Z.-C. Zhao, “Global climate projections,” in *Climate Change 2007: The Physical Science Basis. Contribution of Working Group I to the Fourth Assessment Report of the Intergovernmental Panel on Climate Change*, S. Solomon, D. Qin, M. Manning, Z. Chen, M. Marquis, K. B. Averyt, M. Tignor, and H. L. Miller, Eds. Cambridge, United Kingdom and New York, NY, USA.: Cambridge University Press, 2007.

[147] S. Rahmstorf, “A Semi-Empirical Approach to Projecting Future Sea-Level Rise,” *Science*, vol. 315, no. 5810, pp. 368–370, 2007, doi: 10.1126/science.1135456.

[148] W. T. Pfeffer, J. T. Harper, and S. O’Neel, “Kinematic Constraints on Glacier Contributions to 21st-Century Sea-Level Rise,” *Science*, vol. 321, no. 5894, pp. 1340–1343, 2008, doi: 10.1126/science.1159099.

[149] A. Arns, S. Dangendorf, J. Jensen, S. Talke, J. Bender, and C. Pattiaratchi, “Sea-level rise induced amplification of coastal protection design heights,” *Scientific Reports*, vol. 7, 2017, doi: 10.1038/srep40171.

[150] M. D. Pickering, N. C. Wells, K. J. Horsburgh, and J. A. M. Green, “The impact of future

sea-level rise on the European Shelf tides," *Continental Shelf Research*, vol. 35, pp. 1–15, 2012, doi: 10.1016/j.csr.2011.11.011.

[151] M. D. Pickering, K. J. Horsburgh, J. R. Blundell, J. J. M. Hirschi, R. J. Nicholls, M. Verlaan, and N. C. Wells, "The impact of future sea-level rise on the global tides," *Continental Shelf Research*, vol. 142, pp. 50–68, 2017, doi: 10.1016/j.csr.2017.02.004.

[152] S. P. Neill, P. E. Robins, and I. Fairley, "The Impact of Marine Renewable Energy Extraction on Sediment Dynamics," in *Marine Renewable Energy: Resource Characterization and Physical Effects*, Z. Yang and A. Copping, Eds. Springer International Publishing, 2017, pp. 279–304. doi: 10.1007/978-3-319-53536-4_12.

[153] A. Rivier, A. C. Bennis, V. Magar, G. Pinon, and M. Gross, "Regional numerical modelling of offshore monopile wind turbine impacts on hydrodynamics and sediment transport," in *Proceedings of the 1st International Conference on Renewable Energies Offshore*, 2014.

[154] M. A. Hemer, "The magnitude and frequency of combined flow bed shear stress as a measure of exposure on the Australian continental shelf," *Continental Shelf Research*, vol. 26, no. 11, pp. 1258–1280, 2006, doi: 10.1016/j.csr.2006.03.011.

4 Development and dynamic of sediment waves in a complex morphological and tidal dominant system: southern Irish Sea

Development and dynamics of sediment waves in a complex morphological and tidal dominant system: southern Irish Sea

Shauna Creane[1,2,3], Mark Coughlan[4,5,3], Michael O'Shea[1,2], Jimmy Murphy[1,2]

[1]School of Civil & Environmental Engineering, University College Cork, College Road, T12 K8AF Cork, Ireland; shauna.creane@ucc.ie (S.C.); michaeloshea@ucc.ie (M.O.); jimmy.murphy@ucc.ie (J.M.)

[2]SFI Research Centre for Energy, Climate and Marine (MaREI), Beaufort Building, Environmental Research Institute, University College Cork, Ringaskiddy, P43 C573 Cork, Ireland

[3]Gavin and Doherty Geosolutions, Unit A2, Nutgrove Office Park, Rathfarnham, D14 X627 Dublin, Ireland

[4]School of Earth Sciences, Science Centre West, University College Dublin, Belfield, D04 N2E5 Dublin, Ireland; mark.coughlan@icrag-centre.org (M.C.)

[5]SFI Research Centre for Applied Geosciences (iCRAG), O'Brien Centre for Science East, University College Dublin, D04 N2E5 Dublin, Ireland

Abstract

With the recent push for a transition towards a climate-resilient economy, the demand on marine resources is accelerating. For many economic exploits, a comprehensive understanding of environmental parameters underpinning seabed morphodynamics in tidally-dominated shelf seas, and the relationship between local and regional scale sediment transport regimes as an entire system, is imperative. In this paper, high-resolution, time-lapse

bathymetry datasets, hydrodynamic numerical modelling outputs and various theoretical parameters are used to describe the morphological characteristics of sediment waves and their spatio-temporal evolution in a hydrodynamically and morphodynamically complex region of the Irish Sea. Analysis reveals sediment waves in a range of sizes (height = 0.1 to 25.7 m, and wavelength = 17 to 983 m), occurring in water depths of 8.2 to 83 mLAT, and migrating at a rate of 1.1 to 79 m/yr. Combined with numerical modelling outputs, a strong divergence of sediment transport pathways from the previously understood predominantly southward flow in the south Irish Sea is revealed, both at offshore sand banks and independent sediment wave assemblages. This evidence supports the presence of a semi-closed circulatory hydrodynamic and sediment transport system at Arklow Bank (an open-shelf linear sand bank). Contrastingly, the Lucifer–Blackwater Bank complex and associated sediment waves are heavily influenced by the interaction between a dominant southward flow and a residual headland eddy, which also exerts a strong influence on the adjacent banner bank. Furthermore, a new sediment transfer system is defined for offshore independent sediment wave assemblages, whereby each sediment wave field is supported by circulatory residual current cells originating from offshore sand banks. These new data and results improve knowledge of seabed morphodynamics in tidally-dominated shelf seas, which has direct implications for offshore renewable developments and long-term marine spatial planning.

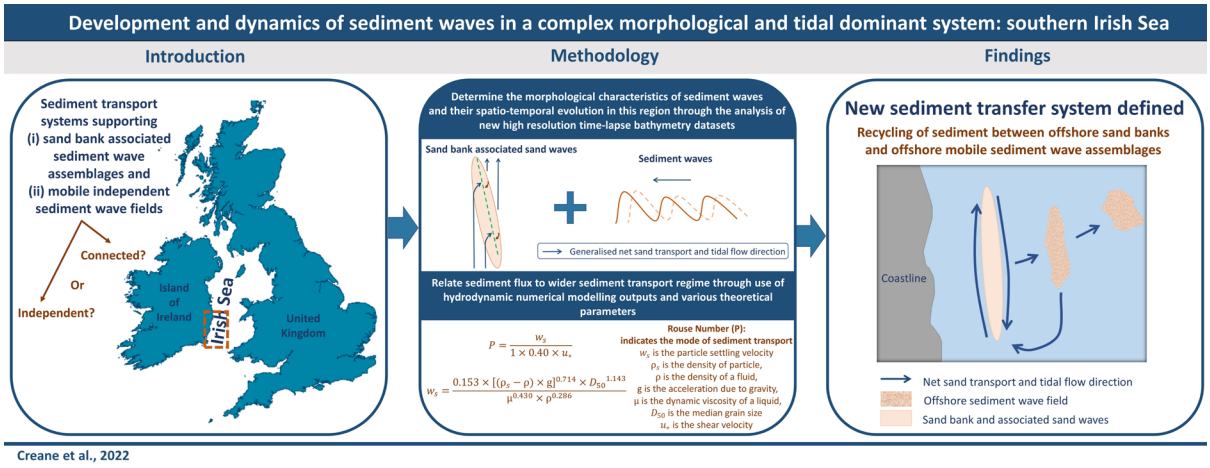


Figure 4-1 Graphical Abstract for peer-reviewed paper 'Development and dynamics of sediment waves in a complex morphological and tidal dominant system: southern Irish Sea'.

4.1 Introduction

4.1.1 Seabed morphodynamics

A comprehensive understanding of sediment dispersal and seabed morphodynamic processes on tidally-dominated shelf seas [1]–[8] is paramount for a wide range of economic exploits including: the location and evolution of benthic habitats directly impacting fisheries [9], [10], the need to monitor the volume of marine aggregates [11], the impact of coastal flooding and erosion protection measures [12]–[14], the prevention of free-spanning and burial of offshore infrastructure such as pipelines and cables [15], [16], and reducing the risk of scour formation around offshore wind turbine foundations inherently leading to critical infrastructural instability [17], [18]. With the recent push for a transition towards a climate resilient economy, both at national and regional levels, ambitious 2030 offshore wind capacity targets have been set at 7 GW and 50 GW for the Republic of Ireland and UK respectively [19]–[21]. This heightened demand on marine resources calls for efficient marine spatial planning. With the recent push for a transition towards a climate-resilient economy, both at national and regional levels, ambitious 2030 offshore wind capacity targets have been set at

7 GW and 50 GW for the Republic of Ireland and UK respectively [19]–[21]. This heightened demand on marine resources calls for efficient marine spatial planning. With predicted future sea level rise potentially altering the spatial distribution of tidal constituents across tidally-dominated continental shelves [22], [23], the dependent sediment transport regime subsequently could be altered [5]. Consequently, a fundamental knowledge of environmental parameters underpinning seabed mobility and evolution over time, and the relationship between local and regional scale sediment transport regimes as an entire system, is imperative. Investigation into the present-day interaction between these processes will ultimately facilitate the composition and implementation of more robust long-term marine spatial planning. The formation of submarine morphological features is dependent upon the interaction between regional sedimentary systems and local hydrodynamic conditions. Two main categories of submarine geological features have been described by Stow et al [24]; (i) linear bedforms that develop elongated, parallel or oblique to flow direction, and (ii) transverse bedforms that are relatively regular undulating features occurring perpendicular to flow. Plan- and cross-sectional analysis of sediment banks (linear bedforms) and sediment waves (transverse bedforms) are used to define bed load transport pathways in tidally-dominated shelf seas and are very important to understanding seabed evolution over time.

4.1.1.1 Sediment banks and sediment waves as indicators of sediment transport dynamics

Sediment banks are widespread across the European continental shelf, having formed under a variety of conditions [5], [25]. In the Irish Sea and North Sea, sand banks are potential sites for present and future offshore wind farm developments, for example, Arklow Bank and Scroby Sands respectively. Where sand bank geometry can indicate regional scale net tidal flow and net sediment transport pathways [26]–[28], sediment waves associated with sand banks indicate localised sediment transport regimes. As sediment wave migration rates

(migrating up to tens of metres per year [29], [30]) are one order magnitude higher than sand banks they pose significant threat to the offshore wind industry [31]. For example, exposure or burial of submarine cables [15], and interaction with turbine foundations and protection structures inherently lead to infrastructural instability [18]. Therefore, the temporal and spatial evolution of bedform morphology, and the localised transport pathways, are of critical importance to offshore industries. The impact of migrating sediment waves and other bedforms on manmade seabed structures remains understudied. Using a combination of repeat bathymetric survey data and hydrodynamic modelling, Couldrey et al [32] analysed the morphological evolution of a barchan dune as it passed a monopile foundation at an average migration rate of 25 m/yr to assess its impact on sedimentary processes at the base of the structure. Overall, despite changes in seabed morphology at the site including scouring processes, they found that the dune's presence did not impact significantly on the stability of the wind turbine, nor its operational performance. However, this represents a single study of an isolated sediment wave (a barchan dune) passing a structure, whereas in areas such as the Irish Sea, multiple individual sediment waves of varying heights may pass and interact with a particular feature.

The oblique alignment of a linear sand bank axis to the net tidal flow generates a flood and ebb dominance on either flank of the bank [33]. On active sand banks this is ultimately reflected in sediment wave asymmetry, where sediment lee slopes face in opposite directions on either side of the bank [25], [34]. Identification of symmetrical sediment waves at end of sand banks, in conjunction with the progressive orientation change of the sediment wave crests, from bank base to bank crest, towards almost parallel alignment with the bank crest, led to the conclusion that circulation around and over the bank is what maintains the sand bank [35], [36]. Leenders et al [37] supports this theory by successfully modelling the

migration directions of sediment waves up and over sand banks in the North Sea, reasonably matching observational studies. Horrillo-Caraballo et al [38] further supports the presence of this circulatory flow pattern by identifying residual gyre patterns around sand banks in the Irish Sea by plotting the vorticity of the residual flow. Nevertheless, Johnson et al [28] suggests circulation around sand banks doesn't necessarily suggest a closed circulatory hydrodynamic and sediment transport system. Creane et al [5] supports this concept by using numerically modelled residual tidal current and bed shear stress to identify two residual transport pathways capable of providing sediment flux into Arklow Bank's (Irish Sea) (Figure 4-2) localised circulatory system. However, ground-truthing evidence such as analysis of repeat bathymetric datasets to quantify bedform spatial and temporal evolution, and net transport pathways, are absent in the area.

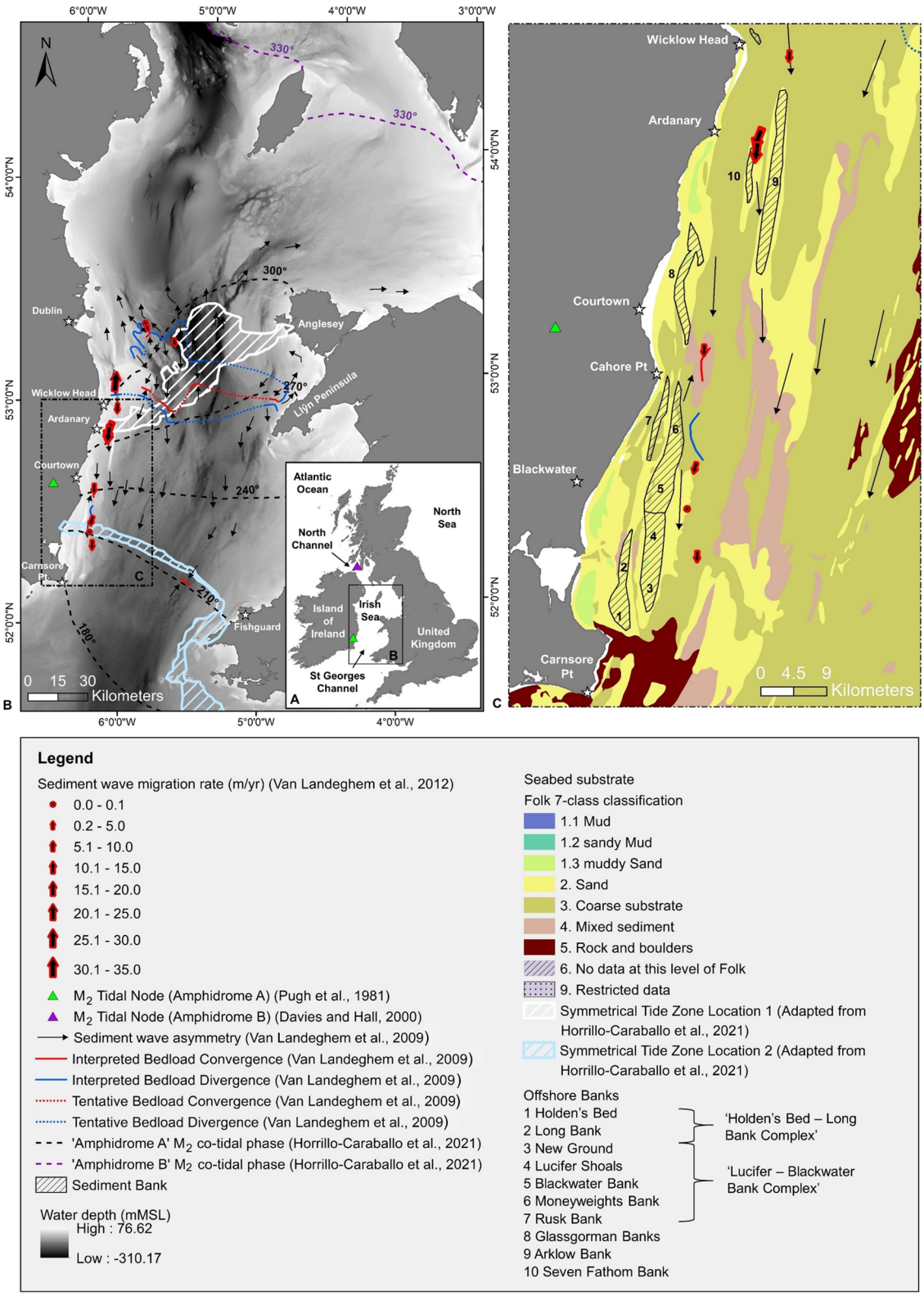


*Figure 4-2 Maps showing pre-existing knowledge of Irish Sea sediment transport. (**A**) Location of the Irish Sea on the north-western European continental shelf. (**B**) Irish Sea hydrodynamic and sediment transport characteristics. The location of the bedform derived bed load parting zone, defined by Van Landeghem et al* [39]*, characterised by one main sediment transport convergence zone and two divergent zones, is indicated. Bathymetry source: EMODnet Bathymetry Consortium* [40]*. (**C**) Study*

area displaying sediment distribution and main offshore sediment banks. Seabed substrate source: European Marine Observation Data Network (*EMODnet) Seabed Habitats initiative* (*http://www.emodnet-seabedhabitats.eu/ [Accessed: 25 June 2021]*) [41].

Under uni-directional flow, sediment wave migration is found to be in direction of asymmetry. This is found to be mostly true under bi-directional flow. This assumption has been used to estimate migration rates [29], [42], [43], and to depict sediment transport pathways on a regional scale across tidally dominated shelf seas [5], [26], [27], [39], [44]. Analysis of high resolution time-lapse bathymetric data challenges this assumption through observations of counter-current migration and reversals in sediment wave asymmetry [30]. Damen et al [45] found a negative correlation between sediment wave asymmetry and residual transport direction, further falsifying this theory. Thus, this strongly suggests that ground-truthing datasets are necessary to aid the quantification of spatial and temporal evolution in tidally-dominated seas. Furthermore, the comparison of repeat multibeam echo sounder datasets against environmental and theoretical-based indicators may further resolve gaps in academic knowledge.

4.1.1.2 Controlling factors on sediment wave growth

On tidally-dominated shelves, sediment waves also occur independently of larger bedforms (i.e. sand banks, marine channels or troughs), existing in isolation or in assemblages, in two- or three- dimensional form [46]. The basic description of sediment wave geomorphology is predominately based on the sediment wave height (H) to wavelength (L) ratio whereby local datasets are commonly compared to their positive exponential relationship ($H_{mean} = 0.0677L^{0.8098}, r = 0.98, n = 1491$) derived from the global dataset established by Flemming [47] (Table 4-1). This relationship was previously thought to represent an equilibrium state of active sediment waves, however, Flemming [48] re-defined it to

represent an approximate generalised global trend whereby departures from the trend indicate the influence of local process-response mechanisms characteristic of in-situ environments [4], [39], [45], [49]. Flemming [48] further suggests an upper limit to sand wave growth ($H_{max} = 0.16L^{0.84}$) depending on water depth, flow velocity and grain size. To date, numerous research results (e.g. Blondeauz and Vittori [50] and van Santen et al [51]) show that quantifying the sensitivity of sediment waves to individual local environmental parameters has proven to be a difficult task.

Yalin [52] suggests a relationship between sand wave height and water depth, however this association has been highly debated [48], [53], [54]. Where Van Der Veen et al [53] found a good correlation between the occurrence of sediment waves in the North Sea and grain size, water depth and flow velocity, many research studies show poor correlations with sand wave dimensions and water depth [55], [56]. Flemming [48] suggests water depth does not play an important role on sediment wave vertical growth in deeper waters, instead grain size is the dominant controlling factor [48]. Contrastingly, Zhou et al [4] found that sand waves tend to grow higher and shorter with decreasing water depths, and lower and longer with increasing water depths. This is attributed to a higher growth rate in wavelength in comparison to wave height due to the amalgamation process, leading to a more subdued bedform. Nonetheless Zhou et al [4] does not include grain size, current velocity and other influencing environmental parameters in their analysis, therefore external factors may be influencing this relationship. For instance, a moderate to good correlation between sand wave growth and water depth may signify a relationship with environmental parameters associated with water depth variations, i.e. current velocity acceleration/deceleration, rather than water depth itself acting as the controlling factor. A modelling study by Blondeaux and Vittori [50] revealed a correlation between increasing sediment wave wavelengths and increasing water depths

and/or decreasing tidal current velocities. Similarly, van Santen et al [51] found that an increase in depth-averaged maximum tidal current velocity correlated very well with decreasing wavelength under both field and modelled datasets. However, the same study could not detect a dependence of wavelength on water depth or grain size in field data as indicated by theoretical predictions [51]. Consequently, in the natural environment, a complex, dynamic coupling of a variety of environmental factors most likely impact sediment wave growth, therefore process-based indicators may be more suited to this investigation.

Process-based indicators (e.g., Rouse numbers that indicate the mode of sediment transport) have proven useful at quantifying large scale sediment wave dynamics. Hulscher [57] shows that under linear stability analysis, sediment wave growth is due to a residual vertical circulation by the tidal flow. Over an ebb and flood tidal cycle, the upslope flow is dominant over the downslope flow, resulting in a convergence of sediment transport pathways at the bedform crest, triggering bedform growth. Damen et al [45] supports this existing theory suggesting that the mode of sediment transport is an important sediment wave growth damping mechanism. Specifically, on the Dutch Continental Shelf, Damen et al [45] found a strong positive relationship between the occurrence of sand wave fields and bed load transport dominance, and a negative relationship with increasing suspended transport dominance. An increase in the ratio of suspended load transport to bedload transport represents an enhanced entrainment of finer grains into the water column, thus inhibiting the growth of sediment wave heights [45], [58]–[60]. Consequently, as critical suspension velocity is higher for coarser grains, sediment wave heights positively correlate with increasing grain sizes [4], [45], [56]. Positive correlations between grain sizes and Rouse numbers with sediment wave heights suggests the relative dominance of bed load transport over suspended load affects bedform growth [45], [60]. The mode of sediment transport is

considered an important damping mechanism by many studies [45], [48], [61]. Consequently, it is evident that the dynamic coupling of multiple environmental parameters and processes must be considered when investigating bedform growth and development.

Furthermore, in addition to tidal current, sediment source and sink pathways are a major control on whether independent sediment wave fields remain active or become moribund. A lack of studies on these mechanisms in tidally-dominated shelf seas is evident. Investigation into these mechanisms is key to understanding the sediment transport regime as a whole system.

Table 4-1 Geometrical relationships of sediment waves from previous studies

Reference	Power regression equation	Correlation coefficient (r)	Environment
Van Landeghem et al [56]	$H_{mean} = 0.0692L^{0.802}$	0.85	Irish Sea in water depths of 20 to 179 m
Flemming [47]	$H_{mean} = 0.0677L^{0.8089}$		Global dataset
Flemming [47]	$H_{max} = 0.16L^{0.84}$		Global dataset
Zhou et al [4]	$H_{mean} = 0.0625L^{0.8125}$	0.94	Giant sand waves on Taiwan Banks (full dataset)
Zhou et al [4]	$H_{mean} = 0.052L^{0.86}$	0.96	Giant sand waves on Taiwan Banks (symmetrical to symmetrical-asymmetrical sand waves)
Zhou et al [4]	$H_{mean} = 0.0005L$	0.1	Giant sand waves on Taiwan Banks (double-crested sand waves)
Zhou et al [4]	$H_{mean} = 0.0018L$	0.2	Giant sand waves on Taiwan Banks (asymmetrical sand waves)
Francken et al [62]	$H_{mean} = 0.0321L^{0.918}$	0.9	Scheldt Estuary
Dalrymple et al [63]	$H_{mean} = 0.0635L^{0.733}$	0.791	Bay of Fundy, Canada

4.1.2 Study aims

The complex hydrodynamic and morphodynamic regime in the southern Irish Sea provides a unique opportunity to analyse both independent and sand bank associated sediment wave fields separately in their localised environments, as well as the relationship between sand banks and associated sediment wave assemblages, and independent offshore assemblages. Therefore, this study will address the following hypotheses;

1. Mobile independent sediment wave assemblages and sand bank associated sediment wave assemblages are supported by independent sediment transport systems.
2. Linear sediment banks do not exhibit a closed circulatory transport system yet reveal a semi-closed circulatory transport system.

To investigate these hypotheses, this study aims to:

a) Describe the morphological characteristics of sediment waves and their spatio-temporal evolution in a tidally dominated, shallow shelf setting in NW Europe;
b) Estimate sediment wave migration rate and infer sediment transport flux, relating the data to the wider sediment transport and hydrodynamic regime of the region;
c) Investigate whether there is a relationship between sand banks and independent sediment wave assemblages.

4.2 Regional setting

Located on the western European continental shelf, the Irish Sea is a semi-enclosed body of water connected to the Atlantic Ocean via two openings; the North Channel and St Georges Channel (Figure 4-2A). The focus of this study is the south-western section within 30km from the east coast of Ireland, which incorporates a complex degenerate amphidrome [5] (Figure 4-2C). This area exhibits intricate seabed morphologies and a complex sediment transport

regime. The Irish Sea is driven by tidal forcing, wind shear stress and baroclinic flow which in turn are major drivers of seabed mobility and sediment distribution. Tide-induced bed shear stress is shown to be the dominant physical process driving seabed mobility in the south-western Irish Sea, with wave-action enhancing mobility in relatively shallow areas such as the southern banks (e.g. Lucifer-Blackwater Bank complex) [64]. Due to intricate basin geometry a convoluted tidal regime exists. Tidal vectors in the Irish Sea are dominated by M_2 and S_2 constituents, whereby M_2 dominates. The tidal wave propagates into the Irish Sea through St Georges Channel and is continuously both deflected to the right by Coriolis Forcing, and reflected northwards by intricate bathymetry and coastline topography. Ultimately, this generates an anticlockwise rotary wave around a degenerate amphidromic point (Amphidrome A) pinpointed on the east coast of Ireland at Courtown (Figure 4-2). This anticlockwise rotation produces high tidal ranges on the east coastline of the Irish Sea and near net zero tidal ranges at this degenerate amphidrome on the west coastline. The flood tidal wave entering through the North Channel, rotates around a similar yet pure (offshore tidal node) anticlockwise amphidromic system (Amphidrome B) (Figure 4-2). These two flooding tidal waves intersect at an angle along a transect approximately from Ardanary to Anglesey, generating a symmetrical tidal system [38] and a bed load parting zone [26]–[28], [39] (Figure 4-2). The shape and location of this bed load parting zone is further controlled by the change in tidal character at abrupt bathymetric changes, headlands and intricate coastline topography, and large-scale constrictions [5].

This bed load parting zone marks the ‘head’ of regional scale divergent bedload transport paths. These are supported by divergent residual flow and bed shear stress vectors [5]. These residual flows support previously bedform-derived bedload transport pathways [26], [27], [30], [39] in the south-western Irish Sea to a certain point [5]. However, this region is highly

dynamic containing many morphodynamic bedforms, and many large morphological features known to diverge from regional scale patterns (sand bank systems and sediment wave assemblages) have yet to be analysed in detail using repeat time-lapse geophysical datasets.

Sediment distribution in the Irish Sea has been characterised by multiple studies [27], [39], [65]–[69]. The south-western Irish Sea is dominated by coarse non-cohesive sands and gravels (clastic sediments) [68] (Figure 4-2C). In regions where sediment supply is limited, the upper mobile layer of Holocene sediments may be limited or absent, resulting in the exposure of the Pleistocene glacial till, or rarely exposed bedrock. In areas of high sediment supply, a transition from coarse-lag gravels and gravelly sands into thick mobile sand sheets (up to 40 m thick) are evident [5], [9]. Both active and moribund sediment waves (some reaching 36 m high) characterise the south-western Irish Sea [56], with migration rates reaching a maximum average of 32 m/yr [30]. Additionally, a series of coast-parallel bedforms are located in approximately 20–40 m water depth rising to only a couple of metres below sea level (Figure 4-2). A variety of studies characterise these sandbanks as being ‘active’, displaying a highly mobile top layer of surficial sediments [66], [70], [71], however, there is a significant paucity of high spatial and temporal resolution sand bank morphodynamic and seabed stability studies under present day hydrodynamics. These complex bathymetries diverge from the net southward residual bedload transport pathway and increase the complexity of localised sediment transport pathways in the region, yet the extent of this divergence and the driving factors are poorly understood.

4.3 Materials and methods

4.3.1 Multibeam echo sounder data acquisition and processing

Since 2006, high resolution swath bathymetry data has been collected across the Irish sector of the Irish Sea by the Republic of Ireland's INFOMAR (Integrated Mapping for the Sustainable Development of Ireland's Marine Resource) programme, a joint venture between the Geological Survey of Ireland and the Marine Institute funded by the Department of the Environment, Climate and Communications (DECC). These acoustic datasets were collected either using i) the hull-mounted Kongsberg Simrad EM2040 and EM3002 multibeam echo sounder (MBES) models via the *RV Celtic Voyager* and *RV Keary*, or ii) the Teledyne Reson Seabat T20-P MBES model which is mounted to a retractable A-frame onboard the *RV Lir*. The vessel and thus instrument used predominately depended on water depth and vessel availability.

All relevant INFOMAR datasets were collated at the highest available spatial resolution (2 m or 5 m) and integrated into a mosaic raster dataset using ArcGIS v10.8 (Figure 4-3). This dataset was used as baseline bathymetry for a preliminary interpretation framework that aimed to identify seabed features and to compute morpho-metric measurements of transverse marine bedforms. Preliminary seabed characterisation and mapping was carried out using elements of the ArcGIS' Benthic Terrain Modeller [72], and geomorphon analysis [73] within GRASS GIS. Based on these interpretations, 12 sub-areas were identified for further geophysical surveying and geological sampling (Figure 4-3).

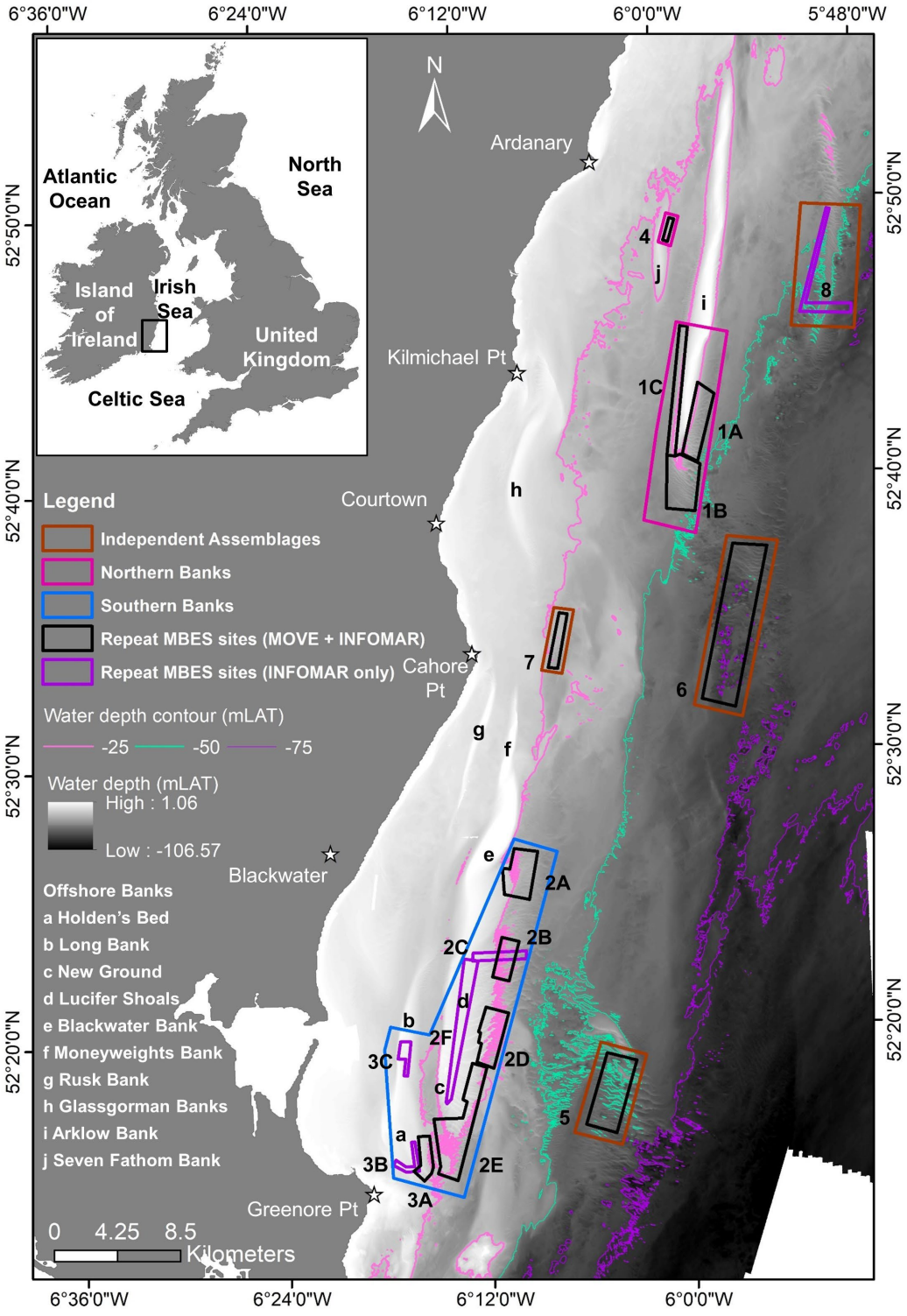


Figure 4-3 Location of multi-beam echo sounder (MBES) bathymetry datasets analysed in this study. Available datasets at each site are presented in Table 4-2. Sites are grouped into three environments for sediment wave analysis: Independent Assemblages, Northern Banks and Southern Banks, which are indicated by blue, pink, and green polygons respectively.

Bathymetry source: composite map produced from INFOMAR datasets (https://www.infomar.ie/data [Accessed: 10 June 2021]) (see section 4.3.1).

Additional repeat MBES data was acquired on three targeted surveys in 2020 and 2021 onboard the *RV Celtic Voyager* (Table 4-2).

The Mobility of Sand Waves and Sediment Banks (MOVE) offshore survey campaigns involved targeted MBES work over the 12 identified sites, onboard the *RV Celtic Voyager*. A Kongsberg dual head EM2040 was used operating at 300 kHz and a beam angle of 69° to 75° on both port and starboard side, depending on water depth. Accurate positioning was provided by an Integrated GNSS/L-Band receiver CNAV 3050 (horizontal/vertical accuracies of +/- 5 cm/ 10 cm. Data was logged onboard using the Kongsberg's Seafloor Information System (SIS) v. 3.83 acquisition software. A Valeport Sound Velocity Profiler (SVP) Mini instrument was used to acquire SVP profiles, which were imported into SIS and fed directly into the echosounder. Using Qimera v2.3.1, all MBES datasets were processed to remove erroneous pings and correct for tidal and water displacement offsets. MBES-derived bathymetry datasets were reduced to Lowest Astronomical Tide (LAT) using a Vertical Offshore Reference Frame (VORF). Quality control was performed using crosslines where available. Datasets were georeferenced using GCS WGS 1984 geographic co-ordinate system and output in raster format at 1 m spatial resolution.

Table 4-2 Details of MBES bathymetry datasets used in this study. Location of each site is presented in Figure 4-3.

		INFOMAR bathymetry datasets						Mobility of Sand Waves and Sediment Banks (MOVE) bathymetry datasets		
Year collected		2009	2011	2012	2015	2016	2017	2020 (Sep)	2020 (Oct)	2021 (Mar)
Offshore Survey Codes		CV09_03	KRY11_02 CV11_03	CV12_02 CV12_01	KRY15_03	KRY16_03 GEO16_03 KRY16_02	LIR17_01 KRY17_02	CV20010	CV20035	CV21035
Spatial resolution (m)		2	2 5	2 5	2	2	2	1	1	1
Sites	1A		√	√		√		√		√
	1B		√	√		√		√		
	1C		√	√		√		√		√
	2A			√			√	√		√
	2B	√		√				√	√	√
	2C	√		√						
	2D	√						√		√
	2E	√						√		√
	2F				√		√			
	3A	√						√		
	3B	√	√							
	3C	√	√				√			

	4		√					√		√
	5			√				√		√
	6			√				√		
	7			√				√		√
	8		√	√						

4.3.2 Sediment wave analysis

Areas of time-lapse bathymetric data were identified for further analysis. These included datasets from the MOVE offshore survey campaigns, and areas of relatively small overlap between the INFOMAR datasets. Eight main areas, comprising 17 sub-areas in total, were identified. The location and available datasets for each site are presented in Figure 4-3 and Table 4-2.

4.3.2.1 Sediment wave geometric characteristics

Sediment wave characterisation is a key component in classifying the geomorphology of a sediment wave and in inferring bedform dynamics over time. Previously, the delineating of sediment wave crests has largely relied on manual digitisation based on MBES and MBES-derived datasets (e.g. slope) [30]. Similarly, the derivation of bedform dimensions has mainly depended on cross-sectional profiles derived from these MBES datasets [56]. More automated methods have included geomorphometry [73], object-based image analysis [74], the second derivative [75], curvature [76], and zero-crossing analysis [77]. The application of Fourier analysis has also proven successful in sediment wave characterisation [78]. Following a review of applications, it was found the approach of Wang et al [78] was the most appropriate for sediment wave characterisation due to its ease of use and accuracy of results.

The automated MATLAB-based method for analysing bedform geometry parameters was applied to the baseline (earliest) bathymetry dataset at each site. This tool combines 2D Fourier analysis, wavelet transform, zero-crossing analysis and a variety of filters. Sediment wave dimensions defined by this tool and adopted by this study are given in Figure 4-4, where sediment wave asymmetry (A) is given as

$$A = \frac{L_1 - L_2}{L} \quad (1)$$

and water depth (d) of a sediment wave is defined as

$$d = d(cr) + H \quad (2)$$

where $d(cr)$ is the water depth of the sediment wave crest and H is sediment wave height and L is sediment wave wavelength. Sediment wave parameters were used to classify bedforms at each site according to the sizing system adopted by Van Landeghem et al [56] and Evans et al [79], originally adapted from Ashley [46] and Berne et al [80] (Table 4-3). Similar to Van Landeghem et al [56], the term 'sediment wave' is used in this study to describe large flow-transverse bedforms and the terms 'sand wave' or 'gravel wave' are used when sediment composition could be determined.

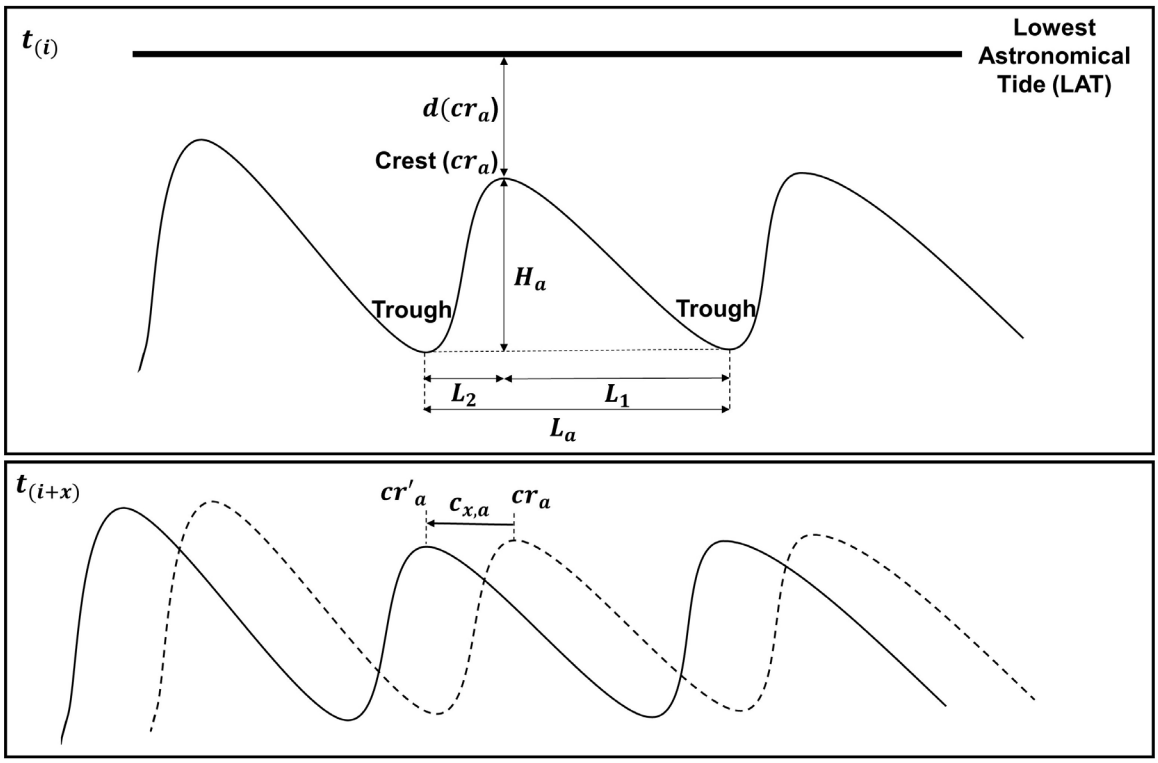


Figure 4-4 Illustration representing sediment wave (SW) characteristics used in this study. For SW "a", the figure denotes cr = SW crest, $d(cr)$ = water depth of SW crest; H = SW height; L = SW wavelength (and length components L_1 and L_2); $t_{(i)}$ = time of first bathymetric survey over SW field; $c_{(x)}$ = displacement of SW crest over time interval x; cr′ = position of displaced SW crest over time interval x.

Table 4-3 Sediment wave size classification scheme used in this study. Source: Van Landeghem et al [56] *and Evans et al* [79]*, originally adapted from Ashley* [46] *and Berne et al* [80]

Sediment wave classification	Height (m)	Wavelength (m)
Small	0.04 – 0.25	0.6 – 5
Medium	0.25 – 0.44	5 – 10
Large	0.44 – 2.8	10 – 100
Very large	> 2.8	> 100

4.3.2.2 Sand wave migration direction and rates

Previous studies calculate migration rate over two-dimensional (2-D) cross-sectional profiles perpendicular to the crest [4], [30]. These provide a good estimate of migration rate and direction in localised areas, but fail to represent changes in rate and direction along the crest and in the wider assemblage and give a more regional view of the sediment transport system and hydrodynamic drivers. This study calculates migration direction and rates through an iterative process using a combined method in GRASS GIS v.7.6.1, QGIS v.3.8.1 and ArcGIS v.10.8.

The methodology of Di Stefano and Mayer [81] for extracting sediment wave crests by geomorphon analysis [73] was adapted by this study. Georeferenced polyline shapefiles of delineated sediment wave crests in plan-view were produced from each individual bathymetric raster dataset (Table 4-2). These datasets were quality controlled (QC) in ArcGIS v.10.8 using the slope and Terrain Ruggedness (VRM) tool [72]. Taking two time-lapse shapefiles at a time and starting with the earlier time-step, several steps were taken to calculate the direction and magnitude of sediment wave crest displacement over time (Figure 4-4) in ArcGIS v.10.8 and QGIS v.3.8.0. A step-by-step guide can be found in the supplementary material to this article. Annual migration rates along the crest of each sediment wave were subsequently calculated based on the dates of each survey.

Crest perpendicular cross-sections were extracted from time-lapse bathymetric datasets for further morphological and geomorphological analysis. This study uses a combination of the two-part geomorphological classification scheme developed by Dove et al [82] and the classification scheme adopted by Van Landeghem et al [56]. Digital Elevation Models (DEM) of difference (DOD) were calculated to quantify the volumetric change between successive

bathymetric surveys, highlight geomorphic changes in a three-dimensional (3-D) surface, and QC sediment wave migration directions. This aided the quantification of change in a one-dimensional (1-D), 2-D and 3-D manner, allowing for a better understanding of bedform development across a sediment wave assemblage. This allows the interpretation of trends in the wider hydrodynamic-morphodynamic system.

4.3.3 Sediment samples

Surficial sediment samples were collected using either the Day Grab sampler or the Shipek sampler during the three MOVE survey campaigns (Figure 4-3). All sediment samples were processed by sieving or laser granulometry. Furthermore, sediment samples containing raw granulometric data was compiled from Geological Survey of Ireland (GSI). The MOVE and GSI datasets were combined, and statistical analysis was carried out using the R package 'geotech' [83]. The resulting median grain size, D_{50}, values were interpolated into a raster dataset in ArcGIS v10.8. This raster dataset is used for two levels of analysis:

a) At an individual site level: The resulting point file produced from the Wang et al [78] method (section 4.3.2.1), that delineates the crest of sediment waves in each of the 17 sites (Figure 4-3), is used to extract D_{50} values from the interpolated raster. These extracted values are used in the investigation of statistical relationships between individual sediment wave dimensions and environmental parameters/processes such as median grain size, D_{50}, and Rouse number, P (which indicates the mode of sediment transport).
b) At a coarse level to elucidate the dynamics of the wider sediment transport system. The raster dataset was interpolated onto a 500 m resolution point grid, covering the entire south-western Irish Sea region. This dataset was used to calculate P,

entrainment function, F_S, and shear Reynold's number, Re_*. Formulae used are presented in section 4.3.5.

4.3.4 Hydrodynamic modelling

A validated, two-dimensional, hydrodynamic model covering the entire Irish Sea, developed using the Danish Hydraulics Institute's MIKE 21 suite of tools [84], [85], was used to simulate bed shear stress and tidal current u and v magnitude components for a one-month period using a time-step of 30 s. Model set-up and validation is published in Coughlan et al [64].

The hydrodynamic model [85] determines bottom shear stress, τ_b, by quadratic friction law:

$$\tau_b = C_d \rho \overline{U}^2 \quad (3)$$

where C_d is a drag coefficient, ρ is the density of the fluid medium in seawater and $\overline{U}$ is the depth averaged velocity. The drag coefficient is determined as;

$$C_d = \frac{g}{(Mh^{1/6})^2} \quad (4)$$

where h is the total water depth and g is the acceleration due to gravity and M is the Manning number. A constant Manning number of 32 $m^{(1/3)}s^{-1}$ was applied in this case. Model outputs were interpolated on to a 1 km² grid where the residual bed shear stress and residual tidal currents were calculated. These datasets were used by Creane et al [5] and used again in this study.

Raster datasets of mean and maximum current velocities, produced by Coughlan et al [64] were also used in this study.

All four datasets were interpolated onto the same two shapefiles as grain size data in section 4.3.3, i.e.

a) the 500 m resolution matrix, for coarse level theoretical parameter calculations, and
b) the resulting point shapefile produced from the Wang et al [78] method in section 4.3.2.1, for investigation into the relationship between environmental parameters and individual sand wave dimensions.

4.3.5 Theoretical parameters

The Rouse number, P, which indicates the mode of sediment transport is calculated similar to that of Borsje et al [86],

$$P = \frac{w_s}{1 \times 0.40 \times u_*} \tag{5}$$

Where w_s is the particle settling velocity according to Allen's Law,

$$w_s = \frac{0.153 \times [(\rho_s - \rho) \times g]^{0.714} \times {D_{50}}^{1.143}}{\mu^{0.430} \times \rho^{0.286}} \tag{6}$$

where ρ_s is the density of particle, ρ is the density of a fluid, g is the acceleration due to gravity, μ is the dynamic viscosity of a liquid, D_{50} is the median grain size and u_* is the shear velocity according to

$$u_* = \sqrt{\frac{\tau_b}{\rho}} \tag{7}$$

where τ_b is the bottom shear stress as given in section 4.3.4 under tidal current only. In this case, C_d is calculated as below

$$C_d = \left[\frac{k}{\ln\left(\frac{h}{z_0}\right) - 1}\right]^2 \tag{8}$$

where h is water depth, k is the von Karman constant and z_0 is the hydraulic roughness given from the following equation

$$z_0 = \frac{2.5 \times D_{50}}{30} \tag{9}$$

Bedload transport is dominant when $P > 2.5$, whereas suspended load transport is the dominant mode when $0.8 < P < 1.2$.

Shields [87] found that a plot of the entrainment function, F_s, against the shear Reynolds number, Re_*, produced a useful chart for predicting the threshold of motion and bedform type when threshold conditions are exceeded. The entrainment function is the ratio of the lift force on a sediment particle to its submerged weight, given by

$$F_s = \frac{\tau_b}{\left(\frac{\rho_s}{\rho} - 1\right) \rho g D_{50}} = \frac{{u_*}^2}{\left(\frac{\rho_s}{\rho} - 1\right) g D_{50}} \tag{10}$$

The shear Reynolds number is proportional to the ratio of the sediment particle diameter to the thickness of the viscous sub-layer

$$Re_* = \frac{u_* D_{50}}{v} \tag{11}$$

where critical shear stress is exceeded by bottom shear stress, sediment is mobilised. The Mobilisation Frequency Index (MFI), developed by Coughlan et al [64], showing the yearly exceedance of critical shear stress (τ_{cr}) under current-induced (τ_c) and combined current- and wave-induced bed shear stress (τ_{cw}), is used in this study.

4.4 Results

4.4.1 Sand wave characteristics

4.4.1.1 Sediment wave shape

Figure 4-5 exhibits the variation of sediment wave shape across the south-western Irish Sea. The morphological definition is two-fold, with waves occurring as either asymmetric (i.e., progressive) or symmetric (i.e., trochoidal), and with crests that are either round, sharp and/or bifurcating. Sediment waves can be compound (superimposed by smaller sediment waves) or simple, and occur in two- or three-dimensional form.These morphological characteristics often occur within the same sediment wave field and/or environment, and frequently change over time between time-lapse survey intervals, for example, the same sediment wave may transition from round- to sharp- crested or from simple to compound or vice versa. An example of each of these types is represented in Figure 4-6.

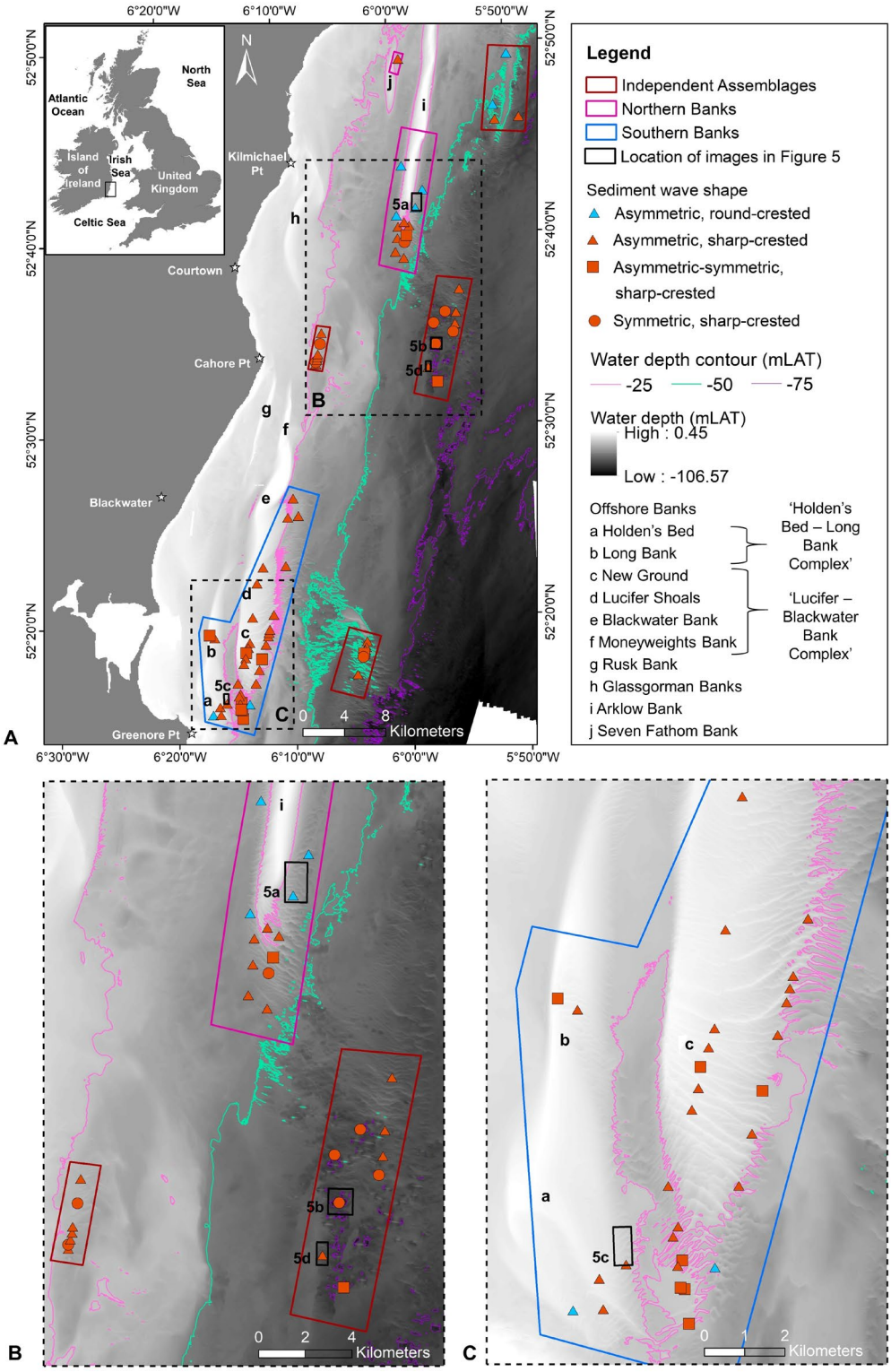


*Figure 4-5 Interpreted average sediment wave shape across the south-western Irish Sea. The location of (**B**) and (**C**) are provided in (**A**). Black boxes and labels indicate the location of figures in Figure 4-6. Bathymetry source: composite map produced from INFOMAR datasets https://www.infomar.ie/data [Accessed: 10 June 2021]) (see section 4.3.1)*

Independent sediment wave assemblages display predominately round to sharp-crested, asymmetric sediment waves, interspersed with very large sharp-crested trochoidal sediment waves. Sediment waves associated with sand banks display a much greater variance in sediment wave type over a relatively small spatial extent in comparison to these independent wave fields (Figure 4-5).

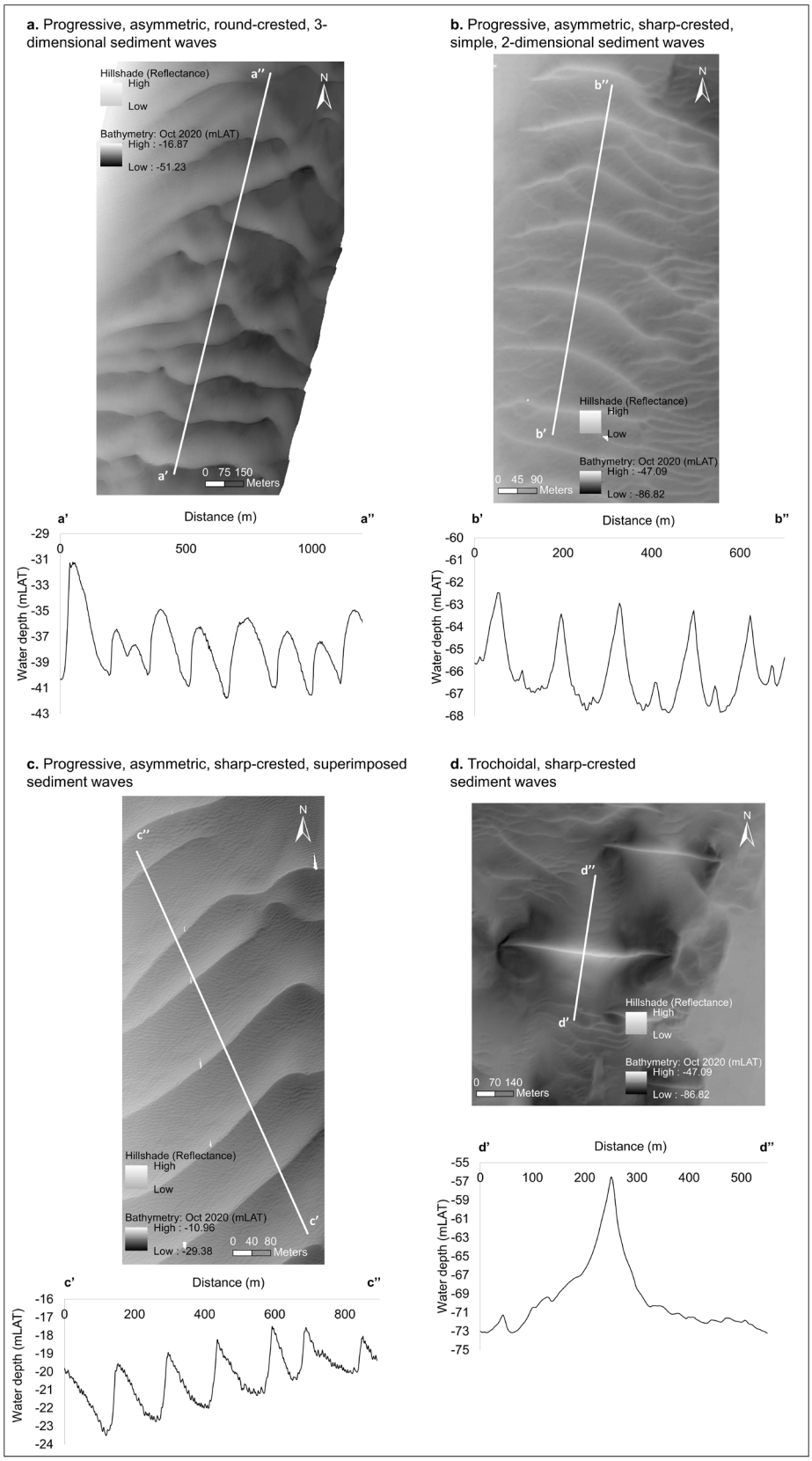


Figure 4-6 Selection of sediment wave types observed in the south-western Irish Sea; a. progressive, asymmetric, round-crested, 3-dimensional sediment waves, b. progressive, asymmetric, sharp-crested, simple, 2-dimensional sediment waves, c.

progressive, asymmetric, sharp-crested, superimposed sediment waves, and d. trochoidal, sharp-crested sediment waves. A representative cross-section is given for each type. Locations are given in Figure 4-5. Bathymetry source: MOVE 2020 survey (see site 1A, 6 and 3A in Table 4-2).

4.4.1.2 Sediment wave dimensions

Analysed sediment waves occur in a range of water depths from 8.2 to 83 mLAT, exhibiting wave heights and wavelengths ranging from 0.1 to 25.7 m and 17 to 983 m respectively. A summary of sediment wave dimensions for each individual site is given in Table 4-4. Markedly, the highest maximum sediment wave heights occur in independent sediment wave assemblages at sites 5 and 6 (Figure 4-3). These large dimensions correspond to very large, isolated trochoidal sediment waves. Contrastingly, the largest maximum wavelength values are evident along the eastern slope of Lucifer Bank at sites 2D and 2E. These large wavelengths are connected to a sequence of relatively large sediment waves, or transverse sediment ridges, extending in a curvilinear form from the sand bank crest to bank base. However, as shown in Table 4-4 these very large sediment waves do not represent the entire sites and are instead encompassed by relatively smaller large to very large sediment waves with a mean wave height of 2.9 to 4.7m (at sites 2D and 2E) and mean wavelength of 157.4 to 215.1 m (at sites 5 and 6). These morphological variations will be discussed further in sections 4.4.2.2.1 and 4.5.1.2.

Table 4-4 Sediment wave characteristics for each individual study site based on first time-lapse bathymetric dataset

Site		Wave Height (m)	Wave Length (WL) (m)	Left WL (m)	Right WL (m)	Asymmetry	Steepness	Average lee slope angle (°)	Water depth (mLAT)	D50 (mm)
7	mean	2.1	114.5	65.1	49.4	0.12	0.019	3.0	30.2	0.3
	max	5.2	355.0	213.0	241.0	0.72	0.053	9.3	32.5	0.5
	min	0.3	43.0	10.0	14.0	-0.82	0.002	0.3	27.5	0.2
2A	mean	2.4	142.2	60.8	81.4	-0.14	0.018	2.9	30.2	0.4

	max	7.5	474.0	343.0	337.0	0.82	0.060	16.1	38.8	0.8
	min	0.2	22.0	4.0	7.0	-0.92	0.001	0.0	18.8	0.2
2B and 2C	mean	4.0	150.2	90.3	59.9	0.18	0.027	4.6	26.3	0.6
	max	11.7	494.0	446.0	280.0	0.82	0.069	14.2	38.1	2.2
	min	0.6	30.0	5.9	12.0	-0.87	0.002	0.5	13.1	0.3
2D	mean	4.7	215.1	114.4	100.6	0.06	0.023	3.8	25.3	1.2
	max	11.7	813.0	620.0	617.1	0.84	0.085	11.6	44.9	1.9
	min	0.7	59.0	9.0	11.9	-0.89	0.002	0.4	11.6	0.4
2E	mean	2.9	157.4	76.4	81.1	-0.04	0.021	3.3	25.4	1.1
	max	12.3	983.0	842.0	883.0	0.91	0.071	16.0	38.5	2.6
	min	0.4	28.3	5.0	4.0	-0.90	0.001	0.3	8.2	0.3
3A and 3B	mean	1.5	126.1	67.6	58.5	0.04	0.013	2.1	20.2	0.8
	max	6.3	281.0	239.0	224.1	0.83	0.063	11.9	29.2	1.5
	min	0.2	30.0	4.0	7.0	-0.91	0.001	0.2	9.3	0.3
1A	mean	3.0	140.2	56.3	83.9	-0.19	0.022	4.1	34.7	0.8
	max	15.2	421.0	310.0	335.0	0.88	0.083	27.3	52.2	5.0
	min	0.2	28.0	5.0	4.0	-0.92	0.001	0.1	15.8	0.3
1B	mean	4.7	165.4	80.5	84.9	-0.02	0.029	4.7	38.0	0.3
	max	18.1	581.0	442.0	481.0	0.84	0.092	18.0	51.1	0.9
	min	0.6	33.0	9.9	10.9	-0.89	0.003	0.2	19.1	0.1
1C	mean	2.3	123.5	56.6	66.9	-0.06	0.020	3.2	26.1	0.3
	max	7.5	422.1	242.1	338.0	0.91	0.082	15.6	39.7	0.8
	min	0.2	26.0	6.0	4.0	-0.87	0.001	0.0	8.5	0.1
4	mean	0.6	124.8	63.9	60.9	0.02	0.005	0.9	28.7	0.4
	max	1.2	291.0	240.0	229.0	0.70	0.016	3.2	29.7	0.7
	min	0.1	50.0	13.0	12.0	-0.65	0.001	0.1	27.1	0.3
5	mean	6.1	216.7	106.5	110.2	-0.02	0.029	4.8	57.9	0.6
	max	23.5	681.0	505.0	576.1	0.86	0.088	17.4	72.9	2.3
	min	0.9	52.0	4.9	13.0	-0.91	0.002	0.5	36.6	0.2
6	mean	4.7	163.7	77.2	86.5	-0.05	0.030	4.8	65.9	1.3
	max	25.7	614.0	428.1	460.1	0.80	0.120	23.0	83.0	5.0
	min	0.4	34.0	5.9	9.9	-0.90	0.002	0.5	52.8	0.3
3C	mean	1.4	101.8	51.5	50.3	0.00	0.015	2.5	18.7	1.0
	max	3.7	313.0	196.0	213.0	0.77	0.044	8.5	26.8	2.8
	min	0.2	29.0	3.0	9.0	-0.87	0.001	0.0	10.4	0.8
2F	mean	1.5	174.9	62.9	112.0	-0.27	0.009	1.8	11.2	0.8
	max	4.4	599.0	336.0	391.0	0.73	0.043	8.0	14.2	1.1
	min	0.2	45.0	9.0	22.0	-0.92	0.001	0.1	7.8	0.3

8	mean	3.4	159.8	93.6	66.3	0.11	0.022	3.7	53.5	0.5
	max	10.2	478.0	365.1	303.0	0.83	0.068	15.4	72.0	1.0
	min	0.1	17.0	3.0	5.0	-0.87	0.001	0.3	40.0	0.3

Table 4-5 and Figure 4-7 display the power regression relationship between sediment wave height and wavelength for i) the full dataset, ii) three separate environments, and iii) each individual study site (Figure 4-3; Figure 4-4). The full dataset and each environment show moderately to strong positive relationships (r = 0.52 to 0.71) between these two parameters, indicating a relatively large scatter of data points. The relationship derived from the full dataset ($H_{mean} = 0.03L^{0.90}$) is relatively lower than the power relation described from the global dataset ($H_{mean} = 0.0677L^{0.8089}$), yet almost identical to that found by Francken et al [62] (Table 4-1). Sediment waves at both the northern banks and independent assemblages display similar relationships to the full dataset yet the southern banks display a relatively higher relationship of $H_{mean} = 0.05L^{0.77}$, correlating well with the relationship derived from giant sand waves on the Taiwan Banks, in the Taiwan Strait [4] (Table 4-1).

On an individual site level, sediment wave assemblages associated with sediment banks display relatively higher power relationships in comparison to those independent from larger bedforms i.e. sites 5, 6 and 8. These higher relationships grow closer to the upper limit of sand wave growth ($H_{max} = 0.16L^{0.84}$) defined by Flemming [48]. Additionally, these higher relationships correlate better with the height-spacing power-law relationships derived by Van Landeghem et al [56] in the Irish Sea under different depth intervals; a) 20 – 30 m ($H = 0.1082L^{0.6174}, r = 0.870$), b) 20 – 40 m ($H = 0.0921L^{0.6651}, r = 0.856$), and c) 20 – 60 m ($H = 0.0921L^{0.6651}, r = 0.869$). Site 2D exceeds this upper limit with a moderate positive correlation (r = 0.43).

Table 4-5 Relationship between bedform heights and wavelengths in the south-western Irish Sea. The Full dataset has been broken into three environments i.e. Southern Banks, Northern Banks and Independent Assemblages, and each individual study site.

Dataset	Power regression equation	r^2	Correlation coefficient (r)	Correlation description
Full dataset	$H_{mean} = 0.03L^{0.90}$	0.33	0.58	Moderate positive
Southern Banks	$H_{mean} = 0.05L^{0.77}$	0.27	0.52	Moderate positive
Northern Banks	$H_{mean} = 0.02L^{0.95}$	0.28	0.52	Moderate positive
Independent Assemblages	$H_{mean} = 0.03L^{0.96}$	0.50	0.71	Strong positive
8	$H_{mean} = 0.03L^{0.91}$	0.53	0.73	Strong positive
2F	$H_{mean} = 0.08L^{0.56}$	0.15	0.39	Weak positive
3C	$H_{mean} = 0.12L^{0.52}$	0.12	0.34	Weak positive
6	$H_{mean} = 0.04L^{0.92}$	0.48	0.69	Strong positive
5	$H_{mean} = 0.06L^{0.83}$	0.38	0.62	Strong positive
4	$H_{mean} = 0.29L^{0.13}$	0	0.07	Very weak positive or no association
1C	$H_{mean} = 0.08L^{0.78}$	0.30	0.55	Moderate positive
1B	$H_{mean} = 0.10L^{0.63}$	0.14	0.38	Weak positive
1A	$H_{mean} = 0.01L^{1.04}$	0.30	0.55	Moderate positive
3A and 3B	$H_{mean} = 0.06L^{0.64}$	0.13	0.36	Weak positive
2E	$H_{mean} = 0.11L^{0.63}$	0.31	0.56	Moderate positive
2D	$H_{mean} = 0.22L^{0.55}$	0.19	0.43	Moderate positive
2B and 2C	$H_{mean} = 0.11L^{0.71}$	0.31	0.56	Moderate positive
2A	$H_{mean} = 0.07L^{0.69}$	0.26	0.51	Moderate positive
7	$H_{mean} = 0.08L^{0.67}$	0.19	0.43	Moderate positive

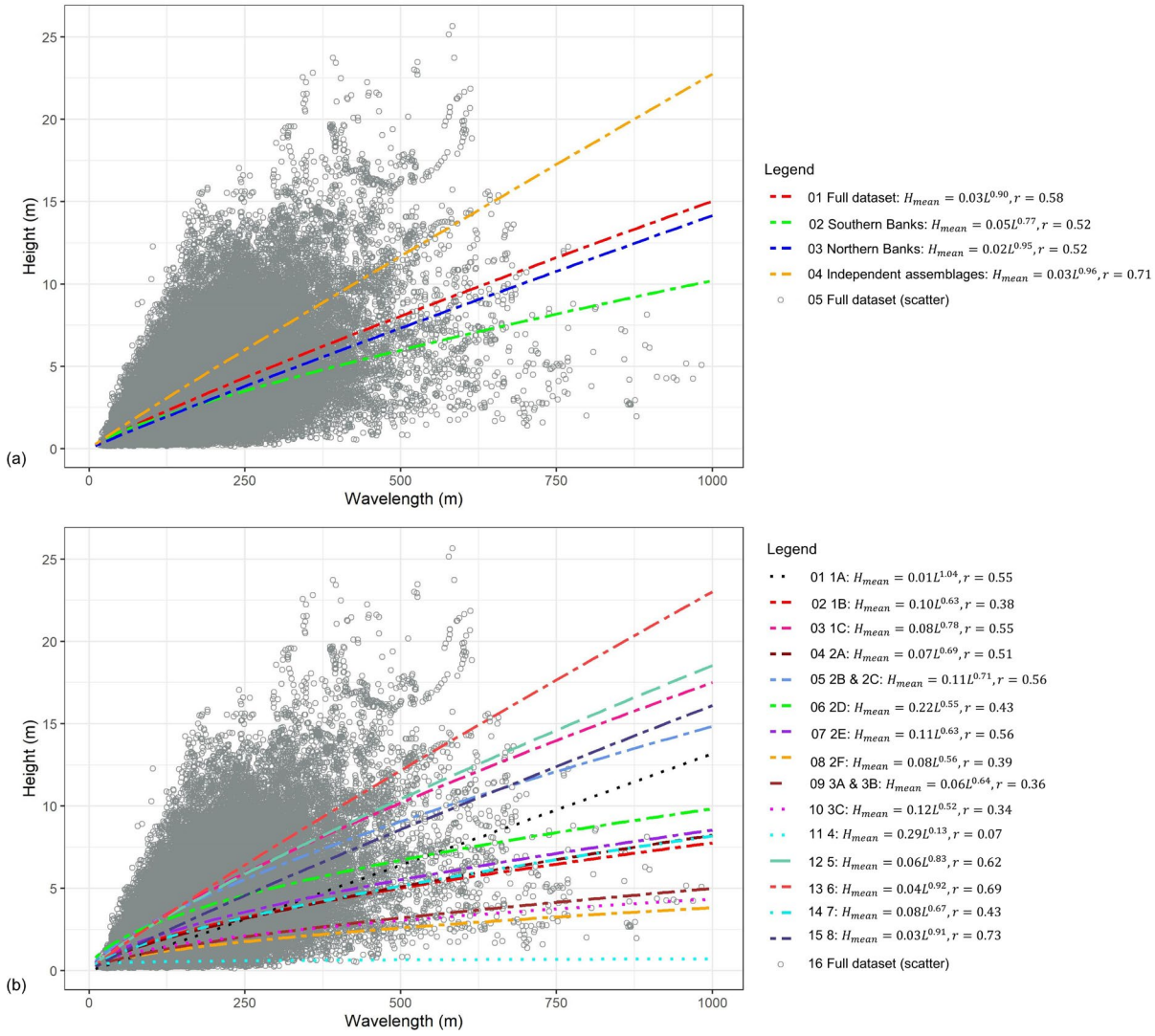


Figure 4-7 *Relationship between sediment wave heights and wavelengths in the south-western Irish Sea: (**a**) displays the results for the full dataset and for three compiled environments i.e., Southern Banks, Northern Banks and Independent Assemblages, and (**b**) displays the results for each individual study site.*

4.4.2 Spatial and temporal evolution of sediment waves

Figure 4-8 presents the average annual sediment wave migration directions and rates, derived from plan-view crest displacement over time. Each arrow in Figure 4-8 accurately represents the average migration parameter of a set of consecutive sediment waves (Figure 4-4) travelling in the same direction and approximately at a similar rate.

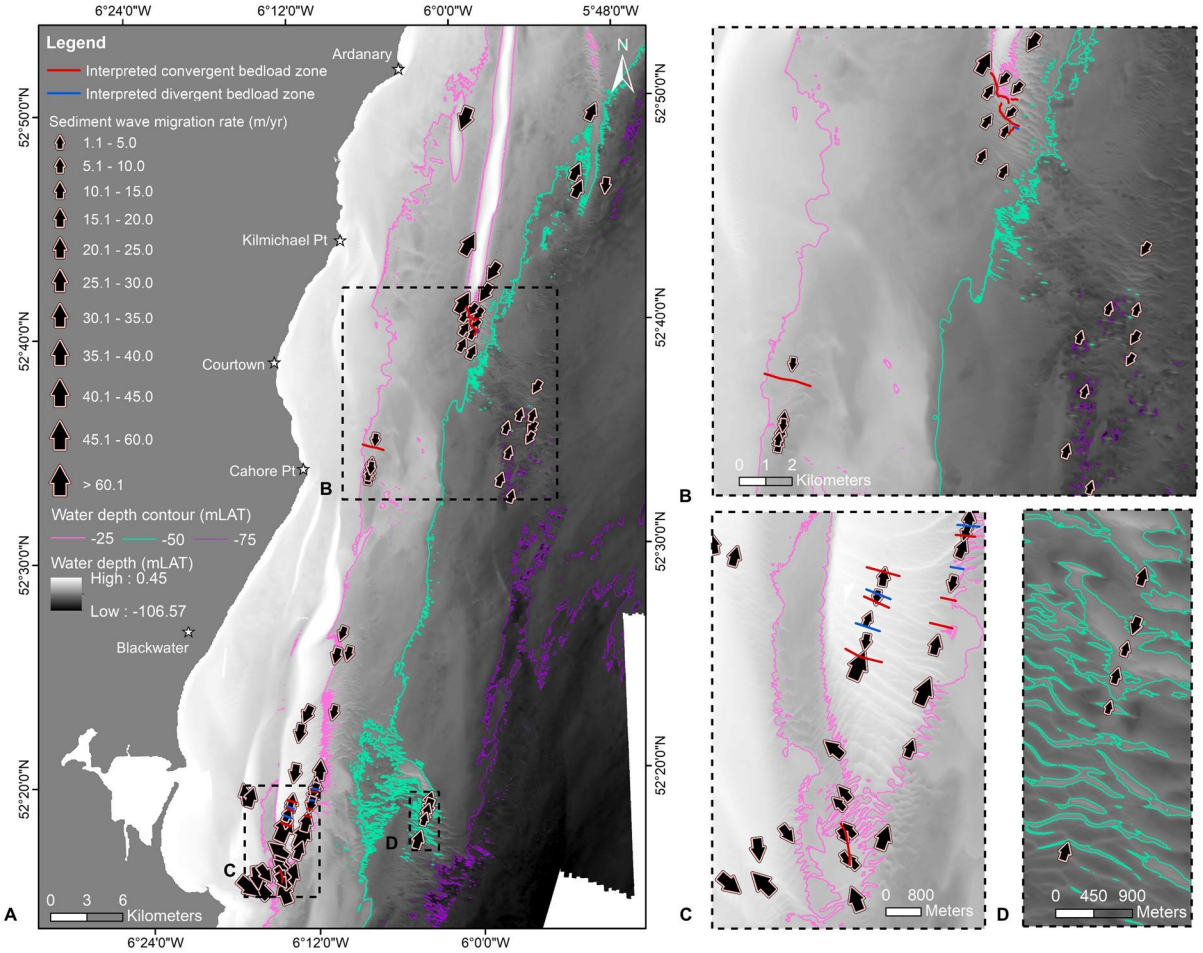


*Figure 4-8 Average annual sediment wave migration rates updated with new time-lapse multi-beam echo sounder bathymetry datasets: (**A**) an overview of south-western Irish Sea, whereby the locations of (**B**) to (**D**) are indicated; (**B**) inset of study sites 1, 6 and 7; (**C**) inset of study sites 2 and 3; (**D**) inset of study site 5. See Figure 4-3 for study site boundaries. Figure bathymetry data source: composite map produced from INFOMAR datasets (referenced to Lowest Astronomical Tide (LAT)) https://www.infomar.ie/data [Accessed: 10 June 2021]) (see section 4.3.1)*

At many study sites, time intervals between various time-lapse bathymetry datasets were too long to accurately derive migration parameters. This was predominately due to; a) sediment waves had migrated more than one wavelength and so could not be accurately identified as the same wave in two consecutive datasets, or b) the sediment wave had undertaken a significant amount of morphological change (e.g. crest deterioration, amalgamation of two sediment waves), and so the same wave could not be identified in consecutive datasets.

Nevertheless, at each location at least two bathymetric datasets could be used to accurately measure migration parameters. Newly identified local convergence and divergence zones are also delineated. Distinct spatial and temporal variability and morphological evolution observed at each site will be described in more detail in the following sections.

4.4.2.1 Sediment waves associated with Arklow Bank

On the south-east side of Arklow Bank, a progressive, asymmetric, round-crested, irregular sediment wave assemblage migrates in a south-westerly direction at a rate of 23 m/yr (Figure 4-9). These very large sediment waves transition abruptly from an irregular assemblage that is limited to the lower slope and base of the bank, to a regular assemblage that covers a larger spatial area, extending eastward from the bank crest to bank base.

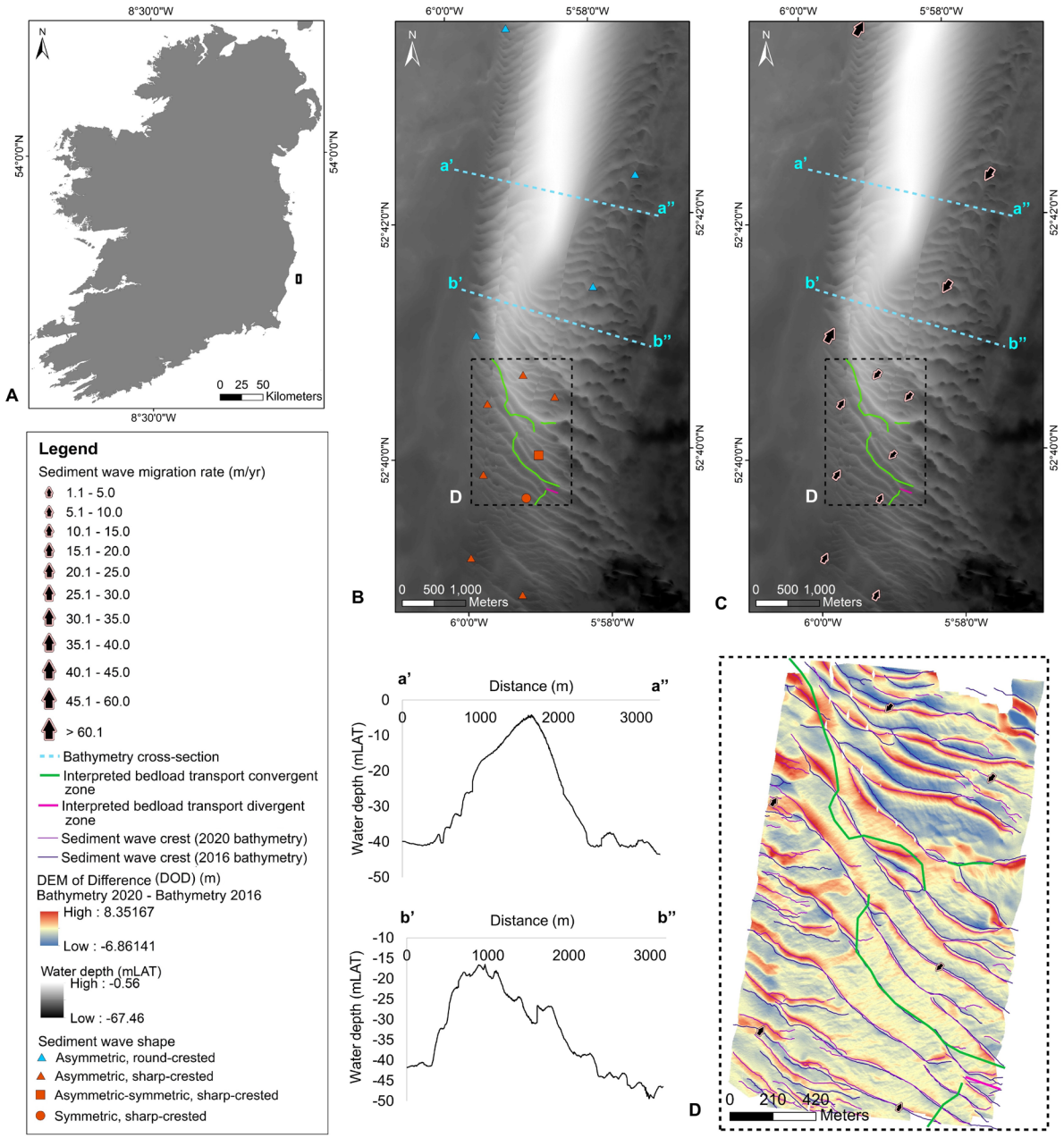


*Figure 4-9 Sediment wave translation rates and shapes at the southern extent of Arklow Bank in the Irish Sea: (**A**) location of Arklow Bank; (**B**) sediment wave shape with locations of cross-sections a and b; (**C**) and (**D**) sediment wave translation rates.(**B**) and (**C**) bathymetry source: composite map produced from INFOMAR datasets (https://www.infomar.ie/data [Accessed: 10 June 2021]) (see section 4.3.1). (**D**) bathymetry source: 2016: INFOMAR survey; 2020: MOVE survey (see site 1B in Table 4-2)*

This abrupt transition correlates with a sudden change in sand bank morphology at its southern end. Sand bank height is markedly reduced whilst wavelength is increased, revealing

a more elongated, subdued asymmetric shape (Figure 4-9). This is associated with increased water depth at the bank crest and a distinct westward facing lee slope indicating a potential westward migration at this section. Sediment wave crests extend along the entire length of the bank's stoss slope, changing progressively from a perpendicular to curvilinear alignment to the bank crest. Specifically, sediment waves display a distinct reduction in migration rate from 23 m/yr to 8.5 m/yr where the crest alignment transitions from E-W to SSE-NNW. Additionally, this combined migration rate reduction and crest orientation change marks a distinct morphological change in the sediment wave assemblage from round- to sharp-crested. Migration rate continues to reduce to 2.8 m/yr to almost zero mobility at a curvilinear convergence zone (Figure 4-9), whereby these southward migrating bedforms are met with a northward flowing assemblage. This convergence zone is marked by a relatively larger, sharp-crested, symmetrical, curvilinear sediment ridge, marking a build-up of sediment (accretion) in this zone. This ridge is bound on either side by asymmetrical waves moving in the opposite directions, of which grow progressively more asymmetric with increasing distance from the convergence zone.

South of this convergent zone on the eastern side of the bank, a progressive, sharp-crested, symmetric to slightly asymmetric sediment wave assemblage, migrates northwards towards the convergent zone at an average rate of 2.5 m/yr. Moving westwards and north-westwards along the convergent line, on the outer edge of the sediment wave assemblage, asymmetric sediment waves move northwards at a higher rate of 9.8 m/yr. South of this region, sand bank flattens more rapidly, water depth increases progressively, and northward migrating sediment waves (at 8.1 m/yr) are asymmetric, progressive and sharp-crested. Furthermore, at the foot of the lee slope of the bank, where there is an increase in sediment wave northward migration rate (9.8 m/yr to 32.7 m/yr), a distinct morphological change from

sharp-crested sediment waves to round-crested sediment waves is observed. This is consistent with the sudden morphological changes on the stoss slope. These lee-slope northward migrating waves migrate faster (32.7 m/yr) than southward moving waves on the stoss slope (23 m/yr). They continue migrating northwards at an average rate of 32.7 m/yr on the lee slope.

On both sides of the bank, in plan-view, sediment wave crests markedly alter their orientation from approximately E – W to SW – NE when transitioning from base to slope. Ultimately, the sediment wave crest orientation adjusts to a curvilinear configuration to adjust progressively towards parallel alignment with the bank crest. However, except for the southern extent of the bank where its morphology becomes more subdued, no sediment waves have been observed reaching the crest of the bank. This may be due to limited water depth and complex hydrodynamic and wave climate conditions.

4.4.2.2 Sediment waves associated with Lucifer-Blackwater bank and Holdens Bed-Long bank complexes

4.4.2.2.1 Southern extent of Lucifer-Blackwater bank complex

Sediment waves in the southern section of Lucifer-Blackwater Bank complex (sites 2D, 2E and 2F) (Figure 4-3) are highly mobile and highly morpho-dynamic whereby their shape, migration direction and migration rate progressively change throughout the study area (Figure 4-10). In contrast to Arklow Bank, the southern section of Lucifer-Blackwater Bank complex does not display an circulatory bedform migration pattern around the bank itself. Instead, sediment waves migrate approximately north-westwards and north-eastwards on the western and eastern sides of the bank respectively (Figure 4-10B). This general northward migratory trend becomes increasingly intricate with addition of the following observations;

a) the presence of a clear reversal in sediment wave migration direction or 'pivoting' phenomenon over an approximate 1000m transect on the lower slope of the south-western side of the bank (Figure 4-10D),
b) the presence of multiple reversals in migration direction that ultimately generate a localised, complex sediment transport convergence and divergence pattern within a restricted area (over approximately 2400m) on the south-eastern side of the bank (Figure 4-10B and C), and
c) the dominant north-eastward moving bedforms are met with a dominant southward sediment transport pathway originating along the Blackwater Bank ('F' in Figure 4-10B).

These three observations will be discussed in detail.

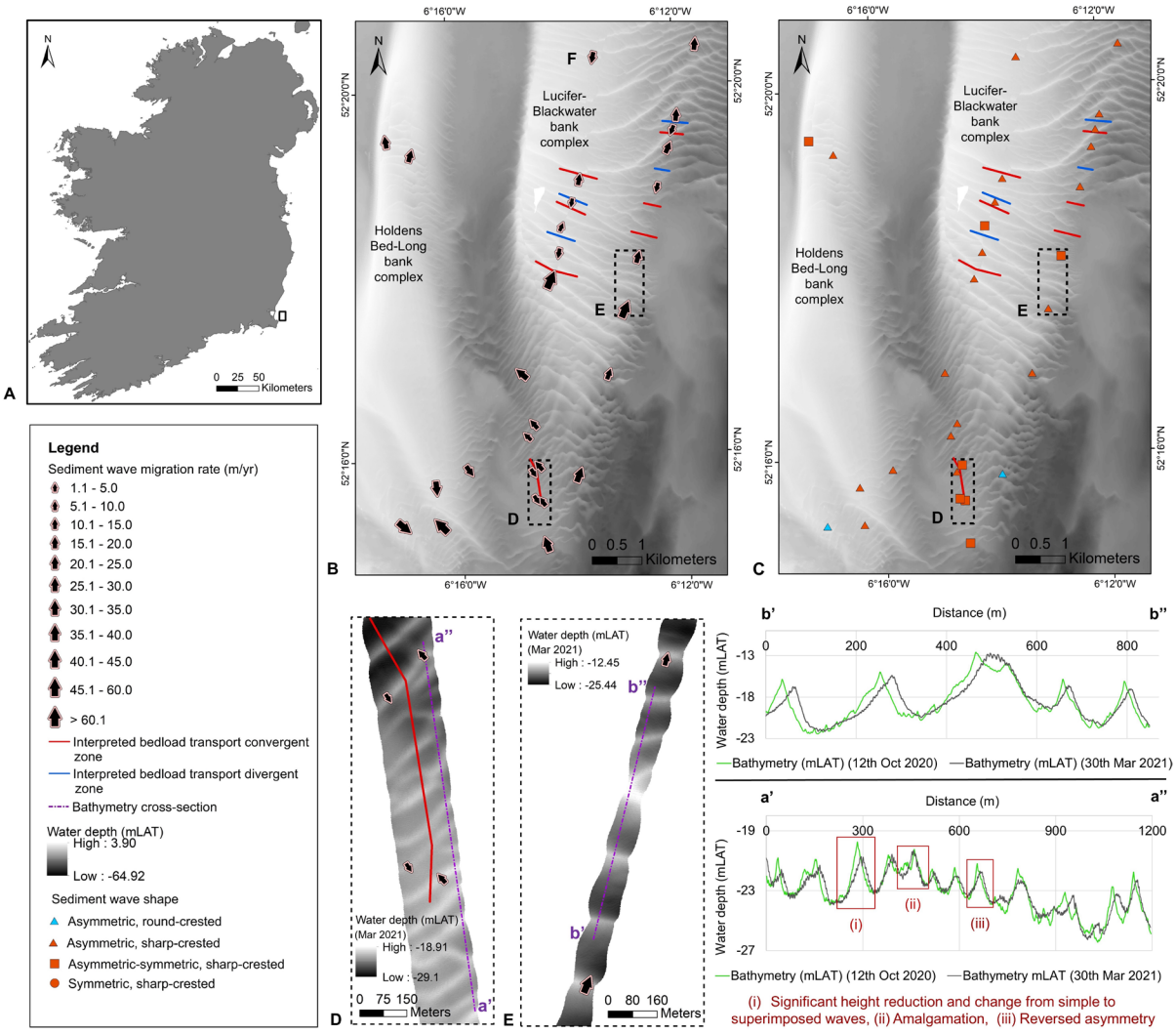


*Figure 4-10 Sediment wave dynamics at southern extent of Lucifer–Blackwater Bank and Holden's Bed–Long Bank complexes. (**A**) Location of analysed site. (**B**) Distribution of sediment wave migration direction and rates. (**C**) Distribution of sediment wave shape. B and C bathymetry source: composite map produced from INFOMAR datasets (https://www.infomar.ie/data [Accessed: 10 June 2021]) (see section 4.3.1). (**D**) Cross-section 'a' location. (**E**) Cross-section 'b' location. D and E bathymetry source: site 2E in Table 4-2.*

Lucifer Bank is asymmetric, with its lee and stoss slope facing westward and eastward (offshore) respectively. In plan-view, sediment wave crests at the southern extent of the bank are orientated at an inclined angle (NW – SE and NE – SW on the stoss and lee slopes respectively) so that they join at an acute angle at the bank crest. This connection point suggests a potential convergence zone. Nevertheless, this pattern is not continued

throughout the central and northern extent of the Lucifer-Blackwater Bank complex, instead the sediment waves diminish towards the bank crest and are relatively absent on the lee slope.

These sediment waves on the southern extent of the bank have migrated more than one wavelength between the 2009 and 2020 bathymetric surveys therefore migratory patterns and morphological changes could not be resolved over this time frame. Consequently, the observations presented here are from the analysis of a long stretch of repeat time-lapse swath bathymetry data (October 2020 and March 2021) that is approximately 200 – 400 m wide.

The most southwestern section of the site reveals slightly asymmetric to symmetric sediment waves moving north-westward at approximately 37.7 m/yr (sand wave migration vector directly south of inset 'D' in Figure 4-10B). Approximately 800m north westwards of this, sediment waves transition into more symmetrical shape and exhibit a bi-directional migration pattern (Figure 4-10D). The section of the sediment wave crests closest to the bank crest continues to move northwards at an average rate of 19.8 m/yr, yet the section of the same sediment wave crests closer to the bank base migrates southwards at an average rate of 13.9 m/yr. This generates a pivoting motion along each sediment wave crest over an approximate 1000 m transect. At the meeting point of these pivoting crests there is a very slow to no migration zone. Sediment waves tend to be symmetrical and may indicate a convergence or a coincidence of opposite moving sediment transport pathways (Figure 4-10D). This pivoting phenomenon of the sediment wave crests is like that revealed at the southern end of Arklow Bank. This trend extends approximately 1000m until the bedforms reverse back to a north-westward migratory direction.

At this transition point, the sediment wave assemblage continues to move at a differential migration rate, with slower rates (14 m/yr) exhibited towards the bank base and faster rates (19.8 m/yr) towards the bank crest. Sediment waves progressively return to a relatively constant rate of 34.2 m/yr, continuing in this north-westward direction.

Significant sediment wave morphological changes over time are observed in this area, which help to gain insight into the sediment wave growth and development processes in a complex tidal current regime. Between the 2009 to 2020 datasets, bedforms could not be compared like for like as migration has been greater than one wavelength. However, over this time interval, the general symmetrical to slightly symmetrical shape of sediment waves are maintained, and bedforms remain simple (not superimposed) and sharp-crested. Contrastingly, from 2020 to 2021, morphological changes are evident. Over this time period, sediment waves show similar symmetric to slightly asymmetric shape/bedform profile however a slight increase in their asymmetry into the direction of migration is evident. Some sediment waves notably migrate in the opposite direction to asymmetry. In this case, their asymmetry in the first time-step is in the opposite direction to their migratory direction, however in the second time-step, their asymmetry changes to slightly asymmetric in the direction of migration (cross-section a in Figure 4-10D). In 2020, bedforms are simple and sharp-crested, yet in 2021 they become compound waves (superimposed by smaller sediment waves) with bifurcating crests. Additionally, there is a notable sediment wave height decrease over the 169-day period. Amalgamation of smaller waves into larger waves is common, potentially indicating a growth mechanism (cross-section a in Figure 4-10D).

At the south-eastern section of the Lucifer-Blackwater Bank complex (site 2E (Figure 4-3)), round-crested, symmetric to slightly asymmetric, widely spaced (~ 200 m) sediment waves

migrate north-eastward at an average rate 36 m/yr (Figure 4-10B and C). Approximately 2000 m north-east from the southern tip of the assemblage, these bedforms abruptly decrease to an average migration rate of 16 m/yr. This decrease is directly correlating with three morphological changes; i) an increase asymmetry (in the direction of migration), ii) a change from round- to sharp-crests, and iii) a transition from wide to tightly spaced rhythmic bedforms. These dramatic morphological changes are consistent in all three time-lapse geophysical surveys.

A significant increase in migration rate from 16 m/yr to 59.1 m/yr (in 18 mLAT water depth) is observed north of this section (site 2D (Figure 4-3)), moving in a similar north-eastward direction (Figure 4-10B and C). These lower slope observations coincide with high average migration rates of 71.6 m/yr observed along the same sediment wave crest on the upper slopes of the bank (site 2F (Figure 4-3)), in approximately 11 mLAT water depth. Similar morphological changes are resolved compared to previous sections. Bedform asymmetry remains in the direction of migration. Sediment waves in 2009 and 2020 tend to be compound and sharp-crested. However, from 2020 to 2021, there is notable slight rounding of the crests, an amalgamation of sediment waves, and averaged bedform heights are reduced.

A decrease in north-eastward sediment wave migration rate along this pathway from 59 m/yr to an average of 21 m/yr is observed. This reduction is marked by a relatively larger sediment wave and a notable increase in bed level indicating sediment accretion (cross-section b in Figure 4-10E). Sediment waves remain asymmetric in direction of propagation.

From this point, a sediment transport convergence and divergence pattern are observed along a 500 – 900 m SSW – NNE trending transect (Figure 4-10B and C). North-westward migrating sediment waves notably transition gradually from asymmetric to symmetric and

back to asymmetric in the opposite direction. A distinct migration directional change is associated with these morphological observations whereby bedforms migrate south-westwards at an average rate of 11 m/yr. This signifies a zone of convergence. This is further supported by the increase in bed level over this transect in comparison to the seabed directly north and south of the zone, whereby the trough bases decreases in water depth (become shallower) by approximately 1 m over this short section. Bifurcation of the crests are evident in all three timestamps. Furthermore, over this transect, some sediment waves that are asymmetric towards the south-west continue to migrate north-westward until further along the transect where migration direction is in the direction of this new asymmetry direction. This may signify a delay in morphological change or adaptation to local hydrodynamics.

An alternating convergent and divergent zone pattern continues along the lower slope of the bank and is reflected on the upper slopes closer to the crest, yet at slightly different locations and rates (Figure 4-10B and C). The most northern convergent zone on the upper slope marks the location of the first of a sequence of five relatively large sediment ridges that extend in a curvilinear form from bank crest to bank base. This curvilinear form corelates with differential migration directions of the sediment wave crests located on the upper slopes compared to lower slopes, i.e. these north-westward migrating waves on the upper slope is met with longer fetched sediment transport pathway earlier (more south) than the part of the same sediment wave crest on the lower slope (denoted by 'F' in Figure 4-10B). This ultimately leads to the curvilinear form of the ridge. The following ridges do not show such a distinct curvilinear form yet correspond to similar orientation change from bank base to bank slope as with Arklow Bank sediment waves.

4.4.2.2.2 Lucifer-Blackwater Bank complex associated waves

All derived sediment wave fields North of this site within the Lucifer-Blackwater Bank complex (site 2A, 2B, 2C and 2F) (Figure 4-3) display asymmetric, sharp-crested sediment waves (Figure 4-5) migrating at an average 6.6 m/yr to 10.4 m/yr in a southward direction on the lower slopes of the banks and a distinct increase to 15.7 to 18 m/yr in a similar direction on the upper slopes (Figure 4-8). This decrease in migration rate with increasing water depth and distance from the bank crest is distinctly shown in site 2B and 2C as multiple time-lapse bathymetric datasets were analysed of which provided a relatively good spatial extent to allow accurate analysis. Amalgamation process was similarly observed between time-lapse datasets. Whilst 2B and 2C sediment waves are generally simple, waves at site 2A tend towards compound. The orientation of the sediment wave crests at site 2A are heavily linked to the bank topography. At least four distinct orientation changes of the crests are evident that correlate directly with the undulating topography of Blackwater Bank. Nonetheless, although a crest orientation change is detected, sediment wave direction and rate does not seem to be affected.

4.4.2.2.3 Long Bank associated sediment waves

Holdens Bed-Long Bank complex (Figure 4-2) displays a similar asymmetry to Lucifer Bank, whereby its lee and stoss slope face landward and offshore respectively. However, its shape is quite different whereby a large rounded form characterises its southern extent, which narrows and tapers as you progress northwards. The southern rounded extent of the bank displays progressive, asymmetric southward migrating sediment waves on both east and west side of the bank at a rate of 31.2 m/yr and 41.2 m/yr respectively (site 3B) (Figure 4-8). The south-western sediment waves are more rounded whereas the south-east sediment waves are sharp-crested (Figure 4-5). As distance increases away from the eastern side of the bank,

sediment waves of similar morphology migrate southwards at a decreased rate of 21.3 m/yr (site 3A). Intricately, at the southern tip of the bank, sediment waves reverse direction and migrate up on to the bank at a rate of 45.5 m/yr. Furthermore, the upper slopes of the relatively narrow mid to northern section of Long Bank (site 3C) exhibits relatively widely spaced (~ 150 – 200 m), sharp-crested, progressive waves migrating in a northward direction at a rate of 23.1 m/yr. Sediment waves closer to the crest of the bank tend towards a symmetrical form, yet the waves slightly downslope are asymmetric.

Evidently, sand bank associated sediment wave morphologies and migration parameters vary immensely over a relatively small distance. The spatio-temporal evolution of these bedforms reveals a highly complex bed load sediment transport regime that divert from the previously understood southward, regional scale sediment transport pathway. Drivers of these patterns is discussed in section 4.5.1.

4.4.2.3 Sediment waves independent of sediment banks

4.4.2.3.1 Site 6

Only two time-lapse bathymetric datasets, of low temporal resolution (approximately 3068 day or 8.4 yr), are available for site 6 (Figure 4-3). Consequently, only a limited amount of sediment waves could be accurately analysed to derive migration parameters. In this context, the highly morphodynamic site can be split into three main sub-regions considering both sediment wave type and migration parameters (see the south-eastern set of sediment waves in Figure 4-5B and Figure 4-8B);

i) The north-western sector, characterised by very large southward migrating (7.4 m/yr) asymmetric sediment waves;

ii) The south-eastern sector, characterised by very large northward migrating (8.2 m/yr) asymmetric sediment waves;

iii) The central and southern sector, dominated by very large trochoidal (symmetrical) sediment waves, whereby their complete bedform remains relatively immobile but sediment wave crests and/or upper slopes notably migrate at an average rate of 1.8 m/yr.

The north-eastern sector of the site is characterised by very large, regular, asymmetric, progressive, sharp-crested sediment wave assemblage that migrate south-south westward at an average rate of 7.4 m/yr. The southern extent of this assemblage is bound by several irregularly spaced very large trochoidal (symmetrical) sediment waves. The crest of these trochoidal waves seem to migrate north-eastward at an average of 1.8 m/yr, yet their troughs remain immobile. This suggests that a) flexing of the crest may be occurring or b) mobilisation of just the upper slopes of these sediment waves, while the bedform unit remains relatively immobile. Spatial resolution discrepancies between the two time-lapse bathymetric datasets were considered an underlying reason for these observations. However, surrounding these very large sediment waves are a limited amount of irregular, large, asymmetric sediment waves that migrate in the same north-eastward direction at an average rate of 2.4 m/yr, thus supporting the low mobility characteristics of the upper layer of the trochoidal waves. Deep scour marks are evident at the eastern and western troughs of these trochoidal waves (Figure 4-6d). This subsequently support their general immobility as these bedforms must have been relatively stationary over a relatively long period of time for local hydrodynamics to carve out such significant scour marks, where none are evident on coincident mobile bedforms.

The southern limit of these trochoidal sediment waves are bound by an assemblage of asymmetric, large sediment waves from which migration parameters could not be resolved. South of this assemblage, large trochoidal sediment waves of similar form and migration parameters scatter across the site. Concurrently, at the eastern perimeter of the site, a limited amount of trochoidal waves exhibit an upper slope mobility of 1.3 m/yr in the opposite direction (southwards). This is coincident with an asymmetric, sharp-crested, progressive sediment wave assemblage migrating southwards at an average rate of 5.6 m/yr.

The asymmetric, progressive sediment wave assemblage in the south-western section of the site is of similar shape and size to the north-eastern assemblage but migrates north-eastward at an average rate of 8.2 m/yr.

4.4.2.3.2 Site 5

Site 5 (Figure 4-3) is dominated by very large, asymmetric, sharp-crested, progressive sediment waves, intermixed with scattered, isolated, very large, trochoidal sediment waves that are encompassed by deep scour marks (Figure 4-5; Table 4-4). These trochoidal waves resemble those identified at site 6. Migration parameters and sediment wave characteristics are derived from two time-lapse bathymetric datasets of time interval 189 days.

Most of the site is characterised by asymmetric, progressive, sharp-crested sediment waves migrating north-eastwards at an average rate of 15.8 m/yr (Figure 4-8). Interrupting this migration pattern are the presence of very large trochoidal sediment waves, whereby the bedform crest migrates or 'flexes' in the same north-eastward direction at approximately 2.5 m/yr, yet the bedform unit remains immobile. This phenomenon is analogous to site 6 (Figure 4-3). This northward migration is further locally interrupted in a north-eastern area of the site whereby northward migration is reduced to 7.5 m/yr and is met with large sediment waves

migrating in the opposite direction at 17.7 m/yr. This sediment transport convergence zone is marked by a relatively larger sediment wave or ridge. North of this area, sediment waves continue migrating north-eastwards at 18.8 m/yr.

4.4.2.3.3 Site 8

The sediment wave assemblage at site 8 markedly combine to form an elongated curvilinear (N – S trending) wave field, extending approximately 16 km long and 2 km wide (Figure 4-11B). Sediment wave crests orientate approximately NW to SE. At various intervals along the assemblage sand accretion notably increases along an approximate mid-line/zone, and sediment waves begin to resemble a N to S trending sand ridge. At these sections, transverse bedforms noticeably align with the slope of the ridge. This ridge formation is discontinuous and is integrated with relatively subdued, flat-bedded independent sediment waves (see cross-sections a – e in Figure 4-11). This study analyses sediment wave characteristics and evolution over time from a $200 \times 7000\ m$ segment of time-lapse bathymetric datasets (Table 4-2) along the western section of the assemblage, and $500 \times 3000\ m$ segment that stretches across the assemblage from west to east in the southern half of the wave field (Figure 4-11).

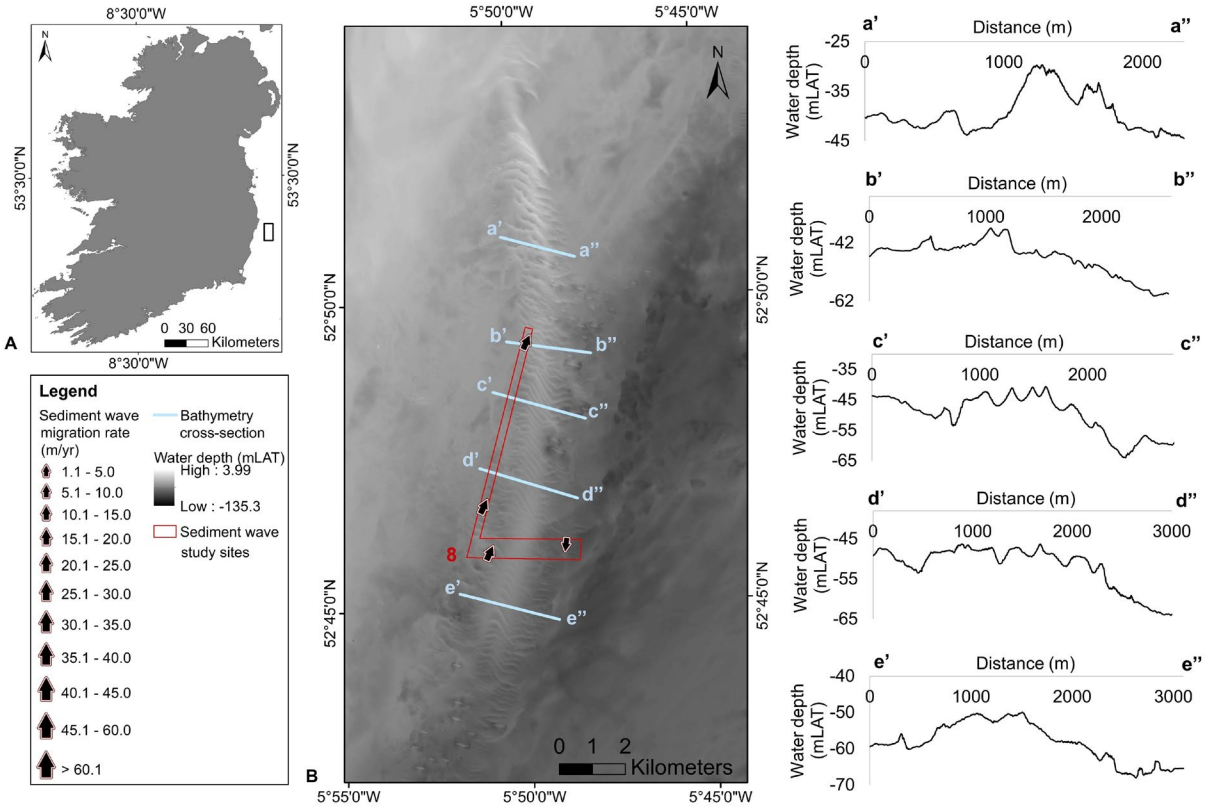


*Figure 4-11 Sediment wave dynamics at offshore independent sediment wave assemblage at site 8 in the Irish Sea. Location of cross-sections a to e are provided in (**B**). Location of (**B**) is given in (**A**). Bathymetry source: composite map produced from INFOMAR datasets (https://www.infomar.ie/data [Accessed: 10 June 2021]) (see section 4.3.1).*

From the analysed sections, large to very large, asymmetric, progressive, round-crested sediment waves migrate at an average rate of 16.5 m/yr along the western perimeter of the site over a 7 km distance (Figure 4-5; Figure 4-11). Contrastingly, on the eastern side of the ridge, large, asymmetric, round-crested sediment waves migrate southwards at 13.5 m/yr. Sediment wave asymmetry is predominately in the direction of migration. The amalgamation of sediment waves is evident from the time-lapse bathymetry datasets.

4.4.2.3.4 Site 7

At site 7 (Figure 4-3), migration parameters and morphological evolution of sediment waves over time could only be derived from 2020 and 2021 datasets (except for immobile trochoidal

waves) as the time interval between these and the 2012 dataset were too long to derive accurate results.

The south is characterised by large, asymmetric, sharp-crested sediment waves travelling north-eastwards at 12.8 m/yr (Figure 4-5; Figure 4-8). Amalgamation between these sediment waves is observed over this 167-day period. This northward migration is locally interrupted by very large sharp-crested trochoidal waves (Figure 4-6d) that show an overall immobility over the three time-steps yet exhibit a northward movement, or flexing, of 2.9 m/yr at the bedform crest. Scour marks around these isolated bedforms are present, comparable to those at sites 5 and 6. Large sediment waves continue to migrate northwards, gradually reducing in rates to 12.2 m/yr to 9.5 m/yr. These reducing migration rates correlate with the transition into a regular, sharp-crested, very large sediment wave assemblage that progressively change from asymmetrical towards the north-west, to a symmetrical form, to asymmetrical in the opposite direction (south-eastwards). Towards the northern section of the site south-eastward facing sediment waves migrate at a rate of 2 m/yr. Clearly, this marks the presence of a convergent sediment transport pathway.

Clearly, sediment wave migration dynamics and morphological changes over time in offshore sediment wave fields vary immensely, both locally within individual sites and between sites, indicating a highly complex bedload sediment transport and hydrodynamic regime. Drivers of these observations and their context in terms of the wider sediment transport regime is discussed in section 4.5.

4.4.3 Comparison between sand wave characteristics, environmental parameters and theory-based indicators

4.4.3.1 Correlation of individual sand wave characteristics with environmental parameters

For the full dataset and for each of the three separate environments, results show a weak to moderate positive correlation [88] between sediment wave height and water depth. However, no association is determined between wavelength and water depth (see supplementary material for statistical correlations). The Sand Wave Index (SWI) (L/H) was adopted from Zhou et al [4] in order to understand the impact of water depth on sediment wave shape. A weak to moderate negative power-law relationship was derived from the full dataset and each of the three compiled environments (see supplementary material for full results). This negative correlation suggests the prevalence of more subdued sediment waves (long wavelengths relative to shorter wave heights) in shallow water, and taller, sharper sediment waves (shorter wavelengths relative to higher wave heights) in deeper waters.

No distinct relationship can be determined between individual sediment wave dimensions and D_{50}, maximum or mean tidal current velocity or P (Rouse number as in Equation (9)). A decrease in height with increasing residual current magnitude is evident ($H = 1.7{U_{c_{res}}}^{-0.12}, r = 0.114$) yet this correlation is very weak. Statistical correlations are provided in tabular format as supplementary material.

4.4.3.2 Relationship between the spatial distribution of environmental parameters/processes and the occurrence of sand waves

The spatial distribution of P reveals a non-statistical relationship with sediment wave assemblages, whereby increasing P corresponds to a decrease in observed mobile bedforms. Particularly, five distinct regions of relatively higher P are identified. These will henceforth be

referred to as ‘transition zones’ (labelled T1 to T5 in Figure 4-12). As P is dependent on w_s, this parameter displays a strong positive correlation with increasing grain sizes. The spatial distribution of P across the study area reveals a widespread dominance of bedload transport. Significantly, sediment wave assemblages from both environments tend to occur in regions where 3 < P < 25 with a median value of 5.7. Outside these zones, relatively higher median P are evident, and correlate well with less mobile, coarser sediments in the transition zones (Figure 4-12; Figure 4-2C). As P increases with increasing grain sizes and decreasing flow strength, where P is high, this is attributed to low current velocities relative to high grain sizes.

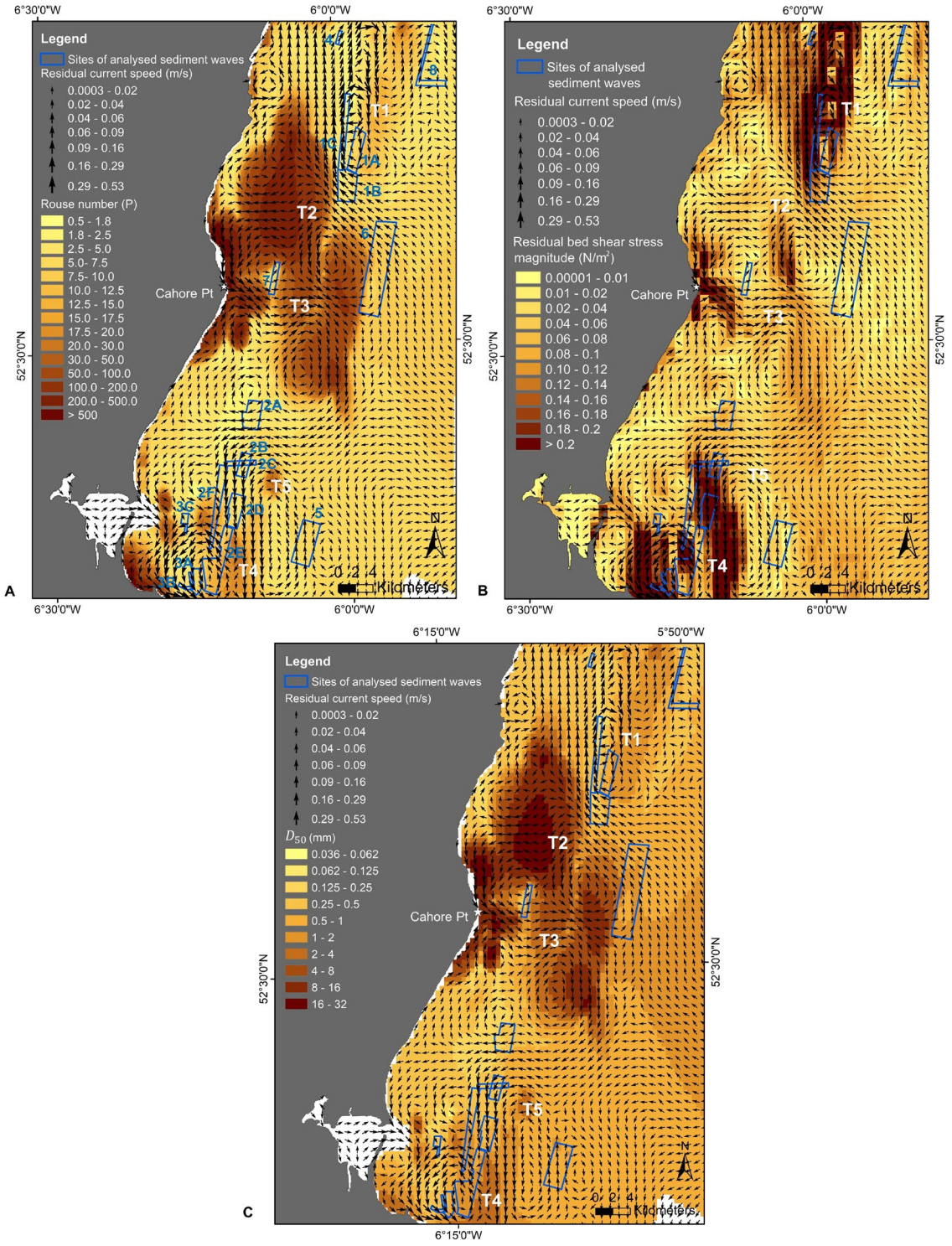


*Figure 4-12 Spatial distribution of (**A**) dimensionless Rouse number, (**B**) residual bed shear stress (N/m²) and (**C**) median grain size (D_{50}) overlain by residual current velocity with location of newly analysed sediment wave assemblages. Transition zones (labelled in white as T1 to T5) refer to areas of relatively higher Rouse number, higher residual current velocity and coarse grain sizes along a residual transport pathway between offshore sand banks and independent sediment wave assemblages.*

A reduction in residual bed shear stress and current magnitudes along a transport pathway corresponds well with the occurrence of independent sediment wave assemblages (Figure 4-12). All analysed independent sediment wave fields follow this trend. The opposite is found to be true in relation to the transition coarser grained zones (T1 to T5), identified using P. Additionally, migration directions generally agree with residual current flow and bed shear stress directions. This will be discussed in section 4.5.1.2.

4.5 Discussion

4.5.1 Connection between average net sediment wave migration directions and the wider sediment transport regime in the Irish Sea

Previous bedform- and numerically-derived sediment transport pathways suggest a net southward sediment transport pathway in the southern Irish Sea (Figure 4-2) [5], [26], [27], [39]. However, the analysis detailed in this study suggests that there is greater complexity to sediment wave behaviour which has subsequent implications for sediment transport sources and sinks. In particular, sediment banks exert a significant influence on these patterns. With this new ground-truthing knowledge presented in section 4.4, this section aims to elucidate the complex interaction of closed/semi-closed sand bank sediment transport systems and offshore mobile sediment. This investigation combines residual current and bed shear stress datasets calculated by Creane et al [5] with newly derived ground-truthing evidence.

4.5.1.1 Sediment waves associated with sandbanks

The south- and north-ward migrating sediment waves on the east and west sides of Arklow Bank reveal an ebb and flood dominance respectively. This is due to the slight anti-clockwise rotation of Arklow Bank to the principle tidal current axis, leaving the east and west sides of the bank exposed to the ebb and flood tidal phase respectively [28], [89], [90]. Residual tidal

current and bed shear stress vectors support these observations (Figure 4-13). This bi-directional sediment transport on either sides of linear sand banks also agrees with many numerical modelling and field studies [28], [35], [37]. The relatively higher sediment wave migration rates on the west side of the bank (32.7 m/yr) in comparison to the east side of the bank (23 m/yr) suggests a higher strength in the flood tidal flow.

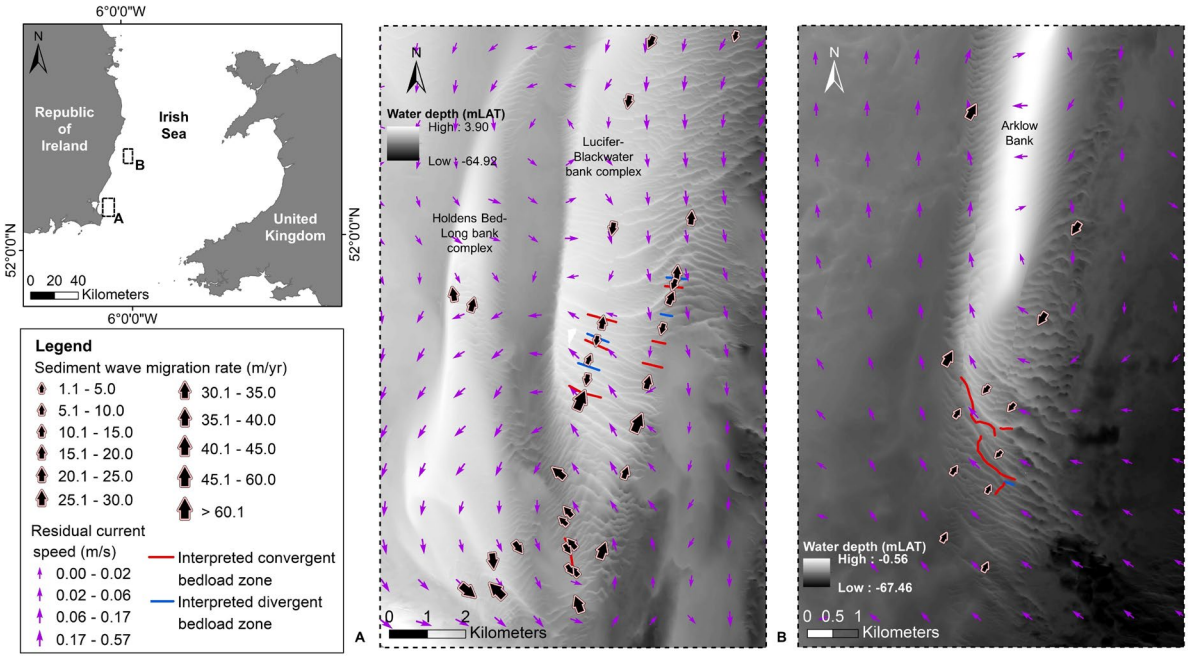


*Figure 4-13 Newly derived sediment wave migration rates and bedload transport divergence and convergence zones overlain by modelled residual tidal current vectors at (**A**) the southern extent of Lucifer–Blackwater and Holden's Bed–Long Bank complexes, and (**B**) the southern half of Arklow Bank in the Irish Sea. Bathymetry source: composite map produced from INFOMAR datasets (https://www.infomar.ie/data [Accessed: 10 June 2021]).*

Furthermore, a clear semi-closed clockwise circulatory sediment transport system is revealed by a of the following observations;

i) A convergence zone at the southern end of Arklow Bank, marking the limiting extent of southward migrating sediment waves;

ii) Sudden changes in migration rate and morphological character of sediment waves at the intricate pivoting phenomenon at the southern end of the bank (section 4.4.2.1);

iii) Southward and northward residual flow on the east and west sides of the bank respectively;

iv) North-westward flow coming from the south-east of the bank, travelling across the southern extent of the bank and pushing northwards on the western side.

This north-westward flow limits the southern extent of the southward residual flow on the east side of the bank, ultimately driving sediment across the southern extent of the bank and back up along the western side of the bank. This north-westward residual flow propagates over the sediment wave assemblage at site 6 (Figure 4-3) prior to reaching Arklow Bank (Figure 4-12) and so has the potential to transport additional sediment into this circulatory system (section 4.5.1.2). These provide a hydrodynamic mechanism for a clockwise semi-open hydrodynamic and sediment transport regime around Arklow Bank. This supports Johnson et al [28] who suggested a circulatory flow system doesn't necessarily represent a closed-system.

Furthermore, the refraction of tidal flow across the bank is evident at Arklow Bank. Similar observations has been noted at other banks on the European Continental Shelf [91]. This cross-flow aligns well with the progressive orientation change of sand wave crests along the bank slopes, indicating a convergence at the bank crest.

Contrastingly, the Lucifer-Blackwater bank complex does not display a similar circulatory sediment transport system to Arklow Bank. Instead, sediment wave migration and residual tidal flow reveal a predominately southward net sediment transport pathway along the

eastern side of these banks (Figure 4-8; Figure 4-13). This is accompanied by a residual anti-clockwise current eddy extending from the headland at Greenore Point (Figure 4-13; Figure 4-3). This residual eddy ultimately acts as a driving mechanism for the intricate migration characteristics and maintenance of sediment waves at the southern end of Lucifer-Blackwater and Holdens Bed-Long bank complexes.

The central zone of this residual gyre (Figure 4-13A) is characteristic of relatively reduced residual tidal currents and bed shear stresses, and the meeting point of opposing flows. This zone perfectly overlays the 1000 m section of pivoting sediment wave crests located on the south-western side of the Lucifer-Blackwater Bank complex (Figure 4-10D; Figure 4-13). Specifically, the progressive south to north-west sediment wave sequence of;

i) uni-directional (north-westward) and constant migratory rate along the same wave crest,
ii) bi-directional migration along the same wave crests,
iii) uni-directional (north-westwards) yet differential rate migration along the same wave crest, and
iv) uni-directional (north-westward) and constant rate,

align with the placement of the central zone of this residual gyre. This anticlockwise flow proceeds across Holdens Bed-Long bank complex and back towards Greenore Point, driving the southward migration of sediment waves at sites 3A and 3B (Figure 4-3). On Lucifer Bank, the increased residual current and bed shear stress magnitudes at the outer circumference of the circulatory flow correlate extremely well with significant increases in sediment wave migration rates i.e. 59.1 – 72.6 m/yr. Concurrently, the transition zone beyond this point, where a convergence of the residual gyre with the southward transport pathway is revealed,

marks the location of the intricate bedload convergence-divergence sequence outlined in section 4.4.2.2 (Figure 4-13A; Figure 4-10D). Fundamentally, this circular motion of the residual gyre suggests a continuous recycling of material between Long and Lucifer Banks and associated sediment waves.

The pear-shaped form of Holdens Bed-Long bank complex, the nature of sediment wave migration and morphological characteristics, and the presence of this residual eddy provides evidence that Holdens Bed-Long bank complex should be categorised as 'Type 3A: headland associated banks - banner bank' [25] as opposed to the neighbouring Lucifer-Blackwater bank complex and Arklow Bank which are clearly 'Type 1: Open shelf linear sand banks'. Banner banks are described to have formed and maintained predominantly by headland-generated residual eddies, which trap sediment produced by coastal erosion or arising from seafloor erosion. While many studies suggest these secondary convergent flows generate sand banks at the centre of the residual eddy [25], [92], [93], further research reveal that the centre of the modelled residual current eddy is not necessarily located over the banner bank but offset at a certain distance [94]–[96]. Similar results are shown here whereby the centre of the residual gyre is offset to the east of the bank (Figure 4-13A). This supports the concept that sediment deposition at the centre of these eddies are not the main element for the formation of banner banks around headlands [96]. Instead, the interaction between tidal current vectors, bed shear stress and sediment transport pattern through the duration of the tidal cycle governs the development and maintenance of banner banks [96].

4.5.1.2 Offshore sediment wave assemblages – source and sink mechanisms

When analysing residual bed shear stress and current vectors, multiple circulatory cells are revealed that originate from sand banks and propagate towards offshore independent sediment wave assemblages. From here, these residual flows either;

a) connect back with sand bank associated localised flows, suggesting a potential recycling of sediment between sand banks and offshore sand deposits, or
b) connect with circulatory cells over the offshore sediment wave field, from which partial diversions extend out to mobile sediments further offshore. In this way, these relatively closer sediment wave fields act as intermediary transport zones to sediment wave fields in deeper waters.

This provides a potential sediment source and sink mechanism for the maintenance of offshore, independent sediment wave assemblages. Three major circulatory systems are identified;

i) The dynamic interaction of the sediment transport regimes at site 7 and site 6 (Figure 4-14a) with the southern extent of Arklow Bank and the northern extent of the Lucifer-Blackwater bank complex (Figure 4-14b);
ii) The circulatory residual flow between the eastern edge of Arklow Bank and the sediment wave assemblage at site 8 (Figure 4-14c);
iii) The circulatory cell connecting the Lucifer-Blackwater bank complex with site 5 (Figure 4-14d).

The average migratory direction of sediment waves aligns well with the residual transport directions in all three circulatory systems.

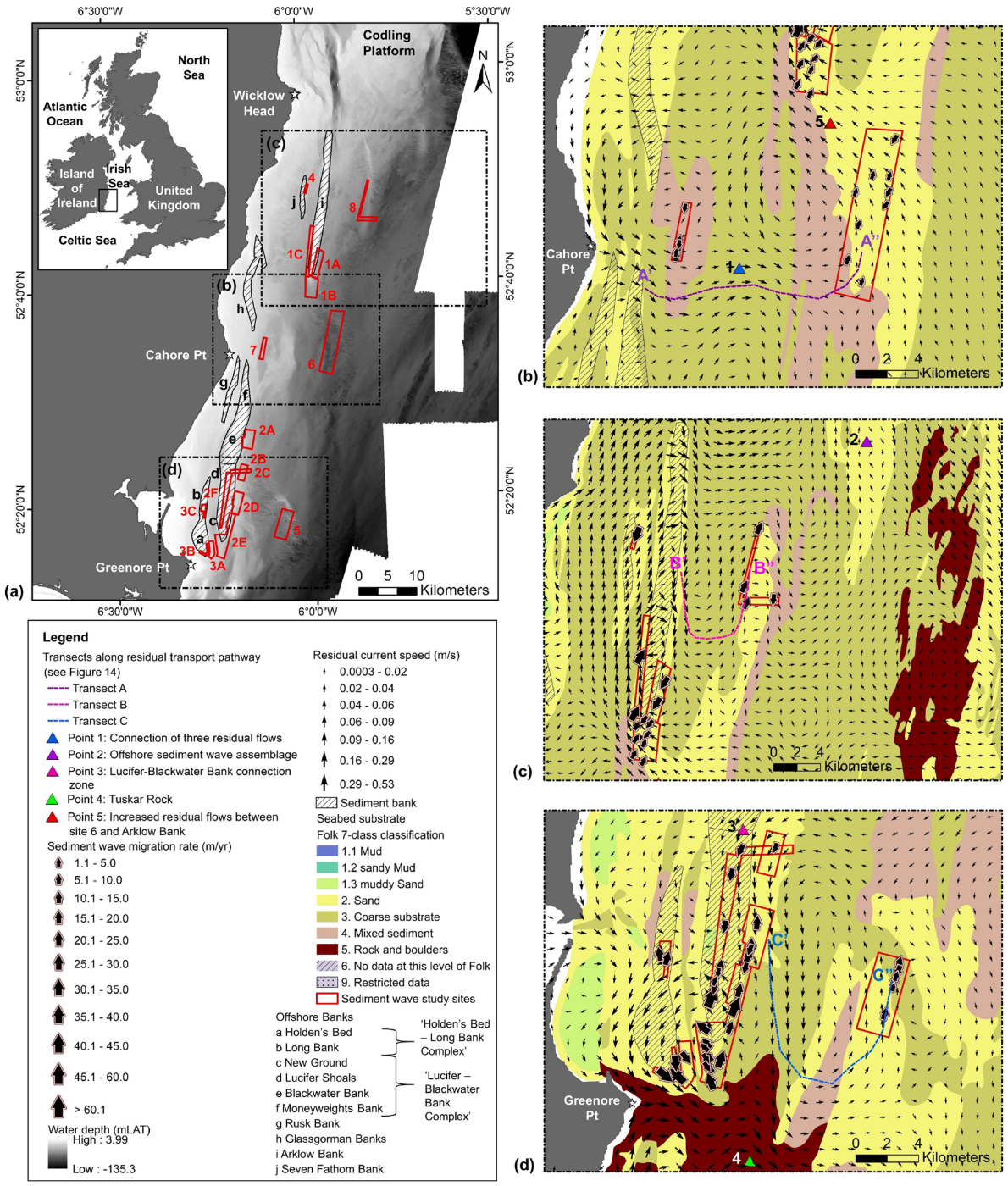


*Figure 4-14 Overview of three residual circulatory transport systems in the south-western Irish Sea connecting offshore sediment banks with independent offshore sediment wave assemblages: (**a**) Location of three circulatory systems, main offshore sediment banks mentioned in the text and areas of analysed sediment waves by this study, (**b**) circulatory system (i) outlined in the text (4.5.1.2), connecting assemblages at site 6 and site 7 with Lucifer–Blackwater Bank complex and Arklow Bank, (**c**) circulatory system (ii) outlined in the text connecting sediment wave assemblage at site 8 and the further offshore assemblage at Point 2 with Arklow Bank, and (**d**) circulatory system (iii) outlined in the text, connecting the sediment wave assemblage at site 5 with the Lucifer–Blackwater Bank complex. Transects in A, B, and C are presented in Figure 4-15.*

Bathymetry source: composite map produced from INFOMAR datasets (https://www.infomar.ie/data [Accessed: 10 June 2021]) (see section 4.3.1). Seabed substrate source: EMODnet Seabed Habitats initiative (http://www.emodnet-seabedhabitats.eu/ [Accessed: 25 June 2021]) [41].

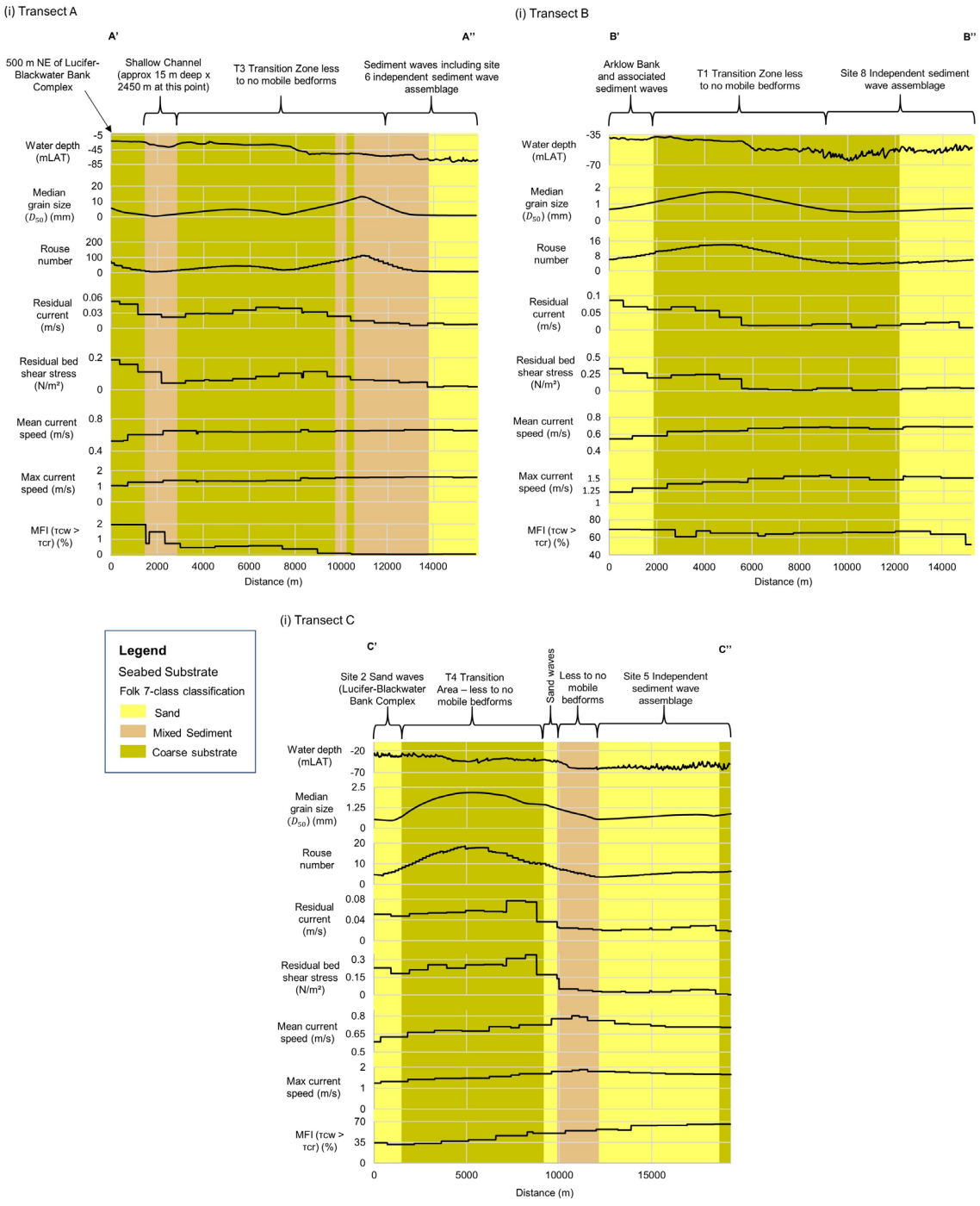


Figure 4-15 Transects along residual transport pathways in each circulatory system connecting offshore sediment banks with independent offshore sediment wave assemblages. Location of transects are presented in Figure 4-14. Data used in this figure

is described in section 4.3.3 to 4.3.5. Mobilisation Frequency Index (MFI) data source: Coughlan et al [64]. *Seabed substrate source: EMODnet Seabed Habitats initiative* (*http://www.emodnet-seabedhabitats.eu/ [Accessed: 25 June 2021]*) [41].

The first circulatory cell originates from the north-eastern region of the Lucifer-Blackwater bank complex, pushing north-eastward, where it merges with two residual flows (Point 1 in Figure 4-14b); i) an eastward flow originating from Cahore Point, and ii) a southward flow that diverges from the southern tip of Arklow Bank. This integration of three flows marks the point of contact of the outer circumferences of three circulatory flow cells offshore Cahore Point. This merged flow of high magnitude residual current and bed shear stress migrates towards site 6 (Figure 4-14). A significant reduction in residual magnitudes is evident as the flow approaches site 6, where it is met with residual flows coming from relatively deeper waters to the south-east and east. These combined flows migrate north-westward across site 6, up towards the southern tip of Arklow Bank. Net sediment wave migration direction correlates well with these pathways.

A sudden increase in residual current and bed shear stress directly beyond these progressive asymmetric transverse bedforms is evident, flowing towards the base of Arklow Bank (Point 5 in Figure 4-14b). This sediment transfer out of the independent sediment wave field acts as an additional sediment supply for Arklow Bank. This flow pattern provides evidence of a high suspended sediment concentration within the north-westward residual flow pathway that has been identified previously by Creane et al [5]. This supports the hypothesis that this pathway transfers additional sediment into the dynamic circulatory hydrodynamic and sediment transport cell around Arklow Bank, ultimately defining the system as semi-open [5]. This flow continues northwards into the locally-driven flow around Arklow Bank and diverts

southwards in two routes: (i) south-westward towards Cahore Point and (ii) southwards, completing the circulatory cells feeding into site 6.

Furthermore, the centre of the circulatory cell approximately 5 km east of Cahore Point marks an area of highly reduced residual current and bed shear stress magnitudes. This coincides with the newly derived convergent sediment transport pattern at site 7. The high migration rates revealed in the southern section of the site correlate well with high residual magnitudes of the outer circumference of the circulatory field. However, relatively reduced, immobile waves in the north correlate with the centre of the residual cell.

The second circulatory cell connects the eastern side of Arklow Bank with the sediment wave assemblage at site 8, approximately 5.5 km east of Arklow Bank (Figure 4-14(c)). A relatively high residual transport pathway moves southward along the eastern edge of Arklow Bank. Part of the flow at the northern half of Arklow Bank diverts eastwards to north-eastwards across the northern section of the offshore site and continues towards the bed load parting zone (Figure 4-2) [5]. The main flow continues further south along the edge of Arklow Bank, correlating well with southward migrating sediment waves on the east side of the bank. Over the southern half of the bank, the high magnitude flow turns progressively eastwards towards the offshore sediment wave field progressively reducing in magnitude. The flow progresses northwards pushing up along the western side of the analysed site, aligning well with the northward migrating sediment waves (~16.5 m/yr) in this area. At the approximate halfway line of the sediment wave assemblage, the residual flow reverses direction once again, continuing southwards, correlating well with the southward migrating sediment waves (~13.5 m/yr) at this site. This residual flow generates a residual circulatory cell over approximately half of the sediment wave assemblage, whereby flow is continuously fed in via the Arklow

Bank. Where this indicates a retainment of sediment within the sediment wave field, minor pathways are identified exiting the localised area, migrating towards both the offshore sediment wave assemblage located ~11 km north-east of this site (Point 2 in Figure 4-14(c)), and the bed load parting zone at Codling Platform (Figure 4-14(a)).

Finally, the third circulatory system connects the sediment wave field at site 5 to the Lucifer-Blackwater bank complex (Figure 4-14(d)). A high magnitude southward residual flow begins on the eastern side of the connection between Lucifer and Blackwater Banks (Point 3 in Figure 4-14(d)), migrating southwards gradually progressing further away from the banks. At an approximate alignment with the southern end of Long Bank, the flow is partially merged with a pathway originating from Greenore Point and the western side of Tusker rock (Point 4 in Figure 4-14(d)). This marks progressive divergence of the southward flow eastwards then northwards, pushing offshore towards the sediment wave field at site 5. A similar reduction in residual current and bed shear stress magnitude with the occurrence of finer sediments and the sediment wave fields is noted. The northward flow aligns well with the northward moving progressive asymmetric sediment waves (~15.8 m/yr) in this region. This residual transport pathway continues northwards to the Lucifer-Blackwater Bank connection zone where a circulatory cell is formed. Several immobile, very large trochoidal sediment waves west of site 5 align with the centre of the circulatory cell which exhibits relatively reduced residuals and converging flow pathways. However, this bedform type in the Irish Sea have also been determined as originating from post-glacial hydrodynamics when sea-levels were lower, tidal currents were stronger and sediment supply was abundant [39].

Along each of the transport pathways defined above, the transition area between sand banks and the independent sediment wave fields are associated with relatively higher residual bed

shear stress and residual current magnitudes. These transition areas are characterised by relatively coarse sediment (mainly sandy gravel to gravelly sand) and are absent of sediment waves. Residual currents notably decrease along the transport pathway at each of the three sites, positively correlating with decreasing grain size, giving rise to sandy sediments where sand wave assemblages occur independently offshore.

These relatively higher residual currents in the transitional gravelly dominated areas represent a scoured seabed whereby critical bed shear stress is exceeded above a certain threshold so that fine to medium sediment grains (silt and fine to medium sands [97]) are lifted into suspension and transported as suspended load. This causes a winnowing of finer material out of the region. While numerically modelled mean and max current velocities don't display higher magnitudes over these coarser transitional areas in comparison to the offshore sediment wave fields, relatively higher residual current and residual bed shear stress magnitudes are exhibited (Figure 4-12; Figure 4-15). This indicates that the residual flow parameters, which correspond to tidal asymmetry, may play a greater role in these circulatory feedback systems in comparison to the strength of the mean or max peak currents. Higher residual currents and bed shear stresses indicate a higher asymmetry in the transport system, therefore high residual currents provide a mechanism for more sediment to be transported out of and/or bypass the region as suspended load in comparison to a symmetrical system. This suggests that sediment originating from the sand banks, at the beginning of each the transport pathway, may be transported as suspended load, remaining entrained in the water column, bypassing these transitional zones, until residual current and bed shear stress magnitudes (thus tidal asymmetry) is reduced. The reduction in tidal asymmetry allows sediment to settle out of suspension [98]. This reduction correlates well with the occurrence of independent sediment wave fields in the south-western Irish Sea (Figure 4-14; Figure 4-15).

A high bed level change is not expected in these areas as shear stresses exerted on the seafloor are not high enough to readily exceed critical bed shear stress for mobilisation of relatively coarse grain sizes. Furthermore, according to Neill and Couch [98] higher tidal asymmetry zones theoretically display a lower bed level change in comparison to maximum bed level changes at tidal symmetry zones. This is supported by the mobility frequency index (MFI) produced by Coughlan et al [64] whereby in each of these transitional zones, the critical bed shear stress is exceeded less frequently by both (a) tidal current- and (b) combined tidal current- and wave-induced bed shear stress, in comparison to sediment wave field zones.

The occurrence and absence of mobile bedforms along a transect at each circulatory system also aligns very well with the theoretical predictor of bed forms defined by Shields [87]. A plot of calculated entrainment function (F_S) against the shear Reynold's number (Re_*) (under mean and maximum current velocities) along each transect is displayed in Figure 4-16, where 'ripples' refer to transverse bedforms with $L < 0.6\,m$. It is clearly shown that under mean current velocities, sediments do not meet the threshold of motion criteria in the transitional zones; therefore, no mobile bedforms are present. Contrastingly, the plot predicts mobile bedforms further along the transport pathway in the independent sediment waves fields at site 5 and 8. Under mean current velocities, the threshold of motion in site 6 is not exceeded yet under maximum current velocities sediments are mobilised in this localised area. As expected, under maximum current velocities, the threshold of motion is exceeded more readily for all three transport pathways.

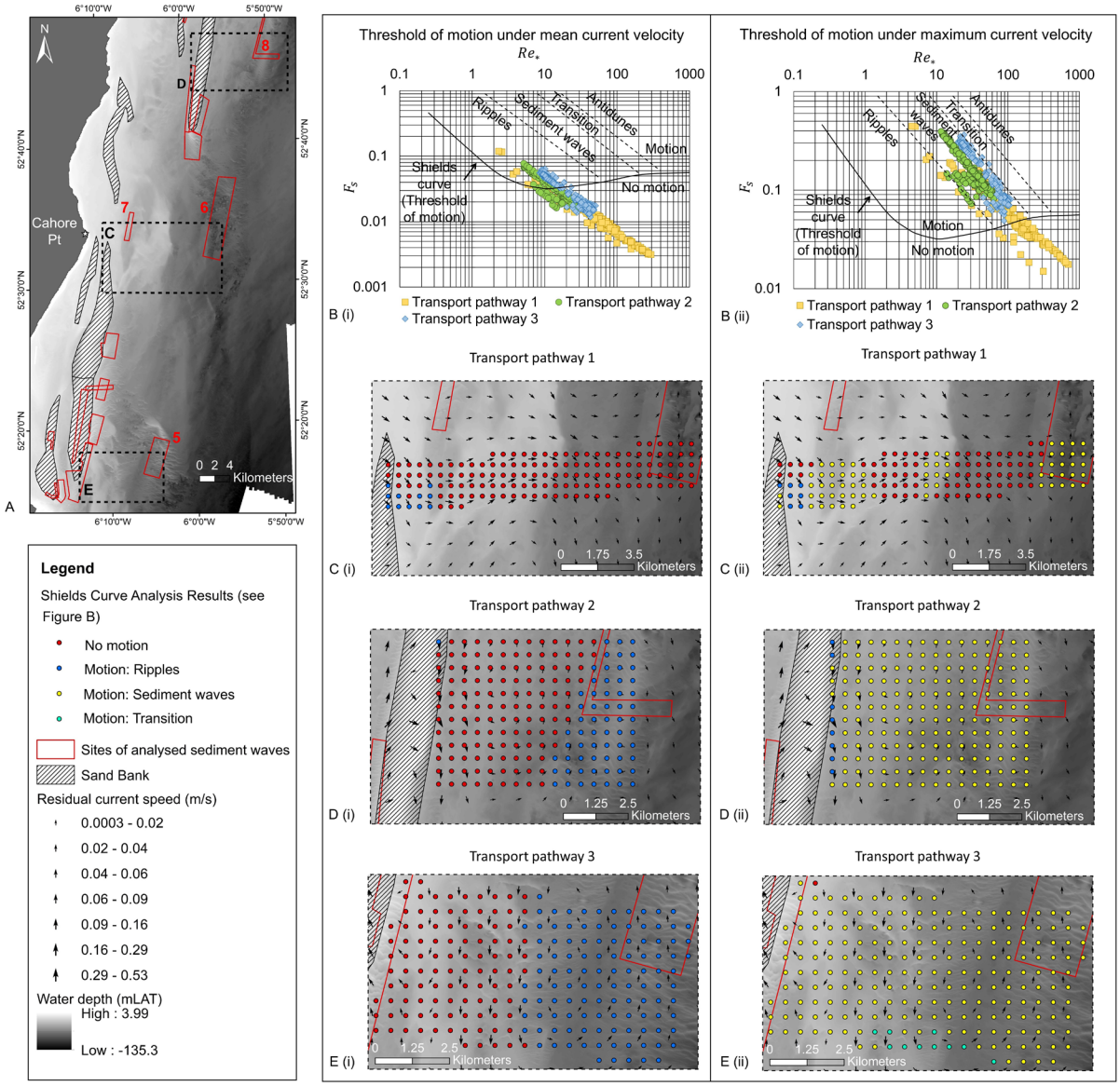


*Figure 4-16 (**A**) The location of (**C**–**E**) in the south-western Irish Sea. (**Bi**,**Bii**): The Shields curve* [87] *overlain with values of Re_* and F_S derived from the sediment surface samples calculated under mean and maximum current velocities, respectively. Sampling locations are displayed in C to E, which form a 500 × 500 m grid that transects along residual circulatory cell systems 1, 2, and 3 outlined in Figure 4-14. From (**Bi**,**Bii**), each point is designated as (a) No motion or (b) Motion: Ripples, Sediment waves or Transition, the location of which are displayed in (**C**–**E**). Bathymetry source: INFOMAR (https://www.infomar.ie/data [Accessed: 10 June 2021]).*

To investigate the mode of sediment transport within these circulatory systems, the spatial distribution of the dimensionless Rouse number (P) was analysed (Figure 4-12; Figure 4-15). Previous studies [45], [60] found a strong correlation between P and the prevalence of sand

wave fields. Specifically, Damen et al [45] found that dominant bedload transport ($P > 2.5$) aligns very well with sand wave field boundaries. Although dominant bed load transport extends beyond the sand wave field boundaries, no sand waves assemblages are found in areas dominated by suspended load transport ($0.8 < P < 1.2$). Subsequently, the Rouse number is incorporated into this study as it has the potential to elucidate the hypothesised circulatory transport systems connecting sand banks and associated sediment waves to independent sediment wave fields.

Each stage of the three circulatory systems displays $P > 2.5$, indicating a dominant bedload transport regime (Figure 4-12). Furthermore, transition zones clearly display a distinctive relative increase in P in comparison to the location of sediment wave fields and sand banks (Figure 4-15). This contrasts to what was found by Borsje et al [60] and Damen et al [45]. Although sediment wave fields too correlated with the bedload transport mode, outside of these areas were dominated by suspended load. Additionally, a dampening mechanism to sediment wave growth was attributed to suspension of material at the sediment wave crests. Discrepancies between the studies can be explained by the difference in sediment grain sizes between these two previous studies and this study. The seabed in earlier studies are dominated by grain sizes (D_{50}) ranging from 0.1 to 0.5 mm, yet the south-western Irish Sea displays a wide range of sediment types varying from 0.5 to 30 mm (section 4.3.3). While dominant suspended load transport, in areas outside sediment wave fields, were attributed to the fine grain sizes characterising the seabed in Damen et al [45], relatively coarser sediment characterises the seabed in the transitions zones in this study. As P is dependent on the particle settling velocity of a grain, there is a distinct positive correlation between P and grain size (P increases with increasing grain size). Subsequently, Rouse numbers are only

representative of sediment at the seabed and does not consider sediment already in suspension, i.e., sediment sourced from sand banks and bypassing the 'transitional' areas as suspended load. Therefore, P in this case does not account for the mode of transport in these circulatory cell systems. A transect along all three transport pathways summarise these findings (Figure 4-15). The MFI dataset, produced by Coughlan et al [64], is less accurate for Transect A compared to B and C (Figure 4-15) due to the lack of available sediment samples for site 6 in the grain size dataset used by Coughlan et al [64]. As a result, the grain size dataset used for MFI calculations shows a higher D_{50} value than what is present at the seabed, subsequently a lower MFI than reality is returned. However a higher number of sediment samples were compiled for this study (see section 4.3.3), therefore median grain size and Rouse numbers (Figure 4-14 and Figure 4-15) calculated by this study have a relatively higher accuracy.

4.5.2 Local variations in sand wave morphology

4.5.2.1 Singular environmental parameters as an unreliable indicator for sediment wave growth

Quantifying the role of individual environmental parameters on sediment wave growth and development is difficult and ultimately proven inconclusive in a number of studies (section 4.1.1.2). The limited very weak to moderate relationships derived from this study (section 4.4.3.1) reinforces the deficiency of robust derivatives from statistical correlations between singular environmental parameters and sediment wave growth. Ultimately, the different sediment wave morphological variations are most likely driven by a combination of physical processes, therefore the use of singular environmental parameters to understand these

bedform dynamics should be made redundant. Instead, a coupled or process-driven approach should be incorporated in future studies.

Results given in section 4.4.3.1 coincide with inconclusive findings of several studies outlined in section 4.1.1.2. For example, this study found a similar strength yet opposite sign correlation (moderate; r = 0.42 – 0.43) between SWI and water depth to sediment waves on the Taiwan Banks [4]. This implies that sand wave shape is more elongated and smaller in relatively shallow water (subdued) and shorter and taller in deeper waters, opposite to that found on the Taiwan Banks. However, although both studies are influenced by locally-driven environmental conditions, both correlations are not statistically strong, have a large scatter of data points, and do not incorporate other potential control factors such as grain size, tidal current velocity and mode of sediment transport. Consequently, singular relationships like these ones are considered inadequate for a robust interpretation.

Alternatively, analysis of the spatial distribution of sediment waves with process-based parameters such as Rouse numbers, to indicate the dominant mode of sediment transport, and residual parameters such as tidal current and bed shear stress, show promise (Figure 4-12). The mode of sediment transport has shown to be highly useful in understanding sediment wave growth by previous studies [45], [60]. Although these studies show that increasing suspended load dominance over bedload transport has a dampening effect on sediment wave heights [45], [60], this study does not resolve the same finding, mostly likely due to a difference in the range of in-situ grain sizes (section 4.5.1.2). However, a clear correlation is still evident whereby sediment waves occur where $P > 2.5$ (bed load transport dominance), with a median value of $P = 5.7$, and tend to be absent in transitional zones where P is relatively increased ($\sim P > 8$). Therefore, increasing P above a certain threshold

may indicate winnowing of sediment from the seafloor, subsequently dampening sediment wave growth and development. Combining this with previous knowledge, this indicates that sediment wave assemblages may only occur within a limited range of P, whereby:

a) increasing suspended load dominance ($0.8 < P < 1.2$) over bed load dominance dampens sediment wave growth, and
b) increasing bed load dominance ($P > 2.5$) above approximately $P > 8$ (Figure 4-12) indicates winnowing of finer sediment from the seafloor, leading to sediment starvation and subsequently also inhibiting sediment wave growth.

Similarly, a clear correlation between the reduction in residual tidal current and bed shear stress along a transport pathway with the occurrence of independent offshore sediment wave assemblages (Figure 4-12; Figure 4-13) suggests that asymmetry of the tide could be considered a sediment wave growth mechanism. According to Neill and Couch [98], where maximum tidal asymmetry ($2\phi_{M_2} = \phi_{M_4}$, where ϕ is the phase of the tidal constituent noted in its subscript) and maximum bed shear stress occurs, low bed level change is expected. Contrastingly, as tidal asymmetry progresses towards a symmetrical tide ($2\phi_{M_2} = \phi_{M_4} + 90°$), bed level change theoretically increases, thus coinciding with increased sediment deposition or erosion. Similarly, a reduction in tidal asymmetry (lower residual bed shear stress and tidal current velocity) corresponds to a lower level of tide-averaged net sediment transport movement out of a region in comparison to high tidal asymmetry (relatively higher residual currents). Subsequently, a reduction in residual current along a transport pathway not only supplies sediment to these independent offshore sediment wave assemblages (section 4.5.1.2) but also indicates a relatively higher retainment of sediment in the local area, potentially allowing the growth of sediment wave heights. Clearly, multiple parameters and

processes interlink to form a highly complex hydrodynamic system resulting in an intricate morphodynamic and sediment transport regime.

4.5.2.2 Geological history of the Irish Sea as a required background knowledge for present day sediment wave dynamics

In this region, geological history of the Irish Sea must be considered when interpreting bedform origin, growth and evolution. Changes in tidal current velocities [99], relative sea level, and an abundant sediment supply during post-glacial marine transgression provide an adequate hydrodynamic and sediment regime for submarine bedform (e.g. sediment bank and sediment wave) formation [5]. Specifically, detailed geophysical analysis and paleo-tidal modelling by Van Landeghem et al [39] suggests very large trochoidal sediment waves in the Irish Sea could not have grown to such large heights under present day hydrodynamics. Instead, these most likely formed during post-glacial dynamics at approximately 7 – 10 ka BP, when relative sea levels were lower, and tide and wave driven current velocities were higher. Subsequent bed shear stress reductions are suggested to have made these sediment waves immobile after 5 ka BP, when hydrodynamic conditions stabilised. These trochoidal waves are dominated by coarse-grained material with a thin veneer of fine-grained sediment on the crest and upper slopes. These thin veneers of finer sediments are thought to be active under present day conditions, altering the shape of the slope and crests over time, without shifting the base of the bedform. Scour occurs around the margins of these very large sediment waves due to intensified vortices around its edges, ultimately supplying fine sediment that migrates over the central part of these coarse-grained bedforms. These observations by Van Landeghem et al [39] correlate very well with very large trochoidal waves associated at sites 5, 6 and 7. Finer sediments at the slope and crests of the bedforms tend to migrate under present day hydrodynamic conditions whilst the core bedform remains immobile.

4.5.2.3 Wave-influence on sediment wave dynamics

Analysis of time-lapse bathymetric datasets have also revealed (a) a reduction in wave height (b) a change from simple to compound waves, (c) counter-current migration, (d) reverse-asymmetry migration, and (e) sand-bank-associated waves displaying higher migration rates in comparison to independent sediment wave assemblages (section 4.4.2.2).

Observations (a) and (b) are most significant over the 169-day period at the Lucifer–Blackwater Bank complex. According to Coughlan et al [64] these banks experience a mixed dominance of tide- and wave- induced bed shear stress. In shallow water, where oscillatory wave motion reaches the seafloor, critical bed shear stress and the mode of sediment transport is affected. The complex tide-wind interaction can specifically have a large impact on residual sediment transport pathways [100], whereby in regions of low tidal amplitude, even moderate wind speeds can reverse residual tidal flows [101], [102]. Similarly, numerical modelling works reveal that the interaction between storm waves and tidal currents not only increase bed shear stresses on sand banks, resulting in net erosion and sediment transport, but further influence the direction of net sediment transport associated with these bedforms [103]–[105]. Mitchell et al [105] found that on a tidal sand ridge in the Bristol Channel, sand transport is likely enhanced by surface waves during slack water by maintaining particles above the threshold of motion and providing a bed stress vector in the direction of wave propagation. Although Damen et al [45] showed only a weak correlation between Shield's parameter and sediment wave heights, many studies have shown a high influence of storm waves dampening sediment wave height and generating a more subdued bedform [59].

Sand bank associated sediment waves analysed in this study occur at a maximum water depth of 30 mLAT. For a wave to reach the seafloor at this water depth or shallower the wave period

needs to be at least 6.2 s. In-situ wave data from the M5 weather buoy, located off the south coast of Ireland (51.690425, -6.704336), was analysed for the 169-day time period. Wave period readily exceeded this 6.2 s threshold. Furthermore, at least four storm events were recorded where the wave period reached 8 s, significant wave heights reached greater than 6 m, and maximum wave heights were greater than 10 m, some reaching 16.4 m. During these storms, the base of the wave could reach the seafloor at water depths less than 50 mLAT, thus implying wave action could easily influence these sediment waves over this time period. The occurrence of these storm waves enhances shear stress exerted on the seabed causing increased erosion, sediment stirring, and flattening of sediment waves, partially distributing local sediment through relatively smaller superimposed sediment waves (shifting the wave from simple to compound). Over time, tidal currents are predicted to transform these sediment waves back to their original sharp-crested, simple, asymmetric form.

Migration rates of sand bank associated sediment waves are notably higher than bedforms in independent assemblages. Two main physical drivers for this may be:

a) the lower residual tidal current (tidal symmetry/bi-directional flow) at offshore assemblages in comparison to higher residual tidal flow (tidal asymmetry/uni-directional flow) at sand bank associated assemblages, and
b) pure tide-induced bed shear stress at offshore sediment wave fields in comparison to combined tide- and wave- induced bed shear stress at sand bank associated sediment wave fields [64].

Under combined tide- and wave- induced bed shear stress, a higher volume of material is mobilised and potentially transported by the tidal current due to increased stirring by wave action, consequently increasing bedform migration rate [105], [106].

Furthermore, in complex hydrodynamic areas such as at bedload convergent zones (e.g. site 7) or at the southern extents of sediment banks (e.g. sites 2E, 2D and 1C), counter-current and reverse-asymmetry migration is evident. These observations support the findings of Van Landeghem et al [30] and further falsify the theory that the migration of sediment waves is predominately in the direction of their asymmetry.

4.6 Conclusions

Targeted repeat high-resolution bathymetry data from the Irish Sea reveals large to very large sediment waves, of varying morphology, with mean wave heights of 0.6 to 6.1 m. These sediment waves exhibit migration rates of 1.1 to 79 m/yr. Sediment wave characteristics were quantified and compared with similar data from previous studies, significantly augmenting the global dataset. Modelled output for bed shear stress magnitude and direction, as well as other environmental parameters and theoretical indicators, were compared with these sediment wave characteristics to determine influencing factors on sediment wave development and migration. The dataset and results provide valuable insights into the spatio-temporal evolution of sediment waves over a large area of a tidally-dominated shelf sea that is geologically complex in terms of morphology and sedimentology.

Individual environmental parameters were found to be unreliable indicators for sediment wave growth. By contrast, the mode of sediment transport is identified as a controlling factor on sediment wave growth and development. It is suggested that sediment waves are restricted to areas where ~$2.5 < P > \sim 8$ for two reasons: a) suspended load dominance over bed load dominance $0.8 < P < 1.2$ dampens sediment wave growth, and b) increasing bed load dominance above $P > \sim 8$ indicates winnowing of finer sediment from the seafloor, leading to sediment starvation and subsequent dampening of sediment wave growth.

Residual tidal current and residual bed shear stress is also a suggested controlling factor for sediment wave growth. The reduction in residual tidal current along a transport pathway supplies sediment to sediment waves, thus facilitating bedform growth, by allowing the settlement of sediment out of suspension, and by retaining sediment within the assemblage due to the associated lower level of tide-averaged net sediment transport movement out of a region in comparison to high tidal asymmetry. In addition, the theoretical predictor of bedforms defined by Shields [87], plotting the entrainment function against the shear Reynold's number, aligns well with the occurrence and absence of mobile bedforms in this region. Therefore, this theoretical predictor has the potential to predict seabed mobility and bedform type in other tidally-dominated shelves, and therefore a coupled or process-driven approach (e.g., Rouse numbers) to understanding bedform dynamics should be incorporated in future studies.

The dataset also allowed for the study of sand bank morphodynamics and the interaction between offshore sand banks, associated sediment waves and independent sediment wave assemblages. A key finding of this study is that the net sediment transport pathways in the south-western Irish Sea derived in this study falsify the previously thought consistent southward flow. Divergence from this pattern is clearly seen both at offshore sand banks and at independent offshore sediment wave assemblages, and a number of key observations can be drawn:

1. Arklow Bank contains a semi-closed circulatory hydrodynamic and sediment transport system.
2. Lucifer–Blackwater Bank complex's sediment transport and morphodynamic regime does not show a similar circulatory pattern to Arklow Bank. Instead, a predominant

southward transport pathway dominates the eastern slope of the bank complex, and a residual headland eddy heavily influences the southern section of the bank. This residual eddy is most likely a controlling factor for the formation and maintenance of the adjacent banner bank (Holden's Bed-Long Bank complex).

The offset of the centre of this residual gyre to the east of the banner bank supports the concept that sediment deposition at the centre of these eddies are not the main element for the formation of banner banks.

3. The circulatory residual flow between the Lucifer–Blackwater and the Holden's Bed–Long Bank complexes, combined with newly derived sediment wave migration and morphodynamic patterns, suggests a continuous recycling of material between these two bank complexes and associated sediment waves.
4. Offshore independent sediment wave fields are supported through circulatory residual tidal current cells, originating from offshore linear sand banks. From this, two new phenomena are suggested: (a) a potential recycling of sediment between sand banks and offshore sand deposits, and (b) offshore independent sediment wave fields act as intermediary transport zones to sediment wave fields in deeper waters.

Observations from this study show that the rate of sediment wave migration and morphological change varies hugely both regionally in a tidal dominant shelf, and within individual study sites, depending on local environmental factors including residual tidal current, mode of sediment transport, and wave influence. It underpins the necessity for investigating further the complex interaction between flow and seafloor bedforms, including the need for higher-resolution temporal datasets to qualify bed-level change over short time periods and the value of numerical modelling of bed stress magnitude and direction at a local level. This new information concerning sediment wave dimensions,

migration parameters, and the nature of morphological change, can be used not only to optimise infrastructural design but also optimise the monitoring strategy and monitoring frequency for navigation channels, pipelines, cables and turbine foundations, and are highly valuable to the development of more robust marine spatial planning.

4.7 Data Availability

The bathymetry data used in Figure 4-3, Figure 4-5, Figure 4-8 – Figure 4-11, and Figure 4-13 – Figure 4-16, and Figure 4-2 is sourced from INFOMAR (https://www.infomar.ie/data [Accessed: 10 June 2021]) and EMODnet Bathymetry Consortium (2020). Seabed substrate data used in Figure 4-2, Figure 4-14 and Figure 4-15 come from EMODnet Seabed Habitats initiative *(*http://www.emodnet-seabedhabitats.eu/ [Accessed: 25 June 2021]*).* The set-up and validation of the numerical model described in section 4.3.4 has been published in a previous paper [64]. Supplementary methodology and results outlined in section 4.3.2.2 and 4.4.3.1 respectively are provided as supplementary material to this paper.

4.8 Acknowledgments

SC is funded by the Irish Research Council (IRC) through grant EBPPG/2019/158 (Employment-Based Postgraduate Programme Scholarship). MC is funded under an Irish Research Council Enterprise Partnership Scheme Postdoctoral Fellowship (EPSPD/2020/109) and in part by a research grant from Science Foundation Ireland (SFI) under Grant Number 13/RC/2092, with support from Gavin and Doherty Geosolutions Ltd and the Geological Survey of Ireland (GSI). This project benefitted from funded industry-academic collaboration involving Gavin and Doherty Geosolutions, University College Dublin (iCRAG) and University College Cork (MaREI), supported by the Marine Institute under the Marine Research Programme 2014-2020 (Grant-Aid Agreement No. IND/18/18). Ship time on the RV Celtic Voyager was funded by the Marine

Institute through the 2020-2021 ship-time programme under the National Marine Research and Innovation Strategy 2017-2021. The authors would gratefully like to acknowledge the Mobility of Sediment Waves and Sand Banks in the Irish Sea (MOVE) (CV20010, CV20036 and CV21035) shipboard crew and scientists, and onshore Marine Institute and INFOMAR support personnel for assistance with data acquisition. The authors are appreciative for access to the seabed sediment sample data and would like to acknowledge colleagues collecting and preparing these data through the projects and surveys mentioned. The authors wish to thank Xavi Monteys and Charise McKeon (both GSI) in particular for aiding with the INFOMAR dataset. *Seabed substrate information contained here has been derived from data that is made available under the European Marine Observation Data Network (EMODnet) Seabed Habitats initiative (*http://www.emodnet-seabedhabitats.eu/*), financed by the European Union under Regulation (EU) No 508/2014 of the European Parliament and of the Council of 15 May 2014 on the European Maritime and Fisheries Fund.*

4.9 Author statement

Shauna Creane: Conceptualization, Methodology, Investigation, Formal Analysis, Writing – Original Draft, Writing - Review & Editing, Visualisation, Validation.

Mark Coughlan: Supervision, Conceptualization, Writing – Review & Editing.

Michael O'Shea: Supervision, Writing – Review & Editing.

Jimmy Murphy: Supervision, Conceptualization, Writing – Review & Editing.

4.10 Supplementary Material A: Methodology – sediment wave crest delineation and migration direction and rates

4.10.1 Crest Delineation

The methodology of Di Stefano and Mayer [81] for extracting sediment wave crests by geomorphon analysis [73] was adapted by this study. The r.geomorphon tool used in this method was originally developed for the terrestrial environment [73] but has since proven to be highly proficient at seabed characterisation [81]. This tool identifies the 10 most frequent landforms based on elevation differences between the central cell and its eight surrounding cells. These landforms consist of flat, summit, ridge, shoulder, spur, slope, hollow, footslope, valley and depression. The r.geomorphon tool was applied to each bathymetry dataset at each site. Runtime parameters were varied depending on the condition of each dataset. The resulting raster was reclassified to extract the classified 'summit' and 'ridge' (classifications 2 and 3 respectively) pixels as sediment wave crests. The resulting raster was thinned, filtered by length, and vectorised. Topological cleaning was carried out to remove any unwanted dangles and the sediment wave crests were smoothed to aid the next process of migration rate calculation, whilst ensuring the accuracy of the crest delineations were retained. Georeferenced polyline shapefiles were produced. These datasets were quality controlled (QC) in ArcGIS v.10.8 using slope and Terrain Ruggedness (VRM) tool in the Benthic Terrain Modeller.

4.10.2 Sand wave migration calculation

The QGIS 'Points along the line' tool was applied to QC shapefiles to generate 10m spaced points along each crest, whereby the angle of the crest line at each point is calculated and

presented in the point shapefile attribute table. All polyline and point shapefiles were taken into ArcGIS v10.8 where migration rate was calculated.

Taking two time-lapse datasets at a time and starting with the earlier time-stamp, several steps were taken to calculate migration rate and direction. Depending on the migration direction of the sediment wave (determined using the 'minus' tool or generating a Difference of DTM (DOD) whereby displacement direction of the wave crest is clearly identified) the angle from the crest to a perpendicular line was calculated in the point shapefile by either adding or subtracting 90° from the line angle at that point. The 'bearing distance to line' tool was used to generate a perpendicular line from each point on the crest using this newly calculated bearing angle, the x and y coordinate of each point, and an estimated fixed maximum extended distance. These lines were intersected with the crest of the next time-lapse dataset to generate a corresponding second point shapefile. Each corresponding a and b points were connected via a polyline shapefile whereby the length of each line corresponds to the perpendicular horizontal displacement of the sediment wave crest from one time-stamp to another (Figure 4-17). Annual migration rates are subsequently calculated based on the dates of each survey.

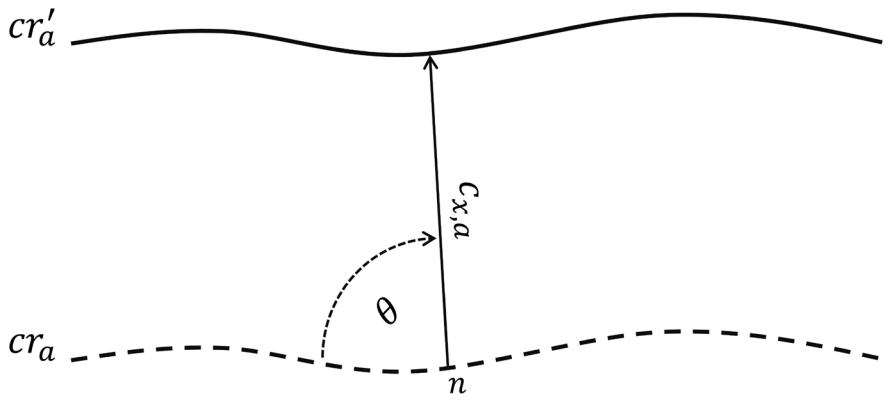


Figure 4-17 Schematic of sediment wave (SW) migration rate calculation, using plan-view delineation of sediment wave crests from bathymetry datasets. For SW "a", the figure denotes cr = SW crest at time of first bathymetric survey; c_x = displacement of SW crest over time interval x, cr'= position of displaced SW crest over time interval x; θ = bearing perpendicular to the crest at point n.

Crest perpendicular cross-sections over time-lapse data were extracted using various ArcGIS tools (Stack Profile) for further morphological and geomorphological analysis. This study uses a combination of the two-part geomorphological classification scheme developed by Dove et al [82] and the classification scheme adopted by Van Landeghem et al [56]. Digital Elevation Models (DEM) of difference (DOD) were calculated to quantify the volumetric change between successive bathymetric surveys and reveal geomorphic changes in a 3-dimensional (3D) surface. This aided the quantification of change in a 1-D, 2D and 3D manner allowing for a better understanding of bedform development on a regional scale and allow interpretation of trends in the wider hydrodynamic-morphodynamic system.

4.11 Supplementary Material B: Results - statistical correlation between sediment wave dimensions and individual environmental parameters

The Pearson correlation coefficient is used to describe the strength of a relationship between independent variables and dependent variables. The interpretation of the strength of the

correlation described by Evans [88] is adopted by this study (Table 4-6). Table 4-7 to Table 4-13 display the resultant relationships between sediment wave dimensions in the south-western Irish Sea and environmental parameters highlighted in section 4.4.3.1 of the main research paper, “Development and dynamics of sediment waves in a complex morphological and tidal dominant system: southern Irish Sea”.

Table 4-6 Interpretation of Pearson correlation coefficient (r)

Correlation coefficient (r)	Strength
+ 1.00	Perfect positive
+ 0.8 to 1.0	Very strong positive
+ 0.6 to 0.8	Strong positive
+ 0.4 to 0.6	Moderate positive
+ 0.2 to 0.4	Weak positive
0.0 to + 0.2	Very weak positive/no association
0.0 to - 0.2	Very weak negative/no association
- 0.2 to - 0.4	Weak negative
- 0.4 to - 0.6	Moderate negative
- 0.6 to - 0.8	Strong negative
- 0.8 to - 1.0	Very strong negative
- 1.0	Perfect negative

Table 4-7 Relationship between sediment wave heights (H) and wavelengths (L) in the south-western Irish Sea. The Full dataset has been broken into three environments i.e. Southern Banks, Northern Banks and Independent Assemblages, and each individual study site.

Dataset	Power regression equation	r^2	Correlation coefficient (r)	Correlation description
Full dataset	$H_{mean} = 0.03L^{0.90}$	0.33	0.58	Moderate positive
Southern Banks	$H_{mean} = 0.05L^{0.77}$	0.27	0.52	Moderate positive
Northern Banks	$H_{mean} = 0.02L^{0.95}$	0.28	0.52	Moderate positive
Independent Banks	$H_{mean} = 0.03L^{0.96}$	0.50	0.71	Strong positive
8	$H_{mean} = 0.03L^{0.91}$	0.53	0.73	Strong positive
2F	$H_{mean} = 0.08L^{0.56}$	0.15	0.39	Weak positive
3C	$H_{mean} = 0.12L^{0.52}$	0.12	0.34	Weak positive
6	$H_{mean} = 0.04L^{0.92}$	0.48	0.69	Strong positive
5	$H_{mean} = 0.06L^{0.83}$	0.38	0.62	Strong positive
4	$H_{mean} = 0.29L^{0.13}$	0	0.07	Very weak positive/no association
1B	$H_{mean} = 0.08L^{0.78}$	0.30	0.55	Moderate positive
1C	$H_{mean} = 0.10L^{0.63}$	0.14	0.38	Weak positive
1A	$H_{mean} = 0.01L^{1.04}$	0.30	0.55	Moderate positive
3A & 3B	$H_{mean} = 0.06L^{0.64}$	0.13	0.36	Weak positive
2E	$H_{mean} = 0.11L^{0.63}$	0.31	0.56	Moderate positive
2D	$H_{mean} = 0.22L^{0.55}$	0.19	0.43	Moderate positive

2B & 2C	$H_{mean} = 0.11L^{0.71}$	0.31	0.56	Moderate positive
2A	$H_{mean} = 0.07L^{0.69}$	0.26	0.51	Moderate positive
7	$H_{mean} = 0.08L^{0.67}$	0.19	0.43	Moderate positive

Table 4-8 Relationship between sediment wave heights (H), wavelengths (L), and Sand Wave Index (SWI) with Rouse Number (P) in the south-western Irish Sea.

Dataset	Power Regression Equation	r^2	Correlation coefficient (r)	*Correlation description*
Full	$SWI = 51.02P^{0.036}$	0.0019	0.043474	Very weak positive/no association
Independent sediment waves	$SWI = 44.57P^{-0.051}$	0.0063	0.079429	Very weak negative/no association
Northern Banks	$SWI = 47.91P^{0.078}$	0.0073	0.085545	Very weak positive/no association
Southern Banks	$SWI = 69.89P^{-0.072}$	0.0049	0.06976	Very weak negative/no association
Full	$L = 132.14P^{0.035}$	0.0028	0.05332	Very weak positive/no association
Independent sediment waves	$L = 167.48P^{-0.013}$	0.0004	0.0191	Very weak negative/no association
Northern Banks	$L = 117.59P^{0.072}$	0.01474	0.1214	Very weak positive/no association

Southern Banks	$L = 121.67P^{0.061}$	0.0057	0.0757	Very weak positive/no association
Full	$H = 2.59P^{-0.001}$	-4.62E-06	N/A	no association
Independent sediment waves	$H = 3.76P^{0.038}$	0.0017	0.0413	Very weak positive /no association
Northern Banks	$H = 2.45P^{-0.006}$	2.74E-06	0.001654	Very weak negative/no association
Southern Banks	$H = 1.74P^{0.132}$	0.01254	0.111982	Very weak positive/no association

Table 4-9 Relationship between sediment wave heights (H), wavelengths (L), and Sand Wave Index (SWI) with Water depth (D) in the south-western Irish Sea.

Dataset	Power Regression Equation	r^2	Correlation coefficient (r)	*Correlation description*
Full	$SWI = 382.32D^{-0.56}$	0.177	0.421	Moderate negative association
Independent sediment waves	$SWI = 539D^{-0.64}$	0.051	0.226	Weak negative association
Northern Banks	$SWI = 895.24D^{-0.83}$	0.1664	0.408	Moderate negative association

Southern Banks	$SWI = 639.79D^{-0.75}$	0.1503	0.388	Moderate negative association
Full	$L = 88.83D^{0.134}$	0.0157	0.125	Very weak/no association
Independent sediment waves	$L = 69.77D^{0.21}$	0.0052	0.072	Very weak/no association
Northern Banks	$L = 69.62D^{0.178}$	0.018	0.134	Very weak/no association
Southern Banks	$L = 153.05D^{-0.035}$	0.00054	0.0232	Very weak/no association
Full	$H = 0.232D^{0.71}$	0.1813	0.426	Moderate positive association
Independent sediment waves	$H = 0.129D^{0.85}$	0.045	0.213	Weak positive association
Northern Banks	$H = 0.078D^{1.01}$	0.1781	0.422	Moderate positive association
Southern Banks	$H = 0.239D^{0.711}$	0.1032	0.321	Weak positive association
7	$H_{mean} = 0D^{2.593}$	0.014	0.119	Very weak/no association
2A	$H_{mean} = 2.82D^{-0.092}$	0	0.018	Very weak/no association
2B & 2C	$H_{mean} = 0.315D^{0.747}$	0.108	0.328	Weak positive association
2D	$H_{mean} = 0.441D^{0.699}$	0.110	0.332	Weak positive association
2E	$H_{mean} = 1.971D^{0.075}$	0.001	0.032	Very weak/no association
3A & 3B	$H_{mean} = 0.071D^{0.965}$	0.137	0.370	Weak positive association
1A	$H_{mean} = 0.311D^{0.565}$	0.034	0.185	Very weak/no association

1C	$H_{mean} = 0.044D^{1.178}$	0.287	0.535	Moderate positive association
1B	$H_{mean} = 1.919D^{0.204}$	0.006	0.077	Very weak/no association
4	$H_{mean} = 0.001D^{1.874}$	0.003	0.057	Very weak/no association
5	$H_{mean} = 0.014D^{1.454}$	0.031	0.176	Very weak/no association
6	$H_{mean} = 0D^{2.156}$	0.051	0.227	Weak positive association
3C	$H_{mean} = 0.950D^{0.085}$	0.001	0.227	Weak positive association
2F	$H_{mean} = 0.024D^{1.672}$	0.084	0.290	Weak positive association
8	$H_{mean} = 221949.933D^{-2.853}$	0.203	0.451	Moderate positive association

Table 4-10 Relationship between sediment wave heights (H), wavelengths (L), and Sand Wave Index (SWI) with median grain size (D_{50}) in the south-western Irish Sea.

Dataset	Power Regression Equation	r^2	Correlation coefficient (r)	*Correlation description*
Full dataset	$SWI = 55.41{D_{50}}^{0.041}$	0.0021	0.046	Very weak positive/no association
Independent sediment waves	$SWI = 39.93{D_{50}}^{-0.056}$	0.0051	0.072	Very weak negative/no association
Northern Banks	$SWI = 57.82{D_{50}}^{0.094}$	0.011	0.104	Very weak positive/no association
Southern Banks	$SWI = 59.91{D_{50}}^{-0.045}$	0.00172	0.0415	Very weak negative/no association
Full dataset	$L = 142.82{D_{50}}^{0.037}$	0.0273	0.0523	Very weak positive/no association

Independent sediment waves	$L = 158.23{D_{50}}^{-0.061}$	0.006	0.0755	Very weak negative/no association
Northern Banks	$L = 137.71{D_{50}}^{0.072}$	0.072	0.015	Very weak positive/no association
Southern Banks	$L = 139.25{D_{50}}^{0.053}$	0.004	0.064	Very weak positive/no association
Full dataset	$H = 2.58{D_{50}}^{-0.0043}$	8.77E-06	0.002962	Very weak negative/no association
Independent sediment waves	$H = 3.96{D_{50}}^{-0.0057}$	-4.61E-06	N/A	no association
Northern Banks	$H = 2.38{D_{50}}^{-0.022}$	0.00041	0.02	Very weak negative/no association
Southern Banks	$H = 2.32{D_{50}}^{0.098}$	0.0063	0.079	Very weak negative/no association

Table 4-11 Relationship between sediment wave heights (H), wavelengths (L), and Sand Wave Index (SWI) with maximum current speed ($U_{c_{max}}$) in the south-western Irish Sea.

Dataset	Power Regression Equation	r^2	Correlation coefficient (r)	*Correlation description*
Full dataset	$SWI = 56.39{U_{c_{max}}}^{-0.23}$	0.005	0.0729	Very weak negative/no association

Independent sediment waves	$SWI = 40.1{U_{c_{max}}}^{0.09}$	0.0017	0.0418	Very weak positive/no association
Northern Banks	$SWI = 48.19{U_{c_{max}}}^{0.51}$	0.0063	0.079	Very weak positive/no association
Southern Banks	$SWI = 59.9{U_{c_{max}}}^{0.12}$	0.0011	0.033	Very weak positive/no association
Full dataset	$L = 139.26{U_{c_{max}}}^{0.033}$	0.00018	0.0134	Very weak negative/no association
Independent sediment waves	$L = 182.83{U_{c_{max}}}^{-0.32}$	0.0213	0.146	Very weak negative/no association
Northern Banks	$L = 119.65{U_{c_{max}}}^{0.40}$	0.009	0.095	Very weak negative/no association
Southern Banks	$L = 138.86{U_{c_{max}}}^{-0.12}$	0.0018	0.042	Very weak negative/no association
Full dataset	$H = 2.47{U_{c_{max}}}^{0.26}$	0.0047	0.069	Very weak positive/no association
Independent sediment waves	$H = 4.56{U_{c_{max}}}^{-0.403}$	0.0188	0.137	Very weak negative/no association
Northern Banks	$H = 2.48{U_{c_{max}}}^{-0.1121}$	0.00019	0.0139	Very weak negative/no association
Southern Banks	$H = 2.32{U_{c_{max}}}^{-0.2327}$	0.00331	0.058	Very weak negative/no association

Table 4-12 Relationship between sediment wave heights (H), wavelengths (L), and Sand Wave Index (SWI) with residual current speed ($U_{c_{res}}$) in the south-western Irish Sea.

Dataset	Power Regression Equation	r^2	Correlation coefficient (r)	*Correlation description*
Full dataset	$SWI = 72.52{U_{c_{res}}}^{0.87}$	0.0094	0.097	Very weak positive/no association
Independent sediment waves	$SWI = 30.88{U_{c_{res}}}^{-0.07}$	0.0051	0.071	Very weak negative/no association
Northern Banks	$SWI = 33.3{U_{c_{res}}}^{-0.159}$	0.0099	0.099	Very weak negative/no association
Southern Banks	$SWI = 66.03{U_{c_{res}}}^{0.026}$	0.0006	0.025	Very weak positive/no association
Full dataset	$L = 123.61{U_{c_{res}}}^{-0.037}$	0.0028	0.053	Very weak negative/no association
Independent sediment waves	$L = 412.82{U_{c_{res}}}^{0.22}$	0.048	0.22	Weak positive
Northern Banks	$L = 104.09{U_{c_{res}}}^{-0.072}$	0.0048	0.069	Very weak negative/no association
Southern Banks	$L = 158.64{U_{c_{res}}}^{0.045}$	0.0031	0.056	Very weak positive/no association

Full dataset	$H = 1.7{U_{c_{res}}}^{-0.12}$	0.013	0.114	Very weak negative/no association
Independent sediment waves	$H = 13.37{U_{c_{res}}}^{0.294}$	0.045	0.212	Weak positive
Northern Banks	$H = 3.17{U_{c_{res}}}^{0.87}$	0.0021	0.046	Very weak positive/no association
Southern Banks	$H = 2.4{U_{c_{res}}}^{0.02}$	0.0003	0.016	Very weak positive/no association

Table 4-13 Relationship between sediment wave heights (H), wavelengths (L), and Sand Wave Index (SWI) with mean current speed ($U_{c_{mean}}$) in the south-western Irish Sea.

Dataset	Power Regression Equation	r^2	Correlation coefficient (r)	*Correlation description*
Independent sediment waves	$SWI = 45.28{U_{c_{mean}}}^{0.2}$	0.0043	0.065	Very weak positive/no association
Northern Banks	$SWI = 94.14{U_{c_{mean}}}^{0.97}$	0.011	0.105	Very weak positive/no association
Southern Banks	$SWI = 69.48{U_{c_{mean}}}^{0.22}$	0.0034	0.058	Very weak positive/no association
Independent sediment waves	$L = 134.67{U_{c_{mean}}}^{-0.43}$	0.018	0.135	Very weak negative/no association

Northern Banks	$L = 168.92{U_{c_{mean}}}^{0.46}$	0.006	0.077	Very weak positive/no association
Southern Banks	$L = 129.61{U_{c_{mean}}}^{-0.09}$	0.00093	0.031	Very weak negative/no association
Independent sediment waves	$H = 2.97{U_{c_{mean}}}^{-0.63}$	0.021	0.15	Very weak negative/no association
Northern Banks	$H = 1.79{U_{c_{mean}}}^{-0.51}$	0.0022	0.047	Very weak negative/no association
Southern Banks	$H = 1.87{U_{c_{mean}}}^{-0.31}$	0.0051	0.071	Very weak negative/no association

4.12 References

[1] F. Gamberi, G. Della Valle, M. Marani, A. Mercorella, S. Di Stefano, and A. Di Stefano, "Tectonic Controls on Sedimentary system along the Continental Slope of the central and southeastern Tyrrhenian Sea," *Italian Journal of Geosciences*, vol. 138, no. 3, pp. 317–332, 2019, doi: 10.3301/IJG.2019.08.

[2] A. D. Short, "Sediment transport around Australia - Sources, mechanisms, rates, and barrier forms," *Journal of Coastal Research*, vol. 26, no. 3, pp. 395–402, 2010, doi: 10.2112/08-1120.1.

[3] J. Zhou, Z. Wu, D. Zhao, W. Guan, Z. Cao, and M. Wang, "Effect of topographic background on sand wave migration on the eastern Taiwan Banks," *Geomorphology*, vol. 398, p. 108030, 2022, doi: 10.1016/j.geomorph.2021.108030.

[4] J. Zhou, Z. Wu, D. Zhao, W. Guan, C. Zhu, and B. Flemming, "Giant sand waves on the

Taiwan Banks, southern Taiwan Strait: Distribution, morphometric relationships, and hydrologic influence factors in a tide-dominated environment," *Marine Geology*, vol. 427, p. 106238, 2020, doi: 10.1016/j.margeo.2020.106238.

[5] S. Creane, M. O'Shea, M. Coughlan, and J. Murphy, "The Irish Sea bed load parting zone: Is it a mid-sea hydrodynamic phenomenon or a geological theoretical concept?," *Estuarine, Coastal and Shelf Science*, vol. 263, p. 107651, 2021, doi: 10.1016/j.ecss.2021.107651.

[6] D. S. Galvez, S. Papenmeier, L. Sander, A. Bartholomä, and K. H. Wiltshire, "Ensemble mapping as an alternative to baseline seafloor sediment mapping and monitoring," *Geo-Marine Letters*, vol. 42, no. 3, pp. 1–13, 2022, doi: 10.1007/s00367-022-00734-x.

[7] C. Auguste, P. Marsh, J. R. Nader, I. Penesis, and R. Cossu, "Modelling morphological changes and migration of large sand waves in a very energetic tidal environment: Banks Strait, Australia," *Energies*, vol. 14, no. 13, 2021, doi: 10.3390/en14133943.

[8] W. Szczuciński, R. Jagodziński, T. J. J. Hanebuth, K. Stattegger, A. Wetzel, M. Mitrega, D. Unverricht, and P. Van Phach, "Modern sedimentation and sediment dispersal pattern on the continental shelf off the Mekong River delta, South China Sea," *Global and Planetary Change*, vol. 110, pp. 195–213, 2013, doi: 10.1016/j.gloplacha.2013.08.019.

[9] K. A. Robinson, K. Ramsay, C. Lindenbaum, N. Frost, J. Moore, D. Petrey, and T. Darbyshire, *Habitat Mapping for Conservation and Management of the Southern Irish Sea (HABMAP). II: Modelling & Mapping*, vol. 5, no. 2. 2009.

[10] B. R. Wilson, C. J. Brown, J. A. Sameoto, M. Lacharité, A. M. Redden, and V. Gazzola,

"Mapping seafloor habitats in the Bay of Fundy to assess megafaunal assemblages associated with Modiolus modiolus beds," *Estuarine, Coastal and Shelf Science*, vol. 252, 2021, doi: 10.1016/j.ecss.2021.107294.

[11] G. Sutton, *Irish Sea Marine Aggregate Initiative (IMAGIN) Project Synthesis Report Including: Geological Assessment, Environmental Assessment, Morphodynamic Modelling Web-based GIS System, Cost Benefit Analysis, Aggregate Resources and Markets-Wales.*, Marine Env., no. 36. 2008.

[12] M. J. Lewis, S. P. Neill, and A. J. Elliott, "Interannual variability of two offshore sand banks in a region of extreme tidal range," *Journal of Coastal Research*, vol. 31, no. 2, pp. 265–275, 2015, doi: 10.2112/JCOASTRES-D-14-00010.1.

[13] M. R. Phillips and A. L. Jones, "Erosion and tourism infrastructure in the coastal zone: Problems, consequences and management," *Tourism Management*, vol. 27, no. 3, pp. 517–524, 2006, doi: 10.1016/j.tourman.2005.10.019.

[14] S. Distefano and F. Gamberi, "Preservation of Transgressive System Tract Geomorphic Elements during the Holocene Sea Level Rise in the South-Eastern Sicilian Tyrrhenian Margin," *Journal of Marine Science and Engineering*, vol. 10, no. 8, 2022, doi: 10.3390/jmse10081013.

[15] R. Morelissen, S. J. M. H. Hulscher, M. A. F. Knaapen, A. A. Németh, and R. Bijker, "Mathematical modelling of sand wave migration and the interaction with pipelines," *Coastal Engineering*, vol. 48, no. 3, pp. 197–209, 2003, doi: 10.1016/S0378-3839(03)00028-0.

[16] M. Yaghoobi, S. Mazaheri, and E. Jabbari, "Determining Natural Frequency of Free

Spanning Offshore Pipelines by Considering the Seabed Soil Characteristics," *Journal of the Persian Gulf*, vol. 3, no. 8, pp. 25–34, 2012.

[17] B. M. Sumer, J. Fredsøe, and N. Christiansen, "Scour around vertical pile in waves," *Journal of Waterway, Port, Coastal, and Ocean Engineering*, vol. 118, no. 1, pp. 15–31, 1992, doi: 10.1061/(ASCE)0733-950X(1992)118:1(15).

[18] R. J. S. Whitehouse, J. M. Harris, J. Sutherland, and J. Rees, "The nature of scour development and scour protection at offshore windfarm foundations," *Marine Pollution Bulletin*, vol. 62, no. 1, pp. 73–88, 2011, doi: 10.1016/j.marpolbul.2010.09.007.

[19] Department of the Environment Climate and Communications, "Climate Action Plan 2021," 2021.

[20] European Commission, "REPowerEU: A plan to rapidly reduce dependence on Russian fossil fuels and fast forward the green transition," *Press Release*, 2022. https://ec.europa.eu/commission/presscorner/detail/en/IP_22_3131 (accessed Sep. 27, 2022).

[21] National Grid ESO, "Pathway to 2030: A holistic network design to support offshore wind deployment for net zero," 2022.

[22] M. D. Pickering, N. C. Wells, K. J. Horsburgh, and J. A. M. Green, "The impact of future sea-level rise on the European Shelf tides," *Continental Shelf Research*, vol. 35, pp. 1–15, 2012, doi: 10.1016/j.csr.2011.11.011.

[23] M. D. Pickering, K. J. Horsburgh, J. R. Blundell, J. J. M. Hirschi, R. J. Nicholls, M. Verlaan, and N. C. Wells, "The impact of future sea-level rise on the global tides,"

Continental Shelf Research, vol. 142, pp. 50–68, 2017, doi: 10.1016/j.csr.2017.02.004.

[24] D. A. V. Stow, F. J. Hernández-Molina, E. Llave, M. Sayago-Gil, V. Díaz-del Río, and A. Branson, "Bedform-velocity matrix: The estimation of bottom current velocity from bedform observations," *Geology*, vol. 37, no. 4, pp. 327–330, 2009, doi: 10.1130/G25259A.1.

[25] K. R. Dyer and D. A. Huntley, "The origin, classification and modelling of sand banks and ridges," *Continental Shelf Research*, vol. 19, no. 10, pp. 1285–1330, 1999, doi: 10.1016/S0278-4343(99)00028-X.

[26] R. Holmes and D. R. Tappin, "DTI Strategic Environmental Assessment Area 6, Irish Sea, seabed and surficial geology and processes." British Geological Survey Commissioned Report, CR/05/057, p. 82, 2005. [Online]. Available: http://nora.nerc.ac.uk/11259/

[27] D. I. Jackson, A. A. Jackson, D. J. A. Evans, R. T. R. Wingfield, R. P. Barnes, and M. J. Arthur, *United Kingdom offshore regional report: the geology of the Irish Sea*. London: HMSO for the British Geological Survey, 1995.

[28] M. A. Johnson, N. H. Kenyon, R. H. Belderson, and A. H. Stride, "Sand transport," in *Offshore Tidal Sands: Processes and Deposits*, A. H. Stride, Ed. Chapman and Hall, 1982, pp. 58–94. doi: 10.1007/978-94-009-5726-8_4.

[29] M. A. F. Knaapen, "Sandwave migration predictor based on shape information," *Journal of Geophysical Research: Earth Surface*, vol. 110, no. 4, pp. 1–9, 2005, doi: 10.1029/2004JF000195.

[30] K. J. J. Van Landeghem, J. H. Baas, N. C. Mitchell, D. Wilcockson, and A. J. Wheeler,

"Reversed sediment wave migration in the Irish Sea, NW Europe: A reappraisal of the validity of geometry-based predictive modelling and assumptions," *Marine Geology*, vol. 295–298, pp. 95–112, 2012, doi: 10.1016/j.margeo.2011.12.004.

[31] A. Nemeth, S. J. M. H. Hulscher, and H. J. de Vriend, "Offshore sand wave dynamics, engineering problems and future solutions," *Pipeline and gas journal*, vol. 230, no. 4, pp. 67–69, 2003.

[32] A. J. Couldrey, T. Benson, M. A. F. Knaapen, K. V Marten, and R. J. S. Whitehouse, "Morphological evolution of a barchan dune migrating past an offshore wind farm foundation," *Earth Surface Processes and Landforms*, vol. 45, no. 12, pp. 2884–2896, 2020, doi: https://doi.org/10.1002/esp.4937.

[33] H. Park and C. E. Vincent, "Evolution of Scroby Sands in the East Anglian coast , UK," *Journal of Coastal Research*, pp. 868–873, 2007.

[34] T. Schmitt, N. C. Mitchell, and T. S. Ramsay, "Use of swath bathymetry in the investigation of sand dune geometry and migration around a near shore 'banner' tidal sandbank," *Geological Society Special Publication*, vol. 274, pp. 53–64, 2007, doi: 10.1144/GSL.SP.2007.274.01.07.

[35] V. N. D. Caston, "Linear sand banks in the southern North Sea," *Sedimentology*, vol. 18, no. 1–2, pp. 63–78, 1972, doi: 10.1111/j.1365-3091.1972.tb00003.x.

[36] N. H. Kenyon and B. Cooper, "Sand banks, sand transport and offshore wind farms: DTI SEA 6 Technical Report," ABPmer for Department of Trade and Industry, London, 2005.

[37] S. Leenders, J. H. Damveld, J. Schouten, R. Hoekstra, T. J. Roetert, and B. W. Borsje,

"Numerical modelling of the migration direction of tidal sand waves over sand banks," *Coastal Engineering*, vol. 163, p. 103790, 2021, doi: 10.1016/j.coastaleng.2020.103790.

[38] J. M. Horrillo-Caraballo, Y. Yin, I. Fairley, H. Karunarathna, I. Masters, and D. E. Reeve, "A comprehensive study of the tides around the Welsh coastal waters," *Estuarine, Coastal and Shelf Science*, vol. 254, p. 107326, 2021, doi: 10.1016/j.ecss.2021.107326.

[39] K. J. J. Van Landeghem, K. Uehara, A. J. Wheeler, N. C. Mitchell, and J. D. Scourse, "Post-glacial sediment dynamics in the Irish Sea and sediment wave morphology: Data-model comparisons," *Continental Shelf Research*, vol. 29, no. 14, pp. 1723–1736, 2009, doi: 10.1016/j.csr.2009.05.014.

[40] EMODnet Bathymetry Consortium, "EMODnet Digital Bathymetry (DTM 2020)." 2020. doi: https://doi.org/10.12770/bb6a87dd-e579-4036-abe1-e649cea9881a.

[41] EMODnet Geology, "Seabed Substrates," 2019. https://www.emodnet-geology.eu/data-products/seabed-substrates/

[42] Y. A. Cataño-Lopera and M. H. García, "Geometry and migration characteristics of bedforms under waves and currents. Part 1: Sandwave morphodynamics," *Coastal Engineering*, vol. 53, no. 9, pp. 767–780, 2006, doi: 10.1016/j.coastaleng.2006.03.007.

[43] J. P. Xu, F. L. Wong, R. Kvitek, D. P. Smith, and C. K. Paull, "Sandwave migration in Monterey Submarine Canyon, Central California," *Marine Geology*, vol. 248, no. 3–4, pp. 193–212, 2008, doi: 10.1016/j.margeo.2007.11.005.

[44] M. R. Dobson, W. E. Evans, and K. H. James, "The sediment on the floor of the southern Irish Sea," *Marine Geology*, vol. 11, no. 1, pp. 27–69, 1971, doi:

10.1016/0025-3227(71)90083-1.

[45] J. M. Damen, T. A. G. P. van Dijk, and S. J. M. H. Hulscher, “Spatially Varying Environmental Properties Controlling Observed Sand Wave Morphology,” *Journal of Geophysical Research: Earth Surface*, vol. 123, no. 2, pp. 262–280, 2018, doi: 10.1002/2017JF004322.

[46] G. M. Ashley, “Classification of large-scale subaqueous bedforms: a new look at an old problem; SEPM bedforms and bedding structures,” *Journal of Sedimentary Petrology*, vol. 60, no. 1, pp. 160–172, 1990, doi: 10.1306/212f9138-2b24-11d7-8648000102c1865d.

[47] B. W. Flemming, “Zur klassifikation subaquatischer, strömungstransversaler Transportkörper,” *Bochumer geologische und geotechnische Arbeiten*, vol. 29, no. January 1988, pp. 93–97, 1988.

[48] B. W. Flemming, “The role of grain size, water depth and flow velocity as scaling factors controlling the size of subaqueous dunes,” *Marine Sandwave Dynamics*, vol. 154, no. March, pp. 55–60, 2000.

[49] Y. Kubo, W. Soh, H. Machiyama, and H. Tokuyama, “Bedforms produced by the Kuroshio Current passing over the northern Izu Ridge,” *Geo-Marine Letters*, vol. 24, no. 1, pp. 1–7, 2004, doi: 10.1007/s00367-003-0134-1.

[50] P. Blondeaux and G. Vittori, “A parameterization of the wavelength of tidal dunes,” *Earth Surface Processes and Landforms*, vol. 36, no. 9, pp. 1152–1161, 2011, doi: 10.1002/esp.2137.

[51] R. B. van Santen, H. E. de Swart, and T. A. G. P. van Dijk, “Sensitivity of tidal sand

wavelength to environmental parameters: A combined data analysis and modelling approach," *Continental Shelf Research*, vol. 31, no. 9, pp. 966–978, 2011, doi: 10.1016/j.csr.2011.03.003.

[52] M. S. Yalin, "Geometrical properties of sand wave," *Journal of Hydraulics Division*, vol. 90, no. 5, pp. 105–119, 1964.

[53] H. H. Van Der Veen, S. J. M. H. Hulscher, and M. A. F. Knaapen, "Grain size dependency in the occurrence of sand waves," *Ocean Dynamics*, vol. 56, no. 3–4, pp. 228–234, 2006, doi: 10.1007/s10236-005-0049-7.

[54] M. Franzetti, P. Le Roy, C. Delacourt, T. Garlan, R. Cancouët, A. Sukhovich, and A. Deschamps, "Giant dune morphologies and dynamics in a deep continental shelf environment: Example of the banc du four (Western Brittany, France)," *Marine Geology*, vol. 346, pp. 17–30, 2013, doi: 10.1016/j.margeo.2013.07.014.

[55] J. Bartholdy, A. Bartholomae, and B. W. Flemming, "Grain-size control of large compound flow-transverse bedforms in a tidal inlet of the Danish Wadden Sea," *Marine Geology*, vol. 188, no. 3–4, pp. 391–413, 2002, doi: 10.1016/S0025-3227(02)00419-X.

[56] K. J. J. Van Landeghem, A. J. Wheeler, N. C. Mitchell, and G. Sutton, "Variations in sediment wave dimensions across the tidally dominated Irish Sea, NW Europe," *Marine Geology*, vol. 263, no. 1–4, pp. 108–119, 2009, doi: 10.1016/j.margeo.2009.04.003.

[57] S. J. M. H. Hulscher, "Tidal-induced large-scale regular bed form patterns in a three-dimensional shallow water model," *Journal of Geophysical Research: Oceans*, vol.

101, no. C9, pp. 20727–20744, 1996, doi: 10.1029/96JC01662.

[58] P. Blondeaux and G. Vittori, “Formation of tidal sand waves: Effects of the spring-neap cycle,” *Journal of Geophysical Research: Oceans*, vol. 115, no. 10, pp. 1–7, 2010, doi: 10.1029/2010JC006400.

[59] G. H. P. Campmans, P. C. Roos, H. J. de Vriend, and S. J. M. H. Hulscher, “The Influence of Storms on Sand Wave Evolution: A Nonlinear Idealized Modeling Approach,” *Journal of Geophysical Research: Earth Surface*, vol. 123, no. 9, pp. 2070–2086, 2018, doi: 10.1029/2018JF004616.

[60] B. W. Borsje, W. M. Kranenburg, P. C. Roos, J. Matthieu, and S. J. M. . Hulscher, “The role of suspended load transport in the occurrence of tidal sand waves,” *Journal of Geophysical Research: Earth Surface*, vol. 119, pp. 701–716, 2014, doi: 10.1002/2013JF002828.

[61] V. B. Ernstsen, R. Noormets, C. Winter, D. Hebbeln, A. Bartholomä, B. W. Flemming, and J. Bartholdy, “Development of subaqueous barchanoid-shaped dunes due to lateral grain size variability in a tidal inlet channel of the Danish Wadden Sea,” *Journal of Geophysical Research: Earth Surface*, vol. 110, no. 4, 2005, doi: 10.1029/2004JF000180.

[62] F. Francken, W. Stanislas, R. Parker, and E. Taverniers, “Factors influencing subaqueous dunes in the Scheldt Estuary,” *Geo-Marine Letters*, vol. 24, pp. 14–21, 2004, doi: 10.1007/s00367-003-0154-x.

[63] R. W. Dalrymple, R. J. Knight, and J. J. Lambiase, “Bedforms and their hydraulic stability relationships in a tidal environment, Bay of Fundy, Canada,” *Nature*, vol. 275,

no. 5676, pp. 100–104, 1978, doi: 10.1038/275100a0.

[64] M. Coughlan, M. Guerrini, S. Creane, M. O'Shea, S. L. Ward, K. J. J. Van Landeghem, J. Murphy, and P. Doherty, "A new seabed mobility index for the Irish Sea: modelling seabed shear stress and classifying sediment mobilisation to help predict erosion, deposition, and sediment distribution," *Continental Shelf Research*, vol. 229, p. 104574, 2021, doi: https://doi.org/10.1016/j.csr.2021.104574.

[65] D. R. Tappin, R. A. Chadwick, A. A. Jackson, R. T. R. Wingfield, and N. J. P. Smith, *United Kingdom offshore regional report: The geology of Cardigan Bay and the Bristol Channel*. London: HMSO for the British Geological Survey, 1994.

[66] A. J. Wheeler, J. Walshe, and G. D. Sutton, "Geological appraisal of the Kish, Burford, Bray and Fraser Banks, Outer Dublin Bay Area," in *Marine Resources Series*, Dublin: Marine Institute, 2000.

[67] M. Kozachenko, R. Fletcher, G. Sutton, X. Monteys, K. Van Landeghem, A. Wheeler, Y. Lassoued, A. Cooper, and C. Nicoll, *A geological appraisal of marine aggregate resources in the southern Irish Sea. Technical report produced for the Irish Sea Marine Aggregates Initiative (IMAGIN) project funded under the INTERREG IIIA Community Initiative Programme 2000-2006*. University College Cork, Ireland, 2008.

[68] S. L. Ward, S. P. Neill, K. J. J. Van Landeghem, and J. D. Scourse, "Classifying seabed sediment type using simulated tidal-induced bed shear stress," *Marine Geology*, vol. 367, pp. 94–104, 2015, doi: 10.1016/j.margeo.2015.05.010.

[69] M. Coughlan, M. Long, and P. Doherty, "Geological and geotechnical constraints in the Irish Sea for offshore renewable energy," *Journal of Maps*, vol. 16, no. 2, pp. 420–

431, 2020, doi: 10.1080/17445647.2020.1758811.

[70] J. E. Hanna and J. A. G. Cooper, “Mesoscale Morphological Changes on Linear, Nearshore Sandbanks, Co.Wexford, SE Ireland.,” *Journal of Coastal Research*, vol. 36, pp. 356–364, 2002, doi: 10.2112/1551-5036-36.sp1.356.

[71] J. K. Panigrahi, P. N. Ananth, and P. A. Umesh, “Coastal morphological modeling to assess the dynamics of Arklow Bank, Ireland,” *International Journal of Sediment Research*, vol. 24, no. 3, pp. 299–314, 2009, doi: 10.1016/S1001-6279(10)60005-4.

[72] S. Walbridge, N. Slocum, M. Pobuda, and D. J. Wright, “Unified Geomorphological Analysis Workflows with Benthic Terrain Modeler,” *Geosciences*, vol. 8, no. 3, 2018, doi: 10.3390/GEOSCIENCES8030094.

[73] J. Jasiewicz and T. F. Stepinski, “Geomorphons-a pattern recognition approach to classification and mapping of landforms,” *Geomorphology*, vol. 182, pp. 147–156, 2013, doi: 10.1016/j.geomorph.2012.11.005.

[74] G. Summers, A. Lim, and A. J. Wheeler, “A scalable, supervised classification of seabed sediment waves using an object-based image analysis approach,” *Remote Sensing*, vol. 13, no. 12, pp. 1–29, 2021, doi: 10.3390/rs13122317.

[75] T. A. G. P. van Dijk, R. C. Lindenbergh, and P. J. P. Egberts, “Separating bathymetric data representing multiscale rhythmic bed forms: A geostatistical and spectral method compared,” *Journal of Geophysical Research: Earth Surface*, vol. 113, no. 4, pp. 1–16, 2008, doi: 10.1029/2007JF000950.

[76] G. P. Duffy, “Patterns of morphometric parameters in a large bedform field: Development and application of a tool for automated bedform morphometry,” *Irish*

Journal of Earth Sciences, vol. 30, pp. 31–39, 2012, doi: 10.3318/IJES.2012.30.31.

[77] C. F. Van der Mark and A. Blom, "A new and widely applicable tool for determining the geometric properties of bedforms. Report number: CE&M Research Report 2007R-003/WEM-002," 2007. doi: 10.13140/RG.2.2.17637.40161.

[78] L. Wang, Q. Yu, Y. Zhang, B. W. Flemming, Y. Wang, and S. Gao, "An automated procedure to calculate the morphological parameters of superimposed rhythmic bedforms," *Earth Surface Processes and Landforms*, vol. 45, no. 14, pp. 3496–3509, 2020, doi: 10.1002/esp.4983.

[79] W. Evans, S. Benetti, F. Sacchetti, D. W. T. Jackson, P. Dunlop, and X. Monteys, "Bedforms on the northwest Irish Shelf: indication of modern active sediment transport and over printing of paleo-glacial sedimentary deposits," *Journal of Maps*, vol. 11, no. 4, pp. 561–574, 2015, doi: 10.1080/17445647.2014.956820.

[80] S. Berne, P. Castaing, E. Le Drezen, and G. Lericolais, "Morphology, internal structure, and reversal of asymmetry of large subtidal dunes in the entrance to Gironde Estuary (France)," *Journal of Sedimentary Petrology*, vol. 63, no. 5, pp. 780–793, 1993, doi: 10.1306/d4267c03-2b26-11d7-8648000102c1865d.

[81] M. Di Stefano and L. A. Mayer, "An automatic procedure for the quantitative characterization of submarine bedforms," *Geosciences*, vol. 8, no. 1, pp. 1–26, 2018, doi: 10.3390/geosciences8010028.

[82] D. Dove *et al.*, "Seabed Geomorphology: a two-part classification system. Marine Geoscience Programme. Open Report OR/16/001," British Geological Survey, 2016.

[83] J. Kaklamanos and K. Elmy, "R Package 'geotech,'" 2016.

[84] DHI Group, “MIKE 21 Toolbox: user guide.” 2017.

[85] DHI Group, “MIKE 21 Flow Model: Hydrodynamic Module User Guide.” 2017.

[86] B. W. Borsje, W. M. Kranenburg, P. C. Roos, J. Matthieu, and S. J. M. H. Hulscher, “The role of suspended load transport in the occurrence of tidal sand waves,” *Journal of Geophysical Research: Earth Surface*, vol. 119, pp. 701–716, 2014, doi: https://doi.org/10.1002/2013JF002828.

[87] A. Shields, “Anwendung der Aehnlichkeitsmechanik und der Turbulenzforschung auf die Geschiebebewegung,” Preussischen Versuchsanstalt für Wasserbau, 1936.

[88] J. D. Evans, *Straightforward statistics for the behavioral sciences*. Pacific Grove, CA: Brooks/Cole Publishing, 1996.

[89] J. M. Huthnance, “On one mechanism forming linear sand banks,” *Estuarine, Coastal and Shelf Science*, vol. 14, no. 1, pp. 79–99, 1982, doi: 10.1016/S0302-3524(82)80068-6.

[90] S. J. M. H. Hulscher, H. E. de Swart, and H. J. de Vriend, “The generation of offshore tidal sand banks and sand waves,” *Continental Shelf Research*, vol. 13, no. 11, pp. 1183–1204, 1993, doi: 10.1016/0278-4343(93)90048-3.

[91] I. Fairley, I. Masters, and H. Karunarathna, “Numerical modelling of storm and surge events on offshore sandbanks,” *Marine Geology*, vol. 371, pp. 106–119, 2016, doi: 10.1016/j.margeo.2015.11.007.

[92] R. J. McCarroll, G. Masselink, N. G. Valiente, M. Wiggins, T. Scott, D. C. Conley, and E. V. King, “Impact of a headland-associated sandbank on shoreline dynamics,” *Geomorphology*, vol. 355, p. 107065, 2020, doi: 10.1016/j.geomorph.2020.107065.

[93] R. D. Pingree, “The formation of the Shambles and other banks by tidal stirring of the seas,” *Journal of Marine Biological Association of the United Kingdom*, vol. 58, pp. 211–226, 1978, doi: 10.1017/S0025315400024504.

[94] A. Bastos, M. Collins, and N. Kenyon, “Water and sediment movement around a coastal headland: Portland Bill, southern UK,” *Ocean Dynamics*, vol. 53, no. 3, pp. 309–321, 2003, doi: 10.1007/s10236-003-0031-1.

[95] A. Berthot and C. Pattiaratchi, “Mechanisms for the formation of headland-associated linear sandbanks,” *Continental Shelf Research*, vol. 26, no. 8, pp. 987–1004, 2006, doi: 10.1016/j.csr.2006.03.004.

[96] M. Z. Li, J. Shaw, B. J. Todd, V. E. Kostylev, and Y. Wu, “Sediment transport and development of banner banks and sandwaves in an extreme tidal system: Upper Bay of Fundy, Canada,” *Continental Shelf Research*, vol. 83, pp. 86–107, 2014, doi: 10.1016/j.csr.2013.08.007.

[97] C. K. Wentworth, “A Scale of Grade and Class Terms for Clastic Sediments,” *The Journal of Geology*, vol. 30, no. 5, pp. 377–392, 1922, doi: 10.1086/622910.

[98] S. P. Neill and S. J. Couch, “Impact of Tidal Energy Converter (TEC) Array Operation on Sediment Dynamics,” in *9th European Wave and Tidal Energy Conference (EWTEC)*, 2011.

[99] K. Uehara, J. D. Scourse, K. J. Horsburgh, K. Lambeck, and A. P. Purcell, “Tidal evolution of the northwest European shelf seas from the Last Glacial Maximum to the present,” *Journal of Geophysical Research: Oceans*, vol. 111, no. 9, pp. 1–15, 2006, doi: 10.1029/2006JC003531.

[100] M. P. O'Shea, "Monitoring and modelling the morphodynamic evolution of a breached barrier beach system," University College Cork, 2015. [Online]. Available: https://cora.ucc.ie/handle/10468/3359

[101] I. Colosimo, P. L. M. de Vet, D. S. van Maren, A. J. H. M. Reniers, J. C. Winterwerp, and B. C. van Prooijen, "The impact of wind on flow and sediment transport over intertidal flats," *Journal of Marine Science and Engineering*, vol. 8, no. 11, pp. 1–26, 2020, doi: 10.3390/jmse8110910.

[102] J. J. Daniell, "Bedload parting in western Torres Strait, northern Australia," *Continental Shelf Research*, vol. 93, pp. 58–69, 2015, doi: 10.1016/j.csr.2014.11.008.

[103] A. Giardino and J. Monbaliu, "Wave effects on the morphodynamic evolution of an offshore sand bank," *Journal of Coastal Research SI*, vol. 51, pp. 127–140, 2010, doi: 10.2112/SI51-012.1.

[104] D. Idier, A. Ehrhold, and T. Garlan, "Morphodynamique d'une dune sous-marine du détroit du pas de Calais," *Comptes Rendus Geoscience*, vol. 334, no. 15, pp. 1079–1085, 2002, doi: 10.1016/s1631-0713(02)01852-7.

[105] N. C. Mitchell, R. Jerrett, and R. Langman, "Dynamics and stratigraphy of a tidal sand ridge in the Bristol Channel (Nash Sands banner bank) from repeated high-resolution multibeam echo-sounder surveys," *Sedimentology*, vol. 69, no. 3, pp. 1051–1082, 2022, doi: 10.1111/sed.12935.

[106] T. A. G. P. Van Dijk and M. G. Kleinhans, "Processes controlling the dynamics of compound sand waves in the North Sea, Netherlands," *Journal of Geophysical Research: Earth Surface*, vol. 110, no. 4, pp. 1–15, 2005, doi: 10.1029/2004JF000173.

5 Estimation of suspended solids concentration from Acoustic Doppler Current Profiler in a tidally-dominated continental shelf sea setting and its use as a numerical modelling validation technique

Estimation of suspended solids concentration from Acoustic Doppler Current Profiler in a tidally-dominated continental shelf sea setting and its use as a numerical modelling validation technique

Shauna Creane[1,2,3], Michael O'Shea[1,2], Mark Coughlan[4,5,3], Jimmy Murphy[1,2]

[1]School of Civil & Environmental Engineering, University College Cork, College Road, T12 K8AF Cork, Ireland; shauna.creane@ucc.ie (S.C.); michaeloshea@ucc.ie (M.O.); jimmy.murphy@ucc.ie (J.M.)

[2]SFI Research Centre for Energy, Climate and Marine (MaREI), Beaufort Building, Environmental Research Institute, University College Cork, Ringaskiddy, P43 C573 Cork, Ireland

[3]Gavin and Doherty Geosolutions, Unit A2, Nutgrove Office Park, Rathfarnham, D14 X627 Dublin, Ireland

[4]School of Earth Sciences, Science Centre West, University College Dublin, Belfield, D04 N2E5 Dublin, Ireland; mark.coughlan@icrag-centre.org (M.C.)

[5]SFI Research Centre for Applied Geosciences (iCRAG), O'Brien Centre for Science East, University College Dublin, D04 N2E5 Dublin, Ireland

Abstract

With the acceleration of the offshore renewable energy (ORE) industry, an increased knowledge of the impact of ORE technologies and supporting infrastructure on the marine environment is imperative. Novel sediment transport numerical modelling approaches allow engineers and scientists to investigate these physical interactions both in the near and far

field. However, a lack of confidence in simulated sediment transport results is evident in many coastal and offshore studies, mainly due to limited access to validation datasets. This study addresses the need for cost-effective sediment validation datasets by investigating the applicability of four new suspended load validation techniques to a 2D model of the south-western Irish Sea. This involves integrating an estimated spatial time series of suspended solids concentration (SSC_{solids}) derived from acoustic doppler current profiler (ADCP) acoustic backscatter with several in situ water sample-based SSC_{solids} datasets.

Ultimately, a robust spatial timeseries of ADCP-based SSC_{solids} was successfully calculated in this offshore, tidally-dominated setting, where the correlation coefficient between estimated SSC_{solids} and directly measured SSC_{solids} is 0.87. Three out of the four assessed validation techniques are deemed advantageous in developing an accurate 2D suspended sediment transport model given the assumptions of the depth-integrated approach. These recommended techniques include i) validation of 2D modelled suspended sediment concentration ($SSC_{sediment}$) using water sample-based SSC_{solids}, ii) validation of the flood-ebb characteristics of 2D modelled suspended load transport and $SSC_{sediment}$ using ADCP-based datasets and iii) validation of the 2D modelled peak $SSC_{sediment}$ over a spring-neap cycle using the ADCP-based SSC_{solids}. Overall, the multi-disciplinary method of collecting in situ metocean and sediment dynamic data via acoustic instruments (ADCPs) is a cost-effective in situ data collection method for future ORE developments and other engineering and scientific projects.

5.1 Introduction

Reliable coastal and offshore sediment transport data is a requirement for many engineering and environmental projects, including port and harbour design [1], dredging and beach

nourishment [2], [3], sea shoreline protection [4], inland navigation [5], marine pollution monitoring [6], benthic habitat mapping [7] and offshore renewable energy (ORE) development projects including wave [8], [9], tidal [10]–[12] and wind energy [13], [14]. With the increased demand in marine resources for offshore renewable energy developments [15]–[17], a comprehensive understanding of sediment transport regimes on a local and regional scale in a coastal and offshore environment is imperative. The installation of infrastructure on the seabed, for example wave and tidal energy converters and wind turbine foundations, alters wave propagation, flow patterns and sediment circulation [12], [18]–[22]. Specific oceanographic parameters effected may include turbulence, mixing and vertical stratification, potentially impacting sediment resuspension, sedimentation, temperature change, nutrient transport and substrate availability [23], [24]. In the far field, subsequent physical impacts to the marine environment could be detrimental, causing beach width reduction [25], or could be beneficial, aiding coastal protection [9], [26]. The nature of this impact depends on the local oceanographic regime, the type and size of the ORE development, and lay-out configurations.

In the near field, these changes have the potential to alter marine biogeochemistry including marine life behaviour, phytoplankton dynamics and benthic habitats [13], [24]. Evidently, baseline information is critical in order to qualify and quantify changes that may occur in the sediment transport system as a result of these developments. Additionally, developing baseline risk maps to identify areas of regional stability may aid developers on choosing low risk zones in terms of scour (e.g. Coughlan et al [27]). The determination of cable burial depths may also be aided through the knowledge of seabed mobility potential [28]. Furthermore, it is imperative to simulate near seabed velocities to quantify seabed shear stress and scour in order to mitigate infrastructural instability [29], [30].

Numerical modelling is an excellent tool that can be used to gather this qualitative and quantitative baseline (natural regime) information on hydrodynamics, waves and sediment transport dynamics in coastal and oceanic regions [8], [31]–[33]. It can also be used to simulate the responses of the physical environment imposed by the installation of these marine structures [8], [11], [12], [26], [34], [35]. State-of-the-art sediment transport numerical modelling techniques takes many forms including one-dimensional (1D) [36], two-dimensional (2D) [12], two-dimensional vertical (2DV) [37], [38], three-dimensional (3D) [39] and smoothed-particle hydrodynamics (SPH) [40] modelling. Across many environments (fluvial, coastal and offshore), the assumptions underlying the depth-integrated (2D) modelling approach are commonly accepted and adopted when considering several project variables including, environmental conditions, model scale, model resolution, computational power, project timelines and project budget [27], [32]. On the other hand, 3D models are becoming increasingly more feasible with the advancement of technology such as high-performance computing [41]. Regardless, a common challenge to all techniques is the paucity of in situ sediment data to calibrate/validate these numerical modelling techniques.

In many sediment transport studies, only the underlying hydrodynamic and wave models are validated using in situ field data [8]. Where field sediment properties such as median grain size, sorting, grain density etc. is available, they act as input into these models, yet modelled sediment transport outputs are generally not validated. This may be due to limited data availability and associated high costs for data collection campaigns. Few studies have managed to quantify bed load transport through the use of bed level changes and sand wave migration characteristics derived from geophysical datasets [12], [39], [42]. Comparably, a limited amount of studies have managed to validate suspended sediment transport variables using optical backscatter sensors and transmissometers [11], [43]–[45]. For example, a study

off the coast of Anglesey, in the Irish Sea [11], validates a two-dimensional (2D) suspended sediment transport model using estimated suspended sediment concentration (SSC) from a Sequoia 100-X LISST (Laser In Situ Scattering and Transmissometry) calibrated via a number of water samples. Nevertheless, there is clear paucity of investigation into the development of suspended sediment transport model validation techniques. Increased validation would ultimately improve the accuracy of numerical models, which is imperative for the acceleration of cost-effective engineering projects with a sustainable and environmental focussed ambition.

This study will focus on potential validation techniques for suspended sediment transport variables of 2D numerical models. The conventional (laboratory-based) method for measuring suspended solids concentration (SSC_{solids}) is the most accurate, yet sole direct sampling via sediment traps or water sampling is expensive and time-consuming. It requires a high sampling time at the observation site, collecting samples at different time stamps and water column depths in order to capture the full dynamics of the system. It requires a high processing time, and does not provide a full spatial and temporal timeseries.

On the other hand, the use of optical backscattering sensors (OBS) and transmissometers overcome this spatial and temporal resolution issue with the capability of producing a time series of high-frequency measurements of suspended mass concentration. Although this captures the variable nature of SSC_{solids} in the water column, the calibration of these instruments is highly complex as the response function of the OBS sensor depends on grain size and is nonlinear with the concentration of suspended solids. Additionally, optical sensors are especially sensitive to biological fouling problems [46].

Alternatively, acoustics sensors which are less susceptible to effects of biological fouling, such as Acoustic Doppler Current Profilers (ADCPs), are typically used to measure ocean currents and velocity profiles, yet also record acoustic backscattering intensity which is directly related to suspended solids concentration. The estimation of SSC from this recorded echo intensity using the sonar equation is not a straightforward process yet has been under development for many years [47]–[54]. This method development is predominately focussed on fluvial environments where high mass concentrations dominate [50]–[52], [55], [56] with few applications in high energy coastal systems [57]. This method of estimation depends on multiple environmental factors, including water temperature, salinity and pressure, and instrument characteristics such as operational frequency, power and transducer size. Early studies account for beam spreading and water absorption in the calculation of transmission losses but exclude corrections for the attenuation from suspended particles and non-spherical spreading in the transducer near field. Other studies incorporate these factors [58]–[60]. In general the application of this method has proven very successful in many fluvial and coastal environments across the globe [61]–[63] and is gaining increasing acceptance amongst coastal engineers and sedimentologists.

This method comes with various limitations which have been outlined in previous studies [54], [57]. For example, the choice of instrument is highly important in terms of frequency, in order to fully capture expected particle size in the water column [54], [64]. Generally, higher frequency ADCPs have the ability to detect finer grain sizes in the water column [65], yet have lower maximum blanking distances and ranges (along the beam path) [52]. For example, a 300kHz ADCP has a maximum range and blanking distance of 300 m and 1 m respectively, yet a 1000kHz ADCP has a maximum range and blanking distance of 25 m and 0.2 m respectively [52]. When used in an offshore environment, a combination of ADCP frequency,

environmental considerations, such as water depth and particle size distribution, and other measurement needs (whether the ADCP is being used to measure ocean currents and waves simultaneously) need to be considered on a case-by-case basis, especially when using single frequency systems. Additionally, single frequency instruments cannot differentiate between changes in concentrations versus changes in particle size distribution (PSD) over the deployment time period. Therefore, in fluvial environments, where PSD is highly variable, this must be taken into consideration during the conversion process. Multi-use frequencies can help overcome this issue. The calibration of such systems is under investigation [53], yet this approach increases complexity and costs.

There is a lack of investigation into the application and limitations of ADCP-based SSC in offshore tidal-dominated environments where mass concentrations in the water column are far less compared to fluvial environments, and non-cohesive medium to very coarse sands dominate the seabed. Nevertheless, the success of this method in fluvial and estuarine environments shows a high potential for its successful application offshore. If ADCP-based SSC_{solids} can be adequately quantified in this way in tidally-dominated shallow shelf sea environments, it could be established as a very cost-effective multi-purpose instrument for the simultaneous collection of metocean and sediment dynamic parameters for numerical model validation.

Consequently, in this paper we address the following two hypotheses:

1. SSC_{solids} can be adequately estimated from the echo intensity recorded by a 300kHz Acoustic Doppler Current Profiler (ADCP), in a shallow shelf sea environment.
2. The spatial timeseries of ADCP-based SSC_{solids} can be used as a validation technique for a 2D (suspended) sediment transport numerical model.

From these hypotheses, this study aims to:

1. Using equations developed by previous authors, estimate SSC_{solids} from the acoustic amplitudes recorded by a 300kHz ADCP deployed in a tidally-dominated shallow shelf setting characterised by complex hydrodynamics and non-cohesive seabed substrate (Figure 5-1).
2. Explore different model validation techniques to validate the suspended load transport and SSC aspect using a combination of direct sampling and ADCP-estimated SSC_{solids}.
3. Evaluate the applicability and advantages of the new validation techniques presented and provide best practice recommendations for future studies.

Section 5.2 outlines the methodology used in this study, including; ADCP deployment and water sample collection, background theory of the sonar principle and equations used in the estimation of SSC_{solids} from ADCP, numerical model development, and novel seabed substrate map development. Section 5.3 provides an overview of results including water sampling, ADCP-based SSC_{solids}, a comparison against ADCP-based SSC_{solids} and measured datasets, and the outcome of four tested model validation techniques using a combination of directly measured SSC_{solids} and ADCP-estimated SSC_{solids} timeseries. Section 5.4 and 5.5 provides a discussion and conclusion of project results respectively.

5.2 Methods

5.2.1 ADCP Deployment and water sample collection

In order to analyse suspended solids concentration (SSC_{solids}) in the south-western Irish Sea, 90 water samples were obtained across eight sampling stations, onboard the RV Celtic Voyager during three offshore survey campaigns (CV20010, CV20036 and CV21034) in

September/October 2020 and December 2021. These survey campaigns were carried out under the 'Mobility of Sediment Waves and Sand Banks in the Irish Sea (MOVE)' project. A Teledyne Workhorse Sentinel 300kHz Acoustic Doppler Current Profiler (ADCP) was also deployed inside a Trawl Resistant bottom mount frame during this project from 27th September to 14th October 2020 at 52.722°, -6.028° (Figure 5-1). Half of these water sampling stations (stations 1 to 4) (Figure 5-1) provide in situ measurements for the estimation of an SSC_{solids} timeseries derived from echo intensity recorded by the ADCP. The use of water samples in this way determined their collection methodology in terms of location, timing and water depth of sample.

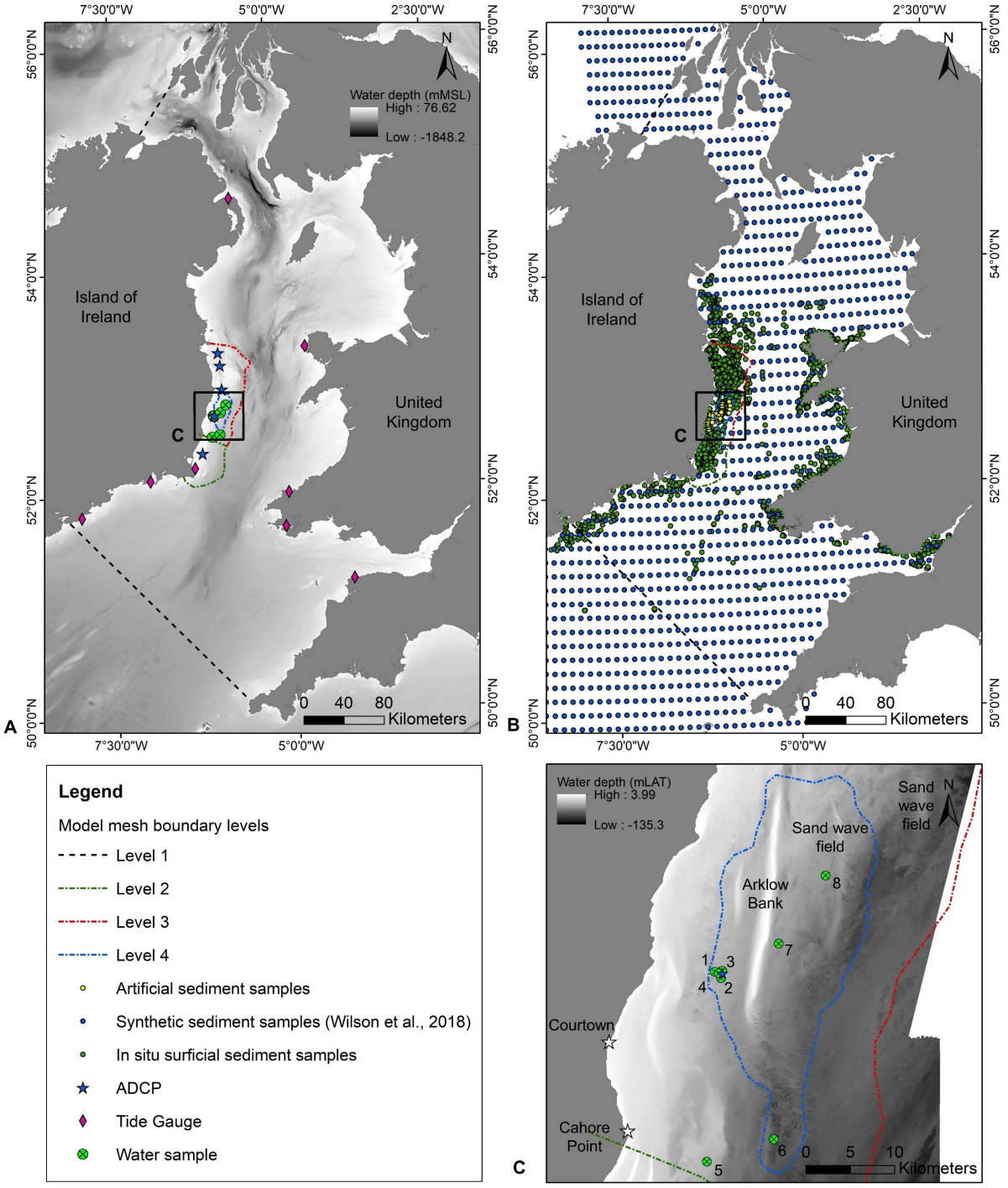


Figure 5-1 A. Site map displaying the area of interest (C), numerical model mesh boundary levels and numerical model validation and calibration points; B. Three sediment sample datasets used in the sediment transport model: i) manually added

artificial samples, ii) synthetic samples from Wilson et al [66]*, and iii) in situ surficial sediment samples; C. Study site displaying water sampling and ADCP stations. (Bathymetry source: A:* [67] *C:* [68]*)*

The timing of each sample was targeted at peak ebb and peak flood tide. This was to ensure the presence of a relatively high amount of suspended sediment in the water column during sampling times, corresponding to relatively high current speeds. To determine these tidal times pre-survey, a timeseries of currents and water levels was extracted for each of the eight water sampling stations from the North East Atlantic (NEATL) hydrodynamic model held by the Marine Institute. The NEATL is an implementation of the three-dimensional Regional Modelling System (ROMS) and can provide an estimate of tidal times across the Irish Sea. Harmonic analysis was carried out on these datasets from which a tidal prediction over the survey time-frame was executed. These were further analysed to derive desired estimated tidal times.

The four stations within 200 m to 800 m of the ADCP site were taken as close as possible to both the deployed ADCP and to the estimated peak flood/ebb tidal time. The setup of the ADCP deployment (e.g. avoidance of the surface marker buoy), drifting of the vessel due to strong tidal currents, vessel safety procedures, and limitations of the NEATL model predictions had to be taken into account at each sampling time and location. Water sampling was carried out using a rosette sampler containing 12 five litre Niskin bottles. Each water sample was taken at a different water depth corresponding to each ADCP bin. The dimensions of the ADCP setup is presented in Figure 5-2. As shown, the first water sample was taken approximately 3.81 m above the seabed and at 1 m intervals from here. From each five-litre bottle, a two-litre sample was retained and tested for Total Suspended Solids (TSS). The same methodology was carried out for stations 5 to 8.

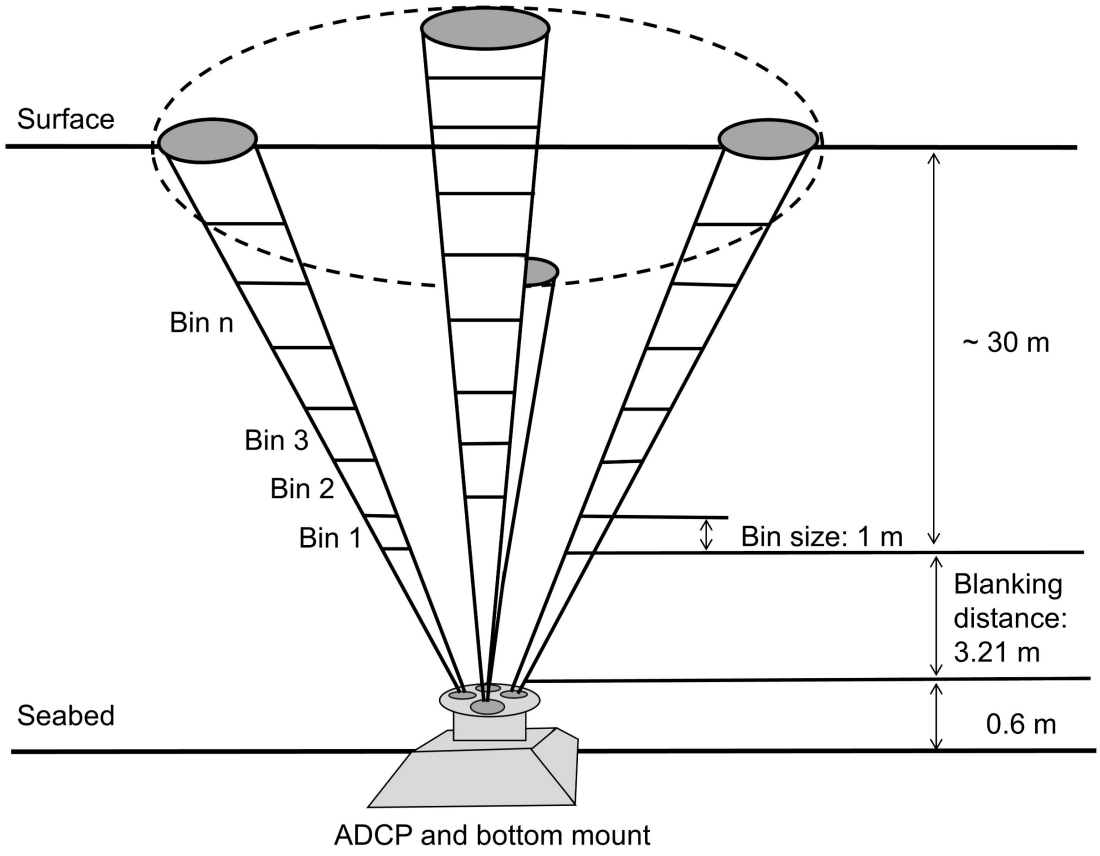


Figure 5-2 Schematic diagram of set-up of the upward-looking Teledyne RDI Workhorse Sentinel 300kHz Acoustic Doppler Current Profiler (ADCP) at the study site

5.2.2 ADCP derived SSC

The method of estimating suspended solids concentration from echo intensity recorded by an ADCP employs a formula based on the sonar equation for sound scattering of small particles [51], [57], [69].

$$SSC_{solids} = 10^{A+B\times RB} \quad (1)$$

where A and B is the intercept and slope respectively determined by the regression of ADCP relative acoustic backscatter (RB) with known measured SSC_{solids} on a semi-log plane in the form of [51], [57], [69]

$$\log\left(SSC_{solids}\right) = A + B \times RB \quad (2)$$

Therefore, in order to derive an estimated timeseries for SSC_{solids} throughout the water column at one location, the echo intensity (E) (counts) recorded along one beam (in this case, beam 4) of the deployed ADCP was processed and converted to relative backscatter (RB) (decibels) through the following equation [51], [65];

$$RB = RL + 2TL \quad (3)$$

where RL is the reverberation level and $2TL$ accounts for two-way travel transmission losses. Based on the sonar equation [70], the reverberation level is given as

$$RL = SL - 2TL + TS \quad (4)$$

where SL is the source level, and TS is the target strength of suspended sediment. When measuring with an ADCP, the reverberation level can be given as [48];

$$RL = 10\log\left(10^{\frac{k_c(E-E_r)}{10}} - 1\right) \quad (5)$$

where E is the measured Returned Signal Strength Indicator (RSSI) amplitude recorded by the ADCP for each bin along each beam, in counts. E_r is the amplitude seen by the ADCP in the absence of any signal or the baseline amplitude. k_c is the RSSI slope which is a factor specific to each beam of each instrument used to convert E counts to decibels. In this case the k_c for beam 4 is 0.4048. This value was received from the manufacturer. The equation used for the correction of the two-way transmission loss ($2TL$) is given as [51];

$$2TL = 20log_{10}(\psi R) + 2R\alpha_s + 2R\alpha_w \quad (6)$$

Where the term $20log_{10}(\psi R)$ accounts for the loss due to spreading, and $2R(\alpha_s + \alpha_w)$ accounts for loss due to absorption whereby α_s is absorption coefficient for sediments and α_w is absorption coefficient due to water.

R is the slant range and varies with height from the sensor (N) and is calculated here as [47]

$$R = \left[\frac{B + \frac{L+D}{2} + \left((N-1) \times D\right) + (\frac{D}{4})}{\cos\theta}\right] \times \frac{c'}{c_1} \quad (7)$$

whereby N is the depth cell number of the scattering layer being measured, B is the blank after transmit (m), L is the transmit pulse length (m), D is the depth cell length (m), θ is the beam angle, $c_1$is the speed of sound in the water used by the ADCP, and c' is the average sound speed from the transducer to the range cell that depends on the depth and is computed by means of the equation by Mackenzie [71] and is calculated for each bin at each timestep;

$$\begin{aligned} c' = {} & 1448.96 + 4.591T - 5.304 \times 10^{-2}T^2 + 2.374 \times 10^{-4}T^3 \\ & + 1.340(S-35) + 1.630 \times 10^{-2}D + 1.675 \times 10^{-7}D^2 \\ & - 1.025 \times 10^{-2}T(S-35) - 7.139 \times 10^{-13}TD^3 \end{aligned} \quad (8)$$

where T is temperature in degrees Celsius, S is salinity in parts per thousand and D is depth in metres.

Additionally, the spreading loss is different in the near and far fields. For this, the R critical (R_{cr}) was calculated as [65]

$$R_{cr} = \frac{\pi R_0}{4} \quad (9)$$

where R_0 represents Rayleigh Distance (m) which depends on the frequency used. The Rayleigh Distance for RDI Workhorse Sentinel 300 kHz is 0.87 m, which is taken from Mullison [48]. This value does not vary but is fixed for each bin and each timestep.

From this, the near field correction for spreading loss (ψ) is calculated by [72]

$$\psi = \frac{[1 + 1.35Z + (2.5Z)^{3.2}]}{[1.35Z + (2.5Z)^{3.2}]} \tag{10}$$

where $Z = R/R_{cr}$, therefore ψ varies for each bin and timestep. Next, the transmission loss due to the absorption of seawater $2\alpha_w$, depends on a variety of environmental conditions and the frequency of the ADCP [48]. This is calculated as [73]

$$\alpha_w = 0.106\frac{f_1 f^2}{f_1^2 + f^2}e^{(pH-8)/0.56} + 0.52\left(1 + \frac{T}{43}\right)\left(\frac{S}{35}\right)\frac{f_2 f^2}{f_2^2 + f^2}e^{-\frac{D}{6}} + 0.00049 f^2 e^{-(\frac{T}{27}+\frac{D}{17})} \tag{11}$$

$$f_1 = 0.78(\frac{S}{35})^{1/2}e^{T/26} \tag{12}$$

$$f_2 = 42e^{T/17} \tag{13}$$

whereby pH is the typical pH value of seawater, T is temperature in degrees Celsius measured by ADCP, S is salinity (psu) measured by the ADCP, D is the maximum depth (km), f_1 is boric acid, f_2 is magnesium sulphate and f is the frequency of the ADCP (kHz). The resulting α_w correlate very well with absorption coefficient given in Mullison [48], 0.068 dB/m, which was calculated for a 300 kHz ADCP in a 4 °C water temperature and 35 ppm salinity. This study uses a water temperature of 14.7 °C, salinity of 35 ppm and a 300kHz ADCP giving an α_w value

of 0.087 dB/m. In order to calculate α_s we use Urick's [74] equation which gives a coefficient for the attenuation of acoustic energy by sediment (expressed in dB/cm);

$$\alpha_s = SSC_v \left[k(\gamma - 1)^2 \left\{ \frac{s}{s^2 + (\gamma + \tau)^2} \right\} + \frac{1}{6}(k^4 a_s^3) \right] 4.34 \qquad (14)$$

Where SSC_v is the dimensionless volumetric sediment concentration (SSC divided by sediment density), k is the wave number, $2\pi/\lambda$, λ is the wavelength in cm, γ is the specific gravity of the sediment, $a_s$is the mean sediment radius in cm, s is equal to $[9/(4\beta a_s][1 + 1/(\beta a_s]$, τ is equal to $[0.5 + 9/(4\beta a_s)]$, in which β is equal to $[\omega/2v]^{0.5}$, ω is $2\pi f$, f is frequency in hertz (Hz), v is the kinematic viscosity of the water, in stokes [51]. The calculated α_s concentration for 1 mg/L is 0.000482 dB/m. This shows a very good agreement with the α_s value determined in the study by Baranya and Józsa [55]

Once the RB is calculated, values are input back into equations (2) and (1) in order to derive an estimated spatial timeseries of SSC_{solids}.

5.2.3 Numerical modelling

A dynamically coupled two-dimensional (2D) hydrodynamic and sediment transport model was developed using DHI's MIKE 21 suite of tools [75]–[77] in order to investigate the complex feedback sediment transport system between offshore sand banks and offshore independent sediment wave fields identified in previous studies [78]. An integral part of this model development is the need to understand the relationship between bed load and suspended load sediment transport in this dynamic system. Subsequently, this study focusses on developing validation techniques for the suspended sediment transport variables of this model. The techniques developed will feed directly into future local and regional work, but also be applicable to a broad-spectrum of model applications in other geographical regions.

Section 5.2.3.1 and 5.2.3.2 describes the coupled hydrodynamic and sediment transport modelling approach used.

5.2.3.1 HD modelling

Two attempts at developing a high resolution, medium-scale, 2D hydrodynamic model of the south-western Irish Sea was carried out using the DHI's MIKE 21 suite of tools [75], [77] in an effort to produce a computationally efficient model for the area of interest. Both the model domain and unstructured, flexible mesh were kept consistent for both models, whereby the south and north boundaries extended eastwards from the east coast of Ireland at Courtown (52.530835°, -6.215659° to 52.479936°, -5.81943°) and Wicklow Head (53.096108°, -6.036121° to 53.084429°, -5.640141°) respectively. The water level boundary conditions were driven by (i) the DHI Global Tide Model [79], and (ii) the MIKE 21 FM hydrodynamic model developed by Coughlan et al [27]. After multiple calibration iterations and output examination, it was decided that these local models failed to capture the full complexity of hydrodynamics in this region, previously identified in Creane et al [31] and Creane et al [78]. As a result, the hydrodynamic model covering the entire Irish Sea developed in Coughlan et al [27] was used in this study.

This 2D model was updated with additional geophysical datasets; a new refined mesh was implemented, and a new validation point was utilised. An outline of the original hydrodynamic model is presented in Coughlan et al [27] whilst new updates and modifications to the model setup includes:

1. An addition of 16 bathymetric datasets to increase the accuracy and resolution of the seabed topography in the south-western Irish Sea.

- 15 of these datasets were collected via the INFOMAR (Integrated Mapping for the Sustainabe Development of Ireland's Marine Resource) programme between 2011 and 2017 onboard a range of survey vessels. These datasets were provided at spatial resolution between 2 m and 5 m and vertical referenced to Lowest Astronomical Tide (LAT). These datasets were converted to XYZ format which were then converted to OD Malin. All 15 surveys ultimately replaced the coarse resolution EMODnet (European Marine Observation and Data Network) datasets (referenced to Mean Sea Level (MSL)) along the south-east coast of Ireland in the original model setup.
- The final bathymetric dataset was collected in September/October 2020 onboard the RV Celtic Voyager under the project 'Mobility of Sediment Waves and Sand Banks in the Irish Sea', and encompasses approximately 7.2 km² of the ADCP deployment site (Figure 5-1). This was to ensure maximum potential model validation using the ADCP at this location.

2. A higher 5 m resolution INFOMAR bathymetry dataset, vertically referenced to OD Malin was produced for Arklow Bank, an area of targeted investigation in terms of sand bank morphodynamics. This dataset replaced the coarser 30 m resolution dataset from the same source.
3. This model is designed to couple with a MIKE 21 spectral wave model [80], [81] in ongoing studies therefore it was necessary to remove the unrealistic high current values at the boundaries evident in the original model in order to feasibly generate sediment transport tables using the quasi-three dimensional method (Q3D) [76], [82] As a result, the boundary shapes/locations were modified slightly and a varying bed resistance map was generated. In this model, the simulated drag coefficient is

calculated by resolving the Manning number (M) for bed friction [83]. The updated model retains a constant M for bed friction of $32\ m^{\frac{1}{3}}$ over majority of the model domain, but M is decreased up to $10\ m^{\frac{1}{3}}$ along the bounaries.

4. An unstructured triangular flexible mesh is refined for the study site. The four levels of resolution (Figure 5-1) are defined as:
    - Level 4: 150 m to 200 m around the Arklow Bank system (approximately 7.2 km²);
    - Level 3: 500 m to 600 m buffer zone, extending from the approximate -70 m water depth contour to the coastline from Howth Head (53.37861°, -6.057222°) to Courtown (52.645°, -6.228333°), and covering any sand banks outside these areas off the south-east coast of Ireland;
    - Level 2: 800 m to 1000 m extending along the -70 m contour to the coast from Courtown to Carnsore Point (52.17056°, -6.355278°);
    - Level 1: 2500 m to 3000 m resolution for the rest of the model domain.
5. The ADCP dataset described in section 5.2.1 is used as an additional validation point.

Due to the above updates in the original model, the calibration of the model were checked at various locations and new validation statistics were generated. These validation results are presented in section 5.2.3.1.1.

5.2.3.1.1 Model Validation

The hydrodynamic model was validated using coastal tide gauge data for surface elevation and acoustic doppler current profiler data for surface elevation, and current speed and direction. Assessed tide gauge data was sourced from the Marine Institute and the British Oceanographic Data Centre (BODC). These datasets underwent harmonic analysis and tidal

prediction in order to filter out tidal residuals such as storm surge and enable a direct comparison to the modelled data points. Four pre-existing ADCP datasets were used [27] with one new additional ADCP dataset labelled 'Arklow', the details of which are outlined in section 5.2.1 and Table 5-2. Due to the south-western Irish Sea being the area of interest, some of these ADCPs were also used to validate the water levels in this area of the Irish Sea.

A number of statistics were generated to assess the fit between measured and simulated datasets. Where the correlation coefficient is a measure of linear correlation between measured and simulated variables, bias represents the mean difference between both datasets. The root-mean-square-error (RMSE) is the standard deviation of residuals and the scatter index presents the percentage of RMS difference with respect to mean observation. Results are presented in Table 5-1, Table 5-2, Figure 5-3 and Figure 5-4.

Water levels were re-assessed at eight tide gauges and four ADCPs along the Irish Sea coast and offshore the south-east coast of Ireland respectively, over the time periods outlined in Table 5-1. A strong positive relationship is evident between all measured and simulated water levels (Table 5-1) where the average correlation coefficient across all locations is 0.99.

Similarly, simulated current speeds and directions were re-assessed against measured data at four locations, including the newly collected Arklow ADCP site. Generally, a strong positive correlation is evident with correlation coefficients ranging from 0.84 to 0.95 (Table 5-2). The notable 30° shift in the major axis of the tidal ellipse on Lucifer Bank shown Coughlan et al [27] is still evident in this re-analysis. This may be due to the merging of at least two different bathymetry datasets in this location, none of which was captured at the time of the ADCP deployment. Changes in seabed morphology over time have the potential to subsequently alter local hydrodynamics.

Table 5-1 Comparison between the simulated and observed water level data from tide gauge and ADCP locations

Location	Comparison time frame	Instrument (Tide Gauge (TG) or ADCP)	Bias (m)	RMSE (m)	R
Wicklow (ADCP) (52.95601°, −5.90135°)	September 30, 2009 (00:00) – October 26, 2009 (11:00)	ADCP	0.02	0.16	0.97
Lucifer Bank (52.3867°, −6.2183°)	June 27, 2005 (20:00) – July 08, 2005 (11:10)	ADCP	-0.01	0.13	0.97
Kish Bank 1 (53.28422°, −5.9361°)	August 23, 2012 (12:50) – September 19, 2012 (11:20)	ADCP	-0.02	0.22	0.98
Kish Bank 2 (53.16978°, −5.912767°)	August 23, 2012 (15:00) – September 18, 2012 (05:10)	ADCP	0.01	0.24	0.98
Ballycotton (51.8278°, −8.0007°)	May 01, 2021 (00:00) – May 31, 2021 (23:00)	TG	-0.196	0.22	0.99
Bangor (54.665°, −5.669167°)	May 01, 2021 (00:00) – May 31, 2021 (23:00)	TG	0.00	0.12	0.99
Dunmore (52.1477°, −6.9919°)	May 01, 2021 (00:00) – May 31, 2021 (23:00)	TG	-0.217	0.25	0.99
Fishguard (52.01272°, −4.982778°)	May 01, 2021 (00:00) – May 31, 2021 (23:00)	TG	0.00	0.17	0.99
Ilfracombe (51.211139°, −4.112389°)	May 01, 2021 (00:00) – May 31, 2021 (23:00)	TG	0.18	0.26	1.00
Milford Haven (51.70686°, −5.050639°)	May 01, 2021 (00:00) – May 31, 2021 (23:00)	TG	0.20	0.24	1.00
Rosslare (52.254600°, −6.334861°)	May 01, 2021 (00:00) – May 31, 2021 (23:00)	TG	-0.02	0.16	0.98
Holyhead (53.30889°, −4.630556°)	May 01, 2021 (00:00) – May 31, 2021 (23:00)	TG	0.0001	0.22	0.99

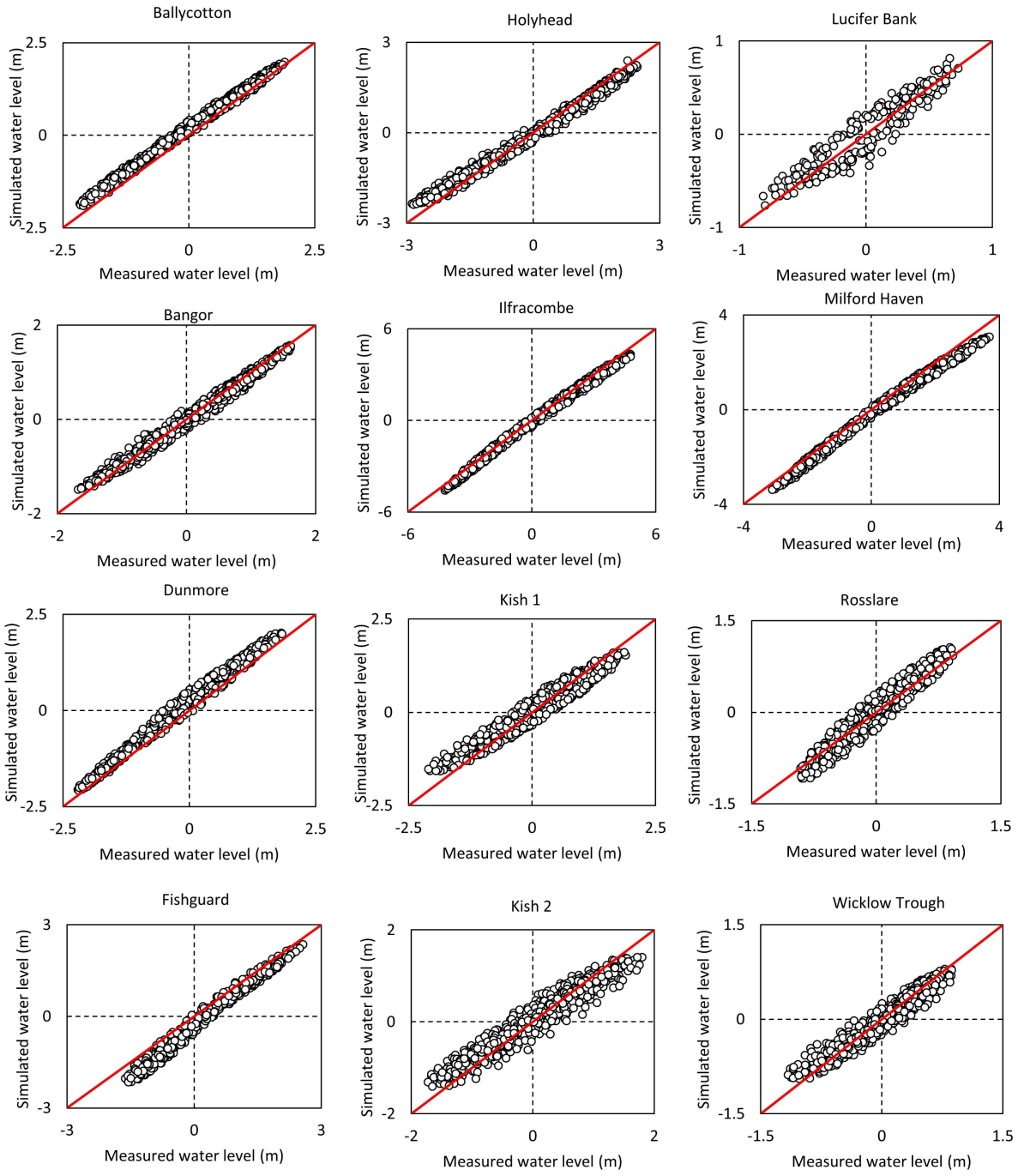


Figure 5-3 Comparison between measured and simulated water levels. See Table 5-1 for location.

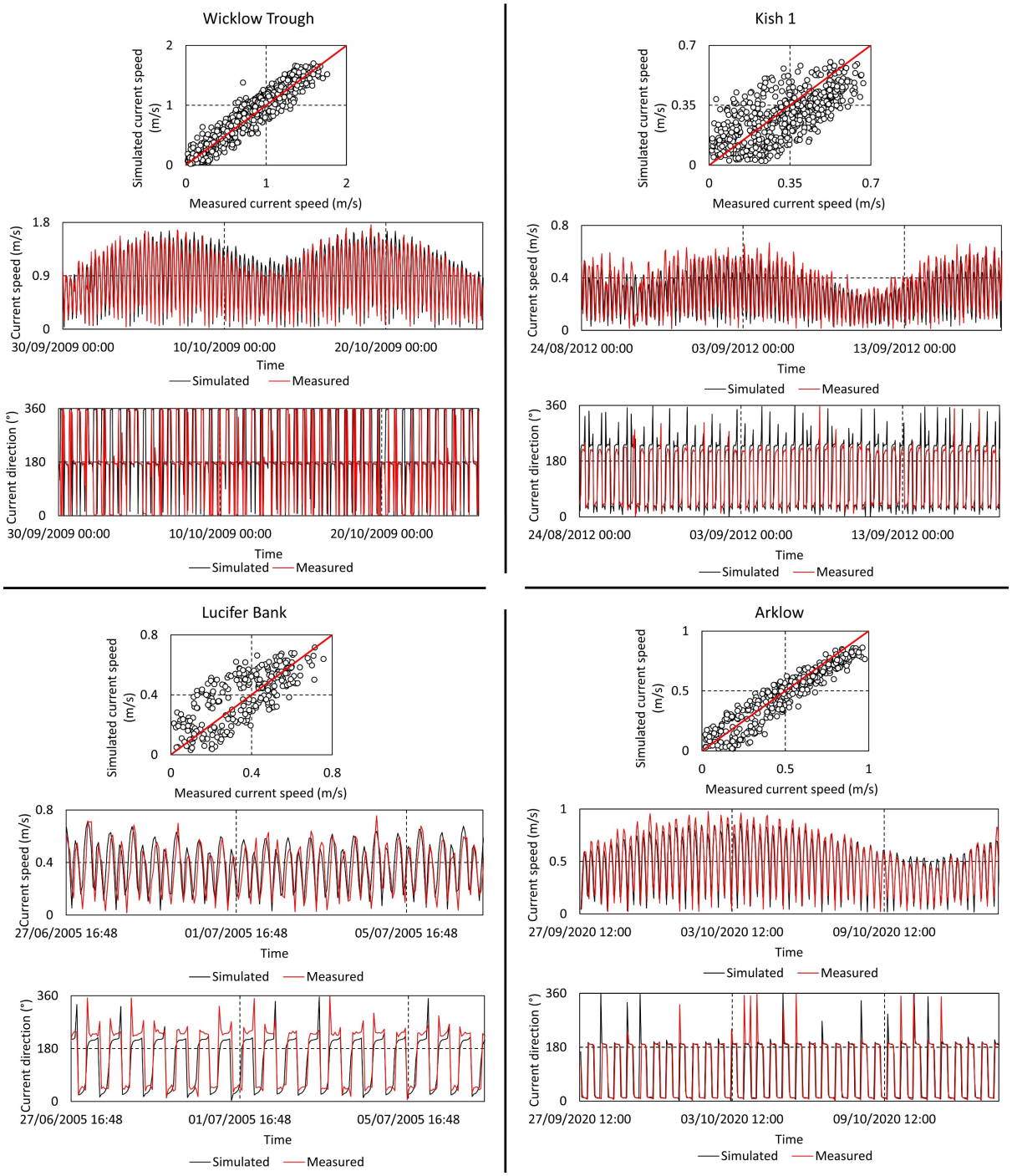


Figure 5-4 Calibration profiles of current speed and direction at each of the four ADCP locations (Table 5-2)

Table 5-2 Comparison between the simulated and observed current data from ADCP locations.

Location	Data collection period	Bias (m/s)	RMSE (m/s)	R	SI (%)
Arklow (52.72153°, -6.0278°)	September 27, 2020 (14:20) - October 10, 2020 (09:10)	0.02	0.10	0.95	19.57
Kish Bank 1 (53.28422°, −5.9361°)	August 23, 2012 (12:50) - September 19, 2012 (11:20)	0.04	0.11	0.84	37.33
Wicklow Trough (52.95601°, −5.90135°)	September 30, 2009 (00:00) – October 26, 2009 (11:00)	-0.05	0.19	0.95	22.62
Lucifer Bank (52.3867°, −6.2183°)	June 27, 2005 (20:00) – July 08, 2005 (11:10)	-0.03	0.13	0.85	35.89

5.2.3.2 ST modelling set-up

The MIKE 21 sand transport module [76], [82] was used to calculate the sediment transport rates of non-cohesive sediment under 'pure current' whereby the effects due to wind and wave forcing are not included. The mesh used in the simulation of the sand transport rates is the same as that is used to calculate the flow field in the hydrodynamic model (section 5.2.3.1). A coupled morphological model was generated, whereby the governing equations for flow and sediment transport are merged into a set of equations, which are solved simultaneously. Coupling the hydrodynamic and sand transport modules in this way allowed morphological development to be captured by updating the bathymetry for every time step with the net sedimentation:

$$Z^{n+1} = Z^n + \Delta z^n \tag{15}$$

Where Z^n is the bathymetry level at present time step, Z^{n+1} is the bathymetry level at the next time step, Z^{n+1} is net sedimentation at present time step, and n is time step. Further details are presented in the MIKE 21 sand transport manual [82]. The key parameter for determination of bed level changes is the rate of bed level change, $\frac{\partial z}{\partial t}$, at the element cell centres. This parameter is based on the Exner equation, or sediment continuity equation, written as:

$$-(1-n)\frac{\partial z}{\partial t} = \frac{\partial S_x}{\partial x} + \frac{\partial S_y}{\partial y} - \Delta S \tag{16}$$

Where n is bed porosity, z is bed level, t is time, S_x is bed load or total load transport in the x direction, S_y is bed load or total load transport in the y direction, x and y are horizontal cartesian coordinates, and ΔS is sediment sink or source rate. For a non-equilibrium model such as this, the sediment sink/source term can be written as

$$\Delta S = \varphi_0(\eta_0) w_s (c - c_e) \tag{17}$$

Where η_0 is normalised no slip level above the bed, φ_0 is unit profile function for the sediment concentration, w_s is settling velocity for the suspended sediment, c is depth-averaged sediment concentration, and c_e is depth-averaged equilibrium concentration. The bed is updated continuously through a morphological simulation (at every HD-time step, in this case 30 second intervals) based on the estimated bed level change rates. The initial bed thickness of the erodible bed was designated as constant and unlimited throughout the model domain. Slope failure is not included in this morphological model.

The pure current sediment transport theory used in this model was the Engelund and Hansen [84] total-load transport theory. The model by Engelund and Hansen [84] is a total load model that needs user-specified information in order to divide the total load S_{tl} sediment transport

into bed load S_{bl} and suspended load S_{sl} transport rates (m²/s) [82]. Transport rates are obtained from the relations:

$$S_{bl} = k_b S_{tl} \tag{18}$$

$$S_{sl} = k_s S_{tl} \tag{19}$$

Whereby k_b and k_s are user defined bed load calibration factor and suspended load calibration factor respectively. In this case, both parameters are kept as the default value of 1. Total sediment transport is obtained by:

$$S_{tl} = 0.05 \frac{C^2}{g} \theta^{\frac{5}{2}} \sqrt{(s-1) g D_{50}^3} \tag{20}$$

Where the Shields parameter θ is defined as

$$\theta = \frac{\tau}{\rho g (s-1) D_{50}} \tag{21}$$

Where τ is the flow shear stress, ρ is density of water, g is the acceleration due to gravity, s is ρ/ρ_s relative density of sediment and ρ_s is density of sediment. C is the Chezy number and D_{50} is the median grain size. Flow shear stress is divided into form drag τ'' and skin friction τ'. The total shear stress $\tau' + \tau''$ is estimated from the local flow velocity u and the local Chezy number C:

$$\tau = \rho g \frac{V^2}{C^2} \tag{22}$$

For skin friction the following approximate friction formula is applied

$$\theta' = 0.06 + 0.4\theta^2 \tag{23}$$

Sediment density and porosity were defined as constant 2.65 and 0.40 respectively.

The equilibrium mass concentration (c_e) (g/m³) is calculated as the suspended load divided by the water flux and converted from volumetric concentration to mass concentration [82]:

$$c_e = \frac{S_{sl}}{Vh} s 10^6 \tag{24}$$

Where V is velocity (m/s) and h is water depth.

The following correction is applied to account for the slope effect on the sediment transport rate:

$$S_s = \left(1 - \alpha \frac{\partial z_b}{\partial s}\right) S_{bl} \tag{25}$$

Where z_b is bed level, s is stream-wise (horizontal) coordinate, α is model calibration parameter, S_s is bed load along streamline, s, and S_{bl} is bed load as calculated from sediment transport formula [82].

A varying grain diameter (D_{50}) map was defined for the model domain comprising both surficial and synthetic sediment samples. Surficial sediment samples were collected using either a Day Grab sampler or the Shipek sampler during four MOVE offshore survey campaigns in September 2020 (CV20010), September/October 2020 (CV2036), March 2021 (CV21035) and December 2021 (CV21034). All sediment samples were processed by sieving or laser granulometry. Furthermore, sediment samples containing raw granulometric data was compiled from Geological Survey of Ireland (GSI). The MOVE and GSI datasets were combined, and statistical analysis to derive D_{50} values was carried out using the R package 'geotech' [85].

Due to limited grain size availability outside our area of interest, the synthetic sand D_{50} dataset produced by Wilson et al [66] was utilised. This dataset was clipped to represent the model domain beyond the -70 m contour line extending geographically from Carnsore Point

(52.17056°, -6.355278°) to Skerries (53.58389°, -6.101111°). This was to ensure mostly in situ measured grab samples would represent the south-western Irish Sea.

A number of artificial D_{50} values were also placed in the target area using combined analysis of bathymetry, backscatter, surrounding D_{50} values and the EMODnet seabed substrate map. These artificial samples were placed in areas where a significant deficit of measured samples was evident in order to produce the most realistic interpolated dataset when comparing against coarse seabed substrate maps such as the EMODnet seabed substrate map [86].

5.2.4 Generation of seabed substrate map representing the ADCP deployment time frame

High quality seabed substrate maps of the Irish Sea have been produced by many organisations such as the Integrated Mapping for Sustainable Development of Ireland's Marine Resource (INFOMAR) programme [68], the British Geological Survey (BGS) [87], and the European Marine Observation and Data Network (EMODnet) [86]. These seabed classification maps provide a fantastic first indication of surficial sediment type across the continental shelf sea at a coarse resolution. However, the BGS dataset for example Westhead et al [88] is mainly based on in situ sediment samples that only represent the seabed at one point in time and do not resolve local areas at a fine resolution. Therefore, due to the high mobility of sediment in this area of the Irish Sea [27], [31], [78] and the lack of existing fine-scale seabed substrate maps, the production of a seabed substrate map on a fine scale over the time period of the ADCP deployment time-frame is imperative to understand the potential particle distribution of sediment in the water column.

During offshore survey CV20010, a multibeam echo sounder (MBES) dataset and two sediment samples, using a day grab sampler, were collected at the site. These datasets were collected on 26/09/2020 and 27/09/2020 respectively. The raw MBES files (.all) were

processed for bathymetry and backscatter through Qimera v2.3.1 and FMGT v7.9.5 respectively whereby the latter is a measure of the strength of the return signal and provides information on the 'hardness' of the seabed. This dataset was subsequently classified into 2 classes using the Iso Cluster Unsupervised Classification Tool in ArcGIS v10.8 using a similar method to Evans et al [89].

Simultaneously, the sediment samples underwent particle size analysis using the sieve analysis technique. The resulting raw granulometric dataset was processed through the 'geotech' R package to derive relevant statistics, such as median grain size (D_{50}) and the grading coefficient. These sediment samples were used to ground-truth and further classify the backscatter, ultimately producing a new spatial map of seabed substrate at the site. The processing workflow and end results are provided in Figure 5-5.

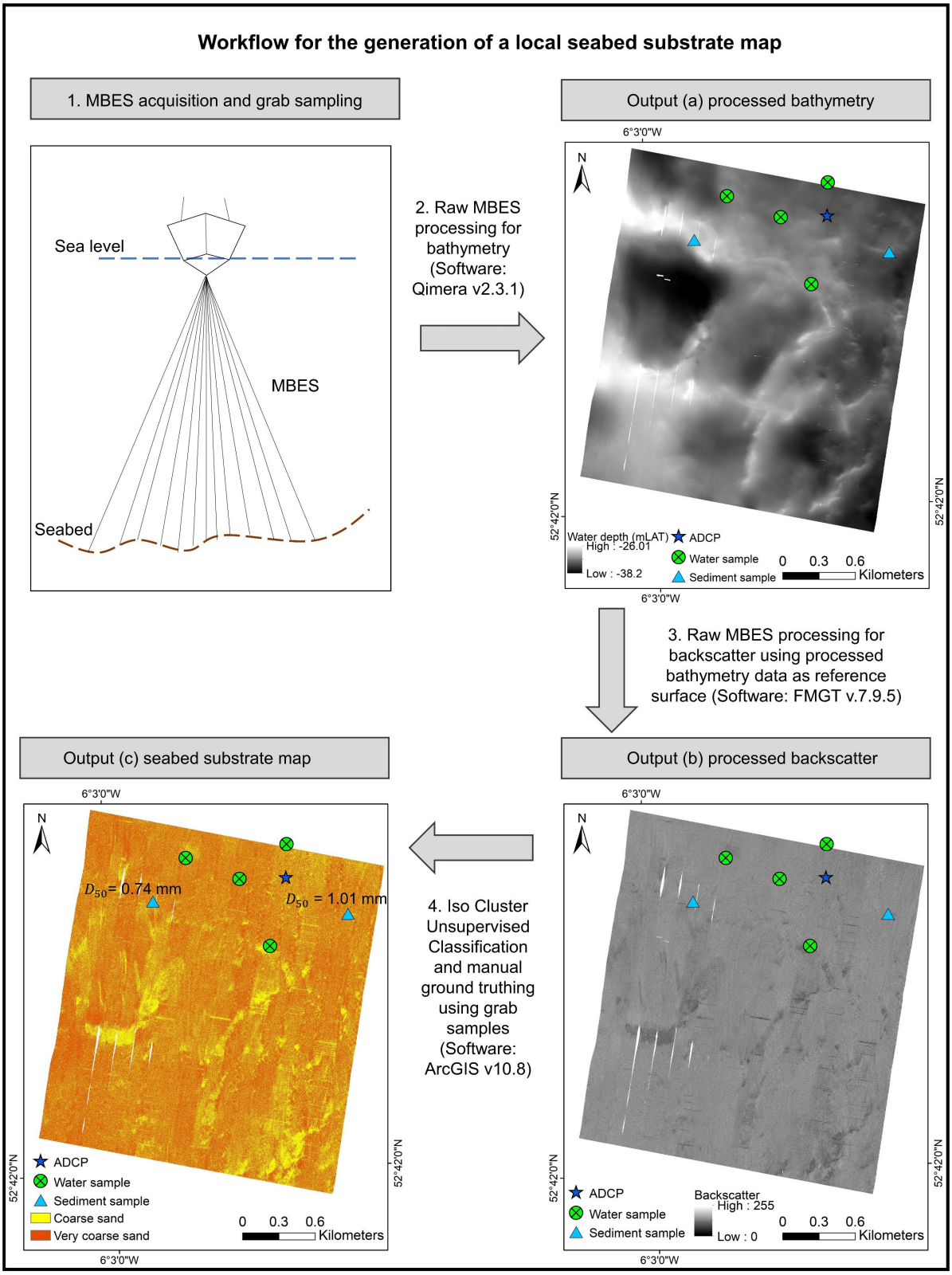


Figure 5-5 Workflow diagram of multi-beam echo sounder (MBES) processing and derivation of seabed substrate map over ADCP deployment time period

5.3 Results

5.3.1 Water sample based SSC_{solids}

All water samples were tested in the laboratory for total suspended solids (TSS), the results of which are summarised in Table 5-3. The range of SSC_{solids} across stations 1 to 4 (Figure 5-1) is 3.10 mg/L to 13.50 mg/L. These samples were taken between 4 m and 15 m above the seabed at 1 m intervals and between a 270 m and 840 m radius of the deployed ADCP. They represent approximate slack, peak ebb and peak flood tidal times. The depth-averaged SSC_{solids} across this 11 m section of the water column, across all four time-periods, are consistent, displaying values between 7.26 mg/L and 8.10 mg/L (Figure 5-6).

Stations 5 to 8 (Figure 5-1) are standalone and disassociated from an ADCP deployment. Samples at station 5 and 6 are taken within a one-hour timeframe. Due to the distance of 8 km between stations and the rotary nature of tidal movements in the south Irish Sea around the degenerate amphidromic point located approximately at Courtown [31], both timestamps represent approximately peak ebb for each location. These samples are taken approximately between 4 m and 15 m above the seabed. The depth-averaged SSC_{solids} across this 11 m section of the water column is 3.6 mg/L for both stations, whereas the range varies slightly from 3.1 to 4.2 mg/L and 2.9 to 4.0 mg/L for stations 5 and 6 respectively (Figure 5-6).

Stations 7 and 8 are also taken within a one-hour time-frame and at a separation distance of 9.5 km. They represent approximate peak ebb tide. Similar to stations 1 to 6, samples at stations 7 and 8 are taken between 4 m and 15 m above the seabed. Station 7 displays a higher SSC_{solids} values compared to station 8. Where station 7 SSC_{solids} ranges from 6.4 mg/L to 13.0 mg/L with a depth-averaged value of 9.3 mg/L, station 8 SSC_{solids} ranges from 5.6 mg/L to 7.2 mg/L (Figure 5-6) with a depth-averaged concentration of 6.3 mg/L.

Table 5-3 Details of water sampling stations including water depth of samples and resulting SSC_{solids}

Survey Code	Site	Station ID	Date time (UTC) of sample	Location	Water depth at station (m)	Water depth of samples (m)	Sampling interval (m)	Number of successful samples	Range of processed SSC (mg/l)	Mean across all samples (mg/l)	Approx. tide time
CV20010	ADCP	1	27/09/2020 13:32	-6.040°, 52.7223°	-34	-29 to -18	1	12	6 to 9.5	7.74	Slack tide
CV20036	ADCP	2	10/10/2020 07:03	-6.030°, 52.716°	-34	-30 to -19	1	12	5 to 11.8	7.28	Peak ebb
CV20036	ADCP	3	10/10/2020 13:10	-6.028°, 52.724°	-36	-32 to -21	1	12	3.1 to 13.5	8.1	Peak flood
CV20036	ADCP	4	13/10/2020 10:30	-6.033°, 52.722°	-34	-30 to -19	1	12	5.7 to 10	7.26	Peak ebb
CV21034	D1 T	5	09/12/2021 17:00	-6.066°, 52.532°	-32	-28 to -17	1	10	3.1 to 4.2	3.6	Peak ebb
CV21034	D1	6	09/12/2021 17:57	-5.953°, 52.551°	-68	-64 to -53	1	10	2.9 to 4.0	3.6	Peak ebb
CV21034	8 T	7	10/12/2021 18:04	-5.931°, 52.749°	-42	-38 to -27	1	12	6.4 to 13.0	9.3	Peak ebb
CV21034	8	8	10/12/2021 18:50	-5.848°, 52.816°	-57	-53 to -42	1	10	5.6 to 7.2	6.3	Peak ebb

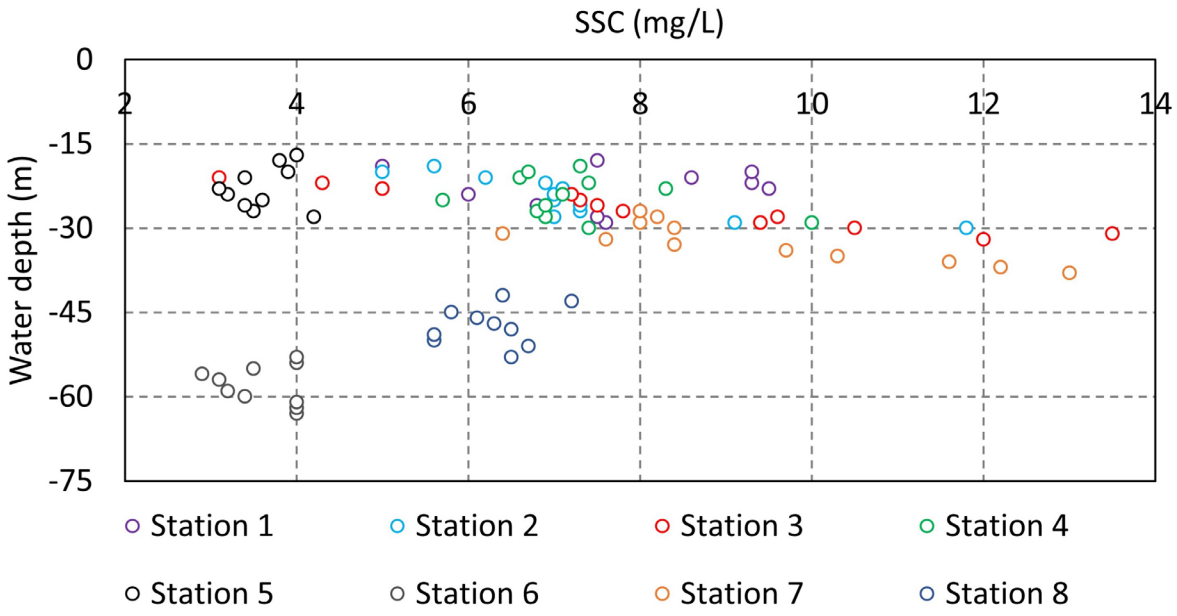


Figure 5-6 Scatter plot of all water sample-based SSC_{solids} samples at stations 1 to 8

5.3.2 ADCP based SSC_{solids}

A quality check of the processed relative acoustic backscatter identified noise and inconsistencies in bin 1 and bins 27 to 30. As a result, these 5 bins were removed, leaving the processed relative acoustic backscatter recorded in bins 2 to 26, corresponding to 5 m to 29 m above the seabed, as input into the estimation of SSC_{solids}. Subsequently, approximately 71 % of the water column is captured by the processed ADCP relative acoustic backscatter.

Accuracy and precision were considerable factors for the quantification of SSC_{solids} from the processed relative acoustic backscatter. The directly measured SSC_{solids} samples, outlined in Table 5-4, were used in linear regression analysis against ADCP acoustic backscatter.

Table 5-4 Directly measured samples used in linear regression analysis to estimate SSC_{solids} from ADCP relative acoustic backscatter

Survey Code	Site	Station ID	Date time (UTC) of sample	Location	Number of samples used	Range of processed SSC (mg/l)	Mean across selected samples (mg/l)	Approx. tide time
CV20010	ADCP	1	27/09/2020 13:32	-6.040°, 52.7223°	4	7.5 to 9.5	8.73	Slack tide
CV20036	ADCP	2	10/10/2020 07:03	-6.030°, 52.716°	8	5 to 9.1	6.74	Peak ebb
CV20036	ADCP	3	10/10/2020 13:10	-6.028°, 52.724°	8	3.1 to 10.5	6.86	Peak flood
CV20036	ADCP	4	13/10/2020 10:30	-6.033°, 52.722°	4	5.7 to 10	7.43	Peak ebb

A strong positive correlation exists between ADCP relative acoustic backscatter and water sample-based SSC_{solids}, where the correlation coefficient (R) is 0.89 (Figure 5-7). The resulting linear regression equation gives a slope of 0.6992 and intercept of -38.848. These slope and intercept values were used in equation (1) to estimate the time series and spatial distribution of suspended sediment concentration which is presented in Figure 5-8. This equation is specific to this dataset and not applicable to other studies.

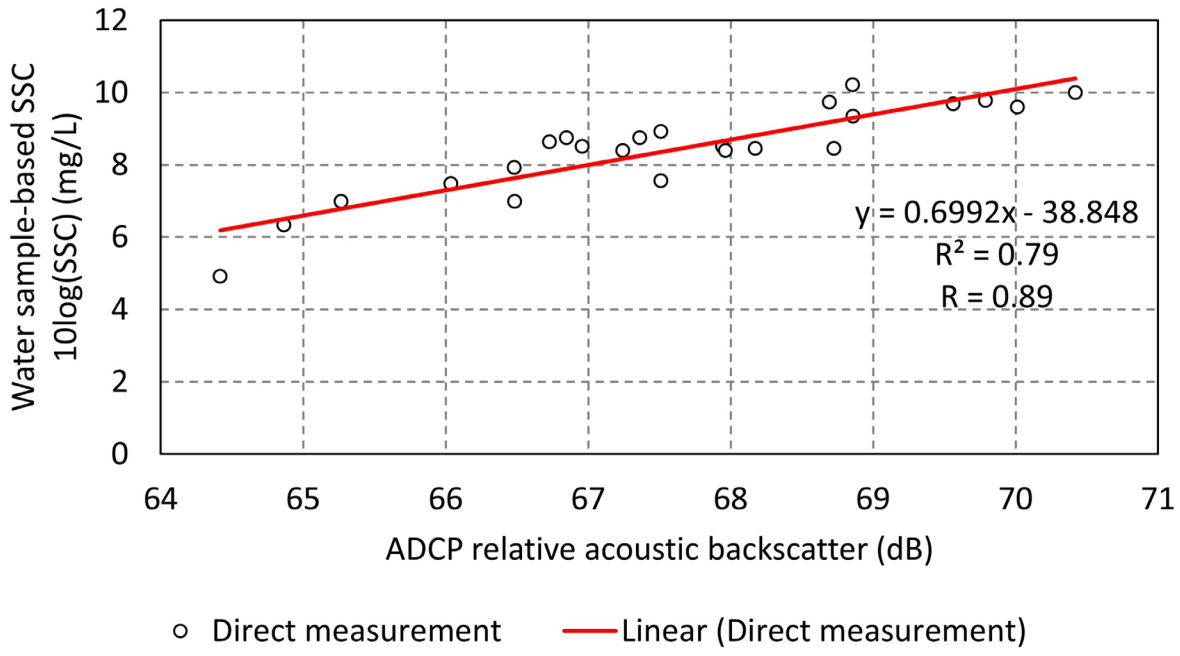


Figure 5-7 Calibration of ADCP relative acoustic backscatter data (Beam 4) using the laboratory-analysed SSC_{solids}.

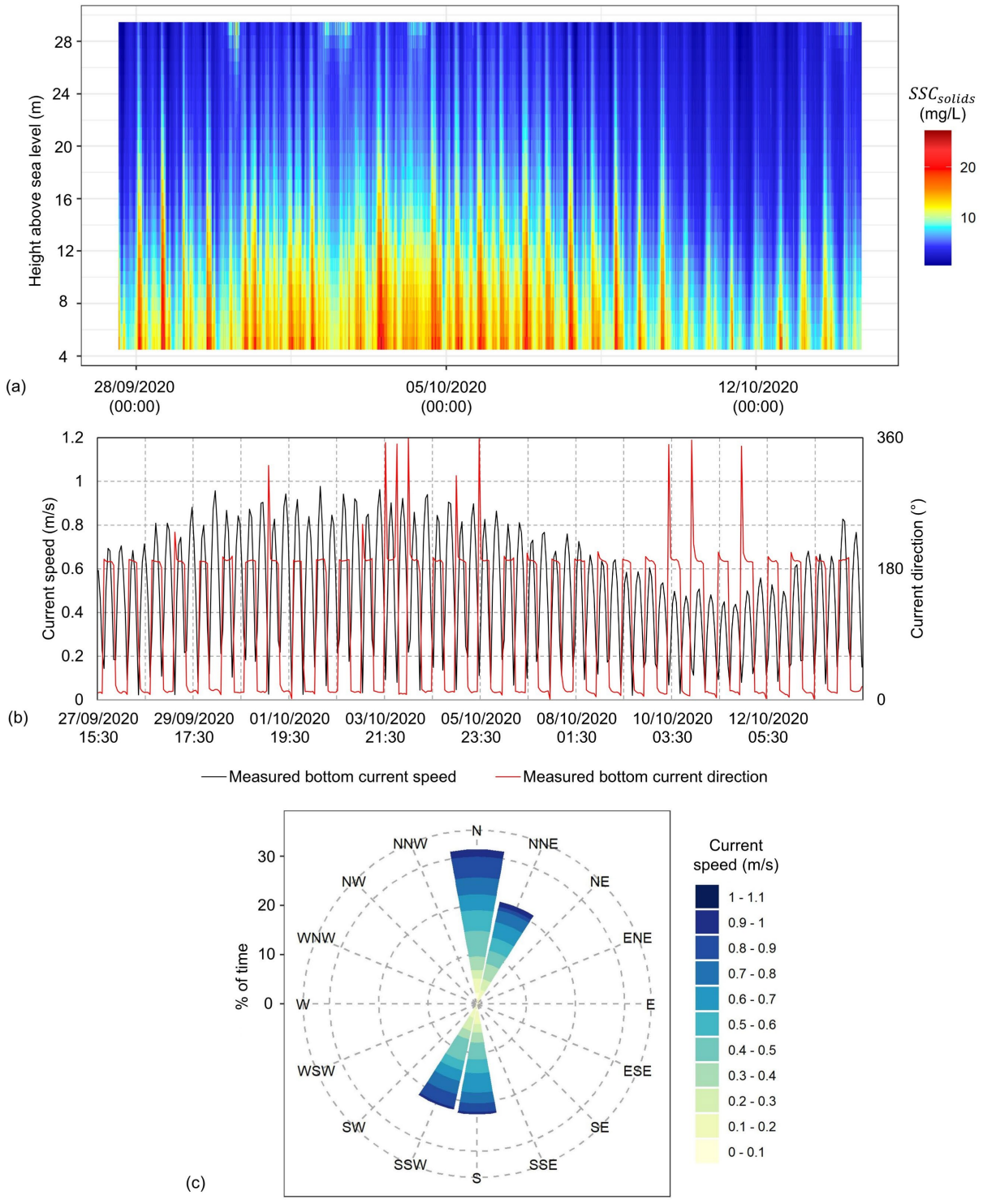


Figure 5-8 a) Beam 4 ADCP-derived SSC_{solids} spatial time series, b) bottom current speed and direction recorded by the ADCP, c) rose diagram of bottom current speed and direction recorded by the ADCP

From the ADCP-based SSC_{solids} spatial timeseries (Figure 5-8), it is clear that the highest fluctuation in concentrations occur between 5 m and 20 m above the seabed. Above this

stratum of the water column, SSC_{solids} significantly reduces, notably varying at a much lesser degree throughout the spring-neap cycle. The maximum and minimum estimated SSC_{solids} occurs at 5 m and 29 m above the seabed on 03/10/2020 12:30 (during spring tidal phase) and 11/10/2020 15:10 (during neap tidal phase) respectively. The suspended material in the water column most likely comprises substrate material from the seabed, plankton (mainly zooplankton) and other floating microorganisms and particles.

Figure 5-5 shows the seabed substrate surrounding the ADCP and water sample locations to be approximately coarse to very coarse sand with two sediment samples (52.7186 N, 6.0204 W and 52.7201 N, 6.0442 W) in the area displaying a D_{50} of 1.01 mm and 0.74 mm respectively. Due to the consistent sandy nature of the seabed substrate at this location and the consistent flood-ebb nature of the tidal flow, the particle distribution of sediment in the water column is expected to be quite consistent. The resuspension of this seabed sediment is highly linked with the tidal cycle whereby the threshold of motion is more readily exceeded during peak and flood tidal times when relatively higher current speeds exert the highest bed shear stress on the seabed. Some of this sediment may be transported in suspension, given the progressive nature of the tide in a northerly direction (Figure 5-8), yet some particles may re-settle on the seabed as bed shear stress decreases over slack tide. This settling effect is evident when comparing the recorded water levels and current speeds and directions to the estimated ADCP based SSC_{solids} spatial timeseries (Figure 5-8).

In particular, it is clear from Figure 5-8 that the suspended sediment is highly linked to the flood and ebb tide. From the current rose produced from the ADCP (Figure 5-8) and the modelled residual currents, a progressive tidal wave is present at this location in the Irish Sea [31], with the flood currents (N to NNE) being more dominant. This is reflected in suspended

sediment profile whereby a relatively higher amount of sediment is present in the water column during flood tides in comparison to neaps. Additionally, short drops in concentration along the timeseries in between the flood and ebb tides correlate with 'slack' tide imitating the rectilinear nature of the current at this location. Similarly, the longer increasing and decreasing trend of SSC_{solids} over this two-week period, mimic current patterns over the spring-neap cycle. Where current magnitudes are relatively higher over spring tides (approximately 1st to 6th October 2020) compared to neap tides, a higher concentration of SSC_{solids} is notably present in the water column. As the average current speeds over spring tides is higher than neaps, it is more likely for a higher percentage of sediment to remain in the water column over the flood-ebb cycle rather than completely settle to the seafloor compared to neap currents.

5.3.3 Comparison between ADCP-based SSC_{solids} and Water sample based SSC_{solids}

In order to quality check the accuracy of the ADCP estimated SSC_{solids}, ADCP-based SSC_{solids} values corresponding directly to the timestamp and water depth of the water sample-based SSC_{solids}, were extracted and compared. A strong positive linear relationship ($R = 0.87$) exists between the measured and estimated SSC_{solids} values (Figure 5-9), ultimately providing a high level of confidence for the ADCP-derived SSC_{solids} timeseries. This shows that SSC_{solids} is accurately estimated from the ADCP's acoustic backscatter.

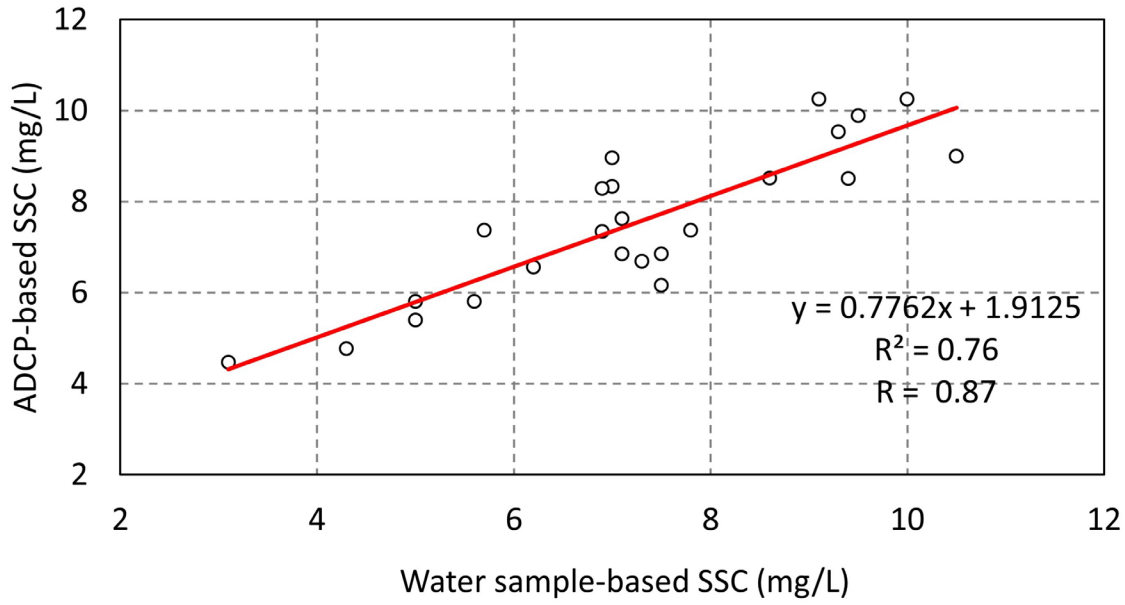


Figure 5-9 Linear regression between water sample-based SSC_{solids} samples and ADCP-derived SSC_{solids}

5.3.4 Suspended sediment model validation

In this section, four validation techniques are explored to try understand the most appropriate method to best validate a 2D suspended sediment transport model. These are outlined below:

1. Validation of 2D modelled $SSC_{sediment}$ using water sample-based SSC_{solids}
2. Validation of the flood-ebb characteristics (tidal asymmetry) of (i) 2D modelled suspended load transport and (ii) $SSC_{sediment}$ using ADCP-based datasets
3. ADCP-based validation of 2D modelled $SSC_{sediment}$ using full-timeseries statistics
4. Validation of the 2D modelled peak $SSC_{sediment}$ over a spring-neap cycle using ADCP-based SSC_{solids}

5.3.4.1 Technique 1: Validation of 2D modelled $SSC_{sediment}$ using water sample-based SSC_{solids}

Technique 1 involves the comparison between modelled $SSC_{sediment}$ and directly measured SSC_{solids} collected via water sampling at four stations non-associated with ADCP deployments. These include stations 5 to 8, the details of which are provided in Table 5-3. Each of these samples were taken at approximately peak flood or peak ebb tidal times. In order to validate the model using these samples, the modelled peak $SSC_{sediment}$ at these corresponding timestamps, and the modelled peak $SSC_{sediment}$ 7 days before and after the sampling date, representing a full spring-neap tidal cycle, were extracted and subsequently plotted in Figure 5-10.

Notably, each location displays a strong relationship between directly measured SSC_{solids} and modelled $SSC_{sediment}$. Figure 5-10a displays results at station 5. Modelled values at the time of sampling, and the modelled peak mean concentration over the spring-neap cycle, is 3.3 mg/L and 3.1 mg/L respectively. These values show a very good agreement with the mean measured SSC_{solids} of 3.6 mg/L.

Similarly, output at the time of direct sampling at station 6 is 4.6 mg/L, where the overall modelled peak mean over the spring-neap cycle is 4.0 mg/L. These compare well with mean measured SSC_{solids}, 3.6 mg/L.

Figure 5-10c displays results at station 7. Direct sampling results range from 6.4 mg/L to 13.0 mg/L with an average of 9.3 mg/L. The modelled output at this timestamp, 7.1 mg/L and the modelled peak mean over the spring-neap cycle, 6.9 mg/L, compare well with these values.

Furthermore, Figure 5-10d displays very good agreement between mean measured SSC_{solids}, 6.3 mg/L, and modelled values whereby modelled $SSC_{sediment}$ at that timestamp is 5.1 mg/L and modelled peak mean over the spring-neap cycle is 6.2 mg/L.

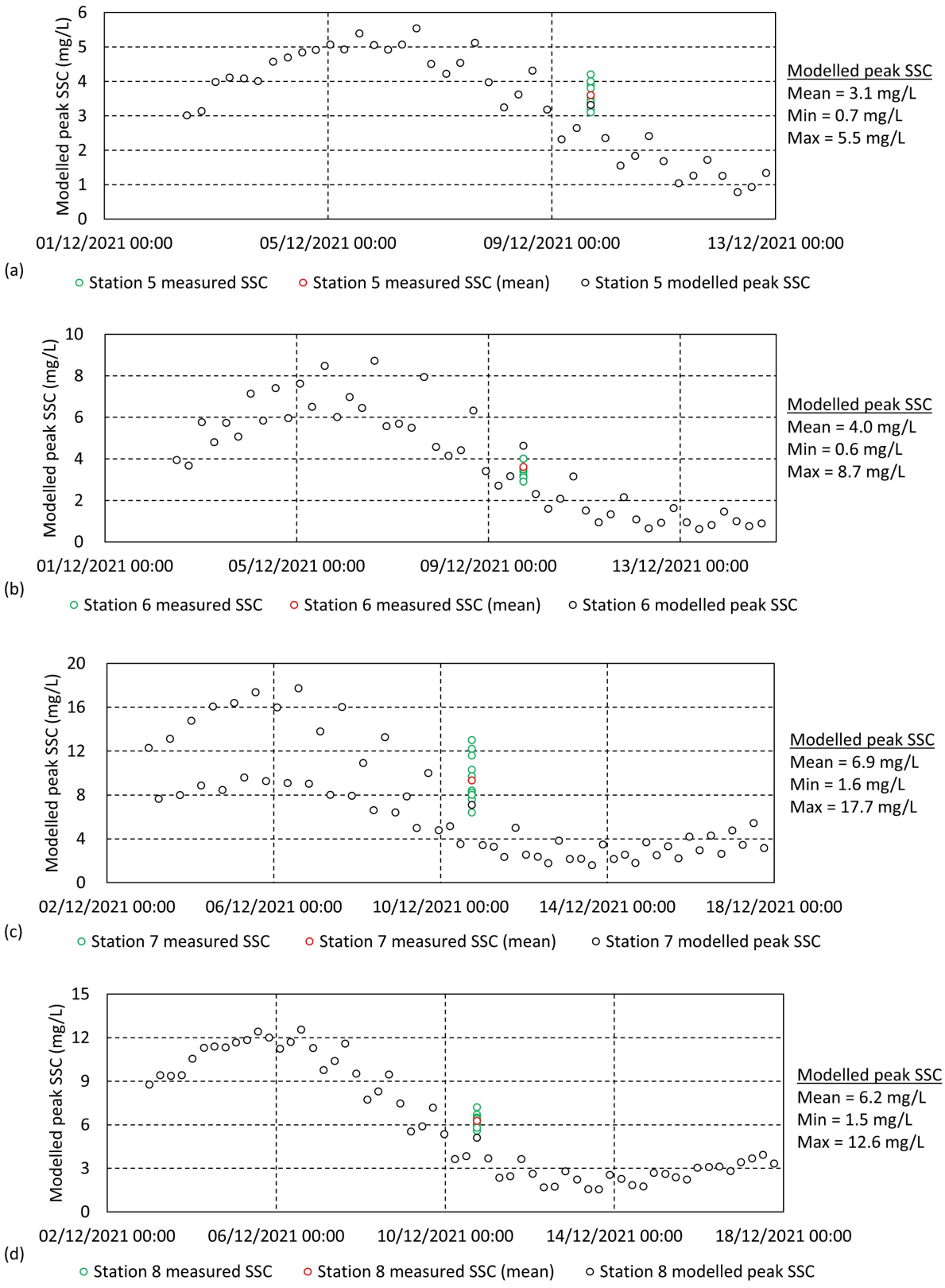


Figure 5-10 Comparison of 2D modelled peak $SSC_{sediment}$ against measured SSC_{solids} samples at four sampling stations non-associated with ADCP deployments. Sampling station locations are presented in Figure 5-1.

5.3.4.2 Technique 2: Validation of the flood-ebb characteristics (tidal asymmetry) of (i) 2D modelled suspended load transport and (ii) $SSC_{sediment}$, using ADCP-based datasets

5.3.4.2.1 Validation of tidal asymmetry in 2D modelled suspended load transport

As outlined in section 5.3.2, measured currents at the site exhibit a flood-dominant tidal current in a north to north-north-easterly direction. Modelled residual tidal current and residual suspended load transport agree with the nature of this tidal asymmetry (Figure 5-11), ultimately providing a high degree of confidence for directional component of modelled suspended sediment transport at this location.

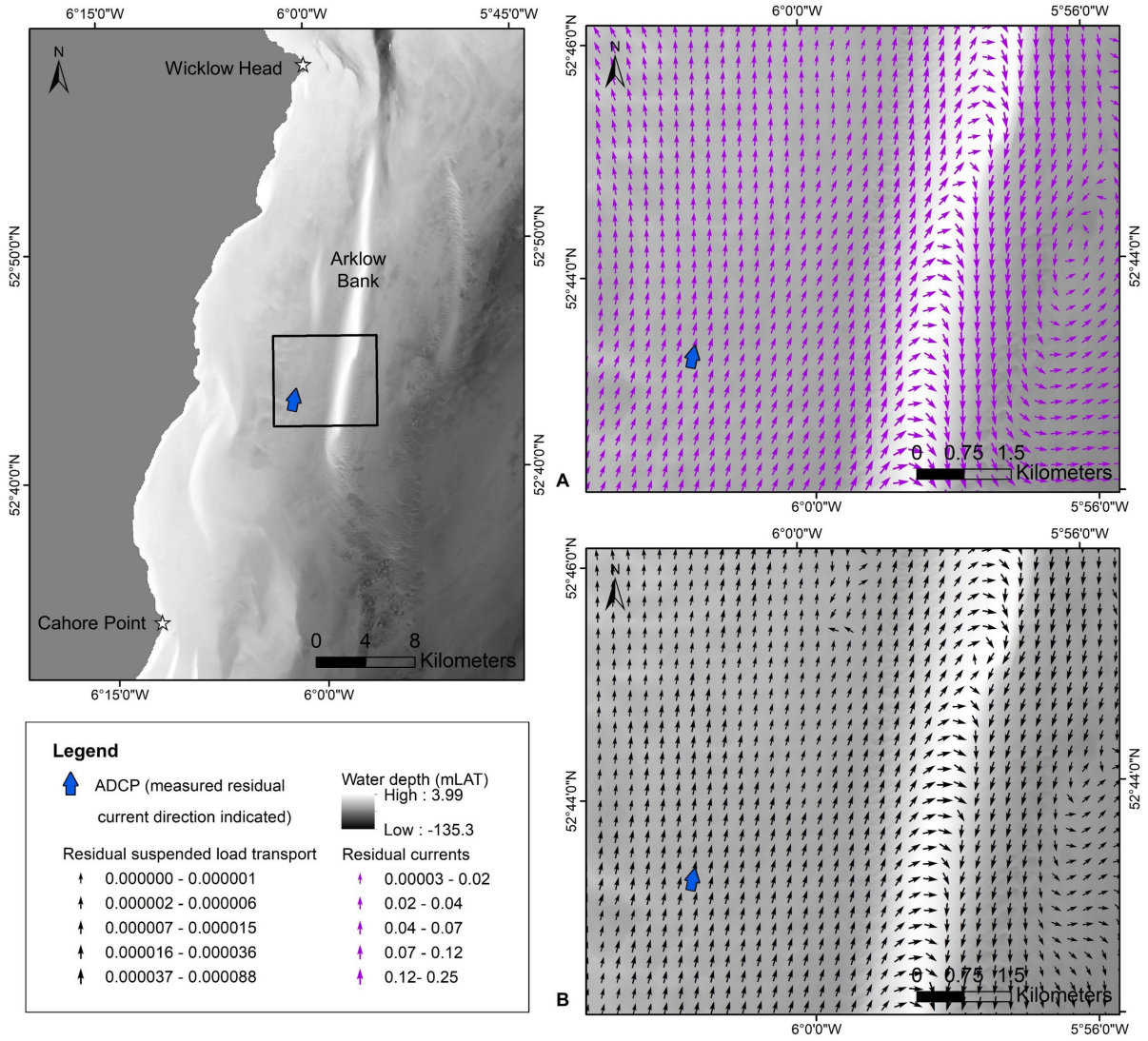


Figure 5-11 A. Modelled residual currents, B. Modelled residual suspended sediment transport

5.3.4.2.2 Validation of tidal asymmetry in 2D modelled $SSC_{sediment}$

In parallel, the ADCP-based SSC_{solids} spatial timeseries can be used as a calibration/validation technique for the relative magnitude of modelled $SSC_{sediment}$ in the water column over a flood-ebb tidal cycle. For example, the impact of the progressive tidal wave on suspended sediment transport in this local environment is clear when analysing the rose diagram (Figure 5-12) of estimated bottom-water, mid-water, surface-water and depth-averaged ADCP-based SSC_{solids} alongside measured current directions. All four timeseries (Figure 5-12) display a higher concentration of SSC_{solids} in the water column for a higher percentage of time during

the flood tide compared to ebb tide. This is a direct consequence of the flood-dominance nature of the tide. The rose diagram of modelled $SSC_{sediment}$ alongside modelled current directions show a very good agreement with this asymmetrical tide-SSC relationship whereby a higher concentration of $SSC_{sediment}$ is present in the water column also over flood tide (N – NNE) in comparison to ebb tide (S – SSW) (Figure 5-12).

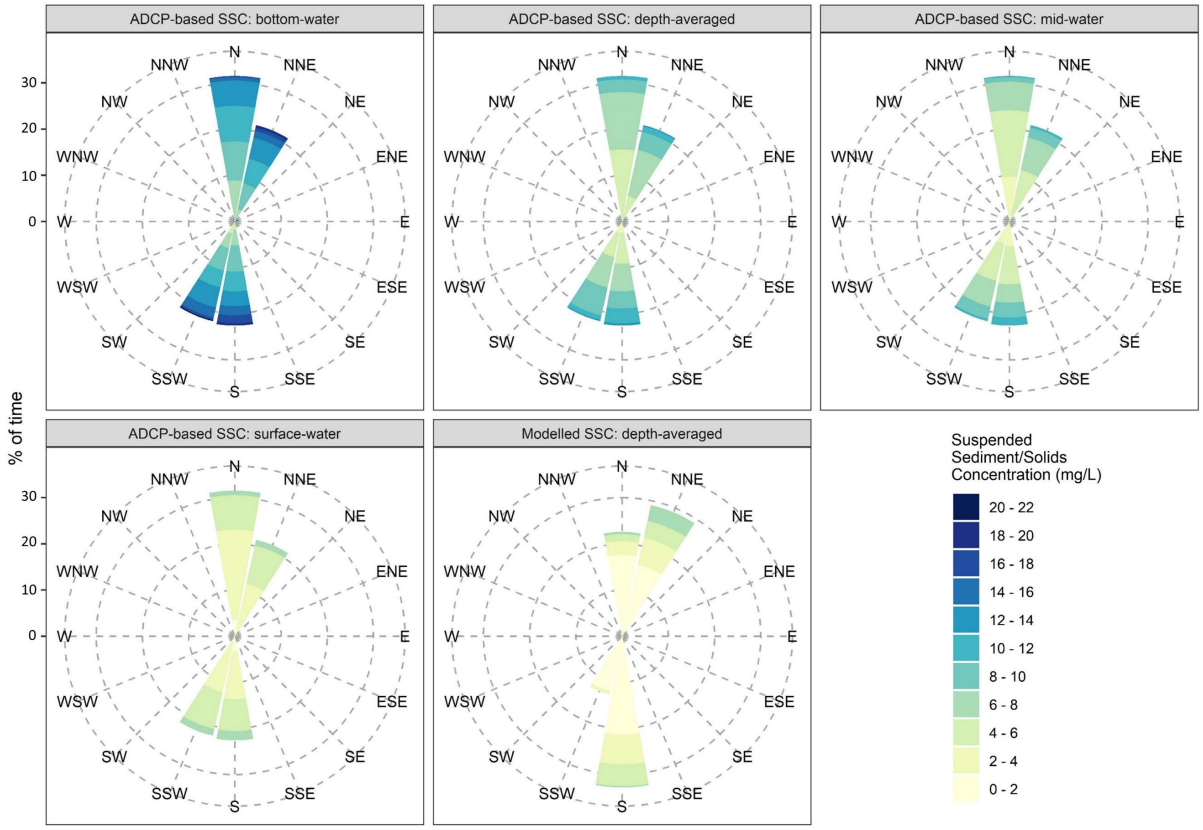


Figure 5-12 Roses of bottom-water, mid-water, surface-water and depth-averaged ADCP-based suspended solids concentration with measured current directions from 27/09/2020 15:00 to 14/10/2020 09:00. Modelled depth-averaged suspended sediment concentration with modelled current directions over the same time period.

5.3.4.3 Technique 3: ADCP-based validation of 2D modelled $SSC_{sediment}$ using full timeseries statistics

Full timeseries statistics are generated for bottom-water, mid-water and surface-water ADCP-based SSC_{solids} and are compared against modelled $SSC_{sediment}$ over the same time period. Results are displayed in Table 5-5 where variation between modelled and estimated datasets is evident. These will be discussed further in section 5.4.2.

Table 5-5 Minimum, maximum and mean ADCP-based SSC_{solids} at bottom-water, mid-water, surface water and depth-averaged, and statistics from full dataset of modelled $SSC_{sediment}$

Statistic	ADCP-based SSC_{solids} (mg/L)				Modelled $SSC_{sediment}$ (mg/L)
	Depth-averaged	Bottom-water	Mid-water	Surface-water	
Min	2.29	3.85	1.86	0.66	0.00
Mean	6.79	10.51	5.63	3.61	1.62
Max	13.37	21.84	11.48	6.95	7.90
Standard deviation	2.07	3.09	1.94	1.32	1.91
Variance	4.29	9.52	3.74	1.74	3.63

5.3.4.4 Technique 4: Validation of the 2D modelled peak $SSC_{sediment}$ over a spring-neap cycle using ADCP-based SSC_{solids}

Modelled peak $SSC_{sediment}$ values (maximum concentration over each flood and ebb tide) from 27/09/2020 15:00 to 14/10/2020 09:00 were extracted, corresponding to the time-frame of the ADCP deployment. Simultaneously, three timeseries were generated from the ADCP-based spatial time series, by calculating the minimum, mean (depth-averaged) and maximum SSC_{solids} values across all ADCP bins, for all timesteps. Subsequently, the minimum, mean and maximum ADCP-based SSC_{solids}, corresponding to the same timestep of the modelled peak values, were extracted and compared. The resulting comparison is presented in Figure 5-13.

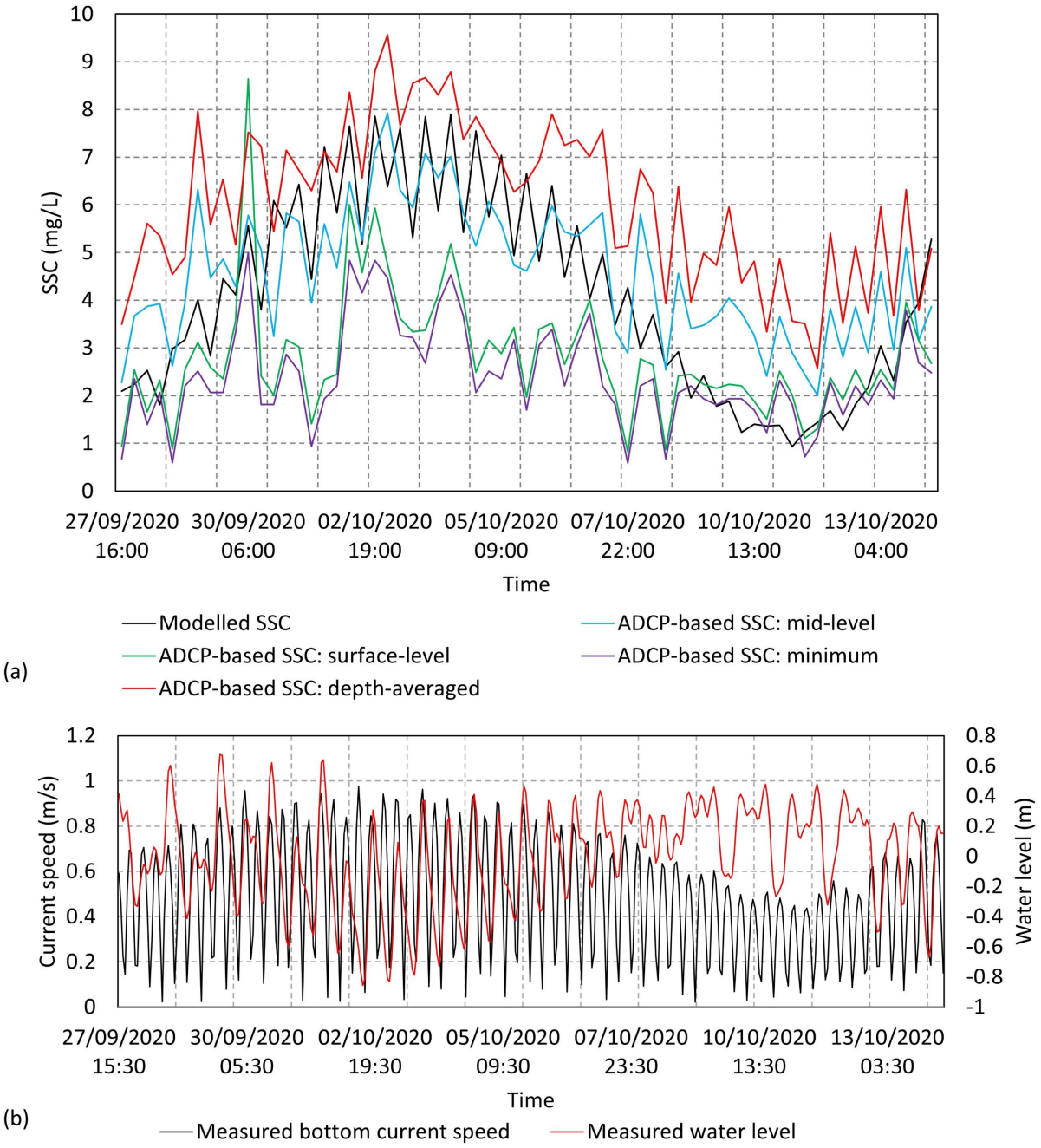


Figure 5-13 a) Comparative time series plot of 2D modelled suspended sediment concentration against ADCP-derived suspended solids concentration, b) water level and bottom current speed recorded by the ADCP

An overall increase and decrease of modelled peak $SSC_{sediment}$ is evident over the spring and neap tidal phases respectively. This same trend is reflected both in the full spatial ADCP-based timeseries (Figure 5-8) and in the depth-averaged profile (Figure 5-13). The modelled output has a better agreement with depth-averaged ADCP-based SSC_{solids} over spring tides yet

agrees better with the minimum profile over the neap tidal phase (Figure 5-13). Nevertheless, the peak modelled $SSC_{sediment}$ lie between the minimum and depth-averaged ADCP-based profiles. A strong positive relationship exists between the depth-averaged SSC_{solids} and modelled peak $SSC_{sediment}$, where R is 0.82 (Figure 5-14a). Additionally, a moderate positive relationship is present between the minimum SSC_{solids} and modelled peak $SSC_{sediment}$ where R is 0.58 (Figure 5-14b). Overall, a good agreement is evident.

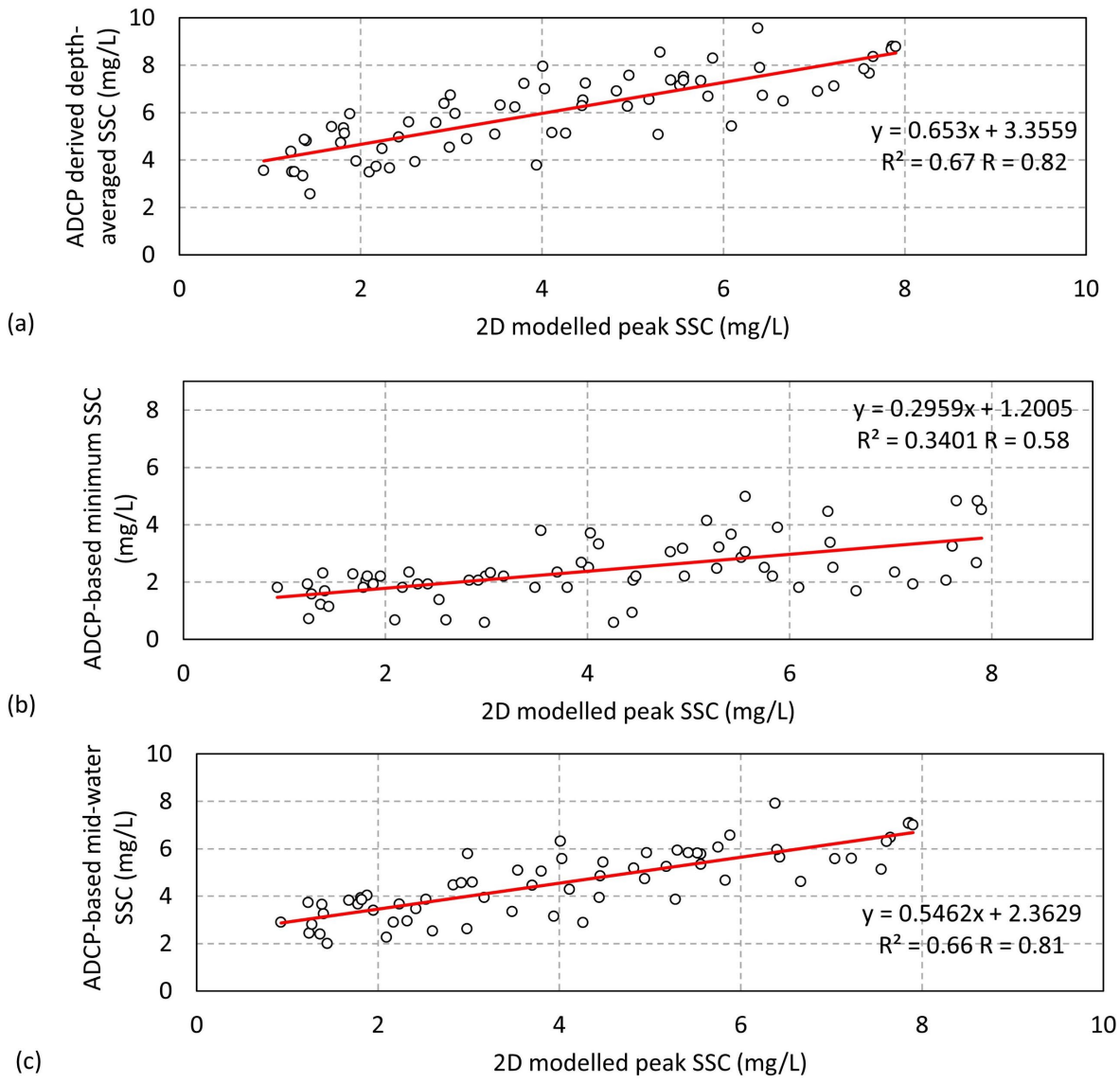


Figure 5-14 Correlation between a) 2D modelled peak $SSC_{sediment}$ and ADCP-based depth-averaged SSC_{solids}, b) 2D modelled peak $SSC_{sediment}$ and ADCP-based minimum SSC_{solids} and c) 2D modelled peak $SSC_{sediment}$ and ADCP-based mid-water SSC_{solids}

These modelled peak SSC values are further compared to the ADCP-based bottom-water, mid-water and surface-water $SSC_{sediment}$ values (Figure 5-13). The modelled dataset shows a very good agreement with mid-water ADCP-based SSC_{solids} over the full spring-neap timeframe. Where correlation drops slightly over the neap tidal phase from approximately 09th Oct to 13th Oct 2020, the modelled output aligns very well with surface-water

estimations. The relationship between these modelled values and the mid-water ADCP based SSC_{solids} is strong positive, where R is 0.81 (Figure 5-14c).

5.4 Discussion

5.4.1 Evaluation of the ability to estimate SSC_{solids} from ADCP relative acoustic backscatter in a shallow shelf sea environment

To convert echo intensity recorded by the ADCP to a clean, processed relative acoustic backscatter dataset, a literature review was first carried out to select the most suitable equations and to establish a robust workflow. The ultimate equations adopted in this study account for spreading losses in both the far and near fields [65], [72], and transmission losses due to both the absorption of seawater [73] and the attenuation of acoustic energy by suspended particles [74]. Comparing results at various stages of the processing workflow, provided in section 5.2.2, to previous studies, yielded very good correlations. The absorption coefficient due to water (α_w) calculated in this study (0.087 dB/m) shows good agreement with that presented in Mullison [48] (0.068 dB/m). Similarly, Baranya and Józsa's [55] α_s concentration value of 0.0005 dB/m for 1 mg/L, correlates very well with the concentration value of 0.00048 dB/m calculated in this study. Additionally, when plotting the reverberation level (RL) (equation 5), the RL when corrected for spreading losses ($RL + 20log_{10}(\psi \mathrm{R})$), and the RL when corrected for spreading losses and fluid and suspended particle losses ($RL + 20log_{10}(\psi \mathrm{R}) + 2\mathrm{R}\alpha_s + 2\mathrm{R}\alpha_w$) on the same line chart, the relative change in their line slope gradients is similar to that presented in Landers [51].

A high degree of confidence is also revealed in the estimation of ADCP-based SSC_{solids}, whereby a strong positive correlation exists between i) ADCP relative acoustic backscatter and water sample-based SSC_{solids} and ii) measured and estimated SSC_{solids} values, with a

correlation coefficient of 0.89 and 0.87 respectively. The magnitude of these correlation coefficients are analogous to results in previous studies [55], [62], [65], [69].

As previously discussed, single frequency systems cannot differentiate between the change in concentration of suspended material in the water column and the change in particle size distribution (PSD) of suspended sediment [57]. The magnitude of error varies depending on the instrument frequency and the amount of change in PSD [57]. This error could be considered negligible in this case when considering three variables; i) the successful production of an estimated seabed substrate map at the study site for the beginning of the ADCP deployment revealing a relatively consistent sandy seabed (section 5.2.4 and 5.3.2), ii) combining (i) with a consistent flood-ebb semi-diurnal tidal system implies a relatively consistent PSD in the suspended sediment load, and iii) the relatively low frequency of the ADCP (300kHz) means a lower sensitivity to very fine particles in comparison to higher frequency instruments, thus reducing the potential for error.

The ability to produce an estimated spatial timeseries of SSC_{solids} using processed relative acoustic backscatter has therefore proven successful in this study. The processed acoustic dataset provides excellent coverage of the water column at the ADCP deployment site, capturing approximately 71% of the water column over a full spring-neap tidal cycle. The resulting estimated spatial time series in combination with ADCP-based hydrodynamic parameters provides invaluable information in terms of SSC_{solids} dynamics in this complex hydrodynamic system. The impacts of the prominent tidal asymmetry phenomenon on sediment dynamics could be observed both over the flood-ebb and spring-neap tidal cycles. These ADCP-based datasets provide a more wholistic understanding of the interaction of these phenomena than sole water-sampling or OBS sensor deployments.

5.4.2 Evaluation of model validation techniques

The suspended sediment transport component of the 2D model is deemed successfully validated at multiple locations off the east coast of Ireland to a relatively high accuracy given underlying assumptions of the model using tested validation techniques.

Specifically, three out of four assessed validation techniques are deemed useful in developing the most accurate 2D suspended sediment transport model. In particular, combined use of technique 1, 2 and 4 provide (i) validation at one timestamp, (ii) validation of tidal asymmetry (flood-ebb characteristics) averaged over a full spring-neap tidal phase, and (iii) validation of the dissected trends and magnitudes across a full spring-neap cycle, or the length of an ADCP deployment.

Technique 1 displays very good validation results and proves highly useful as extra validation points across a model domain. Depending on the size of the numerical model in question or the area of interest within a large model domain, water sampling used in this way may be useful as supplementary validation points to ADCP deployments. This technique is recommended to combine with technique 2 and 4.

Technique 2 provides a very good method to validate the characteristics of suspended load transport and SSC_{solids} directly linked with tidal asymmetry. This method is best combined with technique 1 and 4.

Technique 3 is deemed unsuitable as a validation technique for 2D modelled $SSC_{sediment}$. The results highlight variations between modelled $SSC_{sediment}$ and ADCP-estimated SSC_{solids}. The potential reasons for these variations include:

(i) The ADCP-based time series, representing approximately 71% of the water column, is estimated for suspended solids concentration. This comprises mainly sediment but may also contain floating micro-organisms and other particles. Therefore, this estimated dataset may naturally display a higher concentration of suspended solids compared to 2D modelled suspended sediment.

(ii) The ADCP-based SSC_{solids} time series could not capture the bottom 5 m and the top 5 m of the water column. The bottom 5 m of the water column generally contains the highest concentrations of suspended sediment, these concentrations generally decrease as you progress toward the surface. The absence of these strata may skew full-timeseries general (mean/minimum/maximum) statistics.

(iii) At every slack water over this spring-neap timeframe, the 2D modelled $SSC_{sediment}$ drops down to approximately 0. Realistically, this does not naturally occur in this continental shelf environment, showing the limitation of this depth-integrated approach for suspended sediment transport modelling. This 2D modelled timeseries doesn't fully capture the full complexity of the natural environment therefore it may not be practical to compare SSC magnitude like for like through these general statistics.

The three points outlined above suggests a three-dimensional model may be more useful in terms of trying to capture the full complexity of hydrodynamics and sediment transport over the full water column. However, this is not always practically feasible when taking into account computational time, model resolution and project budget. Therefore, the best calibration/validation technique to provide the most accurate 2D suspended sediment transport model is to compare the peak modelled $SSC_{sediment}$ against corresponding peak ADCP-based SSC_{solids}. This is explored as technique number 4.

Technique 4, whereby 2D modelled $SSC_{sediment}$ is compared against minimum, depth-averaged, mid-water and surface-water ADCP-based SSC_{solids} profiles over a spring-neap cycle, provides the best validation technique for this location. Analysing the 2D modelled peak $SSC_{sediment}$ in this way allows the disintegration of general data trends and magnitude ranges over a full spring-neap cycle. Additionally, although 2D modelled peak $SSC_{sediment}$ lie within the minimum and depth-averaged ADCP-based thresholds and show moderate to strong positive relationships, a comparison against the mid-water and surface-water ADCP-based SSC_{solids} proves more useful at this site. In this case, the modelled peak SSC correlates very well with mid-water ADCP-estimates. Contrastingly, it is found that using the bottom-water ADCP-based SSC_{solids} timeseries as a calibration/validation dataset would be inappropriate, as this stratum contains much higher concentrations over a relatively small proportion of the water column and therefore is not representative of a depth-averaged water column. As a result, it is not recommended to compare like for like against depth-averaged modelled $SSC_{sediment}$. A similar view has been determined for the maximum ADCP-based SSC_{solids} profile.

Although technique 1 is considered highly useful, the ability to dissect the timeseries across a full spring-neap cycle using ADCP-based methods in techniques 2 and 4 is invaluable. Depending on the size of the sediment transport model developed or the area of interest within a numerical model, multiple ADCP deployments and/or water sample stations will enhance model validation accuracy. These ADCP-based techniques are considered very cost-effective as the deployment of acoustic instruments are already necessary in order to provide validation information for hydrodynamic models, and in some cases, wave models [90]. An additional water sampling campaign over the ADCP deployment period, both in the proximity of the deployed ADCP and in other areas of the model domain, could be of huge benefit and

add a wealth of knowledge to the site area. These three techniques can ultimately be combined with bed load validation techniques, for example, bed level changes using bathymetry datasets [12], [39], to provide an increasingly accurate sediment transport model in tidally-dominated environments.

5.4.3 Potential improvements/future work

Potential improvements in methods, and areas of future investigation have been identified in two distinct subject areas; (i) the estimation of ADCP-based SSC_{solids}, and (ii) the validation and calibration of numerical modelling work. Details of these are outlined below.

(i) The estimation of ADCP-based SSC_{solids}:

a) Increasing the number of water samples over the ADCP deployment time frame may further improve correlation between ADCP relative acoustic backscatter and water sample-based SSC_{solids}

b) Improvements in the ADCP deployment set-up. This could involve the use of an acoustic release to allow the ability of survey vessel instrumentation to obtain water samples closer to the deployed ADCP. Practically however, even with the use of an acoustic release, the ability to improve proximity to the ADCP may not be feasible given the relatively high surface current speeds in the south-western Irish Sea and other offshore environments during peak flood and ebb times due to vessel drift. In this case, vessel specifications such as dynamic positioning and operability statistics could be considered more specifically for this purpose if project budget allows. Other techniques such as the use of a hull-mounted ADCP [65] could also be investigated for the purpose of numerical model validation.

c) The methods and techniques developed in this study could be directly applied to other tidally-dominated continental shelf seas on a global scale. However, the south-western Irish Sea is dominated by sand to gravelly sand [31] and exhibits a semi-diurnal tidal cycle [31]. Other offshore environments earmarked for ORE developments diversify from these hydrodynamic and sediment characteristics. Therefore, the estimation of SSC_{solids} from ADCP acoustic backscatter could be further tested in other continental shelf seas around the world.

(ii) Calibration and validation of numerical modelling work:

a) As outlined in section 5.4.2, techniques 1, 2 and 4 prove very good validation methods for 2D numerical modelling work. However, technique 3 highlights the limitation of the depth-integrated modelling approach to capture the full dynamics of the natural sediment transport regime. In many coastal and offshore modelling studies, the underlying assumptions of a 2D modelling approach is accepted, and is commonly the most feasible approach in comparison to other numerical modelling techniques such as 3D and SPH. In making this decision, many variables are commonly considered including model domain size, spatial and temporal resolution requirements, computational power, project scope, timeline and budget, but also site-specific environmental variables such as water stratification, the consistency of the vertical current profile, and the complexity of regional scale hydrodynamics and morphodynamics. On a small to medium scale, 3D sediment transport models in coastal and offshore environments are becoming increasingly more feasible. In this case, the direct application of these newly tested validation techniques to a 3D model could be investigated. Additionally, the full 71 % coverage of the ADCP-based SSC_{solids} spatial timeseries has high potential for additional validation of various layers of the

modelled water column. In doing so, the limitations of the depth-integrated 2D modelling approach of fully characterising suspended load transport could be compared to a 3D modelling approach.

5.5 Conclusions

The main conclusions that have emerged from this research are summarised as follows:

1. The estimation of SSC_{solids} from ADCP acoustic backscatter based on sonar equations has proven successful in a tidally-dominated shallow shelf sea setting. A strong positive correlation is evident both between water sample-based SSC_{solids} and ADCP acoustic backscatter ($R = 0.89$), and water sample-based SSC_{solids} and ADCP-estimated SSC_{solids} ($R = 0.87$). These relationships provide a high degree of confidence in the accuracy of the ADCP-estimated SSC_{solids} spatial timeseries.
2. The ADCP-derived SSC_{solids} spatial timeseries provides excellent coverage of the water column at the ADCP deployment site, capturing 71% of the water column over a full spring-neap cycle.
3. The suspended sediment transport component of the 2D model is deemed successfully validated using three of the four tested model validation techniques.
4. The successful model validation techniques include;
    a. Validation of 2D modelled $SSC_{sediment}$ using water sample-based SSC_{solids},
    b. Validation of the flood-ebb characteristics (tidal asymmetry) of (i) 2D modelled suspended load transport and (ii) $SSC_{sediment}$ using ADCP-based datasets, and
    c. Validation of the 2D modelled peak $SSC_{sediment}$ over a spring-neap cycle using ADCP-based SSC_{solids}.

These techniques have produced highly acceptable results for this area of interest and have a high potential for applicability to other locations.

5. The development of a local seabed substrate map using ground-truthed MBES backscatter proved a useful technique to provide crucial information on site specific seabed sediment characteristics over the ADCP deployment time-frame.
6. The ADCP-based SSC_{solids} spatial timeseries has potential to provide additional validation of the vertical layers in a 3D model. The application of the ADCP-based techniques in this way could reveal how or if a 3D model could overcome the limitations of a depth-integrated 2D modelling approach in fully characterising the natural variability of SSC_{solids} in a tidally-dominated shallow shelf sea setting. Further investigation is recommended.
7. The multi-disciplinary method of collecting in situ metocean and sediment dynamic data via acoustic instruments (ADCP) is a cost-effective procedure for future ORE development projects and other engineering and scientific works.

5.6 Acknowledgments

SC is funded by the Irish Research Council (IRC) through grant EBPPG/2019/158 (Employment-Based Postgraduate Programme Scholarship). MC is funded under an Irish Research Council Enterprise Partnership Scheme Postdoctoral Fellowship (EPSPD/2020/109) and in part by a research grant from Science Foundation Ireland (SFI) under Grant Number 13/RC/2092, with support from Gavin and Doherty Geosolutions Ltd and the Geological Survey of Ireland (GSI). This project benefitted from funded industry-academic collaboration involving Gavin and Doherty Geosolutions, University College Dublin (iCRAG) and University College Cork (MaREI), supported by the Marine Institute under the Marine Research Programme 2014-2020 (Grant-

Aid Agreement No. IND/18/18). Ship time on the RV Celtic Voyager was funded by the Marine Institute through the 2020-2021 ship-time programme under the National Marine Research and Innovation Strategy 2017-2021. The authors would gratefully like to acknowledge the Mobility of Sediment Waves and Sand Banks in the Irish Sea (MOVE) (CV20010, CV20036, CV21034 and CV21035) shipboard crew and scientists, and onshore Marine Institute and INFOMAR support personnel for assistance with data acquisition. The authors are appreciative for access to the seabed sediment sample data and would like to acknowledge colleagues collecting and preparing these data through the projects and surveys mentioned. The authors wish to thank Xavi Monteys and Charise McKeon (both GSI) in particular for aiding with the INFOMAR dataset.

5.7 Author Statement

Shauna Creane: Conceptualization, Methodology, Investigation, Formal Analysis, Writing – Original Draft, Writing - Review & Editing, Visualisation.

Michael O'Shea: Supervision, Writing – Review & Editing.

Mark Coughlan: Supervision, Investigation, Writing – Review & Editing.

Jimmy Murphy: Supervision, Writing – Review & Editing.

5.8 References

[1] S. Aijaz, A. Driscoll, A. Sayce, K. Kaegaard, M. Klabbers, and S. Misra, "Fine sediment transport modelling for design of port facilities," in *Coasts and Ports 2013: 21st Australasian Coastal and Ocean Engineering Conference and the 14th Australasian Port and Harbour Conference*, 2013.

[2] RPS, "Rosslare Dredging & Beach Nourishment Study Sediment Transport Modelling

IBE0938 R01 Rev03 NS July 2014," 2014. [Online]. Available: http://webcache.googleusercontent.com/search?q=cache:Yi20AoF0zo0J:www.housing.gov.ie/sites/default/files/migrated-files/en/Foreshore/ApplicationsandDeterminations/RosslareEuroport/ApplicationDetails/FileDownLoad%252C38566%252Cen.pdf+&cd=1&hl=fr&ct=clnk&gl

[3] T. V. Karambas and A. G. Samaras, "Soft shore protection methods: The use of advanced numerical models in the evaluation of beach nourishment," *Ocean Engineering*, vol. 92, pp. 129–136, 2014, doi: 10.1016/j.oceaneng.2014.09.043.

[4] G. Benassai, *Introduction to coastal dynamics and shoreline protection*. Southampton, UK: Wit Press, 2006.

[5] C. T. Creech, R. S. Amorim, A. N. A. O. Castanon, S. A. Gibson, W. C. Veatch, and T. J. Lauth, "A planning framework for Improving reliability of inland navigation on the Madeira River in Brazil," in *PIANC-World Congress Panama City, Panama 2018*, 2018, pp. 1–20.

[6] M. Duman, F. Kucuksezgin, M. Atalar, and B. Akcali, "Geochemistry of the northern Cyprus (NE Mediterranean) shelf sediments: Implications for anthropogenic and lithogenic impact," *Marine Pollution Bulletin*, vol. 64, no. 10, pp. 2245–2250, 2012, doi: 10.1016/j.marpolbul.2012.06.025.

[7] F. Mcbreen, J. G. Wilson, A. S. Y. Mackie, and C. Nic Aonghusa, "Seabed mapping in the southern Irish Sea: predicting benthic biological communities based on sediment characteristics," *Hydrobiologia*, vol. 606, no. 1, pp. 93–103, 2008, doi: 10.1007/978-1-4020-8808-7.

[8] C. Jones, J. Magalen, and J. Roberts, “Wave energy converter (WEC) array effects on wave, current, and sediment circulation: Monteray Bay, CA,” Sandia National Laboratories, Santa Cruz, CA; Albuquerque, New Mexico, 2014.

[9] J. Abanades, D. Greaves, and G. Iglesias, “Wave farm impact on the beach profile: A case study,” *Coastal Engineering*, vol. 86, pp. 36–44, 2014, doi: 10.1016/j.coastaleng.2014.01.008.

[10] S. P. Neill, P. E. Robins, and I. Fairley, “The Impact of Marine Renewable Energy Extraction on Sediment Dynamics,” in *Marine Renewable Energy: Resource Characterization and Physical Effects*, Z. Yang and A. Copping, Eds. Springer International Publishing, 2017, pp. 279–304. doi: 10.1007/978-3-319-53536-4_12.

[11] P. E. Robins, S. P. Neill, and M. J. Lewis, “Impact of tidal-stream arrays in relation to the natural variability of sedimentary processes,” *Renewable Energy*, vol. 72, pp. 311–321, 2014, doi: 10.1016/j.renene.2014.07.037.

[12] C. Auguste, J. R. Nader, P. Marsh, I. Penesis, and R. Cossu, “Modelling the influence of Tidal Energy Converters on sediment dynamics in Banks Strait, Tasmania,” *Renewable Energy*, vol. 188, pp. 1105–1119, 2022, doi: 10.1016/j.renene.2022.02.077.

[13] E. Ivanov, A. Capet, E. De Borger, S. Degraer, E. J. M. Delhez, K. Soetaert, J. Vanaverbeke, and M. Grégoire, “Offshore Wind Farm Footprint on Organic and Mineral Particle Flux to the Bottom,” *Frontiers in Marine Science*, vol. 8, 2021, doi: 10.3389/fmars.2021.631799.

[14] R. J. S. Whitehouse, J. M. Harris, J. Sutherland, and J. Rees, “The nature of scour development and scour protection at offshore windfarm foundations,” *Marine*

Pollution Bulletin, vol. 62, no. 1, pp. 73–88, 2011, doi: 10.1016/j.marpolbul.2010.09.007.

[15] European Commission, "REPowerEU: A plan to rapidly reduce dependence on Russian fossil fuels and fast forward the green transition," *Press Release*, 2022. https://ec.europa.eu/commission/presscorner/detail/en/IP_22_3131 (accessed Sep. 27, 2022).

[16] Department of the Environment Climate and Communications, "Climate Action Plan 2021," 2021.

[17] National Grid ESO, "Pathway to 2030: A holistic network design to support offshore wind deployment for net zero," 2022.

[18] A. Rivier, A.-C. Bennis, G. Pinon, V. Magar, and M. Gross, "Parameterization of wind turbine impacts on hydrodynamics and sediment transport," *Ocean Dynamics*, vol. 66, no. 10, pp. 1285–1299, 2016, doi: 10.1007/s10236-016-0983-6.

[19] M. Baeye and M. Fettweis, "In situ observations of suspended particulate matter plumes at an offshore wind farm, southern North Sea," *Geo-Marine Letters*, vol. 35, no. 4, pp. 247–255, 2015, doi: 10.1007/s00367-015-0404-8.

[20] I. Fairley, I. Masters, and H. Karunarathna, "The cumulative impact of tidal stream turbine arrays on sediment transport in the Pentland Firth," *Renewable Energy*, vol. 80, pp. 755–769, 2015, doi: 10.1016/j.renene.2015.03.004.

[21] J. M. Harris, R. J. S. Whitehouse, and J. Sutherland, "Marine scour and offshore wind - Lessons learnt and future challenges," in *Proceedings of the International Conference on Offshore Mechanics and Arctic Engineering - OMAE*, 2011, vol. 5, pp. 849–858. doi:

10.1115/OMAE2011-50117.

[22] R. A. Lind and R. J. S. Whitehouse, “Understanding and Assessing Scour Development at Offshore Structures,” *Journal of Oilfield Technology*, vol. 5, no. 6, pp. 63–67, 2012.

[23] J. van Berkel, H. Burchard, A. Christensen, L. O. Mortensen, O. Svenstrup Petersen, and F. Thomsen, “The Effects of Offshore Wind Farms on Hydrodynamics and Implications for Fishes,” *Oceanography*, vol. 33, no. 4, pp. 108–117, 2020, doi: https://doi.org/10.5670/oceanog.2020.410.

[24] S. Clark, F. Schroeder, and B. Baschek, “The influence of large offshore wind farms on the North Sea and Baltic Sea – a comprehensive literature review (Report No. HZG Report 2014-6),” Geesthacht, Germany: Helmholtz-Zentrum Geesthacht, Zentrum für Material-und Küstenforschung, 2014.

[25] L. Bat, M. Sezgin, and F. Sahin, “Impacts of OWF installations on fisheries: A Literature Review,” *Journal of Coastal Life Medicine*, vol. 1, no. 3, pp. 241–252, 2013, doi: 10.12980/jclm.1.2013j17.

[26] F. Onea, L. Rusu, G. B. Carp, and E. Rusu, “Wave farms impact on the coastal processes—A case study area in the portuguese nearshore,” *Journal of Marine Science and Engineering*, vol. 9, no. 3, pp. 1–20, 2021, doi: 10.3390/jmse9030262.

[27] M. Coughlan, M. Guerrini, S. Creane, M. O’Shea, S. L. Ward, K. J. J. Van Landeghem, J. Murphy, and P. Doherty, “A new seabed mobility index for the Irish Sea: modelling seabed shear stress and classifying sediment mobilisation to help predict erosion, deposition, and sediment distribution,” *Continental Shelf Research*, vol. 229, p. 104574, 2021, doi: https://doi.org/10.1016/j.csr.2021.104574.

[28] T. Roetert, T. Raaijmakers, and B. W. Borsje, “Cable Route Optimization for Offshore Wind Farms in Morphodynamic Areas,” in *Proceedings of the 27th International Ocean and Polar Engineering Conference, ISOPE 2017*, 2017, pp. 595–606.

[29] J. M. Harris and R. J. S. Whitehouse, “Scour management – a risk based approach,” in *Proceedings of the 6th International Conference of Scour and Erosion (ICSE-6)*, 2012.

[30] J. van der Tempel, M. B. Zaaijer, and H. Subroto, “The effects of Scour on the design of offshore wind turbines,” in *Proceedings of the 3rd International Conference on Marine Renewable Energy*, 2004, pp. 27–35.

[31] S. Creane, M. O’Shea, M. Coughlan, and J. Murphy, “The Irish Sea bed load parting zone: Is it a mid-sea hydrodynamic phenomenon or a geological theoretical concept?,” *Estuarine, Coastal and Shelf Science*, vol. 263, p. 107651, 2021, doi: 10.1016/j.ecss.2021.107651.

[32] M. Z. Li, C. G. Hannah, W. A. Perrie, C. C. L. Tang, R. H. Prescott, and D. A. Greenberg, “Modelling seabed shear stress, sediment mobility, and sediment transport in the bay of fundy,” *Canadian Journal of Earth Sciences*, vol. 52, no. 9, pp. 757–775, 2015, doi: 10.1139/cjes-2014-0211.

[33] J. M. Brown and A. G. Davies, “Methods for medium-term prediction of the net sediment transport by waves and currents in complex coastal regions,” *Continental Shelf Research*, vol. 29, no. 11–12, pp. 1502–1514, 2009, doi: 10.1016/j.csr.2009.03.018.

[34] A. Rivier, A. C. Bennis, V. Magar, G. Pinon, and M. Gross, “Regional numerical modelling of offshore monopile wind turbine impacts on hydrodynamics and

sediment transport," in *Proceedings of the 1st International Conference on Renewable Energies Offshore*, 2014.

[35] A. J. Couldrey, T. Benson, M. A. F. Knaapen, K. V Marten, and R. J. S. Whitehouse, "Morphological evolution of a barchan dune migrating past an offshore wind farm foundation," *Earth Surface Processes and Landforms*, vol. 45, no. 12, pp. 2884–2896, 2020, doi: https://doi.org/10.1002/esp.4937.

[36] S. P. Neill and S. J. Couch, "Impact of Tidal Energy Converter (TEC) Array Operation on Sediment Dynamics," in *9th European Wave and Tidal Energy Conference (EWTEC)*, 2011.

[37] B. W. Borsje, P. C. Roos, W. M. Kranenburg, and S. J. M. H. Hulscher, "Modeling tidal sand wave formation in a numerical shallow water model: The role of turbulence formulation," *Continental Shelf Research*, vol. 60, pp. 17–27, 2013, doi: https://doi.org/10.1016/j.csr.2013.04.023.

[38] J. Krabbendam, A. Nnafie, H. de Swart, B. Borsje, and L. Perk, "Modelling the past and future evolution of tidal sand waves," *Journal of Marine Science and Engineering*, vol. 9, no. 10, 2021, doi: 10.3390/jmse9101071.

[39] S. Leenders, J. H. Damveld, J. Schouten, R. Hoekstra, T. J. Roetert, and B. W. Borsje, "Numerical modelling of the migration direction of tidal sand waves over sand banks," *Coastal Engineering*, vol. 163, p. 103790, 2021, doi: 10.1016/j.coastaleng.2020.103790.

[40] T. Tran-Duc, N. Phan-Thien, and B. C. Khoo, "A smoothed particle hydrodynamics (SPH) study of sediment dispersion on the seafloor," *Physics of Fluids*, vol. 29, no. 8, p.

83302, 2017, doi: 10.1063/1.4993474.

[41] I. Fairley, I. Masters, and H. Karunarathna, “Numerical modelling of storm and surge events on offshore sandbanks,” *Marine Geology*, vol. 371, pp. 106–119, 2016, doi: 10.1016/j.margeo.2015.11.007.

[42] C. Auguste, P. Marsh, J. R. Nader, I. Penesis, and R. Cossu, “Modelling morphological changes and migration of large sand waves in a very energetic tidal environment: Banks Strait, Australia,” *Energies*, vol. 14, no. 13, 2021, doi: 10.3390/en14133943.

[43] L. M. Ashall, R. P. Mulligan, and B. A. Law, “Variability in suspended sediment concentration in the Minas Basin, Bay of Fundy, and implications for changes due to tidal power extraction,” *Coastal Engineering*, vol. 107, pp. 102–115, 2016, doi: 10.1016/j.coastaleng.2015.10.003.

[44] C. Ulses, C. Estournel, X. Durrieu de Madron, and A. Palanques, “Suspended sediment transport in the Gulf of Lions (NW Mediterranean): Impact of extreme storms and floods,” *Continental Shelf Research*, vol. 28, no. 15, pp. 2048–2070, 2008, doi: 10.1016/j.csr.2008.01.015.

[45] J. Guillén, A. Palanques, P. Puig, X. D. de Madron, and F. Nyffeler, “Field calibration of optical sensors for measuring suspended sediment concentration in the western Mediterranean,” *Scientia Marina*, vol. 64, no. 4, pp. 427–435, 2000, doi: 10.3989/scimar.2000.64n4427.

[46] A. Kerr, M. J. Cowling, C. M. Beveridge, M. J. Smith, A. C. S. Parr, R. M. Head, J. Davenport, and T. Hodgkiess, “The early stages of marine biofouling and its effect on two types of optical sensors,” *Environment International*, vol. 24, no. 3, pp. 331–343,

1998, doi: https://doi.org/10.1016/S0160-4120(98)00011-7.

[47] K. L. Deines, “Backscatter estimation using broadband acoustic Doppler current profilers,” in *Proceedings of the IEEE Sixth Working Conference on Current Measurement*, 1999, pp. 249–253. doi: 10.1109/ccm.1999.755249.

[48] J. Mullison, “Backscatter estimation using broadband acoustic doppler current profilers - updated,” in *ASCE Hydraulic Measurements & Experimental Methods Conference*, 2017.

[49] M. G. Sassi, A. J. F. Hoitink, and B. Vermeulen, “Impact of sound attenuation by suspended sediment on ADCP backscatter calibrations,” *Water Resources Research*, vol. 48, no. 9, pp. 1–14, 2012, doi: 10.1029/2012WR012008.

[50] M. Guerrero, N. Rüther, S. Haun, and S. Baranya, “A combined use of acoustic and optical devices to investigate suspended sediment in rivers,” *Advances in Water Resources*, vol. 102, pp. 1–12, 2017, doi: 10.1016/j.advwatres.2017.01.008.

[51] M. N. Landers, “Review of Methods To Estimate Fluvial Suspended Sediment Characteristics From Acoustic Surrogate Metrics,” in *2nd Joint Interagency Conference*, 2010.

[52] M. N. Landers, T. D. Straub, M. S. Wood, and M. M. Domanski, “Sediment acoustic index method for computing continuous suspended-sediment concentrations,” in *U.S. Geological Survey Techniques and Methods: Book 3, Applications of Hydraulics*, U.S. Department of the Interior; U.S. Geological Survey, 2016, p. 63. doi: http://dx.doi.org/10.3133/tm3C5.

[53] K. F. E. Betteridge, P. D. Thorne, and R. D. Cooke, “Calibrating multi-frequency

acoustic backscatter systems for studying near-bed suspended sediment transport processes," *Continental Shelf Research*, vol. 28, no. 2, pp. 227–235, 2008, doi: 10.1016/j.csr.2007.07.007.

[54] P. D. Thorne and D. Hurther, "An overview on the use of backscattered sound for measuring suspended particle size and concentration profiles in non-cohesive inorganic sediment transport studies," *Continental Shelf Research*, vol. 73, pp. 97–118, 2014, doi: 10.1016/j.csr.2013.10.017.

[55] S. Baranya and J. Józsa, "Estimation of suspended sediment concentrations with ADCP in danube river," *Journal of Hydrology and Hydromechanics*, vol. 61, no. 3, pp. 232–240, 2013, doi: 10.2478/johh-2013-0030.

[56] G. R. Wall, E. A. Nystrom, and S. Litten, "Use of an ADCP to Compute Suspended-Sediment Discharge in the Tidal Hudon River, New York," United States Geological Survey Scientific Investigations Report 2006-5055, New York, 2006.

[57] J. W. Gartner, "Estimating suspended solids concentrations from backscatter intensity measured by acoustic Doppler current profiler in San Francisco Bay, California," *Marine Geology*, vol. 211, no. 3–4, pp. 169–187, 2004, doi: 10.1016/j.margeo.2004.07.001.

[58] D. C. Hill, S. E. Jones, and D. Prandle, "Derivation of sediment resuspension rates from acoustic backscatter time-series in tidal waters," *Continental Shelf Research*, vol. 23, no. 1, pp. 19–40, 2003, doi: 10.1016/S0278-4343(02)00170-X.

[59] D. A. Jay, P. Orton, D. J. Kay, A. Fain, and A. M. Baptista, "Acoustic determination of sediment concentrations, settling velocities, horizontal transports and vertical fluxes

in estuaries," in *Proceedings of the IEEE Sixth Working Conference on Current Measurement (Cat. No.99CH36331)*, 1999, pp. 258–263. doi: 10.1109/CCM.1999.755251.

[60] G. P. Holdaway, P. D. Thorne, D. Flatt, S. E. Jones, and D. Prandle, "Comparison between ADCP and transmissometer measurements of suspended sediment concentration," *Continental Shelf Research*, vol. 19, no. 3, pp. 421–441, 1999, doi: 10.1016/S0278-4343(98)00097-1.

[61] Y. Wang and S. Gao, "ADCP measurements of suspended sediment flux at the entrance to Jiaozhou Bay, western Yellow Sea," *Acta Oceanologica Sinica*, vol. 32, no. 12, pp. 96–103, 2013, doi: 10.1007/s13131-013-0395-0.

[62] P. A. de Oliveira, C. J. C. Blanco, A. L. A. Mesquita, D. F. Lopes, and M. D. C. F. Filho, "Estimation of suspended sediment concentration in Guamá River in the Amazon region," *Environmental Monitoring and Assessment*, vol. 193, no. 2, p. 10661, 2021, doi: 10.1007/s10661-021-08901-w.

[63] A. I. Santos, A. Oliveira, D. Carinhas, J. P. Pinto, and M. C. Freitas, "Hydrodynamic and Sediment Transport Patterns in the Minho and Douro Estuaries (NW Portugal) Based on ADCP Monitoring Data: Part 2—Statistical Interpretation of Bottom Moored Datasets," *Coasts*, vol. 1, no. 1, pp. 56–72, 2021, doi: 10.3390/coasts1010004.

[64] S. A. Moore, J. Le Coz, D. Hurther, and A. Paquier, "Using multi-frequency acoustic attenuation to monitor grain size and concentration of suspended sediment in rivers," *The Journal of the Acoustical Society of America*, vol. 133, no. 4, pp. 1959–1970, 2013, doi: 10.1121/1.4792645.

[65] A. Dwinovantyo, H. M. Manik, T. Prartono, and S. Susilohadi, “Quantification and Analysis of Suspended Sediments Concentration Using Mobile and Static Acoustic Doppler Current Profiler Instruments,” *Advances in Acoustics and Vibration*, vol. 2017, 2017, doi: 10.1155/2017/4890421.

[66] R. J. Wilson, D. C. Speirs, A. Sabatino, and M. R. Heath, “A synthetic map of the north-west European Shelf sedimentary environment for applications in marine science,” *Earth System Science Data*, vol. 10, no. 1, pp. 109–130, 2018, doi: 10.5194/essd-10-109-2018.

[67] EMODnet Bathymetry Consortium, “EMODnet Digital Bathymetry (DTM 2020).” 2020. doi: https://doi.org/10.12770/bb6a87dd-e579-4036-abe1-e649cea9881a.

[68] INFOMAR, “INFOMAR Marine Data Download Portal,” 2022. https://experience.arcgis.com/experience/50f0522dceaa4582a808558c0cbe8bb0/

[69] H. M. Manik, D. A. Gultom, Firdaus, and L. Elson, “Evaluation of ADCP backscatter computation for quantifying suspended sediment concentration,” in *IOP Conference Series: Earth and Environmental Science*, 2020, vol. 429, no. 1. doi: 10.1088/1755-1315/429/1/012035.

[70] R. J. Urick, *Principles of underwater sound*. New York: McGraw-Hill, 1975.

[71] K. V. Mackenzie, “Nine-term equation for sound speed in the oceans,” *The Journal of the Acoustical Society of America*, vol. 70, pp. 807–812, 1981, doi: https://doi.org/10.1121/1.386920.

[72] A. Downing, P. Thorne, and C. Vincent, “Backscattering from a suspension in the near field of a piston transducer,” *The Journal of the Acoustical Society of America*, vol. 97,

no. 3, pp. 1614–1620, 1995, doi: https://doi.org/10.1121/1.412100.

[73] M. Ainslie and J. McColm, “A simplified formula for viscous and chemical absorption in sea water,” *The Journal of the Acoustical Society of America*, vol. 103, pp. 1671–1672, 1998, doi: https://doi.org/10.1121/1.421258.

[74] R. J. Urick, “The Absorption of Sound in Suspensions of Irregular Particles,” *The Journal of the Acoustical Society of America*, vol. 20, pp. 283–289, 1948, doi: https://doi.org/10.1121/1.1906373.

[75] DHI Group, “MIKE 21 Flow Model: Hydrodynamic Module User Guide.” 2017.

[76] DHI Group, “MIKE 21 FLOW MODEL FM: Sand Transport Module, incl. Shoreline Morphology - User Guide.” 2017.

[77] DHI Group, “MIKE 21 Toolbox: User guide.” 2017.

[78] S. Creane, M. Coughlan, M. O’Shea, and J. Murphy, “Development and dynamics of sediment waves in a complex morphological and tidal dominant system: southern Irish Sea,” *Geosciences*, vol. 12, no. 12, p. 46, 2022, doi: 10.3390/geosciences12120431.

[79] DHI Group, “MIKE 21 Toolbox: Global Tide Model - Tidal prediction.” 2017.

[80] DHI Group, “MIKE 21 Spectral Waves FM.” 2017.

[81] DHI Group, “MIKE 21/3 Coupled Model FM.” 2017.

[82] DHI Group, “MIKE 21 & MIKE 3 Flow Model FM Sand Transport Module Scientific Documentation.” 2017.

[83] R. Manning, J. P. Griffith, T. F. Pigot, and L. F. Vernon-Harcourt, “On the flow of water

in open channels and pipes," *Transactions of the Institution of Civil Engineers of Ireland*, vol. 20, pp. 161–207, 1890.

[84] F. Engelund and E. Hansen, "A monograph on sediment transport in alluvial streams," Teknisk Forlag, Copenhagen, Denmark, 1967.

[85] J. Kaklamanos and K. Elmy, "R Package 'geotech,'" 2016.

[86] EMODnet Geology, "Seabed Substrates," 2019. https://www.emodnet-geology.eu/data-products/seabed-substrates/

[87] British Geological Survey, "BGS Seabed Sediments 250k version 3.0," 2011. doi: https://doi.org/10.5285/e0df9db6-09ac-4fa3-a815-1394c1988654.

[88] K. Westhead, D. Diaz Doce, R. Cooper, and A. Stevenson, "User Guide for the British Geological Survey DiGSBS250K Dataset," 2010.

[89] W. Evans, S. Benetti, F. Sacchetti, D. W. T. Jackson, P. Dunlop, and X. Monteys, "Bedforms on the northwest Irish Shelf: indication of modern active sediment transport and over printing of paleo-glacial sedimentary deposits," *Journal of Maps*, vol. 11, no. 4, pp. 561–574, 2015, doi: 10.1080/17445647.2014.956820.

[90] J. D. Flanagan, F. Dias, E. Terray, B. Strong, and J. Dudley, "Extreme Water Waves off the West Coast of Ireland: Analysis of ADCP Measurements," in *The 26th International Ocean and Polar Engineering Conference*, 2016.

6 Hydrodynamic processes controlling sand bank mobility and long-term base stability: A case study of Arklow Bank

Hydrodynamic processes controlling sand bank mobility and long-term base stability: A case study of Arklow Bank

Shauna Creane[1,2,3], Michael O'Shea[1,2], Mark Coughlan[4,5,3], Jimmy Murphy[1,2]

[1]School of Civil & Environmental Engineering, University College Cork, College Road, T12 K8AF Cork, Ireland; shauna.creane@ucc.ie (S.C.); michaeloshea@ucc.ie (M.O.); jimmy.murphy@ucc.ie (J.M.)

[2]SFI Research Centre for Energy, Climate and Marine (MaREI), Beaufort Building, Environmental Research Institute, University College Cork, Ringaskiddy, P43 C573 Cork, Ireland

[3]Gavin and Doherty Geosolutions, Unit A2, Nutgrove Office Park, Rathfarnham, D14 X627 Dublin, Ireland

[4]School of Earth Sciences, Science Centre West, University College Dublin, Belfield, D04 N2E5 Dublin, Ireland; mark.coughlan@icrag-centre.org (M.C.)

[5]SFI Research Centre for Applied Geosciences (iCRAG), O'Brien Centre for Science East, University College Dublin, D04 N2E5 Dublin, Ireland

Abstract

Offshore sand banks are an important resource for coastal protection, marine aggregates, and benthic habitats and are the site of many offshore wind farms. Consequently, a comprehensive understanding of the baseline processes controlling sand bank morphodynamics is imperative. This knowledge will aid the development of a long-term robust marine spatial plan and help address the environmental instability arising from

anthropogenic activities. This study uses a validated, dynamically coupled, two-dimensional hydrodynamic and sediment transport model to investigate the hydrodynamic processes controlling the highly mobile upper layer of Arklow Bank, while maintaining overall long-term bank base stability. The results reveal a flood and ebb tidal current dominance on the west and east side of the bank, respectively, ultimately generating a large clockwise residual current eddy encompassing the entire bank. This residual current flow distributes sediment along the full length of the sand bank. The positioning of multiple off-bank anticlockwise residual current eddies on the edge of this cell is shown to influence east–west fluctuations of the upper slopes of the sand bank and act as a control on long-term stability. These off-bank eddies facilitate this type of movement when the outer flows of adjacent eddies, located on both sides of the bank, flow in a general uniform direction. Whereas they inhibit this east–west movement when the outer flows of adjacent eddies, on either side of the bank, flow in converging directions towards the bank itself. These residual eddies also facilitate sediment transport in and out of the local sediment transport system. Within Arklow Bank's morphological cell, eight morphodynamically and hydrodynamically unique bank sections or 'sub-cells' are identified, whereby a complex morphodynamic–hydrodynamic feedback loop is present. The local east–west fluctuation of the upper slopes of the bank is driven by migratory on-bank stationary and transient clockwise residual eddies and the development of 'narrow' residual current cross-flow zones. Together, these processes drive upper slope mobility but maintain long-term bank base stability. This novel understanding of sand bank morphodynamics is applicable to bedforms in tidally dominated continental shelf seas outside the Irish Sea.

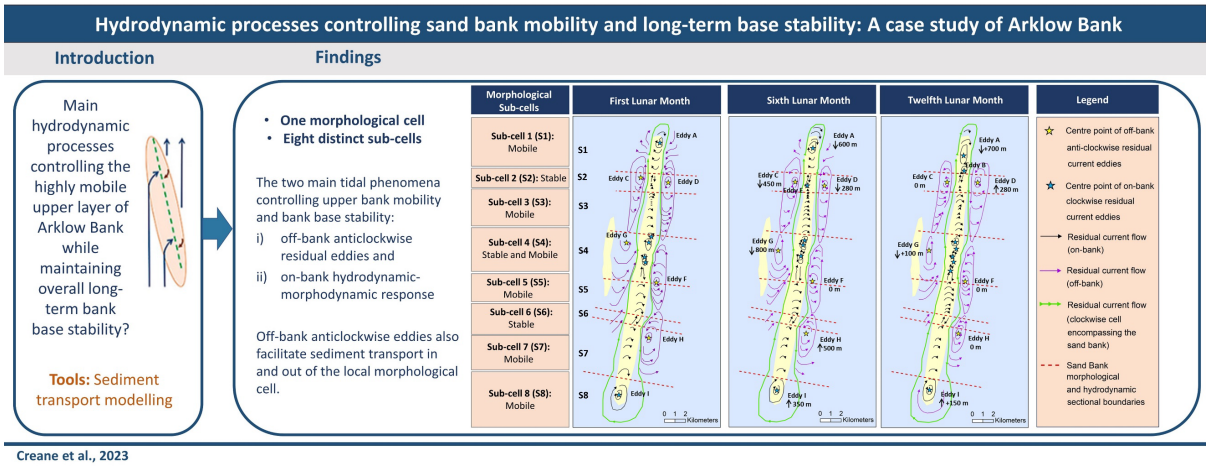


Figure 6-1 Graphical Abstract for peer-reviewed paper 'Hydrodynamic processes controlling sand bank mobility and long-term base stability: A case study of Arklow Bank' [1]

6.1 Introduction

Offshore linear sand banks are elongated sedimentary bedforms located in tidally-dominated continental shelf seas. They are important features, providing a habitat for many epifaunal, infaunal and fish species [2]–[4], as a source of marine aggregates [5], [6], and as sites for offshore renewable energy developments, for example, Scroby Sands Wind Farm in the North Sea. Consequently, a comprehensive understanding of sand bank dynamics and stability is imperative for sustainable, long-term marine spatial planning.

Arklow Bank, located off the south-east coast of Ireland, hosts Ireland's only presently constructed offshore wind farm (OWF) (Arklow Wind Park Phase 1) which is earmarked for further expansion (Arklow Wind Park Phase 2) [7] (Figure 6-2). Additionally, a number of OWFs are at the planning stage in the south-western Irish Sea, spread across the complex inter-related sediment transport pathways identified by Creane et al [8]. Arklow Bank is proposed to have formed during the Early Holocene, during post glacial marine transgression conditions, when a stronger-than-present hydrodynamic regime and abundant sediment supply supported the potential for submarine bedform formation [9]–[14]. The glacial and

post-glacial sediments comprising the bank and its surroundings continue to be modified and re-worked by modern-day hydrodynamics [15]–[18]. Although the positioning of Arklow Bank is relatively stable over a long term period [14], [19], it hosts an upper highly mobile layer of surficial sandy sediments [8], [15], [19], [20]. Coughlan et al [15] developed a mobilisation frequency index (MFI) to calculate the yearly exceedance of critical bed shear stress under pure current, pure wave and combined current and wave-induced bed shear stress. Notably, areas of the Arklow Bank display an MFI of 55 % to 70 % under both pure current and combined current- and wave-induced bed stress. Only restricted parts of the bank display an exceedance of the critical bed shear stress under solely wave conditions, with an MFI of approximately 10 % to 15 %.

Global and local scour are important engineering challenges in offshore wind farm design. Global scour is overall seabed movement, including migrating sand waves and sand banks, whereas local scour is erosion around a foundation caused by the formation of horseshoe vortices around the pile in a flow. Scour influences the bearing capacity of the monopile foundation and the dynamic behaviour of the structure and thus could cause structural instability. Therefore, the ability to accurately predict natural seabed level change and local scour depth are important prerequisites to the calculation of design loads and the determination of an optimized embedment depth of the monopile. This knowledge also informs the selection of optimal mitigation strategies, which will ultimately reduce project cost and risk. During the development of Arklow Wind Park Phase 1, turbine locations on the bank were prone to the development of scour which led to infrastructural instability, resulting in mitigation measures to be put in place [21], [22]. However, still relatively little is known about the processes that drive both on bank seabed mobility yet maintain overall bank base stability. This will be an important challenge to consider for Arklow Wind Park Phase 2.

Creane et al [8] shows that Arklow Bank obliquely aligns to the prevailing tidal flow giving rise to a flood-ebb tidal dominance on either side of the bank. This characteristic compares with other linear sand banks across the northern hemisphere [9], [14], [23], [24]. The nature of this tidal dominance is ultimately reflected in sand wave dynamics where recent studies show that on the south-eastern side of the bank, sand waves with a mean height and wave length of 3 m and 140 m respectively migrate southwards at mean rate of 23 m/yr [8]. Contrastingly, sand waves on the south-western side of the bank display a mean height and wave length of 2.3 m and 123.5 m respectively and migrate northwards at a rate of 32.7 m/yr [8] (Figure 6-2). Furthermore, sand wave analysis reveals the presence of a bed load convergence zone at the southern tip of Arklow Bank, indicating the limiting point of southward bed load sediment transport [8]. The convergence of a southward moving flow on the eastern side of the bank with a north-westward residual current flow coming from an offshore independent sand wave field located approximately 10 km south-east of Arklow Bank influences these bed load dynamics [8].

Creane et al [8], [14] show that Arklow Bank's local sediment transport system is linked with offshore sand deposits unattached to sand banks and the bed load parting zone in the central Irish Sea. During the flood tidal phase, the dominant M_2 tidal wave enters the Irish Sea through the North Channel and St. George's Channel to the north and south, respectively. The complex rotation of these tidal waves around two amphidromic points (one real and one degenerate) causes an intersection of the tidal waves between Ardanary (52.860°N, 6.058°W) on the east coast of Ireland and Anglesey (53.248°N, 4.607°W) on the UK coastline [14]. This interaction generates a tidal symmetry zone (Figure 6-2), giving rise to a bed load parting zone (BLP) [14]. BLPs are areas of maximum bed shear stress [25], [26] that mark the 'head' of divergent sediment transport pathways and hence are important components of the

sediment dispersal regime on tidally dominated continental shelves. This BLP directly influences the sediment transport regime across the south-western Irish Sea including Arklow Bank. Through the combined use of hydrodynamic modelling, repeat geophysical bathymetric surveys, theoretical parameters and multiple environmental variables, Creane et al [8] highlighted three residual circulatory transport pathways in the south-western Irish Sea, whereby sediment is recycled between offshore sand banks and offshore independent sand wave fields. Two of these systems include Arklow Bank, details of which are discussed in Creane et al [8]. Evidence is provided to support a semi-closed clockwise residual current flow around the bank whereby potential external sediment source pathways have been identified through modelled residual tidal currents. Adding to the complexity of this continental shelf sea's oceanography, evidence to support the presence of a semi-diurnal tidal node oscillation zone on the south-east coast of Ireland is presented by Creane et al [14] from which tidal ranges increase outwards from this location across the Irish Sea (Figure 6-2).

This study will focus on addressing the following hypothesis: the upper mobile layer of Arklow Bank and the long-term bank base stability are controlled by the positioning of residual current eddies on and around this bedform.

From this, three research questions will be addressed:

1. How does the hydrodynamics and bank mobility vary along the length of Arklow Bank?
2. What are the underlying hydrodynamic processes driving this variation?
3. What hydrodynamic phenomena control the bank's long-term stable positioning?

Addressing these research questions is critical in order to reduce risk in detailed design of wind farm foundations, export cables [27] and associated protection structures [28], but also to aid the understanding of these bank systems in order to conserve benthic habitats and

reduce risk of environmental instability due to anthropogenic seabed disturbances. Knowledge derived from this study can be applied to other tidally dominated sand bank systems around the globe.

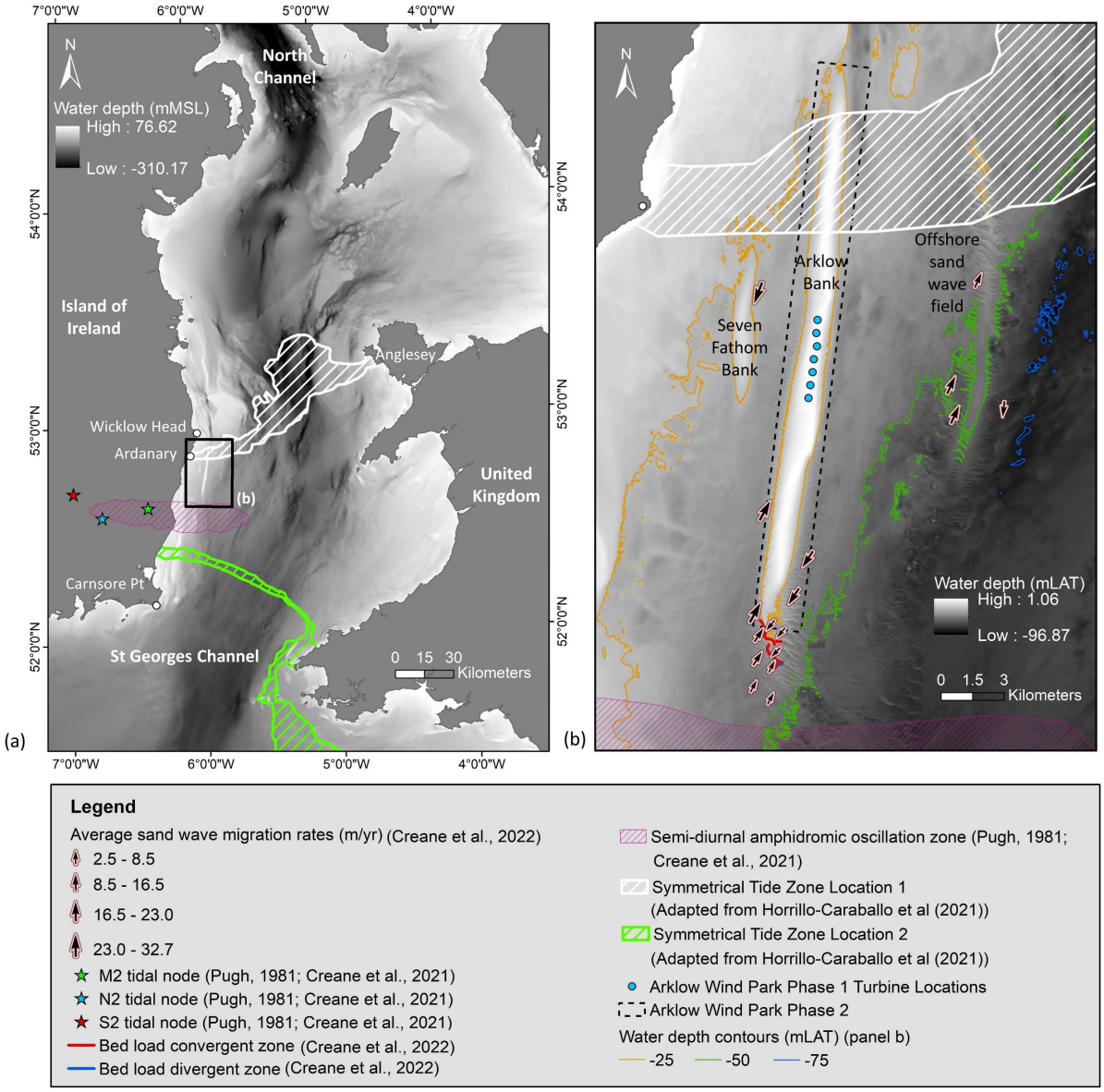


Figure 6-2 (a) Overview of Irish Sea oceanographic phenomena impacting the study site [8], [14], [24], [29]*; (b) the area of interest, Arklow Bank. Panel (a) bathymetry source: EMODnet* [30] *where MSL is mean sea level; Panel (b) bathymetry source: INFOMAR (https://www.infomar.ie/ (accessed on 20 March 2020)) where LAT is lowest astronomical tide.*

6.2 Methodology

A dynamically coupled two-dimensional (2D) hydrodynamic and sediment transport model was developed using DHI's MIKE 21 suite of tools [31], [32]. The setup of the model is detailed in Creane et al [33] and provided as supplementary material to this article along with

validation details for water levels, currents and suspended sediment transport. Notably, Creane et al [33] successfully validate the suspended sediment transport component of the 2D model using three newly tested model validation techniques. The locations of the collected ADCP-based suspended solids concentration (SSC_{solids}) dataset and water sample-based SSC_{solids} stations are displayed in Figure 6-3.

For this study, the levels of resolution of the unstructured triangular flexible mesh are increased from four to five. The five levels of resolution are defined as (Figure 6-3):

- Level 5: 50 to 80 m over Arklow Bank and Seven Fathom Bank;
- Level 4: 150 to 200 m encompassing the Arklow Bank system including offshore independent sand wave field identified in Creane et al [8];
- Level 3: 500 m to 600 m buffer zone, extending from the approximate -70 m water depth contour to the coastline from Howth Head (53.37861°, -6.057222°) to Courtown (52.645°, -6.228333°), and covering any sand banks outside these areas off the south-east coast of Ireland;
- Level 2: 800 m to 1000 m extending along the -70 m contour to the coast from Courtown to Carnsore Point (52.17056°, -6.355278°);
- Level 1: 2500 m to 3000 m resolution for the rest of the model domain.

The set-up of the sediment transport model is consistent with Creane et al [33]. As in Creane et al [33], artificial samples were placed in areas where a significant deficit of measured samples was evident, in order to produce the most realistic interpolated dataset when comparing against coarse seabed substrate maps such as the EMODnet seabed substrate map [34]. In this case, a constant D_{50} value of 0.7 mm which correlates with course sand according to the Wentworth scale [20] characterizes Arklow Bank.

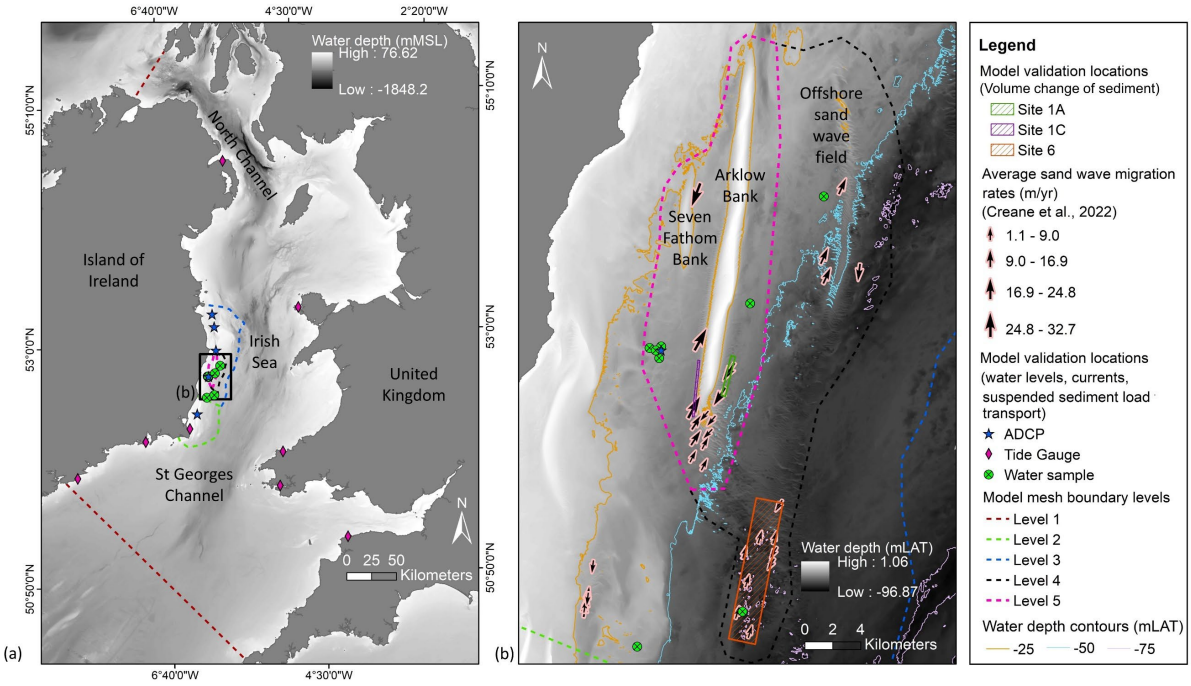


Figure 6-3 (a,b) Numerical model boundaries, mesh resolution levels and validation points [8], [33]. *Panel (a) bathymetry source: EMODnet* [30] *where MSL is mean sea level; Panel (b) bathymetry source: INFOMAR (https://www.infomar.ie/ (accessed on 20 March 2020)), where LAT is lowest astronomical tide.*

As there were no publicly available time-lapse bathymetry datasets extending across the upper bank, validation of simulated bed levels across the bank could not be carried out. Instead, volumetric analysis of repeat bathymetry datasets and simulated bed level changes was carried out in areas where limited repeat bathymetry data were available. Three different sites were assessed (Figure 6-3), whereby targeted repeat bathymetry datasets were collected during three offshore research survey campaigns (CV20010, CV21034 and CV21035) under the research project 'Mobility of Sand Waves and Sediment Banks (MOVE) Phase 1 and Phase 2' [8]. These sites are numbered 1a, 1c and 6 as per the nomenclature in Creane et al [8]. For each site, two bathymetry datasets were utilized. The volume of sediment above a certain reference level was first calculated from the earliest measured bathymetry dataset, followed by the later measured bathymetry dataset. The measured volume change over this

time period between the two surveys was calculated (Table 6-1). Simultaneously, the earliest bathymetry dataset was interpolated to the model mesh, and a simulation was run to predict bed levels for the second time-stamp using a time step of 30 s. The volume of sediment was then calculated above a certain reference level from the interpolated bathymetry dataset and then from the final simulated bed level. The simulated volume change over this time period was calculated. A comparison between measured and modelled volume change was carried out. All three analysed sites present a variance between measured and simulated bed levels of less than 1.1 % (Table 6-1).

Table 6-1 Comparison of simulated bed level changes against measured repeat bathymetry datasets at different sites in the model domain

Site	Location	Data type	Date of survey; Simulation start/end date	Overlap surface area (km²)	Volume Change ΔV (%)	Variance (%)
6	8 km south-east of Arklow Bank	Measured bathymetry	27th Sep 2020	19.7	+ 3.5	0.2
			06th Dec 2021			
		Modelled bed level	27th Sep 2020		+ 3.7	
			06th Dec 2021			
1A	South-eastern side of Arklow Bank	Measured bathymetry	10th Oct 2020	0.7	+ 0.6	1.1
			30th Mar 2021			
		Modelled bed level	10th Oct 2020		+ 1.7	
			30th Mar 2021			
1C	South-western side of Arklow Bank	Measured bathymetry	10th Oct 2020	0.5	+ 1.8	0.8
			30th Mar 2021			
		Modelled bed level	10th Oct 2020		+ 1.0	
			30th Mar 2021			

This coupled hydrodynamic and sediment transport model was run over a typical one-year period (12 lunar month tidal cycles) from September 2020 to September 2021 to analyse the interaction between tidal current dynamics and morphological changes over this time scale.

6.3 Results and Discussion

6.3.1 General bank morphodynamics from a flood-neap tidal cycle to full lunar cycle

In order to assess bank morphodynamics over a flood-neap tidal cycle, simulated bed level changes were calculated over two 6-hour slack to slack tidal phases, ending directly after a flood tide and an ebb tide. From Figure 6-4(a)–(b), it is clear that the upper bank migrates from west to east and east to west over the flood and ebb tidal phases respectively due to the nature of the cross-flows during each tidal phase [35]. Peak flood and peak ebb currents over this time period are presented in Figure 6-5. Over this time period, the bank moves in the same direction along the full length of the bank with the exception of at least three morphologically ‘stable’ zones. These stable zones correlate with relatively shallow areas of the bank (< 3 mMSL). The maximum erosion over the flood and ebb tidal phases is -0.32 m and -0.33 m respectively, and the maximum accretion is +0.29 m and +0.76 m.

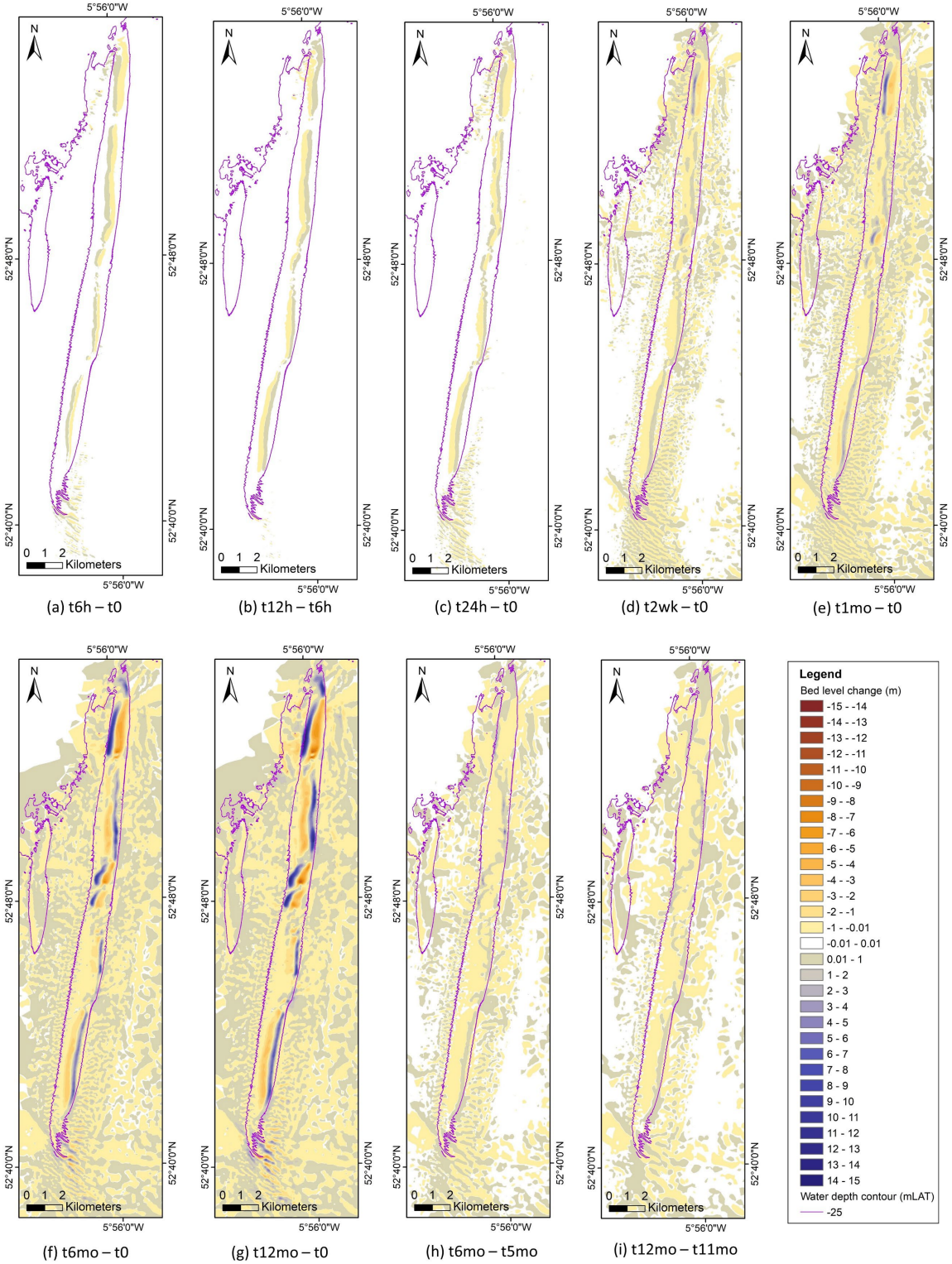


Figure 6-4 Bed level changes over various time periods calculated from extracted simulated bed levels; (a) after one ebb tidal phase, (b) after one flood tidal phase, (c) after two ebb and two flood tides, (d) after one spring-neap cycle, (e–g) after one, six and 12 lunar month simulations, (h–i) after one spring-neap cycle between simulation months five and six and 11 and 12

respectively. A −25 m water depth contour is provided based on INFOMAR bathymetry data referenced to Lowest Astronomical Tide (LAT). INFOMAR data available at: https://www.infomar.ie/, (accessed on 20 March 2020).

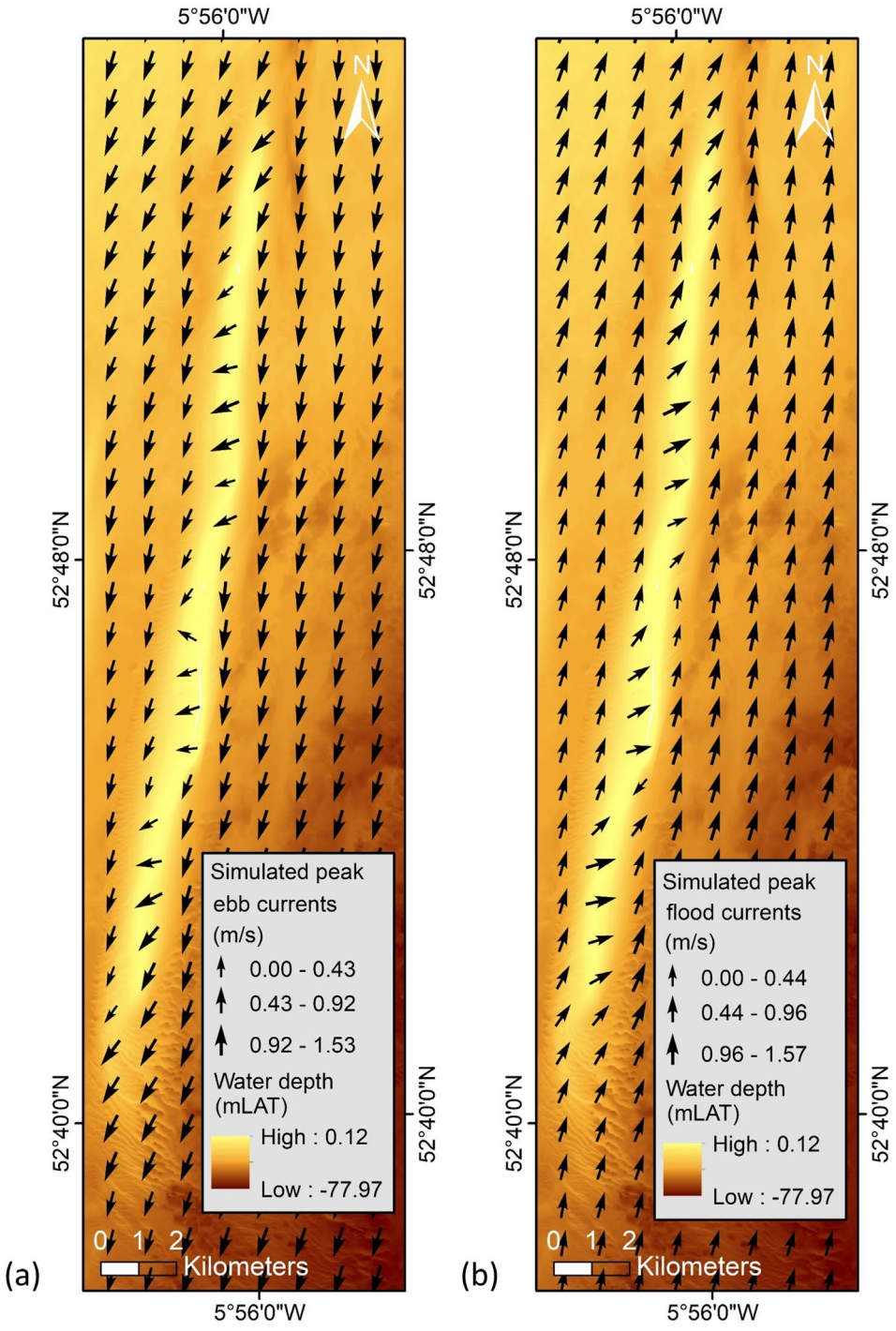


Figure 6-5 (a,b) Simulated peak ebb and flood depth-averaged currents, respectively. Bathymetry source: INFOMAR (https://www.infomar.ie/ (accessed on 20 March 2020)).

Analysis of bed level changes over a flood-ebb (Figure 6-4(c)), spring-neap (Figure 6-4(d)) and one lunar month tidal cycle (Figure 6-4(e)) reveals an inconsistent pattern of tidal dominance along the length of the bank, separating the bank into morphological sections. From the northern tip moving southwards in Figure 6-4(e), an approximate 3.3 km section of the bank crest migrates westwards. Next, an immobile zone dominates for approximately 800 m, followed by a successional eastward, westward, eastward, westward migration over an 8 km section of the bank. Another stability zone is then observed for approximately 1 km, followed by 4 km of eastward migration, 600 m of stability, until finally a relatively higher degree of eastward migration dominates over a 5.8 km section of the bank. These upper bank migration patterns coincide with the direction of tidal asymmetry presented in Figure 6-6(a)-(c).

The impact of tidal asymmetry on upper bank migration patterns remains evident over a one-year simulation period (e.g., Figure 6-4(e)–(g)). However, Figure 6-4(h)–(i) shows that the nature of each individual lunar month's dynamics are different from one another, whereby over the mobile sections, erosion occasionally takes place in a previously noted accretion zone and vice versa. This suggests that tidal current residuals alter from month to month, dynamically adjusting in strength and direction, with a constant change in bank morphology. As a result, although Figure 6-4(g) reveals relatively large bed level changes along the bank (ranging from +14.5 m to −11 m), the direct comparison of t12mo bed levels to t0 bed levels fails to capture the morphological changes of the sand bank occurring over shorter timescales within this one-year period (as highlighted in Figure 6-4(h)–(i)). Thus, a maximum bed level change of +14.5 m and −11 m over this time period (Figure 6-4(g)) does not represent direct accretion or erosion; instead, these are resultant net changes after continuous upper bank east–west fluctuation over time. Additionally, as the upper bank fluctuates in an east–west migration pattern, bed level changes occur from the shift in bank slope positioning over time

rather than solely traditional erosion and accretion processes. Therefore, bed level changes represented along the sand bank comprise the resultant changes due to the shift in bank slope positioning and due to traditional erosion and accretion processes and therefore must be interpreted with caution.

To investigate this east-west morphodynamic fluctuation, the residual tidal currents for each lunar month over a 12-month period were calculated (Figure 6-6). Hereafter, each lunar month cycle will be referred to as 'tXmo' whereby the first and twelfth lunar month cycles are referred to as t1mo and t12mo, respectively. Analysis shows that residual bed shear stress patterns are consistent with the inferences derived.

Similar to other offshore linear sand banks on the European continental shelf [9], [35], the first lunar month's residual tidal currents reveal a strong flood (northward) and ebb (southward) dominance on the western and eastern side of the bank, respectively (Figure 6-6(a)–(c)). This correlates well with sand wave migration dynamics on either sides of the bank [8] (Figure 6-2(b)). Clearly a strong, clockwise residual current eddy encompasses the bank, suggesting a semi-closed sediment transport system. Multiple off-bank anticlockwise residual current eddies are pinpointed on the outside of this cell (Figure 6-6(a)–(c)), including a complex partial anticlockwise curvilinear flow originating from Seven Fathom Bank (Eddy G in Figure 6-6(a)–(c). Additionally, a number of clockwise residual eddies are distributed along the length of the bank, the most prominent being Eddy A and Eddy I, illustrated in (Figure 6-6(a)–(c)). These eddies are intermittent, with regions of strong residual cross-flows and areas of limited cross-flows. For each lunar month up to the 12th lunar month, similar features are noted with slight variations, reiterating the potential for a hydrodynamic–morphodynamic feedback system along the length of the bank. This is evident in Figure

6-6(a)–(c), where the migration of the eddy centres from t1mo to t6mo to t12mo are pinpointed. These notable monthly variations in bed levels and residual currents are discussed in more detail in Section 6.3.2.

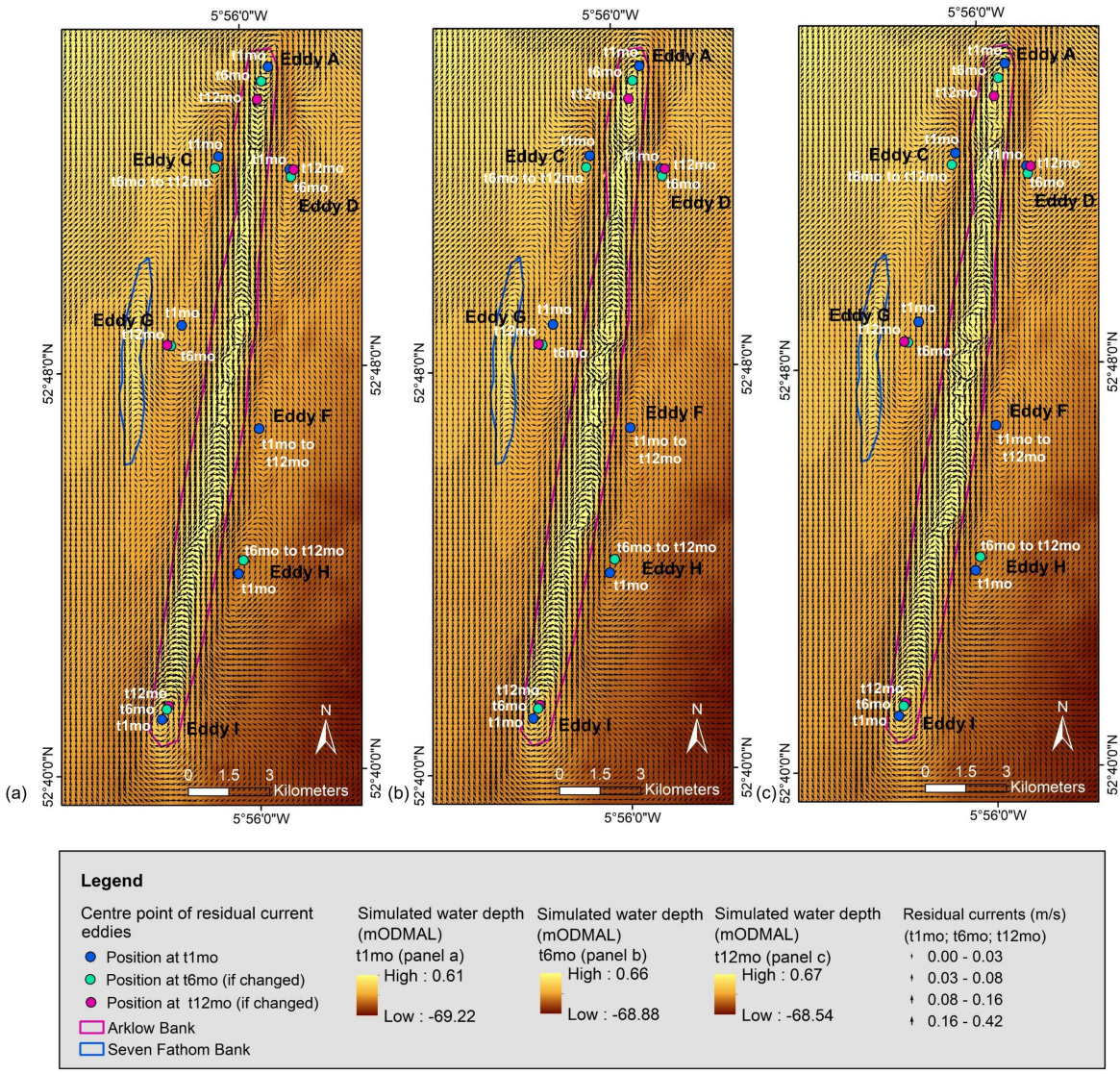


Figure 6-6 Simulated residual currents for the (a) first (t1mo), (b) sixth (t6mo) and (c) twelfth (t12mo) month of a one-year simulation period. Simulated bed levels at the end of each simulated month are also presented; t1mo is the simulated bed level at the end of the first month.

6.3.2 Detailed analysis of hydrodynamic-morphodynamic feedback loop

From combined cross-sectional analysis of simulated monthly bed levels, and monthly variation in residual tidal currents, a complex morphodynamic-hydrodynamic feedback

system is evident. Clearly, the development and migration of both clockwise and anticlockwise residual current eddies both on and off the bank, and associated residual tidal flows, are directly linked to both east-west migration patterns of the bank and vertical erosion/accretion patterns. To present and discuss the variation of this phenomenon along the length of the bank, the bank will be split into eight sub-cells which directly link to natural changes in the morphodynamic-hydrodynamic system.

6.3.2.1 Sub-cell 1

The morphodynamics of sub-cell 1 (Figure 6-7), the most northern sub-cell, is highly linked to:

i) a clockwise on-bank residual current eddy (Eddy A) that migrates southwards,
ii) the development of a clockwise on-bank residual current eddy (Eddy B) at the southern extent of this sub-cell, and
iii) a morphodynamic stability point controlled by two off-bank, adjacent, anticlockwise residual current eddies (Eddy C and Eddy D).

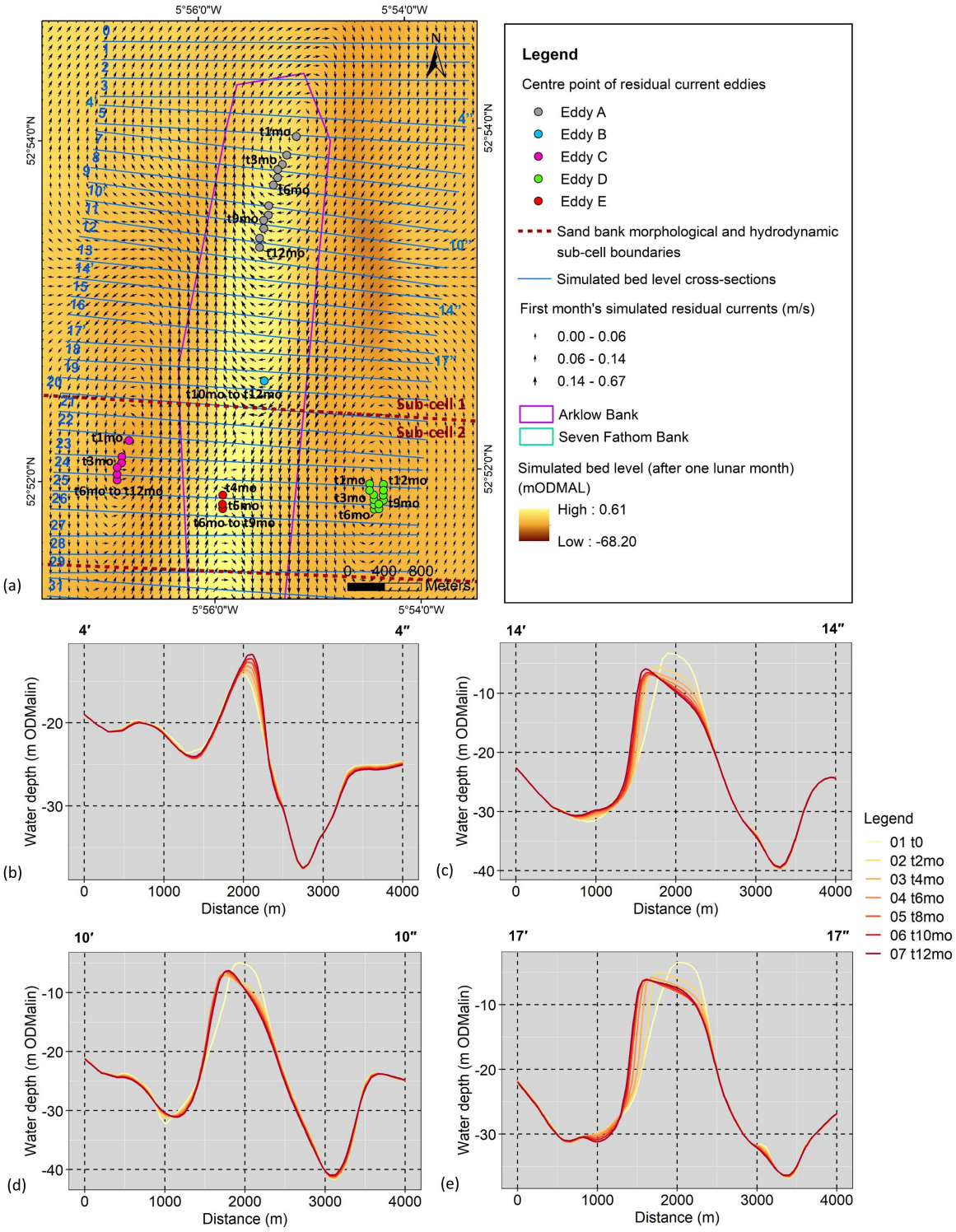


Figure 6-7 Morphodynamics and hydrodynamics at Sub-cell 1 of Arklow Bank (a) Simulated bed level change after one lunar month and associated residual current vectors, overlain by the location of the centre point of residual eddies from residual currents during each subsequent lunar month simulation whereby 't6mo' is the sixth lunar simulation month; (b) to (e)

Simulated bed level over a one year simulation at cross-sections 4, 14, 10 and 17 whereby 't0' is the starting bed level and 'h', 'wk' and 'mo' is subsequent months.

At t1mo, the centre of the northern most clockwise residual eddy, hereafter referred to as Eddy A, lies approximately over cross-section L5 (Figure 6-7(a)). Tracking the location of the centre of Eddy A over the one-year simulation period reveals a continuous southwards migration by approximately 1.3 km. At t12mo, it lies approximately between L11 and L14. Due to the circular nature of this clockwise residual current eddy, the dominant cross-flow over the bank is eastwards and westwards respectively, directly north and south of the centre of the eddy. Consequently, as the centre of Eddy A shifts southwards, the nature of the surrounding flow vectors subsequently adjusts.

In particular, the northern tip of the bank, an area outside the migration route of Eddy A's centre, shows evidence of residual current vector adjustment, which directly impacts the morphodynamic response of the bank. Over this northern tip of the bank, observations show a simultaneous reduction in residual current magnitudes and consistent rotation of the eastward current vectors to southward, as Eddy A migrates south (Figure 6-7(a)). Cross-sections L0 to L4 highlight the existing hydrodynamic-morphodynamic feedback loop whereby the bank crest simultaneously migrates eastward and shallows (up to 7 m), ultimately aligning with the gradual rotation of residual current vectors, allowing a build-up of sediment on the upper slopes and crest (Figure 6-7(b)). Additionally, the gradual development of a southward flow on the east side of the bank acts as a limitation to accretion on the eastern slope and a barrier to further eastward migration; thus, accretion takes place mostly on the upper stoss slope or crest of the bank.

Over a longer simulation period, the continuous rotation of these vectors at the northern tip of the bank suggests the formation of another on-bank clockwise residual eddy. In this way, as Eddy A develops and migrates southwards, another eddy develops in its place, ultimately acting as a conveyor belt of continuous migratory clockwise residual current eddies dynamically responding to and influencing the east-west morphodynamics of the bank.

Over the one-year period, the upper bank from L5 to L12, shifts migratory direction from westwards to eastwards as the centre of Eddy A and associated outer ring flows migrate southwards across these cross-profiles (Figure 6-7(a), (d)). The centre of the eddy signifies a reduction of tidal residuals and an area of tidal symmetry, indicating potential for sediment accretion. Therefore, as the eddy migrates south over one point along the bank, a progressive morphodynamic response should be evident in the cross-sectional profiles; these include (i) a westward migration of the bank, (ii) slowing of east–west migration in conjunction with sediment accretion, i.e., increased bed levels, and finally (iii) eastward migration of the bank. This is evident in cross-sections L5 to L12 (Figure 6-7(a), (d)).

As expected, the timing of the shift in migration direction varies along the length of this section of the bank, progressing through cross-sectional lines L5 to L12, aligning directly with the continuous progression of the centre of the residual eddy southwards. Whilst the mobility of the bank varies from above the −15 m contour to above the −25 m contour in some areas of the bank, the base of the bank remains relatively stable over time.

Furthermore, L13 to L14 only display morphodynamic responses (i) and (ii), whereby the slowing of westward crest migration and coincident sediment accretion at approximately t10mo and t12mo align with the ending position of the centre of the residual eddy (Figure 6-7(a), (c)).

Directly south of this region, approximately located between L15 to L19, at t6mo there is a noticeable shift in the westward residual cross-flow to a north-westward direction. From t6mo to t9mo, a continuous clockwise rotation of these residual current vectors is noticeable, coinciding with the southward migration of Eddy A, until the full formation of Eddy B at t10mo (Figure 6-7(a)). The centre of the eddy is located approximately between cross-sections L18 and L19. The coverage area of Eddy B is approximately 500 m to 700 m wide along the crest of the bank. The intersection between the northern-most eastward crossflow of Eddy B and the southern-most westward crossflow of Eddy A lies between L16 and L17 (Figure 6-7(a) and (e). As a result of reduced magnitudes of residual currents and reduced extent of cross-flows both at (i) the centre of Eddy B and (ii) the intersection of Eddy B with Eddy A, this area is characterised by westward migration and erosion of up to approximately 2 m, directly followed by slowed migration and sediment accretion (Figure 6-7(e)). A temporary stability zone is evident due to these two hydrodynamic phenomena.

Sub-cell 1 is bound to the south by sub-cell 2, which is characterised by a morphodynamic stability point generated by the intersection of two off-bank anti-clockwise residual current eddies (Eddy C and Eddy D). This is described in detail in Section 6.3.2.2.

6.3.2.2 Sub-cell 2

A clear hydrodynamic and morphodynamic transition point is evident from approximately L20 to L21 (Figure 6-8(a)). The southern-most westward residual cross-flows of Sub-cell 1 (including the outer-most ring of Eddy B) remain stable in terms of direction and positioning over this one-year period (Figure 6-8(a)). The southward shifting of these residuals is restricted by the dramatic change in bank morphology, shallowing from 5 to 10 m below mean sea level (MSL) to close to MSL. This shallow, symmetrical structure of the bank continues for

circa. 800 m. Notably, relatively low mobility and high stability is observed in cross-sections L21 to L24 over the one-year time period (Figure 6-8(b)). At L25 and L26, the bank deepens in comparison to this first 800 m zone to approximately 3 m below MSL. However, a relative low mobility and high stability is still evident in bank morphology for approximately another 750 m (L25 to L29) (Figure 6-8(c)).

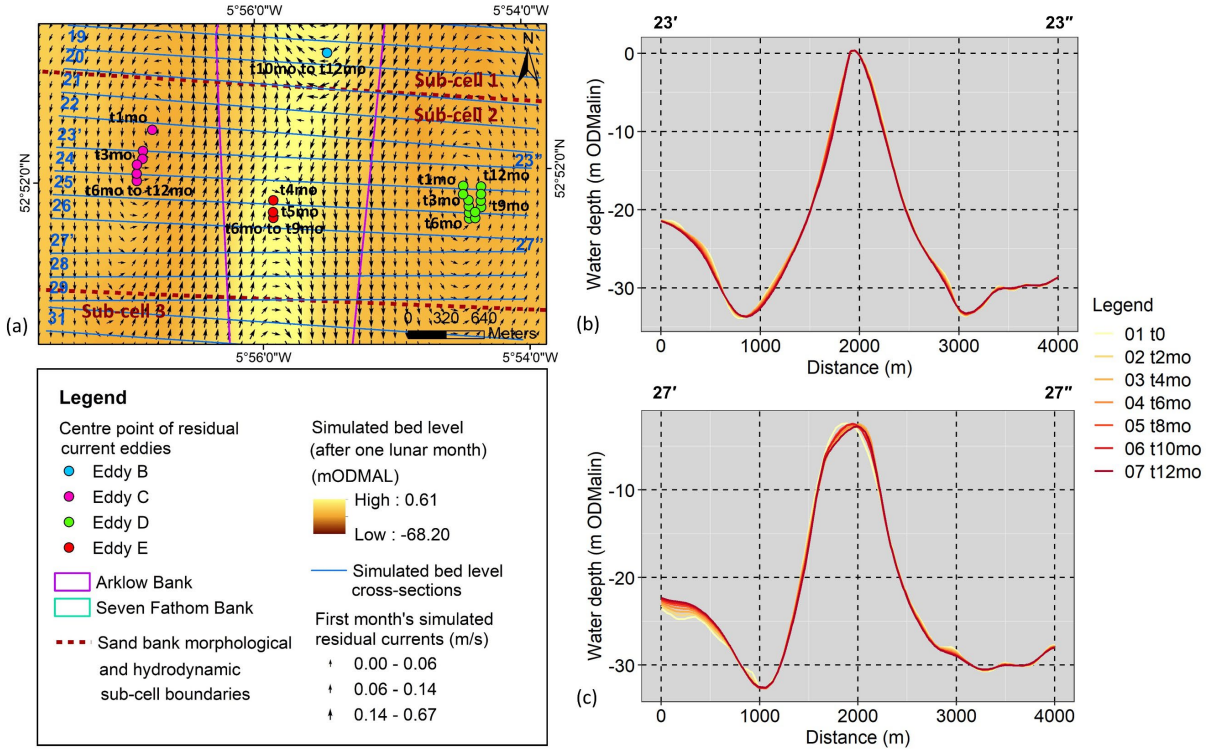


Figure 6-8 Morphodynamics and hydrodynamics at Sub-cell 2 of Arklow Bank. (a) Simulated bed level change after one lunar month and associated residual current vectors, overlain by the location of the centre point of residual eddies from residual currents during each subsequent lunar month simulation; 't6mo' is the sixth lunar simulation month. (b,c) Simulated bed level over a one year simulation at cross-sections 23 and 27; 't0' is the starting bed level, and 'mo' is subsequent months.

The maintenance of this ~1550 m morphological stability zone is driven by the presence of two anticlockwise residual current eddies located adjacently on the eastern and western side of the bank respectively. These will hereafter be referred to as Eddy C and Eddy D (Figure 6-8(a)). The intersection of these eddies occurs along the crest/upper slopes of the bank, directly limiting residual cross-flows at very shallow areas and reducing both the width and

magnitude of the cross-flows in other areas along this section. This ultimately reduces east–west fluctuation of the bank crest and increases the potential for sediment accretion/bank stability.

Unlike the transient and migratory nature of the on-bank clockwise residual current eddies identified in Sub-cell 1, the existence of these off-bank eddies remains constant throughout the simulation period. The positioning of the centre of Eddy C and D also remain relatively stable over time (Figure 6-8(a)). For example, from t1mo to t6mo, Eddy C migrates southwards by approximately 450 m, where it remains in the same location from t6mo to t12mo. On the other hand, Eddy D migrates approximately 280 m southwards from t1mo to t6mo. From t6mo to t12mo, it gradually migrates back up north, close to its original position (Figure 6-8(a)).

The first 800 m of the on-bank intersection of Eddy C and Eddy D, where the bank is at or above MSL, show little impact from these minor migration patterns; the length and position of the stability zone remains relatively constant over the same time period (Figure 6-8(a), (b)). At the transition zone to the southern half of Sub-cell 2, the deepening of the bank permits an increase in current-driven mobility at this location. A relatively weak on-bank transient eddy (Eddy E) forms and disappears over time, corresponding to the movements of Eddy D, influencing a shift in crest migration from eastwards to westwards over a small section of the bank (L25-L27) (Figure 6-8(a), (c)).

Overall, observations show that the general conveyor belt of clockwise on-bank residual current eddies tends to drive the east–west fluctuation of the bank in Sub-cell 1. This area of mobility is restricted and bound to the south by Sub-cell 2, a zone of relative stability,

ultimately maintained and driven by the stability of two off-bank anticlockwise residual current eddies.

6.3.2.3 Sub-cell 3

Sub-cell 3 marks a transition to a region of high mobility (Figure 6-9(a)). Initially, eastward migration of the upper bank profile dominates the length of the bank. When a maximum 'threshold' of eastward asymmetry is reached, westward migration ensues. Unlike Sub-cell 1, on-bank residual eddy formation is absent. Instead, the reversal of crest migration direction correlates with increasing and decreasing width of westward residual cross-flows, combined with partial rotation of residual current vectors southward and northward on the eastern and western side of the upper slopes of the bank, respectively. Although a full rotation of vectors forming an eddy is absent, this reduction in width of the cross-flow and the rotation of current vectors on either side of the bank stimulate migration of the upper bank in the opposite direction, while the base of the bank remains stable. Reduced current magnitudes facilitate sediment accretion both at the crest and on the stoss slope, whilst the new southern flow stimulates erosion on the east side of the bank and inhibits further eastward migration. In this way, the bank migrates back towards a more symmetrical shape. Clearly, a morphodynamic–hydrodynamic looped response system controls the east–west fluctuation of the crest while maintaining bank base stability.

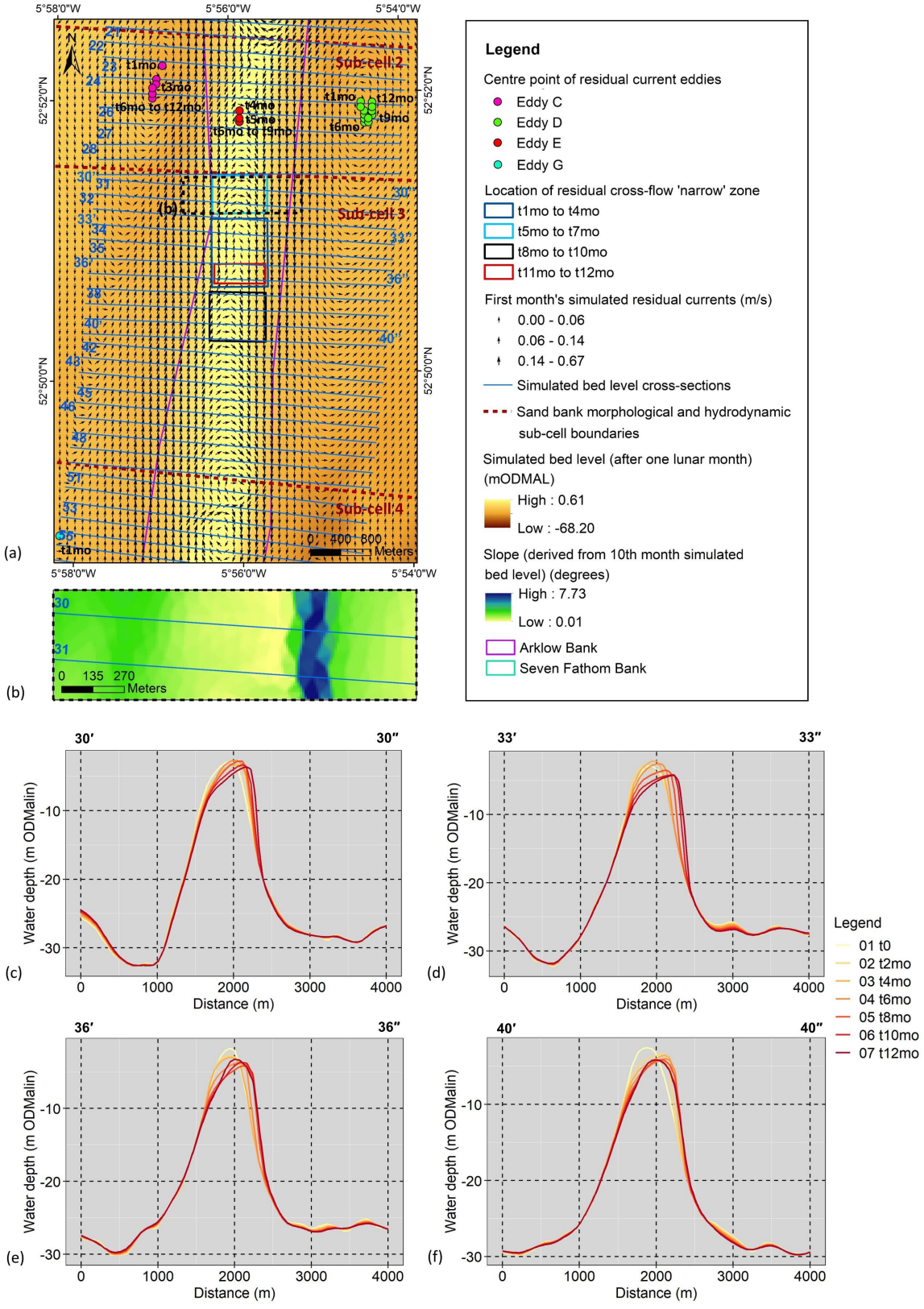


Figure 6-9 Morphodynamics and hydrodynamics at Sub-cell 3 of Arklow Bank. (a) Simulated bed level change after one lunar month and associated residual current vectors, overlain by the location of the centre point of residual eddies from residual currents during each subsequent lunar month simulation; 't6mo' is the sixth lunar simulation month. (b) Slope derived from

the resulting bed level after 10 lunar month simulation, overlain by cross-section L30. (c–f) Simulated bed level over a one year simulation at cross-sections 30, 33, 36, and 40; 't0' is the starting bed level, and 'mo' is subsequent months.

Over the one-year time period, most of Sub-cell 3 is dominated by an eastward residual cross-flow between 400 and 600 m wide. The area of reduced cross-flow (approximately 100 m wide), outlined previously, hereafter will be referred to as a 'narrow' area. This narrow area coincides with bank rejuvenation and intermittently moves to different areas of the bank over the one-year period. As the narrow area moves, the wider cross-flow replaces it and dominates that same area once again. The migratory nature of this 'narrow' area over the one-year simulation period is illustrated in Figure 6-9(a). A number of representative cross-sectional profiles presented in Figure 6-9(c)–(f) exhibit the expected morphodynamic response of (i) eastward migration, (ii) bank rejuvenation back towards a symmetrical shape (westward migration), and in some cases (iii) eastward migration once again. The variation in each cross-sectional profile follows the timeline of successional wide-narrow-wide residual current changes.

As there is evidence of a reversed migration pattern over the majority of Sub-cell 3, the slope of the bank at this transition point was analysed from monthly extracted simulated bed levels. Notably, at cross-sections L30, L33, L36 and L40, a shift in migration direction occurred when the upper slopes reached an angle of approximately 5.5° to 6° (Figure 6-9(b)). When this approximate angle is reached, a hydrodynamic response is stimulated that alters the upper slope's erosion–accretion regime, thus influencing the east–west fluctuation of the crest and the bank's shape. In this way, the slope angle of the upper bank acts as a 'threshold' that stimulates tidal residuals to alter and reverse upper bank migration in the opposite direction. As the analysed bed levels are 'snapshots' at monthly intervals, this threshold angle may vary.

Although the bank alters its migration direction corresponding to a certain slope threshold, the maximum horizontal displacement of the crest, the maximum vertical bed level changes are difficult to quantify, even under pure current conditions. For example, cross-section L30 shows that the lee slope has the ability to reach this threshold angle multiple times during an overall eastward migratory direction over this one-year time period (Figure 6-9(c)). An oscillatory-type upper slope migration exists, whereby multiple 'reversals' in upper slope migration occur in an overall consistently eastward migration. Over this one-year time period, the maximum horizontal displacement along this cross-section is not reached. The timing of this process varies along the length of Sub-cell 3. Detailed analysis of simulated bed levels at each timestep would help to elucidate this process at a finer scale. Furthermore, although sediment transport in this area of the Irish Sea is predominately driven by tidal current, wind and wave conditions are known to influence sediment transport in shallow water; thus, their influence on the east–west fluctuation of the upper bank should be investigated in future studies. Sub-cell 3 is bound to the south by the approximate southern limits of the outer flows of off-bank residual current eddies, Eddy C and D (Figure 6-9(a)).

6.3.2.4 Sub-cell 4

Sub-cell 4 is longitudinally bound between the intersection point of the outer flows of Eddy D and Eddy F, and the approximate centre point of Eddy F (Figure 6-9(a); Figure 6-10(a)). The outer flows associated with the northern half of off-bank Eddy F drive westward and south-westward residual current flow toward the eastern side of the bank, potentially inhibiting the dominant eastward cross-flows originating from the western side of the bank. As a result, this region of the bank is characterised by a very complex morphodynamic and hydrodynamic regime driven by the interaction between this anticlockwise, off-bank residual eddy (Eddy F) on the eastern side of the bank, and the anticlockwise residual partial eddy-type flow (Eddy

G) on the western side of the bank, located between Arklow Bank and Seven Fathom Bank (Figure 6-10(a)). The centre point of Eddy F maintains a relatively stable positioning over the 12-month simulation period. On the other hand, the centre point of the partial eddy, Eddy G, migrates 800 m south-westward from t1mo to t6mo, where it migrates an extra ~100 m in the same direction over the final 6-month time period (Figure 6-10(a)).

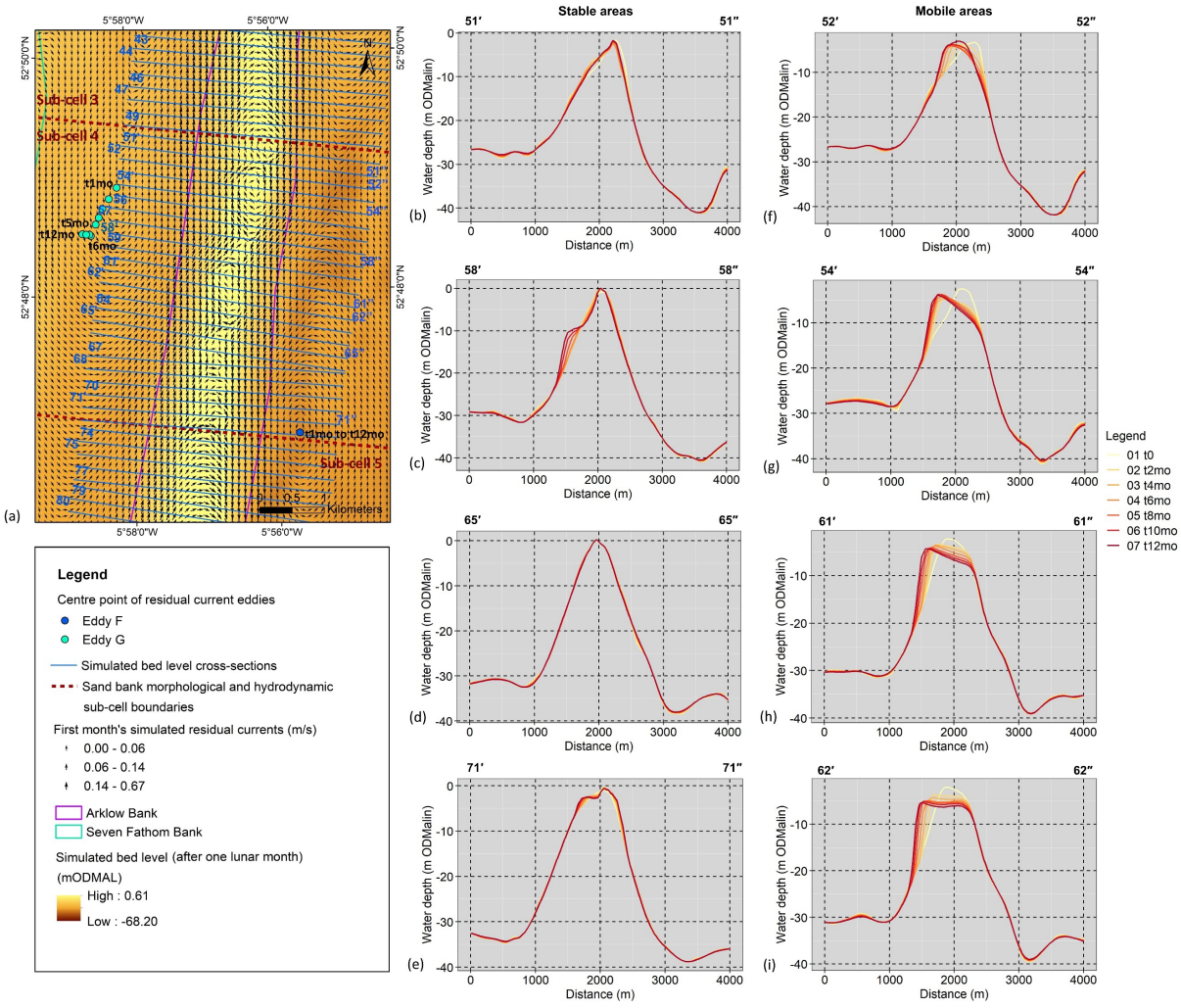


Figure 6-10 Morphodynamics and hydrodynamics at Sub-cell 4 of Arklow Bank. (a) Simulated bed level change after one lunar month and associated residual current vectors, overlain by the location of the centre point of residual eddies from residual currents during each subsequent lunar month simulation; 't6mo' is the sixth lunar simulation month. (b–e) Simulated bed

level over a one year simulation at cross-sections 51, 58, 65 and 71, representing 'stable' areas; 't0' is the starting bed level and 'mo' is subsequent months; (f–i) cross-sections 52, 54, 61 and 62 representing 'mobile' areas.

The line of intersection of Eddy F and Eddy G gives rise to a complex hydrodynamic region of constant and transient on-bank clockwise residual eddies, where the centre point and the intersection point of the individual eddies are dominated by reduced residual current magnitudes and quantity of cross-flow. These points are intermixed with relatively higher eastward and westward residual cross-flows that increase outwards from the centre point of each eddy. This sequence of residual clockwise eddies along this section directly influences the morphodynamics of the bank, where areas displaying a symmetrical bank shape in combination with high upper bank stability and relatively shallow water conditions (ca. <3 mMSL water depth) (Figure 6-10(a)–(e)) alternate with relatively deeper water conditions (ca. >3 mMSL water depth) and lower upper bank stability regions (Figure 6-10(a), (f)–(i)). Most notably, the relatively 'stable' areas over this one-year period are evident in cross-sections L51, L58–59, L64–69 and L71–72 (Figure 6-10(b)–(e)). These areas generally display very shallow morphology and align with the central point or intersections of the on-bank residual eddies. Over this time period, two notable regions show continuously high westward crest migration, geographically located over cross-sections L52–L56 (Figure 6-10(f)–(g)) and L60–L63 (Figure 6-9(h)–(i)). Given the long-term stable positioning of the bank, a longer simulation time period may highlight a threshold, as a result of which the westward crest migration is restricted and a reversal in crest direction is stimulated. In this way, the on-bank residual eddies might shift a few hundred metres to allow bank re-generation until the cycle re-starts.

6.3.2.5 Sub-cell 5

An abrupt change in hydrodynamics and bank morphology is observed at the transition from Sub-cell 4 to Sub-cell 5 (Figure 6-11(a)). Notably, the upper bank deepens, and transitions from a relatively symmetric to eastward asymmetric shape. This asymmetric shape and direction remain relatively stable over the one-year period for approximately 3 km of the bank, with sediment transport only causes minor vertical fluctuations (within $\pm 2\ m$ bed level change) at the crest over the simulation period. This is visible in cross-sections L82-L86 (Figure 6-11(a), (b)).

Modelled current residuals align with these morphological observations, with relatively consistent westward cross-flows noted. This hydrodynamic and morphodynamic consistent zone is pinpointed between the approximate centre point of Eddy F and the intersection of outer flows of Eddy F and Eddy H on the eastern side of the bank (Figure 6-11(a)). The curvilinear southward and south-eastward flows associated with the southern half of Eddy F on the eastern side of the bank generally do not converge against flows coming from the western side of the bank, opposite to that observed in Sub-cell 4. Instead, they align with the westward flows coming from the Seven Fathom Bank, partial Eddy G. In this way, instead of a tidal asymmetric, morphologically 'stable' zone developing along the upper bank, a consistent eastward bank asymmetry and eastward residual cross-flow is evident along this section. This shows that the existence and positioning of the off-bank residual eddies provide a strong control on long-term east–west fluctuation of the bank.

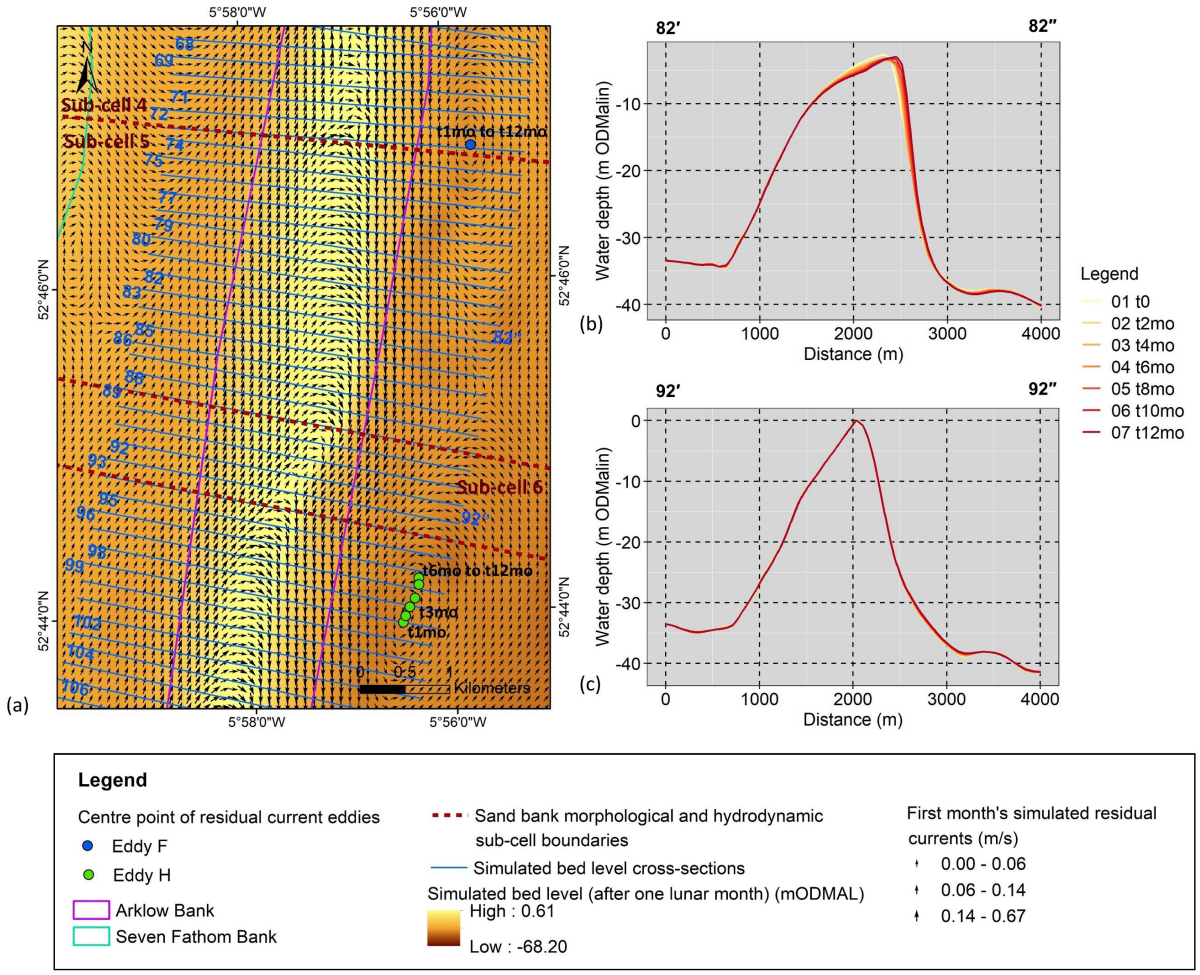


*Figure 6-11 Morphodynamics and hydrodynamics at Sub-cells 5 and 6 of Arklow Bank. (**a**) Simulated bed level change after one lunar month and associated residual current vectors, overlain by the location of the centre point of residual eddies from residual currents during each subsequent lunar month simulation; 't6mo' is the sixth lunar simulation month. (**b**,**c**) Simulated bed level over a one year simulation at cross-sections 82 and 92; 't0' is the starting bed level, and 'mo' is subsequent months.*

6.3.2.6 Sub-cell 6

Similar to Sub-cell 2 and 4, the curvilinear south-westward, south-south-westward and southerly flows associated with the anticlockwise residual eddy, Eddy H, located on the eastern side of the bank, seems to inhibit westward cross-flows coming from the western side of the bank, ultimately generating another morphological 'stable' zone (Figure 6-11(a)). Over the simulation period, the bank retains its symmetrical shape, and little to no crest mobility is evident (see cross-sections L90 to L93) (Figure 6-11(a), (c)). The centre point of Eddy H

remains relatively stable over the simulation period; it migrates northwards 500 m from t1mo to t6mo, where it remains in this position for t6mo to t12mo. This is a similar migratory pattern to Eddy C but in the opposite direction.

6.3.2.7 Sub-cell 7

As the influence of the curvilinear flows from Eddy H on the upper bank is reduced, westward residual current flows dominate once again (Figure 6-12(a)). Westward migration of the upper bank dominates, but evidence of slowed migration and/or slight reversal in migration direction is shown in some areas, for example, cross-section L96 (Figure 6-12(c)). This may be related to the hydrodynamic–morphodynamic response described in other sub-cells of the bank, whereby a maximum slope threshold is reached, which modifies residual current flow dynamics, allowing bank rejuvenation of the bank through sediment accretion build up on the upper slopes and ultimately causing further hydrodynamic modification and a process re-start.

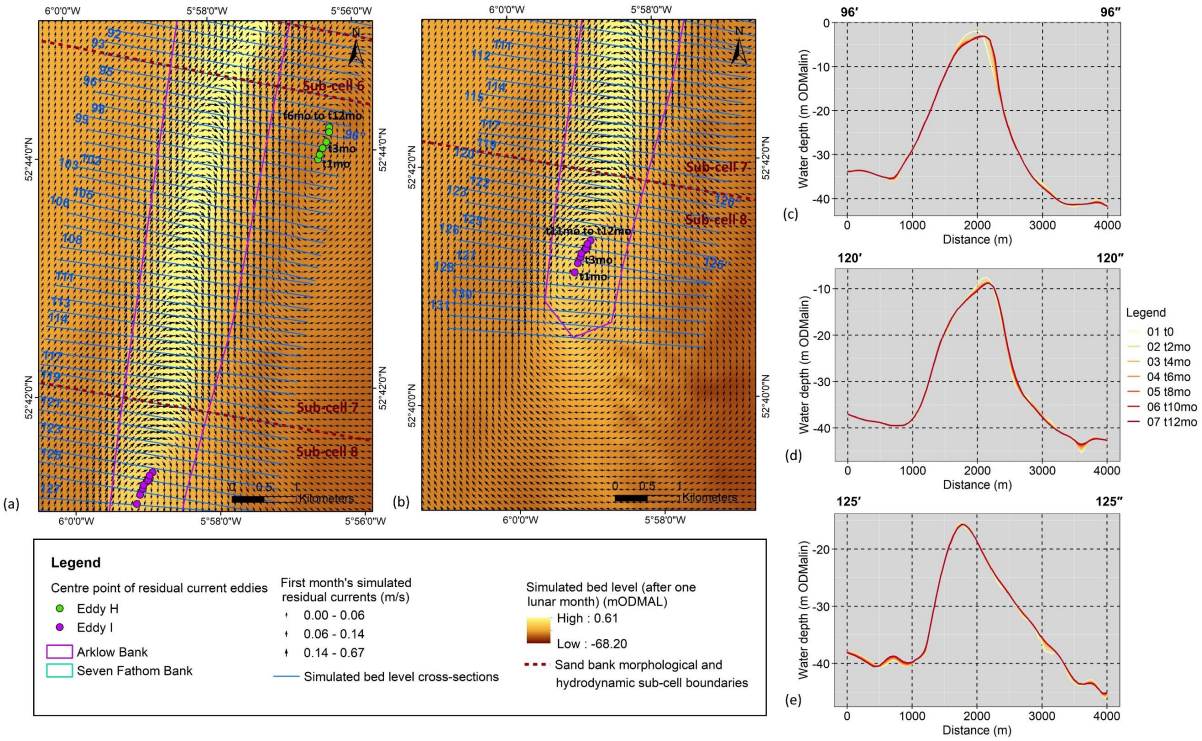


Figure 6-12 Morphodynamics and hydrodynamics at Sub-cells 7 and 8 of Arklow Bank. (a,b) Simulated bed level change after one lunar month and associated residual current vectors, overlain by the location of the centre point of residual eddies from residual currents during each subsequent lunar month simulation; 't6mo' is the sixth lunar simulation month. (c–e) Simulated bed level over a one year simulation at cross-sections 96, 120 and 125; 't0' is the starting bed level, and 'mo' is subsequent months.

6.3.2.8 Sub-cell 8

Sub-cell 8 marks the transition of bank asymmetry from eastward to westward. This transition occurs over an approximate 700 m section of the bank (Figure 6-12(b), (d), (e)). The rest of Sub-cell 8 encompasses the tail of the bank, in which a westward asymmetry dominates. This aligns well with the existence of a clockwise residual current eddy over the southern extent of the bank, hereafter referred to as Eddy I, ultimately connecting the dominant southward flow on the eastern side of the bank with the northern flow on the western side of the bank (Figure 6-12(b)). The turning of the flows in a clockwise motion re-iterates a semi-closed sediment transport regime over the bank. This is combined with a residual current flow

coming from the south-eastern side of the bank and pushing north-westward across the southern tip of the bank and connecting with the residual northward flow on the western side of the bank. This flow acts as an additional sediment source for the bank [8]. The centre point of Eddy I notably migrates approximately 350 m north-eastward from t1mo to t6mo, then 150 m in the same direction over the following 6-month period. The mobility of sediment along the southern extent of the bank is mainly in the form of bed load transport via sand waves [8].

6.3.3 Summary discussion of hydrodynamic controls on Arklow Bank high mobility and bank base stability

As a result of the flood and ebb tidal dominance on the west and east side of the bank, respectively, an overall clockwise residual current eddy encompasses the bank, ultimately recycling sediment material within the bank cell. However, two different phenomena play a role in controlling upper bank mobility and bank base stability: (i) off-bank anticlockwise residual eddies; (ii) on-bank hydrodynamic-morphodynamic response.

The positioning of multiple off-bank anticlockwise residual eddies both facilitate and inhibit east–west fluctuation of the bank and act as a control on long-term base stability. They do this in two ways: firstly, when the outer flows of the residual eddy on the eastern side of the bank are in a west to south-westward direction, these converge with residual eastward cross-flows coming from the western side of the bank. This generates a zone of absent or reduced residual cross-flow, inhibiting the mobility of the upper slopes of the bank and preserving bank base stability. Secondly, when outer flows of the residual eddy on the eastern side of the bank are in a south-east to eastward direction, these align with residual cross-flows

coming from the western side of the bank instead of converging with them. This facilitates upper slope mobility.

In the case of this second mechanism, the control on the maximum limit or 'threshold' of east–west fluctuation, and thus base bank stability, is the on-bank hydrodynamic-morphodynamic feedback loop. This occurs in two forms:

1. a morphodynamic–hydrodynamic feedback loop allowing the generation of a conveyor belt of on-bank residual eddies and/or stationary transient residual eddies, continuously influencing east–west fluctuation of the bank;
2. the reduction and expansion of residual current cross-flow, ultimately allowing the regeneration of the bank after a certain slope threshold has been reached.

The positioning of these off-bank anticlockwise residual current eddies on the outer edge of the larger clockwise eddy encompassing the entire bank, facilitates sediment transfer in and out of the local morphological cell. An overview of each morphological sub-cell and controlling hydrodynamic processes are summarised in Figure 6-13.

This new process-based understanding of Arklow Bank's complex hydrodynamic and morphodynamic regime can be used to guide the planning of offshore fieldwork to measure these morphological changes across the bank, thus improving the predictability of seabed level change in this region. This is crucial for the accurate and detailed design of OWF turbine foundations, cables and associated protection structures on and surrounding this bedform. Furthermore, by elucidating the baseline processes that maintain long-term seabed stability, this improves the ability to assess the risk of environmental instability due to future increased anthropogenic seabed disturbances in the south-western Irish Sea.

On a wider scale, this new comprehension of the hydrodynamic processes controlling bedform mobility has potential applicability to other offshore linear sand banks in tidally dominated shelf sea environments [9], [23], [35]–[37]. If proven similar, the outcomes of this study may re-define how these sand bank systems are analysed. Consequently, using similar methods as applied in this study to investigate the applicability of these controlling phenomena on other sand bank systems is imperative.

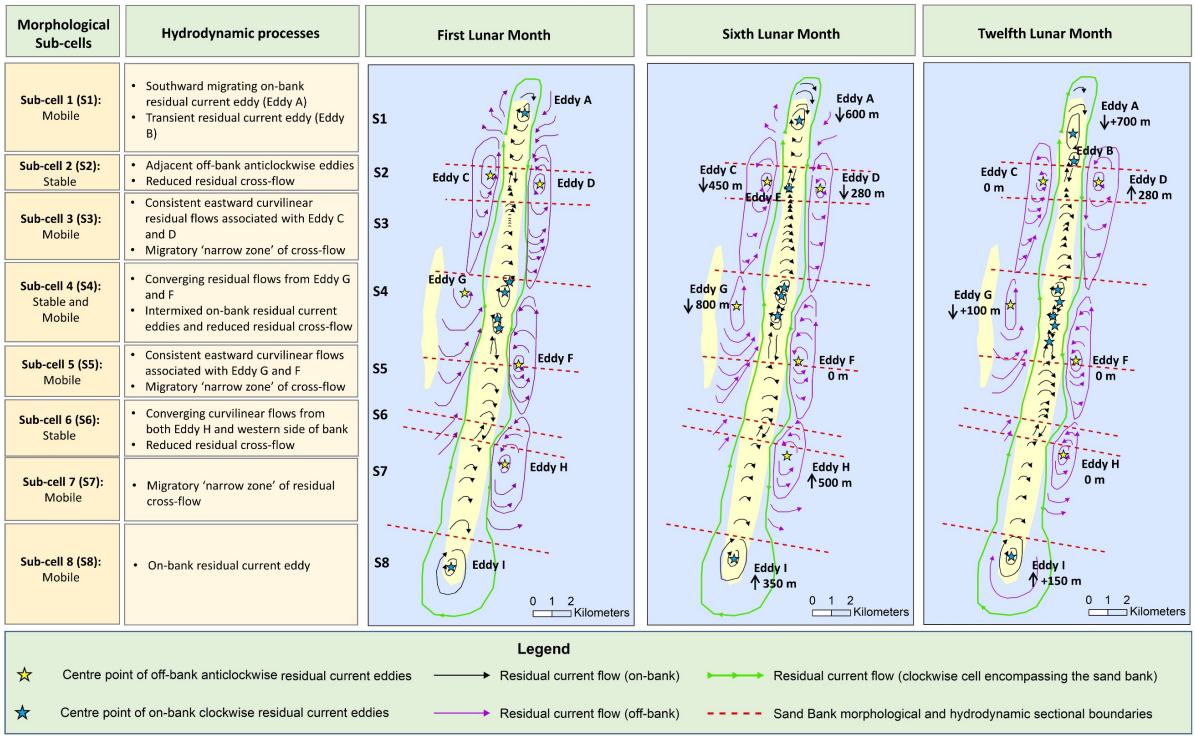


Figure 6-13 A schematic diagram summarising the hydrodynamic processes driving Arklow Bank's upper slope mobility and bank base stability.

6.4 Conclusions

This study uses a two-dimensional, dynamically coupled, hydrodynamic and sediment transport numerical model to investigate the hydrodynamic processes driving the morphodynamics of the offshore linear sand bank, Arklow Bank. Over a one-year simulation period, combined analysis of numerically modelled residual currents and bed levels elucidates

the complex interconnected hydrodynamic and sediment transport regime in this area of the south-western Irish Sea. Ultimately, this study aims to define the hydrodynamic processes controlling morphodynamic variability and long-term stable positioning of Arklow Bank over time. The main conclusions drawn from this study are provided below.

1. A flood and ebb tidal dominance is evident on the west and east side of the bank, respectively, generating a residual clockwise tidal current eddy encompassing the entire bank. This ultimately recycles sediment material within the bank cell.
2. During an individual flood and ebb tide, sediment on the upper slopes is transported eastward and westward respectively along the full length of the bank due to the directional nature of tidal current cross-flow during these tidal phases. From a full semi-diurnal tidal cycle (divided into two flood and two ebb tidal phases) onwards, a variation in the direction of tidal asymmetry along the upper slopes of the bank is evident. This divides the bank into a variety of morphological sections migrating in different directions.
3. Eight unique sub-cells of the bank are identified whereby a complex morphological-hydrodynamic feedback system is evident. These individual sub-cells display a variety of on-bank and off-bank hydrodynamic and morphological features yet fit together as one linear offshore sand bank, with high upper slope mobility and long-term bank base stability. The two main tidal phenomena that control upper bank mobility and bank base stability are (i) off-bank anticlockwise residual eddies and (ii) on-bank hydrodynamic–morphodynamic response.
4. The positioning of multiple off-bank anticlockwise residual current eddies on the edge of this cell is shown to influence east–west fluctuations of the upper slopes of the sand bank and act as a control of long-term stability. These off-bank eddies facilitate this

type of movement when the outer flows of adjacent eddies, located on both sides of the bank, flow in a generally uniform direction. Whereas they inhibit this east–west movement when the outer flows of adjacent eddies, on either side of the bank, flow in converging directions towards the bank itself. Off-bank anticlockwise eddies also facilitate sediment transport in and out of the local morphological cell.

5. The control of the maximum limit of upper bank east–west fluctuation is the on-bank hydrodynamic-morphodynamic feedback loop through (i) the formation of migratory and stationary transient on-bank clockwise residual tidal current eddies and (ii) the formation of transient 'narrow' residual tidal current cross-flow zones.
6. The concept of a 'threshold slope angle' is also introduced. When the upper slopes of the bank reach a certain threshold angle, a hydrodynamic response is stimulated that reverses upper bank migration in the opposite direction. By taking into consideration this concept in conjunction with the identified controlling hydrodynamic processes, analysis of this system at a higher temporal scale and over a longer time period could help determine the maximum limits of vertical and horizontal bed level changes along the bank, as well as the rate and frequency at which these limits are reached. The information provided in this study can be used to guide offshore survey planning for existing and planned OWF projects in order to measure these morphological changes on Arklow Bank. The details provided in this study can reduce costs for such an expedition.
7. The new process-based understanding of Arklow Bank's complex hydrodynamic and morphodynamic regime introduced in this study aids the predictability of future seabed level changes in this highly mobile sand-dominated environment. Where the maximum bed level change over a one-month period along the bank is +7.3 m to −3.4

m, the magnitude and rate of bed level change varies hugely along the length of the bank. This highlights the need for careful selection of scour and bed level change mitigation strategies for each potential wind turbine generator (WTG) position. Resultingly, the information provided in this study not only informs offshore geophysical survey design to confirm these modelled morphological changes but also informs concept layout design and foundation design.

8. This comprehension of Arklow Bank's morphodynamic system has the potential to re-define how we analyse offshore linear sand banks. Consequently, the methods used in this study should be applied to offshore linear sand banks in other tidally dominated environments to investigate this wider connection.

6.5 Acknowledgments

SC is funded by the Irish Research Council (IRC) through grant EBPPG/2019/158 (Employment-Based Postgraduate Programme Scholarship). MC is funded under an Irish Research Council Enterprise Partnership Scheme Postdoctoral Fellowship (EPSPD/2020/109) and in part by a research grant from Science Foundation Ireland (SFI) under Grant Number 13/RC/2092, with support from Gavin and Doherty Geosolutions Ltd and the Geological Survey of Ireland (GSI). This project benefitted from funded industry-academic collaboration involving Gavin and Doherty Geosolutions, University College Dublin (iCRAG) and University College Cork (MaREI), supported by the Marine Institute under the Marine Research Programme 2014-2020 (Grant-Aid Agreement No. IND/18/18). Ship time on the RV Celtic Voyager was funded by the Marine Institute through the 2020-2021 ship-time programme under the National Marine Research and Innovation Strategy 2017-2021.

6.6 Author Contributions

Shauna Creane: Conceptualization, Methodology, Investigation, Formal analysis, Writing – original draft, Writing – review & editing, Visualisation

Michael O'Shea: Supervision, Conceptualization, Writing – review & editing

Mark Coughlan: Supervision, Investigation, Writing – review & editing

Jimmy Murphy: Supervision, Conceptualization, Writing – review & editing

6.7 Supplementary Material: Numerical Modelling

6.7.1 Hydrodynamic Model

The two-dimensional (2D) hydrodynamic model covering the entire Irish Sea developed in Coughlan et al [15] was used in this study. This 2D model was updated with additional geophysical datasets, a new refined mesh was implemented, and a new validation point was utilised. The full set-up, extent and validation details of the original pure hydrodynamic model is presented in Coughlan et al [15] whilst new updates and modifications to the model setup are outlined in Creane et al [33].

The MIKE 21 hydrodynamic model [32] determines bottom shear stress, τ_b, by quadratic friction law:

$$\tau_b = C_d \rho \overline{U}^2$$

Where C_d is a drag coefficient, ρ is the density of the fluid medium in seawater and $\overline{U}$ is the depth averaged velocity. The drag coefficient is determined as;

$$C_d = \frac{g}{(Mh^{1/6})^2}$$

Where h is the total water depth and g is the acceleration due to gravity and M is the Manning number. The original model uses a constant M for bed friction of $32\ m^{\frac{1}{3}}$ over the entire model domain. The updated model retains a constant M for bed friction of $32\ m^{\frac{1}{3}}$ over majority of the model domain, but M is decreased up to $10\ m^{\frac{1}{3}}$ along the boundaries. Due to the updates on the original model, the calibration of the model was checked at various locations and new validation statistics were generated. Full validation results are outlined in Creane et al [33] and are summarised in section 6.7.1.1.

6.7.1.1 Model Validation

Water levels were re-assessed using data from eight tide gauges along the Irish Sea coast, and from four Acoustic Doppler Current Profilers (ADCPs) located off the south-east coast of Ireland (Figure 6-3). A strong positive correlation was evident between all measured and simulated water levels where the average correlation coefficient across all locations was 0.99.

Similarly, simulated current speeds and directions were re-assessed against measured data at four locations, including a new ADCP dataset labelled 'Arklow' in Creane et al [33] collected at 52.72153°, -6.0278°. Generally, a strong positive correlation was evident with correlation coefficients ranging from 0.84 to 0.95. Example validation plots are provided in Figure 6-14 whereby full validation results are detailed in Creane et al [33].

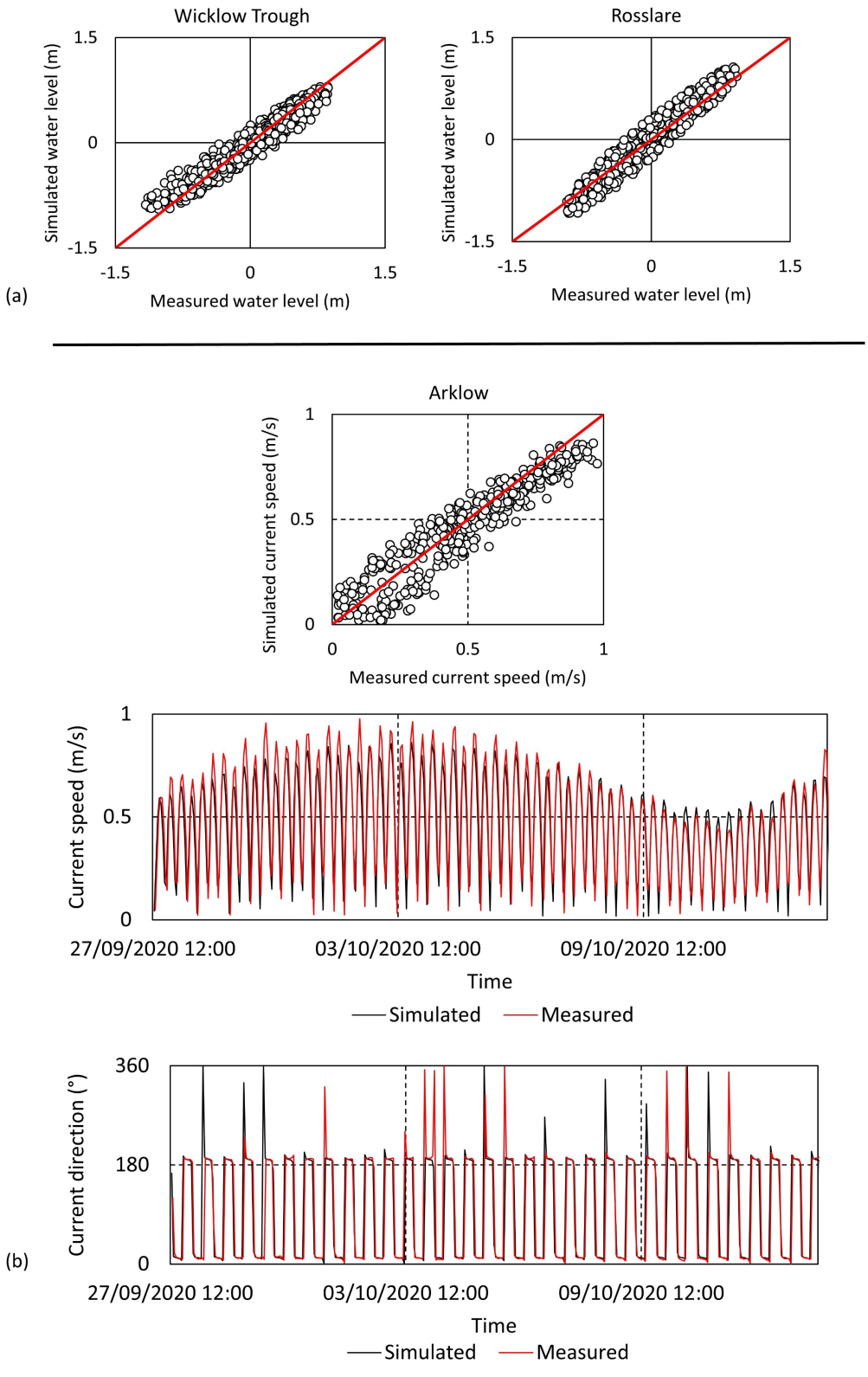


Figure 6-14 Comparison between measured and simulated (a) water levels from Wicklow Trough ADCP (52.95601°, −5.90135°) and Rosslare tide gauge (52.254600°, −6.334861°), and (b) current speed and directions from Arklow ADCP (52.72153°, -6.0278°). Data source: Creane et al [33].

6.7.2 ST modelling set-up

The MIKE 21 sand transport module [31], [38] was used to calculate the sediment transport rates of non-cohesive sediment under 'pure current' whereby the effects due to wind and wave forcing are not included. The mesh used in the simulation of the sand transport rates is the same as that is used to calculate the flow field in the hydrodynamic model (section 6.2). A coupled morphological model was generated, whereby the governing equations for flow and sediment transport are merged into a set of equations, which are solved simultaneously. Coupling the hydrodynamic and sand transport modules in this way allowed morphological development to be captured by updating the bathymetry for every time step with the net sedimentation:

$$Z^{n+1} = Z^n + \Delta z^n$$

Where Z^n is the bathymetry level at present time step, Z^{n+1} is the bathymetry level at the next time step, Z^{n+1} is net sedimentation at present time step, and n is time step. Further details are presented in the MIKE 21 sand transport manual [31]. The key parameter for determination of bed level changes is the rate of bed level change, $\frac{\partial z}{\partial t}$, at the element cell centres. This parameter is based on the Exner equation, or sediment continuity equation, written as:

$$-(1-n)\frac{\partial z}{\partial t} = \frac{\partial S_x}{\partial x} + \frac{\partial S_y}{\partial y} - \Delta S$$

Where n is bed porosity, z is bed level, t is time, S_x is bed load or total load transport in the x direction, S_y is bed load or total load transport in the y direction, x and y are horizontal cartesian coordinates, and ΔS is sediment sink or source rate. For a non-equilibrium model such as this, the sediment sink/source term can be written as

$$\Delta S = \varphi_0(\eta_0) w_s (c - c_e)$$

Where η_0 is normalised no slip level above the bed, φ_0 is unit profile function for the sediment concentration, w_s is settling velocity for the suspended sediment, c is depth-averaged sediment concentration, and c_e is depth-averaged equilibrium concentration. The bed is updated continuously through a morphological simulation (at every HD-time step, in this case 30 second intervals) based on the estimated bed level change rates. The initial bed thickness of the erodible bed was designated as constant and unlimited throughout the model domain. Slope failure is not included in this morphological model.

The pure current sediment transport theory used in this model was the Engelund and Hansen [39] total-load transport theory. The model by Engelund and Hansen [39] is a total load model that needs user-specified information in order to divide the total load S_{tl} sediment transport into bed load S_{bl} and suspended load S_{sl} transport rates (m²/s) [31]. Transport rates are obtained from the relations:

$$S_{bl} = k_b S_{tl}$$

$$S_{sl} = k_s S_{tl}$$

Whereby k_b and k_s are user defined bed load calibration factor and suspended load calibration factor respectively. In this case, both parameters are kept as the default value of 1. Total sediment transport is obtained by:

$$S_{tl} = 0.05 \frac{C^2}{g} \theta^{\frac{5}{2}} \sqrt{(s-1) g D_{50}^3}$$

Where the Shields parameter θ is defined as

$$\theta = \frac{\tau}{\rho g(s-1)D_{50}}$$

Where τ is the flow shear stress, ρ is density of water, g is the acceleration due to gravity, s is ρ/ρ_s relative density of sediment and ρ_s is density of sediment. C is the Chezy number and D_{50} is the median grain size. Flow shear stress is divided into form drag τ'' and skin friction τ'. The total shear stress $\tau' + \tau''$ is estimated from the local flow velocity V and the local Chezy number C:

$$\tau = \rho g \frac{V^2}{C^2}$$

For skin friction the following approximate friction formula is applied

$$\theta' = 0.06 + 0.4\theta^2$$

Sediment density and porosity were defined as constant 2.65 and 0.40 respectively.

The equilibrium mass concentration (c_e) (g/m³) is calculated as the suspended load divided by the water flux and converted from volumetric concentration to mass concentration [31]:

$$c_e = \frac{S_{sl}}{Vh} s 10^6$$

Where V is velocity (m/s) and h is water depth.

The following correction is applied to account for the slope effect on the sediment transport rate:

$$S_s = \left(1 - \alpha \frac{\partial z_b}{\partial s}\right) S_{bl}$$

Where z_b is bed level, s is stream-wise (horizontal) coordinate, α is model calibration parameter, S_s is bed load along streamline, s, and S_{bl} is bed load as calculated from sediment transport formula [31].

A varying grain diameter (D_{50}) map was defined for the model domain comprising both surficial and synthetic sediment samples. Surficial sediment samples were collected using either a Day Grab sampler or the Shipek sampler during four MOVE offshore survey campaigns in September 2020 (CV20010), September/October 2020 (CV2036), March 2021 (CV21035) and December 2021 (CV21034). All sediment samples were processed by sieving or laser granulometry. Furthermore, sediment samples containing raw granulometric data was compiled from Geological Survey of Ireland (GSI). The MOVE and GSI datasets were combined, and statistical analysis was carried out using the R package 'geotech' [40].

Due to limited grain size availability outside our area of interest, the synthetic sand D_{50} dataset produced by Wilson et al [41] was utilised. This dataset was clipped to represent the model domain beyond the -70 m contour line extending geographically from Carnsore Point (52.17056°, -6.355278°) to Skerries (53.58389°, -6.101111°). This was to ensure mostly in situ measured grab samples would represent the south-western Irish Sea. A number of artificial D_{50} values were also placed in the target area using combined analysis of bathymetry, backscatter, surrounding D_{50} values and the EMODnet seabed substrate map. These artificial samples were placed in areas where a significant deficit of measured samples was evident in order to produce the most realistic interpolated dataset when comparing against coarse seabed substrate maps such as the EMODnet seabed substrate map [34].

6.7.2.1 Suspended sediment model validation at various points in the model domain

Using an ADCP dataset collected at 52.72153°, -6.0278°, Creane et al [33] produces a robust spatial timeseries of ADCP-based SSC_{solids} where the correlation coefficient between estimated SSC_{solids} and directly measured SSC_{solids} is 0.87. Combining this dataset with other ADCP outputs and water-sampled-based SSC_{solids}, Creane et al [33] successfully validates the suspended sediment transport component of the 2D model at multiple locations off the east coast of Ireland to a relatively high accuracy given underlying assumptions of the model, using three out of four tested validation techniques (Technique 1, 2 and 4). The location of these validation points includes all 'water sample' data points and the ADCP located on the western side of Arklow Bank shown in Figure 6-3(b) of the main article. The model validation techniques used include; i) validation of 2D modelled suspended sediment concentration ($SSC_{sediment}$) using water sample-based SSC_{solids} (Technique 1), ii) validation of the flood-ebb characteristics of 2D modelled suspended load transport and $SSC_{sediment}$ using ADCP-based datasets (Technique 2) and iii) validation of the 2D modelled peak $SSC_{sediment}$ over a spring-neap cycle using the ADCP-based SSC_{solids} (Technique 4). Full details are outlined in Creane et al [33] and a summary of the results is provided below:

Technique 1: Validation of 2D modelled modelled $SSC_{sediment}$ using water sample-based SSC_{solids}

This involves the comparison between modelled $SSC_{sediment}$ and directly measured SSC_{solids} collected via water sampling at four stations non-associated with ADCP deployments. This technique displays very good validation results and is recommended to combine with technique 2 and 4. An example comparison at one location is provided in Figure 6-15.

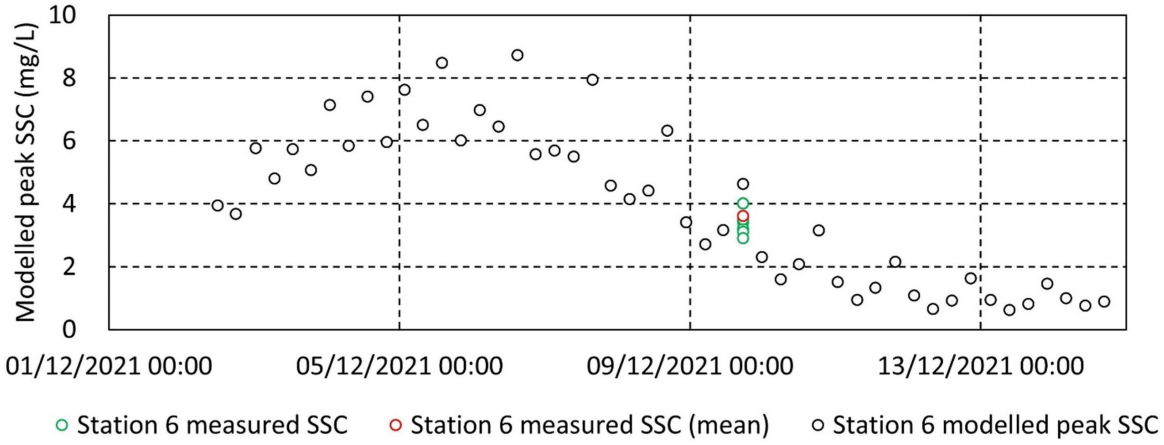


Figure 6-15 Comparison of 2D modelled peak $SSC_{sediment}$ against measured SSC_{solids} samples at sampling station 6 (-5.953°, 52.551°). Data source: Creane et al [33].

Technique 2: Validation of the flood-ebb characteristics (tidal asymmetry) of (i) 2D modelled suspended load transport and (ii) $SSC_{sediment}$, using ADCP-based datasets

Measured currents from the ADCP exhibit a flood-dominant tidal current direction. Both modelled residual tidal current and residual suspended load transport agree with the nature of this tidal asymmetry [33]. This provides a high degree of confidence for the directional component of modelled suspended sediment transport at this location.

In parallel, the ADCP-based SSC_{solids} spatial timeseries can be used as a calibration/validation technique for the relative magnitude of modelled $SSC_{sediment}$ in the water column over a flood-ebb tidal cycle. The bottom-water, mid-water, surface-water and depth-averaged ADCP-based SSC_{solids} datasets were analysed alongside the measured current speeds and directions. All four datasets show a higher concentration of SSC_{solids} in the water column for a higher percentage of time during the flood tide in comparison to the ebb tide. This is a direct consequence of the flood-dominance nature of the tide. When analysing modelled $SSC_{sediment}$ alongside modelled current speeds and directions, there is a very good agreement with this asymmetrical tide-SSC relationship whereby a higher concentration of

$SSC_{sediment}$ is present in the water column over flood tide (N – NNE) in comparison to ebb tide (S – SSW).

Technique 4: Validation of the 2D modelled peak $SSC_{sediment}$ over a spring-neap cycle using ADCP-based SSC_{solids}

A strong positive correlation exists between the depth-averaged SSC_{solids} and modelled peak $SSC_{sediment}$, where R is 0.82 (Figure 6-16). The relationship between these modelled values and the mid-water ADCP based SSC_{solids} is strong positive, where R is 0.81.

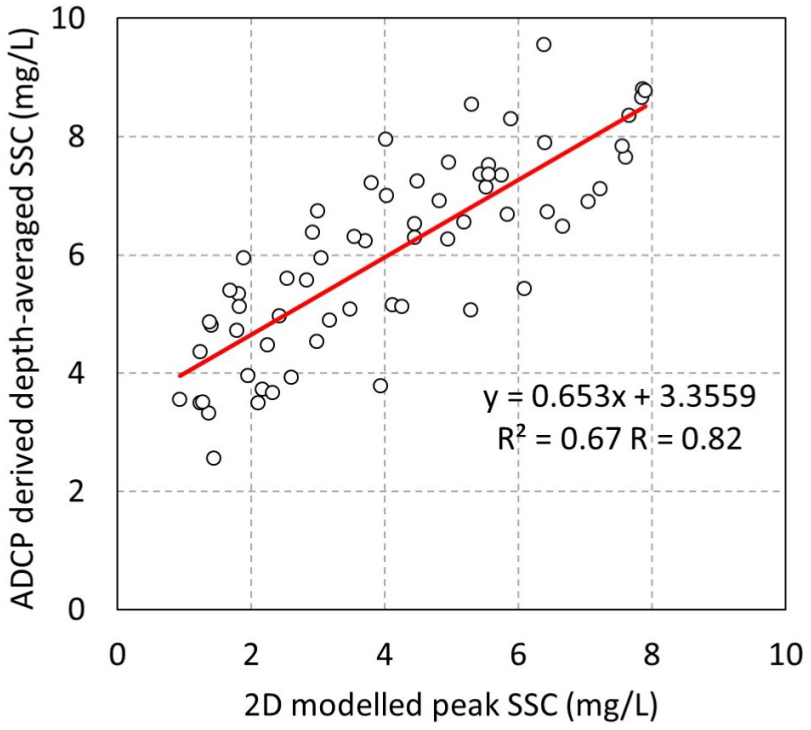


Figure 6-16 Correlation between 2D modelled peak $SSC_{sediment}$ and ADCP-based depth-averaged SSC_{solids} . Data source: Creane et al [33].

6.8 References

[1] S. Creane, M. O'Shea, M. Coughlan, and J. Murphy, "Hydrodynamic processes controlling sand bank mobility and long-term base stability: A case study of Arklow Bank," *Geosciences*, vol. 13, no. 2, p. 60, 2023, doi: 10.3390/geosciences13020060.

[2] J. R. Ellis, T. Maxwell, M. Schratzberger, and S. I. Rogers, “The benthos and fish of offshore sandbank habitats in the southern North Sea,” *Journal of the Marine Biological Association of the United Kingdom*, vol. 91, no. 6, pp. 1319–1335, 2011, doi: 10.1017/S0025315410001062.

[3] A. F. Sell and I. Kröncke, “Correlations between benthic habitats and demersal fish assemblages - A case study on the Dogger Bank (North Sea),” *Journal of Sea Research*, vol. 80, pp. 12–24, 2013, doi: 10.1016/j.seares.2013.01.007.

[4] T. A. G. P. van Dijk, J. A. van Dalfsen, V. Van Lancker, R. A. van Overmeeren, S. van Heteren, and P. J. Doornenbal, “Benthic Habitat Variations over Tidal Ridges, North Sea, the Netherlands,” in *Seafloor Geomorphology as Benthic Habitat*, P. T. Harris and E. K. Baker, Eds. London: Elsevier, 2012, pp. 241–249. doi: https://doi.org/10.1016/B978-0-12-385140-6.00013-X.

[5] A. F. Velegrakis, A. Ballay, S. Poulos, R. Radzevičius, V. Bellec, and F. Manso, “European marine aggregates resources: Origins, usage, prospecting and dredging techniques,” *Journal of Coastal Research*, no. 51, pp. 1–14, 2010, doi: 10.2112/SI51-002.1.

[6] L. Wyns, M. Roche, F. Barette, V. Van Lancker, K. Degrendele, K. Hostens, and A. De Backer, “Near-field changes in the seabed and associated macrobenthic communities due to marine aggregate extraction on tidal sandbanks: A spatially explicit bio-physical approach considering geological context and extraction regimes,” *Continental Shelf Research*, vol. 229, p. 104546, 2021, doi: 10.1016/j.csr.2021.104546.

[7] RPS, “Arklow Bank Wind Park Phase 2 Offshore Infrastructure: Environmental Impact

Assessment Report - Appendix 3.1: Consultation Report," 2021.

[8] S. Creane, M. Coughlan, M. O'Shea, and J. Murphy, "Development and dynamics of sediment waves in a complex morphological and tidal dominant system: southern Irish Sea," *Geosciences*, vol. 12, no. 12, p. 46, 2022, doi: 10.3390/geosciences12120431.

[9] K. R. Dyer and D. A. Huntley, "The origin, classification and modelling of sand banks and ridges," *Continental Shelf Research*, vol. 19, no. 10, pp. 1285–1330, 1999, doi: 10.1016/S0278-4343(99)00028-X.

[10] S. L. Bradley, G. A. Milne, I. Shennan, and R. Edwards, "An improved glacial isostatic adjustment model for the British Isles," *Journal of Quaternary Science*, vol. 26, no. 5, pp. 541–552, 2011, doi: 10.1002/jqs.1481.

[11] J. D. Scourse, S. L. Ward, A. Wainwright, S. L. Bradley, and K. Uehara, "The role of megatides and relative sea level in controlling the deglaciation of the British–Irish and Fennoscandian ice sheets," *Journal of Quaternary Science*, vol. 33, no. 2, pp. 139–149, 2018, doi: 10.1002/jqs.3011.

[12] K. Uehara, J. D. Scourse, K. J. Horsburgh, K. Lambeck, and A. P. Purcell, "Tidal evolution of the northwest European shelf seas from the Last Glacial Maximum to the present," *Journal of Geophysical Research: Oceans*, vol. 111, no. 9, pp. 1–15, 2006, doi: 10.1029/2006JC003531.

[13] S. L. Ward, S. P. Neill, J. D. Scourse, S. L. Bradley, and K. Uehara, "Sensitivity of palaeotidal models of the northwest European shelf seas to glacial isostatic adjustment since the Last Glacial Maximum," *Quaternary Science Reviews*, vol. 151,

pp. 198–211, 2016, doi: 10.1016/j.quascirev.2016.08.034.

[14] S. Creane, M. O'Shea, M. Coughlan, and J. Murphy, "The Irish Sea bed load parting zone: Is it a mid-sea hydrodynamic phenomenon or a geological theoretical concept?," *Estuarine, Coastal and Shelf Science*, vol. 263, p. 107651, 2021, doi: 10.1016/j.ecss.2021.107651.

[15] M. Coughlan, M. Guerrini, S. Creane, M. O'Shea, S. L. Ward, K. J. J. Van Landeghem, J. Murphy, and P. Doherty, "A new seabed mobility index for the Irish Sea: modelling seabed shear stress and classifying sediment mobilisation to help predict erosion, deposition, and sediment distribution," *Continental Shelf Research*, vol. 229, p. 104574, 2021, doi: https://doi.org/10.1016/j.csr.2021.104574.

[16] K. J. J. Van Landeghem, J. H. Baas, N. C. Mitchell, D. Wilcockson, and A. J. Wheeler, "Reversed sediment wave migration in the Irish Sea, NW Europe: A reappraisal of the validity of geometry-based predictive modelling and assumptions," *Marine Geology*, vol. 295–298, pp. 95–112, 2012, doi: 10.1016/j.margeo.2011.12.004.

[17] K. J. J. Van Landeghem, K. Uehara, A. J. Wheeler, N. C. Mitchell, and J. D. Scourse, "Post-glacial sediment dynamics in the Irish Sea and sediment wave morphology: Data-model comparisons," *Continental Shelf Research*, vol. 29, no. 14, pp. 1723–1736, 2009, doi: 10.1016/j.csr.2009.05.014.

[18] K. J. J. Van Landeghem, A. J. Wheeler, N. C. Mitchell, and G. Sutton, "Variations in sediment wave dimensions across the tidally dominated Irish Sea, NW Europe," *Marine Geology*, vol. 263, no. 1–4, pp. 108–119, 2009, doi: 10.1016/j.margeo.2009.04.003.

[19] J. K. Panigrahi, P. N. Ananth, and P. A. Umesh, “Coastal morphological modeling to assess the dynamics of Arklow Bank, Ireland,” *International Journal of Sediment Research*, vol. 24, no. 3, pp. 299–314, 2009, doi: 10.1016/S1001-6279(10)60005-4.

[20] C. K. Wentworth, “A Scale of Grade and Class Terms for Clastic Sediments,” *The Journal of Geology*, vol. 30, no. 5, pp. 377–392, 1922, doi: 10.1086/622910.

[21] J. M. Harris, R. J. S. Whitehouse, and J. Sutherland, “Marine scour and offshore wind - Lessons learnt and future challenges,” in *Proceedings of the International Conference on Offshore Mechanics and Arctic Engineering - OMAE*, 2011, vol. 5, pp. 849–858. doi: 10.1115/OMAE2011-50117.

[22] R. J. S. Whitehouse, J. M. Harris, J. Sutherland, and J. Rees, “The nature of scour development and scour protection at offshore windfarm foundations,” *Marine Pollution Bulletin*, vol. 62, no. 1, pp. 73–88, 2011, doi: 10.1016/j.marpolbul.2010.09.007.

[23] H. Park and C. E. Vincent, “Evolution of Scroby Sands in the East Anglian coast , UK,” *Journal of Coastal Research*, pp. 868–873, 2007.

[24] J. M. Horrillo-Caraballo, Y. Yin, I. Fairley, H. Karunarathna, I. Masters, and D. E. Reeve, “A comprehensive study of the tides around the Welsh coastal waters,” *Estuarine, Coastal and Shelf Science*, vol. 254, p. 107326, 2021, doi: 10.1016/j.ecss.2021.107326.

[25] P. T. Harris, C. B. Pattiaratchi, M. B. Collins, and R. W. Dalrymple, “What is a bedload parting?,” in *Tidal signatures in modern and ancient sediments*, B. W. Flemming and A. Bartholoma, Eds. 1995. doi: 10.1002/9781444304138.ch1.

[26] R. D. Pingree and D. K. Griffiths, “Sand transport paths around the British Isles

resulting from M2 and M4 tidal interactions," *Journal of the Marine Biological Association of the United Kingdom*, vol. 59, no. 2, pp. 497–513, 1979, doi: https://doi.org/10.1017/S0025315400042806.

[27] T. Roetert, T. Raaijmakers, and B. Borsje, "Cable route optimization for offshore wind farms in morphodynamic areas," in *Proceedings of the 27th International Offshore and Polar Engineering Conference*, 2017, pp. 595–606.

[28] T. Fazeres-Ferradosa, J. Chambel, F. Taveira-Pinto, P. Rosa-Santos, F. V. C. Taveira Pinto, G. Giannini, and P. Haerens, "Scour protections for offshore foundations of marine energy harvesting technologies: A review," *Journal of Marine Science and Engineering*, vol. 9, no. 3, 2021, doi: 10.3390/jmse9030297.

[29] D. T. Pugh, "Tidal amphidrome movement and energy dissipation in the Irish Sea," *Geophysical Journal of the Royal Astronomical Society*, vol. 67, no. 2, pp. 515–527, 1981, doi: 10.1111/j.1365-246X.1981.tb02763.x.

[30] EMODnet Bathymetry Consortium, "EMODnet Digital Bathymetry (DTM 2020)." 2020. doi: https://doi.org/10.12770/bb6a87dd-e579-4036-abe1-e649cea9881a.

[31] DHI Group, "MIKE 21 & MIKE 3 Flow Model FM Sand Transport Module Scientific Documentation." 2017.

[32] DHI Group, "MIKE 21 Flow Model: Hydrodynamic Module User Guide." 2017.

[33] S. Creane, M. O'Shea, M. Coughlan, and J. Murphy, "Estimation of suspended solids concentration from Acoustic Doppler Current Profiler in a tidally-dominated continental shelf sea setting and its use as a numerical modelling validation technique," *Coastal Engineering*.

[34] EMODnet Geology, “Seabed Substrates,” 2019. https://www.emodnet-geology.eu/data-products/seabed-substrates/

[35] M. A. Johnson, N. H. Kenyon, R. H. Belderson, and A. H. Stride, “Sand transport,” in *Offshore Tidal Sands: Processes and Deposits*, A. H. Stride, Ed. Chapman and Hall, 1982, pp. 58–94. doi: 10.1007/978-94-009-5726-8_4.

[36] M. B. Collins, S. J. Shimwell, S. Gao, H. Powell, C. Hewitson, and J. A. Taylor, “Water and sediment movement in the vicinity of linear sandbanks: the Norfolk Banks, southern North Sea,” *Marine Geology*, vol. 123, no. 3–4, pp. 125–142, 1995, doi: 10.1016/0025-3227(95)00010-V.

[37] A. H. Stride, “Offshore tidal deposits: sand sheet and sand bank facies,” in *Offshore Tidal Sands: Processes and Deposits*, A. H. Stride, Ed. Dordrecht: Springer, 1982, pp. 95–125. doi: 10.1007/978-94-009-5726-8_5.

[38] DHI Group, “MIKE 21 FLOW MODEL FM: Sand Transport Module, incl. Shoreline Morphology - User Guide.” 2017.

[39] F. Engelund and E. Hansen, “A monograph on sediment transport in alluvial streams,” Teknisk Forlag, Copenhagen, Denmark, 1967.

[40] J. Kaklamanos and K. Elmy, “R Package ‘geotech,’” 2016.

[41] R. J. Wilson, D. C. Speirs, A. Sabatino, and M. R. Heath, “A synthetic map of the north-west European Shelf sedimentary environment for applications in marine science,” *Earth System Science Data*, vol. 10, no. 1, pp. 109–130, 2018, doi: 10.5194/essd-10-109-2018.

7 Morphological modelling to investigate the role of external sediment sources, and wind and waves-induced flow on sand bank sustainability: An Arklow Bank case study

Morphological modelling to investigate the role of external sediment sources, and wind and wave-induced flow on sand bank sustainability: An Arklow Bank case study

Shauna Creane[1,2,3], Michael O'Shea[1,2], Mark Coughlan[4,5,3], Jimmy Murphy[1,2]

[1]School of Civil & Environmental Engineering, University College Cork, College Road, T12 K8AF Cork, Ireland; shauna.creane@ucc.ie (S.C.); michaeloshea@ucc.ie (M.O.); jimmy.murphy@ucc.ie (J.M.)

[2]SFI Research Centre for Energy, Climate and Marine (MaREI), Beaufort Building, Environmental Research Institute, University College Cork, Ringaskiddy, P43 C573 Cork, Ireland

[3]Gavin and Doherty Geosolutions, Unit A2, Nutgrove Office Park, Rathfarnham, D14 X627 Dublin, Ireland

[4]School of Earth Sciences, Science Centre West, University College Dublin, Belfield, D04 N2E5 Dublin, Ireland; mark.coughlan@icrag-centre.org (M.C.)

[5]SFI Research Centre for Applied Geosciences (iCRAG), O'Brien Centre for Science East, University College Dublin, D04 N2E5 Dublin, Ireland

Abstract

Offshore anthropogenic activities such as the installation of Offshore Renewable Energy (ORE) developments and sediment extraction for marine aggregates have shown to disrupt current flow, wave propagation and sediment transport pathways, leading to potential environmental instability. Due to the complexity of the interconnected sediment transport

pathways in the south-western Irish Sea combined with an increase in planned anthropogenic activities, the assessment of this risk is imperative for the development of a robust marine spatial plan. Subsequently, this study uses two-dimensional morphological modelling to build upon previous studies to assess the dependency of Arklow Bank's local sediment transport regime on external sediment sources. Additionally, scenario modelling is used to identify vulnerable areas of this offshore linear sand bank to wind and wave-forcing, and to examine the nature of this impact.

A sediment budget is estimated for Arklow Bank whereby seven source and nine sink pathways are identified. New evidence to support the exchange of sediment between offshore sand banks and offshore independent sand wave fields is also provided. The areas of the bank most vulnerable to changes in external sediment sources and the addition of wind- and wave-induced flow are analogous. These high vulnerability zones (HVZs) align with regions of residual cross-flow under pure current conditions. The restriction of sediment sources off the southern extent of Arklow Bank impact erosion and accretion patterns in the mid and northern sections of the bank after just one lunar month simulation. Where tidal current is the primary driver of sand bank morphodynamics, wind- and wave-induced flow is shown to temporarily alter sediment distribution patterns. Wind and wave-induced flow can both accelerate and decelerate the east-west fluctuation of the upper slopes of the bank yet the nature of this impact is inconsistent due to the mis-alignment of the directionality of these two forces. The methods and new knowledge derived from this study is directly applicable to tidally-dominated environments outside the Irish Sea.

7.1 Introduction

Sand banks are important sites for benthic habitats, coastal protection and marine aggregates, and often host offshore renewable energy developments. Arklow Bank in particular, hosts Ireland's only offshore wind farm (Arklow Wind Park Phase 1) which is earmarked for further expansion (Arklow Wind Park Phase 2) [1] (Figure 7-1). Additional offshore wind farm projects, at various stages of planning, are located across the south-western Irish Sea. With the acceleration of the offshore renewable energy industry, and future needs for aggregate material, the demand on marine resources is increasing. Many of these offshore anthropogenic activities, such as dredging and the installation of offshore renewable energy (ORE) infrastructure, can affect wave propagation, flow patterns and sediment circulation [2]–[9]. In the near field, these changes have the potential to alter marine biogeochemistry including marine life behaviour, phytoplankton dynamics and benthic habitats [10], [11]. In the far field, subsequent physical impacts to the marine environment could be detrimental, causing shoreline change [8], [10] or could be beneficial, aiding coastal protection [12], [13]. The nature of this impact depends on the local oceanographic regime, the type and size of the ORE development and ORE lay-out configurations, or the volume, scale and nature of dredged material. This study investigates the physical controls on the sediment transport regime encompassing Arklow Bank, an offshore linear sand bank in the south-western Irish Sea, in order to reduce the risk of environmental instability due to ongoing and planned anthropogenic activities. In order to reduce the risk of negative environmental repercussions following increased offshore anthropogenic activities, a comprehensive understanding of baseline dynamics is imperative to inform environmental risk assessments (EIA) and long-term marine spatial planning.

The south Irish Sea is a tidally-dominated shallow shelf sea environment, which exhibits a highly complex hydrodynamic and morphodynamic regime influenced by a tidal symmetry zone and bed load parting zone extending approximately from Ardanary on the Irish coastline to Anglesey on the United Kingdom's coastline [14] (Figure 7-1). Additionally, the presence of tidal node oscillation zone extending from the coastline at Courtown for approximately 39 km provides additional complexity to hydrodynamics of the region [14] (Figure 7-1).

Arklow Bank itself displays a flood and ebb tidal dominance on the west and east side of the bank respectively. This ultimately generates a clockwise residual transport pathway that encompasses the entire bank, facilitating sediment distribution within the morphological cell. This is reflected in bed load transport whereby sand waves with a mean height and wave length of 3 m and 140 m respectively migrate southwards at mean rate of 23 m/yr on the south-eastern side of the bank. Contrastingly, sand waves on the south-western side of the bank display a mean height and wave length of 2.3 m and 123.5 m respectively and migrate northwards at a rate of 32.7 m/yr [15] (Figure 7-1). Within this sediment transport cell, Arklow Bank displays a highly mobile upper surficial sediment layer [16], [17]. Eight unique hydrodynamic and morphodynamic sub-cells of the bank are identified that display various levels of upper slope east-west fluctuation [17] yet overall long-term bank base stability is maintained. This highly mobile upper layer has posed issues to anthropogenic activities whereby wind turbines installed during Arklow Wind Park Phase 1 have been effected by scour development [18].

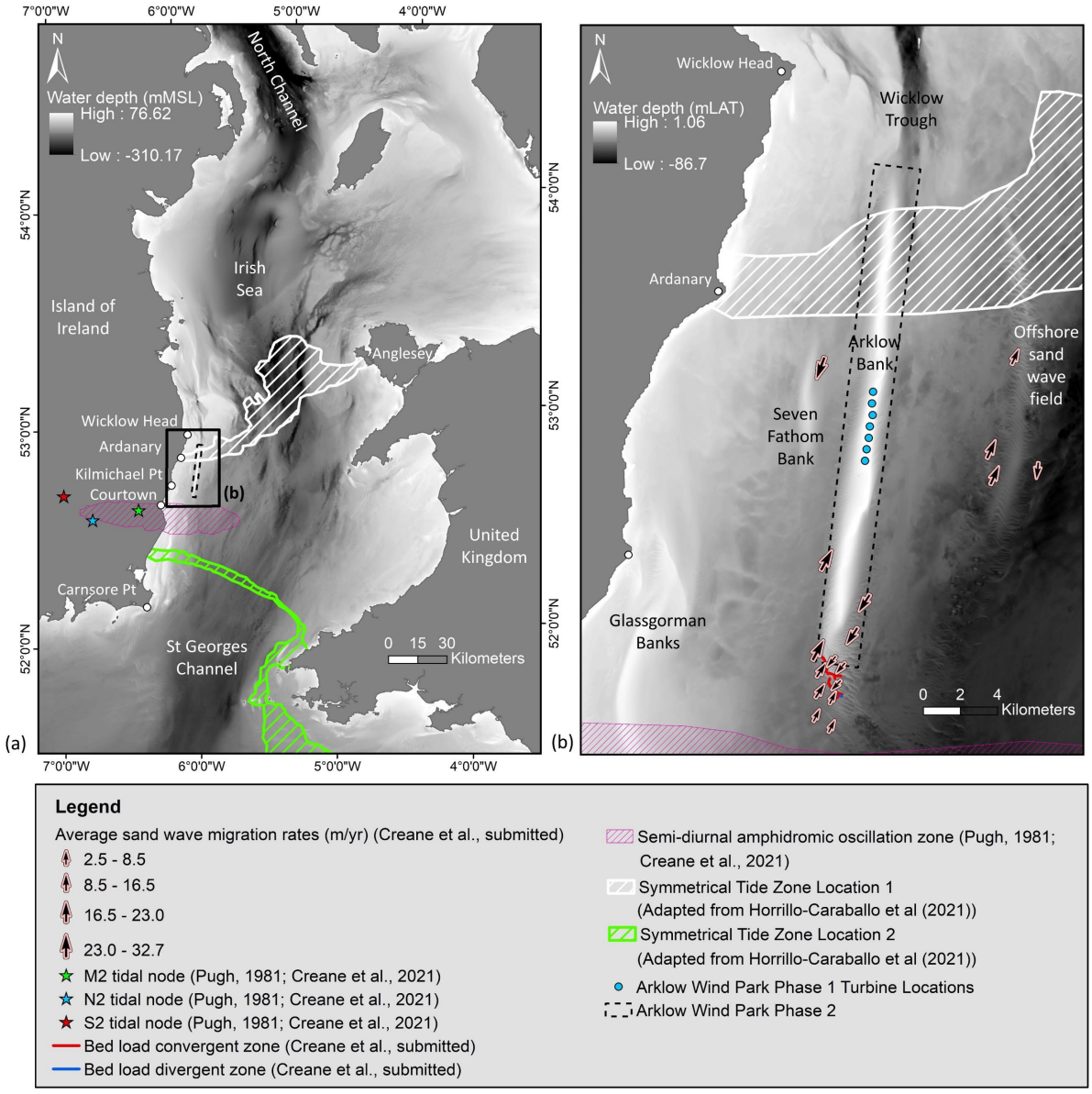


Figure 7-1 (a) Overview of Irish Sea oceanographic phenomena impacting the study site (b), (b) the area of interest, Arklow Bank. Panel (a) bathymetry source: EMODnet [19] where MSL is mean sea level; Panel (b) bathymetry source: INFOMAR (https://www.infomar.ie/ [Accessed on 20 March 2020]) where LAT is lowest astronomical tide.

Evidence of a semi-open circulatory residual sediment transport regime over Arklow Bank is presented by Creane et al [15], who identifies multiple residual transport pathways that facilitate the recycling of sediment material between offshore sand banks and offshore independent sand deposits. In this way, sediment passes in and out of Arklow Bank's local sediment transport cell, implying an influence of external sediment sources on Arklow Bank

sustainability and longevity. Furthermore, Creane et al [17] uses a coupled two-dimensional hydrodynamic and sediment transport model to investigate the hydrodynamic processes that drive upper bank mobility yet maintain long term bank base stability. Ultimately, the positioning of multiple anticlockwise residual current eddies along the circumference of this main large clockwise residual current eddy both facilitate and inhibit upper bank mobility and promotes long term base bank stability. These eddies also promote sediment exchange along the bank margin. Furthermore, a strong hydrodynamic-morphodynamic feedback loop is evident along the length of the upper slopes of the bank. Both on-bank clockwise mobile and stationary residual current eddies, the generation of 'narrow' residual cross-flow zones, and the concept of a 'threshold slope angle' play a role in controlling maximum horizontal and vertical bed level fluctuation limits [17].

Building upon this pure current based approach, it is important to have a comprehensive understanding other physical factors impacting this sediment transport regime, namely wind, wave and external sediment sources.

In shallow areas of the bank, where oscillatory motion of waves reach the sea floor, the combined tidal current- and wave-induced bed shear stress allow grains to exceed the threshold of motion more readily thus increasing erosion and sediment transport. Coughlan et al [16] shows that Arklow Bank displays a mobilisation frequency index (MFI) of approximately 70 % under pure current conditions over a one-year period. Although the dominant seabed disturbance process is tidal currents, areas of the bank display an MFI of up to 20 % under pure wave-induced bed shear stress [16]. Sediment stirring caused by this increased erosion is shown to modify the shape of sand bank-associated sand waves and influence sand wave migration rate and direction [15]. Furthermore, wave-induced flow has

shown to influence net sediment transport directions [20]–[22]. Mitchell et al [22] showed that surface waves enhance sand transport during slack tide by maintaining particles above the threshold of motion and providing a bed shear stress vector in the direction of wave propagation. Additionally, the wind-tidal current interaction is highly complex whereby in areas of low tidal amplitudes even moderate wind speeds can reverse residual tidal currents [23], [24]. In this way, the most vulnerable areas of Arklow Bank to wind and wave conditions and the nature of their impact is important to comprehend.

To elucidate the impact of external sediment on Arklow Bank's sediment transport regime and morphodynamic patterns, the coastal engineering concept, the 'sediment budget', will be adopted. The development of a sediment budget is a commonly used tool to understand how a coastal system functions [25]–[27]. A sediment budget balances the volumes of sediment entering (sources) and leaving (sinks) a selected coastal region with the resulting erosion or accretion in that cell within a defined period of time. This is summarised in the following equation [27]:

$$Residual = \sum Q_{source} - \sum Q_{sink} - \Delta V + P - R \qquad (1)$$

whereby the Q-terms represent the sediment entering and leaving the cell, the P- and R-terms represent the sediment that is 'placed' or 'removed' from the cell by anthropogenic activities such as beach nourishment or dredging respectively, and ΔV is the volume change in the cell. The resulting 'residual' is an indicator of how balanced the cell is and should be zero if all parameters are accounted for. The most common approach to develop a sediment budget is to use the most known variables, such as volume change data and placement and removal data, as the foundation of the budget. Subsequently, a range of longshore transport rates and other relative magnitudes are applied to solve for the budget. This study will test the

applicability of this coastal engineering concept in an offshore setting to estimate a sediment budget for Arklow Bank. Once estimated, the impact of external sediments on the sediment transport regime and morphodynamics can be assessed.

When developing robust hydrodynamic and morphological models for offshore environments, the utilisation of the most efficient mesh resolution upon considering specific study aims and objectives, site-specific environmental considerations, computational power and run time, and project budget and timeline is imperative to resolve the best results. Depending on these variables, various mesh types (unstructured or structured) [28] and resolution have been utilised to model regional scale hydrodynamic and sediment transport trends [14], [16], [29], and specific bedform dynamics such as sand waves under both two-dimensional (2D) [30], two-dimensional vertical (2DV) [31] and three-dimensional modelling techniques (3D) [32], [33], and sand banks [20], [34]–[38]. Performing a mesh sensitivity analysis is a useful technique in the decision-making process.

Specifically, this study addressed the following hypothesis:

'Morphodynamics of offshore sand banks in tidally-dominated continental shelf seas are dominated by tidal current processes yet are influenced by other phenomena including external sediment sources, and wind and wave processes.'

From this hypothesis, this study aimed to:

1. Conduct a numerical model mesh sensitivity analysis to define the most efficient spatial resolution that facilitates the investigation of various processes controlling Arklow Bank morphodynamics;
2. Estimate a sediment budget for Arklow Bank;

3. Examine the influence of external sediment sources on the local sediment transport regime and bank morphodynamics;
4. Identify the most vulnerable areas of the bank due to wind and wave-induced flow and the nature of this impact.

7.2 Methods

7.2.1 Numerical model set-up and validation

7.2.1.1 Hydrodynamic model

A dynamically coupled two-dimensional (2D) hydrodynamic and sediment transport model was developed using MIKE 21 suite of tools [39]–[41]. The setup of the model is provided in Creane et al [42] along with validation details for water levels, currents and suspended sediment transport. Additional validation of bed levels through volumetric analysis is provided in Creane et al [17] (Figure 7-2). The model utilises an unstructured flexible mesh which facilitates a varied spatial resolution across the model domain (Figure 7-2). A variation of four to five levels of refined mesh resolution is utilised in this study, details of which are provided in section 7.2.2.

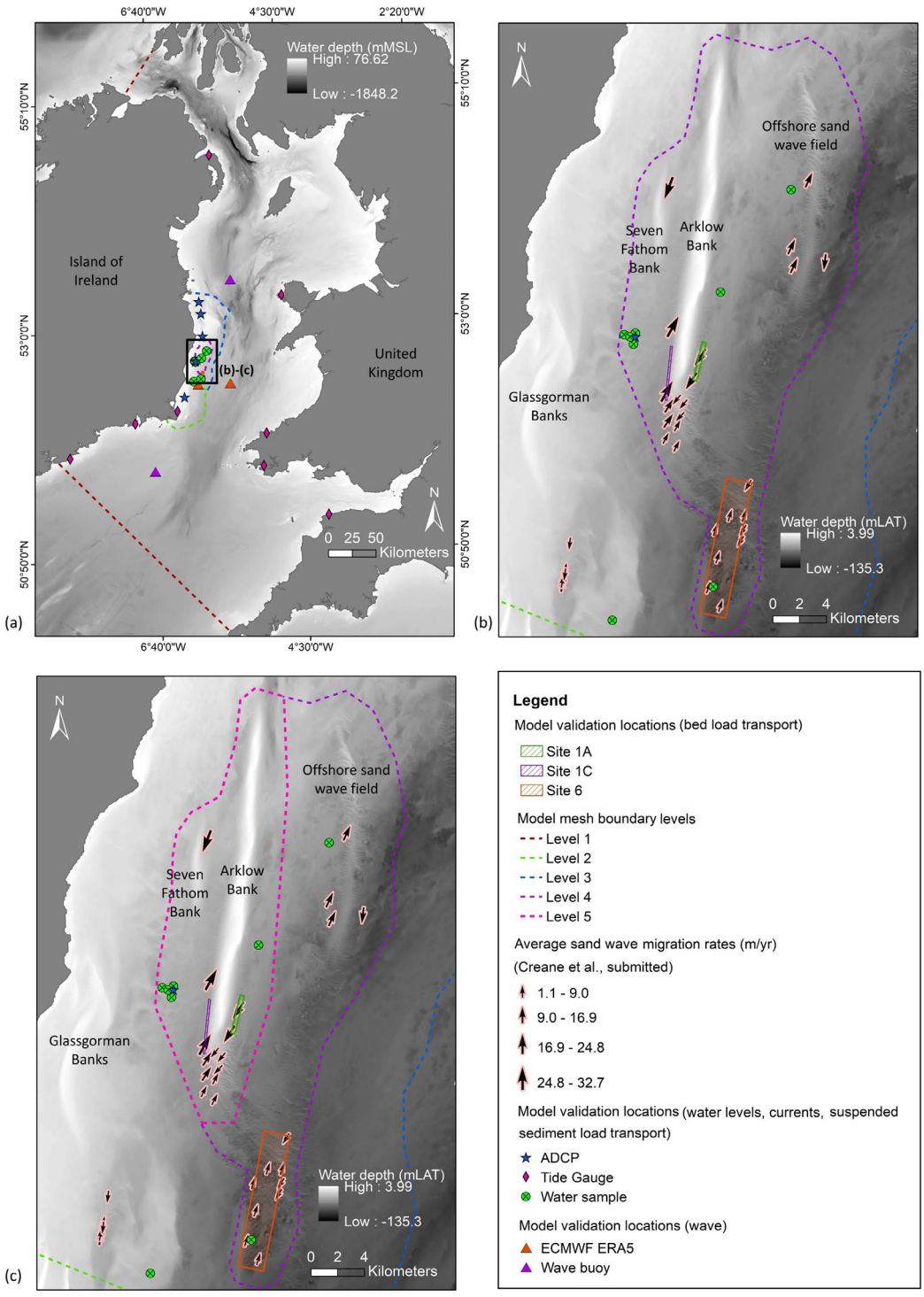


Figure 7-2 (a)-(c) shows numerical model boundaries, mesh resolution levels and validation points whereby (b) specifically displays the four mesh levels used in model runs 2 to 5 and (c) displays the five mesh levels used in model run 1. Panel (a) bathymetry source: EMODnet [19] *where MSL is mean sea level; Panel (b) bathymetry source: INFOMAR (https://www.infomar.ie/ [Accessed on 20 March 2020]) where LAT is lowest astronomical tide.*

7.2.1.2 Spectral wave model

A validated MIKE 21 spectral wave model [43] was developed using the same domain as the hydrodynamic model outlined in section 7.2.1.1 (Figure 7-2). This fully spectral formulation is based on the wave action conservation equation as described in Komen et al [44] and Young [45] where the directional-frequency wave action spectrum is the dependent variable. The discretisation in the geographical and spectral space is performed using a cell-centered finite volume method [43]. The model can include wave growth by action of wind, non-linear wave-wave interaction, wave-current interaction, refraction and shoaling due to depth variations, effect of time-varying water depth and flooding and drying, and dissipation due to white capping, bottom friction and depth-induced wave breaking. This fully spectral model can simulate both swell and wind-generated waves. The quadruplet-wave interaction is described by the Discrete Interaction Approximate (DIA) [44]. White capping driven energy dissipation is based on the formulation of Hasselmann [46] and Bidlot et al [47] where the final dissipation coefficients used in the model, C_{dis} (Cdis) and δ (DELTAdis), are 3.5 and 0.5 respectively. As waves propagate into shallow water, the orbital wave velocities penetrate the water depth and the source function due to wave-bottom interaction become important. Dissipation due to bottom friction depends on the hydrodynamic and sediment conditions as described in Johnson and Kofoed-Hansen [48]. To account for bottom friction a Nikuradse roughness value [49] of 0.04 m was applied as recommended by Weber [50]. Depth induced wave breaking is calculated based on empirical formulations by Battjes and Janssen [51]. In this case, the Gamma parameter used in the breaking formulation was constant at 0.8. The effect of wind forcing on the surface stress is incorporated into the model using empirical relationships that include density, drag coefficient and wind speed.

A wind field comprising wind speed and direction at 10 m above sea level has been incorporated into the model using European Centre for Medium-Range Weather Forecasts' (ECMWF) ERA5 Climate Reanalysis dataset. This wind field varies in time (1-hour intervals) and over the entire domain at a spatial resolution of 0.25°x 0.25°. The two open boundaries (Figure 7-2) are forced with hourly significant wave height, peak wave period, mean wave direction, and directional standard deviation extracted from European Centre for Medium-Range Weather Forecasts' ERA5 Climate Reanalysis dataset at 0.5° x 0.5° resolution. The Global Tide Model developed by DTU Space [52] provides one-hour water levels covering the whole model domain. This ensures that the changes in wave conditions due to varying water depths resulting from tides are properly modelled. The wave model outputs include significant wave height (H_s), peak wave period (T_p), mean spectral wave zero-upcrossing period (T_{02}), mean wave direction (MWD) and three components of radiation stresses (S_{xx}, S_{yy}, S_{xy}) which were output at 1-h intervals for model calibration and validation. Calibration was carried out by altering bottom friction, white capping and wave breaking parameters.

Data from the M2 (53.480° N, 5.425° W) and M5 (51.690° N, 6.704° W) wave buoys were downloaded from the Met Éireann online delivery system for a period between 2014 and 2016 for calibration and validation purposes. In order to compare the MIKE 21 simulated spectral zero crossing period (T_{02}) to the significant wave period (T_s) recorded by the wave buoys, the measured dataset (T_s) was converted to T_{02} using the following equation [53]:

$$T_s = 1.14 T_{02} \quad (2)$$

Due to the limited amount of in-situ data available across the model domain, an additional validation was carried out using two data points extracted from the ECMWF ERA5 climate

reanalysis model to ensure a more robust validation. The location of these two additional validation points is provided in Figure 7-2 and Table 7-1.

Table 7-1 Comparison between the model and measured M2 and M5 datasets and model and output from the ERA5-ECMWF dataset at locations shown in Figure 7-2. The indices shown are bias, the root-mean-square error (RMSE), the correlation coefficient (R) and the scatter index (SI)

Dataset	Dataset Type	Location	Significant wave height (m)			
			Bias (m)	RMSE (m)	R	SI (%)
M2	Measured (wave buoy)	53.480 N, 5.425 W	-0.03	0.24	0.98	19.20
M5	Measured (wave buoy)	51.690 N, 6.704 W	-0.19	0.35	0.97	16.84
ERA5-ECMWF 1	Climate reanalysis (modelled)	52.5 N, 6 W	0.06	0.20	0.98	16.80
ERA5-ECMWF 2	Climate reanalysis (modelled)	52.5 N, 5.5 W	-0.04	0.23	0.98	13.37

The level of agreement between the model output and these observed/ERA5 datasets are assessed both visually and statistically. Visual comparisons allow the assessment of shape, trend, range and limits of model and observed/ERA5 datasets (Figure 7-3), whereas statistical comparisons determine the degree to which the model fits the observations within defined calibration limits. A number of statistics were generated to assess the fit between measured/ERA5 and simulated datasets (Table 7-1 and Figure 7-3). Where the correlation coefficient is a measure of linear correlation between measured and simulated variables, bias represents the mean difference between both datasets. The root-mean-square-error (RMSE) is the standard deviation of residuals and the scatter index presents the percentage of RMS difference with respect to mean observation. The comparisons between in-situ measurements and simulated predictions for H_s, T_{02} and MWD generally showed a good fit, time series plots are presented in Figure 7-3. A strong positive relationship is evident between

measured or ERA5 dataset and the simulated timeseries whereby an average R value of 0.98 across all four data points (Table 7-1; Figure 7-3(g)-(j)). Additionally, a scatter index of < 20 % is evident across all sites, revealing a good correlation.

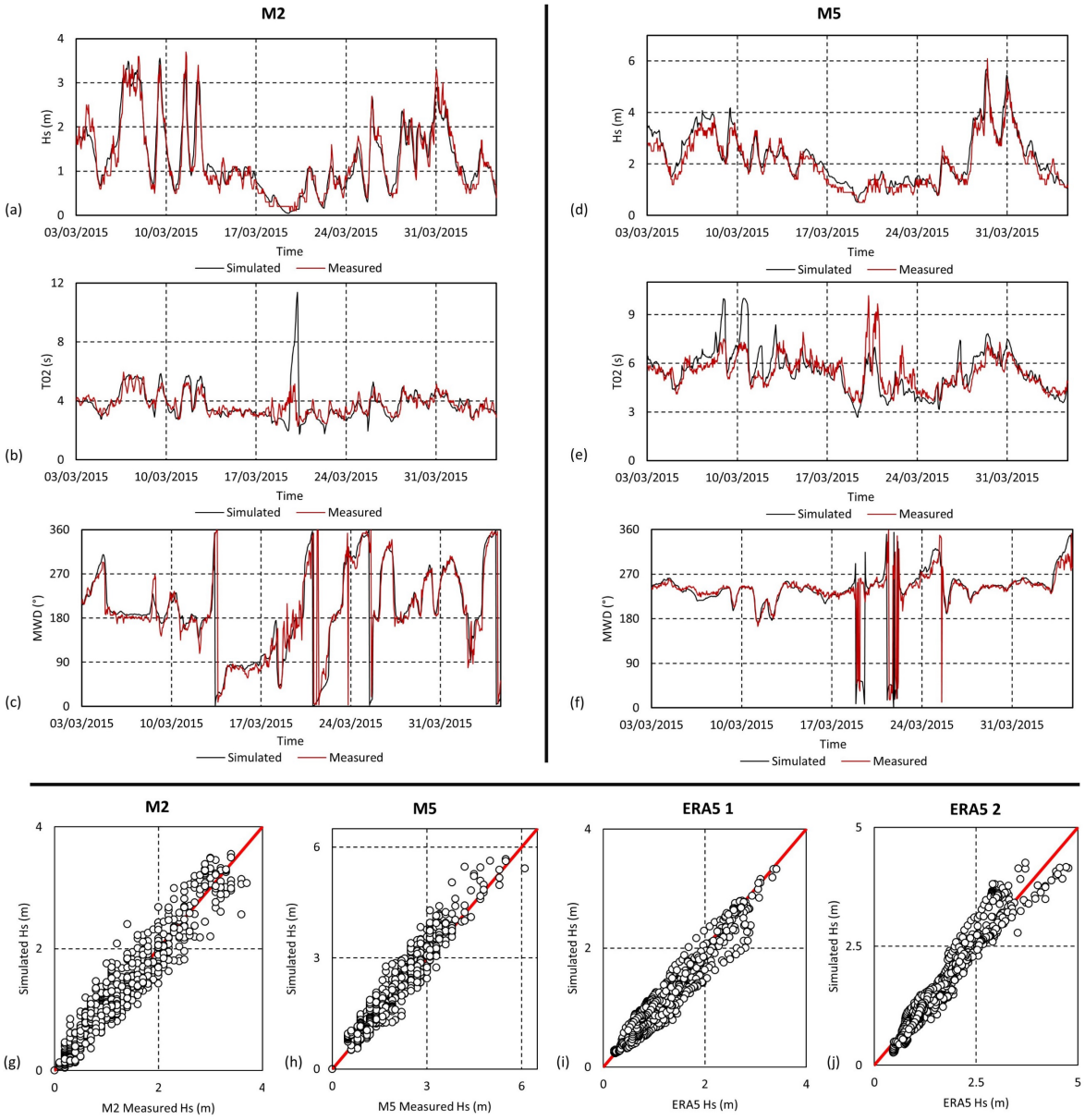


Figure 7-3 Wave model validation plots: (a) to (c) time-series plots of significant wave height (H_s), spectral zero-crossing wave period (T_{02}) and mean wave direction (MWD) at M2 data point; (d) to (e) time-series plots of H_s, T_{02} and MWD at M5 data point; (g) to (j) scatter plots of H_s at M2, M5, ERA5 1 and ERA5 2 data point locations. Coordinates of each data point is provided in Table 7-1.

7.2.2 Scenario modelling

Five scenario model runs were constructed to address the hypothesis outlined in section 7.1. These are summarised in Table 7-2. Run 1 was previously executed by Creane et al [17] and produces one-year baseline sediment transport conditions over Arklow Bank under pure current conditions, utilising a relatively high resolution mesh. The unstructured flexible mesh contains five levels of refinement, the highest of which is 50 m to 80 m over Arklow Bank and Seven Fathom Bank in order to resolve the main features of the bank at an adequate scale to address the objectives of Creane et al [17] (Figure 7-2; Table 7-3).

Run 2 to Run 5 are new simulations carried out specifically for this body of work (Table 7-3). Run 2 represents one-year baseline sediment transport conditions over Arklow Bank under pure current conditions, utilising a relatively lower resolution mesh over Arklow Bank. This unstructured mesh contains four levels of refinement with the highest spatial resolution being 150 to 200 m encompassing the Arklow Bank system [42] (Figure 7-2; Table 7-3). A mesh sensitivity study was carried out by comparing outputs from Run 2 to Run 1 to ensure adequate quality and applicability of this four-level mesh at addressing the study aims.

Run 3 was used to assess the influence of external sediment sources on Arklow Bank's local sediment transport regime. Firstly, the hydrodynamic and sediment transport model outputs from Run 2 were used to estimate a sediment budget for Arklow Bank. On completion, two significant sediment source areas were identified and designated as 'immobile' zones in the sediment transport model of Run 3. This was executed by adjusting the median grain size (D_{50}) of these 'immobile zones' to 1 m to ensure the threshold of motion is not exceeded by bed shear stress exerted on the seabed. The outputs from Run 3 were compared against

baseline outputs from Run 2 to assess the response of the sediment transport regime to this change.

Run 4 utilised the model set-up of Run 2 as a foundation but included an additional 2D spatially-varying grid series of u- and v-wind velocity components and surface pressure in the hydrodynamic model. This hourly dataset has a 0.25 ° spatial resolution and was sourced from the European Centre for Medium-Range Weather Forecasts (ECMWF) ERA5 dataset. Run 4 assessed the influence of wind on Arklow Bank's sediment transport regime.

Run 5 built upon Run 4 to assess the influence of wave-induced flow on this sediment transport system. Firstly, the spectral wave model described in section 7.2.1 was run for a one-year simulation period in order to generate radiation stresses for the entire model domain at a 1-hour temporal resolution. Radiation stresses are second order stresses due to the breaking of short period waves. They acted as driving forces for the mean flow and can be used to calculate wave-induced flow. The three components of radiation stresses (S_{xx}, S_{yy}, S_{xy}) were thus included in the hydrodynamic simulation of Run 5.

Table 7-2 Overview of scenario modelling

Model Runs	Aim of Model Run	Description	Mesh Levels
Run 1	To simulate baseline conditions using a higher spatial resolution over Arklow Bank	Hydrodynamic module: - Pure current Sand transport module: - Baseline conditions	Five
Run 2	To simulate baseline conditions using a lower spatial resolution over Arklow Bank	Hydrodynamic module: - Pure current Sand transport module: - Baseline conditions	Four
Run 3	To test the influence of external sediment sources on baseline conditions (Run 2)	Hydrodynamic module: - Pure current Sand transport module: - Designated 'immobile' zones in identified sediment source areas.	Four
Run 4	To test the influence of wind on baseline conditions (Run 2)	Hydrodynamic module: - Current - Inclusion of wind and surface pressure grid series (1-hour temporal resolution; 0.25° spatial resolution)	Four

		Sand transport module: - Baseline conditions	
Run 5	To test the influence of combined wind and wave on baseline conditions (Run 2)	Hydrodynamic module: - Current - Inclusion of wind and surface pressure grid series (1-hour temporal resolution; 0.25° spatial resolution) - Inclusion of wave radiation stresses produced from separate spectral wave model run. Sand transport module: - Baseline conditions	Four

Table 7-3 Resolution details of the unstructured flexible triangular mesh used in scenario modelling

Mesh Levels		Description	Mesh utilised	
			Original Study	Current Study
5 levels	Level 5	50 to 80 m over Arklow Bank and Seven Fathom Bank	Creane et al [17]	Run 1
	Level 4	150 to 200 m encompassing the Arklow Bank system including offshore independent sand wave field identified in Creane et al [15]		
	Level 3	500 m to 600 m buffer zone, extending from the approximate -70 m water depth contour to the coastline from Howth Head (53.37861°, -6.057222°) to Courtown (52.645°, -6.228333°), and covering any sand banks outside these areas off the south-east coast of Ireland		
	Level 2	800 m to 1000 m extending along the -70 m contour to the coast from Courtown to Carnsore Point (52.17056°, -6.355278°)		
	Level 1	2500 m to 3000 m resolution for the rest of the model domain		
4 levels	Level 4	150 m to 200 m around the Arklow Bank system (approximately 7.2 km²)	Creane et al [42]	Run 2, 3, 4, 5
	Level 3	Same as Level 3 above.		
	Level 2	Same as Level 2 above.		
	Level 1	Same as Level 2 above.		

7.3 Results and discussion

7.3.1 Mesh sensitivity analysis

The hydrodynamic and morphodynamic trends of Run 1 are described in detail in Creane et al [17], which are summarised in Figure 7-4. As outlined previously, a large clockwise residual current eddy encompasses the bank, ultimately circulating sediment throughout the morphological cell. A number of anticlockwise residual tidal current eddies are positioned along the circumference of this residual eddy both facilitating and inhibiting east-west upper

slope fluctuation and controlling long-term bank base stability. These also facilitate sediment transfer in and out of the bank's local sediment transport system. The bank base is described as being relatively stable over time but the upper slopes are highly dynamic, fluctuating on an approximate east-west axis [17]. The bank is split into eight hydrodynamically and morphodynamically unique sub-cells whereby sub-cells 1, 3, 7 and 8 are morphologically mobile zones, sub-cells 2 and 6 are relatively stable, and sub-cell 4 is more complex displaying intermixed zones of stable and mobile upper slopes. East-west fluctuation of the upper slopes are further controlled by both stationary and mobile on-bank clockwise residual tidal current eddies and the development of transient 'narrow' zones of residual cross-flow [17].

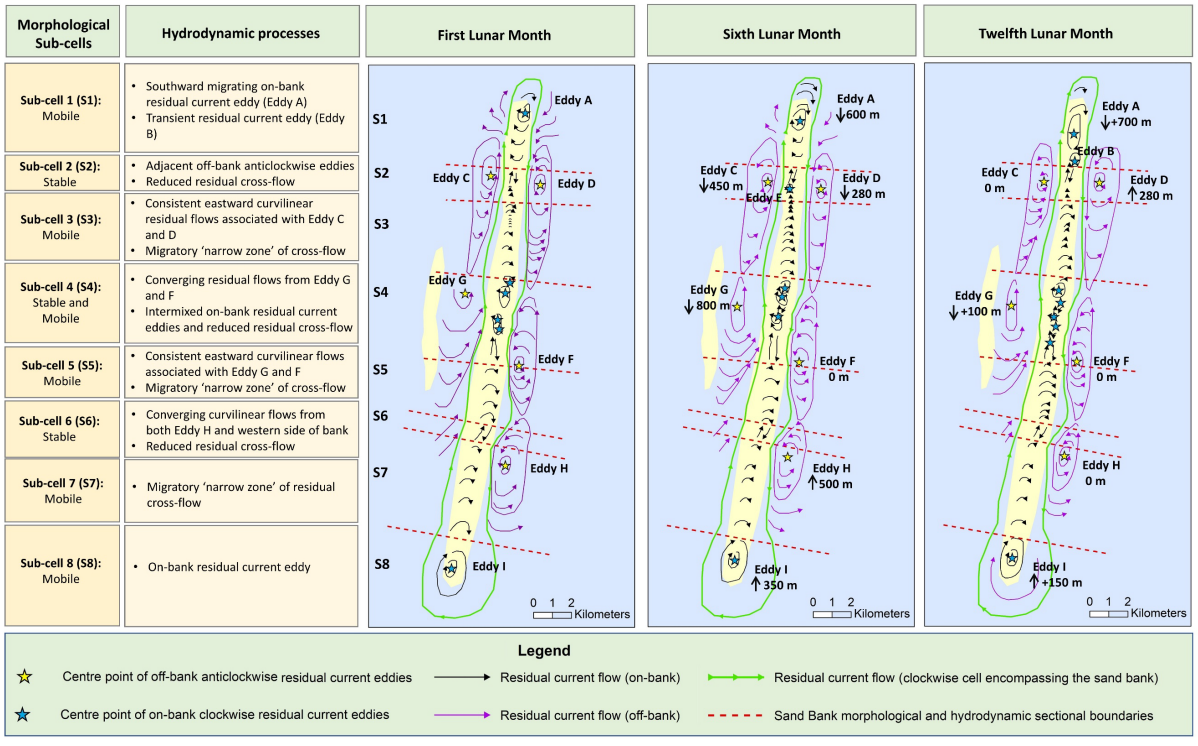


Figure 7-4 Diagram displaying Arklow Bank hydro- and morpho-dynamics under pure current conditions produced by Creane et al [17]

When comparing simulated current residuals between the high- and low-resolution model runs (Run 1 and Run 2 respectively), both gridded to 200 m resolution, broad hydrodynamic

trends are consistent (Figure 7-5). For example, the off-bank anticlockwise residual current eddies, Eddy C, D, F and H, one partial anticlockwise current flow, Eddy G, and the clockwise current eddies over the southern tip of the bank, Eddy I, are all present and located in similar positions in both datasets (Figure 7-5). These current eddies are most likely responsible for stable positioning of the bank over time and facilitate the transfer of sediment in and out of the bank's sediment budget cell [17]. Therefore, on a regional level, the inferred hydrodynamic and sediment transport processes remain unchanged when transitioning from a high-resolution mesh to a lower resolution mesh. Additionally, Figure 7-6(c) represents the difference in bed level at t12mo between Run 1 and Run 2. The lack of bed level change (close to 0 m) on the lower slopes of the bank and along the edge of the sediment budget cell in this figure reiterates the ability of the low-resolution mesh to capture regional processes.

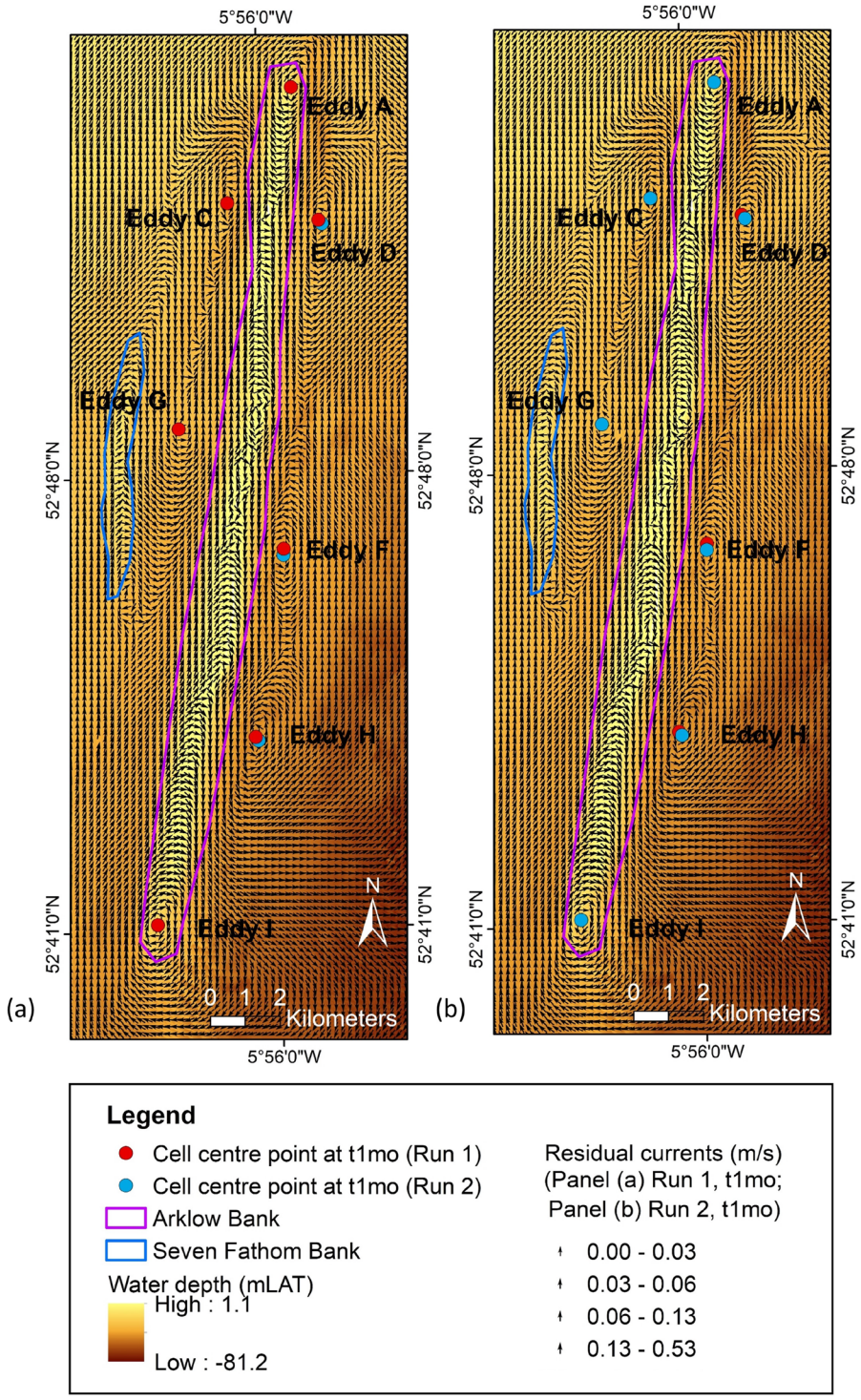


Figure 7-5 (a) and (b) displays residual currents calculated after the first lunar month simulation from Run 1 and Run 2 respectively (Table 7-2). The approximate location of the centre point of each off-bank anticlockwise residual eddy and two on-bank clockwise residual eddies, originally identified in Creane et al [17], are provided in each figure. Bathymetry source: INFOMAR (https://www.infomar.ie/ [Accessed on 20 March 2020])

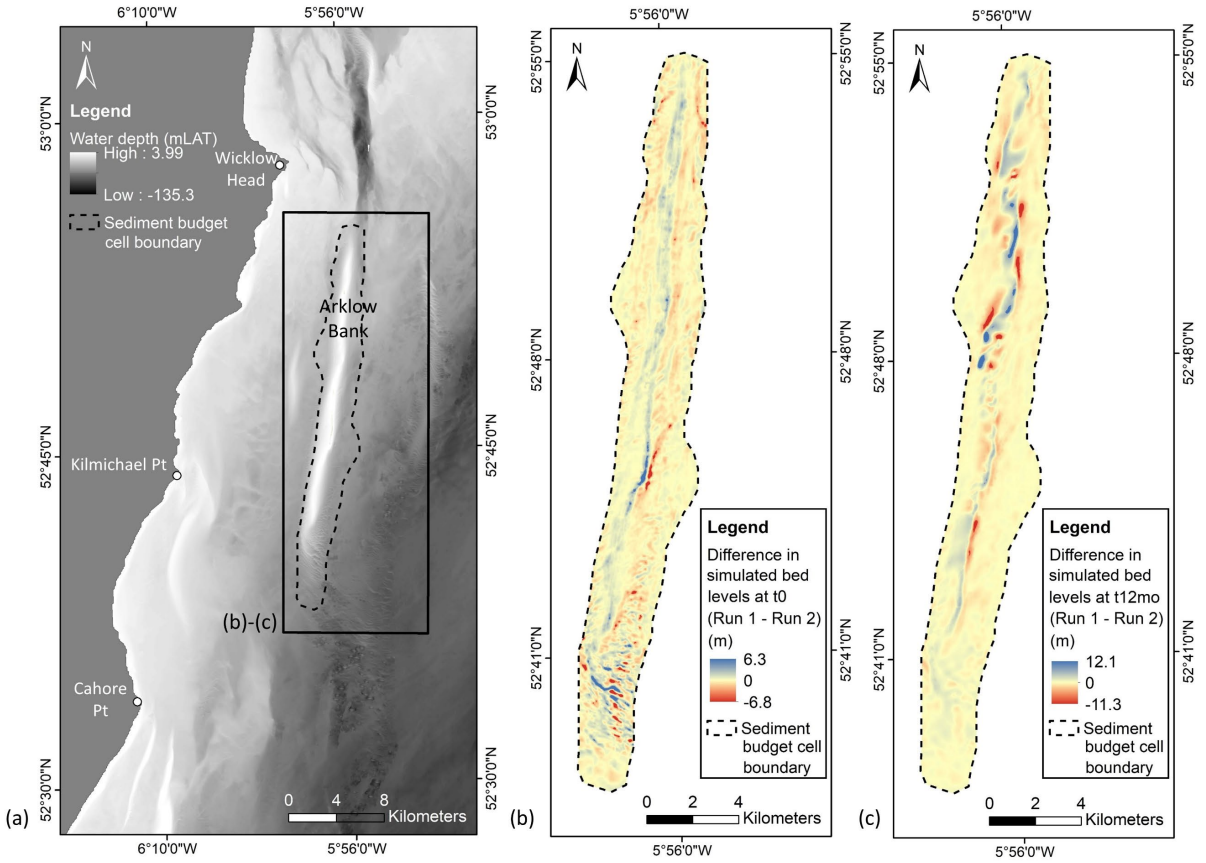


Figure 7-6 (a) Location of Arklow Bank in the south-western Irish Sea, (b) difference in simulated bed levels between Run 1 and Run 2 at the starting model timestep (t0), (c) difference in simulated bed levels between Run 1 and Run 2 after a 12 lunar month simulation period (t12mo). Bathymetry source: INFOMAR (https://www.infomar.ie/ [Accessed on 20 March 2020])

On a local level, Figure 7-6(c) shows 12.1 m to -11.3 m difference in bed level on the upper slopes along the length of the bank. Cross-sectional analysis of bed levels over a one-year period reveals that these changes are a result of differences in timing of east-west fluctuations at various points along the bank. A failure of the low-resolution mesh to fully capture the details of the hydrodynamic-morphodynamic response system, identified from Run 1 in Creane et al [17], across the upper slopes and crest of the bank, is highlighted.

Previously identified morphological 'stability' zones, namely sub-cells 2, 4 and 6, from Run 1 remain quite stable in Run 2. Representative cross-sections are provided in Figure 7-7. This is consistent with the relatively lower bed level difference between Run 1 and 2 (Figure 7-6(c))

at these stability sections in comparison to the rest of the bank. However, minor differences between the two runs are noted in these stability areas. These are mainly due to the inability of the lower resolution input bathymetry to fully capture the detailed shape of the bank (Figure 7-6(b); Figure 7-8(b)), whereby natural variances in water depth occur across the bank between the two input meshes (for example cross-section L65 in Figure 7-8).

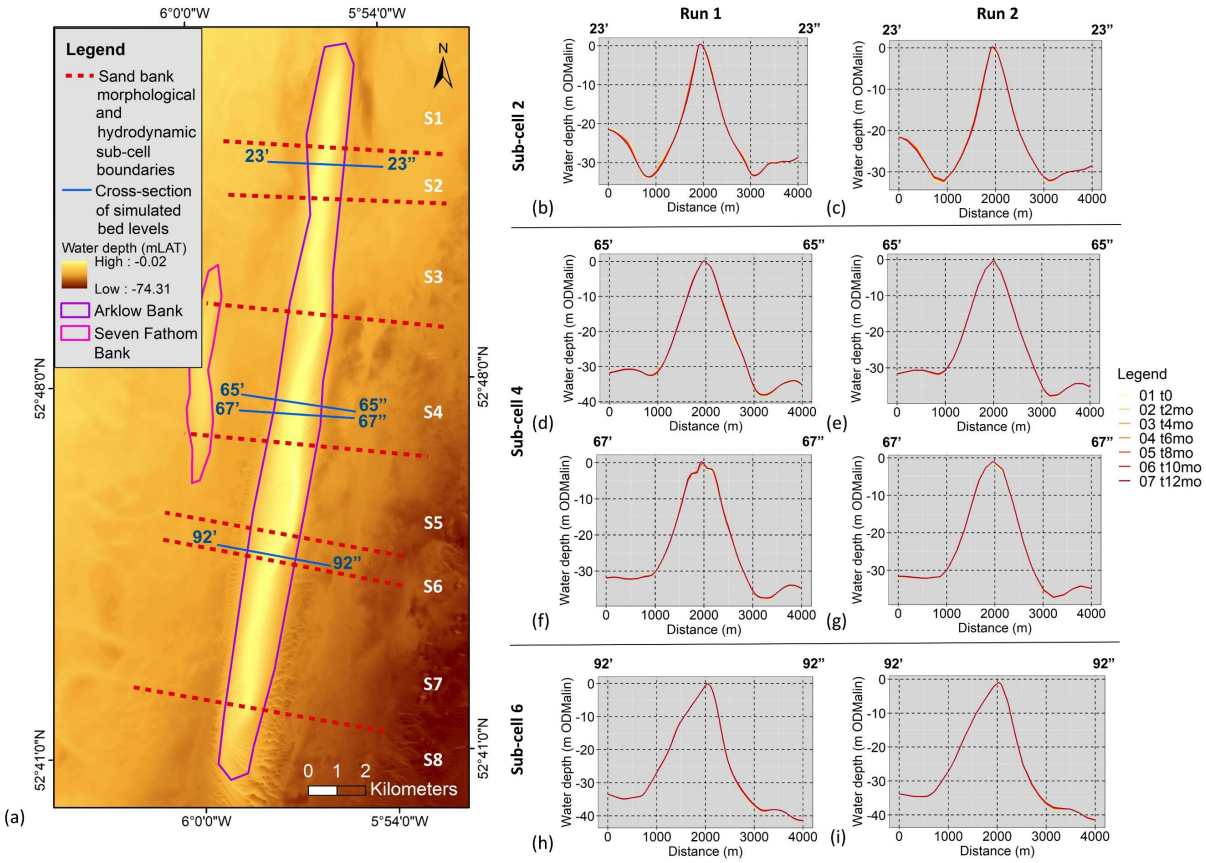


Figure 7-7 Cross-sectional analysis of simulated bed levels of Run 2 against Run 1 in identified 'stable' zones: (b) – (i) display simulated bed level over a one year simulation at cross-sections 23, 63, 67 and 92 whereby 't0' is the starting bed level and 'h', 'wk' and 'mo' is subsequent months; (a) provides the location of these cross-sections. Bathymetry source: INFOMAR (https://www.infomar.ie/ [Accessed on 20 March 2020])

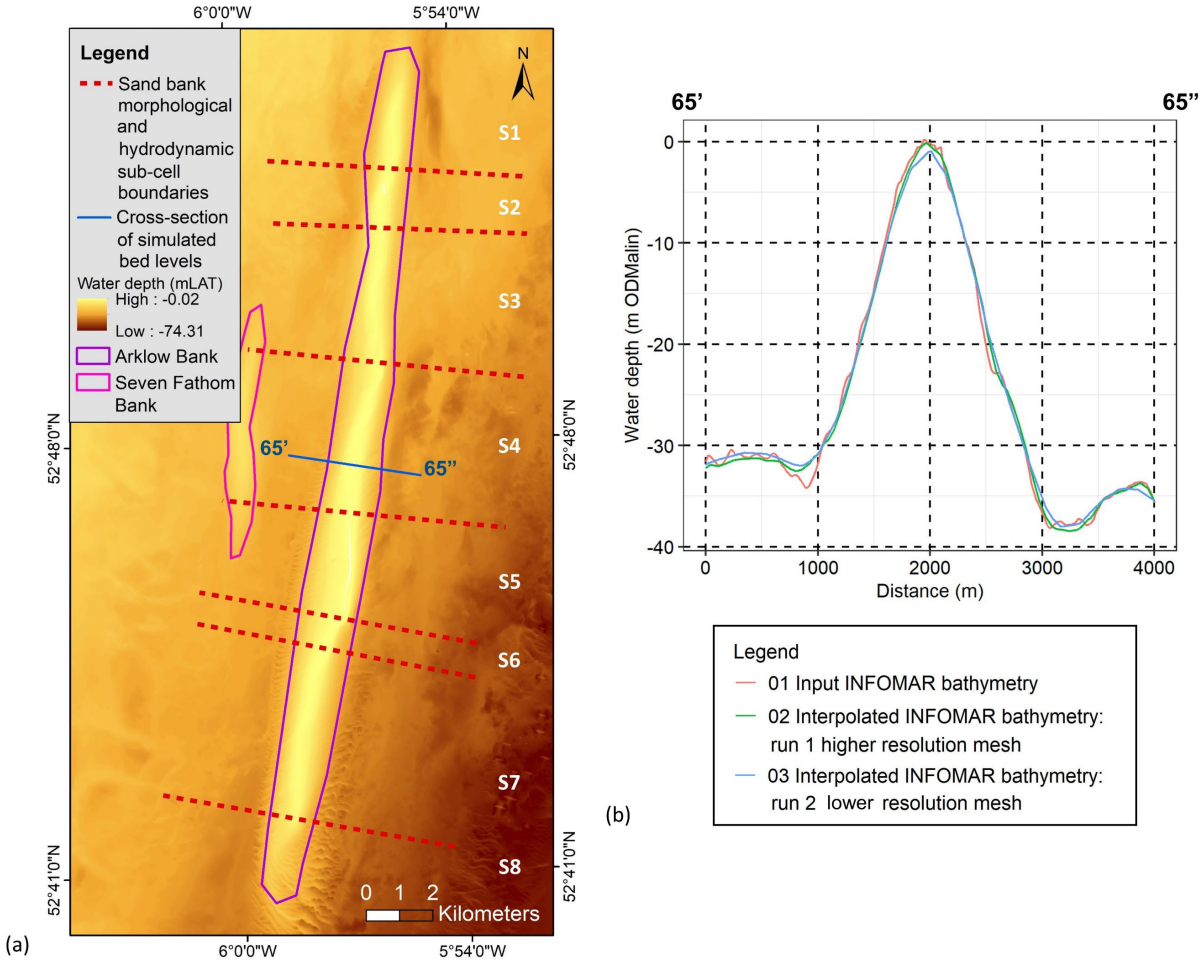


Figure 7-8 Cross-section L65 (b) displays a comparison of bed levels between interpolated INFOMAR bathymetry using the higher and lower resolution unstructured triangular meshes used in Run 1 and Run 2 respectively, against baseline INFOMAR survey data. (a) Displays the location of this cross-section. Bathymetry source: INFOMAR (https://www.infomar.ie/ [Accessed on 20 March 2020]).

This natural variance in the interpolated bathymetry (Figure 7-6(b); Figure 7-8(b)) impacts the previously identified mobile sections of the bank to a higher degree, whereby the low resolution mesh does not capture the morphological details required to model hydrodynamic-morphodynamic response system appropriately (Figure 7-9). In particular, the slope threshold, identified as a potential hydrodynamic response stimulator [17], could not be captured accurately in the low resolution model simulation. As a result, the difference in the timing of the east-west fluctuation and the vertical and horizontal maximum limits of the

upper slopes between the two model results are highest in the high mobility zones. Representative cross-sections of this phenomena are presented in Figure 7-9.

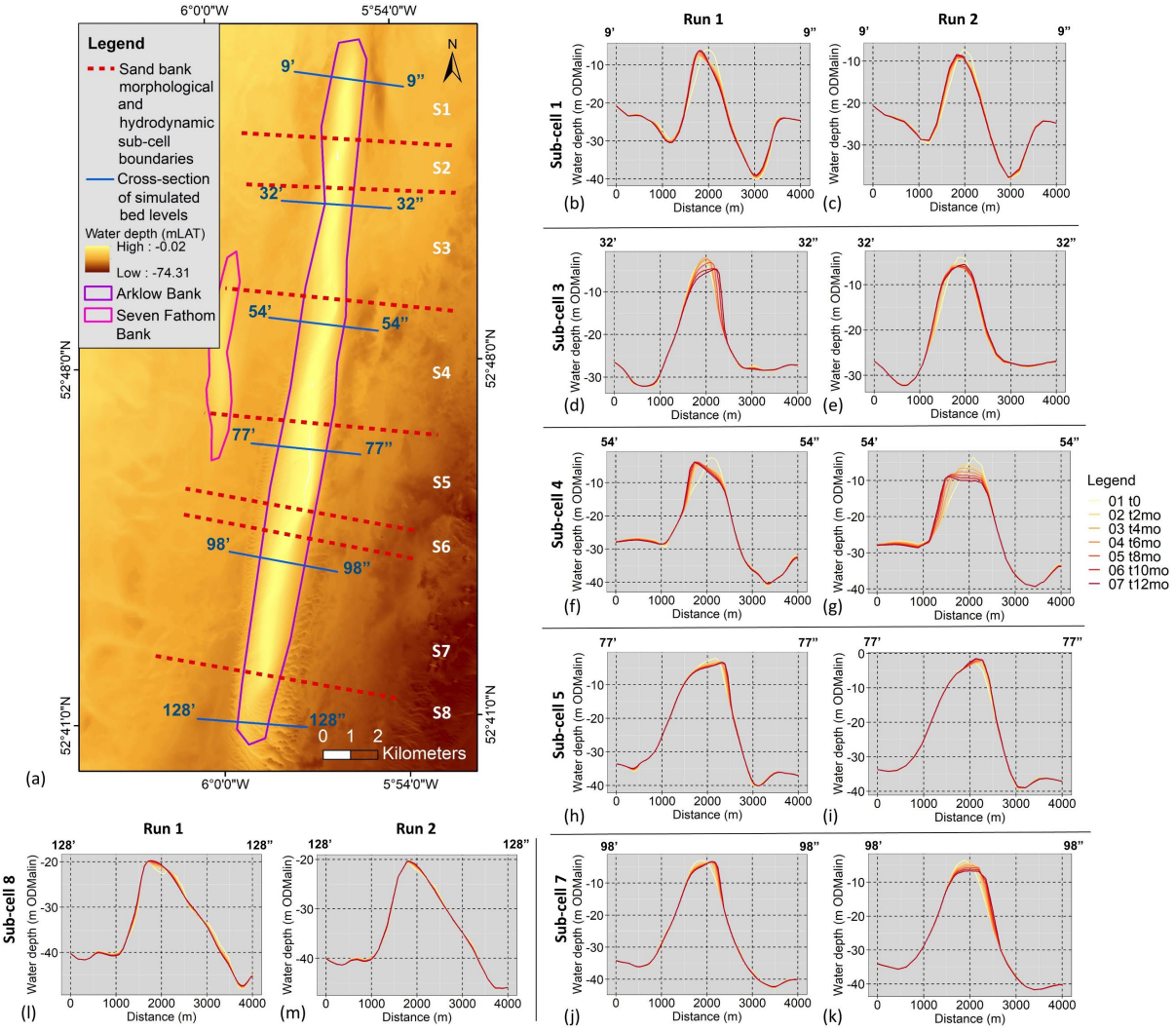


Figure 7-9 Cross-sectional analysis of simulated bed levels of Run 2 against Run 1 in identified 'mobile' zones. (b) – (k) display simulated bed level over a one year simulation at multiple cross-sections whereby 't0' is the starting bed level and 'h', 'wk' and 'mo' is subsequent months; (a) provides the location of these cross-sections. Bathymetry source: INFOMAR (https://www.infomar.ie/ [Accessed on 20 March 2020]).

Ultimately, the change in mesh resolutions does not influence regional hydrodynamics. Therefore, when considering all project variables including computational time, project objectives and site-specific environmental conditions, in this study, the low resolution model is adequate to develop a sediment budget for Arklow Bank in order to test the influence of

external sediment sources on the morphological cell. Run 2 is also deemed adequate to identify vulnerable areas of the bank to wind and wave-induced flow and the nature of this influence.

7.3.2 Sediment budget

The sediment budget cell boundary and associated source and sink pathways were defined through modelled accumulative total sediment load transport, after a one-year simulation period, under pure current conditions (Run 2) (Figure 7-10). The resulting x- and y- velocity components were gridded to a 200 m resolution grid and plotted as magnitude and direction in ArcGIS v10.8. The location of the defined cell boundary was compared, and quality controlled against the clockwise circulatory flow cell encompassing Arklow Bank and anticlockwise flow cells located on the outside of this main morphological cell, identified through tidal current residuals from the first simulated month (Figure 7-4). These source and sink pathways were also compared against the structure of the bank, using bathymetry, bathymetry derivatives e.g. slope, to ensure location accuracy. As expected, the nature of the accumulative total load transport pathway vectors and residual tidal current vectors are quite similar throughout the one-year period (Figure 7-5(b); Figure 7-10(a)).

The volume of sediment crossing each defined source and sink cross-section was calculated for a one-year period. At the same time, the simulated volume change over this same time period was calculated. A balanced sediment budget equation was achieved from which the percentage of the total source or sink sediment volumes were defined for each pathway. These are displayed in Figure 7-10. Seven sink and nine source pathways were defined. The largest amount of external sediment source enters the morphological cell through cross-sections 2 (20.06 %), 7 (15.15 %), 10 (40.41 %) and 15 (12.72 %) whereas the highest volume

of sediment leaving the cell passes through pathways 3 (35.07 %), 9 (15.21 %) and 14 (21.85 %).

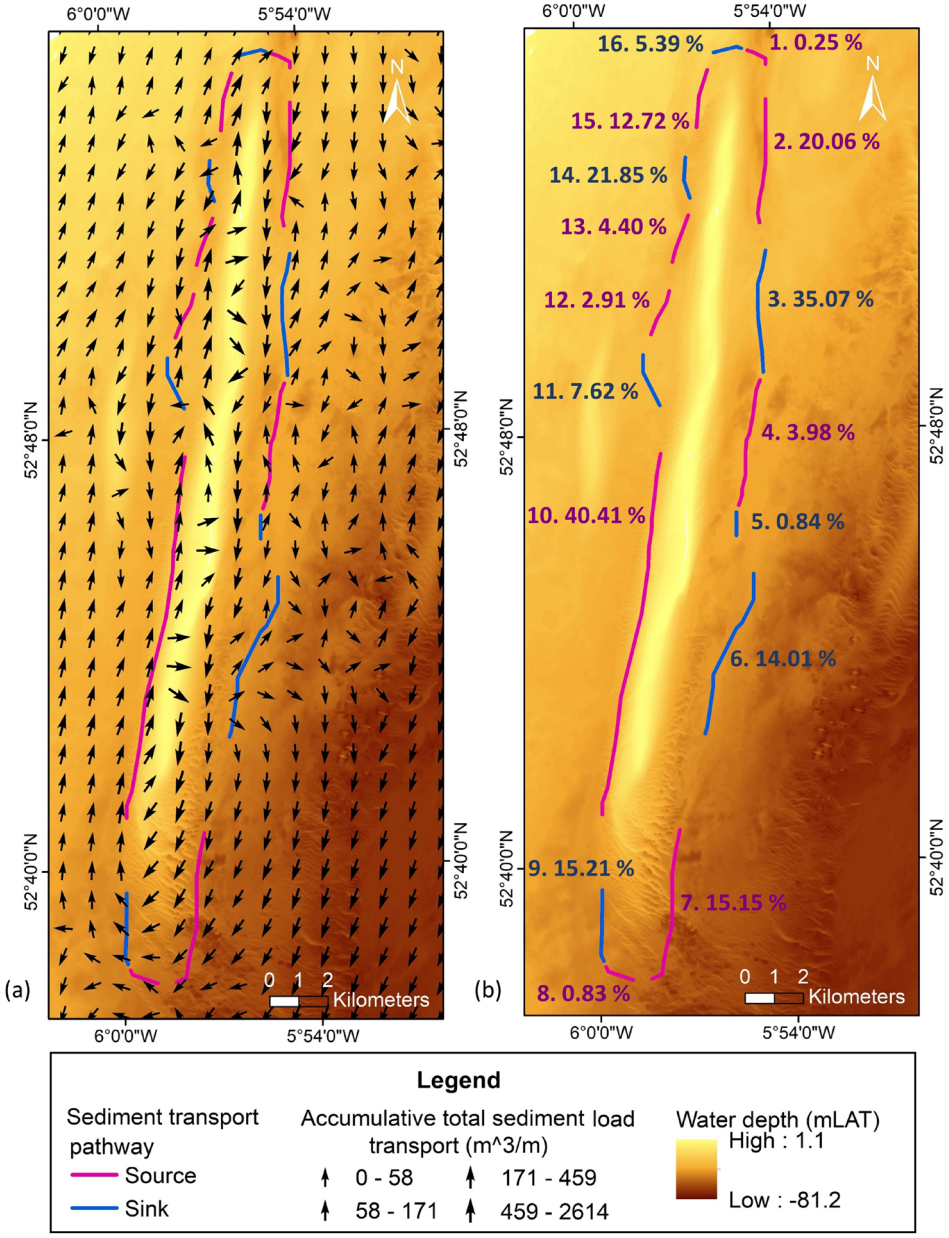


Figure 7-10 (a) Bathymetry map overlain by simulated accumulative total sediment load transport vectors after 12 lunar month simulation period. The identified source and sink pathways are identified along the circumference of the sediment budget cell in red and blue respectively. (b) The percentage of the total sediment entering the sediment budget cell through each source pathway over this 12 month period are presented in red. The percentage of the total sediment exiting the

sediment budget cell at each sink pathway over this 12 month period is identified in blue. Bathymetry source: INFOMAR (https://www.infomar.ie/ [Accessed on 20 March 2020]).

As discussed by Creane et al [17] a complex hydrodynamic system drives sediment exchange along the full circumference of the cell boundary. Residual transport vectors, derived from modelled accumulative total sediment transport and tidal current, show that on the eastern side of the bank, sink pathways 3, 5 and 6 facilitate sediment transport out of the local transport system. From here, partial sediment load returns via pathways 2, 4 and 7 while partial load is transported towards an independent offshore sand wave field approximately 8 km east of Arklow Bank (sand wave field 1 in Figure 7-11) [15]. According to Creane et al [15], sediment then either i) returns back to the offshore sand bank, in this case via source transport pathways 7 and 8, or ii) the offshore independent sand wave field acts as an intermediary stepping stone to independent sand wave fields further offshore (sand wave field 2 in Figure 7-11). Creane et al [15] uses a combination of environmental variables and theoretical factors to determine the mechanism of sediment transport in this circulatory residual transport pathway. Ultimately, this is predominately controlled by tidal asymmetry. For example, over the 'transition zone' where sediment grain sizes are relatively coarser in between the sand bank and the offshore independent sand wave field, residual current magnitudes are high along these transport paths, indicating a strong tidal asymmetry, this correlates with suspended load sediment transport dominance. On the other hand, bedload dominance is present over the sand wave field where residual current magnitudes are relatively low and tidal symmetry is prominent [15].

This study supports this mechanism through the use of sediment transport modelling under pure current conditions. The simulated one-year mean suspended sediment concentration

(SSC) is displayed in Figure 7-11(b). As suspected, the results show high SSC over the offshore sand bank and offshore sand wave fields where mobile bedforms and localised sediment transport systems are present. However, Figure 7-11(b) also highlights residual 'plumes' of SSC over the coarser-grained transition zone, correlating directly with the residual transport pathways derived from residual currents and accumulative total load sediment transport over the same period. This supports the movement of sediment between these independent sand deposits.

The estimation of simulated bed load/suspended load dominance over a one-year period also proves useful in an attempt to support this hypothesis. Bed load dominance is observed over both the offshore sand bank and two offshore sand wave fields, whereas suspended load dominance is noted along the identified residual transport pathways in between these features (Figure 7-11(c)). This ultimately provides additional support to the sediment exchange relationship between offshore sand banks and independent sediment wave fields identified by Creane et al [15].

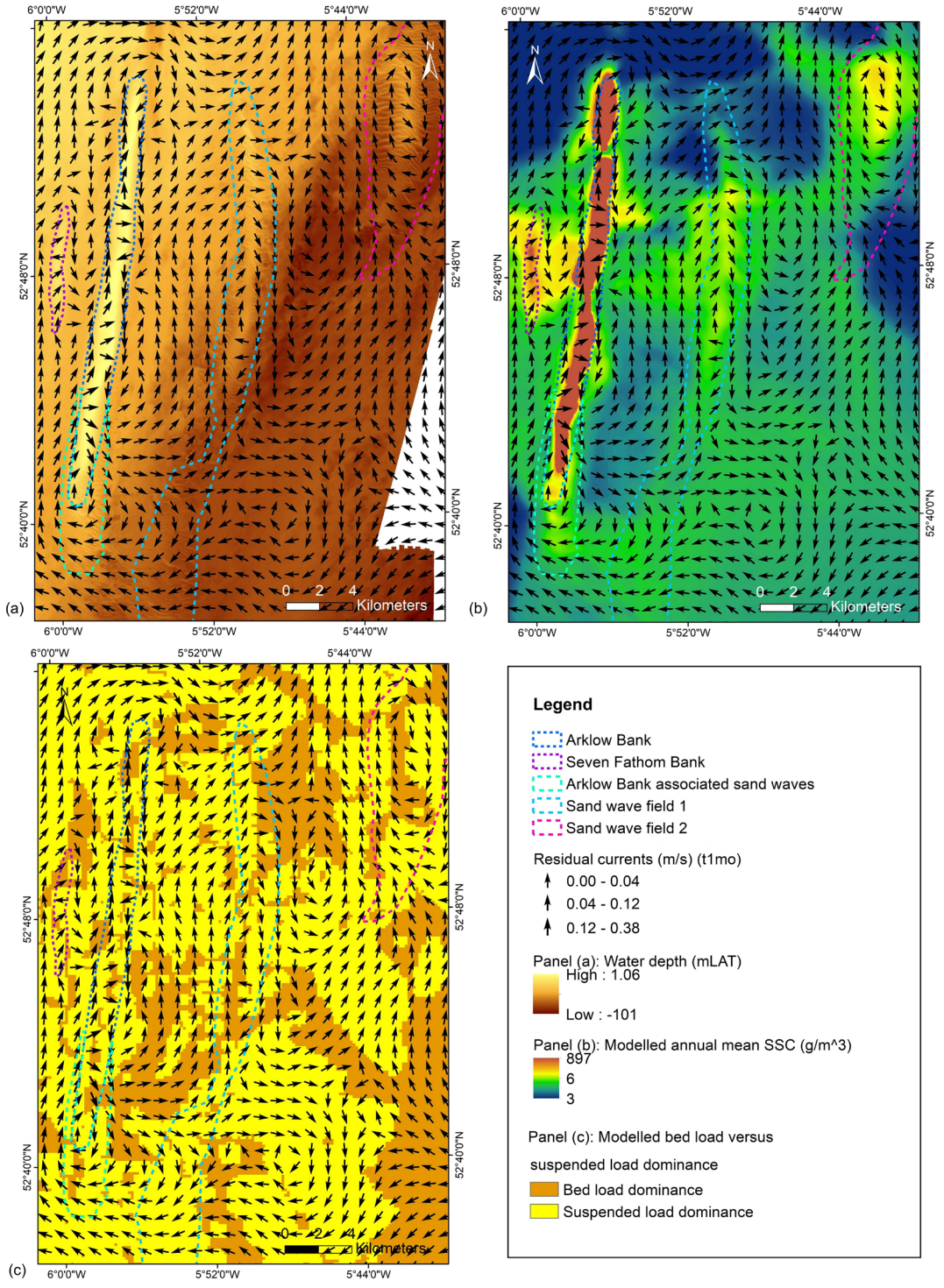


Figure 7-11 (a) Bathymetry (mLAT) overlain by modelled residual currents (m/s), (b) Mean simulated SSC (g/m³) over one-year period under pure current conditions overlain by modelled residual currents (m/s), (c) Bed load versus suspended load dominance calculated from one lunar month simulation under pure current conditions overlain by modelled residual currents (m/s). Bathymetry source: INFOMAR (https://www.infomar.ie/ [Accessed on 20 March 2020]).

The external sediment sources at the northern section of the bank can be linked to a sediment transport pathway originating from the on-land headland, Wicklow Head whereby a south-eastward residual transport pathway is evident, originating from Wicklow Head and entering into Arklow Bank's main morphological cell through source pathway number 1 and 2 (Figure 7-12(b)) [14]. Additionally, high resolution modelling of residual tidal currents reveals a residual anticlockwise eddy over the submarine channel, Wicklow Trough [54], [55], similar to the trend identified in Creane et al [14] and Creane et al [15] (Figure 7-12(b)). This potentially acts as a sediment accumulation/deposition zone for eroded sediment from the encompassing shallower Codling Platform [14]. When analysing the one-year accumulative total load sediment transport vectors, a predominant southward sediment transport pathway is evident, streamlined through the Wicklow Trough towards the northern tip of Arklow Bank and partially through source pathways 1 and 2 (Figure 7-12(c)). These pathways comprise a combined 20.31 % of total external sediment sources. In this way, the Wicklow Trough has the potential of focussing sediment transport from the bed load parting zone [14] to Arklow Bank.

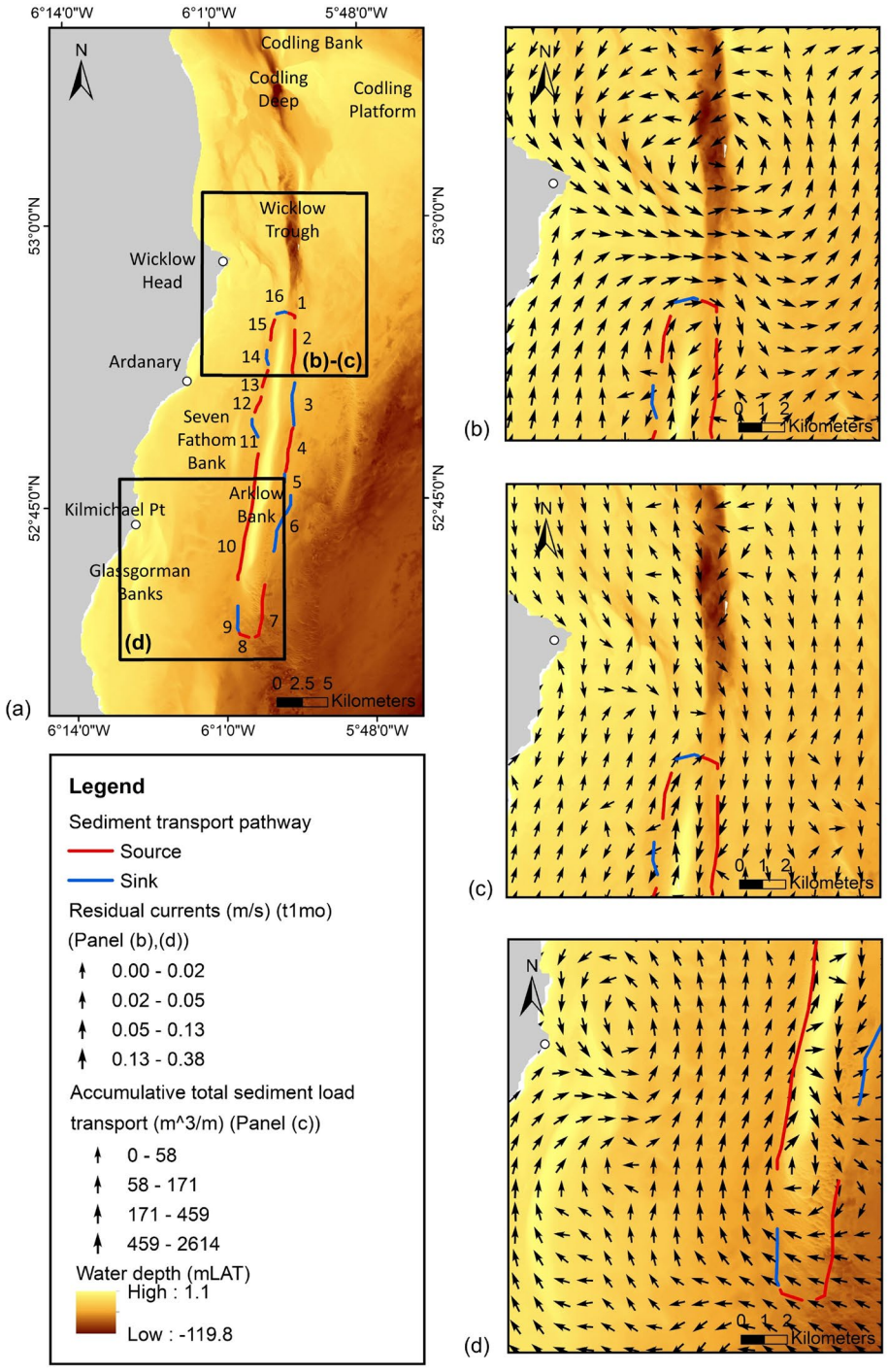


Figure 7-12 (a) Identified sink and source pathways around Arklow Bank's sediment budget cell in relation to the Wicklow Trough and Wicklow Head, (b) Simulated residual currents, after first simulation month (t1mo), over Wicklow Trough and Northern Arklow Bank, (c) Modelled accumulative total sediment load over, after a 12 lunar month simulation, over Wicklow Trough and Northern Arklow Bank, (d) Simulated residual currents t1mo over Glassgorman Banks and Arklow Bank. Bathymetry source: INFOMAR (https://www.infomar.ie/ [Accessed on 20 March 2020]).

However, due to the 'scoured' nature of the bed load parting zone (Figure 7-1) [14], there is a higher potential for currents at the southern half of the bank to carry sediment compared to those focussed through this submarine channel. In this way, pathways 7, 8 and 10 comprise 56.39 % of the total external sediment sources for the Arklow Bank. From analysing residual currents and total sediment transport load residuals over a one-year period, sediment sources at the southern extent of the bank (i.e. pathways 7, 8 and 10) originate from multiple potential sources including;

i) sink pathways 6 and 9,
ii) recycling of sediment from the offshore independent sand wave field (8km east of Arklow Bank (sand wave field 1 in Figure 7-11) [15],
iii) a pathway flowing north-eastward from the northern tip of the Glassgorman Banks (Figure 7-12(a),(d)) and Kilmichael Point (on-land headland) (Figure 7-12(a),(d)) towards pathway 10,
iv) a pathway identified by Creane et al [15], originating from the northern extent of Blackwater Bank, flowing over an offshore sand wave field approximately 10 km off the south-eastern end of Arklow Bank and continuing north-westward across the southern extent of the bank.

In addition, the western side of the bank contains a dynamic exchange system between Arklow Bank and the Seven Fathom Bank through source and sink pathways 10 to 15, potentially recycling material between one another promoting long term stability.

7.3.3 Influence of external sediment sources on Arklow Bank's local sediment transport regime

Sediment source pathways 7 and 10 (Figure 7-10) were selected to test the impact of external sediment sources on Arklow Bank's sediment transport system. These were chosen due to the relatively high portion of external sediment source they account for in the calculated sediment budget. An area of approximately 46 km² and 29 km² directly outside the morphological cell, opposite pathways 7 and 10 respectively, were designated as immobile zones according to the method outlined in section 7.2.2 (Figure 7-13). No other variable was changed from the baseline simulation (Run 2) to ensure the impact of this change could be tested accurately.

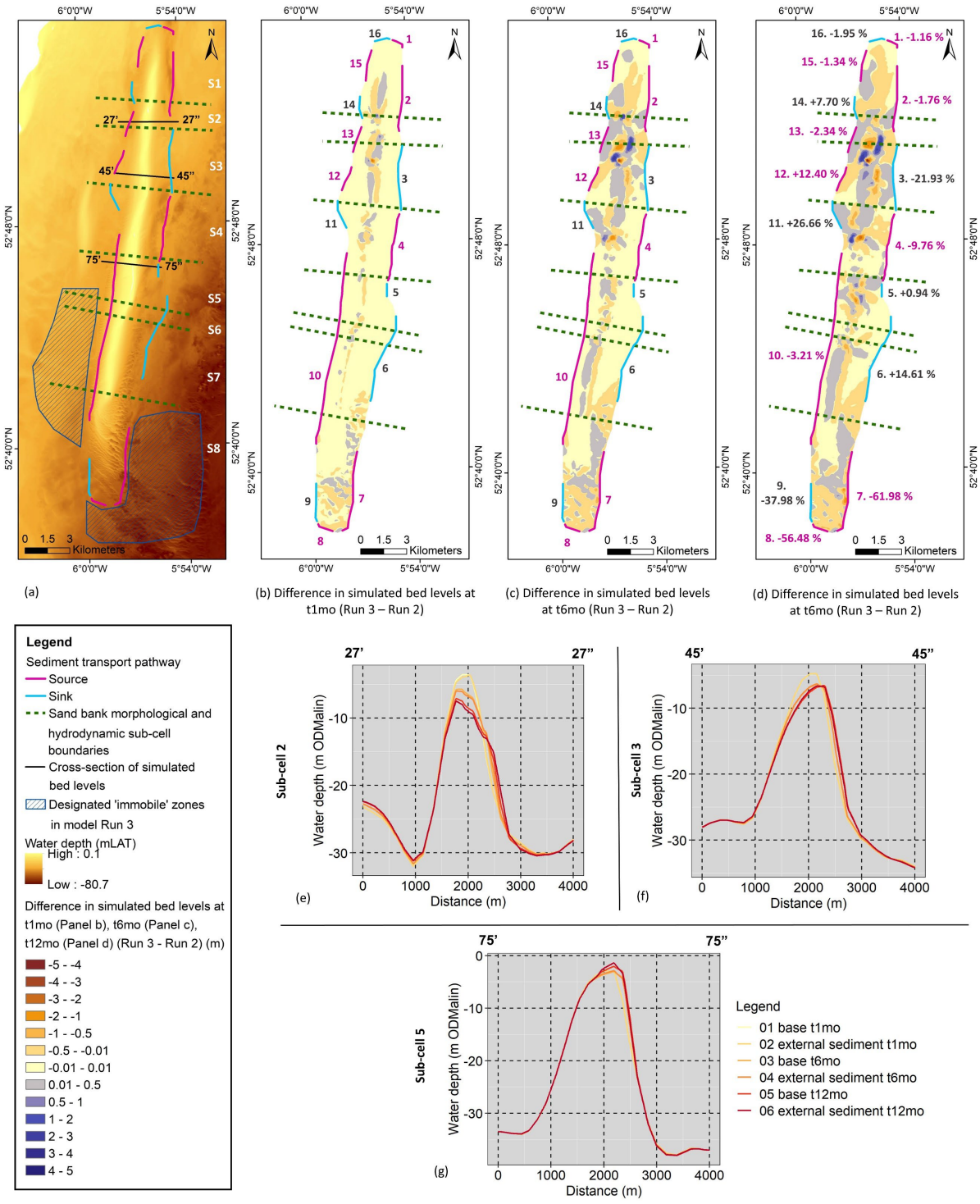


Figure 7-13 (a) Identified sediment sink and source pathways on the circumference of Arklow Bank's sediment budget cell. Location of simulated bed level cross-sections are given. Areas designated as 'immobile zones' in Run 3 are also denoted. (b) to (d) Difference in simulated bed levels after one (t1mo), six (t6mo) and 12 (t12mo) lunar month simulations between Run 2 and Run 3 respectively (Table 7-5). (d) also displays the % total sediment load volume change between Run 3 and Run 2 at each source and sink transport pathway (see Table 7-4). (e) to (g) Cross-sections of simulated bed levels after one (t1mo), six

(t6mo) and 12 (t12mo) lunar month simulations between Run 2 and Run 3 respectively). Panel (a) bathymetry source: INFOMAR (https://www.infomar.ie/ [Accessed on 20 March 2020]).

Results show that the volume change between simulated bed levels within the morphological cell over a one-year period has decreased by 7% compared to baseline calculations. Furthermore, an alteration in the volume of sediment exchanged along the full circumference of the sediment budget cell over this same one-year time period is highlighted (Table 7-4; Figure 7-13).

Compared to baseline results, a decrease in external sediment entering the morphological cell is most significant at source pathways 7 (-62 %), 8 (-56 %) and 10 (-3 %) whereas a decrease in sediment volume exiting the cell is most notable at sink pathways 3 and 9 by 22 % and 38 % respectively. The major reduction in sediment volume passing cross-sections 7, 8 and 9 in Run 3 correlates very well with the adjacent designated 'immobile' zones. As less external sediment passes through pathways 7 and 8, this directly reduces the volume of material exported out of the cell via pathway 9.

Table 7-4 Change in volume of sediment passing through each pathway in Run 3 compared to baseline model Run 2

Pathway Number	Sediment Pathway Type	% Volume change of sediment compared to baseline volumes (negative values = reduction; positive values = increase)
1	Source	-1.16
2	Source	-1.76
3	Sink	-21.93
4	Source	-9.76
5	Sink	0.94
6	Sink	14.62
7	Source	-61.98

8	Source	-56.48
9	Sink	-37.98
10	Source	-3.21
11	Sink	26.66
12	Source	12.40
13	Source	-2.34
14	Sink	7.70
15	Source	-1.34
16	Sink	-1.95

Figure 7-13 presents bed level differences between Run 2 and Run 3 after one, six and 12 lunar month simulation periods. These datasets highlight the direct impact of external sediment sources on upper slope bank morphodynamics. Notably, zones of high bed level differences, i.e. high vulnerability zones (HVZs), are identified as early as a one lunar month simulation, correlating with 'mobile' areas of the bank, namely sub-cells 1, 3, 4, 5 and 7. Partial overlap with southern half of the relatively 'stable' zone of sub-cell 2 is noted, where the bank transitions from at or above mean sea level (MSL) to a slightly deeper water depth [17]. The slight increase in water depth above the bank crest facilitates a relatively higher quantity and magnitude of residual cross-flow [17] in comparison to the northern half of sub-cell 2. Subsequently, this potentially leaves this area of the bank more vulnerable to other forces such as changes in external sediment sources, wind and wave-induced flow. However, the bed level changes at the southern tip of the bank, in sub-cell 8, are directly related to changes in sand wave dynamics rather than upper slope morphodynamic changes [15].

After one, six and 12-month simulation periods, the maximum difference in bed level between Run 2 and Run 3 ranges from +1.29 m to -2.53 m, +3.21 m to -3.56 m and +2.98 m to -4.85 m respectively (Figure 7-13(b)-(d)). The most significant HVZs, located at the mid and

northern sections of the bank, align with the change in sediment volume exchanged across pathways 3, 4, 11, 12 13 and 14. In general, there is an increase in the percentage of sediment transfer on the western side of the bank and a decrease in the percentage of sediment exchanged on the eastern side of the bank in comparison to the baseline run. For example, where volume of sediment exchanged outwards and inwards increase by 26.66 % and 12.4 % at pathways 11 and 12, the volume of sediment transported out pathway 3 reduced by 21.93 % (Figure 7-13(d)). These correlate with the intersection point of the outer flows of off-bank anticlockwise Eddies D and F on the eastern side of the bank, and Eddies E and G on the western side of the bank (Figure 7-5). This also marks the transition point between bank sub-cells 3 and 4. From Figure 7-4, the nature of these residual currents differ on either side of this transition zone, yet most notably, the development of on-bank clockwise residual current and residual total load vector eddies at the northern point of sub-cell 4 implies the recycling of sediment between pathways 12 and 11 (Figure 7-13(d)).

When comparing cross-sections of simulated bed levels between Run 2 and Run 3 over the identified HVZs, the nature of the change is not consistent in each area. This is most likely due to the complex hydrodynamic and sediment transport system, containing:

ii. A high level clockwise residual circular eddy encompassing the whole bank, caused by flood/ebb tidal dominance, and multiple smaller scale on-bank clockwise residual eddies, both of which unevenly distribute sediment within the sediment budget cell, and
iii. Multiple anticlockwise residual current and sediment transport eddies, located on the edge of the larger clockwise flow, that have the potential to transfer sediment in and out of the cell.

Due to these complex sediment distribution mechanisms, although an overall reduction in volume change is observed between Run 2 and Run 3, changes to the morphodynamics of the bank in each HVZ are inconsistent. For example, along cross-sections L15-L17 and L27-30 a higher magnitude and rate of erosion is observed (Figure 7-13(a) and (e)). Contrastingly, a lower rate of both erosion and mobility is observed in cross-sections L45 to L46 and L52 to L55 (Figure 7-13(a) and (f)), and a higher rate of accretion is notable in cross-sections L75 to L76 (Figure 7-13(a) and (g)). While the maximum range of bed level difference between Run 2 and Run 3 after one, six and 12 lunar months simulation is +1.29 m to -2.53 m, +3.21 m to -3.56 m, and +2.98 m to -4.85 m, bed level differences vary between HVZ representative cross-sections (Table 7-5). After the first month simulation, cross-section L17 bed level differences range from +0.06 m to -0.16 m yet L27 ranges from +0.64 m to -0.39 m. By the 12th simulation month, L17 displays a relatively low difference of +0.03 m to -0.21 m in comparison to L27 displaying a difference of +1.91 m to -0.61 m compared to base case. Evidently, the range of impact of external sediment source on bank morphology varies immensely along the bank.

Table 7-5 Difference in bed levels between each scenario run, along targeted cross-sections over the identified HVZs, after a simulation period of 1 month (t1mo), 6 months (t6mo) and 12 months (t12mo). For cross-section locations see Figure 7-13(a).

Model Run Comparison	Variable	Line ID	T1mo			T6mo			T12mo		
			Mean	Max	Min	Mean	Max	Min	Mean	Max	Min
Run 2 Vs Run 3	Baseline Vs Changes to external sediment sources	L17	-0.01	0.06	-0.16	-0.03	0.03	-0.21	-0.05	0.03	-0.21
		L27	0.01	0.64	-0.39	0.05	1.3	-0.34	0.05	1.91	-0.61
		L33	0	0.24	-0.23	0.19	1.97	-0.26	0.21	2.35	-0.48
		L45	0	0.02	-0.03	0.01	0.1	-0.05	-0.02	0.27	-0.69
		L63	0	0	-0.05	-0.01	0.01	-0.05	-0.03	0.07	-0.12
		L75	0	0.01	-0.02	-0.01	0.18	-0.43	0	0.67	-0.9
		L77	0	0.01	-0.02	0	0.13	-0.08	-0.06	0.02	-0.66
		L80	0	0.01	-0.02	0	0.01	-0.05	-0.06	0.92	-1.27

		L111	-0.01	0.01	-0.07	-0.04	0.01	-0.4	-0.08	0.07	-0.83
Run 2 Vs Run 4	Baseline Vs Addition of Wind and surface pressure	L17	-0.01	0.14	-0.37	-0.01	0.4	-0.91	0.04	0.73	-1.04
		L27	0.04	0.74	-0.19	0.05	1.76	-0.26	0.07	3.03	-0.76
		L33	-0.01	0.25	-0.35	0.17	2.04	-2.33	0.31	2.22	-1.65
		L45	0	0.15	-0.12	-0.01	0.05	-0.04	-0.06	0.33	-0.98
		L63	0.01	0.2	-0.01	-0.02	0.28	-0.21	-0.05	0.81	-0.71
		L75	0	0.04	-0.06	-0.01	0.81	-0.49	-0.05	2.43	-1.35
		L77	0	0.05	-0.08	-0.05	1.32	-1.28	-0.04	4.41	-3
		L80	0	0.04	-0.07	-0.04	0.23	-0.53	-0.14	0.66	-1.8
		L111	0	0.02	-0.03	0	0.15	-0.11	0	0.03	-0.04
Run 2 Vs Run 5	Baseline Vs Addition of wind and surface pressure, and wave-induced flow	L17	-0.01	0.17	-0.44	-0.01	0.32	-0.73	-0.05	0.52	-1.02
		L27	-0.01	0.9	-0.52	0.11	2.59	-0.5	0.17	4.65	-1.02
		L33	-0.01	0.3	-0.38	0.12	1.7	-2.79	0.27	2.46	-1.99
		L45	0	0.14	-0.1	-0.02	0.04	-0.06	-0.06	0.32	-0.86
		L63	0.01	0.21	-0.01	-0.02	0.31	-0.23	-0.05	0.92	-0.76
		L75	0	0	-0.02	-0.01	0.44	-0.3	-0.05	1.35	-0.91
		L77	0	0.02	-0.05	-0.03	0.82	-0.71	-0.01	3.98	-2.56
		L80	0	0.03	-0.04	-0.03	0.18	-0.43	-0.03	0.44	-0.46
		L111	0	0.09	-0.07	0.01	0.82	-0.44	0.02	0.78	-0.41
Run 4 Vs Run 5	Addition of wind and surface pressure Vs Addition of wind and surface pressure, and wave-induced flow	L17	0	0.05	-0.07	-0.01	0.19	-0.21	-0.09	0.05	-0.65
		L27	-0.04	0.16	-0.71	0.06	0.83	-0.25	0.1	1.61	-0.33
		L33	0	0.05	-0.06	-0.06	0.25	-0.77	-0.04	0.92	-0.91
		L45	0	0.02	-0.01	-0.01	0.02	-0.06	0	0.13	-0.08
		L63	0	0.02	0	0	0.03	-0.02	-0.01	0.19	-0.07
		L75	0	0.03	-0.04	0	0.19	-0.37	0.01	0.48	-1.08
		L77	0	0.03	-0.02	0.02	0.57	-0.5	0.03	0.44	-0.46
		L80	0	0.03	-0.01	0.01	0.1	-0.05	0.11	1.64	-0.35
		L111	0	0.07	-0.04	0.01	0.67	-0.33	0.02	0.82	-0.44

While Coughlan et al [16] shows that the dominant process controlling seabed disturbance are tidal currents and Creane et al [17] shows that tidal currents are the dominant controlling factor of Arklow Bank's long-term stability and morphodynamic regime, new analysis

ultimately shows that this sedimentary bedform relies on external sediment sources to sustain morphological stability in the existing local sediment transport system.

By introducing a restriction on sediment sources entering the southern part of the bank, a relatively low impact on the one-year bank volume change is revealed. Although the reduction in volume change from Run 2 to Run 3 is quite minimal (7 %), the volume of sediment exchanged across each pathway of the entire circumference of the sediment budget cell is modified. Additionally, this reduction in external sediment sources clearly alters the distribution of sediment along the length of the bank which in turn alters rates and magnitudes of localised erosion/accretion.

This alteration varies along the length of the bank whereby the areas most impacted are the relatively high mobility areas in the mid and northern sections of the bank. The visibility of these changes after a single lunar cycle implies that the residual clockwise sediment transport eddy encompassing the bank has the ability to distribute sediment from the southern to northern extent of the bank over this time-frame. This may take place through a combination of bed load and suspended load sediment transport methods. This knowledge could directly apply to other offshore sand banks in tidally-dominated areas. Furthermore, the nature and timeline of this impact implies that a disturbance to the seabed due to anthropogenic processes such as dredging of materials for OWF cable burial or as a source of marine aggregates has potential to impact erosion and accretion rates and bedform dynamics further along the sediment transport pathway [8]. Similarly, studies have shown that ORE developments alter current and wave propagation [2], [4], [7], [10], [12], [13], [56]. In this way, with the increased in planned anthropogenic activities, a robust marine spatial plan must incorporate a risk assessment that analyses potential changes to the hydrodynamic processes

controlling seabed stability identified in this study and in Creane et al [17]. Ultimately, due to complex local and regional hydrodynamic and sediment transport systems connecting various areas of the south-western Irish Sea [14], [15], it is imperative that an assessment should be carried out to identify and reduce potential risks to environmental stability both in the immediate and wider area of works. Increasing knowledge of this system and protecting against seabed instability will also reduce risk for ORE developments, protect benthic habitats, protect existing marine commercial industries such as fisheries, and aid marine spatial planning.

A long-term simulation may improve knowledge of the extent and timing of the intricate interconnected sediment transport system. For example, disturbance to the offshore independent sand wave off the eastern side of Arklow Bank, presented in Figure 7-11, should be tested to understand the dependence of offshore sand deposits on offshore sand banks, the dependence of offshore sand banks on these offshore sand deposits, and the timeline in which this circulatory system exchanges sediment between these two deposition areas. This will ultimately facilitate the development of a robust, sustainable marine spatial plan.

7.3.4 Impact of wind on Arklow Bank morphodynamics

With the inclusion of a wind field in Run 4, high vulnerability zones (HVZs) are identified along the bank. These HVZs are located in the highly dynamic morphological sub-cells 1, 3, 4 and 5 (Figure 7-14(a)-(d)), yet sub-cells 2, 4, 6, 7 and 8 (Figure 7-14(a)-(d)) show very little impact. These vulnerable areas correlate very well with those areas of the bank susceptible to change under the interference of external sediment sources (section 7.3.3). Additionally, the areas of stability previously observed in Runs 1 to 3, remain relatively immobile showing little to no response to wind-induced flow. The maximum difference in simulated bed levels over the

whole bank between Run 2 and Run 4 after one, six and 12 lunar months, range from +1.37 m to -2.92 m, +5.95 m to -6.90 m, and 6.16 m to -8.32 m respectively (Figure 7-14(b)-(d)). Notably, this maximum range is not observed in each HVZ (Table 7-5). For example, cross-sections L33 and L77 represent typical simulated bed level conditions in these areas (Figure 7-14(f) and (i)). The range of bed level difference between Run 2 and Run 4 after one, six and 12 lunar months along L33 are +0.25 m to -0.35m, +2.04 m to -2.33 m, and +2.22 m to -1.65 m respectively and along L77 are +0.05 m to -0.08 m, +1.32 m to -1.28 m, and +4.41 m to -3.00 m (Table 7-5). Notably, in each profile where a difference is noted, it is most significant in the upper slopes, with the highest impact within the upper five metres of the crest (Figure 7-14(f)-(i)).

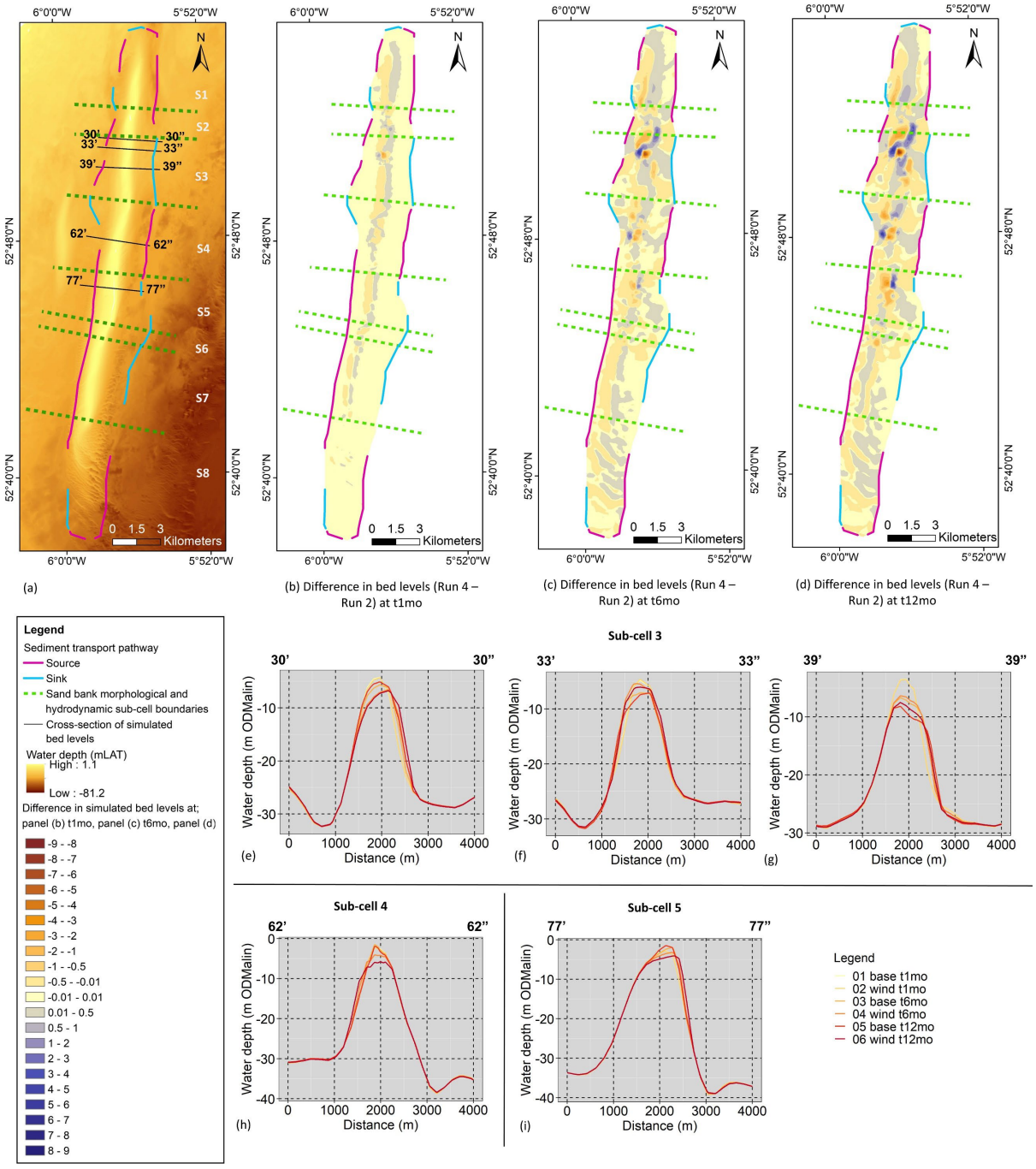


Figure 7-14 (a) Identified sediment sink and source pathways on the circumference of Arklow Bank's sediment budget cell. Location of simulated bed level cross-sections are given. (b) to (d) Difference in simulated bed levels after one (t1mo), six (t6mo) and 12 (t12mo) lunar month simulations between Run 2 and Run 4 respectively (Table 7-5). (e) to (i) Cross-sections of simulated bed levels after one (t1mo), six (t6mo) and 12 (t12mo) lunar month simulations between Run 2 and Run 3 respectively. Panel (a) bathymetry source: INFOMAR (https://www.infomar.ie/ [Accessed on 20 March 2020]).

In shallow environments, wind-induced currents have shown to both induce surface current velocities and temporally reverse surface current directions [23]. This in turn has a direct impact on sediment transport pathways and morphodynamics, especially bedforms located in relatively shallow water. This study shows that wind-induced currents increases erosion at various HVZs along the bank. This phenomenon is reflected in cross-section L62 (Figure 7-14(a) and (h)), located in sub-cell 4, whereby an increased rate of bed level reduction is evident in comparison to the pure current case. Contrastingly, other regions such as over cross-section L39 (Figure 7-14(a) and (g)), a decrease in the rate of bed level reduction is evident. This could be due to a temporary reversal of net current flow in this area, or due to sediment resuspension during slack tide and sediment transport in the opposite direction during these slack tidal current conditions as noted in previous studies in other environments [22]–[24]. This slows this east-west fluctuation behaviour. Subsequent alteration in the timing of the east-west fluctuation of the bank due to this altered flow regime is further visible in cross-section L30 (Figure 7-14(a) and (e)).

Clearly, the magnitude of the altered flow varies depending on the location along the bank and the simulation time step of extracted bed levels. As the dynamically coupled model includes a morphological feedback loop with simulated hydrodynamics, the bed level is continuously updated. These updated morphological changes are used as a base for flow calculations at the following timestep. In this way, it is difficult to directly compare the direct impact of wind to the baseline bed levels at the 6^{th} and 12^{th} simulated months. Using cross-section L33 as an example (Figure 7-14(a), (f)), Run 4 bed levels at the 12^{th} lunar month displays a bank asymmetry in the opposite direction to baseline bed levels for the same simulation month. The addition of wind-influenced flow, continuously modifies the shape of the bank which ultimately alters the timing of the hydrodynamic-morphodynamic response

in the identified vulnerable areas in comparison to the base case. In this way, wind may either accelerate or delay the localised timing of the fluctuation compared to the pure current case.

Although the wind-current interaction implies that shallow areas of the bank should be most influenced by wind-induced flows, this is not always the case here. The relatively 'stable' sub-cells of the bank, namely sub-cell 2 and 6 have crest levels near MSL yet show very little to no impact. On closer examination, the areas mostly impacted align with regions that are relatively shallow (< -5 mMSL) but have an existing relatively high residual cross-flow driving east-west migration of the upper slopes of the bank. The lack of influence of wind on sub-cells 2 and 6 may be due to the absence of a strong residual cross-flow due to the control of wider tidal current phenomena such as off-bank anticlockwise residual eddies and on-bank clockwise eddies [17].

7.3.5 Impact of wave-induced flow on Arklow Bank morphodynamics

The areas of the bank impacted by combined current, wave and wind-induced flow align with those HVZs identified in section 7.3.4. The maximum range of bed level difference between Run 5 (current, wind and wave) and Run 2 (current only) after one, six and 12 lunar months is +1.65 m to -3.55 m, +5.96 m to -7.34 m, and +7.03 m to -8.71 m (Figure 7-15(a), (c), (e)). However, this maximum range varies across each HVZ over the one-year simulation period as highlighted in Table 7-5. For example, the maximum and minimum bed level difference along cross-section L27 (Figure 7-15(g)) between Run 5 and Run 2 after one, six and 12 lunar months is 0.90 m and -0.52 m, 2.59 m and -0.50 m, 4.65 m and -1.02 m respectively. However, under the same scenario, L63 (Figure 7-15(h)) displays a maximum and minimum bed level difference after one, six and 12 lunar months of 0.21 m and -0.01 m, 0.31 m and -0.23 m, 0.92 m and -0.76 m respectively (Table 7-5).

Additionally, variation exists between Run 5 and Run 4 (current and wind) where the maximum range of bed level differences after one, six and 12 lunar months is +1.16 m to -1.52 m, +2.39 m to -1.02 m, and +2.76 m to -1.25 m (Figure 7-15(b), (d), (f)). The variability of this maximum range across each identified HVZ are evident in extracted representative cross-sections presented in Table 7-5. In particular, the maximum and minimum bed level difference across L27 (Figure 7-15(g)) between Run 5 and Run 4 after one, six and 12 lunar months is 0.16 m and -0.71 m, 0.83 m and -0.25 m, 1.61 m and -0.33 m respectively. However, under the same scenario, L63 (Figure 7-15(h)) displays a maximum and minimum bed level difference after one, six and 12 lunar months of 0.02 m and 0.00 m, 0.03 m and -0.02 m, 0.19 m and -0.07 m respectively (Table 7-5).

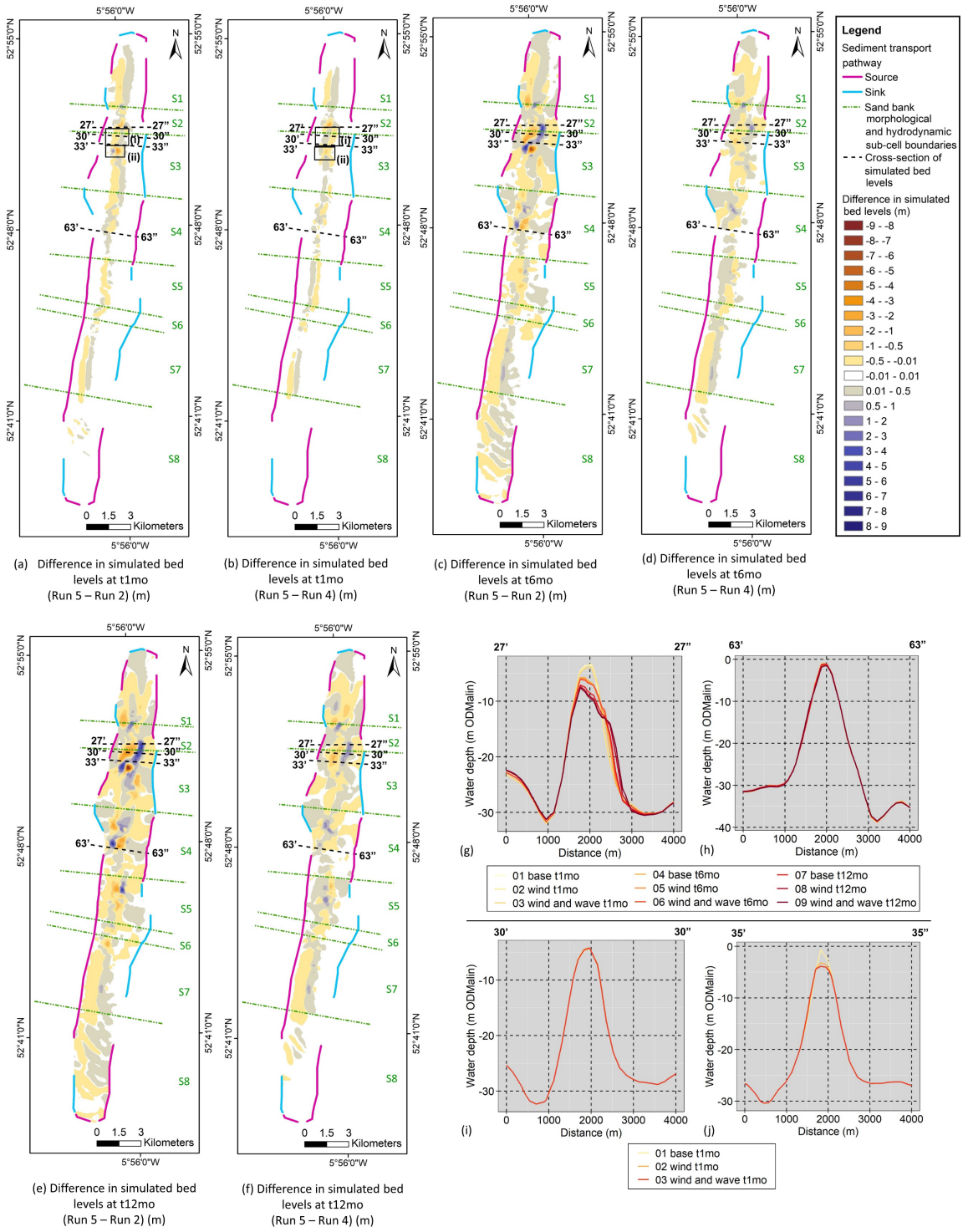


Figure 7-15 (a), (c), (e) Difference in simulated bed levels after one (t1mo), six (t6mo) and 12 (t12mo) month simulation periods respectively between Run 2 and Run 5; (b), (d), (f) Difference in simulated bed levels after one, six and 12 month simulation periods respectively between Run 4 and Run 5 (see Table 7-5); (g) to (j) Cross-sections of simulated bed levels from Run 2 ('base'), Run 4 ('wind') and Run 5 ('wind and wave').

Over each HVZ, wave-induced flow is shown to both increase erosion or accretion in comparison to baseline conditions, similar to that shown in [20], which in this case directly correlate with the delay or acceleration of the east-west fluctuation of the upper slopes of the bank (Figure 7-15(a)-(j)) characterised by Creane et al [17]. This is directly linked to the complex wave-current interaction [57]. Depending on the orientation of wave propagation in relation to the direction of current flow, wave celerity may be increased or decreased [57]. At Arklow Bank, depending on whether wave-induced flow is in the same or opposing direction as tidal currents, the east-west fluctuation of the bank may be delayed or accelerated. Additionally, the general distribution of sediment along the bank may be temporally altered due to this change.

Furthermore, when analysing the difference between simulated bed levels after one lunar month between (i) Run 5 and Run 2 (Figure 7-15(a)), and (ii) Run 5 and Run 4 (Figure 7-15(b)), a complex wind-wave interaction is highlighted. For example, in area (i) in Figure 7-15(a) Run 5 displays increased erosion and accretion on the western and eastern sides of the bank respectively in comparison to baseline conditions. In area (ii) in Figure 7-15(a) Run 5 displays increased accretion and erosion on the western and eastern sides of the bank in comparison to the baseline model run. By analysing one month simulated bed levels in these areas from Run 4 against Run 5 the nature of the impact of wind and wave on sediment transport can be isolated. Therefore, when further analysing area (i) together in Figure 7-15(a) and Figure 7-15(b), the addition of wave forcing actually decreases the magnitude of eastward migration of the upper slope in comparison to combined current and wind forcing over this time period (e.g. cross-section L30 (Figure 7-15(a); Figure 7-15(b); Figure 7-15(i)). However, when analysing area (ii) together in Figure 7-15(a) and Figure 7-15(b), wave forcing increases the rate of westward migration of the upper slope in comparison to combined current and wind

forcing over this time period (e.g. cross-section L35 (Figure 7-15(a); Figure 7-15(b); Figure 7-15(j)). In this way, the addition of wave forcing can further increase or delay the east-west fluctuation of the upper slopes of Arklow Bank. These discrepancies are most likely due to the misalignment of the directionality of wind forcing and swell wave propagation. Surface waves can be separated into wind-waves and swell waves. Wind-waves are waves that propagate in the same direction as the wind whereas swell are waves that have been generated elsewhere or before the wind changes direction. In other words, swell are wind-generated waves that are not significantly affected by the local wind at that time. The radiation stresses generated by the spectral wave model for input into Run 5 incorporate both wind-waves and swell. In this way, the mis-alignment in directionality between the wind forcing and wave-induced flow has the potential to drive these inconsistent morphodynamic changes. Also wave refraction, which is the bending of wave energy in shallow water, adds complexity to this interaction.

From this analysis it is clear that specific areas of the bank are impacted by the wind- and wave-tidal current interaction. These phenomena have shown to either speed up or delay the tidal-current-controlled upper slope east-west fluctuation. However, these forces are not as consistent as tidal currents, instead they vary over time on an hourly, daily and seasonal basis. Consequently, the influence they have on bank morphodynamics do not impact the overall long-term behaviour of the bank.

7.4 Conclusion

This study uses two-dimensional morphological modelling to investigate the level to which Arklow Bank's local sediment transport regime is influenced by external sediment sources, wind forcing and wave forcing. A mesh sensitivity analysis was first carried out to identify the most efficient mesh resolution to investigate various hydrodynamic and morphodynamic

processes along the length of the bank. Secondly, a sediment budget was estimated for Arklow Bank in order to analyse the impact of external sediment sources on the local sediment transport regime. Finally, the areas of the bank most-vulnerable to wind and wave forcing are identified, and the nature of their impact is revealed. The main outcomes from this study are presented below.

1. An unstructured mesh resolution of at least 50 m to 80 m over Arklow Bank is necessary to resolve the timing and nature of the complex east-west fluctuation of the upper slopes of the sand bank. When the mesh resolution over the bank is increased to 150 m to 200 m, the morphological model fails to resolve the timing of this east-west fluctuation, but still captures the general hydrodynamic processes controlling both bank base stability and upper slope mobility. Consequently, when considering all variables of a project such as project objectives, site characteristics, computational time, and project timeline and budget, for a process-understanding study, a coarser resolution model is adequate. However, regardless of the computational time saved by a coarser resolution mesh, to understand maximum limits of vertical and horizontal bed levels along the length of the bank, a higher resolution mesh is required. The adoption of this criteria is important for studies where a detailed understanding of morphological changes is necessary, such as OWF cable burial depth and scour protection design.
2. Using a one-year model simulation, a sediment budget for Arklow Bank is estimated. From this, seven sink and nine source external sediment transport pathways are identified, with the following characteristics:
    a) The identified connection between sink pathways on the eastern side of Arklow Bank with an offshore independent sand wave field 8 km east of Arklow Bank by Creane et al [15] is further supported here through the identification of SSC residual plumes

along the transport pathways and by using a bed load/suspended load dominance factor to support the proposed mechanism of transport.

b) Sediment sources at the southern extent of the bank are partially connected to the return of sediment from these sand deposits yet are also sourced from other offshore sand deposits including the Glassgorman Banks.

c) Sediment exchange at the northern extent of Arklow Bank is linked with Wicklow Head and Wicklow Trough, the latter displaying a potentially funnelling of sediment from the BLP zone [14].

d) Finally, the western side of the bank is dominated by sediment exchange between Arklow Bank and Seven Fathom Bank.

3. Although sediment distribution along Arklow Bank is mainly contributed to the large clockwise residual current eddy encompassing the bank, the bank is also influenced by external sediment sources. External sediment exchange is clearly facilitated by the positioning of multiple anticlockwise residual current eddies along the circumference of this main morphological cell [17]. The restriction of sediment sources off the southern extent of the bank leads to changes in erosion and accretion patterns in the mid and northern sections of the bank after just one simulated lunar month. This highlights the short timescale to which the large clockwise residual current eddy distributes sediment throughout the bank. This implies that anthropogenic activities such as dredging for marine aggregates can highly impact areas further along a transport pathway over a relatively short time-scale. The magnitude of this impact depends on the extent and duration of the works. Given the particular complexity of the interconnected sediment transport pathways in the south-western Irish Sea, the risk of seabed instability arising from increased anthropogenic seabed disturbances is high. Robust marine spatial

planning that considers these processes are key to reducing the risk of environmental instability.

4. The areas of the bank most vulnerable to changes in external sediment sources and the addition of wind forcing and wave forcing are quite consistent. These areas generally align with those regions identified as 'mobile' zones in Creane et al [17] and display a relatively high residual current crossflow under pure current baseline conditions.
5. The influence of wind-induced flow on the bank is concentrated in these HVZs. The addition of these forces is shown to both accelerate and reduce the speed of the east-west fluctuation of the upper slopes of the bank.
6. The impact of wave-induced flow is also focussed in these HVZs. Although the east-west fluctuation can both accelerate or reduce the speed of the upper slope migration dynamics, it is inconsistent with wind-forcing. This is most likely due to the mis-alignment between wind direction with the directionality of wave-induced flow arising from swell.
7. Where tidal currents are the primary control on sediment transport patterns and regulate Arklow Bank morphodynamics, wind and wave forcing are shown to impact vulnerable areas of the system but have a lesser impact the long-term behaviour of the bank.

7.5 Acknowledgments

SC is funded by the Irish Research Council (IRC) through grant EBPPG/2019/158 (Employment-Based Postgraduate Programme Scholarship). MC is funded under an Irish Research Council Enterprise Partnership Scheme Postdoctoral Fellowship (EPSPD/2020/109) and in part by a research grant from Science Foundation Ireland (SFI) under Grant Number 13/RC/2092, with support from Gavin and Doherty Geosolutions Ltd and the Geological Survey of Ireland (GSI). This project benefitted from funded industry-academic collaboration involving Gavin and

Doherty Geosolutions, University College Dublin (iCRAG) and University College Cork (MaREI), supported by the Marine Institute under the Marine Research Programme 2014-2020 (Grant-Aid Agreement No. IND/18/18). Ship time on the RV Celtic Voyager was funded by the Marine Institute through the 2020-2021 ship-time programme under the National Marine Research and Innovation Strategy 2017-2021.

7.6 Author statement

Shauna Creane: Conceptualization, Methodology, Investigation, Formal Analysis, Writing – Original Draft, Writing - Review & Editing, Visualisation.

Michael O'Shea: Supervision, Writing – Review & Editing.

Mark Coughlan: Supervision, Writing – Review & Editing.

Jimmy Murphy: Supervision, Conceptualization, Writing – Review & Editing.

7.7 References

[1] RPS, "Arklow Bank Wind Park Phase 2 Offshore Infrastructure: Environmental Impact Assessment Report - Appendix 3.1: Consultation Report," 2021.

[2] C. Auguste, J. R. Nader, P. Marsh, I. Penesis, and R. Cossu, "Modelling the influence of Tidal Energy Converters on sediment dynamics in Banks Strait, Tasmania," *Renewable Energy*, vol. 188, pp. 1105–1119, 2022, doi: 10.1016/j.renene.2022.02.077.

[3] M. Baeye and M. Fettweis, "In situ observations of suspended particulate matter plumes at an offshore wind farm, southern North Sea," *Geo-Marine Letters*, vol. 35, no. 4, pp. 247–255, 2015, doi: 10.1007/s00367-015-0404-8.

[4] I. Fairley, I. Masters, and H. Karunarathna, "The cumulative impact of tidal stream

turbine arrays on sediment transport in the Pentland Firth," *Renewable Energy*, vol. 80, pp. 755–769, 2015, doi: 10.1016/j.renene.2015.03.004.

[5] J. M. Harris, R. J. S. Whitehouse, and J. Sutherland, "Marine scour and offshore wind - Lessons learnt and future challenges," in *Proceedings of the International Conference on Offshore Mechanics and Arctic Engineering - OMAE*, 2011, vol. 5, pp. 849–858. doi: 10.1115/OMAE2011-50117.

[6] R. A. Lind and R. J. S. Whitehouse, "Understanding and Assessing Scour Development at Offshore Structures," *Journal of Oilfield Technology*, vol. 5, no. 6, pp. 63–67, 2012.

[7] A. Rivier, A.-C. Bennis, G. Pinon, V. Magar, and M. Gross, "Parameterization of wind turbine impacts on hydrodynamics and sediment transport," *Ocean Dynamics*, vol. 66, no. 10, pp. 1285–1299, 2016, doi: 10.1007/s10236-016-0983-6.

[8] H. Demir, E. N. Otay, P. A. Work, and O. S. Börekçi, "Impacts of Dredging on Shoreline Change," *Journal of Waterway, Port, Coastal, and Ocean Engineering*, vol. 130, no. 4, pp. 170–178, 2004, doi: 10.1061/(asce)0733-950x(2004)130:4(170).

[9] L. Wyns, M. Roche, F. Barette, V. Van Lancker, K. Degrendele, K. Hostens, and A. De Backer, "Near-field changes in the seabed and associated macrobenthic communities due to marine aggregate extraction on tidal sandbanks: A spatially explicit bio-physical approach considering geological context and extraction regimes," *Continental Shelf Research*, vol. 229, p. 104546, 2021, doi: 10.1016/j.csr.2021.104546.

[10] S. Clark, F. Schroeder, and B. Baschek, "The influence of large offshore wind farms on the North Sea and Baltic Sea – a comprehensive literature review (Report No. HZG Report 2014-6)," Geesthacht, Germany: Helmholtz-Zentrum Geesthacht, Zentrum für

Material-und Küstenforschung, 2014.

[11] E. Ivanov, A. Capet, E. De Borger, S. Degraer, E. J. M. Delhez, K. Soetaert, J. Vanaverbeke, and M. Grégoire, “Offshore Wind Farm Footprint on Organic and Mineral Particle Flux to the Bottom,” *Frontiers in Marine Science*, vol. 8, 2021, doi: 10.3389/fmars.2021.631799.

[12] J. Abanades, D. Greaves, and G. Iglesias, “Wave farm impact on the beach profile: A case study,” *Coastal Engineering*, vol. 86, pp. 36–44, 2014, doi: 10.1016/j.coastaleng.2014.01.008.

[13] F. Onea, L. Rusu, G. B. Carp, and E. Rusu, “Wave farms impact on the coastal processes—A case study area in the portuguese nearshore,” *Journal of Marine Science and Engineering*, vol. 9, no. 3, pp. 1–20, 2021, doi: 10.3390/jmse9030262.

[14] S. Creane, M. O’Shea, M. Coughlan, and J. Murphy, “The Irish Sea bed load parting zone: Is it a mid-sea hydrodynamic phenomenon or a geological theoretical concept?,” *Estuarine, Coastal and Shelf Science*, vol. 263, p. 107651, 2021, doi: 10.1016/j.ecss.2021.107651.

[15] S. Creane, M. Coughlan, M. O’Shea, and J. Murphy, “Development and dynamics of sediment waves in a complex morphological and tidal dominant system: southern Irish Sea,” *Geosciences*, vol. 12, no. 12, p. 46, 2022, doi: 10.3390/geosciences12120431.

[16] M. Coughlan, M. Guerrini, S. Creane, M. O’Shea, S. L. Ward, K. J. J. Van Landeghem, J. Murphy, and P. Doherty, “A new seabed mobility index for the Irish Sea: modelling seabed shear stress and classifying sediment mobilisation to help predict erosion,

deposition, and sediment distribution," *Continental Shelf Research*, vol. 229, p. 104574, 2021, doi: https://doi.org/10.1016/j.csr.2021.104574.

[17] S. Creane, M. O'Shea, M. Coughlan, and J. Murphy, "Hydrodynamic processes controlling sand bank mobility and long-term base stability: A case study of Arklow Bank," *Geosciences*, vol. 13, no. 2, p. 60, 2023, doi: 10.3390/geosciences13020060.

[18] R. J. S. Whitehouse, J. M. Harris, J. Sutherland, and J. Rees, "The nature of scour development and scour protection at offshore windfarm foundations," *Marine Pollution Bulletin*, vol. 62, no. 1, pp. 73–88, 2011, doi: 10.1016/j.marpolbul.2010.09.007.

[19] EMODnet Bathymetry Consortium, "EMODnet Digital Bathymetry (DTM 2020)." 2020. doi: https://doi.org/10.12770/bb6a87dd-e579-4036-abe1-e649cea9881a.

[20] A. Giardino and J. Monbaliu, "Wave effects on the morphodynamic evolution of an offshore sand bank," *Journal of Coastal Research SI*, vol. 51, pp. 127–140, 2010, doi: 10.2112/SI51-012.1.

[21] D. Idier, A. Ehrhold, and T. Garlan, "Morphodynamique d'une dune sous-marine du détroit du pas de Calais," *Comptes Rendus Geoscience*, vol. 334, no. 15, pp. 1079–1085, 2002, doi: 10.1016/s1631-0713(02)01852-7.

[22] N. C. Mitchell, R. Jerrett, and R. Langman, "Dynamics and stratigraphy of a tidal sand ridge in the Bristol Channel (Nash Sands banner bank) from repeated high-resolution multibeam echo-sounder surveys," *Sedimentology*, vol. 69, no. 3, pp. 1051–1082, 2022, doi: 10.1111/sed.12935.

[23] I. Colosimo, P. L. M. de Vet, D. S. van Maren, A. J. H. M. Reniers, J. C. Winterwerp, and

B. C. van Prooijen, “The impact of wind on flow and sediment transport over intertidal flats,” *Journal of Marine Science and Engineering*, vol. 8, no. 11, pp. 1–26, 2020, doi: 10.3390/jmse8110910.

[24] J. J. Daniell, “Bedload parting in western Torres Strait, northern Australia,” *Continental Shelf Research*, vol. 93, pp. 58–69, 2015, doi: 10.1016/j.csr.2014.11.008.

[25] C. Ulses, C. Estournel, X. Durrieu de Madron, and A. Palanques, “Suspended sediment transport in the Gulf of Lions (NW Mediterranean): Impact of extreme storms and floods,” *Continental Shelf Research*, vol. 28, no. 15, pp. 2048–2070, 2008, doi: 10.1016/j.csr.2008.01.015.

[26] S. Dan and E. Vandebroek, “A sediment budget for a highly deveoped coast - Belgian case,” in *Proceedings of Coastal Dynamics 2017: Helsingør, Denmark*, 2017, pp. 1376–1385.

[27] J. D. Rosati, “Concepts in sediment budgets,” *Journal of Coastal Research*, vol. 21, no. 2, pp. 307–322, 2005, doi: 10.2112/02-475A.1.

[28] A. M. Symonds, T. Vijverberg, S. Post, B. J. van der Spek, J. Henrotte, and M. Sokolewicz, “Comparison between MIKE 21 FM, DELFT3D and DELFT3D FM flow models of Western Port Bay, Australia,” in *Coastal Engineering Proceedings*, 2017, vol. 1, no. 35. doi: 10.9753/icce.v35.currents.11.

[29] M. Z. Li, C. G. Hannah, W. A. Perrie, C. C. L. Tang, R. H. Prescott, and D. A. Greenberg, “Modelling seabed shear stress, sediment mobility, and sediment transport in the bay of fundy,” *Canadian Journal of Earth Sciences*, vol. 52, no. 9, pp. 757–775, 2015, doi: 10.1139/cjes-2014-0211.

[30] C. Auguste, P. Marsh, J. R. Nader, I. Penesis, and R. Cossu, “Modelling morphological changes and migration of large sand waves in a very energetic tidal environment: Banks Strait, Australia,” *Energies*, vol. 14, no. 13, 2021, doi: 10.3390/en14133943.

[31] J. Krabbendam, A. Nnafie, H. de Swart, B. Borsje, and L. Perk, “Modelling the past and future evolution of tidal sand waves,” *Journal of Marine Science and Engineering*, vol. 9, no. 10, 2021, doi: 10.3390/jmse9101071.

[32] S. Leenders, J. H. Damveld, J. Schouten, R. Hoekstra, T. J. Roetert, and B. W. Borsje, “Numerical modelling of the migration direction of tidal sand waves over sand banks,” *Coastal Engineering*, vol. 163, p. 103790, 2021, doi: 10.1016/j.coastaleng.2020.103790.

[33] B. W. Borsje, W. M. Kranenburg, P. C. Roos, J. Matthieu, and S. J. M. H. Hulscher, “The role of suspended load transport in the occurrence of tidal sand waves,” *Journal of Geophysical Research: Earth Surface*, vol. 119, pp. 701–716, 2014, doi: https://doi.org/10.1002/2013JF002828.

[34] M. Z. Li, J. Shaw, B. J. Todd, V. E. Kostylev, and Y. Wu, “Sediment transport and development of banner banks and sandwaves in an extreme tidal system: Upper Bay of Fundy, Canada,” *Continental Shelf Research*, vol. 83, pp. 86–107, 2014, doi: 10.1016/j.csr.2013.08.007.

[35] J. K. Panigrahi, P. N. Ananth, and P. A. Umesh, “Coastal morphological modeling to assess the dynamics of Arklow Bank, Ireland,” *International Journal of Sediment Research*, vol. 24, no. 3, pp. 299–314, 2009, doi: 10.1016/S1001-6279(10)60005-4.

[36] A. Chatzirodou, H. Karunarathna, and D. E. Reeve, “Modelling 3D hydrodynamics

governing island-associated sandbanks in a proposed tidal stream energy site," *Applied Ocean Research*, vol. 66, pp. 79–94, 2017, doi: 10.1016/j.apor.2017.04.008.

[37] A. Chatzirodou, H. Karunarathna, and D. E. Reeve, "3D modelling of the impacts of in-stream horizontal-axis Tidal Energy Converters (TECs) on offshore sandbank dynamics," *Applied Ocean Research*, vol. 91, p. 101882, 2019, doi: 10.1016/j.apor.2019.101882.

[38] R. J. McCarroll, G. Masselink, N. G. Valiente, M. Wiggins, T. Scott, D. C. Conley, and E. V. King, "Impact of a headland-associated sandbank on shoreline dynamics," *Geomorphology*, vol. 355, p. 107065, 2020, doi: 10.1016/J.GEOMORPH.2020.107065.

[39] DHI Group, "MIKE 21 Toolbox: User guide." 2017.

[40] DHI Group, "MIKE 21 Flow Model: Hydrodynamic Module User Guide." 2017.

[41] DHI Group, "Non-Cohesive Sediment Transport Module - MIKE 21 ST," 2017.

[42] S. Creane, M. O'Shea, M. Coughlan, and J. Murphy, "Estimation of suspended solids concentration from Acoustic Doppler Current Profiler in a tidally-dominated continental shelf sea setting and its use as a numerical modelling validation technique," *Coastal Engineering*.

[43] DHI Group, "MIKE 21 Spectral Waves FM." 2017.

[44] G. J. Komen, L. Cavaleri, M. Donelan, K. Hasselmann, S. Hasselmann, and P. Janssen, *Dynamics and modelling of ocean waves*. Cambridge: Cambridge University Press, 1994. doi: 10.1017/CBO9780511628955.

[45] I. R. Young, *Wind generated ocean waves*. Elsevier, 1999.

[46] K. Hasselmann, “On the spectral dissipation of ocean waves due to white capping,” *Boundary-Layer Meteorology*, vol. 6, no. 1, pp. 107–127, 1974, doi: https://doi.org/10.1007/BF00232479.

[47] J.-R. Bidlot, P. A. E. M. Janssen, and S. Abdalla, “A revised formulation of ocean wave dissipation and its model impact,” 2007, doi: 10.21957/m97gmhqze.

[48] H. K. Johnson and H. Kofoed-Hansen, “Influence of Bottom Friction on Sea Surface Roughness and Its Impact on Shallow Water Wind Wave Modeling,” *Journal of Physical Oceanography*, vol. 30, no. 7, pp. 1743–1756, 2000, doi: 10.1175/1520-0485(2000)030<1743:IOBFOS>2.0.CO;2.

[49] J. Nikuradse, “Stromungsgesetze in rauhen Rohren,” *Journal of Applied Mathematics and Mechanics / Zeitschrift für Angewandte Mathematik und Mechanik*, vol. 11, no. 6, pp. 409–411, 1931, doi: https://doi.org/10.1002/zamm.19310110603.

[50] N. Weber, “Bottom friction for wind sea and swell in extreme depth-limited situations,” *Journal of Physical Oceanography*, vol. 21, pp. 149–172, 1991, doi: https://doi.org/10.1175/1520-0485(1991)021<0149:BFFWSA>2.0.CO;2.

[51] J. Battjes and J. Janssen, “Energy loss and set-up due to breaking of random waves,” in *Coastal Engineering Proceedings*, 1978, no. 16. doi: 10.1061/9780872621909.034.

[52] DHI Group, “MIKE 21 Toolbox: Global Tide Model - Tidal prediction.” 2017.

[53] K. D. Suh, H. D. Kwon, and D. Y. Lee, “Some statistical characteristics of large deepwater waves around the Korean Peninsula,” *Coastal Engineering*, vol. 57, no. 4, pp. 375–384, 2010, doi: 10.1016/j.coastaleng.2009.10.016.

[54] B. Dorschel and A. J. Wheeler, “Appraisal of the Irish Sea Seabed Imaging for Tidal

Energy Generation Tidal Energy Potential Assessment. INFOMAR Report INF-11-11-WHE," INFOMAR Programme, Geological Survey Ireland, Dublin, 2012.

[55] M. Coughlan, Z. Tóth, K. J. J. Van Landeghem, S. McCarron, and A. J. Wheeler, "Formational history of the Wicklow Trough: a marine-transgressed tunnel valley revealing ice flow velocity and retreat rates for the largest ice stream draining the late-Devensian British–Irish Ice Sheet," *Journal of Quaternary Science*, vol. 35, no. 7, pp. 907–919, 2020, doi: 10.1002/jqs.3234.

[56] J. van Berkel, H. Burchard, A. Christensen, L. O. Mortensen, O. Svenstrup Petersen, and F. Thomsen, "The Effects of Offshore Wind Farms on Hydrodynamics and Implications for Fishes," *Oceanography*, vol. 33, no. 4, pp. 108–117, 2020, doi: https://doi.org/10.5670/oceanog.2020.410.

[57] USA Corps of Engineers, *Coastal Engineering Manual Part II: Coastal Hydrodynamics (EM 1110-2-1100)*, vol. 1100. Books Express Publishing, 2002.

8 Conclusions and Recommendations

8.1 Chapter Overview

This chapter concludes the thesis aimed at exploring and advancing the knowledge of morphodynamic characteristics and drivers in the Irish Sea.

8.2 Conclusions to the thesis objectives

The outcome from chapters 3 to 7 contributes to the conclusions of this thesis. A synopsis of each chapter's contents are as follows:

- Chapter 3 investigates the highly complex morpho- and hydro-dynamic regimes in the central Irish Sea through a comprehensive review of existing literature, and analysis of new MIKE 21 numerical modelling and observational data.
- Chapter 4 uses high-resolution time-lapse bathymetry datasets, hydrodynamic numerical modelling outputs and various theoretical parameters to describe the morphological characteristics of sediment waves and their spatio-temporal evolution in a hydrodynamic and morphodynamic complex region of the Irish Sea. This chapter builds upon the advanced knowledge produced from Chapter 3.
- Chapter 5 addresses the need for cost-effective sediment validation datasets for two-dimensional (2D) sediment transport models by investigating the applicability of four new suspended load validation techniques in an offshore, tidally-dominated setting (the south-western Irish Sea).
- Chapter 6 uses the validated, depth-integrated hydrodynamic and sediment transport model developed in Chapter 5 to investigate the hydrodynamic processes controlling the highly mobile upper layer of Arklow Bank and overall long-term bank base stability.
- Chapter 7 builds upon the knowledge and tools developed in Chapter 3, 4, 5 and 6 to assess the dependency of Arklow Bank's local sediment transport regime on external

sediment sources, and to examine the influence of wind and wave-forcing on this offshore linear sand bank.

In the following subsections, the outcomes of all chapters are compiled to answer each high-level objective and corresponding sub-objectives to conclude this thesis.

8.2.1 Objective 1: Improve the understanding of hydrodynamics and morphodynamics in the Irish Sea

8.2.1.1 Chapter 3 outcomes and conclusions that address this objective

- The nearshore northward net sand transport pathway off the east coast of Ireland indicated by early bedform interpretation studies [1] is supported by underlying hydrodynamics and peak bed shear stress patterns on a quantitative scale. This is further supported by newly modelled residual tidal currents and bed shear stresses. This is not represented in other bedform-derived transport pathways studies.
- The body of work presented by Van Landeghem et al [2]–[4] is similarly supported and provides an excellent base characterisation study of seabed mobility in the Irish Sea. However, in situ observations of mobile bedforms is needed to fully understand the driving factors behind net sand transport pathways in the direction of the longer tidal phase, opposite to what is most commonly expected. This is addressed in Chapter 4.
- Residual tidal currents and mean tidal bed shear stress patterns reveal an open circulatory flow around Arklow Bank which indicates a strong divergence from earlier-defined net sand transport pathways. This is further investigated in Chapters 4, 6 and 7.
- The presence of the BLP in the central Irish Sea is supported by;

- the reduced magnitude and circulatory nature of both mean tidal currents and mean tidal bed shear stresses,
- the existence of opposing residual flows from this zone,
- the coincident succession of symmetrical and asymmetrical tidal character (defined by tidal constituents) both within and bounding the overall divergent zone,
- numerically modelled peak bed shear stresses, and
- sediment distribution patterns.

- This chapter challenges the classification by Harris et al [5] whereby the BLP is determined as Type A: those associated with flow accelerations under tidal nodes.
- This study proposes that the origin of the BLP is mainly attributed to the intersection of the North and South tidal fronts at an inclined angle due to Coriolis Forcing and coastline interactions.
- Minor factors influencing the shape and location of the BLP are;
    - the alteration of the tidal character as a result of the interaction of the propagating M_2 tidal wave with a rapid change in water depth at the Codling and Welsh Platforms,
    - the alteration of the tidal character at intricate submarine and coastline topographies,
    - flow acceleration due to the large constriction of the St Georges Channel caused by headlands and protruding submarine plateaus.
- Newly interpreted ADCP datasets support the presence of the semi-diurnal tidal node oscillation zone in the south-western Irish Sea.

8.2.1.2 Chapter 4 outcomes and conclusions that address this objective

- Targeted repeat high-resolution bathymetry data in the Irish Sea reveals large to very large sediment waves, of varying morphology, with mean wave heights of 0.6 to 6.1 m. These sediment waves exhibit migration rates of 1.1 to 79 m/yr. Sediment wave characteristics were quantified and compared with similar data from previous studies, significantly augmenting the global dataset.
- Individual environmental parameters were found to be unreliable indicators for sediment wave growth.
- By contrast, the mode of sediment transport is identified as a controlling factor on sediment wave growth and development. It is suggested that sediment waves are restricted to areas where ~$2.5 < P > \sim 8$ for two reasons: a) suspended load dominance over bed load dominance $0.8 < P < 1.2$ dampens sediment wave growth, and b) increasing bed load dominance above $P > \sim 8$ indicates winnowing of finer sediment from the seafloor, leading to sediment starvation and subsequent dampening of sediment wave growth.
- Residual tidal current and residual bed shear stress is also a suggested controlling factor for sediment wave growth. The reduction in residual tidal current along a transport pathway supplies sediment to sediment waves, thus facilitating bedform growth, by allowing the settlement of sediment out of suspension, and by retaining sediment within the assemblage due to the associated lower level of tide-averaged net sediment transport movement out of a region in comparison to high tidal asymmetry.
- The theoretical predictor of bedforms defined by Shields [6], plotting the entrainment function against the shear Reynold's number, aligns well with the occurrence and

absence of mobile bedforms in this region. Therefore, this theoretical predictor has the potential to predict seabed mobility and bedform type in other tidally-dominated shelves and so a coupled or process-driven approach (e.g. Rouse numbers) to understanding bedform dynamics should be incorporated in future studies.

- The net sediment transport pathways in the south-western Irish Sea derived in this study falsify the previously thought consistent southward flow. Divergence from this pattern is clearly seen both at offshore sand banks and at independent offshore sediment wave assemblages, and a number of key observations can be drawn:
    - Arklow Bank contains a semi-closed circulatory hydrodynamic and sediment transport system. This is further investigated in Chapters 6 and 7.
    - Lucifer-Blackwater bank complex's sediment transport and morphodynamic regime does not show a similar circulatory pattern to Arklow Bank. Instead, a predominant southward transport pathway dominates the eastern slope of the bank complex, and a residual headland eddy heavily influences the southern section of the bank. This residual eddy is most likely a controlling factor for the formation and maintenance of the adjacent banner bank (Holdens Bed-Long bank complex).

      The offset of the centre of this residual gyre to the east of the banner bank supports the concept that sediment deposition at the centre of these eddies are not the main element for the formation of banner banks.
    - The circulatory residual flow between the Lucifer-Blackwater and Holdens-Long bank complexes, combined with newly derived sediment wave migration and morphodynamic patterns, suggests a continuous recycling of material between these two bank complexes and associated sediment waves.

- Offshore independent sediment wave fields are supported through circulatory residual tidal current cells, originating from offshore linear sand banks. From this, two new phenomena are suggested: a) a potential recycling of sediment between sand banks and offshore sand deposits and b) offshore independent sediment wave fields act as intermediary transport zones to sediment wave fields in deeper waters. This is further supported by outcomes of Chapter 7.

- Observations from this study show that the rate of sediment wave migration and morphological change varies hugely both regionally in a tidal dominant shelf, and within individual study sites, depending on local environmental factors including residual tidal current, mode of sediment transport, and wave influence.

8.2.1.3 Chapter 6 outcomes and conclusions that address this objective

- A flood and ebb tidal dominance is evident on the west and east side of Arklow Bank respectively, generating a residual clockwise tidal current eddy encompassing the entire bank. This ultimately recycles sediment material within the bank's morphological cell.
- During an individual flood and ebb tide, sediment on the upper slopes is transported eastward and westward respectively along the full length of the bank due to the directional nature of tidal current cross-flow during these tidal phases. From a full semi-diurnal tidal cycle (divided into two flood and two ebb tidal phases) onwards, a variation in the direction of tidal asymmetry along the upper slopes of the bank is evident. This divides the bank into a variety of morphological sections migrating in different directions.

- Eight unique sub-cells of the bank are identified whereby a complex morphological-hydrodynamic feedback system is evident. These individual sub-cells display a variety of on-bank and off-bank hydrodynamic and morphological features yet fit together as one linear offshore sand bank, with high upper slope mobility and long-term bank base stability. The two main tidal phenomena that control upper bank mobility and bank base stability are (i) off-bank anticlockwise residual eddies and (ii) on-bank hydrodynamic–morphodynamic response.
- The positioning of multiple off-bank anticlockwise residual current eddies on the edge of this cell is shown to influence east–west fluctuations of the upper slopes of the sand bank and act as a control of long-term stability. These off-bank eddies facilitate this type of movement when the outer flows of adjacent eddies, located on both sides of the bank, flow in a generally uniform direction. Whereas they inhibit this east–west movement when the outer flows of adjacent eddies, on either side of the bank, flow in converging directions towards the bank itself. Off-bank anticlockwise eddies also facilitate sediment transport in and out of the local morphological cell.
- The control of the maximum limit of upper bank east–west fluctuation is the on-bank hydrodynamic-morphodynamic feedback loop through (i) the formation of migratory and stationary transient on-bank clockwise residual tidal current eddies and (ii) the formation of transient 'narrow' residual tidal current cross-flow zones.
- The concept of a 'threshold slope angle' is also introduced. When the upper slopes of the bank reach a certain threshold angle, a hydrodynamic response is stimulated that reverses upper bank migration in the opposite direction. By taking into consideration this concept in conjunction with the identified controlling hydrodynamic processes, analysis of this system at a higher temporal scale and over a longer time period could

help determine the maximum limits of vertical and horizontal bed level changes along the bank, as well as the rate and frequency at which these limits are reached. The information provided in this study can be used to guide offshore survey planning for existing and planned OWF projects in order to measure these morphological changes on Arklow Bank. The details provided in this study can reduce costs for such an expedition.

- The new process-based understanding of Arklow Bank's complex hydrodynamic and morphodynamic regime introduced in this study aids the predictability of future seabed level changes in this highly mobile sand-dominated environment. Where the maximum bed level change over a one-month period along the bank is +7.3 m to −3.4 m, the magnitude and rate of bed level change varies hugely along the length of the bank. This highlights the need for careful selection of scour and bed level change mitigation strategies for each potential wind turbine generator (WTG) position. Resultingly, the information provided in this study not only informs offshore geophysical survey design to confirm these modelled morphological changes but also informs concept layout design and foundation design.
- This comprehension of Arklow Bank's morphodynamic system has the potential to re-define how we analyse offshore linear sand banks. Consequently, the methods used in this study should be applied to offshore linear sand banks in other tidally dominated environments to investigate this wider connection.

8.2.1.4 Chapter 7 outcomes and conclusions that address this objective

- Using a one-year model simulation, a sediment budget for Arklow Bank is estimated. From this, seven sink and nine source external sediment transport pathways are identified, with the following characteristics:
    - The identified connection between sink pathways on the eastern side of Arklow Bank with an offshore independent sand wave field 8 km east of Arklow Bank by Creane et al [7] (Chapter 4) is further supported here through the identification of residual SSC plumes along the transport pathways and by using a bed load/suspended load dominance factor to support the proposed mechanism of transport.
    - Sediment sources at the southern extent of the bank are partially connected to the return of sediment from these sand deposits yet are also sourced from other offshore sand deposits including the Glassgorman Banks.
    - Sediment exchange at the northern extent of Arklow Bank is highly linked with Wicklow Head and Wicklow Trough, the latter displaying a potentially funnelling of sediment from the BLP zone [8] (outlined in Chapter 3).
    - Finally, the western side of the bank is dominated by sediment exchange between Arklow Bank and Seven Fathom Bank.
- Although sediment distribution along Arklow Bank is mainly contributed to the large clockwise residual current eddy encompassing the bank, the bank is also influenced by external sediment sources. External sediment exchange is clearly facilitated by the positioning of multiple anticlockwise residual current eddies along the circumference of this main morphological cell [9]. The restriction of sediment sources off the

southern extent of the bank leads to changes in erosion and accretion patterns in the mid and northern sections of the bank after just one simulated lunar month.

- The areas of the bank most vulnerable to changes in external sediment sources and the addition of wind forcing and wave forcing are quite consistent. These areas generally align with those regions identified as 'mobile' zones in Creane et al [9] (Chapter 6) and display a relatively high residual current crossflow under pure current baseline conditions.
- The influence of wind-induced flow on the bank is concentrated in these high vulnerability zones (HVZs). The addition of these forces is shown to both accelerate and reduce the speed of the east-west fluctuation of the upper slopes of the bank.
- The impact of wave-induced flow is also focussed in these areas. Although the east-west fluctuation can both accelerate or reduce the speed of the upper slope migration dynamics, it is inconsistent with wind-forcing. This is most likely due to the mis-alignment between wind direction with the directionality of wave-induced flow arising from swell.
- Where tidal currents are the primary control on sediment transport patterns and regulate Arklow Bank morphodynamics, wind and wave forcing are shown to alter sediment distribution patterns in the HVZs but have a lesser impact the long-term behaviour of the bank.

8.2.2 Objective 2: Develop new methods and approaches to investigate hydrodynamics and seabed morphodynamics in an offshore setting

8.2.2.1 Chapter 3 outcomes and conclusions that address this objective

- The combined use of numerically modelled co-tidal phases of individual tidal constituents, tidal asymmetry indicators derived from individual constituent relationships, and numerically modelled residual tidal currents and tidal-induced bed shear stress vectors in this body of work has proven successful to both a) identify and investigate the existence of bed load partings and associated divergent net sediment transport pathways, and b) understand their origin. This approach can be used to elucidate processes in other tidally-dominated shelf seas.

8. By examining the changes in the tidal character over a spring-neap cycle recorded by two spatially separated ADCPs, support is provided for the presence of the semi-diurnal tidal node oscillation zone presented by Pugh [10].

8.2.2.2 Chapter 4 outcomes and conclusions that address this objective

9. This study calculates sand wave migration direction and rates through an iterative process using a combined method in GRASS GIS v.7.6.1, QGIS v.3.8.1 and ArcGIS v.10.8. A streamlined workflow is provided as supplementary material. This is outlined in Chapter 4 of this thesis.
10. Individual environmental parameters were found to be unreliable indicators for sediment wave growth.
11. By contrast, the mode of sediment transport, and residual tidal current and residual bed shear stress are identified as controlling factors on sediment wave growth and development.

12. The theoretical predictor of bedforms defined by Shields (1936), plotting the entrainment function against the shear Reynold's number, aligns well with the occurrence and absence of mobile bedforms in this region. Therefore, this theoretical predictor has the potential to predict seabed mobility and bedform type in other tidally-dominated shelves and so a coupled or process-driven approach (e.g. Rouse numbers) to understanding bedform dynamics should be incorporated in future studies.
13. Combined use of targeted, high resolution, time-lapse repeat bathymetry datasets, hydrodynamic modelling outputs and the process-driven approach outlined above facilitated investigation into the complex sediment exchange relationship between offshore sand banks and associated sediment waves, and offshore independent sediment wave assemblages. This approach can be applied to other areas of the Irish Sea and beyond.

8.2.2.3 Chapter 5 outcomes and conclusions that address this objective

- The estimation of SSC_{solids} from ADCP acoustic backscatter based on sonar equations has proven successful in a tidally-dominated shallow shelf sea setting.
- This ADCP-derived SSC_{solids} spatial timeseries provides excellent coverage of the water column at the ADCP deployment site, capturing 71% of the water column over a full spring-neap cycle.
- The suspended sediment transport component of the developed 2D model is deemed successfully validated using three of the four tested model validation techniques.
- The useful model validation techniques include;
    - Validation of 2D modelled $SSC_{sediment}$ using water sample-based SSC_{solids},

- Validation of the flood-ebb characteristics (tidal asymmetry) of (i) 2D modelled suspended load transport and (ii) $SSC_{sediment}$ using ADCP-based datasets, and
- Validation of the 2D modelled peak $SSC_{sediment}$ over a spring-neap cycle using ADCP-based SSC_{solids}.

These techniques have produced highly acceptable results for this area of interest and have a high potential for applicability to other locations.

- The development of a local seabed substrate map using ground-truthed MBES backscatter proved a useful technique to provide crucial information on site specific seabed sediment characteristics over the ADCP deployment time-frame.
- The ADCP-based SSC_{solids} spatial timeseries has potential to provide additional validation of the vertical layers in a 3D model. The application of the ADCP-based techniques in this way could reveal how or if a 3D model could overcome the limitations of a depth-integrated 2D modelling approach in fully characterising the natural variability of SSC_{solids} in a tidally-dominated shallow shelf sea setting.
- The multi-disciplinary method of collecting in situ metocean and sediment dynamic data via acoustic instruments (ADCP) is a cost-effective procedure for future ORE development projects and other engineering and scientific works.

8.2.2.4 Chapter 6 outcomes and conclusions that address this objective

- Combined analysis of temporally varying numerically modelled residual tidal currents and numerically modelled bed levels facilitate the determination of the hydrodynamic processes controlling long-term base stability and upper slope mobility of Arklow Bank.

- By taking into consideration the newly introduced concept of a 'threshold slope angle', in conjunction with the newly identified controlling hydrodynamic processes, this chapter determines that analysis of this system at a higher temporal scale and over a longer time period could help determine the maximum limits of vertical and horizontal bed level changes along the bank, and the rate and frequency at which these limits are reached. This is critical information for existing and future offshore wind farm developments.
- The comprehension of Arklow Bank's morphodynamic system has the potential to re-define how we analyse offshore linear sand banks. Consequently, the methods used in this study should be applied to offshore linear sand banks in other tidally-dominated environments to investigate this wider connection.

8.2.2.5 Chapter 7 outcomes and conclusions that address this objective

- A numerical modelling mesh sensitivity test reveals that when considering all variables of a project such as project objectives, site characteristics, computational time, and project timeline and budget, for a process-understanding study of an Arklow Bank, an offshore linear sand bank, a coarser resolution model (150 m to 200 m) is adequate. However regardless of the computational time saved by a coarser resolution mesh, to understand maximum limits of vertical and horizontal bed levels along the length of the bank, a higher resolution mesh, of at least 50 m to 80 m, is required.
- The concept of the 'sediment budget', typically a coastal engineering tool, is successfully applied to an offshore linear sand bank. Integrating this concept into a unique numerical modelling approach effectively elucidates the influence of external sediment on the local sand bank sediment transport patterns.

8.2.3 Objective 3: Collect and produce novel datasets that will contribute to the understanding of hydro- and morpho-dynamics in the Irish Sea

A number of high-quality geophysical, geological and oceanographic datasets were successfully collected across four multi-disciplinary offshore research surveys. Details of each survey are outlined in Appendix B. Many of these highly valuable datasets such as multi-beam echo sounder (MBES) data, sound velocity profiles (SVP), surficial sediment samples, acoustic doppler current profiler (ADCP) data, and water samples used to analyse total suspended solids (TSS) in the water column, directly feed into chapters 3 to 7 of this thesis. All collected datasets have the potential to directly feed into future research and commercial engineering projects. Other novel datasets produced in each chapter of this thesis are outlined below.

8.2.3.1 Chapter 3 outcomes and conclusions that address this objective

- A validated, two-dimensional, hydrodynamic model covering the entire Irish Sea, developed using the Danish Hydraulics Institute's MIKE 21 suite of tools (DHI Group, 2019), was used to simulate bed shear stress and tidal current u and v magnitude components for a one-month period. This dataset and subsequent interpretation provide advanced understanding of the hydrodynamic and sediment transport regime in the Irish Sea.

8.2.3.2 Chapter 4 outcomes and conclusions that address this objective

- Targeted repeat high-resolution bathymetry data was processed and analysed to reveal detailed sediment wave morphology and migration characteristics, significantly augmenting the global dataset.
- Surficial sediment samples were collected, processed and analysed from the MOVE survey campaigns (Appendix B). The MOVE and GSI datasets were combined, and

statistical analysis was carried out to produce a high-quality processed sediment sample dataset for the Irish Sea.

- The Rouse number, which indicates the mode of sediment transport, was calculated for the south-western Irish Sea using numerical modelling outputs and surficial sediment sample parameters to analysis the processes controlling sand wave growth and development.

8.2.3.3 Chapter 5 outcomes and conclusions that address this objective

- By integrating the processed water sample-based SSC_{solids} with ADCP acoustic backscatter, an ADCP-derived SSC_{solids} spatial timeseries that provides excellent coverage of the water column was produced.
- This processed dataset, combined with hydrodynamic variables recorded by the ADCP and water sample-based SSC_{solids}, act as novel datasets that contribute to the understanding of hydro- and morpho-dynamics in the Irish Sea.
- The validated hydrodynamic and sediment transport model developed in this chapter can be used in future research and commercial projects.

8.2.3.4 Chapter 6 outcomes and conclusions that address this objective

- The developed hydrodynamic and sediment transport model was further validated in this chapter by volumetric analysis of bed levels and can be used in future research and commercial projects.
- The schematic produced in this study that summarises the hydrodynamic processes controlling upper slope mobility and base stability of Arklow Bank, can be used to inform processes controlling other offshore linear sandbanks.

8.2.3.5 Chapter 7 outcomes and conclusions that address this objective

- The validated spectral wave model covering the entire Irish Sea, developed in this chapter, can be used in future research and commercial projects.

8.2.4 Objective 4: Facilitate the sustainable growth of anthropogenic activities in the Irish Sea

8.2.4.1 Chapter 4 outcomes and conclusions that address this objective

- All new information concerning sediment wave dimensions, migration parameters and the nature of morphological change, can be used not only to optimise infrastructural design but also optimise the monitoring strategy and monitoring frequency for navigation channels, pipelines, cables and turbine foundations, and are highly valuable to the development of more robust marine spatial planning.

8.2.4.2 Chapter 5 outcomes and conclusions that address this objective

- This chapter presents three new useful 2D sediment transport model validation techniques. These techniques are critical in developing a robust numerical model in order to produce hindcast and predictive spatial datasets for offshore engineering projects.
- The multi-disciplinary method of collecting in situ metocean and sediment dynamic data via acoustic instruments (ADCP) is determined a cost-effective procedure for future ORE development projects and other engineering and scientific works.

8.2.4.3 Chapter 6 outcomes and conclusions that address this objective

- The ability to determine the maximum limits of vertical and horizontal bed level changes along Arklow Bank, and the rate and frequency at which these limits are reached is critical information for existing and future offshore wind farm developments. The high-quality results derived from interpreted high resolution

model outputs, the introduction of the 'threshold slope angle', and the advanced knowledge of hydrodynamic controls produced from this study directly increases the predictability of future seabed level changes in this highly mobile sand-dominated environment. This directly impacts the efficiency and accuracy of detailed design scopes of work for existing and planned OWFs.

- Elucidating the hydrodynamic processes that control bedform mobility directly improves the ability to assess the risk of environmental instability due to increased offshore anthropogenic activities, thus facilitating the development of a robust marine spatial plan.

8.2.4.4 Chapter 7 outcomes and conclusions that address this objective

- Results from the model mesh sensitivity analysis conducted in this chapter reveal that when considering all variables of a project such as project objectives, site characteristics, computational time, and project timeline and budget, for a process-understanding study of an Arklow Bank, an offshore linear sand bank, a coarser resolution model (150 m to 200 m) is adequate. However regardless of the computational time saved by a coarser resolution mesh, to understand maximum limits of vertical and horizontal bed levels along the length of the bank, a higher resolution mesh, of at least 50 m to 80 m, is required. The adoption of this criteria is important for studies where a detailed understanding of morphological changes is necessary, such as OWF cable burial depth and scour protection design.
- The restriction of sediment sources off the southern extent of the Arklow Bank leads to changes in erosion and accretion patterns in the mid and northern sections of the bank after just one simulated lunar month. This highlights the short timescale to which

the large clockwise residual current eddy distributes sediment throughout the bank. This implies that anthropogenic activities such as dredging for marine aggregates can highly impact areas further along a transport pathway over a relatively short time-scale.

- Given the particular complexity of the interconnected sediment transport pathways in the south-western Irish Sea, the risk of seabed instability arising from increased anthropogenic seabed disturbances is high. Robust environmental impact assessments (EIA) that considers these processes are key to reducing the risk of environmental instability.
- Where tidal currents are the primary control on sediment transport patterns and regulate Arklow Bank morphodynamics, wind and wave forcing are shown to alter sediment distribution patterns in the HVZ but have a lesser impact the long-term behaviour of the bank. This knowledge is important for EIA in this specific region but also should be considered in other tidally-dominated shelf seas.

8.3 Impact on policy, industry and society

MaREI, the SFI Research Centre for Energy, Climate and Marine research and innovation, focusses its research towards three impact priorities; (i) informing policy, (ii) supporting industry, and (iii) empowering society. How this thesis contributes to these impact priorities are discussed in the following sub-sections.

8.3.1 Policy implications

The concluding synthesis of this thesis confirms that this body of work greatly improves the scientific evidence-base for policy-makers, contributing to both national and international climate action plans, including:

1. The Paris Agreement's [11] and Glasgow Climate Pact's [12] target to limit global temperature rise to 1.5 °C above pre-industrial levels;
2. The European Green Deal's updated target of a 45 % share of renewable energy by 2030 [13];
3. Ireland's Climate Action Plan's target of 7 GW of offshore wind generation by 2030 and 30 GW by 2050 [14];
4. Ireland's Climate Action Plan's [15] and Programme for Government's [16] ambitious targets to reach net zero carbon emissions by 2050.

Additionally, results from this thesis reveal that undertaking offshore activities that disturb the seabed, such as dredging for marine aggregate extraction, impact sediment dispersal patterns further along the sediment transport pathway. This leaves the seabed and associated ecosystem vulnerable to adverse effects. In the south-western Irish Sea, changes to the sediment dispersal system and seabed morphodynamics is evident over a relatively short time scale (one lunar tidal cycle). This reveals the high risk associated with increased offshore anthropogenic activities whereby overlapping or closely located engineering activities may cause adverse effects to each other, and/or the combined occurrence of these activities may negatively impact the natural environment. This significant outcome directly aligns with the EU MSP Directive adopted by all EU Member States in 2014. The implementation of robust environmental risk assessments incorporating newly developed concepts and techniques outlined in this thesis is imperative to preserve environmental stability. This will facilitate early identification of impact and opportunities for multiple use of the marine space.

From the synthesis of concluding arguments, it is also clear that this body of work directly aligns with the United Nations sustainable development goals (SDG) [17]. This thesis

specifically makes a major contribution to the following; Goal 7: Affordable and clean energy - ensuring access to affordable, reliable, sustainable and modern energy for all; Goal 9: Industry, innovation and infrastructure - building resilient infrastructure, promote inclusive and sustainable industrialization and foster innovation; Goal 13: Climate action - taking urgent action to combat climate change and its impacts; Goal 14: Life below water - conserving and sustainably using the oceans, seas and marine resources for sustainable development.

8.3.2 Industry implications

This thesis was produced through an industry-based PhD programme which provides the invaluable opportunity to feed its outcomes directly into industry. Specifically, the advanced numerical models, novel model validation techniques, new approaches and methodologies, and invaluable offshore in-situ datasets produced from this body of work either directly support or indirectly inform commercial metocean and seabed mobility assessments in the Offshore Wind, and Ports and Harbour sectors of industry. A comprehensive understanding of seabed morphodynamics and sediment transport trends over the lifetime of a wind farm is imperative for the design, installation and maintenance of wind turbines and export cables, but also essential for nearshore studies such as Ports and Harbour concept and detailed design works. The combination of advanced modelling and GIS techniques developed in this thesis, and relevant outputted datasets are used to assess future and historic seabed level change and bedform dynamics in a commercial setting. This information concerning seabed stability and variability inform critical decision making and has the potential to reduce uncertainty and minimise risk during development [18], [19].

Similarly, wind farm developers and operators need both an ambient and qualitative understanding of meteorological and oceanographic (metocean) conditions for design,

installation, and maintenance of offshore wind turbines and cables [20]. This criterion is also critical for nearshore engineering works. An early understanding of metocean site conditions is crucial for project planning and costing, as well as for informing offshore surveys. The models, novel datasets and advanced knowledge produced from this thesis inform these scopes of work.

Each paper of this thesis has either been published in an international peer-reviewed journal or is under review. The eventual publication of all chapters from this thesis will further allow the outcomes of this body of work to be used to inform industry on a wider level.

8.3.3 Society implications

This thesis aids the sustainable growth of offshore anthropogenic activities in the Irish Sea and beyond, and informs synergies between various industries for multi-use of the marine space. The socio-economic impact of the acceleration of the growing ORE industry is the large creation of job opportunities and promotion of regional development. A Carbon Trust [21] study states that the offshore wind industry in Ireland has the opportunity to provide 2,500 local development and construction jobs, and 700 local permanent operations and maintenance jobs by 2030. With the projected deployment achievement of 11 GW – 16 GW of onshore wind and 30 GW of offshore wind by 2050, the Sustainable Energy Authority of Ireland have estimated that combined onshore and offshore wind generation could create over 20,000 direct installation and operation and maintenance jobs by 2040 [22]. These additional volumes of renewable power are necessary to attract new foreign direct investment and support the development of energy intensive industries. This research advances Europe's step towards energy independence as necessitated by REPowerEU [13].

Citizens health would also increase over time due to the less exposure to hazardous wastes and emissions as we move away from fossils fuels and towards cleaner energy [23].

Societal acceptance and public attitude are important criteria in the sustainable growth of the offshore sector [24]. The significant challenge to the deployment of large-scale renewable energy projects is balancing the relationship between developing these projects at scale and ensuring a positive impact on local communities. Therefore, stakeholder and public engagement is key at all stages of a project. In addition to the production of this thesis, community outreach was undertaken in the form of contributing to a BBC StoryWorks documentary [25] which explores how seabed mapping can inform offshore renewable energy development, and through organising and participating in two 'OffshoreWind4Kids' demo days [26], which allows families to build offshore wind turbines at different beaches in Ireland and learn about engineering, technology and renewable energy. These two public demo days were organised by OffshoreWind4Kids, in partnership with Gavin and Doherty Geosolutions (PhD programme employment partner). Continuous engagement with stakeholders and the public is key to enable both industry and society to receive the full benefit from the use of the marine space.

8.4 Recommendations and future research

1. Chapter 3 provides new evidence supporting the presence of a semi-diurnal tidal node oscillation zone in the south-western Irish Sea. Further work is needed to understand the full extent of this phenomenon and the impact of this on sediment transport in this region.
2. Chapter 2 introduces a new sediment exchange relationship between offshore sand banks and offshore independent sand wave fields at three locations in the south-

western Irish Sea. This is further supported in Chapter 7. Investigation into whether similar relationships exist outside this region is imperative to form robust arguments that augment the scientific knowledge of this field.

3. The resulting sediment exchange relationships outlined in this thesis complicate previously understood sediment transport patterns in the Irish Sea. Interruption to these pathways by offshore anthropogenic activities may pose a potential risk to both industry and the environment if not accurately assessed. Environmental risk assessments should be carried out that incorporate the findings of this thesis and the accurate knowledge of the source of seabed disturbance, for example, turbine array layout and dredging volumes, duration and extent of the activity. This will effectively optimise design, minimise environmental instability and identify multi-use of the marine space.
4. The multi-disciplinary use of an ADCP to obtain oceanographic and sediment validation datasets is a cost-efficient method for industry, governmental groups and research bodies to develop robust numerical models to accurately characterise nearshore and offshore sites.
5. The ADCP-based SSC_{solids} spatial timeseries produced from this thesis has potential to provide additional validation of the vertical layers in a 3D model. The application of the ADCP-based techniques in this way could reveal how or if a 3D model could overcome the limitations of a depth-integrated 2D modelling approach in fully characterising the natural variability of SSC_{solids} in a tidally-dominated shallow shelf sea setting. Further investigation is recommended.
6. The advanced comprehension of Arklow Bank's morphodynamic system has the potential to re-define how we analyse offshore linear sand banks. Consequently, the

methods used in this study should be applied to offshore linear sand banks in other tidally-dominated environments to investigate this wider connection.

7. Further investigation into why the identified controlling hydrodynamic processes (off-bank anticlockwise residual eddies) exist and form at Arklow Bank is imperative. This will further advance scientific knowledge. This baseline understanding will also reduce the risk of change to these hydrodynamic patterns resulting in seabed instability and adverse effects to offshore infrastructure and the marine environment.
8. Analysing the Arklow Bank system at a higher temporal scale and over a longer time period using the concepts developed in this thesis could help determine the maximum limits of vertical and horizontal bed level changes along the bank, and the rate and frequency at which these limits are reached. This is critical information for existing and future offshore wind farm developments.
9. The sediment flow dynamics through the submarine channel, the Wicklow Trough, should be further investigated. This thesis identifies the potential streamlining of sediment from the bed load parting zone in the central Irish Sea towards the Arklow Bank and the wider south-western Irish Sea. Combined advanced 2D or 3D sediment transport modelling of this submarine channel in conjunction with detailed seabed morphodynamic assessments could elucidate the control of sediment dispersal in this region. Subsequent improved knowledge of this system will inform the offshore renewable energy industry in terms of both cable route design for offshore wind farms and the potential for tidal energy extraction.

8.5 Final Remarks

This PhD work is funded by the Irish Research Council's Employment-Based Postgraduate Programme (grant number EBPPG/2019/158), uniquely linking University College Cork with employment partner, Gavin and Doherty Geosolutions (GDG). The author believes that this thesis successfully delivers a consistent body of work under this co-funded programme that addresses the following central research question;

- What are the morphodynamic characteristics and drivers in the Irish Sea?

Additionally, this thesis successfully addresses the defined project objectives;

1. Improve the understanding of hydrodynamics and morphodynamics in the Irish Sea;
2. Develop new methods and approaches to investigate hydrodynamics and morphodynamics in an offshore setting;
3. Collect novel datasets that will contribute to the understanding of the hydro- and morpho-dynamics in the Irish Sea;
4. Facilitate the sustainable growth of anthropogenic activities in the Irish Sea.

The results have been presented with a local, regional and global outlook and can be applied to regions beyond the Irish Sea. The author hopes that this work will motivate and inspire other researchers to continue contributing to this field of scientific research which will ultimately support and inform policy-makers, industry and society.

8.6 References

[1] M. R. Dobson, W. E. Evans, and K. H. James, "The sediment on the floor of the southern Irish Sea," *Marine Geology*, vol. 11, no. 1, pp. 27–69, 1971, doi: 10.1016/0025-3227(71)90083-1.

[2] K. J. J. Van Landeghem, A. J. Wheeler, N. C. Mitchell, and G. Sutton, “Variations in sediment wave dimensions across the tidally dominated Irish Sea, NW Europe,” *Marine Geology*, vol. 263, no. 1–4, pp. 108–119, 2009, doi: 10.1016/j.margeo.2009.04.003.

[3] K. J. J. Van Landeghem, K. Uehara, A. J. Wheeler, N. C. Mitchell, and J. D. Scourse, “Post-glacial sediment dynamics in the Irish Sea and sediment wave morphology: Data-model comparisons,” *Continental Shelf Research*, vol. 29, no. 14, pp. 1723–1736, 2009, doi: 10.1016/j.csr.2009.05.014.

[4] K. J. J. Van Landeghem, J. H. Baas, N. C. Mitchell, D. Wilcockson, and A. J. Wheeler, “Reversed sediment wave migration in the Irish Sea, NW Europe: A reappraisal of the validity of geometry-based predictive modelling and assumptions,” *Marine Geology*, vol. 295–298, pp. 95–112, 2012, doi: 10.1016/j.margeo.2011.12.004.

[5] P. T. Harris, C. B. Pattiaratchi, M. B. Collins, and R. W. Dalrymple, “What is a bedload parting?,” in *Tidal signatures in modern and ancient sediments*, B. W. Flemming and A. Bartholoma, Eds. 1995. doi: 10.1002/9781444304138.ch1.

[6] A. Shields, “Anwendung der Aehnlichkeitsmechanik und der Turbulenzforschung auf die Geschiebebewegung,” Preussischen Versuchsanstalt für Wasserbau, 1936.

[7] S. Creane, M. Coughlan, M. O’Shea, and J. Murphy, “Development and dynamics of sediment waves in a complex morphological and tidal dominant system: southern Irish Sea,” *Geosciences*, vol. 12, no. 12, p. 46, 2022, doi: 10.3390/geosciences12120431.

[8] S. Creane, M. O’Shea, M. Coughlan, and J. Murphy, “The Irish Sea bed load parting

zone: Is it a mid-sea hydrodynamic phenomenon or a geological theoretical concept?," *Estuarine, Coastal and Shelf Science*, vol. 263, p. 107651, 2021, doi: 10.1016/j.ecss.2021.107651.

[9] S. Creane, M. O'Shea, M. Coughlan, and J. Murphy, "Hydrodynamic processes controlling sand bank mobility and long-term base stability: A case study of Arklow Bank," *Geosciences*, vol. 13, no. 2, p. 60, 2023, doi: 10.3390/geosciences13020060.

[10] D. T. Pugh, "Tidal amphidrome movement and energy dissipation in the Irish Sea," *Geophysical Journal of the Royal Astronomical Society*, vol. 67, no. 2, pp. 515–527, 1981, doi: 10.1111/j.1365-246X.1981.tb02763.x.

[11] UNFCCC, "The Paris Agreement," in *Paris Climate Change Conference*, 2015.

[12] UNFCCC, "Glasgow Climate Pact," in *Conference of the Parties serving as the meeting of the Parties to the Paris Agreement*, 2021.

[13] European Commission, "REPowerEU: A plan to rapidly reduce dependence on Russian fossil fuels and fast forward the green transition," *Press Release*, 2022. https://ec.europa.eu/commission/presscorner/detail/en/IP_22_3131 (accessed Sep. 27, 2022).

[14] Department of the Taoiseach, "Government announces sectoral emissions ceilings, settling Ireland on a pathway to turn the tide on climate change," *Press Release*, 2022. https://www.gov.ie/en/press-release/dab6d-government-announces-sectoral-emissions-ceilings-setting-ireland-on-a-pathway-to-turn-the-tide-on-climate-change/ (accessed Sep. 27, 2022).

[15] Department of the Environment Climate and Communications, "Climate Action Plan

2021," 2021.

[16] Department of the Taoiseach, "Programme for Government," 2020. [Online]. Available: https://www.gov.ie/en/publication/7e05d-programme-for-government-our-shared-future/

[17] United Nations, "Transforming our world: the 2030 Agenda for Sustainable Development," in *UN General Assembly*, 2015. doi: 10.1163/15718093-12341375.

[18] T. Raaijmakers, T. Roetert, and P. Van Steijn, "Scour and scour mitigation for Hollandse Kust," *Deltares*, p. 64, 2017.

[19] R. Morelissen, S. J. M. H. Hulscher, M. A. F. Knaapen, A. A. Németh, and R. Bijker, "Mathematical modelling of sand wave migration and the interaction with pipelines," *Coastal Engineering*, vol. 48, no. 3, pp. 197–209, 2003, doi: 10.1016/S0378-3839(03)00028-0.

[20] B. H. Bailey, M. Filippelli, and M. Baker, "Metocean Data Needs Assessment for U.S. Offshore Wind Energy", doi: 10.2172/1338823.

[21] Carbon Trust, "Harnessing out potential: Investment and jobs in Ireland's offshore wind industry," 2020. [Online]. Available: https://windenergyireland.com/images/files/final-harnessing-our-potential-report-may-2020.pdf

[22] Sustainable Energy Authority of Ireland (SEAI), "Wind Energy Roadmap 2011 to 2050," 2011. [Online]. Available: https://www.seai.ie/publications/Wind_Energy_Roadmap_2011-2050.pdf

[23] G. D'Amato, C. E. Baena-Cagnani, L. Cecchi, I. Annesi-Maesano, C. Nunes, I. Ansotegui,

M. D'Amato, G. Liccardi, M. Sofia, and W. G. Canonica, "Climate change, air pollution and extreme events leading to increasing prevalence of allergic respiratory diseases," *Multidisciplinary Respiratory Medicine*, vol. 8, no. 1, p. 12, 2013, doi: 10.1186/2049-6958-8-12.

[24] Y. Cronin, V. Cummins, and E. Wolsztynski, "Public perception of offshore wind farms in Ireland," *Marine Policy*, vol. 134, no. October, p. 104814, 2021, doi: 10.1016/j.marpol.2021.104814.

[25] BBC StoryWorks, *What do Ireland's shipwrecks have to do with renewable energy?*, (2022). [Online]. Available: https://www.bbc.com/storyworks/unlocking-science/what-do-irelands-shipwrecks-have-to-do-with-renewable-energy

[26] OffshoreWind4Kids, "OffshoreWind4Kids Demo Days." https://www.offshorewind4kids.com/demo-days (accessed Sep. 27, 2022).

Appendix A: Conference deliverables and co-authored peer-reviewed publications

During this PhD programme, several presentations were delivered in both oral and poster format at multiple conferences around Europe (Table A-1). A co-authored conference paper [1] was also produced where I contributed to the following aspects: conceptualisation, investigation, methodology, visualisation, writing – original, writing – editing and reviewing.

Furthermore, I was the co-author on a peer-reviewed journal paper [2] where I contributed to the following: methodology, formal analysis, investigation, conceptualization, visualisation, writing – original draft, and writing – reviewing and editing.

Table A-1 Conference deliverables during this PhD programme

Conference	Location	Date	Presentation Type	Presentation Title
WindEurope Offshore 2019	Copenhagen, Denmark (In-person)	26th – 28th Nov 2019	Poster Presentation (Presenter)	A Morphodynamic Study of the Irish Sector of the Irish Sea [3]
WindEurope Offshore 2019	Copenhagen, Denmark (In-person)	26th – 28th Nov 2019	Conference Paper (co-author)	A Morphodynamic Study of the Irish Sector of the Irish Sea [1]
European Geosciences Union (EGU) 2020	Vienna, Austria (Online)	3rd – 8th May 2020	Oral Presentation (Presenter)	Geological and Geophysical Assessment of Offshore Sediment Banks in the South Western Irish Sea [4]
Wind Energy Science Conference (WESC) 2021	Hannover, Germany (Online)	25th – 28th May 2021	Oral Presentation (Presenter)	Mobility assessment of coastal sediment banks and associated features in the south western Irish Sea utilising a combination of advanced geophysical, geological and morphological modelling techniques [5]
Wind Energy Ireland (WEI) Annual Conference 2022	Dublin, Ireland (In-person)	13th – 14th April 2022	Poster Presentation (Presenter)	Modelling the morphological changes of tidal sand waves in a complex hydrodynamic environment and their interaction with offshore windfarm foundations [6]
European Geosciences Union (EGU) 2022	Vienna, Austria (In-person)	23rd – 27th May 2022	Oral Presentation (Presenter)	Development and dynamics of sediment waves in a complex morphological and tidal dominant system: southern Irish Sea [7]

References

[1] M. Coughlan, M. Guerrini, S. Creane, M. Musialik, M. O'Shea, and J. Murphy, "A Morphodynamic Study of the Irish Sector of the Irish Sea (Conference Paper)," 2019.

[2] M. Coughlan *et al.*, "A new seabed mobility index for the Irish Sea: modelling seabed shear stress and classifying sediment mobilisation to help predict erosion, deposition, and sediment distribution," *Continental Shelf Research*, vol. 229, p. 104574, 2021, doi: https://doi.org/10.1016/j.csr.2021.104574.

[3] M. Coughlan, M. Guerrini, S. Creane, M. Musialik, M. O'Shea, and J. Murphy, "A Morphodynamic Study of the Irish Sector of the Irish Sea (Poster Presentation)," 2019.

[4] S. Creane, M. Coughlan, J. Murphy, J. Clarke, and P. Doherty, "Geophysical and Geological Assessment of Offshore Sediment Banks in the South Western Irish Sea (Oral Presentation)," 2020.

[5] S. Creane, M. Coughlan, J. Murphy, M. O'Shea, P. Doherty, and C. Desmond, "Mobility assessment of coastal sediment banks and associated features in the south western Irish Sea utilising a combination of advanced geophysical, geological and morphological modelling techniques (Oral Presentation)," 2021.

[6] S. Creane, M. O'Shea, M. Coughlan, and J. Murphy, "Modelling the morphological changes of tidal sand waves in a complex hydrodynamic environment and their interaction with offshore windfarm foundations (Poster Presentation)," 2022.

[7] S. Creane, M. Coughlan, M. O'Shea, and J. Murphy, "Development and dynamics of sediment waves in a complex morphological and tidal dominant system: southern

Irish Sea (Oral Presentation),” 2022.

[8] M. Coughlan and S. Creane, “Mobility of Sediment Waves and Sand Banks in the Irish Sea (MOVE 1), Leg 1 and 2,” 2020.

[9] S. Creane and M. Coughlan, “Mobility of Sediment Waves and Sand Banks in the Irish Sea Phase 2 (MOVE 2), Leg 1,” 2021.

[10] S. Creane, R. Strachan, and F. Butchek, “Mobility of Sediment Waves and Sand Banks in the Irish Sea Phase 2 (MOVE 2) Leg 2,” 2021.

Appendix B: Offshore research surveys

Appendix B presents three offshore research survey reports submitted by the Chief Scientist to the Marine Institute upon survey completion. The first report details the activities of the offshore survey campaign entitled 'Mobility of Sediment Waves and Sand Banks in the Irish Sea (MOVE) Phase 1', including both Leg 1 and Leg 2, with survey codes CV20010 and CV20036 respectively [8]. The MOVE Phase 1 campaign was funded under the Marine Institute's national research vessels 2020 ship-time programme. The second and third report details the activities of the offshore survey campaign entitled 'Mobility of Sediment Waves and Sand Banks in the Irish Sea (MOVE) Phase 2' Leg 1 [9] and Leg 2 [10] respectively. The survey codes are CV21035 and CV21034. The MOVE Phase 2 campaign was funded under the Marine Institute's national research vessels 2021 ship-time programme.

References

[1] M. Coughlan, M. Guerrini, S. Creane, M. Musialik, M. O'Shea, and J. Murphy, "A Morphodynamic Study of the Irish Sector of the Irish Sea (Conference Paper)," 2019.

[2] M. Coughlan *et al.*, "A new seabed mobility index for the Irish Sea: modelling seabed shear stress and classifying sediment mobilisation to help predict erosion, deposition, and sediment distribution," *Continental Shelf Research*, vol. 229, p. 104574, 2021, doi: https://doi.org/10.1016/j.csr.2021.104574.

[3] M. Coughlan, M. Guerrini, S. Creane, M. Musialik, M. O'Shea, and J. Murphy, "A Morphodynamic Study of the Irish Sector of the Irish Sea (Poster Presentation)," 2019.

[4] S. Creane, M. Coughlan, J. Murphy, J. Clarke, and P. Doherty, "Geophysical and Geological Assessment of Offshore Sediment Banks in the South Western Irish Sea

(Oral Presentation),” 2020.

[5] S. Creane, M. Coughlan, J. Murphy, M. O’Shea, P. Doherty, and C. Desmond, “Mobility assessment of coastal sediment banks and associated features in the south western Irish Sea utilising a combination of advanced geophysical, geological and morphological modelling techniques (Oral Presentation),” 2021.

[6] S. Creane, M. O’Shea, M. Coughlan, and J. Murphy, “Modelling the morphological changes of tidal sand waves in a complex hydrodynamic environment and their interaction with offshore windfarm foundations (Poster Presentation),” 2022.

[7] S. Creane, M. Coughlan, M. O’Shea, and J. Murphy, “Development and dynamics of sediment waves in a complex morphological and tidal dominant system: southern Irish Sea (Oral Presentation),” 2022.

[8] M. Coughlan and S. Creane, “Mobility of Sediment Waves and Sand Banks in the Irish Sea (MOVE 1), Leg 1 and 2,” 2020.

[9] S. Creane and M. Coughlan, “Mobility of Sediment Waves and Sand Banks in the Irish Sea Phase 2 (MOVE 2), Leg 1,” 2021.

[10] S. Creane, R. Strachan, and F. Butchek, “Mobility of Sediment Waves and Sand Banks in the Irish Sea Phase 2 (MOVE 2) Leg 2,” 2021.

Cruise Report

Mobility of Sediment Waves and Sand Banks in the Irish Sea

MOVE

RV Celtic Voyager – Survey CV20010 & CV20036

23rd– 28th Sept. 2020 & 9th Oct. – 17th Oct. 2020

Compiled by

Dr. Mark Coughlan (Chief Scientist: Irish Centre for Research in Applied Geosciences (iCRAG)
mark.coughlan@icrag-Centre.org)

& Shauna Creane (Co-Chief Scientist: University College Cork (UCC)/GDG)



INDEX

1 Executive Summary 1
2 Background 2
3 Survey Rationale and Objectives 3
4 Equipment 4
4.1 Research Vessel – RV Celtic Voyager 4
4.2 Acoustic Doppler Current Profiler (ADCP) 4
4.3 Multibeam Echosounder 5
4.4 Shipek grab sampler 6
4.5 Van Veen grab sampler 6
4.6 Sea-Bird SBE 9plus conductivity-temperature-depth (CTD) profiler 6
4.7 AML Smart SVPlus 7
5 Technical Difficulties 8
6 Survey Narrative 9
7 Survey Data Examples 16
7.1 Current Profiles 16
7.1.1 ADCP 1 16
7.1.2 ADCP 2 18
7.2 Multibeam Bathymetry 20
7.3 Sediment Samples 21
Appendices 22

1 EXECUTIVE SUMMARY

The Mobility of Sediment Waves and Sand Banks in the Irish Sea (MOVE) survey is a collaborative research survey undertaken by the Irish Research Centre for Applied Geosciences (iCRAG), Centre for Energy, Climate and Marine (MaREI) and Gavin and Doherty Geosolutions (GDG). Its primary purpose is to collect seabed and sub-seabed data in order to investigate seabed mobility and bedform dynamics, in particular offshore banks and sediment wave features.

The survey was split into two legs to facilitate equipment deployment over a full tidal cycle. Due to Covid-19 measures, the number of scientists was restricted to two. However, 24-hour operations were performed as much as possible. During the survey, **fifteen areas** were surveyed using a multi-beam echosounder (MBES) amounting to approximately **80 km^2 of seabed.** These areas were primarily concentrated in the southern Irish Sea, off the coast of Wicklow and Wexford. The data reveals a highly dynamic seabed consisting of a range of mobile bedforms (e.g. sediment waves) as well as sediment banks that exhibit some morphodynamic change over time. Moribund and relic bedforms (e.g. trochoidal sediment waves) were also observed. For the duration of the survey, **two acoustic doppler current profiler (ADCP) units** were deployed at locations 30 km apart and relative to sediment banks of interest. To help groundtruth seabed conditions and to assist in sediment dynamics studies, **39 sediment samples** were retrieved. A total of **200 1 L water samples** were collected at varying water depths above the two ADCP locations at **nine different time intervals** in order to calculate suspended sediment transport levels.

2 BACKGROUND

In general, significant vagrancies exist regarding seabed morphodynamics and the potential for sediment mobility in the Irish Sea. Many processes associated with morphodynamic and hydrodynamic change, such as sediment wave migration, have been well documented and quantified in fluvial environments where hydrodynamic data is more readily available in both high spatial and temporal resolutions. Furthermore, physical testing (e.g. flume tanks) mean that scaled-down real-world testing allows a greater insight into these processes that can be easily studied. However, in deeper offshore environments such as the Irish Sea, this level of data is not available. Additionally, the Irish Sea environment offers more controlling factors on morphodynamic change and so is considerably more complex. Therefore, the technical challenge of gathering data in this environment is a trying one. Data that can be gathered include traditional seabed mapping techniques, such as multi-beam echosounder to image the seabed, and sub-bottom profiling to visualise seabed structure below the surface. Both these methods offer an image of the seabed and sub-seabed at a given point in time at its collection. Scientifically, the challenge is to utilise this data robustly to develop an understanding of how the seabed has developed temporally and spatially. In this respect, we can collect these multibeam and sub-bottom data in repeat surveys to track seabed morphodynamic changes over time. However, depending on the time-lapse between surveys, many fine or significant changes in the seabed may be missed. By deploying seabed mounted, long-term hydrodynamic monitoring equipment such as acoustic doppler current profilers (ADCP) and sediment sampling, we can garner a better understanding of temporal changes at a higher resolution. Therefore, the big scientific challenge to understanding seabed morphodynamics is how to observe these changes in a reasonable resolution with high-confidence. Furthermore, another significant challenge to assessing the risk of morphodynamic evolution, and sediment mobility, posed to critical engineering and environmental projects is how can future changes in seabed morphodynamics be confidently predicted.

3 SURVEY RATIONALE AND OBJECTIVES

The scientific goal of the MOVE project can be broken down into five objectives:

1. To investigate the nature of sediment mobility and morphodynamic changes in an area of the Irish Sea known for complex hydrodynamics;

2. To examine the physical processes occurring on the seafloor with respect to seabed morphodynamics pertinent to engineering projects;

   To provide data to validate 2D/3D hydrodynamic models that will form the basis of understanding the complex morphodynamics in the survey areas;

3. To gather critical site-specific environmental data to feed in to modelling efforts to help predict future changes in seabed morphology in reaction to anthropogenic impacts and climate change;

4. To build up a unique Geographical Information System (GIS) based database, and series of technical maps, of offshore seabed morphology and sediments in the Irish Sea that can be used in future engineering and environmental studies.

These objectives will be achieved at several sites in the south Irish Sea that are potential areas of offshore renewable energy related infrastructural development and contain notable bedforms and seabed morphodynamics.

The data from this project feeds into the existing Post-Doctoral research of Dr. Mark Coughlan (UCD/iCRAG), as well as the joint-industrial research of Gavin and Doherty Geosolutions and MaREI, as well as the PhD research of Shauna Creane (UCC/GDG).

4 EQUIPMENT

4.1 Research Vessel – RV Celtic Voyager

The Celtic Voyager is a 31.4 m multi-purpose research vessel (Figure 1). The vessel has wet, dry and chemical laboratories, which are permanently fitted with standard scientific equipment and can accommodate 6 - 8 scientists with a maximum endurance of 14 days. The vessel is manned by an experienced crew who are highly skilled with the handling and deployment of scientific equipment.

She is equipped with a Trimble NT Differential GPS and Kongsberg Simrad Seapath 200 motion reference unit. A 10,000 kg general purpose winch hooked through the aft, 4 m high A-frame as well as a 500 kg starboard CTD winch and 1000 kg starboard oceanographic winch.



Figure 1 The CV Celtic Voyager in port

4.2 Acoustic Doppler Current Profiler (ADCP)

Two TRDI 300 kHz Workhorse Sentinel ADCPs were deployed on the seabed to profile changes in current speed throughout the water column. The ADCP is housed within TRDI Workhorse Sentinel ADCP Seabed Gimballed Frame with a location transponder (Figure 2). The ADCP was deployed through the A-frame with a tethered

ground line leading to a clump-weight. Attached to the clump weight was a buoyed mooring line which was used to grapple for retrieval.



Figure 2 ADCP housed in trawl-proof frame prior to deployment Clump weight can be seen in right-hand image background

4.3 Multibeam Echosounder

The EM 2040 is a true wide band high resolution shallow water multibeam echo sounder, with an operating frequency range of 200 to 400 kHz.

4.4 Shipek grab sampler

A Duncan & Associates Shipek sampler was used to sample sediment in both muddy, sandy and gravelly substrates. The sampler scoops a sediment sample from the top 10 cm of the seabed. The Shipek grab was deployed on the starboard winch mid-ship. All Shipek grab samples were described, photographed and sub-sampled for later on-shore analyses. All grab samples were stores in the wet lab at ambient temperature.



Figure 3 Shipek deing retrieved during MOVE survey operations

4.5 Van Veen grab sampler

In areas where retrieving samples using the Shipek were unfeasible due to the ground conditions, a Van Veen grab sampler was deployed through the aft A-frame.

4.6 Sea-Bird SBE 9plus conductivity-temperature-depth (CTD) profiler

The Sea-Bird SBE 9plus CTD profiler was used to determine water mass properties. It was lowered into the water and held at the surface until the sensors equilibrated and then lowered steadily to 5 m off the bottom logging in real-time. The capacity to take water samples was used on this survey. The CTD was deployed on the starboard winch mid-ship.



Figure 4 Retrieving water samples from the CTD rosette during MOVE survey operations

4.7 AML Smart SVPlus

The AML SV Plus is a shallow water sound velocity profiler recording sound velocities and pressure through the water column. This equipment was lowered overboard using the starboard mid-ship winch and was used to produce a sound velocity profile to calibrate MBES data acquisition.

5 TECHNICAL DIFFICULTIES

No technical difficulties were encountered during the course of the survey itself.

However, following the retrieval of one of the ADCPs and initial processing of the data, it was determined that the unit was severely tilted on the seabed. Resultingly the data collected was compromised.

6 SURVEY NARRATIVE

ALL TIMES IN UTC

LEG 1

Wednesday, 23rd September

10.30 – Arrived at the vessel on Horgan's Quay. Met crew and had safety briefing. Captain informed us that the weather wasn't looking great and that we would not be sailing this evening, possibly not even tomorrow.

Kieran Adlum (Marine Institute) arrived shortly after to set up ADCP equipment along with crew. Two units all set by 12.30.

15.30 – Damian Crean departed the vessel after a run through of CTD operations. We set up SIS with assistance of Fabio Sacchetti remotely. Weather starting to deteriorate in the forecast with a yellow weather warning in place for Cork. Tomorrow looks particularly bad with wind up to Beaufort 6.

Thursday, 24th September

Quayside (Cork), bright, sunny, 9°C

07.55 - Met with the Captain and Mate after breakfast. Forecast is bad for today and into tomorrow with northerly winds gusting up to Beaufort 7. Plan is to stay Quayside today and aim to leave tomorrow afternoon. This would get us on site for early Saturday morning where we would: (1) multibeam survey the ADCP 1 deployment area; (2) deploy the ADCP at slack tide (12.20); (3) CTD water samples in that area. The fact that the ADCP unit has an extended mooring line (70 m) and not an acoustic release means that the water sampling will have to be done outside a 70 m radius from the final ADCP location. Similarly, no MBES work can be undertaken in close proximity to the ADCP.

Friday, 25th September

Quayside (Cork), bright, sunny, 14°C

07.30 – Met with the Captain after breakfast. Conditions offshore are still variable and forecasted strong, northerly winds could prove problematic tomorrow for ADCP deployment. The current plan is to leave port at 16.00 and transit to the first ADCP

area with a view to being on-site for first light. Captain to update during the day as new forecast comes in.

17.00 – Cast off, finally! Started transit to first ADCP location.

Saturday, 26th September

Area 1 (A12, ADCP station 1), bright, sunny, 10°C, northerly wind 17 knts gusting 23 knts. 1.2 m waves with 0.5 m swell.

08.33 – On Station 1 and preparing to deploy CTD for SVP profile to start MBES survey of A12. Wind is at around Beaufort 4 and northerly-northwesterly. Sea states not ideal for working but hoping it will get better so that by 13.30 we will be able to deploy first ADCP in this area.

08.38 – CTD deployed. 09.02 started MBES surveying A12. Weather generally improving. 10.55 stopped MBES in order to take grab samples in this area. At 11:33 a grab sample was attempt using the Shipek at Station 2. No sample was returned another attempt was made, which also returned no sample. The Day Grab replaced the Shipek and a third attempt was made, which returned a sample. Another sample was retrieved here before moving to a new station where 4 attempts were made returning 2 samples (Station 4 and 5). 12:05 began transit to ADCP 2 site (B6).

15.24 – CTD deployed to get SVP for B6 MBES survey. Started surveying at 15.52. Weather decent.

21.23 – Finished surveying Area 2 (B6) and started transit to Area 3 (D1 & D2).

22.33 – Arrived at Area 3 (D1 & D2) and started MBES survey. Wind 10 kts northwesterly gusting 19 kts.

Sunday, 27th September

Area 3 (D1&D2), night, 10°C, northerly wind 9 knts gusting 16 knts. 0.8 m waves with 0.6 m swell.

04.32 – Area 3 (D1 &D2) partially surveyed. Heading to ADCP 1 for 06.30 slack tide deployment.

06.30 – On site at ADCP 1. Clear, crisp weather. Wind 13 kts blowing northwesterly. Sea state calm with 0.7 m wave height. Crew were efficient and professional as usual and ADCP was deployed with minimal fuss.

Ship locations

ADCP:

52° 27.887’

006° 07.811’

Mooring weight:

52° 27.923’

006° 07.733’

07.19 – A CTD cast was made to collect water samples near the ADCP at slack tide (Station 8). 12 bottles were fired.

08.42 – A CTD cast was made to collect water samples near the ADCP at peak ebb (Station 9). 12 bottles were fired. After which we started transit to the second ADCP location with a view to deploying at slack tide (circa 13.00).

12.12 – On, or near, site for second ADCP deployment. 4 grab samples were attempted and 4 retrieved (Station 10 and 11).

13.13 – ADCP was deployed in slack conditions, much better than yesterday.

Ship locations

ADCP:

52° 43.296’

006° 01.648'

Mooring weight:

52° 43.289'

006° 01.736'

13.32 – After ADCP deployment was completed, a CTD cast was taken near the location to gather water samples at slack tide (Station 13). After this we started to Area 4 (A3) for MBES survey.

16.29 – CTD cast at Area 4 (A3) for SVP profile. MBES survey started at 16.43. Some initial software problems on Line 30, so that was abandoned and the issue resolved.

19.36 – Survey of Area 4 (A3) completed and started transit to Area 5 (C1).

19.59 – Arrived at Area 5 (C1) and began surveying.

Monday, 28th September

Area 5 (C1), night,°C, southwesterly wind 8 knts gusting 12 knts. 0.4 m waves with 0.3 m swell.

00.45 – Finished surveying Area 5 (C1) and started transit for Dublin.

11.45 – Quayside in Dublin Port. Scientists disembark.

LEG 2

Friday, 9th October

14.00 – All scientists onboard. Briefed by Aodhán Fitzgerald. Weather changeable. Planned to sail at 17.00 and steam to Area 3 (D1 & D2) to complete this area before being on site to sample at ADCP 2 location at 07.00 tomorrow. Weather isn't very promising however for Saturday and Sunday. Left port at 17.00.

22.10 – On site (Station 15) for CTD deployment. No power to winch. Tech and Chief Engineer investigated. Apparently, junction box under computer was bypassing deck unit. Problem resolved by 22.30 and CTD (Station 15) successfully deployed. SVP loaded and surveying of Area 3 started at approximately 23.15.

Saturday, 10th October

04.48 – Finished surveying Area 3 (D1 & D2) and started transit to ADCP 2 site for morning water sampling

07.03 – On site at Station 16. Water sampling followed by grab sample at Station 17.

08.35 – Took an SVP profile (Station 18) and started surveying Area 6 (B3). Had to adjust some course for South Arklow Buoy.

Area 6 (B3), cloudy but bright,13°C, southwesterly wind 17 knts gusting 26 knts. 0.9 m waves with 0.3 m swell.

12.20 – Finished Area 6 survey (for now, cross line left) and heading to ADCP 2 site for water sampling.

12.45 – On site near ADCP 2. Initial attempt at water sampling using the CTD was abandoned due to the proximity of the ADCP buoy and entanglement. Second attempt successful (Station 19). Followed by 2 grab samples (Station 20 and 21).

13.31 – Started surveying Area 7 (B2). Conditions good.

22.16 – Finished surveying Area 7. Started transit to east side of Arklow Bank for sediment sampling. 2 grabs completed (Station 22 and 23).

Area 8 (B1), night, 11°C, northwesterly wind 13 knts gusting 19 knts. 0.7 m waves with 0.4 m swell.

23.11 – Started surveying Area 8.

Sunday, 11th October

06.58 – Finished Area 8 and started transit to ADCP 1 site for water sampling.

07.30 – On site for water sampling at Station 24. Start transit to Area 4 (A3) for surveying. Completed by 12.30 and started transit to ADCP 1 site for water sampling

Area 8 (B1), night, 11°C, northeasterly wind 4 knts gusting 12 knts. 0.6 m waves with 0.5 m swell.

14.32 – On station (Station 28) for water sampling at ADCP 1 site. Started transit to Area 9 (A15) for grab samples and survey reconnaissance.

15.23 – Started grab sample transit at Area 9 (A15) (Station 29 – 33). No issues with sample recovery, but the depth varied significantly and indicated the area could be challenging for surveying as highlighted by Mate Lar Kirwan. Depths at times were 8 m. Transited further south and performed grab attempts at Station 34. Had 2 failed efforts (cobbles kept the bucket from closing) before a retrieval was made.

17.00 – SVP was carried out and surveying started of Area 9 (A6/A15). Iterations had to be made to the line plan continually due to shallowing water depths at the Masters request. Current depths close to Lucifer Bank don't match the chart indicating a highly dynamic area.

Monday, 12th October, Area 9 (A5, A6, A7, A15, A20), clear, bright some cloud, 11°C, easterly wind 17 knts gusting 25 knts. 0.6 m waves with 0.4 m swell.

11.33 – Good night and morning of surveying. Heading to Area 5 (C1) for grab sampling. Weather supposed to deteriorate.

12.26 – Started grab sampling at Area 5 (C1). Managed 4 good grabs on a transect across some sediment wave features (Station 36-39). Had planned further grabs in this area, but Mate advised to steam to ADCP 1 site if we wished to be there for 15.55 sampling as weather was deteriorating making the transit longer.

On route assisted Irish Coast Guard with practice manoeuvres.

15.05 – On station (Station 40) for water sampling. Started transit to Area 5 (C1) to complete earlier sampling.

17.05 – Started sampling and completed 5 sample attempts (Station 42-46). Began transit to Area 10 (A4).

18.07 – Completed SVP and began surveying Area 10 (A4).

Tuesday, 13th October, Area 10 (A4), night, 12°C, northerly wind 15 knts gusting 21knts. 1.1 m waves with 0.2 m swell.

00.54 – Finished surveying Area 10 (A4) and started transit to Area 11 (A2). Comparing old data from A2 to ours is nuts. Very dynamic area.

07.36 – Finished surveying at Area 10 (A4) and started transit to ADCP 2 site (Arklow) for water sampling.

10.20 – Water sampling at ADCP 2. After which, decision was taken to transit to Area 12 (E1) as wind is turning northerly.

18.10 – On site at Area 12 (E1). SVP taken (Station 52). Weather conditions poor and deteriorating.

20.50 – Weather conditions too poor for surveying, affecting data quality. Master made the decision to end operations and head back towards Area 13 (B9) slowly. Aim to be there for 05.00.

Wednesday, 14th October, Area 13 (B9), night, 11°C, northerly wind 22 knts gusting 34 knts. 2 m waves with 0.3 m swell.

01.15 – On site at B9. Awaiting clearer weather to start multibeam.

Area 13 (B9), dark, 13°C, northerly wind 12 knts gusting 18 knts. 0.9 m waves with 0.6 m swell.

03.06 – SVP for Area 13 (B9) completed. Started surveying B9 at 03.29.

06.32 – Finished surveying at B9. Started transit to Area 3 ADCP 2. ADCP retrieved at 08.20. Started transit to (D1&D2) for grab samples.

09.47 – On site for grab sampling at trochoidal waves in Area 3. 4 good samples. Moved to second transect line (normal waves). Attempted 10 samples, retrieved 1. Started transit to Area 14 (A1) for surveying.

14.35 – On site ADCP 1 for retrieval. 14.55 ADCP back on deck. 15.22 began Transit to Cork for short survey at Kinsale Gas Platform.

Thursday, 15th October

06.00 – On site at Kinsale Gas Platform. Started survey at 08.04, completed by 10:22. Started home transit to Cork.

15.15 – Tied up quayside, Cork.

Friday, 16th October

11.00 – All scientists off with backed up data and samples.

SURVEY END

7 SURVEY DATA EXAMPLES

7.1 Current Profiles

Current profiles were collected at two locations (Figure 13).

7.1.1 ADCP 1

ADCP 1 was deployed in approximately 40 m of water with data collected in 37 bins of 1 m each at 10-minute intervals. On processing of the data, it became apparent that the ADCP unit had been tilted significantly. This created issues as the ADCP needs accurate tilt readings in order to:

1. Transform from beam to earth coordinates (uvw components) along with the heading data;
2. For bin mapping (The ADCP needs to work with bins that are in the same depth layer);
3. For accurate compass (i.e. heading) reading.

In the end, Bins 28 to 37 did not record any magnitude or direction values, potentially due to noise? Even though echo Intensity is recorded for bins 1-3 (Figure 5).

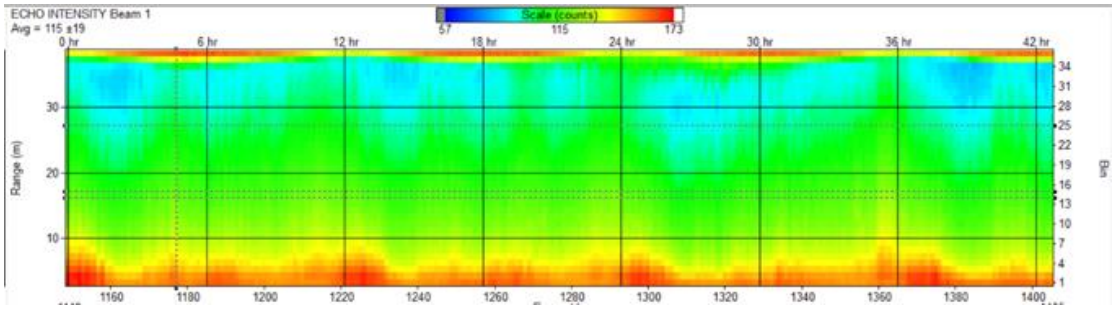


Figure 5 Echo Intensity: Bins 1-37

Bins 26 and 27 record relatively high current speed values (~0.8m/s), which is expected, and a constant rectilinear directional current (Figure 6), however directions are opposite to what was expected.

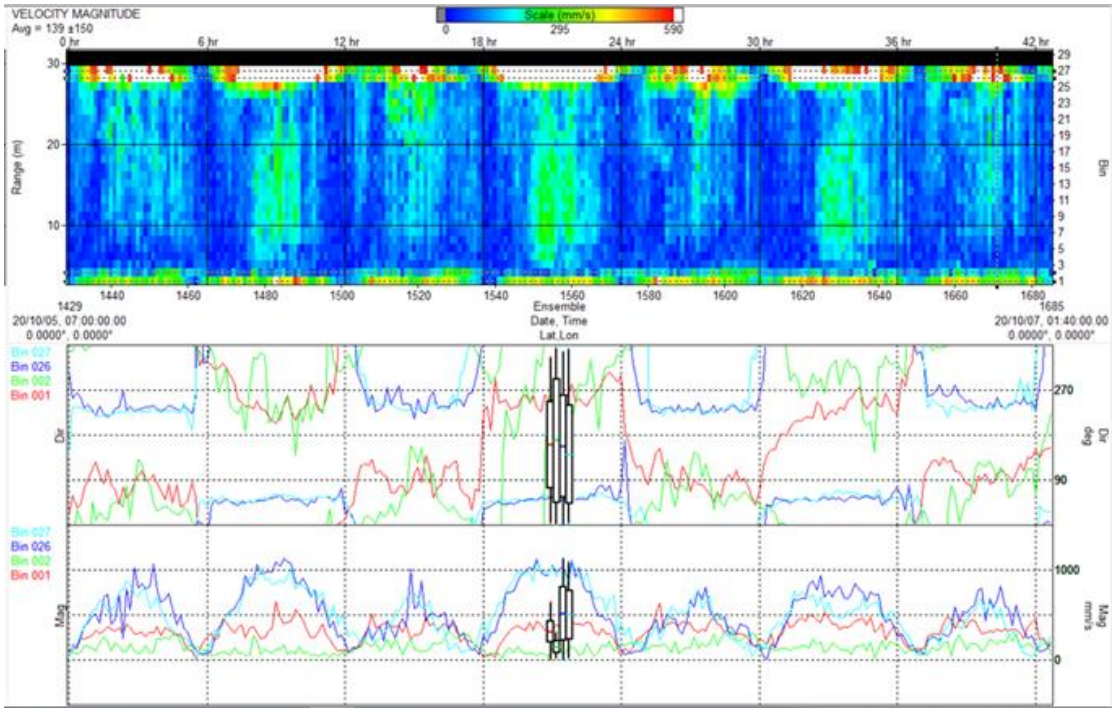


Figure 6 Velocity Magnitude: bins 1-27 recorded. Inconsistency between current directions of bin1 &2 and 26&27. Speeds bins 1-25 v.low compared to what was expected, and compared to bins 26&27

Bins 3-25 suddenly drop to speeds ~0.1m/s and no strong dominant current direction, very scattered, but slight directional trends similar to bins 26-27 above. Bins 1-2 (Figure 6 and Figure 7) shows only slightly higher current speeds than 3-25 and scattered but dominant enough rectilinear current direction but in the opposite direction to the rest of the bins 3-27. Only bins 1-2 show directional trends to what was expected for the area, however currents speeds for the same bins are extremely low.

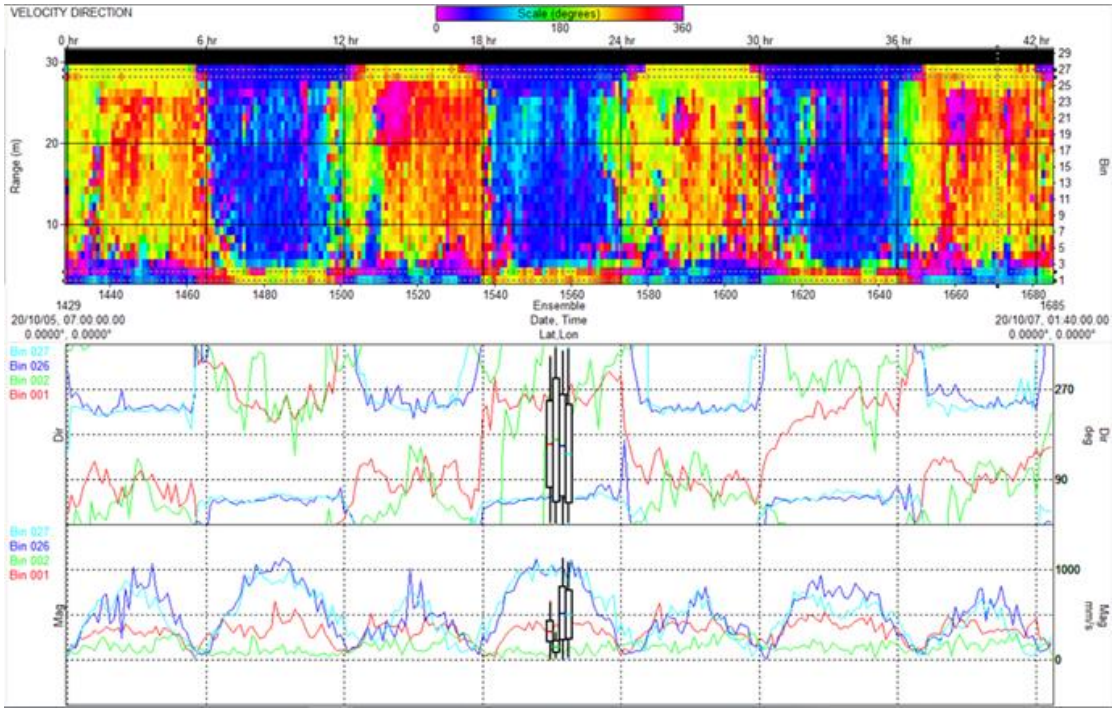


Figure 7 Velocity Direction: bins 1-27 recorded. Inconsistency between current directions of bin1 &2 and 26&27.

7.1.2 ADCP 2

ADCP 2 was deployed in 34 m of water. The u and v-velocity components of each bin were exported. The average of all bins was calculated (i.e. depth averaged) and then converted the u and v-velocity components to direction and speed. This was divided into bottom, mid and surface-water by splitting the water column into thirds and averaging the u and v components in each section, and then converted into to speed and direction (Figure 8).

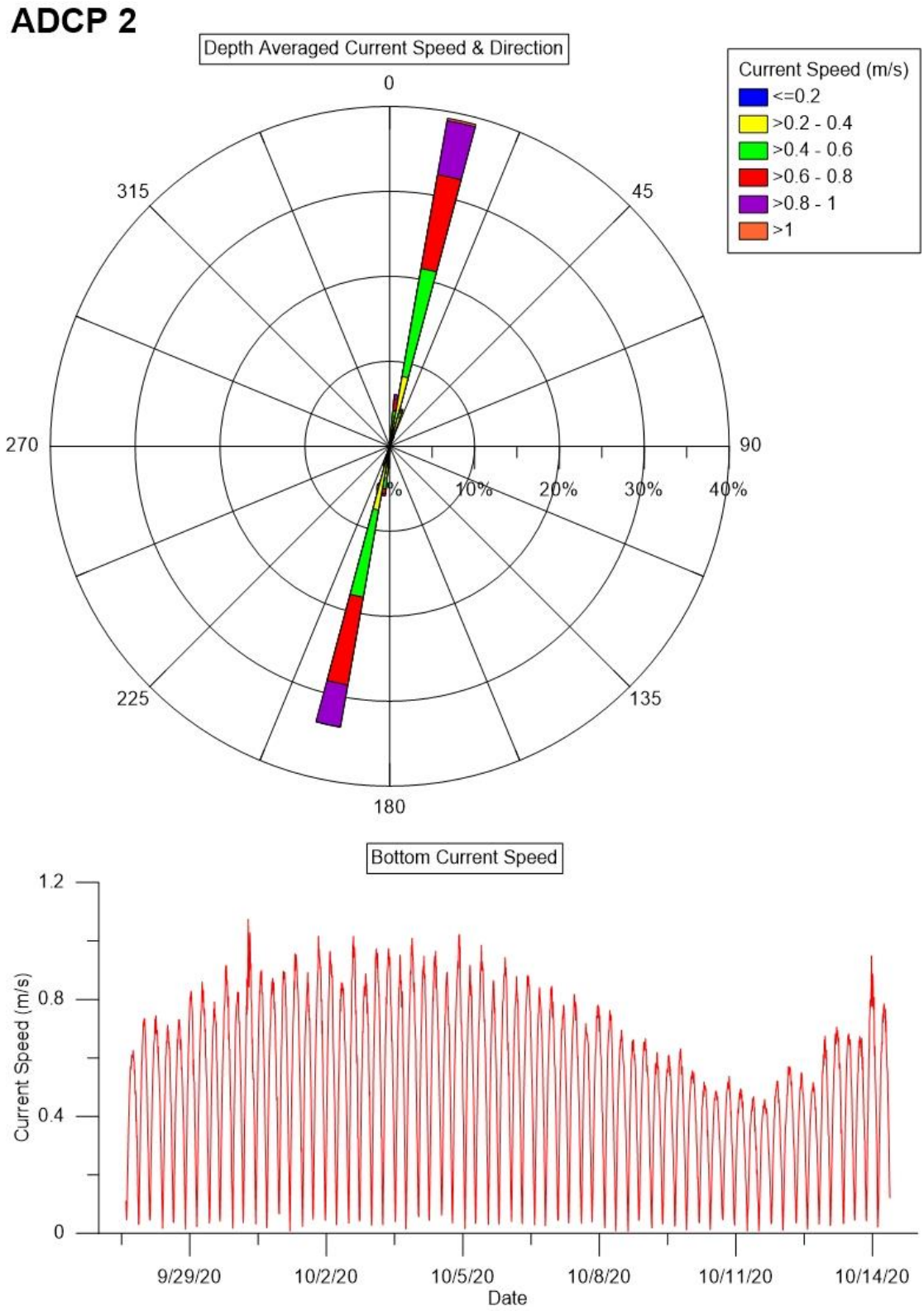


Figure 8 Current speeds and direction at ADCP 2 during survey

To calculate water levels, the pressure/depth was exported and averaged before subtracting the average from the entire dataset. Figure 9 shows the resulting time series data of shows water levels and current speeds on another.

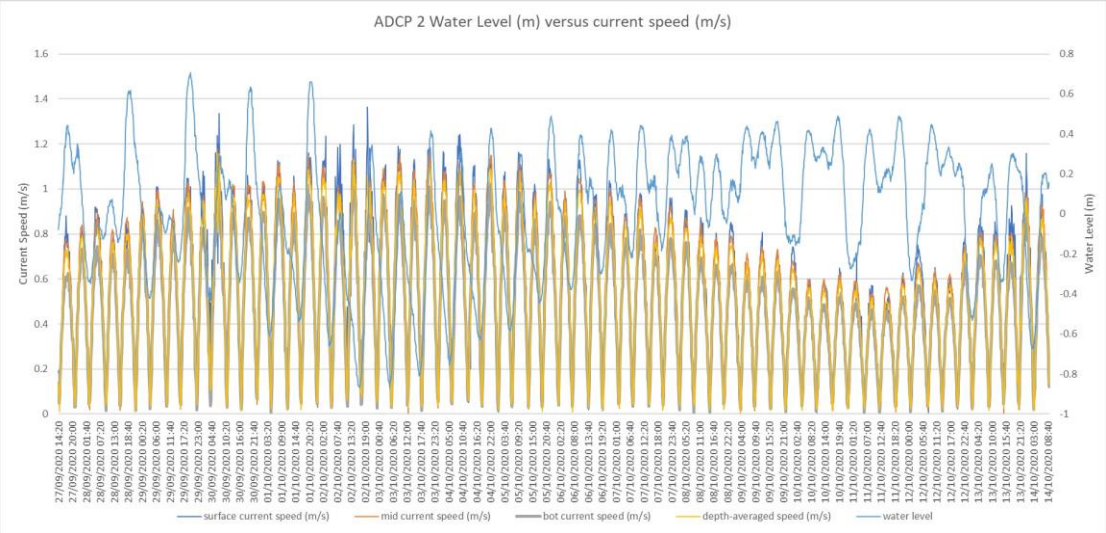


Figure 9 Water levels and current speed for ADCP 2

7.2 Multibeam Bathymetry

Multibeam echosounder (MBES) bathymetry data was collected at 16 individual areas (Figure 11). Data was of good quality, with minor issues during collection mainly due to weather conditions. The data reveals a spectrum of seabed sedimentary features, dominated by sediment waves. Figure 10 displays processed data collected form the C1 area, which exhibits both trochoidal sediment waves (Figure 10A) and normal sediment waves (Figure 10B). Where possible, sediment grab samples were taken in profile across such features. It is the intention of the researchers to process all the MBES data for the areas highlighted in Figure 11 and to develop a geomorphic map of this part of the Irish sea with which to study the morphology, architecture and spatial relationships of these bedforms and their evolution during the Holocene.

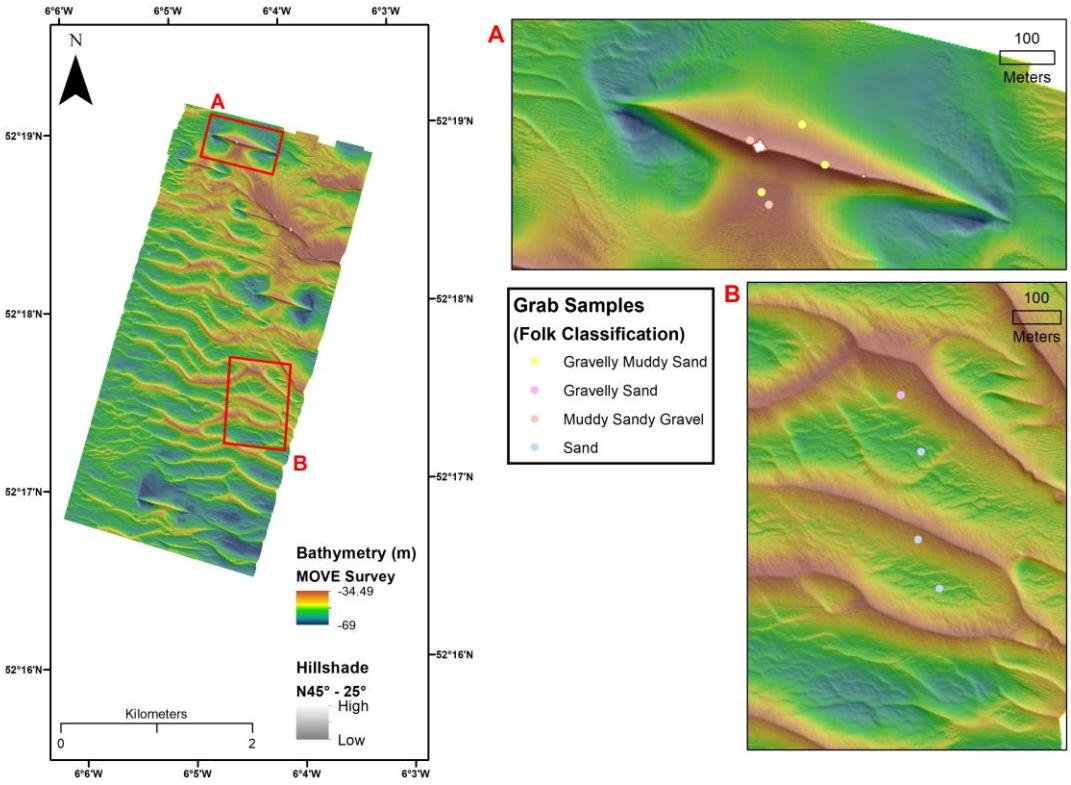


Figure 10 Processed MBES data from survey area C1

7.3 Sediment Samples

Some 43 grab sample attempts were made, of which 38 successfully returned sample material (Figure 12). Samples were processed for grain-size analysis GSA) using sieve and hydrometer methods. The results reveal largely sand-grade material with gravel and silt components. These results will be combined with modelled hydrodynamic data to study sediment mobilisation and bedform development.

Appendices

I. PERSONNEL

LEG 1

Ship' crew	Scientific Party
Colin McBrearty Master	Dr. Mark Coughlan Chief Scientist (UCD/iCRAG)
Stephen Lantry Mate	Shauna Creane Co-Chief Scientist/PhD student (UCC/GDG)
Jason White Chief Engineer	
Martin Goggin 2nd Officer	
Finbar Goggin Motorman	
Tony Reck Cook	
Diarmuid Joyce AB	

LEG 2

Ship' crew	Scientific Party
Philip Baugh Master	Dr. Mark Coughlan Chief Scientist (UCD/iCRAG)
Lar Kirwan Mate	Shauna Creane Co-Chief Scientist/PhD student (UCC/GDG)
Brendan Barry Chief Engineer	
Stephen Barr 2nd Officer	
Tommy Byrne Motorman	
Pat Codd Cook	
Alex Carty AB	
Lukasz Pawlokowski Technician	

II. AREA MAPS: COVERAGES, SAMPLE LOCATIONS AND ADCP LOCATIONS

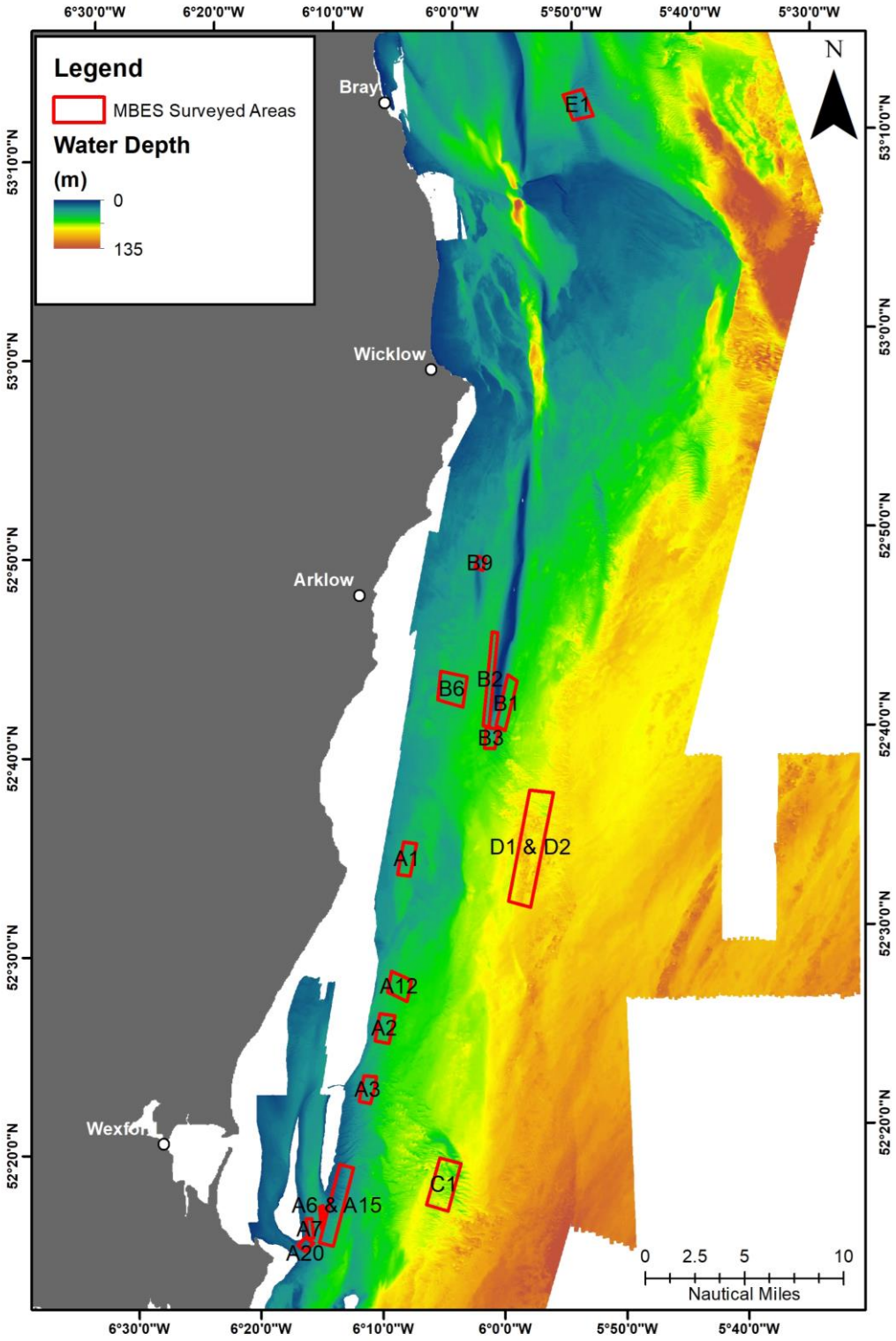


Figure 11 Areas mapped using Multibeam Echosounder (MBES)

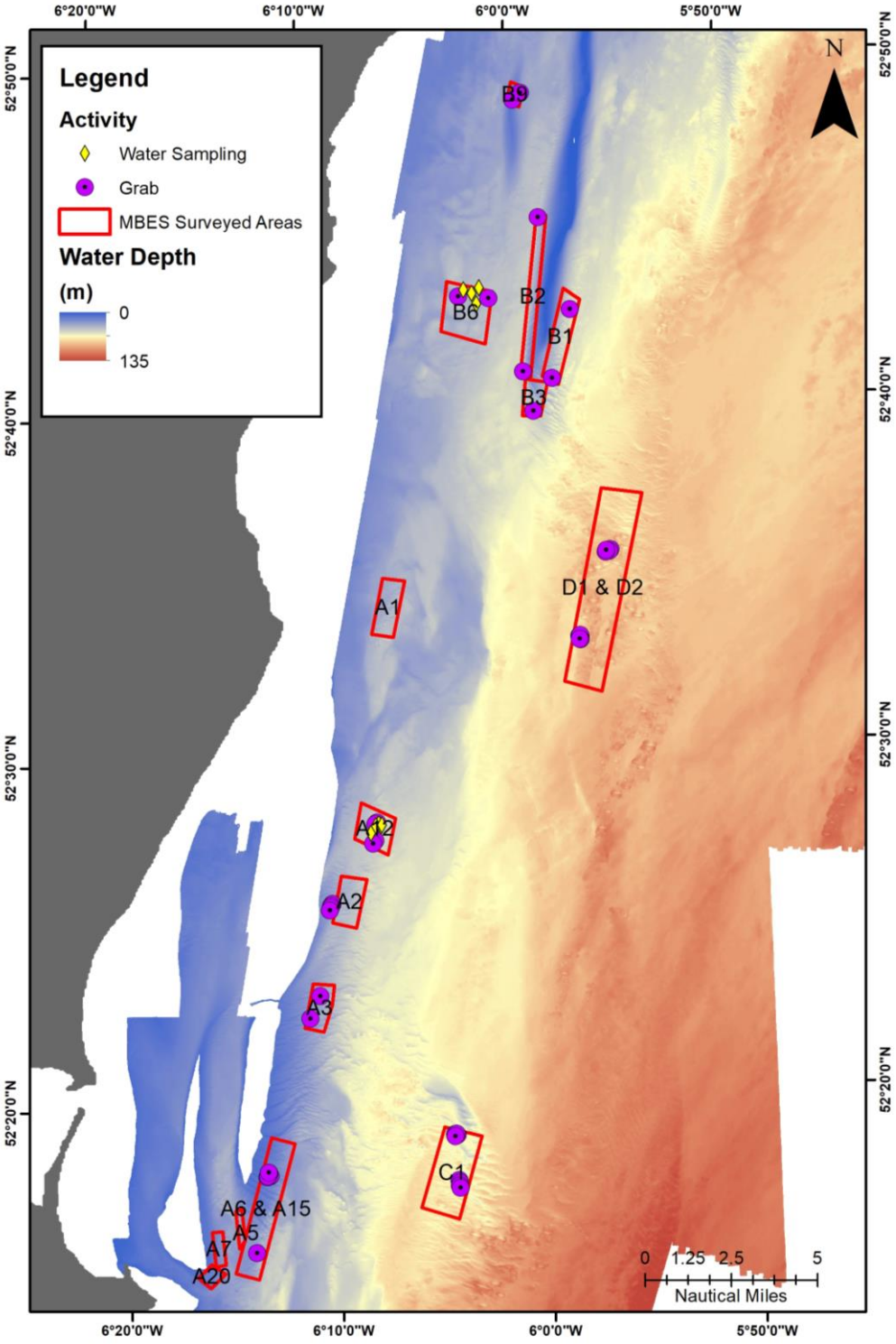


Figure 12 Sampling locations during MOVE survey

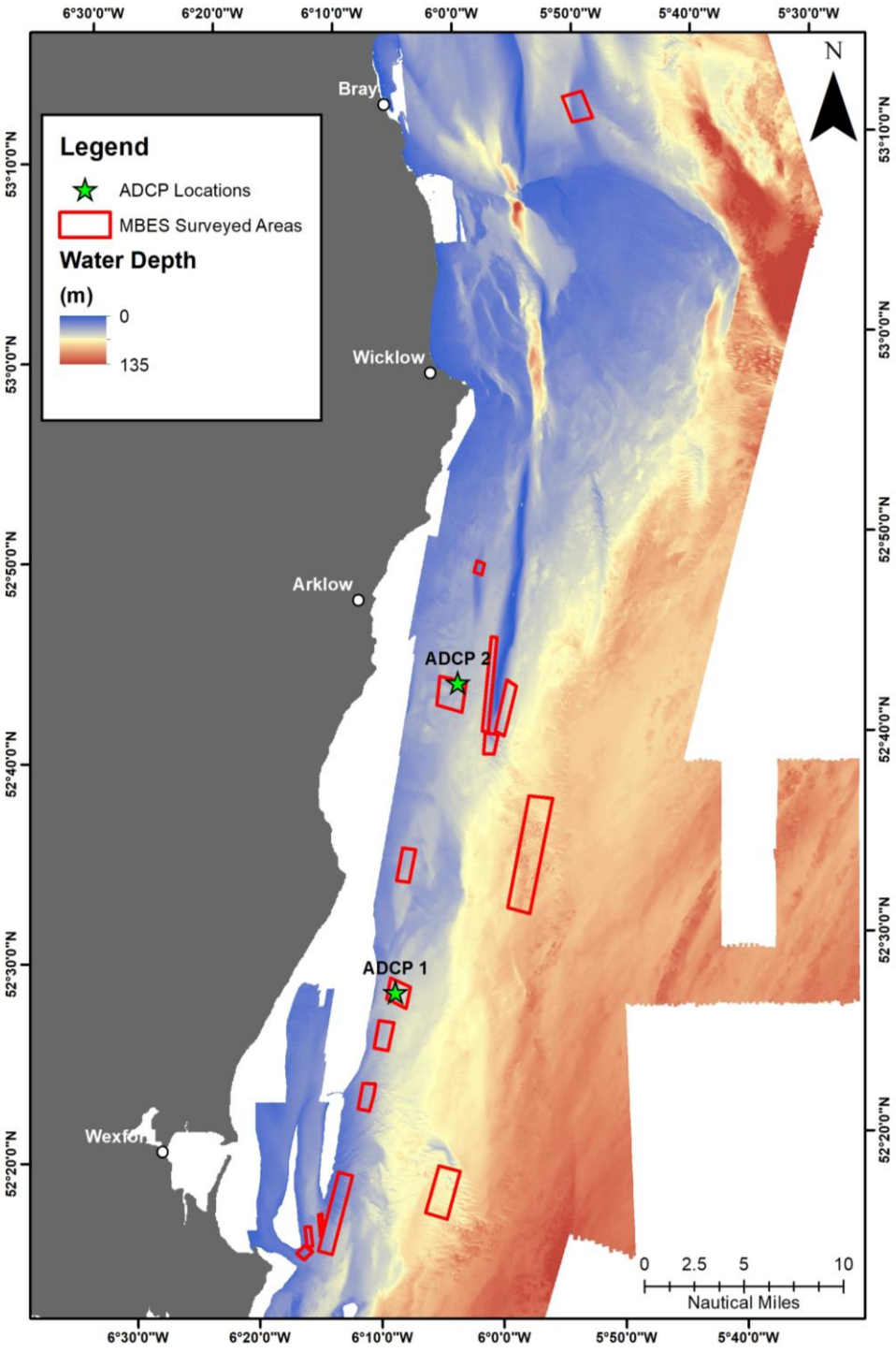


Figure 13 ADCP locations during MOVE survey

III. STATION LOG

Leg No	Stn. No	Activity	Ship Lat		Ship Long		Date	Time	WD	Comments
			Deg	Min	Deg	Min		UTC	m	
1	001	CTD	52	28.2420	6	6.9270	26/09/20	08:38	42m	SVP for Area 1 (A12)
1	002	Grab	52	28.0450	6	7.5280	26/09/20	11:48		After 2 unsuccessful attempts with the Shipek, the Day Grab as used. Silty sand sample with pebbles >1cm
1	003	Grab	52	27.9990	6	7.6170	26/09/20	11:51		Silty sand with 1 cm pebbles
1	004	Grab	52	27.5210	6	7.6420	26/09/20	12:00		
1	005	Grab	52	27.4430	6	7.7610	26/09/20	12:05		Day Grab: After 2 failed prior attempts, a sample was returned. Silty sand with shells and pebbles of up to 1 cm.
1	006	CTD	52	43.3840	6	1.7350	26/09/20	15:24	35m	SVP for MBES Area 2 (B6)
1	007	ADCP	52	27.8870	6	7.8110	27/09/20	06:54	38m	Weight deployed at 06.58 at 52° 27.923', 6° 07.733'. ADCP serial no. 16687 (Frame 008). (Ships Log: ADCP 52° 27.928', 006° 07.719'. Weight: 52° 27.923', 006° 07.733')
1	008	CTD	52	28.0225	6	7.4570	27/09/20	07:19	38m	12 bottles fired for water sampling @ ADCP Station 1 (Wexford) over slack tide
1	009	CTD	52	27.9460	6	7.3470	27/09/20	08:42	38m	12 bottles fired for water sampling @ADCP Station 1 (Wexford) over peak ebb current speeds
1	010	Grab	52	43.1170	6	1.2240	27/09/20	12:12		Silty Sand, shells >1cm, pebbles >1cm
1	011	Grab	52	43.2070	6	2.6500	27/09/20	12:26		Day Grab: After 2 failed attempts, a sample was retrieved on the third attempt. Small sample, sand, pebbled >1cm, rocks >10cm
1	012	ADCP	52	43.2920	6	1.6680	27/09/20	13:13	35.5 m	Weight deployed at 13:15 at 52° 43.287', 006° 01.743'. ADCP serial no. 10489 (Frame 006). (Ships log: ADCP: 52° 43.296', 006° 01.648'. Weight: 52° 43.289', 006° 01.736'.)
1	013	CTD	52	43.3950	6	2.3970	27/09/20	13:32	33.6 m	Water sampling at slack tide. 12 bottles fired.
1	014	CTD	52	23.2750	6	9.8770	27/09/20	16:29	32m	SVP for MBES Area 4 (A3)
2	015	CTD	52	37.9140	5	53.8680	09/10/20	22:44	67m	SVP for MBES Area D1 & D2
2	016	CTD	52	42.9880	6	1.8050	10/10/20	07:03	34m	Water Sampling at Arklow ADCP B6
2	017	Grab	52	39.7970	5	59.2830	10//10/20	07:59	38m	Grab at MBES site B3. Silty sand, shells <1cm
2	018	CTD	52	43.2000	6	1.7000	10/10/20	08:35	40m	SVP for B3
2	019	CTD	52	43.4380	6	1.6530	10/10/20	02:24	36m	12 bottles fired for water sampling @ ADCP Station 2 (Arklow) over peak flood. Initial effort was abandoned due to proximity of buoy.
2	020	Grab	52	45.4030	5	58.6980	10/10/20			(Site B2) Small sample. Silty sand with clay conglomerates.
2	021	Grab	52	40.9570	5	59.7010	10/10/20			(Site B2) Silty sand with clay components
2	022	Grab	52	40.7260	5	58.3250	10/10/20	22.27		Silty sand with some coarser clasts (0.5 cm) and pebbles (1cm) with shell hash
2	023	Grab	52	42.7060	5	57.3490	10/10/20	22.47	40m	Silty sand with pebbles and shell hash (1 cm)
2	024	CTD	52	27.7570	6	7.8280	11/11/20	07:51	41m	Water Sampling at ADCP Station 1 (Wexford site - A12)
2	025	Grab	52	23.0710	6	10.5530	11/10/20	08:31		Silty sand, shell hash (<1cm)

2	026	Grab	52	22.4310	6	11.0560	11/10/20	08:44		Silty sand, shell hash (<1cm)
2	027	CTD	52	22.3760	6	11.0650	11/10/20	09:02	22m	SVP for A3 MBES - issue at Bin average processsing step in 'SBE Data Processing', data disappears from file at this step, only header left in file
2	028	CTD	52	27.9660	6	7.5870	11/10/20	13:44	41 m	12 bottles fired for water sampling @ ADCP Station 1 (Wexford). Bottle 11 fired but leaked so no sample.
2	029	Grab	52	17.9250	6	13.2320	11/10/20	15:23	16 m	light brown silty sand
2	030	Grab	52	17.9910	6	13.2870	11/10/20	15:22		light brown silty sand
2	031	Grab	52	17.8900	6	13.3740	11/10/20	15:36		light brown silty sand
2	032	Grab	52	17.9130	6	13.3650	11/10/20	15:38	17m	light brown silty sand
2	033	Grab	52	18.0160	6	13.3130	11/10/20	15:45	15 m	light brown silty sand
2	034	Grab	52	15.7030	6	14.0020	12/10/20	03:36	25 m	Silty sand but with coarser component including pebbles (1-2 cm) and shell hash.
2	035	SVP	52	16.0890	6	13.4550	12/10/20	00:43	32 m	SVP for Area A6/A15
2	036	Grab	52	17.5840	6	4.3110	12/10/20	12:26	53 m	Grey-Light Brown Silty Sand (fine-medium sand)
2	037	Grab	52	17.5190	6	4.2780	12/10/20	12:29	59 m	Grey-Light Brown Silty Sand (fine-medium sand)
2	038	Grab	52	17.4200	6	4.2900	12/10/20	12:35	50 m	Grey-Light Brown Silty Sand (fine-medium sand)
2	039	Grab	52	17.3640	6	4.2540	12/10/20	12:38	57 m	Grey-Light Brown Silty Sand (fine-medium sand)
2	040	CTD	52	27.9850	6	7.3090	12/10/20	02:24	41 m	12 bottles fired for water sampling @ ADCP Station 1 (Wexford)
2	041	Grab	52	18.8760	6	4.4150	12/10/20	17:05		Coarse Sand to Gravel - dark grey brown
2	042	Grab	52	18.9000	6	4.3110	12/10/20	17:09	37m	Coarse Sand and Gravel - more gravel than 041
2	043	Grab	52	18.9270	6	4.4300	12/10/20	17:17	39m	No sample on first attempt - didn't close. Gravel.
2	044	Grab	52	18.9410	6	4.3450	12/10/20	17:20	52m	Poorly sorted Sand (Fine to Coarse) with Gravel
2	045	Grab	52	18.8630	6	4.4040	12/10/20	17:26	47m	Poorly Sorted Sand and Gravel
2	046	SVP	52	18.9240	6	11.7440	12/10/20	18:07	26m	SVP for area A4
2	047	Grab	52	25.7430	6	9.8090	13/10/20	07:45		Light brown Fine-medium sand
2	048	Grab	52	25.6830	6	9.8660	13/10/20	07:47	27.8m	Light brown Fine-medium sand
2	049	Grab	52	25.6260	6	9.8990	13/10/20	07:50	25.8m	Light brown Fine-medium sand
2	050	Grab	52	25.5580	6	9.9360	13/10/20	07:53	24.09m	Light brown Fine-medium sand, shells >1cm
2	051	CTD	52	43.2920	6	2.0090	13/10/20			Water Sampling at ADCP 2 (Arklow)
2	052	SVP	53	12.6080	5	51.0070	13/10/20	18:10	38m	SVP for E1
2	053	SVP	52	48.7670	5	59.6580	14/10/20	03:36	14m	SVP for B9

2	054	Grab	52	48.8460	5	59.6710	14/10/20	06:56		Grab on the Seven Fathom Bank. Light Brown, Fine Sand
2	055	Grab	52	49.0390	5	59.2940	14/10/20	07:02	24.81m	Grab off the Seven Fathom Bank (eastern side). Light Brown, Fine Sand
2	056	ADCP 2 Retrieval	52	43.2920	6	1.6680	14/10/20	08:20		Retrieved at slack tide
2	057	Grab	52	35.6920	5	55.9030	14/10/20	09:47	75.92m	Poorly sorted Gravel. Fine-Coarse Gravel Pebbles >2cm Dark Grey
2	058	Grab	52	35.6530	5	55.9510	14/10/20	09:51	61.9m	Coarse Sand to Gravel (Finer than 57m)
2	059	Grab	52	35.6240	5	56.1340	14/10/20	10:16	69.9m	Dark Grey - Gravel, pebbles <1cm
2	060	Grab	52	35.6740	5	56.0940	14/10/20	10:32	61m	Dark Grey, Gravel
2	061	Grab	52	33.2190	5	57.5560	14/10/20	11:20	65m	No recovery x 2
2	062	Grab	52	33.1990	5	57.4960	14/10/20	11:34	63m	No recovery and dense silty sand
2	063	Grab	52	33.2510	5	57.5040	14/10/20	11:52	65m	No recovery x 2
2	064	Grab	52	33.1250	5	57.4970	14/10/20	12:02	67m	No recovery x 2
2	065	Grab	52	33.1290	5	57.5420	14/10/20	12:14	65m	No recovery x 2
2	066	ADCP 1 Retrieval	52	28.0000	6	8.0000	14/10/20	14:35		Retrieved at slack tide

IV. MULTIBEAM ECHOSOUNDER LINES

Info					Start				End				Runtime Parameters						
Area	Line id	Type	SVP No.	SOG	Start Date	Start time (UTC)	SOL Lat (dd)	SOL Long (dd)	End Date	End time (UTC)	EOL Lat (dd)	EOL Long (dd)	Coverage	Max Coverage	Pulse Type	Detector	Mode	Frequency	Filters
A12	1	MBES	Stn. 1*	3.5 kts	26/09/2020	09:02	52.4560301	6.1443346	26/09/2020	9.33	52.478	6.135	69|10|69	150/150	SHORT CW	NORMAL	REL. MEAN HEADING	300 kHz	SPIKE: MEDIUM, RANGE GATE:NORMAL, PHASE RAMP: NORMAL
	2	MBES		3.8 kts	26/09/2020	09:39	52.476	6.1275	26/09/2020	09:51	52.453	6.136	69|10|69	150/150	SHORT CW	NORMAL	REL. MEAN HEADING	300 kHz	SPIKE: MEDIUM, RANGE GATE:NORMAL, PHASE RAMP: NORMAL
	3	MBES		3.5 kts	26/09/2020	09:58	52.455	6.137	26/09/2020	10:18	52.474	6.13	69|10|69	150/150	SHORT CW	NORMAL	REL. MEAN HEADING	300 kHz	SPIKE: MEDIUM, RANGE GATE:NORMAL, PHASE RAMP: NORMAL
	4	MBES		3.5 kts	26/09/2020	10:22	52.474	6.126	26/09/2020	10:31	52.456	6.133	69|10|69	150/150	SHORT CW	NORMAL	REL. MEAN HEADING	300 kHz	SPIKE: MEDIUM, RANGE GATE:NORMAL, PHASE RAMP: NORMAL
	5	MBES		3.2 kts	26/09/2020	10:38	52.455	6.131	26/09/2020	10:55	52.473	6.123	69|10|69	150/150	SHORT CW	NORMAL	REL. MEAN HEADING	300 kHz	SPIKE: MEDIUM, RANGE GATE:NORMAL, PHASE RAMP: NORMAL
Finished Area early to undertake grab sampling, then transit to B6																			
Info					Start				End				Runtime Parameters						
Area	Line id	Type	SVP No.	SOG	Start Date	Start time (UTC)	SOL Lat (dd)	SOL Long (dd)	End Date	End time (UTC)	EOL Lat (dd)	EOL Long (dd)	Coverage	Max Coverage	Pulse Type	Detector	Mode	Frequency	Filters
B6	6	MBES	Stn. 6	7.3kts	26/09/2020	15:52	52.7272	6.05014	26/09/2020	16:05	52.7017	6.0585	69|10|69	180/180	SHORT CW	NORMAL	REL. MEAN HEADING	300 kHz	SPIKE: MEDIUM, RANGE GATE:NORMAL, PHASE RAMP: NORMAL
	7	MBES		6.2kts	26/09/2020	16:07	52.7014	6.0557	26/09/2020	16:22	52.7269	6.0471	69|10|69	180/180	SHORT CW	NORMAL	REL. MEAN HEADING	300 kHz	SPIKE: MEDIUM, RANGE GATE:NORMAL, PHASE RAMP: NORMAL
	8	MBES		4.4 kts	26/09/2020	16:26	52.7269	6.0449	26/09/2020	16:40	52.7	6.053	69|10|69	180/180	SHORT CW	NORMAL	REL. MEAN HEADING	300 kHz	SPIKE: MEDIUM, RANGE GATE:NORMAL, PHASE RAMP: NORMAL
	9	MBES		6.2 kts	26/09/2020	16:48	52.698	6.04	26/09/2020	17:03	52.724	6.032	70|10|70	180/180	SHORT CW	NORMAL	REL. MEAN HEADING	300 kHz	SPIKE: MEDIUM, RANGE GATE:NORMAL, PHASE RAMP: NORMAL
	10	MBES		7.5 kts	26/09/2020	17:07	52.7258	6.0297	26/09/2020	17:20	52.6997	6.038	70|10|70	180/180	SHORT CW	NORMAL	REL. MEAN HEADING	300 kHz	SPIKE: MEDIUM, RANGE GATE:NORMAL, PHASE RAMP: NORMAL
	11	MBES		7.5kts	26/09/2020	17:23	52.6995	6.0357	26/09/2020	17:36	52.7239	6.02774	70|10|70	180/180	SHORT CW	NORMAL	REL. MEAN HEADING	300 kHz	SPIKE: MEDIUM, RANGE GATE:NORMAL, PHASE RAMP: NORMAL
	12	MBES		7.3kts	26/09/2020	17:39	52.7246	6.02517	26/09/2020	17:52	52.6975	6.0338	70|10|70	180/180	SHORT CW	NORMAL	REL. MEAN HEADING	300 kHz	SPIKE: MEDIUM, RANGE GATE:NORMAL, PHASE RAMP: NORMAL
	13	MBES		8.1kts	26/09/2020	17:55	52.6985	6.0315	26/09/2020	18:07	52.7247	6.023	70|10|70	180/180	SHORT CW	NORMAL	REL. MEAN HEADING	300 kHz	SPIKE: MEDIUM, RANGE GATE:NORMAL, PHASE RAMP: NORMAL

	14	MBES		8 kts	26/09/2020	18:11	52.7236	6.0209	26/09/2020	18:22	52.6963	6.02999	70|10|70	180/180	SHORT CW	NORMAL	REL. MEAN HEADING	300 kHz	SPIKE: MEDIUM, RANGE GATE:NORMAL, PHASE RAMP: NORMAL
	15	MBES		7.1kts	26/09/2020	18:26	52.6976	6.0274	26/09/2020	18:39	52.7233	6.0188	70|10|70	180/180	SHORT CW	NORMAL	REL. MEAN HEADING	300 kHz	SPIKE: MEDIUM, RANGE GATE:NORMAL, PHASE RAMP: NORMAL
	16	MBES		7.2kts	26/09/2020	18:43	52.7234	6.0165	26/09/2020	18:55	52.696	6.02558	70|10|70	180/180	SHORT CW	NORMAL	REL. MEAN HEADING	300 kHz	SPIKE: MEDIUM, RANGE GATE:NORMAL, PHASE RAMP: NORMAL
	17	MBES		5.9kts	26/09/2020	19:04	52.6995	6.0425	26/09/2020	19:20	52.7252	6.034	70|10|70	180/180	SHORT CW	NORMAL	REL. MEAN HEADING	300 kHz	SPIKE: MEDIUM, RANGE GATE:NORMAL, PHASE RAMP: NORMAL
	18	MBES		5 kts	26/09/2020	19:24	52.7255	6.0362	26/09/2020	19:44	52.695	6.0454	70|10|70	180/180	SHORT CW	NORMAL	REL. MEAN HEADING	300 kHz	SPIKE: MEDIUM, RANGE GATE:NORMAL, PHASE RAMP: NORMAL
	19	MBES		3.8kts	26/09/2020	19:49	52.7	6.0468	26/09/2020	20:13	52.7253	6.03858	70|10|70	180/180	SHORT CW	NORMAL	REL. MEAN HEADING	300 kHz	SPIKE: MEDIUM, RANGE GATE:NORMAL, PHASE RAMP: NORMAL
	20	MBES		6.7 kts	26/09/2020	20:17	52.7611	6.04066	26/09/2020	20:31	52.701	6.0489	70|10|70	180/180	SHORT CW	NORMAL	REL. MEAN HEADING	300 kHz	SPIKE: MEDIUM, RANGE GATE:NORMAL, PHASE RAMP: NORMAL
	21	MBES		4.3 kts	26/09/2020	20:38	52.7016	6.0509	26/09/2020	20:56	52.7263	6.0428	70|10|70	180/180	SHORT CW	NORMAL	REL. MEAN HEADING	300 kHz	SPIKE: MEDIUM, RANGE GATE:NORMAL, PHASE RAMP: NORMAL
	22	MBES		5.7 kts	26/09/2020	21:06	52.7274	6.0486	26/09/2020	21:23	52.7028	6.0566	70|10|70	180/180	SHORT CW	NORMAL	REL. MEAN HEADING	300 kHz	SPIKE: MEDIUM, RANGE GATE:NORMAL, PHASE RAMP: NORMAL

Transit to D1 & D2

Info					Start				End				Runtime Parameters						
Area	Line id	Type	SVP No.	SOG	Start Date	Start time (UTC)	SOL Lat (dd)	SOL Long (dd)	End Date	End time (UTC)	EOL Lat (dd)	EOL Long (dd)	Coverage	Max Coverage	Pulse Type	Detector	Mode	Frequency	Filters
D1/D2	23	MBES	Stn. 6	4.8 kts	26/09/2020	22:33	52.6258	5.9344	26/09/2020	23:22	52.5323	5.9706	70|10|70	180/180	SHORT CW	NORMAL	REL. MEAN HEADING	300 kHz	SPIKE: MEDIUM, RANGE GATE:NORMAL, PHASE RAMP: NORMAL
	24	MBES		6.1 kts	26/09/2020	23:28	52.5308	5.9677	27/09/2020	00:26	52.6247	5.9313	70|10|70	180/180	MEDIUM CW	NORMAL	REL. MEAN HEADING	300 kHz	SPIKE: MEDIUM, RANGE GATE:NORMAL, PHASE RAMP: NORMAL
	25	MBES		8.9 kts	27/09/2020	00:29	52.6243	5.9289	27/09/2020	01:09	52.5325	5.9641	70|10|70	180/180	MEDIUM CW	NORMAL	REL. MEAN HEADING	300 kHz	SPIKE: MEDIUM, RANGE GATE:NORMAL, PHASE RAMP: NORMAL
	26	MBES		7.8 kts	27/09/2020	01:15	52.5299	5.9619	27/09/2020	01:58	52.6235	5.9259	70|10|70	180/180	MEDIUM CW	NORMAL	REL. MEAN HEADING	300 kHz	SPIKE: MEDIUM, RANGE GATE:NORMAL, PHASE RAMP: NORMAL
	27	MBES		7.6 kts	27/09/2020	02:02	52.6244	5.9224	27/09/2020	02:47	52.5312	5.9584	70|10|70	180/180	MEDIUM CW	NORMAL	REL. MEAN HEADING	300 kHz	SPIKE: MEDIUM, RANGE GATE:NORMAL, PHASE RAMP: NORMAL
	28	MBES		7.7 kts	27/09/2020	02:49	52.5281	5.9563	27/09/2020	03:33	52.6221	5.9204	70|10|70	180/180	MEDIUM CW	NORMAL	REL. MEAN HEADING	300 kHz	SPIKE: MEDIUM, RANGE GATE:NORMAL, PHASE RAMP: NORMAL
	29	MBES		7.5	27/09/2020	03:38	52.6231	5.9171	27/09/2020	04:25	52.5279	5.9538							

				kts														
Finished site early to transit to ADCP 1 for slack tide																		
Info					Start				End				Runtime Parameters						
Area	Line id	Type	SVP No.	SOG	Start Date	Start time (UTC)	SOL Lat (dd)	SOL Long (dd)	End Date	End time (UTC)	EOL Lat (dd)	EOL Long (dd)	Coverage	Max Coverage	Pulse Type	Detector	Mode	Frequency	Filters
A3	30	MBES	Stn. 14		27/09/2020	16:43	52.38687	6.166532											
	31	MBES			27/09/2020														
	32	MBES			27/09/2020														
	33	MBES		8 kts	27/09/2020	17:02	52.371	6.175	27/09/2020	17.09	52.383	6.169	69|10|69	150	SHORT CW	NORMAL	REL. MEAN HEADING	300 kHz	SPIKE: MEDIUM, RANGE GATE:NORMAL, PHASE RAMP: NORMAL
	34	MBES		6 kts	27/09/2020	17.11	52.385	6.17	27/09/2020	17:20	52.37	6.177	69|10|69	150	SHORT CW	NORMAL	REL. MEAN HEADING	300 kHz	SPIKE: MEDIUM, RANGE GATE:NORMAL, PHASE RAMP: NORMAL
	35	MBES		5.1 kts	27/09/2020	17.22	52.369	6.179	27/09/2020	17:31	52.385	6.171	69|10|69	150	SHORT CW	NORMAL	REL. MEAN HEADING	300 kHz	SPIKE: MEDIUM, RANGE GATE:NORMAL, PHASE RAMP: NORMAL
	36	MBES		5.0 kts	27/09/2020	17.33	52.3857	6.1729	27/09/2020	17:43	52.3718	6.1796	69|10|69	150	SHORT CW	NORMAL	REL. MEAN HEADING	300 kHz	SPIKE: MEDIUM, RANGE GATE:NORMAL, PHASE RAMP: NORMAL
	37	MBES		5.8 kts	27/09/2020	17.46	52.3711	6.1824	27/09/2020	17.43	52.3844	6.1752	69|10|69	150	SHORT CW	NORMAL	REL. MEAN HEADING	300 kHz	SPIKE: MEDIUM, RANGE GATE:NORMAL, PHASE RAMP: NORMAL
	38	MBES		6.2 kts	27/09/2020	17.55	52.3867	6.1749	27/09/2020	18.03	52.372	6.1826	69|10|69	150	SHORT CW	NORMAL	REL. MEAN HEADING	300 kHz	SPIKE: MEDIUM, RANGE GATE:NORMAL, PHASE RAMP: NORMAL
	39	MBES		6.7 kts	27/09/2020	18.06	52.3689	6.1848	27/09/2020	18:15	52.3849	6.178	69|10|69	150	SHORT CW	NORMAL	REL. MEAN HEADING	300 kHz	SPIKE: MEDIUM, RANGE GATE:NORMAL, PHASE RAMP: NORMAL
	40	MBES		8.4kts	27/09/2020	18:17	52.3867	6.1789	27/09/2020	18:24	52.3727	6.1855	69|10|69	150	SHORT CW	NORMAL	REL. MEAN HEADING	300 kHz	SPIKE: MEDIUM, RANGE GATE:NORMAL, PHASE RAMP: NORMAL
	41	MBES		7.1kts	27/09/2020	18:27	52.3696	6.1889	27/09/2020	18:34	52.3857	6.1807	69|10|69	150	SHORT CW	NORMAL	REL. MEAN HEADING	300 kHz	SPIKE: MEDIUM, RANGE GATE:NORMAL, PHASE RAMP: NORMAL
	42	MBES		7.7kts	27/09/2020	18:36	52.388	6.1812	27/09/2020	18:43	52.3732	6.1881	69|10|69	150	SHORT CW	NORMAL	REL. MEAN HEADING	300 kHz	SPIKE: MEDIUM, RANGE GATE:NORMAL, PHASE RAMP: NORMAL
	43	MBES		7.1kts	27/09/2020	18:05	52.3806	6.1918	27/09/2020	18:57	52.377	6.168	69|10|69	150	SHORT CW	NORMAL	REL. MEAN HEADING	300 kHz	SPIKE: MEDIUM, RANGE GATE:NORMAL, PHASE RAMP: NORMAL
	44	MBES		6 kts	27/09/2020	19:06	52.385	6.1673	27/09/2020	19.36	52.3719	6.1735	69|10|69	150	SHORT CW	NORMAL	REL. MEAN HEADING	300 kHz	SPIKE: MEDIUM, RANGE GATE:NORMAL, PHASE RAMP: NORMAL
Finished site and started transit to C1																			
Info					Start				End				Runtime Parameters						
Area	Line id	Type	SVP	SOG	Start Date	Start	SOL Lat	SOL Long	End Date	End	EOL Lat	EOL Long	Coverage	Max	Pulse	Detector	Mode	Frequency	Filters

			No.			time (UTC)	(dd)	(dd)		time (UTC)	(dd)	(dd)		Coverage	Type				
	45	MBES			27/09/2020	19.59	52.3196	6.0791	27/09/2020	20.22	52.2805	6.1006	69|10|69	150	SHORT CW	NORMAL	REL. MEAN HEADING	300 kHz	SPIKE: MEDIUM, RANGE GATE:NORMAL, PHASE RAMP: NORMAL
	46	MBES			27/09/2020	20.27	52.2775	6.0992	27/09/2020	20.50	52.3179	6.0767	69|10|69	150	SHORT CW	NORMAL	REL. MEAN HEADING	300 kHz	SPIKE: MEDIUM, RANGE GATE:NORMAL, PHASE RAMP: NORMAL
	47	MBES			27/09/2020	20.54	52.3185	6.0736	27/09/2020	21.20	52.2774	6.0961	69|10|69	150	MEDIUM CW	NORMAL	REL. MEAN HEADING	300 kHz	SPIKE: MEDIUM, RANGE GATE:NORMAL, PHASE RAMP: NORMAL
	48	MBES		6.1 kts	27/09/2020	21.25	52.2766	6.0934	27/09/2020	21.53	52.3172	6.0709	69|10|69	150	MEDIUM CW	NORMAL	REL. MEAN HEADING	300 kHz	SPIKE: MEDIUM, RANGE GATE:NORMAL, PHASE RAMP: NORMAL
	49	MBES		7.7 kts	27/09/2020	21.57	52.3175	6.0678	27/09/2020	22.17	52.2781	6.0896	69|10|69	150	MEDIUM CW	NORMAL	REL. MEAN HEADING	300 kHz	SPIKE: MEDIUM, RANGE GATE:NORMAL, PHASE RAMP: NORMAL
C1	50	MBES	Stn. 14	5.7 kts	27/09/2020	22.22	52.2744	6.0883	27/09/2020	22.49	52.3157	6.0656	69|10|69	150	MEDIUM CW	NORMAL	REL. MEAN HEADING	300 kHz	SPIKE: MEDIUM, RANGE GATE:NORMAL, PHASE RAMP: NORMAL
	51	MBES		7.6 kts	27/09/2020	22.54	52.3155	6.0628	27/09/2020	23.15	52.2761	6.0844	69|10|69	150	MEDIUM CW	NORMAL	REL. MEAN HEADING	300 kHz	SPIKE: MEDIUM, RANGE GATE:NORMAL, PHASE RAMP: NORMAL
	52	MBES		7.2 kts	27/09/2020	23.2	52.2737	6.0826	27/09/2020	23.42	52.3139	6.06	69|10|69	150	MEDIUM CW	NORMAL	REL. MEAN HEADING	300 kHz	SPIKE: MEDIUM, RANGE GATE:NORMAL, PHASE RAMP: NORMAL
	53	MBES		7.6 kts	27/09/2020	23.46	52.3144	6.0565	28/09/2020	0.05	52.2737	6.0796	69|10|69	150	MEDIUM CW	NORMAL	REL. MEAN HEADING	300 kHz	SPIKE: MEDIUM, RANGE GATE:NORMAL, PHASE RAMP: NORMAL
	54	MBES		6.9 kts	28/09/2020	0.09	52.2729	6.0768	28/09/2020	0.3	52.3136	6.0544	69|10|69	150	MEDIUM CW	NORMAL	REL. MEAN HEADING	300 kHz	SPIKE: MEDIUM, RANGE GATE:NORMAL, PHASE RAMP: NORMAL
	55	MBES		8.4 kts	28/09/2020	0.35	52.3095	6.0522	28/09/2020	0.45	52.316	6.0866	69|10|69	150	MEDIUM CW	NORMAL	REL. MEAN HEADING	300 kHz	SPIKE: MEDIUM, RANGE GATE:NORMAL, PHASE RAMP: NORMAL

Leg 2

Finished site and started transit to Dublin

Info					Start				End				Runtime Parameters						
Area	Line id	Type	SVP No.	SOG	Start Date	Start time (UTC)	SOL Lat (dd)	SOL Long (dd)	End Date	End time (UTC)	EOL Lat (dd)	EOL Long (dd)	Coverage	Max Coverage	Pulse Type	Detector	Mode	Frequency	Filters
	56	MBES		5.2 kts	09/10/2020	23.15	52.6232	5.905	10/10/2020	00:29	52.5251	5.9427	69|10|69	150	MEDIUM CW	NORMAL	REL. MEAN HEADING	300 kHz	SPIKE: MEDIUM, RANGE GATE:NORMAL, PHASE RAMP: NORMAL
D1/D2	57	MBES	Stn. 15	8.1 kts	10/10/2020	0.34	52.5249	5.9455	10/10/2020	01:21	52.6209	5.9087	69|10|69	150	MEDIUM CW	NORMAL	REL. MEAN HEADING	300 kHz	SPIKE: MEDIUM, RANGE GATE:NORMAL, PHASE RAMP: NORMAL
	58	MBES		7.2 kts	10/10/2020	1.27	52.6238	5.9107	10/10/2020	2.19	52.5258	5.94854	69|10|69	150	MEDIUM CW	NORMAL	REL. MEAN	300 kHz	SPIKE: MEDIUM, RANGE GATE:NORMAL, PHASE

																HEADING		RAMP: NORMAL
	59	MBES		7.2 kts	10/10/2020	2.24	52.5264	5.9511	10/10/2020	02:38	52.6209	5.9148	69|10|69	150	MEDIUM CW	NORMAL	REL. MEAN HEADING	300 kHz	SPIKE: MEDIUM, RANGE GATE:NORMAL, PHASE RAMP: NORMAL
	60	MBES		7.2 kts	10/10/2020	3.47	52.5546	5.9228	10/10/2020	4.00	52.5588	5.9622	69|10|69	150	MEDIUM CW	NORMAL	REL. MEAN HEADING	300 kHz	SPIKE: MEDIUM, RANGE GATE:NORMAL, PHASE RAMP: NORMAL
	61	MBES		7.3 kts	10/10/2020	4.07	52.5594	5.9686	10/10/2020	04:48	52.551	5.9256							
Finished site and started transit to B3																			
Info					Start				End				Runtime Parameters						
Area	Line id	Type	SVP No.	SOG (kts)	Start Date	Start time (UTC)	SOL Lat (dd)	SOL Long (dd)	End Date	End time (UTC)	EOL Lat (dd)	EOL Long (dd)	Coverage	Max Coverage	Pulse Type	Detector	Mode	Frequency	Filters
	62	MBES		6.1	10/10/2020	08:42	52.66	5.99717	10/10/2020	08:52	52.68051	5.992323	55|10|55	100	MEDIUM CW	NORMAL	REL. MEAN HEADING	300 kHz	SPIKE: MEDIUM, RANGE GATE:NORMAL, PHASE RAMP: NORMAL
	64	MBES		6.2	10/10/2020	08:55	52.6794	5.9909	10/10/2020	09:05	52.66	5.99615	55|10|55	100	MEDIUM CW	NORMAL	REL. MEAN HEADING	300 kHz	SPIKE: MEDIUM, RANGE GATE:NORMAL, PHASE RAMP: NORMAL
	65	MBES		5.9	10/10/2020	09:09	52.66154	5.99481	10/10/2020	09:20	52.68	5.98968	69|10|69	100	MEDIUM CW	NORMAL	REL. MEAN HEADING	300 kHz	SPIKE: MEDIUM, RANGE GATE:NORMAL, PHASE RAMP: NORMAL
	66	MBES		6.4	10/10/2020	09:23	52.6797	5.9884	10/10/2020	09:34	52.6596	5.993	69|10|69	100	MEDIUM CW	NORMAL	REL. MEAN HEADING	300 kHz	SPIKE: MEDIUM, RANGE GATE:NORMAL, PHASE RAMP: NORMAL
	67	MBES		5.9	10/10/2020	09:36	52.6614	5.9918	10/10/2020	09:47	52.68	5.98678	69|10|69	150	MEDIUM CW	NORMAL	REL. MEAN HEADING	300 kHz	SPIKE: MEDIUM, RANGE GATE:NORMAL, PHASE RAMP: NORMAL
	68	MBES		6.3	10/10/2020	09:49	52.6795	5.985	10/10/2020	10:01	52.658	5.99	69|10|69	150	MEDIUM CW	NORMAL	REL. MEAN HEADING	300 kHz	SPIKE: MEDIUM, RANGE GATE:NORMAL, PHASE RAMP: NORMAL
B3	69	MBES	Stn. 18	5.9	10/10/2020	10:05	52.66	5.983	10/10/2020	10:16	52.678	5.978	69|10|69	150	MEDIUM CW	NORMAL	REL. MEAN HEADING	300 kHz	SPIKE: MEDIUM, RANGE GATE:NORMAL, PHASE RAMP: NORMAL
	70	MBES		5.7	10/10/2020	10:18	52.678	5.979	10/10/2020	10:29	52.659	5.984	69|10|69	150	MEDIUM CW	NORMAL	REL. MEAN HEADING	300 kHz	SPIKE: MEDIUM, RANGE GATE:NORMAL, PHASE RAMP: NORMAL
	71	MBES		6.3	10/10/2020	10:32	52.65978	5.986	10/10/2020	10:43	52.6789	5.98	69|10|69	150	MEDIUM CW	NORMAL	REL. MEAN HEADING	300 kHz	SPIKE: MEDIUM, RANGE GATE:NORMAL, PHASE RAMP: NORMAL
	72	MBES		5.7	10/10/2020	11	52.681	5.982387	10/10/2020	11.1	52.66	5.987	69|10|69	150	MEDIUM CW	NORMAL	REL. MEAN HEADING	300 kHz	SPIKE: MEDIUM, RANGE GATE:NORMAL, PHASE RAMP: NORMAL
	73	MBES		5.3 kts	10/10/2020	11.15	52.68	5.9837	10/10/2020	11.33	52.6604	5.989	69|10|69	150	MEDIUM CW	NORMAL	REL. MEAN HEADING	300 kHz	SPIKE: MEDIUM, RANGE GATE:NORMAL, PHASE RAMP: NORMAL
	74	MBES		6.5 kts	10/10/2020	11.34	52.6603	5.9871	10/10/2020	12.44	52.6781	5.9767	69|10|69	150	MEDIUM CW	NORMAL	REL. MEAN HEADING	300 kHz	SPIKE: MEDIUM, RANGE GATE:NORMAL, PHASE RAMP: NORMAL

	75	MBES		5.2 kts	10/10/2020	12.53	52.67	5.97755	10/10/2020	12	52.6603	5.9802	69|10|69	150	MEDIUM CW	NORMAL	REL. MEAN HEADING	300 kHz	SPIKE: MEDIUM, RANGE GATE:NORMAL, PHASE RAMP: NORMAL
	76	MBES			10/10/2020	12.08	52.6616	5.9961	10/10/2020	12.18	52.678	5.9916	69|10|69	150	MEDIUM CW	NORMAL	REL. MEAN HEADING	300 kHz	SPIKE: MEDIUM, RANGE GATE:NORMAL, PHASE RAMP: NORMAL
Finished site and started transit to B6																			
Info					Start				End				Runtime Parameters						
Area	Line id	Type	SVP No.	SOG (kts)	Start Date	Start time (UTC)	SOL Lat (dd)	SOL Long (dd)	End Date	End time (UTC)	EOL Lat (dd)	EOL Long (dd)	Coverage	Max Coverage	Pulse Type	Detector	Mode	Frequency	Filters
B2	77	MBES	Stn. 18	7.2 kts	10/10/2020	13.31	52.6785	5.9901	10/10/2020	16.11	52.7584	5.9717	69|10|69	150	MEDIUM CW	NORMAL	REL. MEAN HEADING	300 kHz	SPIKE: MEDIUM, RANGE GATE:NORMAL, PHASE RAMP: NORMAL
	78	MBES		7.2 kts	10/10/2020	16.14	52.7602	5.9726	10/10/2020	16.56	52.6796	5.9914	69|10|69	150	MEDIUM CW	NORMAL	REL. MEAN HEADING	300 kHz	SPIKE: MEDIUM, RANGE GATE:NORMAL, PHASE RAMP: NORMAL
	79	MBES		7	10/10/2020	16.59	52.6767	5.9932	10/10/2020	17:42	52.7591	5.97408	69|10|69	150	MEDIUM CW	NORMAL	REL. MEAN HEADING	300 kHz	SPIKE: MEDIUM, RANGE GATE:NORMAL, PHASE RAMP: NORMAL
	80	MBES		6.5	10/10/2020	17:45	52.761	5.97483	10/10/2020	18:26	52.677	5.9941	69|10|69	150	MEDIUM CW	NORMAL	REL. MEAN HEADING	300 kHz	SPIKE: MEDIUM, RANGE GATE:NORMAL, PHASE RAMP: NORMAL
	81	MBES		7.3	10/10/2020	18:29	52.6768	5.9957	10/10/2020	19:12	52.761	5.9762	69|10|69	150	MEDIUM CW	NORMAL	REL. MEAN HEADING	300 kHz	SPIKE: MEDIUM, RANGE GATE:NORMAL, PHASE RAMP: NORMAL
	82	MBES		7.4	10/10/2020	19:15	52.7611	5.977	10/10/2020	19:58	52.677	5.997	69|10|69	150	MEDIUM CW	NORMAL	REL. MEAN HEADING	300 kHz	SPIKE: MEDIUM, RANGE GATE:NORMAL, PHASE RAMP: NORMAL
	83	MBES		6.4	10/10/2020	20:03	52.677	5.9977	10/10/2020	20:53	52.761	5.98154	69|10|69	150	MEDIUM CW	NORMAL	REL. MEAN HEADING	300 kHz	SPIKE: MEDIUM, RANGE GATE:NORMAL, PHASE RAMP: NORMAL
	84	MBES		3	10/10/2020	20:58	52.7484	5.9849	10/10/2020	21:05	52.74733	5.9727	69|10|69	150	MEDIUM CW	NORMAL	REL. MEAN HEADING	300 kHz	SPIKE: MEDIUM, RANGE GATE:NORMAL, PHASE RAMP: NORMAL
	85	MBES		5.6	10/10/2020	21:22	52.7617	5.9705	10/10/2020	22:16	52.67828	5.9899	69|10|69	150	MEDIUM CW	NORMAL	REL. MEAN HEADING	300 kHz	SPIKE: MEDIUM, RANGE GATE:NORMAL, PHASE RAMP: NORMAL
Finished site and started transit to B1																			
Info					Start				End				Runtime Parameters						
Area	Line id	Type	SVP No.	SOG (kts)	Start Date	Start time (UTC)	SOL Lat (dd)	SOL Long (dd)	End Date	End time (UTC)	EOL Lat (dd)	EOL Long (dd)	Coverage	Max Coverage	Pulse Type	Detector	Mode	Frequency	Filters
B1	86	MBES	Stn. 18	6.1 kts	10/10/2020	23.11	52.719	5.9498	10/10/2020	23.39	52.6777	5.969	69|10|69	150	MEDIUM CW	NORMAL	REL. MEAN HEADING	300 kHz	SPIKE: MEDIUM, RANGE GATE:NORMAL, PHASE RAMP: NORMAL
	87	MBES		6 kts	10/10/2020	23.42	52.6761	5.9709	11/10/2020	0.09	52.7179	5.951	69|10|69	150	MEDIUM CW	NORMAL	REL. MEAN HEADING	300 kHz	SPIKE: MEDIUM, RANGE GATE:NORMAL, PHASE RAMP: NORMAL

	88	MBES		5.2 kts	10/10/2020	0.12	52.7197	5.9516	11/10/2020	0.41	52.6776	5.9715	69|10|69	150	MEDIUM CW	NORMAL	REL. MEAN HEADING	300 kHz	SPIKE: MEDIUM, RANGE GATE:NORMAL, PHASE RAMP: NORMAL
	89	MBES		6.2 kts	11/10/2020	0.44	52.6767	5.973	11/10/2020	1.1	52.7188	5.9532	69|10|69	150	MEDIUM CW	NORMAL	REL. MEAN HEADING	300 kHz	SPIKE: MEDIUM, RANGE GATE:NORMAL, PHASE RAMP: NORMAL
	90	MBES		5.6 kts	11/10/2020	1.13	52.7205	5.9538	11/10/2020	1.41	52.6784	5.9736	69|10|69	150	MEDIUM CW	NORMAL	REL. MEAN HEADING	300 kHz	SPIKE: MEDIUM, RANGE GATE:NORMAL, PHASE RAMP: NORMAL
	91	MBES		6.0 kts	11/10/2020	1.44	52.6758	5.976	11/10/2020	2.1	52.7184	5.9558	69|10|69	150	MEDIUM CW	NORMAL	REL. MEAN HEADING	300 kHz	SPIKE: MEDIUM, RANGE GATE:NORMAL, PHASE RAMP: NORMAL
	92	MBES		5.8 kts	11/10/2020	2.13	52.7211	5.9559	11/10/2020	2.43	52.6791	5.9757	69|10|69	150	MEDIUM CW	NORMAL	REL. MEAN HEADING	300 kHz	SPIKE: MEDIUM, RANGE GATE:NORMAL, PHASE RAMP: NORMAL
	93	MBES		6.4 kts	11/10/2020	2.46	52.6766	5.978	11/10/2020	3.12	52.7204	5.9573	69|10|69	150	MEDIUM CW	NORMAL	REL. MEAN HEADING	300 kHz	SPIKE: MEDIUM, RANGE GATE:NORMAL, PHASE RAMP: NORMAL
	94	MBES		6.6 kts	11/10/2020	3.15	52.7226	5.9575	11/10/2020	3.41	52.6793	5.9781	69|10|69	150	MEDIUM CW	NORMAL	REL. MEAN HEADING	300 kHz	SPIKE: MEDIUM, RANGE GATE:NORMAL, PHASE RAMP: NORMAL
	95	MBES		7.1 kts	11/10/2020	3.44	52.6768	5.9805	11/10/2020	4.09	52.5719	5.9605	69|10|69	150	MEDIUM CW	NORMAL	REL. MEAN HEADING	300 kHz	SPIKE: MEDIUM, RANGE GATE:NORMAL, PHASE RAMP: NORMAL
	96	MBES		7.2 kts	11/10/2020	4.12	52.7232	5.9598	11/10/2020	4.36	52.679	5.9807	69|10|69	150	MEDIUM CW	NORMAL	REL. MEAN HEADING	300 kHz	SPIKE: MEDIUM, RANGE GATE:NORMAL, PHASE RAMP: NORMAL
	97	MBES		6.6 kts	11/10/2020	4.39	52.6769	5.9828	11/10/2020	5.07	52.7215	5.9618	69|10|69	150	MEDIUM CW	NORMAL	REL. MEAN HEADING	300 kHz	SPIKE: MEDIUM, RANGE GATE:NORMAL, PHASE RAMP: NORMAL
	98	MBES		6 kts	11/10/2020	5.26	52.6984	5.9664	11/10/2020	5.3	52.6991	5.9734	69|10|69	150	MEDIUM CW	NORMAL	REL. MEAN HEADING	300 kHz	SPIKE: MEDIUM, RANGE GATE:NORMAL, PHASE RAMP: NORMAL
B3	99	MBES		6.5 kts	11/10/2020	5.39	52.6787	5.9751	11/10/2020	5.43	52.6696	5.9774	69|10|69	150	MEDIUM CW	NORMAL	REL. MEAN HEADING	300 kHz	SPIKE: MEDIUM, RANGE GATE:NORMAL, PHASE RAMP: NORMAL
	100	MBES		5.2 kts	11/10/2020	5.47				5.54	52.6721	5.997	69|10|69	150	MEDIUM CW	NORMAL	REL. MEAN HEADING	300 kHz	SPIKE: MEDIUM, RANGE GATE:NORMAL, PHASE RAMP: NORMAL

Finished Area and started transit to ADCP 1 area

Info					Start				End				Runtime Parameters						
Area	Line id	Type	SVP No.	SOG (kts)	Start Date	Start time (UTC)	SOL Lat (dd)	SOL Long (dd)	End Date	End time (UTC)	EOL Lat (dd)	EOL Long (dd)	Coverage	Max Coverage	Pulse Type	Detector	Mode	Frequency	Filters
A3	101	MBES	Stn. 14/Stn. 18	5.1	11/10/2020	09:27	52.369	6.19	11/10/2020	09:44	52.39231	6.17932	69|10|69	150	MEDIUM CW	NORMAL	REL. MEAN HEADING	300 kHz	SPIKE: MEDIUM, RANGE GATE:NORMAL, PHASE RAMP: NORMAL
	102	MBES	Stn. 18	7.1	11/10/2020	09:46	52.3911	6.17837	11/10/2020	09:57	52.3694	6.1883	69|10|69	150	MEDIUM CW	NORMAL	REL. MEAN HEADING	300 kHz	SPIKE: MEDIUM, RANGE GATE:NORMAL, PHASE RAMP: NORMAL
	103	MBES		6.9	11/10/2020	10:00	52.3688	6.1869	11/10/2020	10:15	52.39175	6.1765	69|10|69	150	MEDIUM	NORMAL	REL.	300 kHz	SPIKE: MEDIUM, RANGE

															CW		MEAN HEADING		GATE:NORMAL, PHASE RAMP: NORMAL
	104	MBES		6.3	11/10/2020	10:17	52.39088	6.1754	11/10/2020	10:29	52.36894	6.18555	69|10|69	150	MEDIUM CW	NORMAL	REL. MEAN HEADING	300 kHz	SPIKE: MEDIUM, RANGE GATE:NORMAL, PHASE RAMP: NORMAL
	105	MBES			11/10/2020	10:34	52.3699	6.1834	11/10/2020	10:46	52.39	6.17391	69|10|69	150	MEDIUM CW	NORMAL	REL. MEAN HEADING	300 kHz	SPIKE: MEDIUM, RANGE GATE:NORMAL, PHASE RAMP: NORMAL
	106	MBES			11/10/2020	10:49	52.39	6.1729	11/10/2020	11:00	52.36728	6.18329	69|10|69	150	MEDIUM CW	NORMAL	REL. MEAN HEADING	300 kHz	SPIKE: MEDIUM, RANGE GATE:NORMAL, PHASE RAMP: NORMAL
	107	MBES		6.7 kts	11/10/2020	11:03	52.36949	6.18	11/10/2020	11.15	52.389	6.1715	69|10|69	150	MEDIUM CW	NORMAL	REL. MEAN HEADING	300 kHz	SPIKE: MEDIUM, RANGE GATE:NORMAL, PHASE RAMP: NORMAL
	108	MBES			11/10/2020	11.17	52.3911	6.1691	11/10/2020	11.3	52.3678	6.1799	69|10|69	150	MEDIUM CW	NORMAL	REL. MEAN HEADING	300 kHz	SPIKE: MEDIUM, RANGE GATE:NORMAL, PHASE RAMP: NORMAL
	109	MBES		7 kts	11/10/2020	11.32	52.3676	6.17844	11/10/2020	10:48	52.3882	6.1688	69|10|69	150	MEDIUM CW	NORMAL	REL. MEAN HEADING	300 kHz	SPIKE: MEDIUM, RANGE GATE:NORMAL, PHASE RAMP: NORMAL
	110	MBES		5.7 kts	11/10/2020	11:16	52.3907	6.1664	11/10/2020	12	52.3686	6.1765	69|10|69	150	MEDIUM CW	NORMAL	REL. MEAN HEADING	300 kHz	SPIKE: MEDIUM, RANGE GATE:NORMAL, PHASE RAMP: NORMAL
	111	MBES		7.2 kts	11/10/2020	00:28	52.3675	6.1756	11/10/2020	12.13	52.3886	6.1656	69|10|69	150	MEDIUM CW	NORMAL	REL. MEAN HEADING	300 kHz	SPIKE: MEDIUM, RANGE GATE:NORMAL, PHASE RAMP: NORMAL
	112	MBES		7 kts	11/10/2020	05:45	52.3772	6.1679	12/10/2020	12.3	52.3802	6.1864	69|10|69	150	MEDIUM CW	NORMAL	REL. MEAN HEADING	300 kHz	SPIKE: MEDIUM, RANGE GATE:NORMAL, PHASE RAMP: NORMAL

Finished Area and started transit to ADCP 1 area

Info					Start				End				Runtime Parameters						
Area	Line id	Type	SVP No.	SOG (kts)	Start Date	Start time (UTC)	SOL Lat (dd)	SOL Long (dd)	End Date	End time (UTC)	EOL Lat (dd)	EOL Long (dd)	Coverage	Max Coverage	Pulse Type	Detector	Mode	Frequency	Filters
A6 & A15	113	MBES	Stn. 35	7.1	11/10/2020	17:37	52.24727	6.23395	11/10/2020	18:13	52.314	6.2	69|10|69	150	MEDIUM CW	NORMAL	REL. MEAN HEADING	300 kHz	SPIKE: MEDIUM, RANGE GATE:NORMAL, PHASE RAMP: NORMAL
	114	MBES		7.7	11/10/2020	18:16	52.315	6.20241	11/10/2020	18:48	52.2474	6.23555	69|10|69	150	MEDIUM CW	NORMAL	REL. MEAN HEADING	300 kHz	SPIKE: MEDIUM, RANGE GATE:NORMAL, PHASE RAMP: NORMAL
	115	MBES		7	11/10/2020	18:52	52.24787	6.2364	11/10/2020	19:29	52.3157	6.2033	69|10|69	150	MEDIUM CW	NORMAL	REL. MEAN HEADING	300 kHz	SPIKE: MEDIUM, RANGE GATE:NORMAL, PHASE RAMP: NORMAL
	116	MBES		6.9	11/10/2020	19:31	52.3161	6.20438	11/10/2020	20:16	52.248	6.2376	69|10|69	150	MEDIUM CW	NORMAL	REL. MEAN HEADING	300 kHz	SPIKE: MEDIUM, RANGE GATE:NORMAL, PHASE RAMP: NORMAL
	117	MBES		6	11/10/2020	20:19	52.2477	6.2389	11/10/2020	20:59	52.31555	6.2058	69|10|69	150	MEDIUM CW	NORMAL	REL. MEAN HEADING	300 kHz	SPIKE: MEDIUM, RANGE GATE:NORMAL, PHASE RAMP: NORMAL
	118	MBES		6.1	11/10/2020	21:00	52.316	6.207	11/10/2020	21:43	52.2485	6.23985	69|10|69	150	MEDIUM CW	NORMAL	REL. MEAN	300 kHz	SPIKE: MEDIUM, RANGE GATE:NORMAL, PHASE

																HEADING		RAMP: NORMAL
119	MBES		6.5	11/10/2020	21:48	52.25261	6.2386	11/10/2020	22:25	52.31607	6.2077	69|10|69	150	MEDIUM CW	NORMAL	REL. MEAN HEADING	300 kHz	SPIKE: MEDIUM, RANGE GATE:NORMAL, PHASE RAMP: NORMAL
120	MBES		5.8	11/10/2020	22:27	52.31558	6.2087	11/10/2020	23:12	52.2498	6.241	69|10|69	150	MEDIUM CW	NORMAL	REL. MEAN HEADING	300 kHz	SPIKE: MEDIUM, RANGE GATE:NORMAL, PHASE RAMP: NORMAL
121	MBES		6 kts	11/10/2020	23:16	52.2489	6.2426	12/10/2020	00:00	52.3155	6.2097	69|10|69	150	MEDIUM CW	NORMAL	REL. MEAN HEADING	300 kHz	SPIKE: MEDIUM, RANGE GATE:NORMAL, PHASE RAMP: NORMAL
122	MBES			12/10/2020	00:02	52.3157	6.211	12/10/2020	00:19	52.2951	6.2209	69|10|69	150	MEDIUM CW	NORMAL	REL. MEAN HEADING	300 kHz	SPIKE: MEDIUM, RANGE GATE:NORMAL, PHASE RAMP: NORMAL
123	MBES		6.4 kts	12/10/2020	00:23	52.295	6.2198	12/10/2020	00:34	52.3135	6.2113	69|10|69	150	MEDIUM CW	NORMAL	REL. MEAN HEADING	300 kHz	SPIKE: MEDIUM, RANGE GATE:NORMAL, PHASE RAMP: NORMAL
124	MBES		4 kts	12/10/2020	00:36	52.3163	6.2119	12/10/2020	00:53	52.2945	6.222	69|10|69	150	MEDIUM CW	NORMAL	REL. MEAN HEADING	300 kHz	SPIKE: MEDIUM, RANGE GATE:NORMAL, PHASE RAMP: NORMAL
125	MBES		5.8 kts	12/10/2020	00:56	52.2954	6.2224	12/10/2020	01:07	52.3142	6.2135	69|10|69	150	MEDIUM CW	NORMAL	REL. MEAN HEADING	300 kHz	SPIKE: MEDIUM, RANGE GATE:NORMAL, PHASE RAMP: NORMAL
126	MBES		6 kts	12/10/2020	01:10	52.3166	6.2131	12/10/2020	01:26	52.95	6.2232	69|10|69	150	MEDIUM CW	NORMAL	REL. MEAN HEADING	300 kHz	SPIKE: MEDIUM, RANGE GATE:NORMAL, PHASE RAMP: NORMAL
127	MBES		6.2 kts	12/10/2020	01:27	52.2958	6.2243	12/10/2020	01:39	52.3143	6.2153	69|10|69	150	MEDIUM CW	NORMAL	REL. MEAN HEADING	300 kHz	SPIKE: MEDIUM, RANGE GATE:NORMAL, PHASE RAMP: NORMAL
128	MBES			12/10/2020	01:55	52.2973	6.207	12/10/2020	02:01	52.2988	6.21877	69|10|69	150	MEDIUM CW	NORMAL	REL. MEAN HEADING	300 kHz	SPIKE: MEDIUM, RANGE GATE:NORMAL, PHASE RAMP: NORMAL
A6	129	MBES		6.3 kts	12/10/2020	02:13	52.2845	6.2266	12/10/2020	02:34	52.2506	6.2425	69|10|69	150	MEDIUM CW	NORMAL	REL. MEAN HEADING	300 kHz	SPIKE: MEDIUM, RANGE GATE:NORMAL, PHASE RAMP: NORMAL
	130	MBES		5.3 kts	12/10/2020	02:36	52.2506	6.2442	12/10/2020	02:53	52.2812	6.2288	69|10|69	150	MEDIUM CW	NORMAL	REL. MEAN HEADING	300 kHz	SPIKE: MEDIUM, RANGE GATE:NORMAL, PHASE RAMP: NORMAL
	131	MBES		5.1 kts	12/10/2020	02:56	52.2843	6.229	12/10/2020	03:17	52.2516	6.2444	69|10|69	150	MEDIUM CW	NORMAL	REL. MEAN HEADING	300 kHz	SPIKE: MEDIUM, RANGE GATE:NORMAL, PHASE RAMP: NORMAL
	132	MBES		7.4 kts	12/10/2020	03:20	52.2506	6.2461	12/10/2020	03:35	52.2805	6.2316	69|10|69	150	MEDIUM CW	NORMAL	REL. MEAN HEADING	300 kHz	SPIKE: MEDIUM, RANGE GATE:NORMAL, PHASE RAMP: NORMAL
	133	MBES		7.2 kts	12/10/2020	03:40	52.2859	6.2305	12/10/2020	04:00	52.2516	6.2469	69|10|69	150	MEDIUM CW	NORMAL	REL. MEAN HEADING	300 kHz	SPIKE: MEDIUM, RANGE GATE:NORMAL, PHASE RAMP: NORMAL
	134	MBES		7.3 kts	12/10/2020	04:03			12/10/2020	04:20	52.2817	6.2335	69|10|69	150	MEDIUM CW	NORMAL	REL. MEAN HEADING	300 kHz	SPIKE: MEDIUM, RANGE GATE:NORMAL, PHASE RAMP: NORMAL
	135	MBES		6.9 kts	12/10/2020	04:23	52.2855	6.233	12/10/2020	04:42	52.253	6.248	69|10|69	150	MEDIUM CW	NORMAL	REL. MEAN HEADING	300 kHz	SPIKE: MEDIUM, RANGE GATE:NORMAL, PHASE RAMP: NORMAL

	136	MBES			12/10/2020	04:46	52.2526	6.25	12/10/2020	05:02	52.2811	6.2362	69|10|69	150	MEDIUM CW	NORMAL	REL. MEAN HEADING	300 kHz	SPIKE: MEDIUM, RANGE GATE:NORMAL, PHASE RAMP: NORMAL
A5	137	MBES			12/10/2020	05:05	52.2847	6.2387	12/10/2020	05:10	52.275322	6.238	69|10|69	150	MEDIUM CW	NORMAL	REL. MEAN HEADING	300 kHz	SPIKE: MEDIUM, RANGE GATE:NORMAL, PHASE RAMP: NORMAL
	138	MBES		7.2	12/10/2020	05:13	52.2742	6.239	12/10/2020	05:18	52.2839	6.2397	69|10|69	150	MEDIUM CW	NORMAL	REL. MEAN HEADING	300 kHz	SPIKE: MEDIUM, RANGE GATE:NORMAL, PHASE RAMP: NORMAL
	139	MBES		6.6	12/10/2020	05:21	52.28508	6.241	12/10/2020	05:27	52.272	6.2395	69|10|69	150	MEDIUM CW	NORMAL	REL. MEAN HEADING	300 kHz	SPIKE: MEDIUM, RANGE GATE:NORMAL, PHASE RAMP: NORMAL
	140	MBES		7	12/10/2020	05:30	52.27107	6.2409	12/10/2020	05:36	52.28406	6.2424	69|10|69	150	MEDIUM CW	NORMAL	REL. MEAN HEADING	300 kHz	SPIKE: MEDIUM, RANGE GATE:NORMAL, PHASE RAMP: NORMAL
	141	MBES		7.7	12/10/2020	05:40	52.2841	6.2438	12/10/2020	05:49	52.26557	6.241638	69|10|69	150	MEDIUM CW	NORMAL	REL. MEAN HEADING	300 kHz	SPIKE: MEDIUM, RANGE GATE:NORMAL, PHASE RAMP: NORMAL
	142	MBES		7	12/10/2020	05:51	52.26628	6.2433	12/10/2020	06:01	52.28499	6.245186	69|10|69	150	MEDIUM CW	NORMAL	REL. MEAN HEADING	300 kHz	SPIKE: MEDIUM, RANGE GATE:NORMAL, PHASE RAMP: NORMAL
	143	MBES		7.5	12/10/2020	06:04	52.2838	6.24664	12/10/2020	06:14	52.26407	6.2443	69|10|69	150	MEDIUM CW	NORMAL	REL. MEAN HEADING	300 kHz	SPIKE: MEDIUM, RANGE GATE:NORMAL, PHASE RAMP: NORMAL
	144	MBES		7.2	12/10/2020	06:17	52.26086	6.2451	12/10/2020	06:30	52.285396	6.24868	69|10|69	150	MEDIUM CW	NORMAL	REL. MEAN HEADING	300 kHz	SPIKE: MEDIUM, RANGE GATE:NORMAL, PHASE RAMP: NORMAL
	145	MBES		7	12/10/2020	06:31	52.285024	6.24989	12/10/2020	06:46	52.2568	6.2457	69|10|69	150	MEDIUM CW	NORMAL	REL. MEAN HEADING	300 kHz	SPIKE: MEDIUM, RANGE GATE:NORMAL, PHASE RAMP: NORMAL
	146	MBES		7.4	12/10/2020	06:49	52.2584	6.2478	12/10/2020	07:02	52.2849	6.2518	69|10|69	150	MEDIUM CW	NORMAL	REL. MEAN HEADING	300 kHz	SPIKE: MEDIUM, RANGE GATE:NORMAL, PHASE RAMP: NORMAL
	147	MBES		7	12/10/2020	07:04	52.2834	6.25284	12/10/2020	07:19	52.2538	6.2486	69|10|69	150	MEDIUM CW	NORMAL	REL. MEAN HEADING	300 kHz	SPIKE: MEDIUM, RANGE GATE:NORMAL, PHASE RAMP: NORMAL
A7	148	MBES		5.4	12/10/2020	07:25	52.2555	6.2577	12/10/2020	07:37	52.274	6.26	69|10|69	150	MEDIUM CW	NORMAL	REL. MEAN HEADING	300 kHz	SPIKE: MEDIUM, RANGE GATE:NORMAL, PHASE RAMP: NORMAL
	149	MBES		8.1	12/10/2020	07:39	52.2729	6.2614	12/10/2020	07:47	52.254	6.25889	69|10|69	150	MEDIUM CW	NORMAL	REL. MEAN HEADING	300 kHz	SPIKE: MEDIUM, RANGE GATE:NORMAL, PHASE RAMP: NORMAL
	150	MBES		6.4	12/10/2020	07:50	52.2543	6.26	12/10/2020	08:00	52.2735	6.26303	69|10|69	150	MEDIUM CW	NORMAL	REL. MEAN HEADING	300 kHz	SPIKE: MEDIUM, RANGE GATE:NORMAL, PHASE RAMP: NORMAL
	151	MBES		6.3	12/10/2020	08:02	52.2733	6.2644	12/10/2020	08:12	52.254	6.262	69|10|69	150	MEDIUM CW	NORMAL	REL. MEAN HEADING	300 kHz	SPIKE: MEDIUM, RANGE GATE:NORMAL, PHASE RAMP: NORMAL
	152	MBES		6.4	12/10/2020	08:14	52.2541	6.26329	12/10/2020	08:26	52.27425	6.26608	69|10|69	150	MEDIUM CW	NORMAL	REL. MEAN HEADING	300 kHz	SPIKE: MEDIUM, RANGE GATE:NORMAL, PHASE RAMP: NORMAL
	153	MBES		6	12/10/2020	08:28	52.1733	6.267	12/10/2020	08:40	52.2498	6.2637	69|10|69	150	MEDIUM CW	NORMAL	REL. MEAN	300 kHz	SPIKE: MEDIUM, RANGE GATE:NORMAL, PHASE

																HEADING		RAMP: NORMAL
	154	MBES		5.1	12/10/2020	08:43	52.2503	6.265	12/10/2020	08:59	52.2742	6.2688	69|10|69	150	MEDIUM CW	NORMAL	REL. MEAN HEADING	300 kHz	SPIKE: MEDIUM, RANGE GATE:NORMAL, PHASE RAMP: NORMAL
	155	MBES		6.4	12/10/2020	09:00	52.2731	6.26922	12/10/2020	09:10	52.2527	6.26624	69|10|69	150	MEDIUM CW	NORMAL	REL. MEAN HEADING	300 kHz	SPIKE: MEDIUM, RANGE GATE:NORMAL, PHASE RAMP: NORMAL
A20	156	MBES		5.3	12/10/2020	09:18	52.25126	6.26	12/10/2020	09:23	52.25654	6.2711	69|10|69	150	MEDIUM CW	NORMAL	REL. MEAN HEADING	300 kHz	SPIKE: MEDIUM, RANGE GATE:NORMAL, PHASE RAMP: NORMAL
	157	MBES		7.3	12/10/2020	09:26	52.255	6.2696	12/10/2020	09:30	52.25075	6.26084	75|10|75	150	MEDIUM CW	NORMAL	REL. MEAN HEADING	300 kHz	SPIKE: MEDIUM, RANGE GATE:NORMAL, PHASE RAMP: NORMAL
	158	MBES		5.4	12/10/2020	09:32	52.24983	6.26158	12/10/2020	09:37	52.25544	6.272	75|10|75	150	MEDIUM CW	NORMAL	REL. MEAN HEADING	300 kHz	SPIKE: MEDIUM, RANGE GATE:NORMAL, PHASE RAMP: NORMAL
	159	MBES		6	12/10/2020	09:38	52.255	6.27266	12/10/2020	09:43	52.24965	6.2625	75|10|75	150	MEDIUM CW	NORMAL	REL. MEAN HEADING	300 kHz	SPIKE: MEDIUM, RANGE GATE:NORMAL, PHASE RAMP: NORMAL
	160	MBES		7.1	12/10/2020	09:46	52.24897	6.2636	12/10/2020	09:52	52.254455	6.27394	75|10|75	150	MEDIUM CW	NORMAL	REL. MEAN HEADING	300 kHz	SPIKE: MEDIUM, RANGE GATE:NORMAL, PHASE RAMP: NORMAL
	161	MBES		6.4	12/10/2020	09:53	52.2541	6.2747	12/10/2020	09:58	52.2483	6.26374	75|10|75	150	MEDIUM CW	NORMAL	REL. MEAN HEADING	300 kHz	SPIKE: MEDIUM, RANGE GATE:NORMAL, PHASE RAMP: NORMAL
	162	MBES		6.5	12/10/2020	10:01	52.24768	6.265054	12/10/2020	10:06	52.2533	6.2767	75|10|75	150	MEDIUM CW	NORMAL	REL. MEAN HEADING	300 kHz	SPIKE: MEDIUM, RANGE GATE:NORMAL, PHASE RAMP: NORMAL
	163	MBES			12/10/2020	10:10	52.25	6.2742	12/10/2020	10:15	52.25599	6.26777	75|10|75	150	MEDIUM CW	NORMAL	REL. MEAN HEADING	300 kHz	SPIKE: MEDIUM, RANGE GATE:NORMAL, PHASE RAMP: NORMAL
A7	164	MBES			12/10/2020	10:15	52.25599	6.26777	12/10/2020	10:22	52.26551	6.26865	75|10|75	150	MEDIUM CW	NORMAL	REL. MEAN HEADING	300 kHz	SPIKE: MEDIUM, RANGE GATE:NORMAL, PHASE RAMP: NORMAL
	165	MBES			12/10/2020	10:22	52.26551	6.26865	12/10/2020	10:26	52.2654	6.2561	75|10|75	150	MEDIUM CW	NORMAL	REL. MEAN HEADING	300 kHz	SPIKE: MEDIUM, RANGE GATE:NORMAL, PHASE RAMP: NORMAL
	166/167	MBES		6.5	12/10/2020	10:35	52.2536	6.263	12/10/2020	10:46	52.2741	6.26534	75|10|75	150	MEDIUM CW	NORMAL	REL. MEAN HEADING	300 kHz	SPIKE: MEDIUM, RANGE GATE:NORMAL, PHASE RAMP: NORMAL
	168	MBES		6.6	12/10/2020	10:48	52.27314	6.2678	12/10/2020	10:52	52.2642	6.2664	75|10|75	150	MEDIUM CW	NORMAL	REL. MEAN HEADING	300 kHz	SPIKE: MEDIUM, RANGE GATE:NORMAL, PHASE RAMP: NORMAL
	169	MBES			12/10/2020	10:55	52.2642	6.264	12/10/2020	11:00	52.2716	6.265	75|10|75	150	MEDIUM CW	NORMAL	REL. MEAN HEADING	300 kHz	SPIKE: MEDIUM, RANGE GATE:NORMAL, PHASE RAMP: NORMAL
	170	MBES		6 kts	12/10/2020	11:03	52.2731	6.2634	12/10/2020	11:07	52.2654	6.2627	75|10|75	150	MEDIUM CW	NORMAL	REL. MEAN HEADING	300 kHz	SPIKE: MEDIUM, RANGE GATE:NORMAL, PHASE RAMP: NORMAL
A5	171	MBES		6.1	12/10/2020	11:14	52.2691	6.2544	12/10/2020	11:19	52.27058	6.2382	75|10|75	150	MEDIUM CW	NORMAL	REL. MEAN HEADING	300 kHz	SPIKE: MEDIUM, RANGE GATE:NORMAL, PHASE RAMP: NORMAL

A6	172	MBES			12/10/2020	11:24	52.269	6.24493	12/10/2020	11:33	52.2661	6.2249	75|10|75	150	MEDIUM CW	NORMAL	REL. MEAN HEADING	300 kHz	SPIKE: MEDIUM, RANGE GATE:NORMAL, PHASE RAMP: NORMAL
Finished Area and started transit to C1																			
Info					Start				End				Runtime Parameters						
Area	Line id	Type	SVP No.	SOG (kts)	Start Date	Start time (UTC)	SOL Lat (dd)	SOL Long (dd)	End Date	End time (UTC)	EOL Lat (dd)	EOL Long (dd)	Coverage	Max Coverage	Pulse Type	Detector	Mode	Frequency	Filters
	173	MBES		6.8	12/10/2020	18:20	52.31444	6.1946	12/10/2020	18:36	52.34634	6.178265	72|10|72	150	MEDIUM CW	NORMAL	REL. MEAN HEADING	300 kHz	SPIKE: MEDIUM, RANGE GATE:NORMAL, PHASE RAMP: NORMAL
	174	MBES		7.1	12/10/2020	18:39	52.3461	6.1798	12/10/2020	18:55	52.31431	6.19611	72|10|72	150	MEDIUM CW	NORMAL	REL. MEAN HEADING	300 kHz	SPIKE: MEDIUM, RANGE GATE:NORMAL, PHASE RAMP: NORMAL
	175	MBES		6.9	12/10/2020	19:00	52.3151	6.1966	12/10/2020	19:17	52.3466	6.1805	72|10|72	150	MEDIUM CW	NORMAL	REL. MEAN HEADING	300 kHz	SPIKE: MEDIUM, RANGE GATE:NORMAL, PHASE RAMP: NORMAL
	176	MBES		7.1	12/10/2020	19:19	52.3467	6.1816	12/10/2020	19:22	52.34134	6.18177	72|10|72	150	MEDIUM CW	NORMAL	REL. MEAN HEADING	300 kHz	SPIKE: MEDIUM, RANGE GATE:NORMAL, PHASE RAMP: NORMAL
	177	MBES		8.1	12/10/2020	19:28	52.3461	6.18209	12/10/2020	19:43	52.3149	6.1981	72|10|72	150	MEDIUM CW	NORMAL	REL. MEAN HEADING	300 kHz	SPIKE: MEDIUM, RANGE GATE:NORMAL, PHASE RAMP: NORMAL
	178	MBES			12/10/2020	19:46	52.31541	6.199	12/10/2020	20:04	52.347	6.182931	72|10|72	150	MEDIUM CW	NORMAL	REL. MEAN HEADING	300 kHz	SPIKE: MEDIUM, RANGE GATE:NORMAL, PHASE RAMP: NORMAL
	179	MBES		7.2	12/10/2020	20:07	52.3467	6.18433	12/10/2020	20:23	52.3155	6.2004	72|10|72	150	MEDIUM CW	NORMAL	REL. MEAN HEADING	300 kHz	SPIKE: MEDIUM, RANGE GATE:NORMAL, PHASE RAMP: NORMAL
A4	180	MBES/Chirp	Stn.46	4.8	12/10/2020	20:27	52.3162	6.2011	12/10/2020	20:48	52.3471	6.1853	72|10|72	150	MEDIUM CW	NORMAL	REL. MEAN HEADING	300 kHz	SPIKE: MEDIUM, RANGE GATE:NORMAL, PHASE RAMP: NORMAL
	181	MBES/Chirp		6.9	12/10/2020	20:52	52.347	6.1866	12/10/2020	21:09	52.3162	6.20236	72|10|72	150	MEDIUM CW	NORMAL	REL. MEAN HEADING	300 kHz	SPIKE: MEDIUM, RANGE GATE:NORMAL, PHASE RAMP: NORMAL
	182	MBES/Chirp		4.4	12/10/2020	21:13	52.3166	6.20336	12/10/2020	21:36	52.3476	6.1875	72|10|72	150	MEDIUM CW	NORMAL	REL. MEAN HEADING	300 kHz	SPIKE: MEDIUM, RANGE GATE:NORMAL, PHASE RAMP: NORMAL
	183	MBES/Chirp		5.4	12/10/2020	21:38	52.3477	6.1887	12/10/2020	21:53	52.3167	6.2046	72|10|72	150	MEDIUM CW	NORMAL	REL. MEAN HEADING	300 kHz	SPIKE: MEDIUM, RANGE GATE:NORMAL, PHASE RAMP: NORMAL
	184	MBES/Chirp		5.7	12/10/2020	21:57	52.3175	6.2052	12/10/2020	22:17	52.3481	6.1897	72|10|72	150	MEDIUM CW	NORMAL	REL. MEAN HEADING	300 kHz	SPIKE: MEDIUM, RANGE GATE:NORMAL, PHASE RAMP: NORMAL
	185	MBES/Chirp		5.8	12/10/2020	22:19	52.3482	6.1906	12/10/2020	22:35	52.317	6.2066	75|10|75	150	MEDIUM CW	NORMAL	REL. MEAN HEADING	300 kHz	SPIKE: MEDIUM, RANGE GATE:NORMAL, PHASE RAMP: NORMAL
	186	MBES/Chirp		7.1	12/10/2020	22:39	52.3176	6.20717	12/10/2020	22:56	52.3483	6.1914	75|10|75	150	MEDIUM CW	NORMAL	REL. MEAN HEADING	300 kHz	SPIKE: MEDIUM, RANGE GATE:NORMAL, PHASE RAMP: NORMAL
	187	MBES		5.7	12/10/2020	22:59	52.3484	6.1922	12/10/2020	23:16	52.3165	6.2085	75|10|75	150	MEDIUM	NORMAL	REL.	300 kHz	SPIKE: MEDIUM, RANGE

															CW		MEAN HEADING		GATE:NORMAL, PHASE RAMP: NORMAL
	188	MBES		5.6 kts	12/10/2020	23:19	52.3162	6.2097	12/10/2020	23:40	52.3477	6.1935	75|10|75	150	MEDIUM CW	NORMAL	REL. MEAN HEADING	300 kHz	SPIKE: MEDIUM, RANGE GATE:NORMAL, PHASE RAMP: NORMAL
	189	MBES		5.5 kts	12/10/2020	23:42	52.3484	6.1939	12/10/2020	23:54	52.3307	6.2032	75|10|75	150	MEDIUM CW	NORMAL	REL. MEAN HEADING	300 kHz	SPIKE: MEDIUM, RANGE GATE:NORMAL, PHASE RAMP: NORMAL
	190	MBES		5.6 kts	12/10/2020	23:56	52.3308	6.204	13/10/2020	00:09	52.347	6.1953	75|10|75	150	MEDIUM CW	NORMAL	REL. MEAN HEADING	300 kHz	SPIKE: MEDIUM, RANGE GATE:NORMAL, PHASE RAMP: NORMAL
	191	MBES			13/10/2020	00:11	52.3496	6.1953	13/10/2020	00:22	52.3325	6.2042	75|10|75	150	MEDIUM CW	NORMAL	REL. MEAN HEADING	300 kHz	SPIKE: MEDIUM, RANGE GATE:NORMAL, PHASE RAMP: NORMAL
	192	MBES		6.1 kts	13/10/2020	00:25	52.3318	6.2053	13/10/2020	00:36	52.3486	6.1968	75|10|75	150	MEDIUM CW	NORMAL	REL. MEAN HEADING	300 kHz	SPIKE: MEDIUM, RANGE GATE:NORMAL, PHASE RAMP: NORMAL
	193	MBES		6.3 kts	13/10/2020	00:38	52.349	6.1987	13/10/2020	00:46	52.3355	6.2054	75|10|75	150	MEDIUM CW	NORMAL	REL. MEAN HEADING	300 kHz	SPIKE: MEDIUM, RANGE GATE:NORMAL, PHASE RAMP: NORMAL
	194	MBES		6.2 kts	13/10/2020	00:46	52.3355	6.2054	13/10/2020	00:54	52.3318	6.1839	75|10|75	150	MEDIUM CW	NORMAL	REL. MEAN HEADING	300 kHz	SPIKE: MEDIUM, RANGE GATE:NORMAL, PHASE RAMP: NORMAL

Finished Area and started transit to A2

Info					Start				End				Runtime Parameters						Filters
Area	Line id	Type	SVP No.	SOG (kts)	Start Date	Start time (UTC)	SOL Lat (dd)	SOL Long (dd)	End Date	End time (UTC)	EOL Lat (dd)	EOL Long (dd)	Coverage	Max Coverage	Pulse Type	Detector	Mode	Frequency	
	195	MBES			13/10/2020	01:38	52.4169	6.1529	13/10/2020	01:52	52.4405	6.1441	70|10|70	150	MEDIUM CW	NORMAL	REL. MEAN HEADING	300 kHz	SPIKE: MEDIUM, RANGE GATE:NORMAL, PHASE RAMP: NORMAL
	196	MBES			13/10/2020	01:54	52.4421	6.1446	13/10/2020	02:07	52.4191	6.1534	70|10|70	150	MEDIUM CW	NORMAL	REL. MEAN HEADING	300 kHz	SPIKE: MEDIUM, RANGE GATE:NORMAL, PHASE RAMP: NORMAL
	197	MBES		6.5 kts	13/10/2020	02:11	54.418	6.154	13/10/2020	02:24	52.4402	6.1465	70|10|70	150	MEDIUM CW	NORMAL	REL. MEAN HEADING	300 kHz	SPIKE: MEDIUM, RANGE GATE:NORMAL, PHASE RAMP: NORMAL
A2	198	MBES	Stn.46		13/10/2020	02:26	52.4431	6.1467	13/10/2020	02:41	52.4195	6.1556	70|10|70	150	MEDIUM CW	NORMAL	REL. MEAN HEADING	300 kHz	SPIKE: MEDIUM, RANGE GATE:NORMAL, PHASE RAMP: NORMAL
	199	MBES		7 kts	13/10/2020	02:44	52.4185	6.157	13/10/2020	02:58	52.4429	6.1477	70|10|70	150	MEDIUM CW	NORMAL	REL. MEAN HEADING	300 kHz	SPIKE: MEDIUM, RANGE GATE:NORMAL, PHASE RAMP: NORMAL
	200	MBES		6 kts	13/10/2020	03:00	52.4438	6.1485	13/10/2020	03:15	52.4183	6.1586	70|10|70	150	MEDIUM CW	NORMAL	REL. MEAN HEADING	300 kHz	SPIKE: MEDIUM, RANGE GATE:NORMAL, PHASE RAMP: NORMAL
	201	MBES		7.6 kts	13/10/2020	03:17	52.4175	6.1598	13/10/2020	03:29	52.4416	6.1509	70|10|70	150	MEDIUM CW	NORMAL	REL. MEAN HEADING	300 kHz	SPIKE: MEDIUM, RANGE GATE:NORMAL, PHASE RAMP: NORMAL
	202	MBES		6 kts	13/10/2020	03:31	52.4443	6.1509	13/10/2020	03:45	52.4201	6.1603	70|10|70	150	MEDIUM CW	NORMAL	REL. MEAN	300 kHz	SPIKE: MEDIUM, RANGE GATE:NORMAL, PHASE

																HEADING		RAMP: NORMAL
203	MBES		6.3 kts	13/10/2020	03:48	52.4189	6.1616	13/10/2020	04:00	52.4408	6.1535	70|10|70	150	MEDIUM CW	NORMAL	REL. MEAN HEADING	300 kHz	SPIKE: MEDIUM, RANGE GATE:NORMAL, PHASE RAMP: NORMAL
204	MBES		7	13/10/2020	04:02	52.445	6.153	13/10/2020	04:16	52.4188	6.1632	70|10|70	150	MEDIUM CW	NORMAL	REL. MEAN HEADING	300 kHz	SPIKE: MEDIUM, RANGE GATE:NORMAL, PHASE RAMP: NORMAL
205	MBES		6	13/10/2020	04:19	52.4182	6.1646	13/10/2020	04:32	52.4413	6.1557	70|10|70	150	MEDIUM CW	NORMAL	REL. MEAN HEADING	300 kHz	SPIKE: MEDIUM, RANGE GATE:NORMAL, PHASE RAMP: NORMAL
206	MBES		6.2	13/10/2020	04:35	52.4451	6.1555	13/10/2020	04:48	52.4213	6.1646	70|10|70	150	MEDIUM CW	NORMAL	REL. MEAN HEADING	300 kHz	SPIKE: MEDIUM, RANGE GATE:NORMAL, PHASE RAMP: NORMAL
207	MBES			13/10/2020	04:51	52.4181	6.1668	13/10/2020	05:04	52.4421	6.1578	70|10|70	150	MEDIUM CW	NORMAL	REL. MEAN HEADING	300 kHz	SPIKE: MEDIUM, RANGE GATE:NORMAL, PHASE RAMP: NORMAL
208	MBES		6.7	13/10/2020	05:07	52.4448	6.1583	13/10/2020	05:20	52.41933	6.1679	70|10|70	150	MEDIUM CW	NORMAL	REL. MEAN HEADING	300 kHz	SPIKE: MEDIUM, RANGE GATE:NORMAL, PHASE RAMP: NORMAL
209	MBES		7.5	13/10/2020	05:23	52.4199	6.1688	13/10/2020	05:35	52.444	6.1596	70|10|70	150	MEDIUM CW	NORMAL	REL. MEAN HEADING	300 kHz	SPIKE: MEDIUM, RANGE GATE:NORMAL, PHASE RAMP: NORMAL
210	MBES		7.2	13/10/2020	05:37	52.449	6.1603	13/10/2020	05:50	52.4198	6.1701	70|10|70	150	MEDIUM CW	NORMAL	REL. MEAN HEADING	300 kHz	SPIKE: MEDIUM, RANGE GATE:NORMAL, PHASE RAMP: NORMAL
211	MBES		7.1	13/10/2020	05:52	52.4195	6.1715	13/10/2020	06:06	52.444	6.1617	70|10|70	150	MEDIUM CW	NORMAL	REL. MEAN HEADING	300 kHz	SPIKE: MEDIUM, RANGE GATE:NORMAL, PHASE RAMP: NORMAL
212	MBES		7.2	13/10/2020	06:08	52.4446	6.16315	13/10/2020	06:20	52.420437	6.1719	70|10|70	150	MEDIUM CW	NORMAL	REL. MEAN HEADING	300 kHz	SPIKE: MEDIUM, RANGE GATE:NORMAL, PHASE RAMP: NORMAL
213	MBES		6.8	13/10/2020	06:24	52.42112	6.17265	13/10/2020	06:36	52.4445	6.16426	70|10|70	150	MEDIUM CW	NORMAL	REL. MEAN HEADING	300 kHz	SPIKE: MEDIUM, RANGE GATE:NORMAL, PHASE RAMP: NORMAL
214	MBES		7.4	13/10/2020	06:40	52.44151	6.1709	13/10/2020	06:45	52.43211	6.17153	70|10|70	150	MEDIUM CW	NORMAL	REL. MEAN HEADING	300 kHz	SPIKE: MEDIUM, RANGE GATE:NORMAL, PHASE RAMP: NORMAL
215	MBES		7.1	13/10/2020	06:45	52.43211	6.17153	13/10/2020	06:52	52.42948	6.14621	70|10|70	150	MEDIUM CW	NORMAL	REL. MEAN HEADING	300 kHz	SPIKE: MEDIUM, RANGE GATE:NORMAL, PHASE RAMP: NORMAL
216	MBES		6.5	13/10/2020	07:02	52.4334	6.1729	13/10/2020	07:08	52.42278	6.173	70|10|70	150	MEDIUM CW	NORMAL	REL. MEAN HEADING	300 kHz	SPIKE: MEDIUM, RANGE GATE:NORMAL, PHASE RAMP: NORMAL
217	MBES		6.6	13/10/2020	07:12	52.42133	6.17357	13/10/2020	07:19	52.4334	6.1741	70|10|70	150	MEDIUM CW	NORMAL	REL. MEAN HEADING	300 kHz	SPIKE: MEDIUM, RANGE GATE:NORMAL, PHASE RAMP: NORMAL
218	MBES		5.2	13/10/2020	07:20	52.4339	6.17525	13/10/2020	07:27	52.4213	6.175	70|10|70	150	MEDIUM CW	NORMAL	REL. MEAN HEADING	300 kHz	SPIKE: MEDIUM, RANGE GATE:NORMAL, PHASE RAMP: NORMAL
219	MBES		4.4	13/10/2020	07:29	52.4226	6.173203	13/10/2020	07:32	52.42477	6.1712	70|10|70	150	MEDIUM CW	NORMAL	REL. MEAN HEADING	300 kHz	SPIKE: MEDIUM, RANGE GATE:NORMAL, PHASE RAMP: NORMAL

	220	MBES		3.5	13/10/2020	07:33	52.4257	6.1711	13/10/2020	07:36	52.4261	6.1768	70|10|70	150	MEDIUM CW	NORMAL	REL. MEAN HEADING	300 kHz	SPIKE: MEDIUM, RANGE GATE:NORMAL, PHASE RAMP: NORMAL
Finished Area and started transit to ADCP 2 area																			
Info					Start				End				Runtime Parameters						
Area	Line id	Type	SVP No.	SOG (kts)	Start Date	Start time (UTC)	SOL Lat (dd)	SOL Long (dd)	End Date	End time (UTC)	EOL Lat (dd)	EOL Long (dd)	Coverage	Max Coverage	Pulse Type	Detector	Mode	Frequency	Filters
E1	221	MBES	Stn. 52		13/10/2020	18:26	53.2069	5.847	13/10/2020	18:37	53.1834	5.8346	70|10|70	150	MEDIUM CW	NORMAL	REL. MEAN HEADING	300 kHz	SPIKE: MEDIUM, RANGE GATE:NORMAL, PHASE RAMP: NORMAL
	222	MBES		4.7	13/10/2020	18:40	53.1839	5.8335	13/10/2020	18:58	53.20594	5.8452	70|10|70	150	MEDIUM CW	NORMAL	REL. MEAN HEADING	300 kHz	SPIKE: MEDIUM, RANGE GATE:NORMAL, PHASE RAMP: NORMAL
	223	MBES		5.9	13/10/2020	19:05	53.207934	5.8399	13/10/2020	19:22	53.1846	5.82734	75|10|75	150	MEDIUM CW	NORMAL	REL. MEAN HEADING	300 kHz	SPIKE: MEDIUM, RANGE GATE:NORMAL, PHASE RAMP: NORMAL
	224	MBES		2.8	13/10/2020	19:25	53.1855	5.8274	13/10/2020	19:50	53.2082	5.8364	75|10|75	150	MEDIUM CW	NORMAL	REL. MEAN HEADING	300 kHz	SPIKE: MEDIUM, RANGE GATE:NORMAL, PHASE RAMP: NORMAL
	225	MBES		6.2	13/10/2020	19:54	53.2082	5.8386	13/10/2020	20:09	53.185	5.826274							
	226	MBES			13/10/2020	20:13	53.185353	5.8254	13/10/2020	20:34	53.2081	5.8375							
	227	MBES		5.1	13/10/2020	20:38	53.2092	5.8358	13/10/2020	20:50	53.1854	5.82286							
Area abandoned and started transit to B9																			
Info					Start				End				Runtime Parameters						
Area	Line id	Type	SVP No.	SOG (kts)	Start Date	Start time (UTC)	SOL Lat (dd)	SOL Long (dd)	End Date	End time (UTC)	EOL Lat (dd)	EOL Long (dd)	Coverage	Max Coverage	Pulse Type	Detector	Mode	Frequency	Filters
B9	228	MBES	Stn. 53	5.3	14/10/2020	03:29	52.824	5.995	14/10/2020	03:37	52.8139	6.0004	70|10|70	150	MEDIUM CW	NORMAL	REL. MEAN HEADING	300 kHz	SPIKE: MEDIUM, RANGE GATE:NORMAL, PHASE RAMP: NORMAL
	229	MBES		6.2	14/10/2020	03:40	52.8111	6.0005	14/10/2020	03:50	52.8219	5.995	70|10|70	151	MEDIUM CW	NORMAL	REL. MEAN HEADING	300 kHz	SPIKE: MEDIUM, RANGE GATE:NORMAL, PHASE RAMP: NORMAL
	230	MBES		5.2	14/10/2020	03:54	52.824	5.9925	14/10/2020	04:04	52.813	5.9983	70|10|70	152	MEDIUM CW	NORMAL	REL. MEAN HEADING	300 kHz	SPIKE: MEDIUM, RANGE GATE:NORMAL, PHASE RAMP: NORMAL
	231	MBES		5.3	14/10/2020	04:07	52.8107	5.9978	14/10/2020	04:17	52.8235	5.9917	75|10|75	153	MEDIUM CW	NORMAL	REL. MEAN HEADING	300 kHz	SPIKE: MEDIUM, RANGE GATE:NORMAL, PHASE RAMP: NORMAL
	232	MBES		4.3	14/10/2020	04:19	52.8243	5.9901	14/10/2020	04:31	52.8103	5.9967	75|10|75	153	MEDIUM CW	NORMAL	REL. MEAN HEADING	300 kHz	SPIKE: MEDIUM, RANGE GATE:NORMAL, PHASE RAMP: NORMAL
	233	MBES		4.4	14/10/2020	04:33	52.8109	5.9954	14/10/2020	04:44	52.8239	5.9892	75|10|75	153	MEDIUM CW	NORMAL	REL. MEAN HEADING	300 kHz	SPIKE: MEDIUM, RANGE GATE:NORMAL, PHASE RAMP: NORMAL
	234	MBES		4.5	14/10/2020	04:46	52.8231	5.9889	14/10/2020	04:56	52.8102	5.9951	75|10|75	153	MEDIUM CW	NORMAL	REL. MEAN	300 kHz	SPIKE: MEDIUM, RANGE GATE:NORMAL, PHASE

																	HEADING		RAMP: NORMAL
	235	MBES		5.4	14/10/2020	04:59	52.8108	5.9939	14/10/2020	05:07	52.8234	5.988	75|10|75	153	MEDIUM CW	NORMAL	REL. MEAN HEADING	300 kHz	SPIKE: MEDIUM, RANGE GATE:NORMAL, PHASE RAMP: NORMAL
	236	MBES		4.3	14/10/2020	00:00	52.823	5.987	14/10/2020	05:19	52.8101	5.99344	75|10|75	153	MEDIUM CW	NORMAL	REL. MEAN HEADING	300 kHz	SPIKE: MEDIUM, RANGE GATE:NORMAL, PHASE RAMP: NORMAL
	237	MBES		4.9	14/10/2020	05:22	52.811	5.9921	14/10/2020	05:30	52.82336	5.9857589	75|10|75	153	MEDIUM CW	NORMAL	REL. MEAN HEADING	300 kHz	SPIKE: MEDIUM, RANGE GATE:NORMAL, PHASE RAMP: NORMAL
	238	MBES		5.7	14/10/2020	05:33	52.82169	5.98596	14/10/2020	05:42	52.8102	5.99158	75|10|75	153	MEDIUM CW	NORMAL	REL. MEAN HEADING	300 kHz	SPIKE: MEDIUM, RANGE GATE:NORMAL, PHASE RAMP: NORMAL
	239	MBES		5.3	14/10/2020	05:45	52.810188	5.99087	14/10/2020	05:53	52.82281	5.98455	75|10|75	153	MEDIUM CW	NORMAL	REL. MEAN HEADING	300 kHz	SPIKE: MEDIUM, RANGE GATE:NORMAL, PHASE RAMP: NORMAL
	240	MBES		4.6	14/10/2020	05:56	52.8227	5.98359	14/10/2020	06:05	52.80988	5.98988	75|10|75	153	MEDIUM CW	NORMAL	REL. MEAN HEADING	300 kHz	SPIKE: MEDIUM, RANGE GATE:NORMAL, PHASE RAMP: NORMAL
	241	MBES		5.1	14/10/2020	06:10	52.81089	5.9975	14/10/2020	06:17	52.822781	5.99146	75|10|75	153	MEDIUM CW	NORMAL	REL. MEAN HEADING	300 kHz	SPIKE: MEDIUM, RANGE GATE:NORMAL, PHASE RAMP: NORMAL
	242	MBES		5.3	14/10/2020	06:26	52.81849	6.0002	14/10/2020	06:32	52.81504	5.985	75|10|75	153	MEDIUM CW	NORMAL	REL. MEAN HEADING	300 kHz	SPIKE: MEDIUM, RANGE GATE:NORMAL, PHASE RAMP: NORMAL
Finished Area and started transit to ADCP 2 area for retrieval																			
Info					Start				End				Runtime Parameters						
Area	Line id	Type	SVP No.	SOG (kts)	Start Date	Start time (UTC)	SOL Lat (dd)	SOL Long (dd)	End Date	End time (UTC)	EOL Lat (dd)	EOL Long (dd)	Coverage	Max Coverage	Pulse Type	Detector	Mode	Frequency	Filters
A1	243	MBES	Stn. 53	6.1	14/10/2020	13:07	52.5564	6.1197	14/10/2020	13:24	52.5872	6.1081	70|10|70	150	MEDIUM CW	NORMAL	REL. MEAN HEADING	300 kHz	SPIKE: MEDIUM, RANGE GATE:NORMAL, PHASE RAMP: NORMAL
	244	MBES		5.5	14/10/2020	13:26	52.5858	6.1069	14/10/2020	13:43	52.5557	6.1159	70|10|70	150	MEDIUM CW	NORMAL	REL. MEAN HEADING	300 kHz	SPIKE: MEDIUM, RANGE GATE:NORMAL, PHASE RAMP: NORMAL
	245	MBES		5.2	14/10/2020	13:46	52.558	6.1152	14/10/2020	13:48	52.5592								
Finished Area and started transit to ADCP 1 area for retrieval																			

National Research Vessels

SHIP-TIME PROGRAMME

RESEARCH SURVEY REPORT

Survey Code:	Survey Name:	Chief Scientist/ Institution
CV21035	Mobility of Sediment Waves and Sand Banks in the Irish Sea Phase 2, Leg 1	Shauna Creane/ University College Cork

Section A: Award Summary

Title of Research Survey and Survey Code:	Mobility of Sediment Waves and Sand Banks in the Irish Sea Phase 2 (MOVE 2), Leg 1 Survey Code: CV21035	
Co-Ordinator/ Chief Scientist:	Shauna Creane	
Vessel used for ship-time:	*RV Celtic Voyager* ☒ *RV Celtic Explorer* ☐	
Total number of days at sea:	7 days: - 4 days (weather downtime – in Dun Laoghaire Harbour) - 1 day (workable at sea) - 2 days (transit to demob port i.e. Galway)	
Total number of grant-aided ship-time days awarded:	12 days in total: - 5 days (MOVE 2 Leg 1; CV21035) - 7 days (MOVE 2 Leg 2; CV21034)	
Dates of survey:	Original Dates: 26th – 30th March 2021 Survey dates changed to 26th – 1st April 2021 while onboard, due to change of demob port location, in order to maximise survey time due to unfavourable weather conditions.	
Mobilisation/Demobilisation Ports	Mobilisation: Dun Laoghaire Demobilisation: Galway	
Survey Personnel:	*No. of Scientists* *2*	*No. of Students* *0*
Final Report Completed by:	Shauna Creane (Chief Scientist) SFI Research Centre for Energy, Climate and Marine (MaREI), University College Cork	**Date**: 17/06/2021

Section B: Description of the Research Survey

B1 Overview of survey personnel

Names	***Institute/ Department/ Course***	***Position (undergraduate/ post graduate etc)***	***Number of Days***
Shauna Creane (Chief Scientist)	School of Civil & Environmental Engineering, University College Cork; SFI Research Centre for Energy, Climate and Marine (MaREI). Funded under the Irish Research Council's Employment-Based Postgraduate Programme, (grant number: EBPPG/2019/158)	PhD (Engineering)	7
Mark Coughlan (Scientist)	School of Engineering, University College Dublin; SFI Research Centre for Applied Geosciences (iCRAG) Funded under the Irish Research Counil Enterprise Partnership Scheme Postdoctoral Fellowship (EPSPD/2020/109) and in part by a research grant from Science Foundation Ireland (SFI) under Grant Number 13/RC/2092, with support from Gavin and Doherty Geosolutions Ltd and the Geological Survey of Ireland (GSI).	Research Fellow	7

B2 Objectives

Briefly outline the overall objectives of the research survey.
Please state if objectives have changed from the original proposal. If survey included a training element please outline clearly.

The Irish Sea is an enclosed, tidal sea with varying bathymetric conditions and distinct geomorphological features. A series of well-documented, linear, north-south trending sandbanks are found close inshore and parallel to the Wexford, Wicklow and South Dublin coast. These banks form a punctuated line parallel to the coast with breaks between them maintained by strong currents and sediment movement (Wheeler et al., 2001). The banks themselves are believed to be quasi-stable over historical time, in dynamic equilibrium with tidal and wave conditions,

and offer important coastal protection (Warren & Keary, 1989). Bathymetry and side-scan sonar records from some banks reveal evidence of seabed mobility on, and adjacent to, the banks (Wheeler et al., 2001). Furthermore, sandwaves increase in amplitude towards the edge of the banks suggesting that currents are highest close to the banks. This is probably responsible for the maintenance of the banks' relative positions. Elsewhere in the Irish Sea, sediment waves of varying sizes and morphologies are well documented, consisting of very large (3–18 m in height), normal-shaped and trochoidal-shaped features (Van Landeghem et al., 2009a). Some features are noted to migrate up to 70 m per year. Others are considered moribund or having formed under previously high hydrodynamic conditions or as part of glacial processes (Van Landeghem et al., 2009b). Some sediment wave features are related to glacial features, such as tunnel valleys, which form seabed channels where current flow is thought to be augmented.

In general, significant vagrancies exist regarding seabed morphodynamics and the potential for sediment mobility in the Irish Sea. Many processes associated with morphodynamic and hydrodynamic change, such as sediment wave migration, have been well documented and quantified in fluvial environments where hydrodynamic data is more readily available in both high spatial and temporal resolutions. Furthermore, physical testing (e.g. flume tanks) mean that scaled-down real-world testing allows a greater insight into these processes that can be easily studied. However, in deeper offshore environments such as the Irish Sea, this level of data is not available. Additionally, the Irish Sea environment offers more controlling factors on morphodynamic change and so is considerably more complex. Therefore, the technical challenge of gathering data in this environment is a trying one. Data that can be gathered include traditional seabed mapping techniques, such as multi-beam echosounder to image the seabed and sub-bottom profiling to visualise seabed structure below the surface. Both these methods offer an image of the seabed and sub-seabed at a given point in time at it's collection but have limited value in fully understanding a mobile sediment environment. Scientifically, the challenge is to utilise this data robustly to develop an understanding of how the seabed has developed temporally and spatially. MOVE 2 (CV21035 & CV21034) will build upon the high-quality geophysical datasets that are collected by MOVE 1 (CV20010 & CV20035) in south Irish Sea. By conducting high precision, high-resolution repeat surveys, time-lapse imagery of the seafloor can be generated. Repeat surveys reveal differences in seafloor bathymetry, accretion and rate of bedform migration (Van Landeghem et al., 2012).

To date the key economic reasons for quantifying seabed change include the needs to monitor dredged shipping channels (Knaapen & Hulscher, 2002); the dispersal of dredged spoil (Stockmann et al., 2009); the volume of marine aggregate resources (Sutton, 2008); and the impact of engineering works such as cables, pipelines and energy infrastructure on the seabed (Morelissen et al., 2003; Yaghoobi et al., 2012). Scientific drivers include the needs to calibrate bedload transport equations and to gain insights into natural geomorphological dynamics such as bedforms (Xu et al., 2008) and implications for benthic habitats (Wilson et al., 2021). However, when sequential multibeam surveys are conducted with long time intervals, short term bedform dynamics may be missed and/or misinterpreted. Currently, there is a distinct paucity of high-resolution repeat bathymetry data in the south Irish Sea and only a limited amount of work has been done on bedform mobility on a local scale (Hanna & Cooper, 2002; Panigrahi et al., 2009; Van Landeghem et al., 2012). Sparse small-scale overlaps have been identified on the edges of INFOMAR surveys allowing only 2D cross-sectional analysis of bedforms. These overlaps fail to include high temporal resolution and eliminates the opportunity to study crest variability along a 3D mobile bedform. For the MOVE project survey areas, INFOMAR's 2009 and 2012 surveys provide great baseline data, however, a difference of 11 years and 8 years respectively

between these datasets and the MOVE 1 survey fail to provide the high temporal resolution necessary for high quality bedform mobility analysis. It is crucial to capture these dynamic changes through frequent interannual bathymetry surveys. MOVE 2 (CV21035 & CV21034) drives this campaign by capturing, repeat interannual high resolution geophysical datasets to be analysed alongside the 2020 MOVE 1 survey campaign.

By combining repeat geophysical data with sediment sampling and long-term hydrodynamic monitoring equipment such as acoustic doppler current profilers (ADCP), we can garner a better understanding of temporal changes at a higher resolution. Therefore, the big scientific challenge to understanding seabed morphodynamics is how to observe these changes in a reasonable resolution with high-confidence. Furthermore, another significant challenge to assessing the risk of morphodynamic evolution, and sediment mobility, poses to critical engineering and environmental projects is how can future changes in seabed morphodynamics be confidently predicted.

Sediment transport modelling offers an innovative means to study this behaviour, and predict where seabed mobility may be an issue in the future. By bringing together geoscientists and engineers, this project will make a significant contribution to the existing knowledge through collaboratively addressing these problems. Precise, interannual surveying is also crucial for robust sediment transport and morphological modelling. For example, a morphological model developed by Fairley et al (2017) produced unrealistic bed level changes of 5m over one lunar month over a sediment wave assemblage in Pentland Firth and Orkley Waters. Without multiple multi-beam bathymetry surveys, it was impossible to determine whether this result was due to model inaccuracies or natural processes. Analysis of repeat bathymetry surveys is key to accurate validation of these types of numerical models. Up-to-date bathymetry data is also a vital basic input into sediment transport and morphological models in order to provide high quality, accurate outputs (Fairley et al., 2017). Outputs are only as good as your input. There is a significant lack of high resolution morphological modelling in the south Irish Sea and it is a critical step in understanding both present day and future hydro- and morphodynamics. MOVE 1 and MOVE 2 combined will not only supply these pivotal repeat geophysical datasets, but also collect a new innovative way of providing sensitivity testing to suspended sediment transport modelling through calculating suspended sediment concentration (SSC) derived from ADCP acoustic backscatter. This method correlates direct measurement of SSC (through water sampling) with ADCP acoustic backscatter, providing a time series of suspended sediment transport throughout the vertical water column at a fixed point.

An integrated use of repeat geophysical data, geological groundtruthing and numerical modelling is key to understanding both regional and local scale hydro- and morphodynamics of the south Irish Sea. With the sudden increase in offshore infrastructure developments in the Irish Sea, expert knowledge of seabed morphodynamics and sediment mobility is of huge importance.

The scientific goal of the MOVE 2 survey can be broken down into six objectives:

1. To build upon MOVE survey phase 1 by gathering critical high resolution interannual geological and geophysical datasets to investigate the nature of sediment mobility and morphodynamic changes in selected sites of the Irish Sea known for highly complex hydrodynamics;
2. To gather interannual geophysical data and time series suspended sediment concentration data to validate and to provide sensitivity analysis for numerical models currently under development;

3. To examine the physical processes occurring on the seafloor with respect to seabed morphodynamics pertinent to engineering projects;
4. To provide data to validate 2D hydrodynamic, sediment transport and morphological numerical models that will form the basis of understanding the complex morphodynamics and it's underlying drivers in the south Irish Sea;
5. To gather critical site specific environmental data to feed in to modelling efforts to help predict future changes in seabed morphology in reaction to anthropogenic impacts and climate change;
6. To build up a unique Geographical Information System (GIS) based database of offshore seabed morphology and sediments in the Irish Sea that can be used in future engineering and environmental studies.

These objectives can be achieved on the with the *RV Celtic Voyager* over the two granted survey legs:

1. Leg 1 (CV21035): 26th to 30th March 2021
2. Leg 2 (CV21034): 6th to 12th December 2021

This report specifically covers the work completed by MOVE 2 Leg 1 whereby the main survey area is located off the east coast of Ireland, in the southern section of the Irish Sea Figure 1.

Leg 1 (CV21035) involves targeted multibeam echo sounder (MBES) and sub-bottom profiler (SBP) survey work. Two areas were identified as MOVE 2 Leg 1 priority areas for investigation; Area A and Area B. Within these areas, multiple subsections were selected and were designated priority levels; high, medium, low. These areas were refined from areas surveyed by MBES during MOVE 1 (CV20010 & CV20035) in October 2020. Two low priority areas were identified as back up in case of unworkable weather conditions around the sediment banks; Area C and Area D Figure 1.

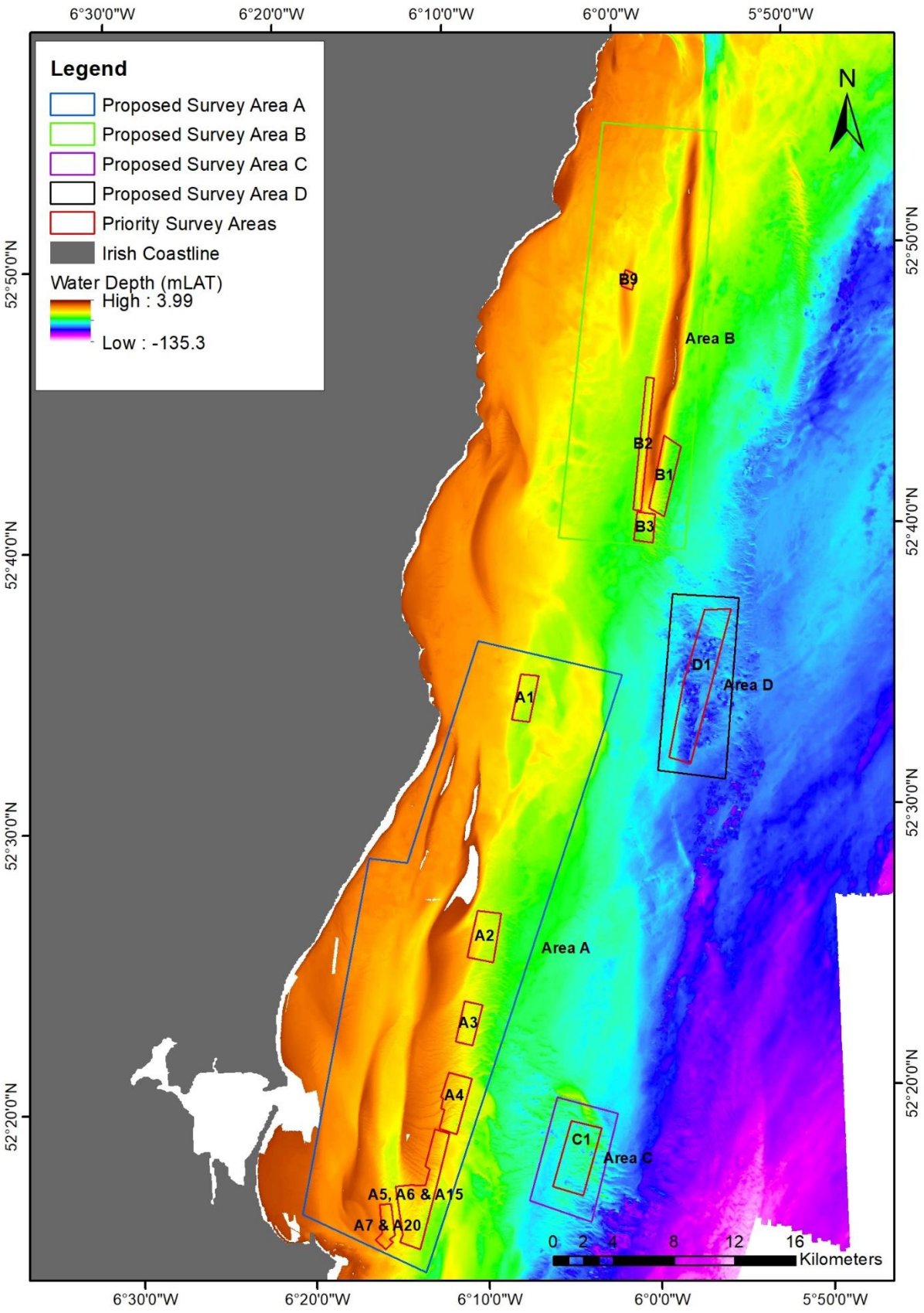


Figure 1 Overview of south-western Irish Sea displaying the location of 4 main study areas (black boxes) and priority MBES and SBP sub-areas (red boxes)

B3 Overview of research survey

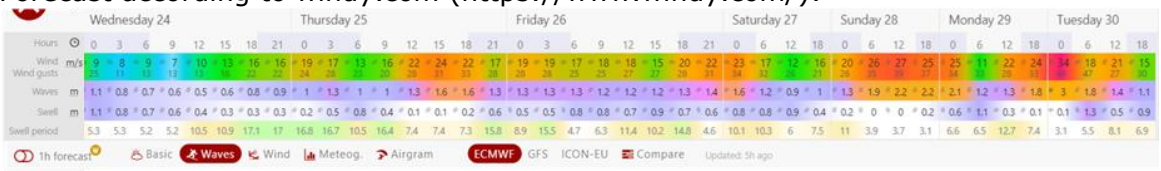
Provide a narrative overview of the research survey including survey timelines
The information provided in this section should not exceed 5 pages (excluding tables and maps)

ALL TIMES IN UTC.

Friday 26th March 2021

10:15 Arrive at RV Celtic Voyager. Follow COVID Procedures onboard.
11:30 Lunch
12:30 Induction to the ship
13:00 Discussion with the captain about weather conditions and accessibility to priority sites.
Decision made not to set sail, conditions too bad. Gail Force, westerly winds, waves >2m in height

Forecast according to windy.com (https://www.windy.com/):



Saturday 27th March 2021

07:30 - Port side in Dun Laoghaire. Weather forecast too bad to sail.

Forecast according to windy.com (https://www.windy.com/) for Site B:



Forecast according to windy.com (https://www.windy.com/) for Site A:



Note: By the time we leave Dun Laoghaire and arrive at our first site, located south of Arklow Bank, we wouldn't have time to do any survey work before we'd have to return to Dun Laoghaire Harbour (original demob location).

Discussion of potential plan: Set sail Monday night to be at Site B early Tuesday morning. Continue to Site A to be onsite at @13:00. Leave the most southerly site at 19:00-20:00 to arrive in Cork 14 hours later for demob.

Sunday 28th March 2021

07:30 - Check in with the captain after breakfast to discuss weather changes and possible plans going forward. Weather forecast for today and tomorrow (Monday) is not workable (~59km/h). Other ships e.g. Navy and Fugro are taking shelter around Dun Laoghaire also.

Note: Plan is still to demob in Dun Laoghaire. Option to demob in Cork TBC depending on weather conditions for transit to Galway Bay post-CV21035.

Forecast according to windy.com (https://www.windy.com/):



Monday 29th March 2021

07:30 – Discussion with the captain after breakfast. Plan is to leave Monday afternoon to potentially arrive and begin surveying at Site B pre-sunset.

Forecast according to windy.com (https://www.windy.com/):



14:00 - Left Dun Laoghaire Habour at 14:00 heading towards the most northerly site (B9). Due to unfavourable working conditions, plan is now to shelter over night and start survey at first light.

Forecast according to windy.com (https://www.windy.com/):

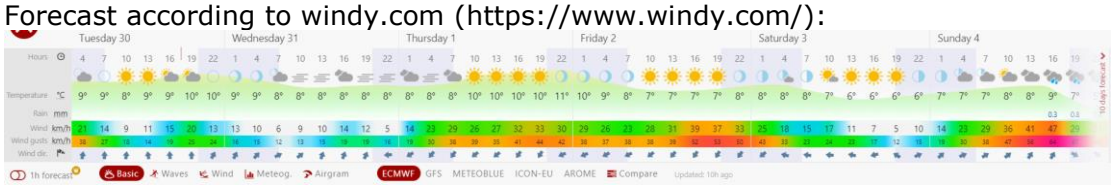


17:30 - Positioned just North of Wicklow Head, conditions too bad to continue further south. Waiting until conditions improve before continuing past Wicklow Head to first site (B9). We wouldn't arrive at B9 before sunset in any case, therefore plan is to start surveying tomorrow at first light.

30th March 2021

06:15 - Arrive at B9 (Seven Fathom Bank) before first light. Carry out SVP Dip.

Forecast according to windy.com (https://www.windy.com/):



07:09 - Begin MBES and Chirp survey at B9
09:35 – Finish survey at B9. Winds are south-westerly, therefore best suitable conditions for surveying in Arklow Bank area are at B1 (south-east side of Arklow Bank).
11:18 - Begin MBES & Chirp at B1.
12:40 - Finish survey at B1. Conditions unworkable for B3 (southern end of Arklow Bank). Winds changed slightly to south-easterly therefore potential

opportunity to run a survey line in B2 (south-western side of Arklow Bank). Transit to B2.
13:06 - Begin MBES & Chirp at B2.
13:54 - Finish survey at B2. Transit to A1 (north of Moneyweights & Blackwater Banks).
14:47 - Begin MBES & Chirp survey at A1.
15:11 - Finish surveying at A1. Transit to A2 (east of Blackwater Bank).
15:46 - Begin MBES & Chirp survey at A2.
16:07 - Finish surveying at A2 and transit to A3 (east of Blackwater/Lucifer Banks).
16:18 - Begin MBES & Chirp survey at A3.
16:35 - Finish survey at A3. Transit to A4 (east of Lucifer Bank).
16:44 - Begin MBES & Chirp survey at A4.
17:13 - Finish survey at A4. Transit to A5/A6/A15. (south-east, south & south-west Lucifer Bank.
17:13 - Begin MBES & Chirp survey at A5/A6/A15.
20:03 - Finish surveying at A5/A6/A15. Transit to C1 (offshore Lucifer Bank).
20:42 - Begin MBES & Chirp survey at C1.
21:43 - Finish surveying at C1. Transit to Cork Harbour for demobilisation.

31st March 2021

08:00 - Arrive offshore Cork Harbour ~8am, dense fog, Cork Harbour closed. Wait until 11am to see if the fog lifts.

11:00 - Received notification that Cork Harbour would not be opening for demob. Start transit to Galway.

1st April 2021

08:00 - On transit to Galway.

11:00 - Offshore Cliffs of Moher, on transit to Galway

Forecast according to windy.com (https://www.windy.com/):



18:00 - Arrive at the docks in Galway for demobilisation. All scientists off with backed up data.

SURVEY END

B4 Benefits, impact and contribution of the outputs to marine research and the marine sector in general.

Outline clearly the specific outcomes and benefits of the research survey.
The information provided in this section should not exceed 1/2 page (excluding tables and maps)

I. Main Deliverables

This survey generated essential data for on-going PhD (Shauna Creane) and group (iCRAG/GDG/MaREI) research as well as future PhD research. The following deliverables will arise from this survey and ongoing research:

1. High resolution multibeam and chirp survey data over previously surveyed sand banks and sediment wave features in the Irish Sea;
2. An evaluation of sediment mobility in the area and subsequent impacts on offshore engineering structures;
3. Presentations at national and international meetings with acknowledgements;
4. Publications in peer-review journals.

These deliverables contribute directly to a significant baseline of data critical for a morphodynamic atlas of the Irish Sea along with a database of sediment hydrodynamic and morphodynamic parameters for designated areas. The objective of which is to be used by stakeholders and infrastructure developers as critical engineering and environmental data for projects.

II. Specific Benefits and Impacts

The MOVE 2 Leg 1 survey fundamentally assists the better understanding of seabed sediment dynamics in the Irish Sea. This has direct implications for a number of sectors, including:

- The construction of offshore renewable energy by identifying areas where it is feasible to profitably build foundations and site cable routes ashore;
- The improving of habitat maps to inform environmental assessments and fisheries research by integrating additional site condition information;
- The developing of critical baseline information and models with which to assess climate change effects including coastal erosion.

Furthermore, the MOVE 2 Leg 1 survey has the following benefits and impacts:

1. Training and sea-going experience for current, active researchers and students;
2. Filling specific data gaps in our understanding of offshore seabed processes and sub-structure;
3. A strengthening of collaboration between parties involved in the project, including iCRAG, UCD, GDG, UCC and MaREI;
4. An increase in research capacity and better interdisciplinary research on the island of Ireland;
5. Development of different techniques and technology in seabed mapping in Irish Waters;
6. Value-add to existing datasets (e.g. INFOMAR);

In general, the MOVE project fosters a firm collaboration between strongly technical researchers actively addressing some of the key challenges facing Ireland in terms of managaing seabed resources and developing offshore renewable energy sources to help us meet our climate change targets. It addresses some of the key priorities set out in Harnessing Our Ocean Wealth Roadmap which aims to build a thriving maritime economy that harnesses economic growth whilst also being being cognisant of healthy ecosystems and

sustainably managing our activities at sea. The MOVE project does so by providing key baseline data and research for both and promotes future collaboration between academia and industry to help achieve these goals. Specifically, the project supports the Ocean Renewable Energy Development Plan (OREDP) in technically assessing key areas for renewable energy installation development and critically de-risking them.

B5 Data

Provide a description of the data collected from the research survey, the usage of the data and how it will be stored.

The information provided in this section should not exceed 1/2 page (excluding tables and maps)

MBES and SBP data were collected at 11 sites (Figure 2) over 15 hours of work. Survey design comprised targeted lines over sediment waves and sand banks identified using INFOMAR and MOVE 1 (CV20010/CV20035) datasets. An example bathymetry dataset collected during this survey is displayed in Figure 3. The collected data act as precise, high resolution, time-lapse information to compare with baseline INFOMAR, MOVE 1, and the future MOVE 2 Leg 2 (planned for December 2021, CV21034) datasets. ADCP deployment, water sampling and sediment sampling that couldn't be carried out over MOVE 2 Leg 1 will be carried out in Leg 2. Table 1 displays the data type collected during CV21035, its usage, and how it will be stored. Preliminary results of sediment wave migration directions and rates using INFOMAR, MOVE 1 (CV20010 & CV20035), and MOVE 2 Leg 1 (CV210035) datasets are displayed in Figure 4.

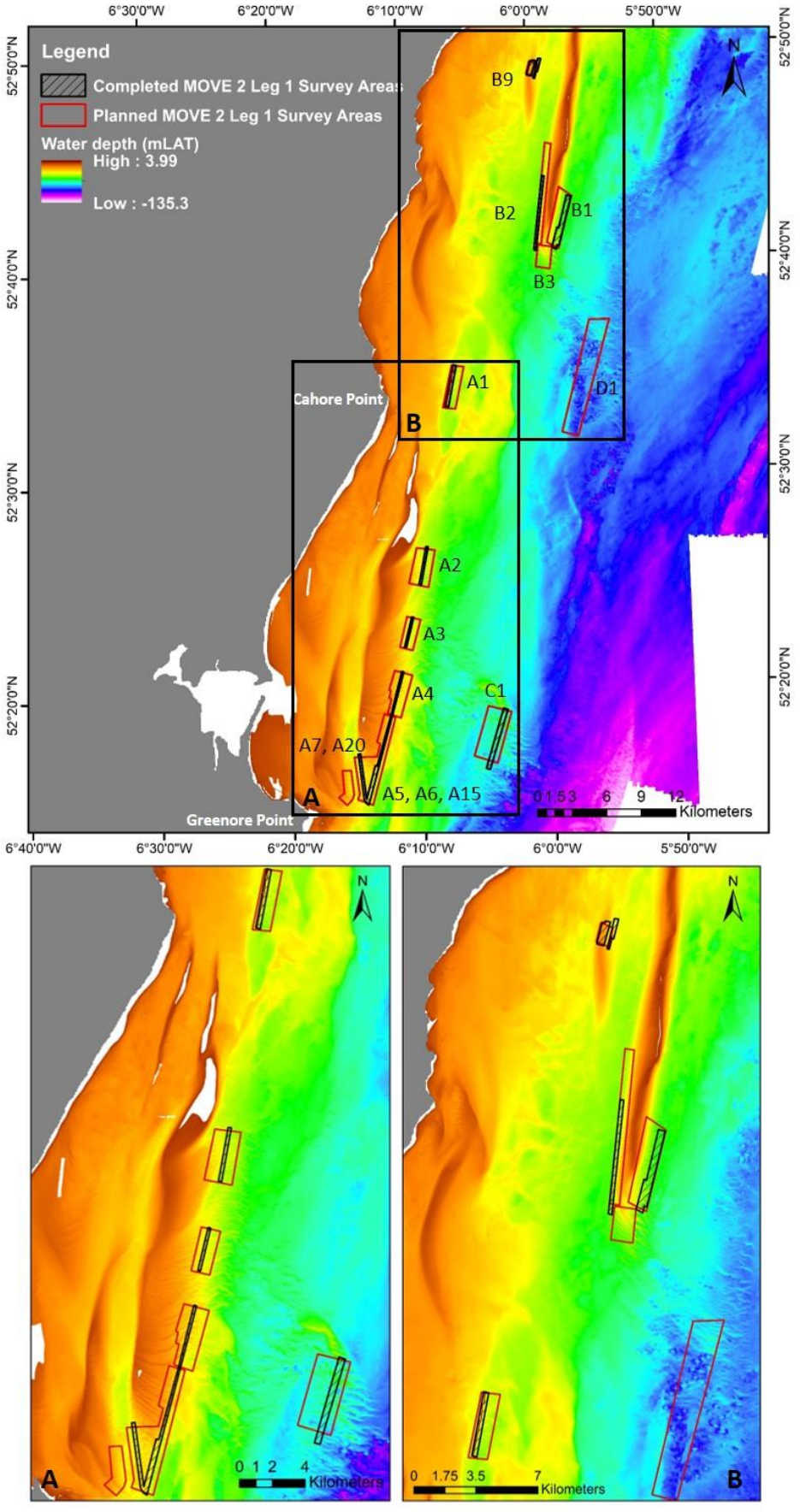


Figure 2 MBES and SBP MOVE 2 Leg 1 planned versus completed

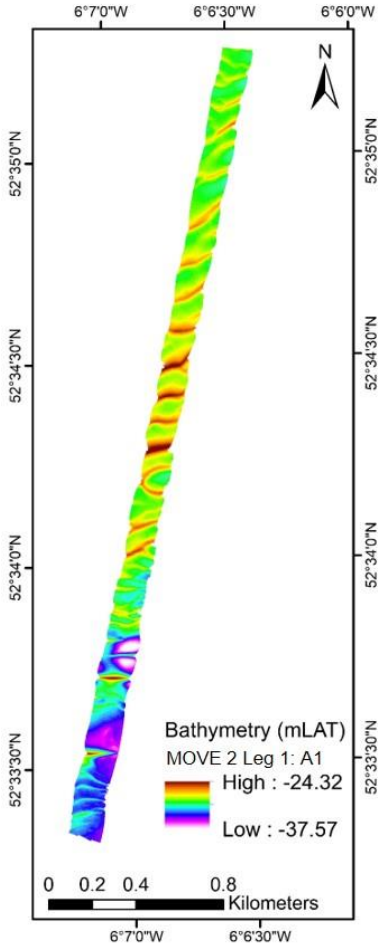


Figure 3 MOVE 2 Leg 1 processed bathymetry dataset revealing sediment waves at site A1

Table 1 Data collected on MOVE 2 Leg 1 (CV21035)

Instrument	***Data Type***	***Usage***	***Storage***
Multibeam Echo Sounder	Bathymetry	Time-lapse data for sediment transport studies; Seabed stability and morphological evolution studies; Input and validation of long term numerical modelling work	Internal server of Gavin and Doherty Geosolutions (GDG); External Hardrives; shared through publications and presentations
	Backscatter	Ground truth with in-situ sediment sampling data and incorporate into seabed mobility and morphological evolution studies alongside bathymetry datasets	Internal server of Gavin and Doherty Geosolutions (GDG); External Hardrives; shared through publications and presentations
Sub-bottom profiler (Chirp system)	Sub-bottom	3D imaging of the sea floor shallow sub-surface and sediment layering; Environemental management, including	Internal server of Gavin and Doherty Geosolutions (GDG); External Hardrives; shared through publications and presentations

		establishing baseline data to support environmental monitoring; Classification maps for seabed habitats; Analyse internal structure of sediment waves and depth of mobile layer for seabed mobility studies for input into offshore infrastructure works;	

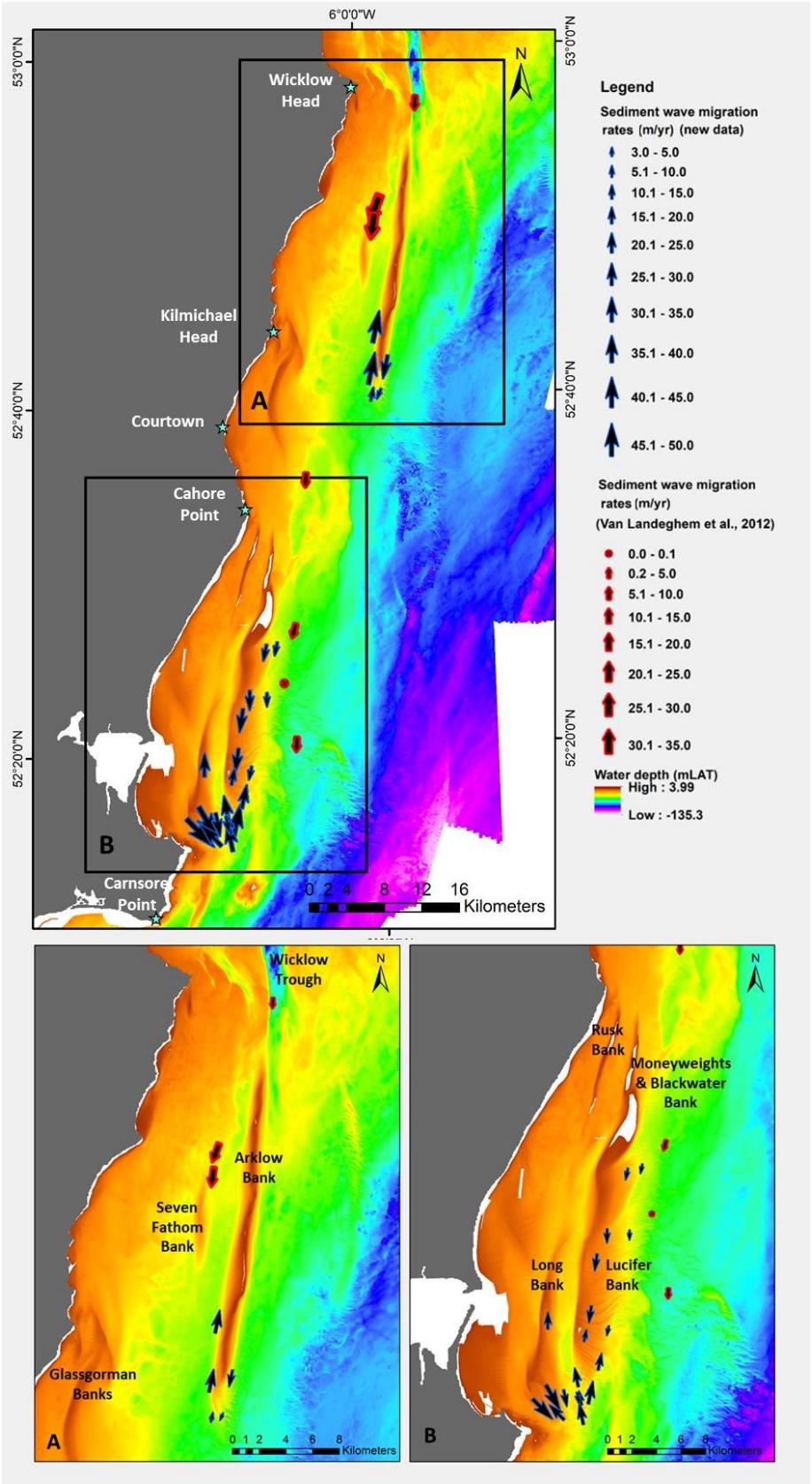


Figure 4 Preliminary Results - Comparison of repeat bathymetry dataset from INFOMAR, MOVE 1 and MOVE 2 Leg 1 datasets. Newly calculated sediment wave migration rates (m/yr) are displayed alongside the work of Van Landeghem et al (2012)

References

Fairley, I., Karunarathna, H., & Chatzirodou, A. (2017). Modelling the Effects of Marine Energy Extraction on Non-Cohesive Sediment Transport and Morphological Change in the Pentland Firth and Orkney Waters. *Scottish Marine and Freshwater Science*, *8*(7), 1–34. https://doi.org/10.7489/1913-1

Hanna, J. E., & Cooper, J. A. G. (2002). Mesoscale Morphological Changes on Linear, Nearshore Sandbanks, Co.Wexford, SE Ireland. *Journal of Coastal Research*, *36*(36), 356–364. https://doi.org/10.2112/1551-5036-36.sp1.356

Knaapen, M. A. F., & Hulscher, S. J. M. H. (2002). Regeneration of sand waves after dredging. *Coastal Engineering*, *46*(4), 277–289. https://doi.org/https://doi.org/10.1016/S0378-3839(02)00090-X

Morelissen, R., Hulscher, S. J. M. H., Knaapen, M. A. F., Németh, A. A., & Bijker, R. (2003). Mathematical modelling of sand wave migration and the interaction with pipelines. *Coastal Engineering*, *48*(3), 197–209. https://doi.org/10.1016/S0378-3839(03)00028-0

Panigrahi, J. K., Ananth, P. N., & Umesh, P. A. (2009). Coastal morphological modeling to assess the dynamics of Arklow Bank, Ireland. *International Journal of Sediment Research*, *24*(3), 299–314. https://doi.org/10.1016/S1001-6279(10)60005-4

Stockmann, K., Riethmüller, R., Heineke, M., & Gayer, G. (2009). On the morphological long-term development of dumped material in a low-energetic environment close to the German Baltic coast. *Journal of Marine Systems*, *75*(3–4), 409–420. https://doi.org/https://doi.org/10.1016/j.jmarsys.2007.04.010.

Sutton, G. (2008). Irish Sea Marine Aggregate Initiative (IMAGIN) Project Synthesis Report Including: Geological Assessment, Environmental Assessment, Morphodynamic Modelling Web-based GIS system, Cost Benefit Analysis, Aggregate Resources and Markets-Wales. *Marine Environment and Health Series,* No. 36.

Van Landeghem, K. J. J., Baas, J. H., Mitchell, N. C., Wilcockson, D., & Wheeler, A. J. (2012). Reversed sediment wave migration in the Irish Sea, NW Europe: A reappraisal of the validity of geometry-based predictive modelling and assumptions. *Marine Geology*, *295–298*, 95–112. https://doi.org/10.1016/j.margeo.2011.12.004

Van Landeghem, K. J. J., Uehara, K., Wheeler, A. J., Mitchell, N. C., & Scourse, J. D. (2009). Post-glacial sediment dynamics in the Irish Sea and sediment wave morphology: Data-model comparisons. *Continental Shelf Research*, *29*(14), 1723–1736. https://doi.org/10.1016/j.csr.2009.05.014

Van Landeghem, K. J. J., Wheeler, A. J., Mitchell, N. C., & Sutton, G. (2009). Variations in sediment wave dimensions across the tidally dominated Irish Sea, NW Europe. *Marine Geology*, *263*(1–4), 108–119. https://doi.org/10.1016/j.margeo.2009.04.003

Warren, W. P., & Keary, R. (1989). The sand and gravel resources of the Irish Sea Basin. *The Irish Sea Basin: A Resource at Risk. Dublin: Geographical Society of Ireland, Special Publication*, (3), 65-79.

Wheeler, A. J., Walshe, J., & Sutton, G. D. (2001). Seabed mapping and seafloor processes in the Kish, Burford, Bray and Fraser Banks area, south-western Irish Sea. *Irish Geography*, *34*(2), 194–211. https://doi.org/10.1080/00750770109555787

Wilson, B. R., Brown, C. J., Sameoto, J. A., Lacharité, M., Redden, A. M., & Gazzola, V. (2021). Mapping seafloor habitats in the Bay of Fundy to assess megafaunal assemblages associated with Modiolus modiolus beds. *Estuarine, Coastal and Shelf Science*, *252*. https://doi.org/10.1016/j.ecss.2021.107294

Xu, J. P., Wong, F. L., Kvitek, R., Smith, D. P., & Paull, C. K. (2008). Sandwave migration in Monterey Submarine Canyon, Central California. *Marine Geology*, *248*(3–4), 193–212.

https://doi.org/10.1016/j.margeo.2007.11.005
Yaghoobi, Mehdi, Mazaheri, ;, Said, Jabbari, & Ebrahim. (2012). Determining Natural Frequency of Free Spanning Offshore Pipelines by Considering the Seabed Soil Characteristics. *Journal of the Persian Gulf*, *3*(June 2012), 25–34. http://jpg.inio.ac.ir/article-1-75-en.pdf

Appendices

I. Multibeam Echo Sounder Line Log

Info					Start				End				Runtime Parameters						Filters
Area	Line id	Type	SVP No.	SOG	Start Date	Start time (UTC)	SOL Lat (dd)	SOL Long (dd)	End Date	End time (UTC)	EOL Lat (dd)	EOL Long (dd)	Coverage	Max Coverage	Pulse Type	Detector	Mode	Frequency	
B9	0000	MBES	2	3.5	30/03/2021	07:09	52.8224493	5.9936971	30/03/2021	07:17	52.81224	5.998606	69|10|69	60/60	AUTO	NORMAL	REL. MEAN HEADING	300 kHz	SPIKE: MEDIUM, RANGE GATE:NORMAL, PHASE RAMP: NORMAL
	0001	MBES		3.3	30/03/2021	07:32	52.814328	5.996396	30/03/2021	07:36	52.82258	5.992205	69|10|69	60/60	AUTO	NORMAL	REL. MEAN HEADING	300 kHz	SPIKE: MEDIUM, RANGE GATE:NORMAL, PHASE RAMP: NORMAL
	0002	MBES		3.3	30/03/2021	07:49	52.82359	5.99089	30/03/2021		52.8118	5.997239	69|10|69	60/60	AUTO	NORMAL	REL. MEAN HEADING	300 kHz	SPIKE: MEDIUM, RANGE GATE:NORMAL, PHASE RAMP: NORMAL
	0003	MBES		3.3	30/03/2021	08:09	52.811314	5.996634	30/03/2021	08:14	52.824394	5.9951	69|10|69	60/60	AUTO	NORMAL	REL. MEAN HEADING	300 kHz	SPIKE: MEDIUM, RANGE GATE:NORMAL, PHASE RAMP: NORMAL
	0004	MBES		3.3	30/03/2021	08:24	52.8229	5.98959	30/03/2021	08:35	52.81128	5.995923	69|10|69	60/60	AUTO	NORMAL	REL. MEAN HEADING	300 kHz	SPIKE: MEDIUM, RANGE GATE:NORMAL, PHASE RAMP: NORMAL
	0005	MBES		3.3	30/03/2021	08:41	52.8111014	5.994801	30/03/2021	08:46	52.82333	5.98869	69|10|69	60/60	AUTO	NORMAL	REL. MEAN HEADING	300 kHz	SPIKE: MEDIUM, RANGE GATE:NORMAL, PHASE RAMP: NORMAL
	0006	MBES		3.3	30/03/2021	08:53	52.82346	5.98787	30/03/2021	09:08	52.810785	5.994186	69|10|69	60/60	AUTO	NORMAL	REL. MEAN HEADING	300 kHz	SPIKE: MEDIUM, RANGE GATE:NORMAL, PHASE RAMP: NORMAL
	0007	MBES		3.3	30/03/2021	09:15	52.80967	5.99004	30/03/2021	09:21	52.8256	5.982331	69|10|69	60/60	AUTO	NORMAL	REL. MEAN HEADING	300 kHz	SPIKE: MEDIUM, RANGE GATE:NORMAL, PHASE RAMP: NORMAL
	0008	MBES		3.3	30/03/2021	09:27	52.8241	5.9814	30/03/2021	09:35	52.814344	5.98615	69|10|69	60/60	AUTO	NORMAL	REL. MEAN HEADING	300 kHz	SPIKE: MEDIUM, RANGE GATE:NORMAL, PHASE RAMP: NORMAL
Info					Start				End				Runtime Parameters						Filters
Area	Line id	Type	SVP No.	SOG	Start Date	Start time (UTC)	SOL Lat (dd)	SOL Long (dd)	End Date	End time (UTC)	EOL Lat (dd)	EOL Long (dd)	Coverage	Max Coverage	Pulse Type	Detector	Mode	Frequency	
B1	0012	MBES	2	4	30/03/2021	11:18	52.6785	5.96786	30/03/2021	11:51	52.71611	5.95097	69|10|69	100/100	Short CW	NORMAL	REL. MEAN HEADING	300 kHz	SPIKE: MEDIUM, RANGE GATE:NORMAL, PHASE RAMP: NORMAL
	0016	MBES		4.5	30/03/2021	11:53	52.7157	5.95304	30/03/2021	12:25	52.67566	5.972349	69|10|69	100/100	Short CW	NORMAL	REL. MEAN HEADING	300 kHz	SPIKE: MEDIUM, RANGE GATE:NORMAL, PHASE RAMP: NORMAL
	0019	MBES		4	30/03/2021	12:28	52.6775	5.97381	30/03/2021	12:40	52.69126	5.9665	69|10|69	100/100	Short CW	NORMAL	REL. MEAN HEADING	300 kHz	SPIKE: MEDIUM, RANGE GATE:NORMAL, PHASE RAMP: NORMAL
Info					Start				End				Runtime Parameters						Filters
Area	Line id	Type	SVP No.	SOG	Start Date	Start time	SOL Lat (dd)	SOL Long (dd)	End Date	End time	EOL Lat (dd)	EOL Long (dd)	Coverage	Max Coverage	Pulse Type	Detector	Mode	Frequency	

						(UTC)				(UTC)									
B2	0022	MBES	2	4.5	30/03/2021	13:06	52.6755	5.99736	30/03/2021	13:54	52.7328	5.984	69|10|69	120/120	Short CW	NORMAL	REL. MEAN HEADING	300 kHz	SPIKE: MEDIUM, RANGE GATE:NORMAL, PHASE RAMP: NORMAL
Info					Start				End				Runtime Parameters						
Area	Line id	Type	SVP No.	SOG	Start Date	Start time (UTC)	SOL Lat (dd)	SOL Long (dd)	End Date	End time (UTC)	EOL Lat (dd)	EOL Long (dd)	Coverage	Max Coverage	Pulse Type	Detector	Mode	Frequency	Filters
A1	0027	MBES	2	5.3	30/03/2021	14:47	52.5875	6.10758	30/02/2021	15:11	52.555	6.1202837	69|10|69	100/100	Short CW	NORMAL	REL. MEAN HEADING	300 kHz	SPIKE: MEDIUM, RANGE GATE:NORMAL, PHASE RAMP: NORMAL
Info					Start				End				Runtime Parameters						
Area	Line id	Type	SVP No.	SOG	Start Date	Start time (UTC)	SOL Lat (dd)	SOL Long (dd)	End Date	End time (UTC)	EOL Lat (dd)	EOL Long (dd)	Coverage	Max Coverage	Pulse Type	Detector	Mode	Frequency	Filters
A2	0030	MBES	2	4	30/03/2020	15:46	52.44605	6.15177	30/03/2021	16:07	52.417	6.1623	69|10|69	100/100	Short CW	NORMAL	REL. MEAN HEADING	300 kHz	SPIKE: MEDIUM, RANGE GATE:NORMAL, PHASE RAMP: NORMAL
Transit to A3																			
Info					Start				End				Runtime Parameters						
Area	Line id	Type	SVP No.	SOG	Start Date	Start time (UTC)	SOL Lat (dd)	SOL Long (dd)	End Date	End time (UTC)	EOL Lat (dd)	EOL Long (dd)	Coverage	Max Coverage	Pulse Type	Detector	Mode	Frequency	Filters
A3	0033	MBES	2		30/03/2021	16:18	52.39179	6.1736		16:35	52.3686	6.183999	69|10|69	100/100	Short CW	NORMAL	REL. MEAN HEADING	300 kHz	SPIKE: MEDIUM, RANGE GATE:NORMAL, PHASE RAMP: NORMAL
Info					Start				End				Runtime Parameters						
Area	Line id	Type	SVP No.	SOG (kts)	Start Date	Start time (UTC)	SOL Lat (dd)	SOL Long (dd)	End Date	End time (UTC)	EOL Lat (dd)	EOL Long (dd)	Coverage	Max Coverage	Pulse Type	Detector	Mode	Frequency	Filters
A4	0035	MBES	2		30/03/2021	16:44	52.35	6.1892		17:13	52.31563	6.205349	69|10|69	100/100	Short CW	NORMAL	REL. MEAN HEADING	300 kHz	SPIKE: MEDIUM, RANGE GATE:NORMAL, PHASE RAMP: NORMAL
Info					Start				End				Runtime Parameters						
Area	Line id	Type	SVP No.	SOG (kts)	Start Date	Start time (UTC)	SOL Lat (dd)	SOL Long (dd)	End Date	End time (UTC)	EOL Lat (dd)	EOL Long (dd)	Coverage	Max Coverage	Pulse Type	Detector	Mode	Frequency	Filters
A5, A6, A15	0038	MBES	2		30/03/2021	17:13	52.31563	6.205349	30/03/2021	18:22	52.2474	6.2392	69|10|69	100/100	Short CW	NORMAL	REL. MEAN HEADING	300 kHz	SPIKE: MEDIUM, RANGE GATE:NORMAL, PHASE RAMP: NORMAL
		MBES			30/03/2021	18:25	52.25	6.242	30/03/2021	18:40	52.28446	6.247	69|10|69	100/100	Short CW	NORMAL	REL. MEAN HEADING	300 kHz	SPIKE: MEDIUM, RANGE GATE:NORMAL, PHASE RAMP: NORMAL
		MBES			30/03/2021		52.2864	6.248378	30/03/2021	19:18	52.25	6.2429	69|10|69	100/100	Short CW	NORMAL	REL. MEAN HEADING	300 kHz	SPIKE: MEDIUM, RANGE GATE:NORMAL, PHASE RAMP: NORMAL
		MBES			30/03/2021	19:24	52.24799	6.23985	30/03/2021	19:39	52.27776	6.22593	69|10|69	100/100	Short CW	NORMAL	REL. MEAN	300 kHz	SPIKE: MEDIUM, RANGE GATE:NORMAL, PHASE

																	HEADING		RAMP: NORMAL
		MBES			30/03/2021	19:42	52.27693	6.227644	30/03/2021	20:03	52.2486	6.24131	69|10|69	100/100	Short CW	NORMAL	REL. MEAN HEADING	300 kHz	SPIKE: MEDIUM, RANGE GATE:NORMAL, PHASE RAMP: NORMAL
Info					Start				End				Runtime Parameters						
Area	Line id	Type	SVP No.	SOG (kts)	Start Date	Start time (UTC)	SOL Lat (dd)	SOL Long (dd)	End Date	End time (UTC)	EOL Lat (dd)	EOL Long (dd)	Coverage	Max Coverage	Pulse Type	Detector	Mode	Frequency	Filters
C1	0056	MBES	2	7.5	30/03/2021	20:42	52.2709	6.08612	30/03/2021	21:04	52.3165	6.06064	69|10|69	100/100	Short CW	NORMAL	REL. MEAN HEADING	300 kHz	SPIKE: MEDIUM, RANGE GATE:NORMAL, PHASE RAMP: NORMAL
		MBES		5.1	30/03/2021	21:09	52.3107	6.05868	30/03/2021	21:43	52.2724	6.0829	69|10|69	100/100	Short CW	NORMAL	REL. MEAN HEADING	300 kHz	SPIKE: MEDIUM, RANGE GATE:NORMAL, PHASE RAMP: NORMAL

National Research Vessels

SHIP-TIME PROGRAMME

RESEARCH SURVEY REPORT

Survey Code:	Survey Name:	Chief Scientist/ Institution
CV21034	Mobility of Sediment Waves and Sand Banks in the Irish Sea Phase 2, Leg 2	Shauna Creane/ University College Cork

Section A: Award Summary

Title of Research Survey and Survey Code:	Mobility of Sediment Waves and Sand Banks in the Irish Sea Phase 2 (MOVE 2), Leg 2 Survey Code: CV21034	
Co-Ordinator/ Chief Scientist:	Shauna Creane	
Vessel used for ship-time:	*RV Celtic Voyager* ☒ *RV Celtic Explorer* ☐	
Total number of days at sea:	10 days: - 2 days (weather downtime – Rosslare Harbour) - 5 day (workable at sea) - 3 day mob/demob at Cork Harbour (4th Dec), Rosslare Harbour (8th Dec) and Dublin (13th Dec)	
Total number of grant-aided ship-time days awarded:	16 days in total: - 5 days (MOVE 2 Leg 1; CV21035) 26th March – 1st April 2021 - 10 days 4th – 13th December (MOVE 2 Leg 2; CV21034) NOTE: 3 additional days were added to CV21034 (increasing the survey to 10 days) due to large amount of weather downtime during CV21035.	
Dates of survey:	4th – 13th December 2021	
Mobilisation/Demobilisation Ports	Mobilisation: Cork (Horgan's Quay) Port Call (Wednesday 8th December 2021): Rosslare Harbour where sparker was demobbed, the sparker technician (Lukasz Pawilowski) and one scientist (Ruaihri Starchan) got off board, and one AB (Frank Kenny) boarded. Demobilisation: Dublin	
Survey Personnel:	*No. of Scientists* *3*	*No. of Students* *0*
Final Report Completed by:	Shauna Creane (Chief Scientist) SFI Research Centre for Energy, Climate and Marine (MaREI), University College Cork	**Date**: 07/04/2022

Section B: Description of the Research Survey

B1 Overview of survey personnel

Leg 1: pre-port call at Rosslare Harbour. 4th – 8th December 2021

Names of crew	***Role***	***Number of Days onboard CV21034***
John O'Regan	Master	10
Stephen Lantry	Mate	10
Brendan Barry	C/Eng	10
Thomas Byrne	Motorman	10
Alec Carthy	AB	10
Paul Shannon	Cook	10
Tim Dennehy	2nd Officer	10
Lukasz Pawlikowski	Tech	5

Names scientific personnel	***Institute/ Department/ Course***	***Position (undergraduate/ post graduate etc)***	***Number of Days***
Shauna Creane (Chief Scientist)	School of Civil & Environmental Engineering, University College Cork; SFI Research Centre for Energy, Climate and Marine (MaREI). Funded under the Irish Research Council's Employment-Based Postgraduate Programme, (grant number: EBPPG/2019/158)	PhD (Engineering)	10
Ruaihri (Scientist & MMO)	University College Cork (UCC)	Research Assisstant	5
Felix Butschek (Scientist)	UCC	Research Assisstant	10

Leg 2: post-port call at Rosslare Harbour. 8th – 13th December 2021

Names of crew	***Role***	***Number of Days onboard CV21034***
John O'Regan	Master	10
Stephen Lantry	Mate	10
Brendan Barry	C/Eng	10
Thomas Byrne	Motorman	10
Alec Carthy	AB	10
Paul Shannon	Cook	10
Tim Dennehy	2nd Officer	10
Frank Kenny	AB 2	6

Names of scientific personnel	***Institute/ Department/ Course***	***Position (undergraduate/ post graduate etc)***	***Number of Days***
Shauna Creane (Chief Scientist)	School of Civil & Environmental Engineering, University College Cork; SFI Research Centre for Energy, Climate and Marine (MaREI). Funded under the Irish Research Council's Employment-Based Postgraduate Programme, (grant number: EBPPG/2019/158)	PhD (Engineering)	10
Felix Butschek (Scientist)	UCC	Research Assisstant	10

B2 Objectives

Briefly outline the overall objectives of the research survey.
Please state if objectives have changed from the original proposal. If survey included a training element please outline clearly.

The Irish Sea is an enclosed, tidal sea with varying bathymetric conditions and distinct geomorphological features. A series of well-documented, linear, north-south trending sandbanks are found close inshore and parallel to the Wexford, Wicklow and South Dublin coast. These banks form a punctuated line parallel to the coast with breaks between them maintained by strong currents and sediment movement (Wheeler et al., 2001). The banks themselves are believed to be quasi-stable over historical time, in dynamic equilibrium with tidal and wave conditions, and offer important coastal protection (Warren & Keary, 1989). Bathymetry and side-scan sonar records from some banks reveal evidence of seabed mobility on, and adjacent to, the banks (Creane et al., under review; Wheeler et al., 2001). Furthermore, sandwaves increase in amplitude towards the edge of the banks suggesting that currents are highest close to the banks. This is probably responsible for the maintenance of the banks' relative positions. Elsewhere in the Irish Sea, sediment waves of varying sizes and morphologies are well documented, consisting of very large (3–18 m in height), normal-shaped and trochoidal-shaped features (Creane et al., under review; Van Landeghem et al., 2009a). Some features are noted to migrate up to 70 m per year. Others are considered moribund or having formed under previously high hydrodynamic conditions or as part of glacial processes (Creane et al., under review; Van Landeghem et al., 2009b). Some sediment wave features are related to glacial features, such as tunnel valleys, which form seabed channels where current flow is thought to be augmented.

In general, significant vagrancies exist regarding seabed morphodynamics and the potential for sediment mobility in the Irish Sea. Many processes associated with morphodynamic and hydrodynamic change, such as sediment wave migration, have been well documented and quantified in fluvial environments where hydrodynamic data is more readily available in both high spatial and temporal resolutions. Furthermore, physical testing (e.g. flume tanks) mean that scaled-down real-world testing allows a greater insight into these processes that can be

easily studied. However, in deeper offshore environments such as the Irish Sea, this level of data is not available. Additionally, the Irish Sea environment offers more controlling factors on morphodynamic change and so is considerably more complex (Creane et al., 2021). Therefore, the technical challenge of gathering data in this environment is a trying one. Data that can be gathered include traditional seabed mapping techniques, such as multi-beam echosounder to image the seabed and sub-bottom profiling to visualise seabed structure below the surface. Both these methods offer an image of the seabed and sub-seabed at a given point in time at it's collection but have limited value in fully understanding a mobile sediment environment. Scientifically, the challenge is to utilise this data robustly to develop an understanding of how the seabed has developed temporally and spatially. MOVE 2 (CV21035 & CV21034) will build upon the high-quality geophysical datasets that are collected by MOVE 1 (CV20010 & CV20035) in south Irish Sea. By conducting high precision, high-resolution repeat surveys, time-lapse imagery of the seafloor can be generated. Repeat surveys reveal differences in seafloor bathymetry, accretion and rate of bedform migration (Creane et al., under review; Van Landeghem et al., 2012).

To date the key economic reasons for quantifying seabed change include the needs to monitor dredged shipping channels (Knaapen & Hulscher, 2002); the dispersal of dredged spoil (Stockmann et al., 2009); the volume of marine aggregate resources (Sutton, 2008); and the impact of engineering works such as cables, pipelines and energy infrastructure on the seabed (Morelissen et al., 2003; Yaghoobi et al., 2012). Scientific drivers include the needs to calibrate bedload transport equations and to gain insights into natural geomorphological dynamics such as bedforms (Xu et al., 2008) and implications for benthic habitats (Wilson et al., 2021). However, when sequential multibeam surveys are conducted with long time intervals, short term bedform dynamics may be missed and/or misinterpreted. Currently, there is a distinct paucity of high-resolution repeat bathymetry data in the south Irish Sea and only a limited amount of work has been done on bedform mobility on a local scale (Creane et al., under review; Hanna & Cooper, 2002; Panigrahi et al., 2009; Van Landeghem et al., 2012). Sparse small-scale overlaps have been identified on the edges of INFOMAR surveys allowing only 2D cross-sectional analysis of bedforms. These overlaps fail to include high temporal resolution and eliminates the opportunity to study crest variability along a 3D mobile bedform. For the MOVE project survey areas, INFOMAR's 2009 and 2012 surveys provide great baseline data, however, a difference of 11 years and 8 years respectively between these datasets and the MOVE 1 survey fail to provide the high temporal resolution necessary for high quality bedform mobility analysis. It is crucial to capture these dynamic changes through frequent interannual bathymetry surveys. MOVE 2 (CV21035 & CV21034) drives this campaign by capturing, repeat interannual high resolution geophysical datasets to be analysed alongside the 2020 MOVE 1 survey campaign.

By combining repeat geophysical data with sediment sampling and long-term hydrodynamic monitoring equipment such as acoustic doppler current profilers (ADCP), we can garner a better understanding of temporal changes at a higher resolution. Therefore, the big scientific challenge to understanding seabed morphodynamics is how to observe these changes in a reasonable resolution with high-confidence. Furthermore, another significant challenge to assessing the risk of morphodynamic evolution, and sediment mobility, poses to critical engineering and environmental projects is how can future changes in seabed morphodynamics be confidently predicted.

Sediment transport modelling offers an innovative means to study this behaviour, and predict where seabed mobility may be an issue in the future. By bringing together geoscientists and engineers, this project will make a significant

contribution to the existing knowledge through collaboratively addressing these problems. Precise, interannual surveying is also crucial for robust sediment transport and morphological modelling. For example, a morphological model developed by Fairley et al (2017) produced unrealistic bed level changes of 5m over one lunar month over a sediment wave assemblage in Pentland Firth and Orkley Waters. Without multiple multi-beam bathymetry surveys, it was impossible to determine whether this result was due to model inaccuracies or natural processes. Analysis of repeat bathymetry surveys is key to accurate validation of these types of numerical models. Up-to-date bathymetry data is also a vital basic input into sediment transport and morphological models in order to provide high quality, accurate outputs (Fairley et al., 2017). Outputs are only as good as your input. There is a significant lack of high resolution morphological modelling in the south Irish Sea and it is a critical step in understanding both present day and future hydro- and morphodynamics. MOVE 1 and MOVE 2 combined will not only supply these pivotal repeat geophysical datasets, but also collect a new innovative way of providing sensitivity testing to suspended sediment transport modelling through calculating suspended sediment concentration (SSC) derived from ADCP acoustic backscatter. This method correlates direct measurement of SSC (through water sampling) with ADCP acoustic backscatter, providing a time series of suspended sediment transport throughout the vertical water column at a fixed point.

An integrated use of repeat geophysical data, geological groundtruthing and numerical modelling is key to understanding both regional and local scale hydro- and morphodynamics of the south Irish Sea. With the sudden increase in offshore infrastructure developments in the Irish Sea, expert knowledge of seabed morphodynamics and sediment mobility is of huge importance.

The scientific goal of the MOVE 2 survey can be broken down into six objectives:

1. To build upon MOVE survey phase 1 by gathering critical high resolution interannual geological and geophysical datasets to investigate the nature of sediment mobility and morphodynamic changes in selected sites of the Irish Sea known for highly complex hydrodynamics;
2. To gather interannual geophysical data and time series suspended sediment concentration data to validate and to provide sensitivity analysis for numerical models currently under development;
3. To examine the physical processes occurring on the seafloor with respect to seabed morphodynamics pertinent to engineering projects;
4. To provide data to validate 2D hydrodynamic, sediment transport and morphological numerical models that will form the basis of understanding the complex morphodynamics and it's underlying drivers in the south Irish Sea;
5. To gather critical site specific environmental data to feed in to modelling efforts to help predict future changes in seabed morphology in reaction to anthropogenic impacts and climate change;
6. To build up a unique Geographical Information System (GIS) based database of offshore seabed morphology and sediments in the Irish Sea that can be used in future engineering and environmental studies.

These objectives can be achieved on the with the *RV Celtic Voyager* over the two granted survey legs:

1. Leg 1 (CV21035): 26th March to 1st April 2021

2. Leg 2 (CV21034): 4th to 13th December 2021

This report specifically covers the work completed by MOVE 2 Leg 2 whereby the main survey area is located off the east coast of Ireland, in the southern section of the Irish Sea.

Leg 2 (CV21034) involved mainly targeted sparker acquisition and MBES in the first half of the survey 4th – 8th Dec). After a port call, the second half (8th – 13th) mainly consisted of gravity coring, water sampling, targeted sediment sampling and MBES and Chirp in specified areas. Three were identified as MOVE 2 priority areas for investigation; Area B, C and D. These areas were refined from areas surveyed by MBES during MOVE phase 1 in October 2020 and MOVE 2 Leg 1 in March 2021. Two low priority areas were identified as back up in case of unworkable weather conditions or plan changes; Area A, E and F.

Area A
Area A is geographically located off the east coast of Wexford. It comprises Long Bank, Lucifer Shoals, Blackwater Bank, Moneyweights Bank and Rusk Bank. Sediment waves are found throughout the area. Whilst the top of the banks are shallow and impossible to survey using the RV Celtic Voyager due to restrictive depths, the flanks and base of the bank, along with sediment wave assemblages have been previously surveyed by CV09_03, CV13_01, CV12_01, CV20036, CV21035. This is a low priority area.

Area B
Area B lies to the east of Area A. It is notable for its variety of sediment wave features including normal-shaped, large sediment waves and troichoidal-shaped features. It was previously investigated by the CV12_02 and CV20036. This a high priority area.

Area C
Area C lies between Area B and Area D. It is notable for its variety of sediment wave features including normal-shaped, large sediment waves and some minor bank-like structures. It was previously investigated by CV12_01, CV20036, CV21035. This is a high priority area.

Area D
Lies between Lucifer-Blackwater Bank complex and Arklow Bank in a bed load convergence zone. This area is characterised by a series of mobile asymmetric sediment waves displaying a bed load convergence zone in conjunction with very large immobile trochoidal sediment waves displaying with associated large scour features. This is a high priority area.

Area E
Area E lies over an offshore independent sediment wave assemblage that contains complex morphologies and migration parameters. This area was previously surveyed by CV11 and CV12. This is a low priority area.

Area F
Area F lies over Wicklow Trough a submarine channel off the coast of Wicklow Head. It contains a variety of active bedforms such as sediment waves. This area is broken down into sub-priority areas. It was previously surveyed by CV09 and KRY16. This is a low priority area.

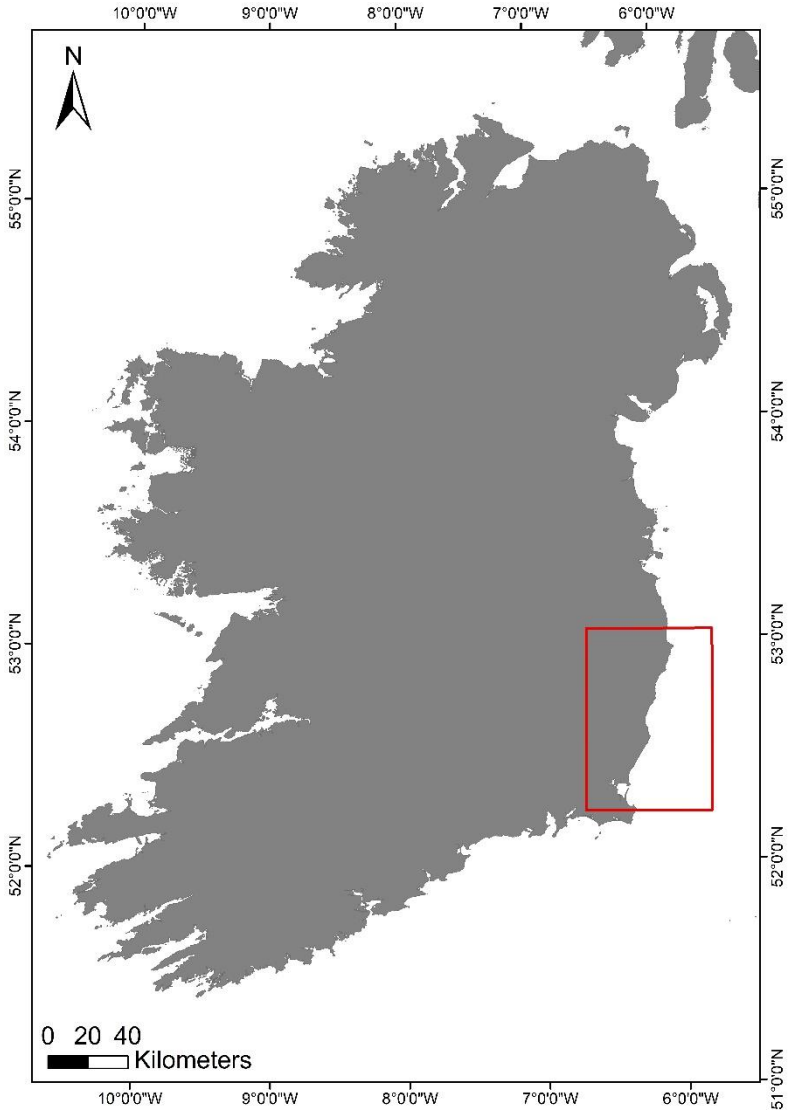


Figure 1 Proposed study area (red box) at a regional scale in the Irish Sea

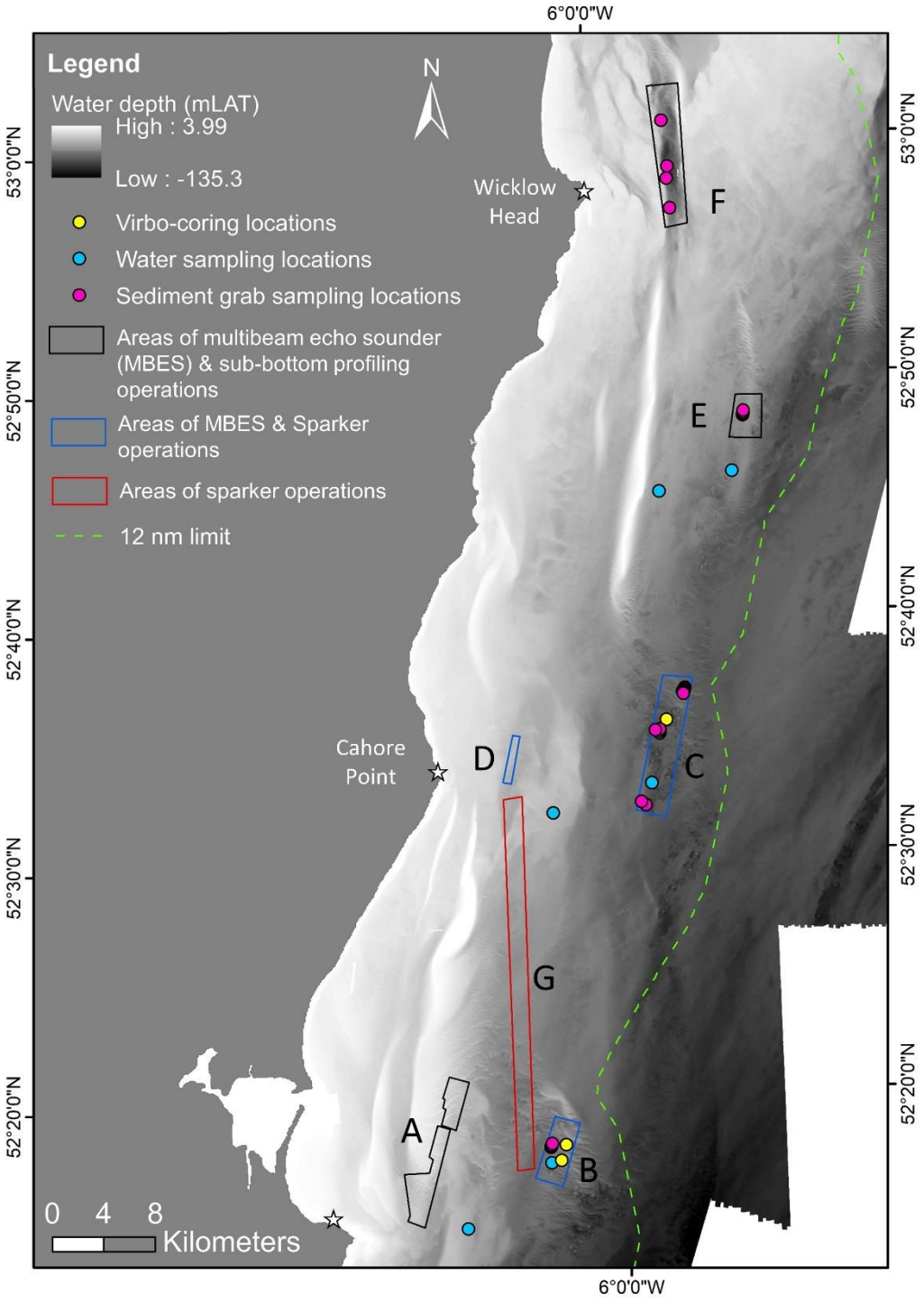


Figure 2 Proposed MOVE 2 Leg 2 survey areas

B3 Overview of research survey

Provide a narrative overview of the research survey including survey timelines
The information provided in this section should not exceed 5 pages (excluding tables and maps)

ALL TIMES IN UTC

Saturday 04th December 2021

12:30 All scientific personnel arrive at vessel at Horgans Quay in Cork Harbour for mobilisation. Follow COVID procedures onboard.

12.35 Induction to the vessel by the master, John O'Regan.

13:30 All crew and all scientific personnel participate in toolbox talk for the use of the Sparker equipment.

14:00 Work with technician, Lukasz Pawilkowski, to ensure sparker equipment is set up correctly ready for use on Sunday 05th December. Also set up of SIS operation ready for acquisition and consult MMO to ensure all plans are set for.

17:30 Dinner

18:00 Depart Horgans Quay for voyage to priority site C. Plan is to begin MMO 30min pre-watch at sunrise on arrival at the site. Carry out an SVP dip and deploy Sparker equipment under strict MMO and health and safety guidelines.

Sunday 05th December 2021

08:00 Wind and wave conditions to dangerous to move out directly to offshore priority site B, transit northwards towards the site at 4 knots closer to shore for shelter. Wind speeds are 34 knots which is 7 on the Beaufort scale.

09:00 Conditions improve slightly where winds are force 6 to allow MBES acquisition but not CTD (SVP) or Sparker deployment. Begin MBES acquisition.

11:30 Conditions improve enough to begin sparker equipment deployment (Figure 3). Wind speeds are force 5. Sea state is choppy.

11:50 MMO 30 minute pre-watch begins. SVP dip.

12:20 Sparker soft start begins

13:00 Sparker at full power – run test line to adjust parameters. Continue MBES acquisition while adjusting Sparker parameters.

13:47 Begin sparker acquisition. Continue MBES acquisition at site C.

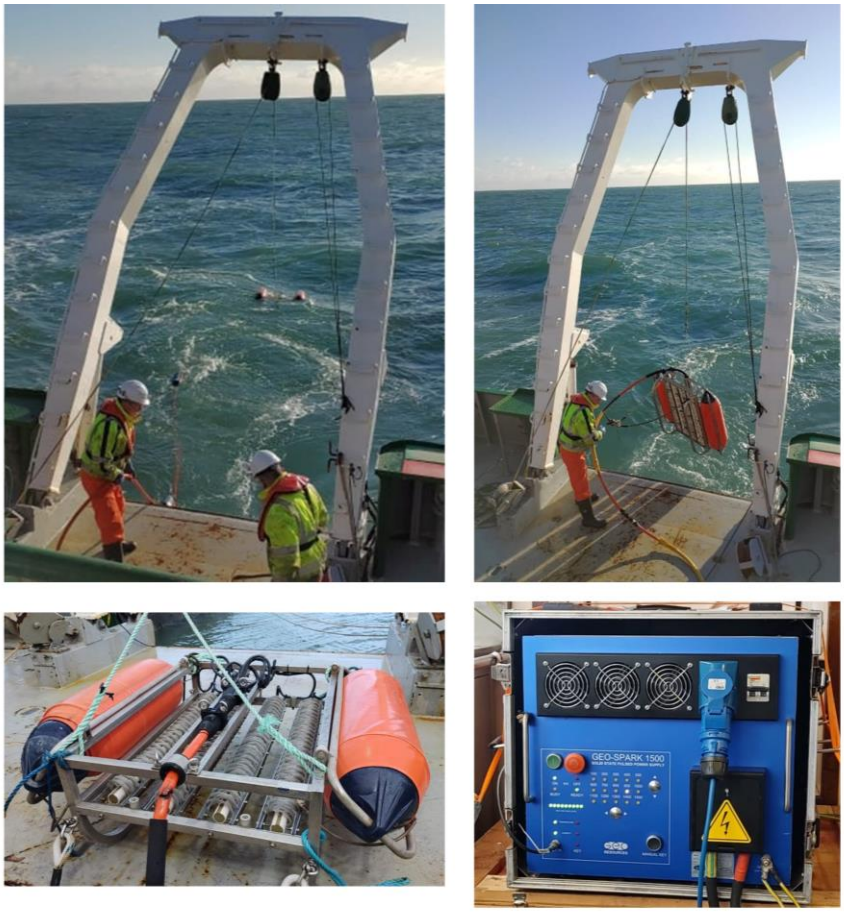


Figure 3 Sparker deployment onboard the RV Celtic Voyager during survey CV21034

Monday 06th December 2021

02:26 Complete MBES and Sparker acquisition at site C.

02:29 Begin sparker and MBES target transit line between site C to site B.

05:31 Complete transition acquisition line and arrive at site B. Begin sparker and MBES acquisition at site B until 10:27.

09:00 Weather forecast predicts unworkable predictions for Monday night right through to Thursday morning due to Storm Barra pushing in from the south-west. Predicted condtions given in screenshot below given taken from https://www.windy.com/ . Previous plan is to have a port call in Rosslare Harbour on Wednesday 8th December 2021 but due to storm we need to be in the port Monday night.



10:42 Begin targetted sparker and MBES transect line in area G.

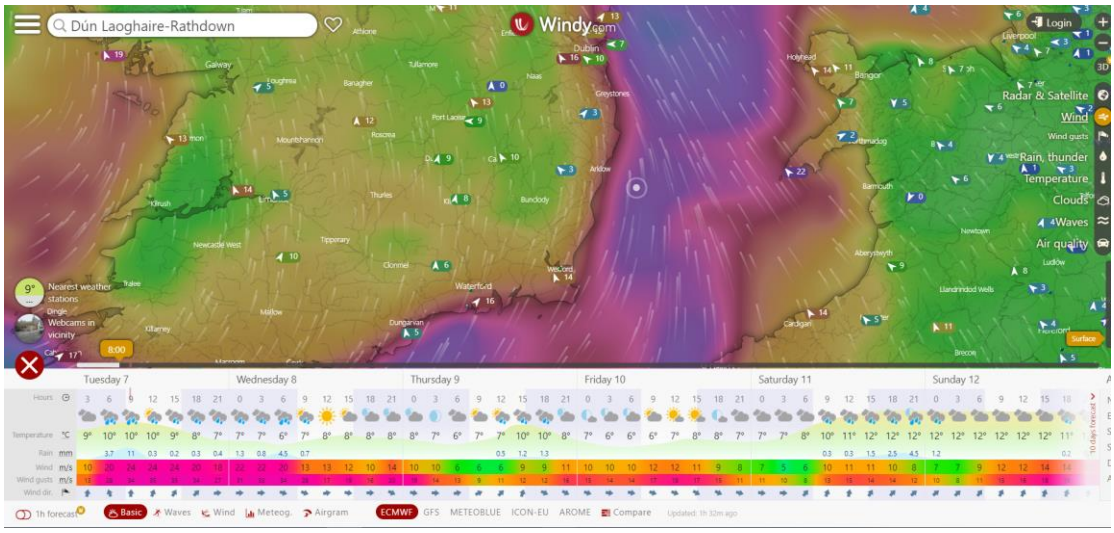
13:51 Finish sparker and MBES acquisition. Crew safely retrieve sparker. Once on deck, burning issue with sparker wire is noted by crew and sparker technician and is subsequently reported.

14:00 Begin transit to Rosslare Harbour for shelter from incoming storm.

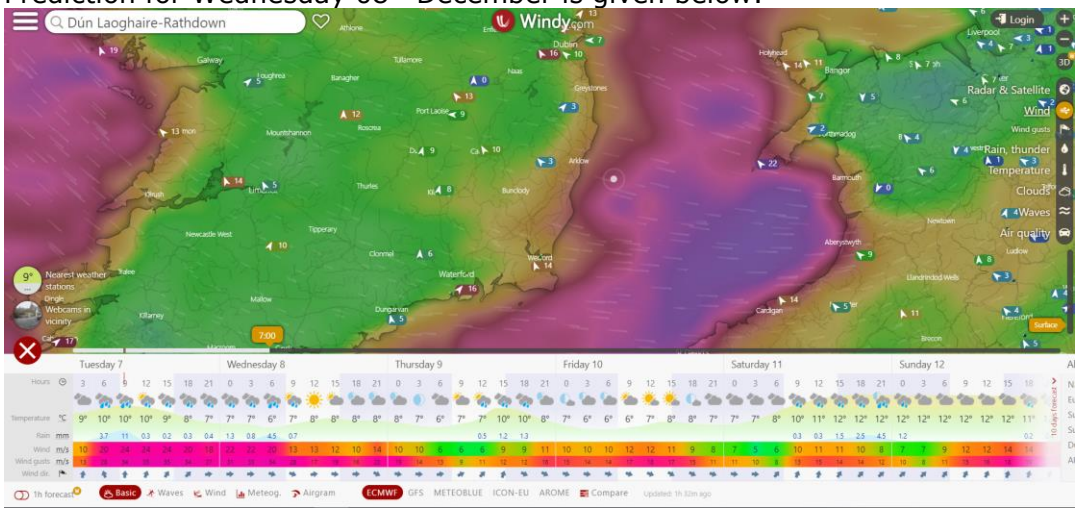
16:00 Arrive at Rosslare Harbour.

Tuesday 07th December 2021

08:00 Port-side in Rosslare Harbour. Weather and sea-state conditions too bad to sail. Screenshot of conditions in the Irish Sea and over our priority site C is outlined below which has been retrieved from https://www.windy.com/.

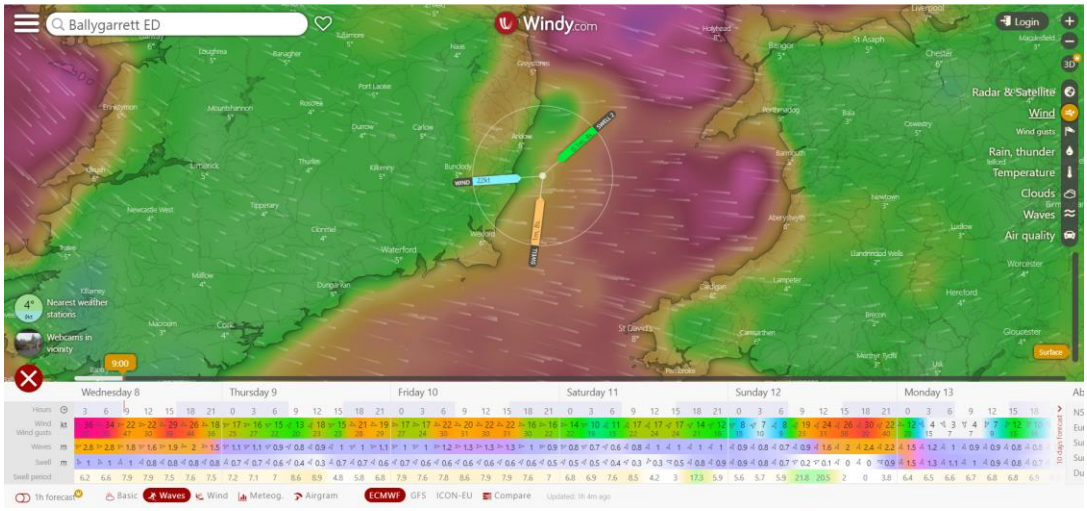


Prediction for Wednesday 08th December is given below:

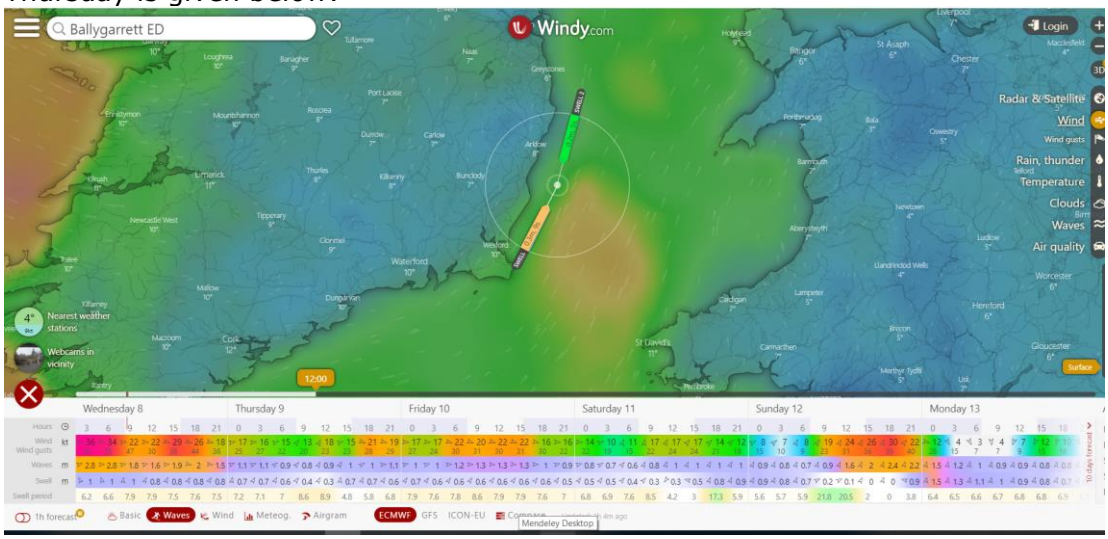


Wednesday 08th December 2021

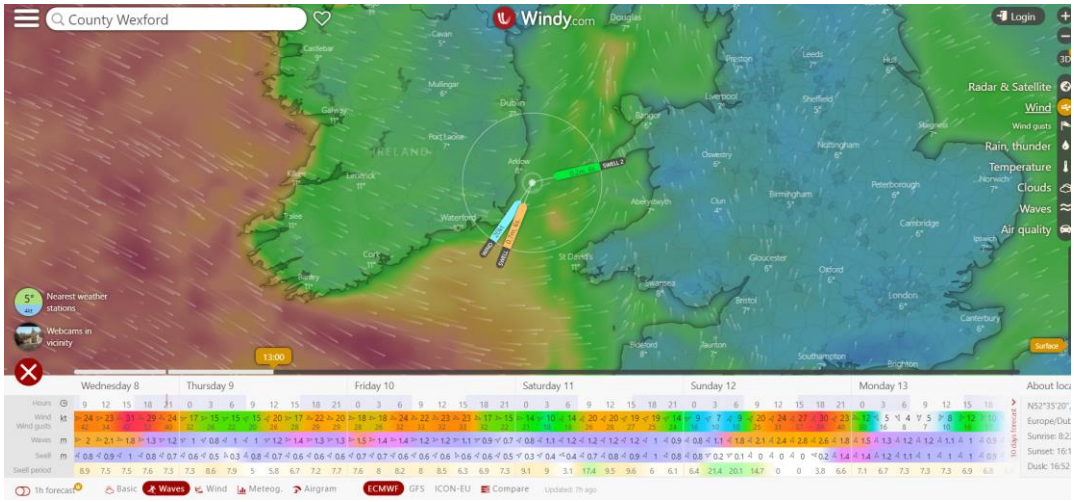
08:00 Port-side in Rosslare Harbour. Conditions too bad to sail. Conditions according to https://www.windy.com/ for today.



08:00 Predicted conditons for Thursday 10th December. According to weather forecast, plan to carry out gravity cores and grab/shipek sediment sampling tomorrow as weather conditions deteriorate later in the week. Prediction for Thursday is given below:

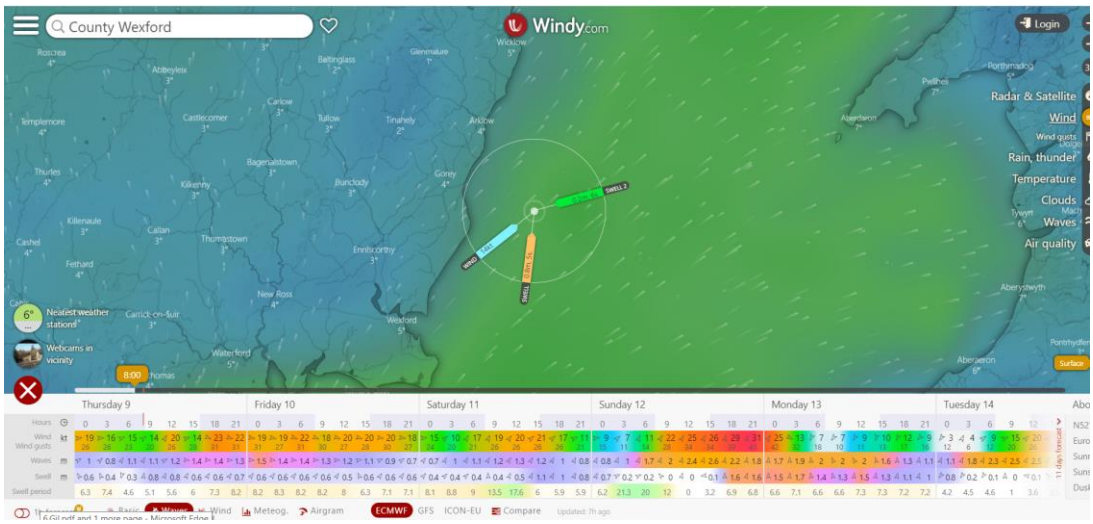


20:30 Weather and sea-state conditions worsen according to updated forecast. Potential window for grab and core sampling before lunch. Plan is to shelter and/or survey near shore sites until windows open to move out to offshore priority sites.



Thursday 09th December 2021

08:00 Depart Rosslare Harbour. Set sail for site C, priority site to carry out gravity coring, grab/shipek sampling and water sampling.



11:06 Arrive at site C. Failed gravity core attempt (Figure 4). There is a strong drift, surface currents are > 2 knots therefore too dangerous to have the gravity core in the water during this strong drift. First attempt showed gravity core at 45° angle to the vessel. Switch to day grab sampler (Figure 5).



Figure 4 Gravity core attempt during CV21034

11:23 12 day grab attempts at site C, 11 successful attempts.



Figure 5 Day grab sampling in the Irish Sea during offshore survey CV21034

13:52 Carry out a CTD deployment in order to retreive an SVP for MBES acquisition.

14:17 MBES acquisition at site C

15:55 Break off MBES line to travel to water sample site W1 at mid-ebb tide. According to ROMS model max ebb depth-averaged current at this location is @17:07.

17:00 CTD and water sampling at W1 (Figure 6). Water samples for suspended sediment concentrations were taken on the upcast. 12 niskin bottles were fired at 1m intervals from the bottom. 10 niskin bottles were successful. Water depth at beginning of CTD was 32.8 m, at the end of CTD was 33.5 m. Sampling started at 28 m.



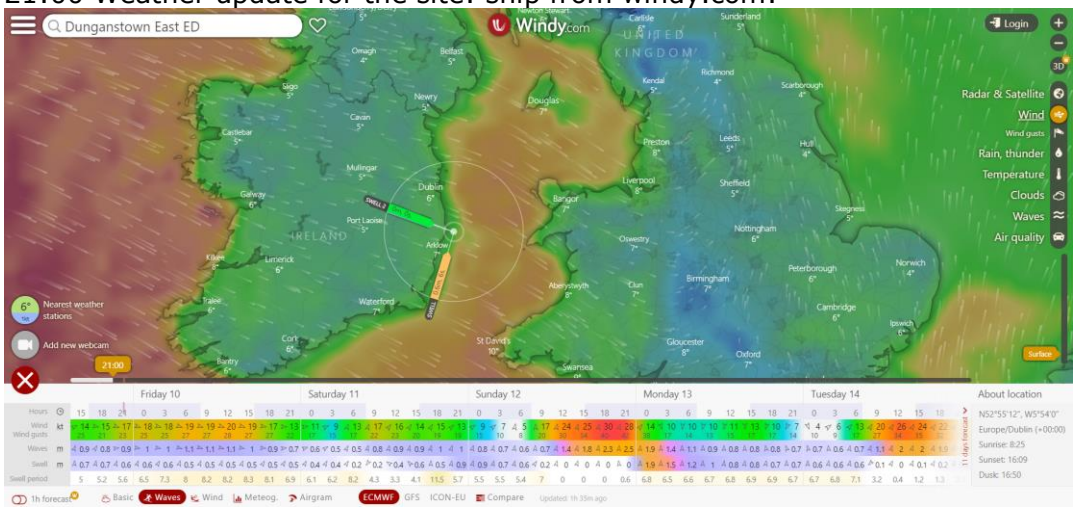
Figure 6 Water sampling during CV21034 in order to analyse suspended sediment concentration in different locations of the Irish Sea

17:05 Begin transit from to water sample site W1 to W2. According to ROMS model, the maximum ebb depth-averaged current at this location occurs @17:25.

17:57 Water sample at site W2. Carry out MBES and chirp acquisiton at site C.

20:10 Finish MBES & chirp acquistionat site C. Transit to site D for MBES.

21:00 Weather update for the site: snip from windy.com:

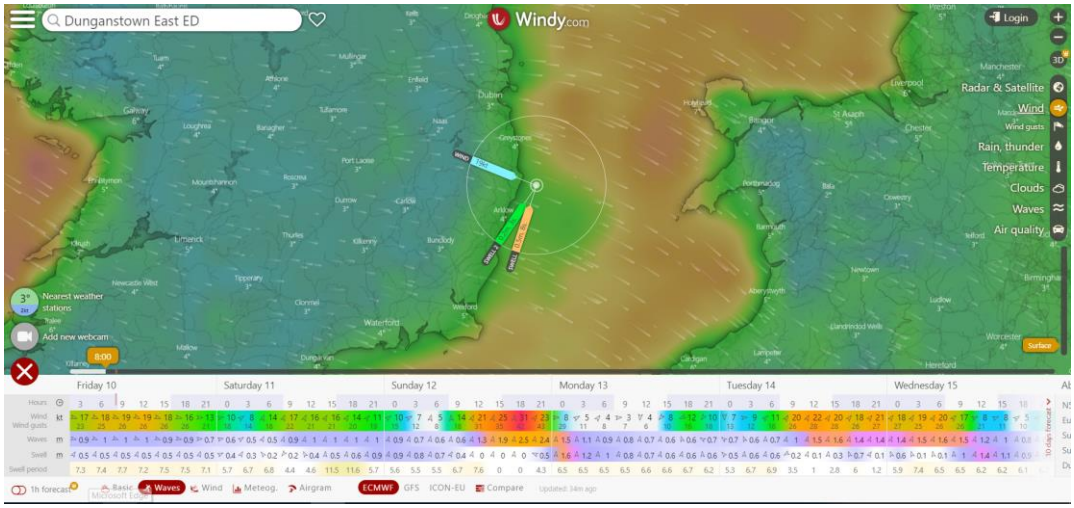


21:07 MBES and chirp at site D until 22:23.

22:23 Transit to site F over night for MBES acquistion on the 10th December.

Friday 10th December 2021

08:00 on-site F, weather conditions workable. See extract from windy.com below.



08:08 CTD deployment at site F to acquire Sound Velocity Profile (SVP) for MBES acquisition. MBES and chirp acquisition at site F.

13:35 Finish MBES acquisition. 7 day grab samples were attempted at the site, 2 were successful due to the presence of very coarse sediment. Transit to site E.

16:02 Collect 4 day grab samples at site E. Carry out MBES acquisition of the crossline at site E.

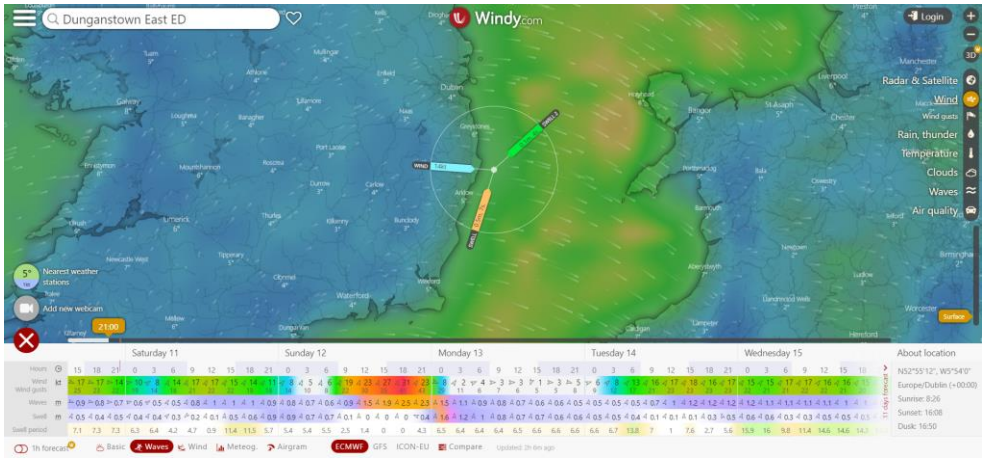
17:05 Transit to water sampling site W5. According to ROMS model, maximum ebb depth-averaged currents at this location are at 17:53.

18:04 Water sample at W5. Transit to water sampling site W6. According to the ROMS model, maximum ebb depth-averaged currents at this location are at 18:15.

18:50 Water sample at W6.

19:11 MBES at site C.

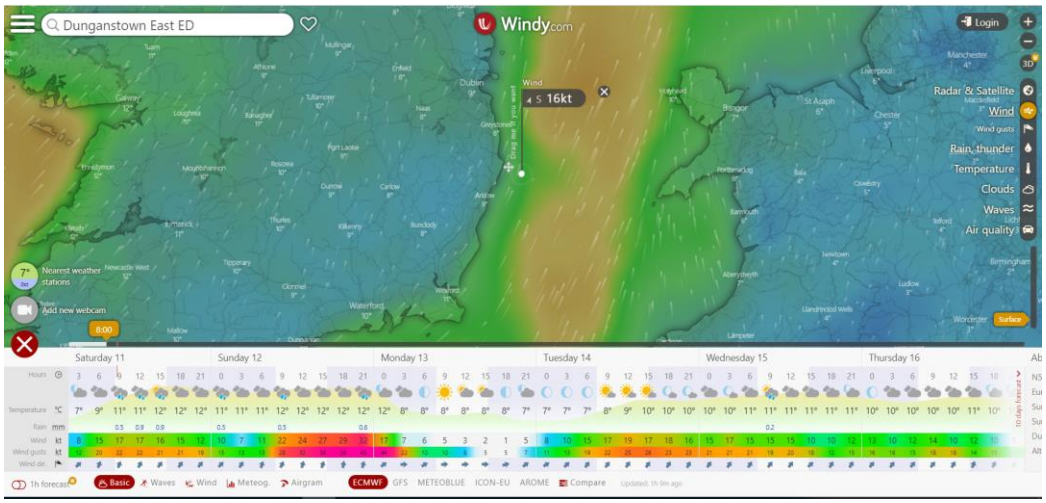
21:00 Weather update, conditions workable. Extract from windy.com below.



00:45 Transit to site F overnight.

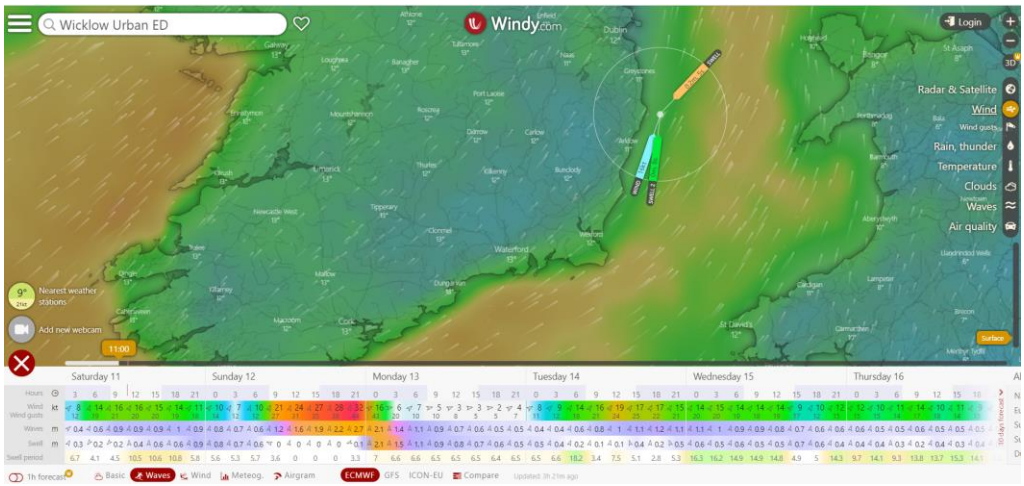
Saturday 11th December 2021

08:00 Weather update, conditions workable. Extract from windy.com given below.



08:20 MBES acquition at site Fa.

11:00 Weather update: conditions workable. Extract from windy.com is given below:

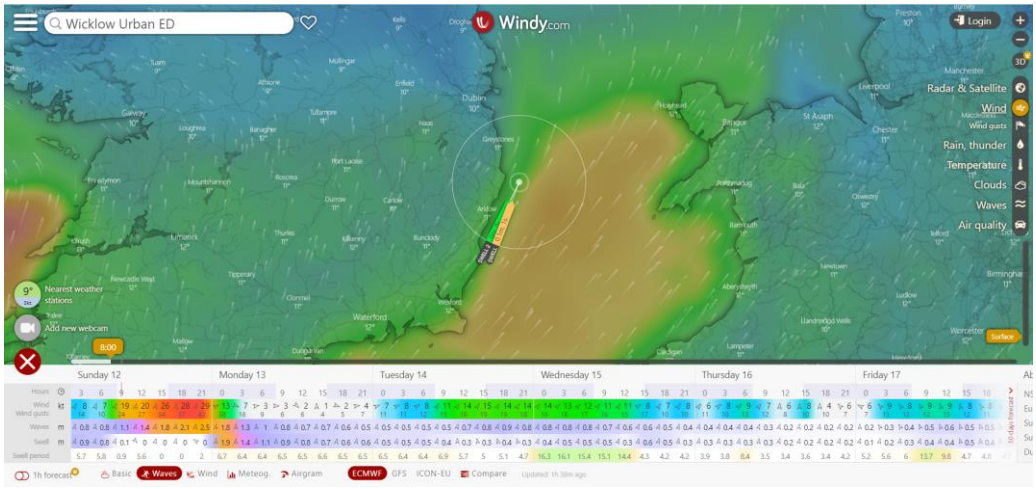


13:18 8 day grabs were attempted at site F, 7 of which were successful.

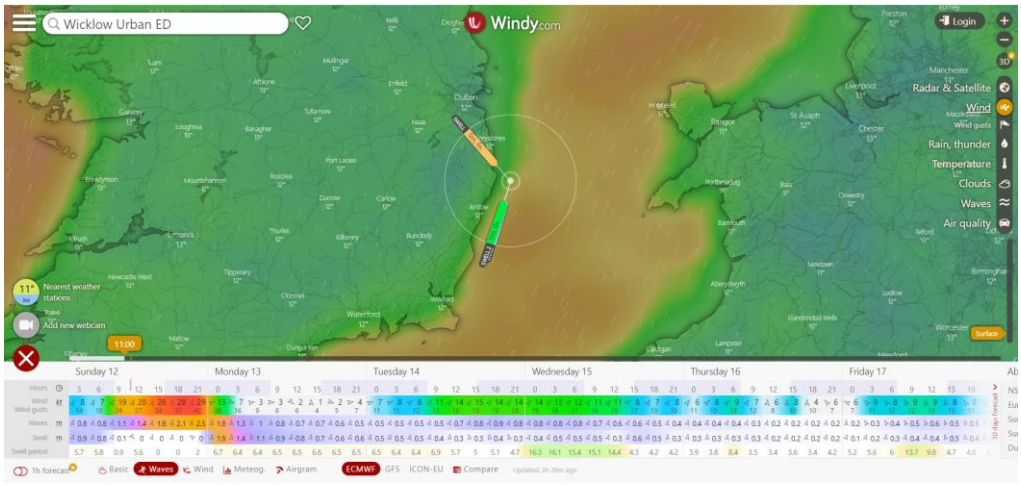
15:02 MBES acquisition at site Fb.

Sunday 12th December 2021

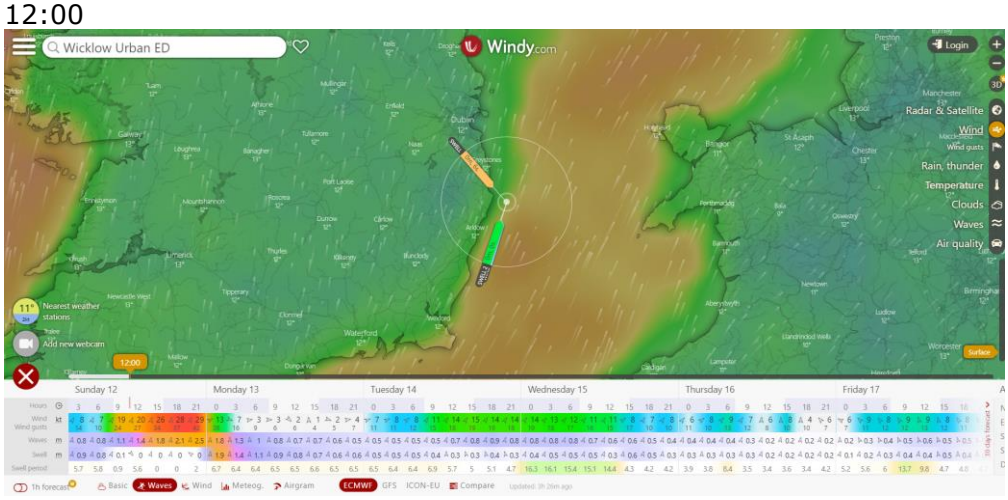
08:00 Weather update: conditions workable. See extract from windy.com below. Begin MBES acquisition at site Fb.



11:00 Weather/sea-state conditions deteriorating but still workable. Extract from wind.com below.



12:00



SURVEY END

B4 Benefits, impact and contribution of the outputs to marine research and the marine sector in general.

Outline clearly the specific outcomes and benefits of the research survey.
The information provided in this section should not exceed 1/2 page (excluding tables and maps)

I. Main Deliverables

This survey generated essential data for on-going PhD (Shauna Creane) and group (iCRAG/GDG/MaREI) research as well as future PhD research. The following deliverables will arise from this survey and ongoing research:

1. High resolution multibeam, chirp and sparker survey data over previously surveyed sediment wave features both independent of large morphological features (e.g. sand banks) and those located within submarine channels in the Irish Sea;
2. Water samples that will be used to calculate suspended sediment concentration (SSC) at different locations in the Irish Sea which will be directly used as a sensitivity analysis for sediment transport modelling outputs alongside ADCP-derived SSC;
3. Elucidate the sediment dispersal and seabed morphodynamic processes in a complex hydrodynamic regime on the south-western sector of the Irish Sea through geophysical data analysis and dynamically coupled hydrodynamic, spectral wave and sediment transport modelling;
4. An evaluation of local scale sediment mobility in the area and subsequent impacts on offshore engineering structures;
5. Presentations at national and international meetings with acknowledgements;
6. Publications in peer-review journals.

These deliverables contribute directly to a significant baseline of data critical for a morphodynamic atlas of the Irish Sea along with a database of sediment hydrodynamic and morphodynamic parameters for designated areas. The objective of which is to be used by stakeholders and infrastructure developers as critical engineering and environmental data for projects.

II. Specific Benefits and Impacts

The MOVE 2 Leg 2 survey fundamentally assists the better understanding of seabed sediment dynamics in the Irish Sea. This has direct implications for a number of sectors, including:

- The construction of offshore renewable energy by identifying areas where it is feasible to profitably build foundations and site cable routes ashore;
- The improving of habitat maps to inform environmental assessments and fisheries research by integrating additional site condition information;
- The developing of critical baseline information and models with which to assess climate change effects including coastal erosion.

Furthermore, the MOVE 2 Leg 2 survey has the following benefits and impacts:

1. Training and sea-going experience for current, active researchers and students;
2. Filling specific data gaps in our understanding of offshore seabed processes and sub-structure;
3. A strengthening of collaboration between parties involved in the project, including iCRAG, UCD, GDG, UCC and MaREI;
4. An increase in research capacity and better interdisciplinary research on the island of Ireland;

5. Development of different techniques and technology in seabed mapping in Irish Waters;
6. Value-add to existing datasets (e.g. INFOMAR);

In general, the MOVE project fosters a firm collaboration between strongly technical researchers actively addressing some of the key challenges facing Ireland in terms of managaing seabed resources and developing offshore renewable energy sources to help us meet our climate change targets. It addresses some of the key priorities set out in Harnessing Our Ocean Wealth Roadmap which aims to build a thriving maritime economy that harnesses economic growth whilst also being being cognisant of healthy ecosystems and sustainably managing our activities at sea. The MOVE project does so by providing key baseline data and research for both and promotes future collaboration between academia and industry to help achieve these goals. Specifically, the project supports the Ocean Renewable Energy Development Plan (OREDP) in technically assessing key areas for renewable energy installation development and critically de-risking them.

B5 Data

Provide a description of the data collected from the research survey, the usage of the data and how it will be stored.

The information provided in this section should not exceed 1/2 page (excluding tables and maps)

MBES, Chirp and Sparker datasets were collected at five, four and two sites respectively. Survey design comprised targeted lines over sediment waves and sand banks identified using INFOMAR and MOVE 1 (CV20010/CV20035) datasets. The collected data act as precise, high resolution, time-lapse information to compare with baseline INFOMAR, MOVE 1, and MOVE 2 Leg 1 datasets. An example bathymetry dataset collected during this survey is displayed in Figure 8. An example DTM of difference is presented in Figure 9 and a classified processed backscatter dataset is shown in Figure 10. ADCP deployment, water sampling and sediment sampling that couldn't be carried out over MOVE 2 will be carried out in late September 2022 upon receipt of appropriate foreshore licence. In total, 25 successful grab samples (Table 1) and 42 water samples were taken (Table 2), locations of both are displayed in Figure 7. Table 3 displays the data type collected during CV21034, its usage, and how it will be stored.

Table 1 Successful day grab sediment samples collected in the south-western Irish Sea during CV21034

LONG	LAT	Survey Code	Sample ID	Description
-5.91407667	52.612425	CV21034	3	Gravelly Sand
-5.911705	52.61496833	CV21034	4	Gravelly Sand
-5.90947333	52.61719833	CV21034	5	Gravelly Sand
-5.912975	52.61443333	CV21034	6	Sandy Gravel
-5.96276667	52.53628667	CV21034	7	Gravelly Sand
-5.96813333	52.54011333	CV21034	9	Sandy Gravel
-5.943005	52.58462833	CV21034	10	Gravelly Sand
-5.94279667	52.586365	CV21034	11	Gravelly Sand
-5.94262167	52.58805167	CV21034	12	Gravelly Sand
-5.94633667	52.58770667	CV21034	13	Sandy Gravel
-5.93353	52.59399667	CV21034	14	Sandy Gravel
-5.91167167	53.01334333	CV21034	20	Gravel
-5.90948	52.97045167	CV21034	25	Slightly Gravelly Sand
-5.90293667	52.951595	CV21034	26	Sandy Gravel

-5.83110667	52.80931	CV21034	27	Gravelly Sand
-5.831085	52.807035	CV21034	28	Sand
-5.83120333	52.80557167	CV21034	29	Gravelly Sand
-5.83151167	52.80423833	CV21034	30	Gravelly Sand
-5.9054383	52.94674	CV21034	33	Gravelly Sand
-5.9053483	52.9591467	CV21034	34	Sandy Gravel
-5.9094033	52.97486	CV21034	36	Slightly Gravelly Sand
-5.9096717	52.990035	CV21034	37	Gravelly Sand
-5.9033967	53.0342983	CV21034	38	Sandy Gravel
-5.902345	53.0462733	CV21034	39	Sandy Gravel
-5.9079683	53.0590033	CV21034	40	Sandy Gravel

Table 2 Location and description of water samples taken during CV21034

Date	09/12/2021	09/12/2021	10/12/2021	10/12/2021
Time (UTC)	17:00	17:57	18:04	18:50
Station No	16	17	31	32
LONG (CTD in water)	-6.06595	-5.95325	-5.93142	-5.84831
LAT (CTD in water)	52.5316	52.5513	52.7491	52.8159
LONG (CTD last bottle fired)	-6.0651	-5.9524	-5.9328	-5.8484
LAT (CTD last bottle fired)	52.5281	52.5470	52.7460	52.8141
Water Depth at Station (m) CTD in	32.8	68	41.8	57
Water Depth at Station (m) CTD out	33.5	71.2	42	57.5
Sampling interval	samples taken at 1 m intervals between 17 m to 28 m water depth	samples taken at 1 m intervals between 53 m to 64 m water depth	samples taken at 1 m intervals between 27 m to 38 m water depth	samples taken at 1 m intervals between 42 m to 53 m water depth
No. of successful samples	10 out of 12	10 out of 12	12 out of 12	10 out of 12

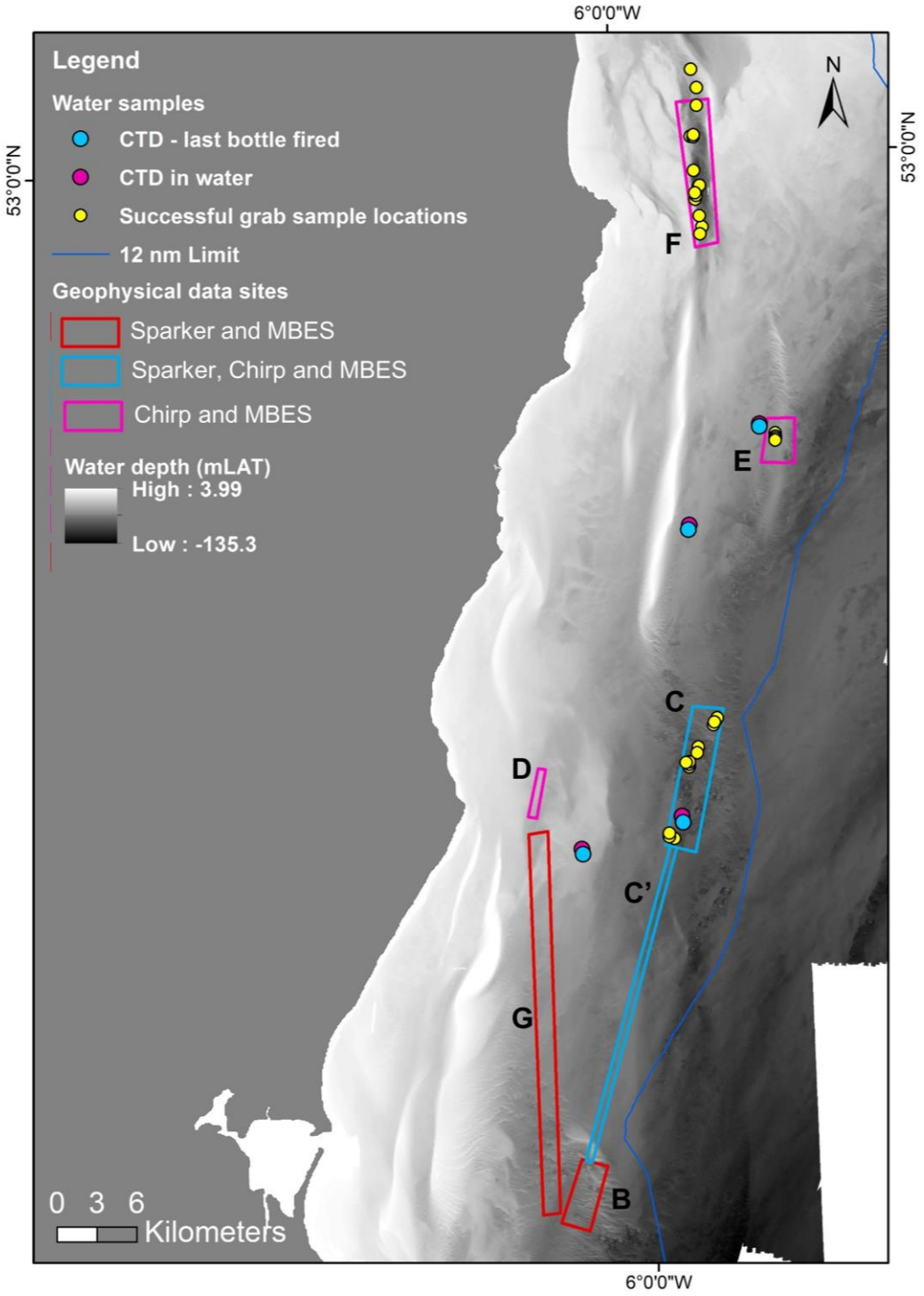


Figure 7 Offshore site locations where geophysical, geological and oceanographic data were collected in the south-western Irish Sea during CV21034

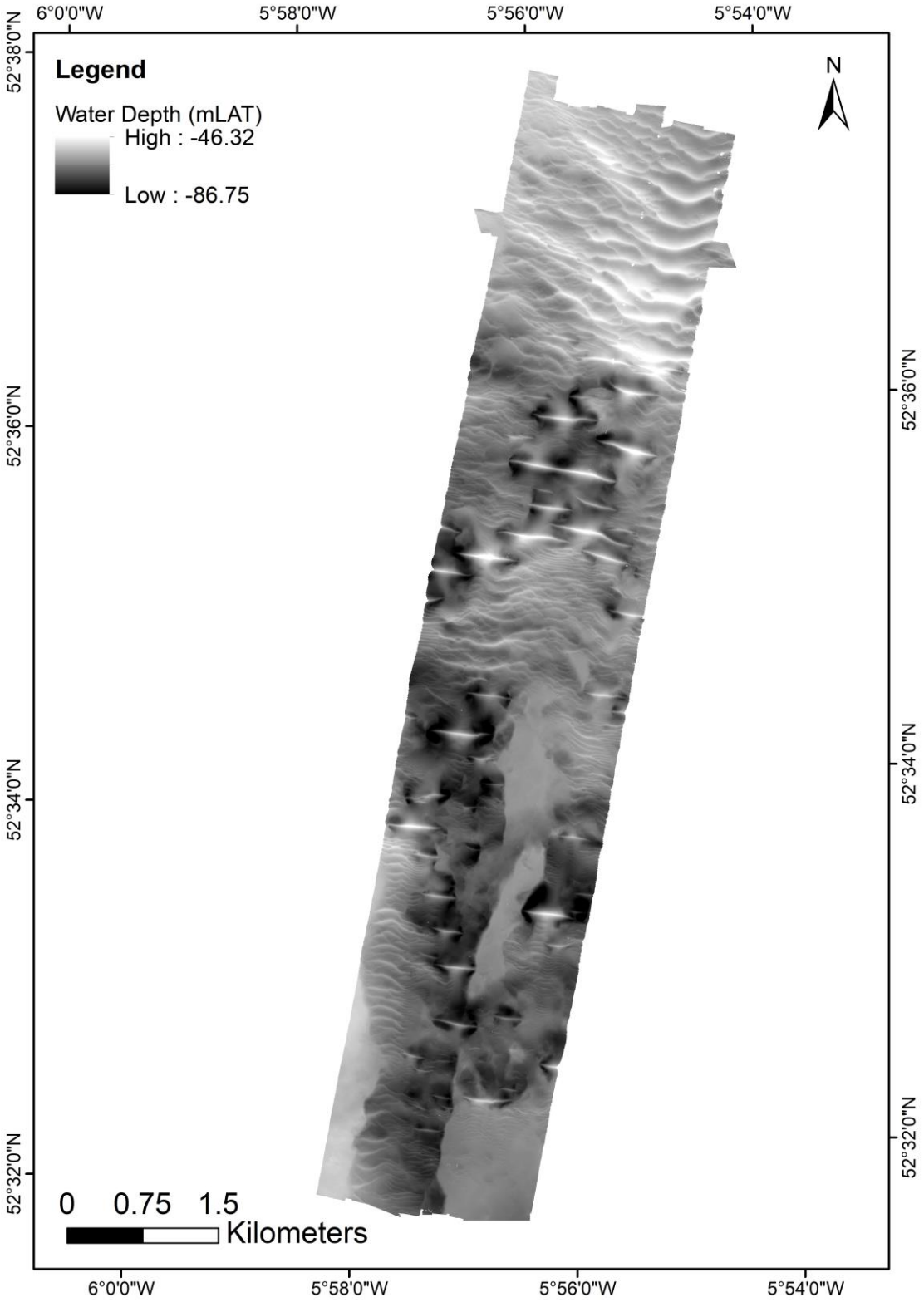


Figure 8 MOVE 2 Leg 2 processed bathymetry dataset revealing sediment waves at site C

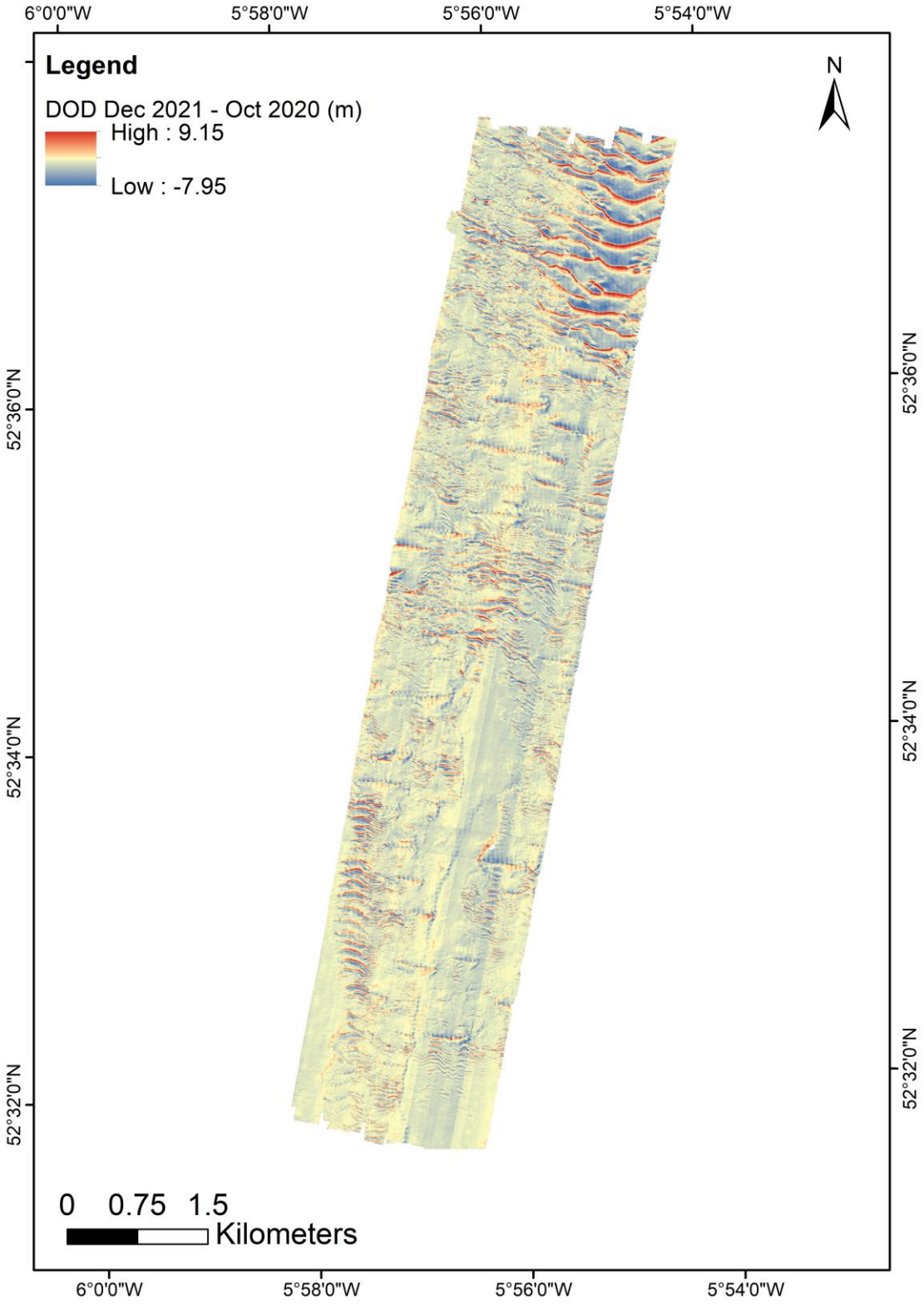


Figure 9 DTM of Difference (DOD) at site C using bathymetry datasets collected in Oct 2020 during MOVE 1 and in December 2021 on MOVE 2 Leg 2 (CV21034)

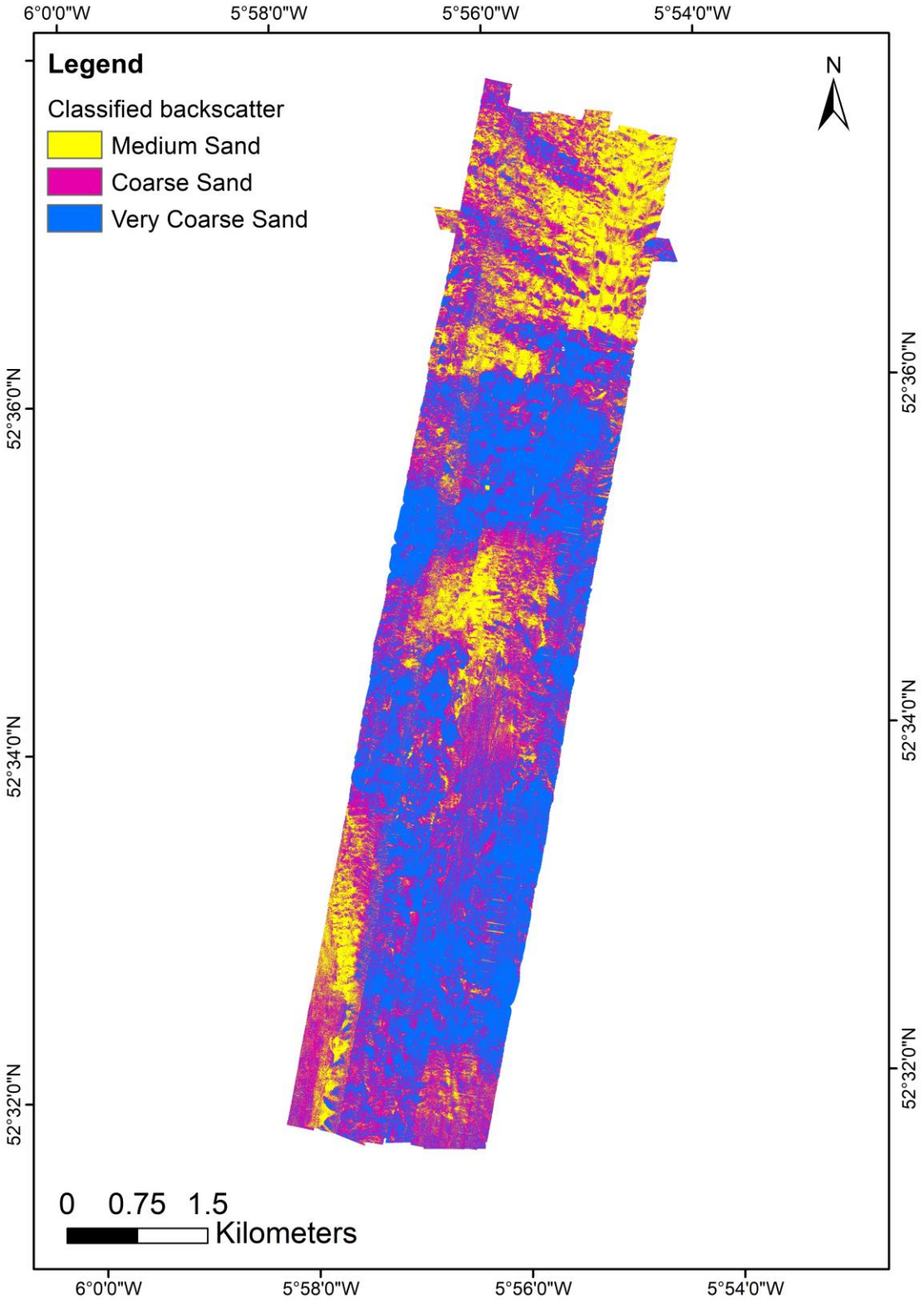


Figure 10 Processed backscatter from site C, collected during CV21034, which has been classified using 'ISO Cluster Unsupervised Classification' in ArcGIS and groundtruthed using collected sediment samples both from MOVE 2 Leg 1 and Leg 2 surveys

Table 3 Data collected on MOVE 2 Leg 2 (CV21034)

Instrument	***Data Type***	***Usage***	***Storage***
Multibeam Echo Sounder	Bathymetry	Time-lapse data for sediment transport studies; Seabed stability and morphological evolution studies; Input and validation of long term numerical modelling work	Internal server of Gavin and Doherty Geosolutions (GDG); External Hardrives; shared through publications and presentations
	Backscatter	Ground truth with in-situ sediment sampling data and incorporate into seabed mobility and morphological evolution studies alongside bathymetry datasets	Internal server of Gavin and Doherty Geosolutions (GDG); External Hardrives; shared through publications and presentations
Sub-bottom profiler (Chirp system) Sparker	Sub-bottom	3D imaging of the sea floor shallow sub-surface and sediment layering; Environemental management, including establishing baseline data to support environmental monitoring; Classification maps for seabed habitats; Analyse internal structure of sediment waves and depth of mobile layer for seabed mobility studies for input into offshore infrastructure works;	Internal server of Gavin and Doherty Geosolutions (GDG); External Hardrives; shared through publications and presentations
Water Samples	Water samples	Water samples will be processed to derive suspended sediment concentration. This will be used for sensitivity analysis of sediment transport modelling outputs.	Water samples sent to laboratory for analysis. Results stored as CSV files and Shapefiles on Internal server of Gavin and Doherty Geosolutions (GDG), External Hardrives and shared through publications and presentations
Grab samples	Grab samples	Both used to assess seabed mobility in conjunction with geophysical datasets and as input into MIKE 21/3 numerical modelling	Processed in lab; PSD results stored on Internal server of Gavin and Doherty Geosolutions (GDG), External Hardrives and shared through publications and presentations

References

Creane , S., O'Shea, M., Coughlan, M., Murphy, J. (2021). The Irish Sea Bed Load Parting Zone: Is it a mid-sea hydrodynamic phenomenon or a geological theoretical concept? Estuarine, Coastal and Shelf Science, 263(107651). https://doi.org/10.1016/j.ecss.2021.107651

Creane, S., Coughlan, M., O'Shea, M., Murphy, J. (under review). Development and dynamics of sediment waves in a complex morphological and tidal dominant system: southern Irish Sea.

Fairley, I., Karunarathna, H., & Chatzirodou, A. (2017). Modelling the Effects of Marine Energy Extraction on Non-Cohesive Sediment Transport and Morphological Change in the Pentland Firth and Orkney Waters. *Scottish Marine and Freshwater Science*, *8*(7), 1–34. https://doi.org/10.7489/1913-1

Hanna, J. E., & Cooper, J. A. G. (2002). Mesoscale Morphological Changes on Linear, Nearshore Sandbanks, Co.Wexford, SE Ireland. *Journal of Coastal Research*, *36*(36), 356–364. https://doi.org/10.2112/1551-5036-36.sp1.356

Knaapen, M. A. F., & Hulscher, S. J. M. H. (2002). Regeneration of sand waves after dredging. *Coastal Engineering*, *46*(4), 277–289. https://doi.org/https://doi.org/10.1016/S0378-3839(02)00090-X

Morelissen, R., Hulscher, S. J. M. H., Knaapen, M. A. F., Németh, A. A., & Bijker, R. (2003). Mathematical modelling of sand wave migration and the interaction with pipelines. *Coastal Engineering*, *48*(3), 197–209. https://doi.org/10.1016/S0378-3839(03)00028-0

Panigrahi, J. K., Ananth, P. N., & Umesh, P. A. (2009). Coastal morphological modeling to assess the dynamics of Arklow Bank, Ireland. *International Journal of Sediment Research*, *24*(3), 299–314. https://doi.org/10.1016/S1001-6279(10)60005-4

Stockmann, K., Riethmüller, R., Heineke, M., & Gayer, G. (2009). On the morphological long-term development of dumped material in a low-energetic environment close to the German Baltic coast. *Journal of Marine Systems*, *75*(3–4), 409–420. https://doi.org/https://doi.org/10.1016/j.jmarsys.2007.04.010.

Sutton, G. (2008). Irish Sea Marine Aggregate Initiative (IMAGIN) Project Synthesis Report Including: Geological Assessment, Environmental Assessment, Morphodynamic Modelling Web-based GIS system, Cost Benefit Analysis, Aggregate Resources and Markets-Wales. *Marine Environment and Health Series,* No. 36.

Van Landeghem, K. J. J., Baas, J. H., Mitchell, N. C., Wilcockson, D., & Wheeler, A. J. (2012). Reversed sediment wave migration in the Irish Sea, NW Europe: A reappraisal of the validity of geometry-based predictive modelling and assumptions. *Marine Geology*, *295–298*, 95–112. https://doi.org/10.1016/j.margeo.2011.12.004

Van Landeghem, K. J. J., Uehara, K., Wheeler, A. J., Mitchell, N. C., & Scourse, J. D. (2009). Post-glacial sediment dynamics in the Irish Sea and sediment wave morphology: Data-model comparisons. *Continental Shelf Research*, *29*(14), 1723–1736. https://doi.org/10.1016/j.csr.2009.05.014

Van Landeghem, K. J. J., Wheeler, A. J., Mitchell, N. C., & Sutton, G. (2009). Variations in sediment wave dimensions across the tidally dominated Irish Sea, NW Europe. *Marine Geology*, *263*(1–4), 108–119. https://doi.org/10.1016/j.margeo.2009.04.003

Warren, W. P., & Keary, R. (1989). The sand and gravel resources of the Irish Sea Basin. *The Irish Sea Basin: A Resource at Risk. Dublin: Geographical Society of Ireland, Special Publication*, (3), 65-79.

Wheeler, A. J., Walshe, J., & Sutton, G. D. (2001). Seabed mapping and seafloor processes in the Kish, Burford, Bray and Fraser Banks area, south-western Irish Sea. *Irish Geography*, *34*(2), 194–211. https://doi.org/10.1080/00750770109555787

Wilson, B. R., Brown, C. J., Sameoto, J. A., Lacharité, M., Redden, A. M., &

Gazzola, V. (2021). Mapping seafloor habitats in the Bay of Fundy to assess megafaunal assemblages associated with Modiolus modiolus beds. *Estuarine, Coastal and Shelf Science*, *252*. https://doi.org/10.1016/j.ecss.2021.107294

Xu, J. P., Wong, F. L., Kvitek, R., Smith, D. P., & Paull, C. K. (2008). Sandwave migration in Monterey Submarine Canyon, Central California. *Marine Geology*, *248*(3–4), 193–212. https://doi.org/10.1016/j.margeo.2007.11.005

Yaghoobi, Mehdi, Mazaheri, ;, Said, Jabbari, & Ebrahim. (2012). Determining Natural Frequency of Free Spanning Offshore Pipelines by Considering the Seabed Soil Characteristics. *Journal of the Persian Gulf*, *3*(June 2012), 25–34. http://jpg.inio.ac.ir/article-1-75-en.pdf

Appendices

I. Multibeam Echo Sounder Line Log

Info					Start				End			
Area	Line id	Type	SVP No.	SOG	Start Date	Start time (UTC)	SOL Lat (dd)	SOL Long (dd)	End Date	End time (UTC)	EOL Lat (dd)	EOL Long (dd)
C	0001	MBES	1	4.5	05/12/2021	09:00	52.5314	5.96776	05/12/2021	09:53	52.5944	5.9442
	0002	MBES		4	05/12/2021	10:01	52.603	5.9405	05/12/2021	10:22	52.6276	5.9315
	0004	MBES		4.5	05/12/2021	10:30	52.6266	5.9296	05/12/2021	10:46	52.5298	5.9668
	0005	MBES		4	05/12/2021	13:10	52.5233197	5.9487624	05/12/2021	14:49	52.6241	5.908
	0006	MBES		5	05/12/2021	14:57	52.6243	5.9124	05/12/2021	16:15	52.5271	5.9497
	0007	MBES		4	05/12/2021	16:22	52.5288	5.9558	05/12/2021	17:45	52.6258	5.9186
	0008	MBES		4	05/12/2021	17:56	52.6245	5.9100	05/12/2021	19:28	52.527047	5.9473742
	0009	MBES		4	05/12/2021	19:45	52.5284952	5.9530337	05/12/2021	20:52	52.6264032	5.9152631
	0010	MBES		4	05/12/2021	21:19	52.6124518	5.9045278	05/12/2021	21:37	52.6166906	5.94157375
	0011	MBES		4	05/12/2021	21:58	52.6294639	5.9307831	05/12/2021	23:17	52.5299	5.969
	0012	MBES		4.5	05/12/2021	23:26	52.5291	5.9583	06/12/2021	00:52	52.6295	5.9211
	0013	MBES		4	06/12/2021	01:00	52.6258	5.9237	06/12/2021	02:26	52.5293	5.9611
	0014	MBES		4 (up to 6 coming online)	06/12/2021	02:29	52.5244	5.9646	06/12/2021	06:17	52.2738	6.0947
B	0015	MBES	1	5 (up to 6)	06/12/2021	06:26	52.2705	6.0848	06/12/2021	06:59	52.318	6.0588
	0016	MBES		4	06/12/2021	07:29	52.3035	6.0896	06/12/2021	07:46	52.2977287	6.0570843
	0017	MBES		4	06/12/2021	08:06	52.3181	6.0611	06/12/2021	08:49	52.2698	6.0875
	0018	MBES		5	06/12/2021	08:56	52.2707	6.0802	06/12/2021	09:29	52.3167	6.0548
	0019	MBES		4	06/12/2021	09:47	52.3170	6.0570	06/12/2021	10:27	52.2697	6.0830
	0020	MBES		3	06/12/2021	10:42	52.2783	6.1139	06/12/2021	13:51	52.4724216	6.1144794

C	0021	MBES	15	5	09/12/2021	14:17	52.5864705	5.9418066	09/12/2021	15:05	52.5292745	5.9637254
	0022	MBES		4	09/12/2021	15:17	52.5269082	5.94245	09/12/2021	15:55	52.5735438	5.9247127
	0023	MBES		4	09/12/2021	18:34	52.5724072	5.9251814	09/12/2021	19:18	52.6237154	5.9053989
	0024	MBES		4	09/12/2021	19:38	52.6264198	5.9263492	09/12/2021	20:10	52.586454	5.9419663
D	0025	MBES	15	4	09/12/2021	21:07	52.5871531	6.1065656	09/12/2021	21:38	52.5528713	6.119188
	0026	MBES		4	09/12/2021	21:45	52.5547203	6.1202842	09/12/2021	22:12	52.588119	6.1077376
	0027	MBES		4	09/12/2021	22:19	52.5845388	6.110884	09/12/2021	22:23	52.5843454	6.1055603
F	0028	MBES	18	4	10/12/2021	08:32	52.9334608	5.9088663	10/12/2021	09:26	52.9966791	5.9179039
	0029	MBES		4	10/12/2021	09:33	52.9967815	5.9149354	10/12/2021	10:24	52.9308833	5.905523
	0030	MBES		5	10/12/2021	10:34	52.9323651	5.9046209	10/12/2021	11:20	52.9984519	5.9141465
	0031	MBES		5	10/12/2021	11:28	52.9970685	5.912308	10/12/2021	12:20	52.9317343	5.9029599
	0032	MBES		5	10/12/2021	12:28	52.9320318	5.9014762	10/12/2021	13:11	52.9970938	5.9106372
	0033	MBES		5	10/12/2021	13:26	52.9950648	5.9082576	10/12/2021	13:35	52.9831716	5.906542
E	0034	MBES	32	5	10/12/2021	16:30	52.805731	5.8407302	10/12/2021	16:50	52.805413	5.8260081
	0035	MBES		5	10/12/2021	16:55	52.805731	5.8407302	10/12/2021	17:05	52.8056275	5.8422789
	0036	MBES		5	10/12/2021	19:11	52.7891718	5.9409942	10/12/2021	19:35	52.8199345	5.8382396
	0037	MBES		5	10/12/2021	19:42	52.8192991	5.8339253	10/12/2021	20:04	52.7884521	5.8362814
	0038	MBES		5	10/12/2021	20:12	52.789786	5.8317244	10/12/2021	20:36	52.8216951	5.892502
	0039	MBES		5.5	10/12/2021	20:40	52.8214701	5.8312922	10/12/2021	21:01	52.7882959	5.8340667
	0040	MBES		5	10/12/2021	21:09	52.7883431	5.8299232	10/12/2021	21:30	52.8200498	5.8273186
	0041	MBES		5	10/12/2021	21:37	52.8192488	5.8253508	10/12/2021	21:57	52.7884472	5.827979
	0042	MBES		5	10/12/2021	22:02	52.7884943	5.8260712	10/12/2021	22:24	52.8195685	5.8234996
	0043	MBES		5.8	10/12/2021	22:29	52.8196634	5.8215551	10/12/2021	22:50	52.787425	5.8223059
	0044	MBES							10/12/2021	23:16	52.8196033	5.8196391
	0045	MBES		5.5	10/12/2021	23:23	52.8206288	5.8359629	10/12/2021	23:45		
	0046	MBES		5.5	10/12/2021	23:52	52.7878165	5.8199842	10/12/2021	23:58	52.7975229	5.8195151
	0047	MBES		5.5	10/12/2021	00:06	52.7978157	5.8153145	10/12/2021	00:13	52.7879929	5.8159786
	0048	MBES		5.6	10/12/2021	00:20	52.7873276	5.8179325	10/12/2021	00:40		
Fa	0049	MBES	18	5.3	11/12/2021	08:20	53.9842824	5.9064852	11/12/2021	08:58	52.9318638	5.8992223
	0050	MBES		5	11/12/2021	09:22	52.9318763	5.8971314	11/12/2021	10:02	52.9977402	5.906489
	0051	MBES		4.6/3	11/12/2021	10:10	52.9977308	5.9044974	11/12/2021	11:38	52.9321938	5.895111
	0052	MBES		6.8	11/12/2021	11:57	52.9330681	5.9073351	11/12/2021	12:07	52.9518499	5.9100665
	0053	MBES		5.7	11/12/2021	12:29	52.9470248	5.9131441	11/12/2021	12:36	52.948727	5.8903867
	0054	MBES		3.8	11/12/2021	12:49	52.9513254	5.8986034	11/12/2021	13:05	52.9315712	5.8958163

Fb	0055	MBES		5	11/12/2021	15:02	53.0732357	5.9220644	11/12/2021	15:35	53.027548	5.9050762
	0056	MBES		5.9	11/12/2021	15:42	53.0328477	5.9054705	11/12/2021	16:13	53.0749314	5.9211912
	0057	MBES		4.8	11/12/2021	16:18	53.0746459	5.9105158	11/12/2021	16:47	53.0294429	5.8935283
	0058	MBES		5	11/12/2021	16:56	53.0322	5.89456	11/12/2021	17:16	53.0563421	5.9023788
	0059	MBES		5	11/12/2021	17:02	53.0562891	5.9012271	11/12/2021	17:42	53.0308662	5.8922769
	0060	MBES		5	11/12/2021	17:47	53.0288683	5.8945822	11/12/2021	18:20	53.0760217	5.9121036
	0061	MBES		5	11/12/2021	18:25	53.0753319	5.9136935	11/12/2021	18:57	53.0290453	5.8962904
	0062	MBES		5	11/12/2021	19:01	53.0296388	5.8975932	11/12/2021	19:38	53.0758625	5.9147971
	0063	MBES		5	11/12/2021	19:44	53.0754139	5.9156558	11/12/2021	20:22	53.0282072	5.8979827
	0064	MBES	18	5	11/12/2021	20:31	53.0287842	5.899407	11/12/2021	21:07	53.075458	5.916784
	0065	MBES		5	11/12/2021	21:22	53.0610977	5.912347	11/12/2021	21:47	53.0283663	5.9001407
	0066	MBES		5.5	11/12/2021	21:56	53.028422	5.9010941	11/12/2021	22:29	53.0751503	5.9185233
	0067	MBES		5	12/12/2021	08:09	53.074932	5.9196651	12/12/2021	08:40	53.0284015	5.9023293
	0068	MBES		5.1	12/12/2021	08:47	53.0290648	5.8955446	12/12/2021	09:40	53.0759507	5.9130123
	0069	MBES		5.2	12/12/2021	09:31	53.0745916	5.917542	12/12/2021	09:44	53.0585554	5.9114121
	0070	MBES		5.2	12/12/2021	09:50	53.0620654	5.9112148	12/12/2021	10:01	53.0759037	5.9163368
	0071	MBES			12/12/2021	10:07	53.0762955	5.9104415	12/12/2021	10:23	53.0547175	5.9021371
	0072	MBES		5.2	12/12/2021	10:29	53.0549733	5.9015492	12/12/2021	10:46	53.0769832	5.9098053
	0073	MBES		5.1	12/12/2021	10:53	53.0769832	5.9098053	12/12/2021	11:13	53.0551671	5.9008576

II. MMO Forms

MARINE MAMMAL RECORDING FORM - COVER PAGE

Regulatory reference number (e.g. DECC no., MMS permit no., OCS lease no., etc.) CV21034	**Country** Ireland	**Ship/ platform name** RV Celtic Voyager
Client N/A	**Contractor** N/A	**Survey type** □ **site** □ 4C √ 2D □ VSP □ 3D □ WAZ □ 4D □ other □ OBC
Start date 05/12/2021	**End date** 06-12-2021	

Number of source vessels 1	**Type of source** (e.g. airguns) Sparker	**Number of airguns** (only if airguns used) N/A	**Source volume** (cu. in.) N/A
Source depth (metres) 70 m	**Frequency** (Hz)	**Intensity** (dB re. 1µPa or bar metres) 900 joules	**Shot point interval** (seconds)
Method of soft start □ increase number of guns □ increase pressure (where permitted) □ increase frequency (where permitted) □ **other**			

Visual monitoring equipment used (e.g. binoculars, big eyes, etc.) Binoculars	**Magnification of optical equipment** (e.g. binoculars) 7x50	**Height of eye** (metres) 1.8	**How was distance of animals estimated?** □ by eye □ with laser rangefinder □ with rangefinder stick/ calipers √ **with reticle binoculars** □ by relating to object at known distance □ other
Number of dedicated MMOs 1	**Training of MMOs** √ **JNCC approved MMO induction course for UK waters** □ PSO training course for the Gulf of Mexico □ MMO training course for Irish waters □ other □ none		

Was PAM used? □ yes √ **no**	**Number of PAM operators**	
Description of PAM equipment		
Range of PAM hydrophones from airguns (metres)	**Bearing of PAM hydrophones from airguns** (relative to direction of travel)	**Depth of PAM hydrophones** (metres)

MARINE MAMMAL RECORDING FORM - OPERATIONS

Regulatory reference number:
(e.g. DECC no., MMS permit no., OCS lease no., etc.)

Ship/platform name: RV Celtic Voyager

Complete this form every time the airguns are used, including overnight, whether for shooting a line or for testing or for any purpose.
Times should be in UTC, using the 24 hour clock.

Date	**Reason for firing** l = line t = test x = test followed immediately by line	**Time soft start/ ramp-up began**	**Time of full power**	**Time of start of line**	**Time of end of line**	**Time of reduced output** (if relevant)	**Time airguns/ source stopped**	**Time pre-shooting search began**	**Time search ended**	**Time PAM began**	**Time PAM ended**	Was it day or night in period prior to firing? d = day n = night w = dawn k = dusk	**Was any mitigating action required?** (yes/ no)
05/12/2021	x	12:20	13:00	13:40	14:05	N/A	N/A	11:50	12:20	N/A	N/A	d	No
05/12/2021	l			14:14	14:49	N/A	N/A			N/A	N/A	d	No
05/12/2021	l			14:57	16:15	N/A	N/A			N/A	N/A	d	No
05/12/2021	x			16:22	16:24	N/A	N/A			N/A	N/A	d	No
05/12/2021	l			16:24	17:45	N/A	N/A			N/A	N/A	k	No
05/12/2021	l			17:56	19:28	N/A	N/A			N/A	N/A	n	No
05/12/2021	l			19:45	20:52	N/A	N/A			N/A	N/A	n	No
05/12/2021	l			21:19	21:37	N/A	N/A			N/A	N/A	n	No
05/12/2021	l			21:58	23:17	N/A	N/A			N/A	N/A	n	No
06/12/2021	l			23:26	00:52	N/A	N/A			N/A	N/A	n	No
06/12/2021	l			01:00	02:26	N/A	N/A			N/A	N/A	n	No
06/12/2021	l			02:29	05:31	N/A	N/A			N/A	N/A	n	No
06/12/2021	l			05:31	06:17	N/A	N/A			N/A	N/A	n	No
06/12/2021	l			06:26	06:59	N/A	N/A			N/A	N/A	n	No
06/12/2021	l			07:29	07:46	N/A	N/A			N/A	N/A	n	No
06/12/2021	l			08:06	08:49	N/A	N/A			N/A	N/A	d	No
06/12/2021	l			08:56	09:29	N/A	N/A			N/A	N/A	d	No
06/12/2021	l			09:47	10:27	N/A	N/A			N/A	N/A	d	No
06/12/2021	l			10:42	13:51	N/A	N/A			N/A	N/A	d	No

MARINE MAMMAL RECORDING FORM - EFFORT

0

Regulatory reference number .
(e.g. DECC no., MMS permit no., OCS lease no., etc.)

Ship/ platform name RV Celtic Voyager

Please record the following for all watches, even if no marine mammals are seen.

Start a new line on form if any one of these changes

Date	Visual watch or PAM v = visual watch p = PAM	Observer's/ operator's name(s)	Time of start of watch (UTC, 24hr clock)	Time of end of watch (UTC, 24hr clock)	**Start position** (latitude and longitude)	**Depth at start** (m)	**End position** (latitude and longitude)	**Depth at end** (m)	**Speed of vessel** (knots)	**Source activity** f = full power s = soft start r = reduced power (not soft start) n = not active	**Wind direction**	**Wind force** (Beaufort scale)	**Sea state** g = glassy (like mirror) s = slight (no or few white caps) c = choppy (many white caps) r = rough (big waves, foam, spray) or Beaufort sea states (0 - 7+)	**Swell** o = low (< 2 m) m = medium (2-4 m) l = large (> 4 m)	**Visibility** **(visual watch only)** p = poor (< 1 km) m = moderate (1-5 km) g = good (> 5 km)	**Sunglare** **(visual watch only)** n = no glare w = weak glare s = strong glare v = variable
05/12/2021	√	Ruaihri Strachan	11:50	12:20	52.5267N 5.9683W	70	52.5265N 5.9833W	65	2	n	329	5	c	o	g	w
05/12/2021	√	Ruaihri Strachan	12:20	12:40	52.5265N 5.9833W	65	52.5135N 5.9728W	62	2	s	322	5	c	o	g	w
05/12/2021	√	Ruaihri Strachan	12:40	13:00	52.5135N 5.9728W	62	52.5774N 5.9258W	74	4	f	348	4	s	o	g	w

MARINE MAMMAL RECORDING FORM - SIGHTINGS

Regulatory reference number (e.g. DECC no., MMS permit no., OCS lease no., etc.) CV21034	**Ship/ platform name** RV Celtic Voyager	**Sighting number** 1	**Acoustic detection number** N/A
Date 05/12/2021		**Time at start of encounter** (UTC, 24hr clock) 12:47	**Time at end of encounter** (UTC, 24hr clock) 12:55

Were animals detected visually and/ or acoustically?	**How were the animals first detected?**
√ **visual** □ acoustic □ both	√ **visually detected by observer keeping a continuous watch** □ visually spotted incidentally by observer or someone else □ acoustically detected by PAM □ both visually and acoustically before operators/ observers informed each other

Observer's/ operator's name	**Position** (latitude and longitude)	**Water depth** (metres)
Ruaihri Strachan	52.5135N, 5.9727W	70 m

Species/ species group Common Seal		**Description** (include features such as overall size; shape of head; colour and pattern; size, shape and position of dorsal fin; height, direction and shape of blow) Smooth body, similar to a fender at surface, small whiskers, large eyes, dark grey/black in colour
Bearing to animal (when first seen or heard) 225°	**Range to animal** (when first seen or heard) (metres) 1m	

Total number 1	**Number of adults** (visual sightings only) 1	**Number of calves** (visual sightings only) N/A

Behaviour (visual sightings only)

Following vessel through wake for several minutes, coming to surface for air and to look around.

Direction of travel (relative to ship)		**Direction of travel** (compass points)	
□ towards ship	□ crossing ahead of ship	□ N	□ S
□ away from ship	□ variable	□ NE	□ SW
√ parallel to ship in same direction as ship	□ milling	□ E	□ W
□ travelling in opposite direction to ship	□ other	□ SE	□ NW
			√ variable

Airgun (or other source) activity when animals first detected	**Airgun (or other source) activity when animals last detected**	**Closest distance of animals from airguns (or other source)** (metres)	**Time of closest approach** (UTC, 24hr clock)
□ full power □ not firing	□ full power □ not firing	10 m	

<table>
<tr>
<td>√ soft start
□ reduced power (other than soft start)</td>
<td>√ soft start
□ reduced power (other than soft start)</td>
<td colspan="2">If seen during soft start give:

First distance Closest distance Last distance
50 m 10 m 50 m

during soft start (metres)</td>
</tr>
<tr>
<td colspan="2">What action was taken?

(according to requirements of guidelines/ regulations in country concerned)

√ none required
□ delay start of firing
□ shut-down of active source
□ power-down of active source
□ power-down then shut-down of active source</td>
<td>Length of power-down and/ or shut-down (if relevant) (length of time until subsequent soft start, in minutes)

N/A</td>
<td>Estimated loss of production (if relevant) due to mitigating actions (km)

N/A</td>
</tr>
</table>